frontiers

RESEARCH TOPICS

NEUROVASCULAR IMAGING

Hosted by
Anna Devor and David Boas

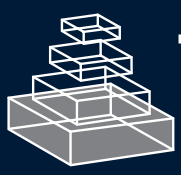

frontiers in
NEUROENERGETICS

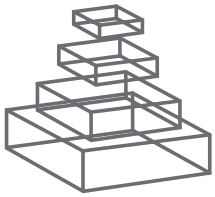

frontiers

Cover image provided by Ibbl sarl, Lausanne CH

ISSN 1664-8714
ISBN 978-2-88919-014-0
DOI 10.3389/978-2-88919-014-0

ABOUT FRONTIERS

Frontiers is more than just an open-access publisher of scholarly articles: it is a pioneering approach to the world of academia, radically improving the way scholarly research is managed. The grand vision of Frontiers is a world where all people have an equal opportunity to seek, share and generate knowledge. Frontiers provides immediate and permanent online open access to all its publications, but this alone is not enough to realize our grand goals.

FRONTIERS JOURNAL SERIES

The Frontiers Journal Series is a multi-tier and interdisciplinary set of open-access, online journals, promising a paradigm shift from the current review, selection and dissemination processes in academic publishing.
All Frontiers journals are driven by researchers for researchers; therefore, they constitute a service to the scholarly community. At the same time, the Frontiers Journal Series operates on a revolutionary invention, the tiered publishing system, initially addressing specific communities of scholars, and gradually climbing up to broader public understanding, thus serving the interests of the lay society, too.

DEDICATION TO QUALITY

Each Frontiers article is a landmark of the highest quality, thanks to genuinely collaborative interactions between authors and review editors, who include some of the world's best academicians. Research must be certified by peers before entering a stream of knowledge that may eventually reach the public - and shape society; therefore, Frontiers only applies the most rigorous and unbiased reviews.
Frontiers revolutionizes research publishing by freely delivering the most outstanding research, evaluated with no bias from both the academic and social point of view.
By applying the most advanced information technologies, Frontiers is catapulting scholarly publishing into a new generation.

WHAT ARE FRONTIERS RESEARCH TOPICS?

Frontiers Research Topics are very popular trademarks of the Frontiers Journals Series: they are collections of at least ten articles, all centered on a particular subject. With their unique mix of varied contributions from Original Research to Review Articles, Frontiers Research Topics unify the most influential researchers, the latest key findings and historical advances in a hot research area!
Find out more on how to host your own Frontiers Research Topic or contribute to one as an author by contacting the Frontiers Editorial Office: researchtopics@frontiersin.org

NEUROVASCULAR IMAGING

Hosted By
Anna Devor, University of California San Diego, USA
David Boas, Massachusetts General Hospital, USA; Massachusetts Institute of Technology, USA; Harvard Medical School, USA

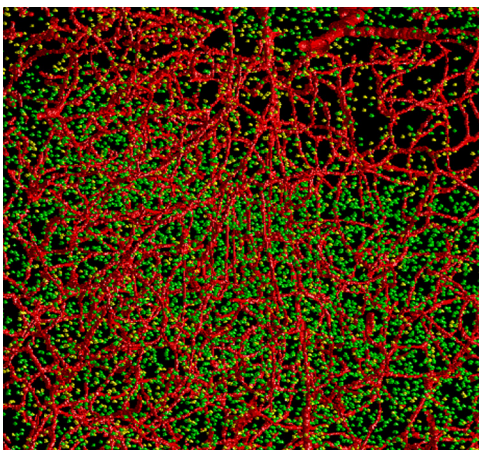

Recent technological advances are significantly enhancing ones ability to image the interplay of neuronal activity, metabolism, and the associated vascular response with high spatial and temporal resolution. This Research Topic will cover these recent technological advances as well as the impact they have had on understanding the coupling of neuronal, metabolic, and vascular responses.

We invite contributions to highlight new original research and to provide a forum for discussion of hot neurovascular topics. Potential contributions include, but are not limited by the following examples:

- Development and application of novel optical technologies for imaging of neuronal, metabolic and vascular activity. Examples include 2-Photon Microscopy, Optical Coherence Tomography, and Second Harmonic Microscopy.
- Intravital imaging of metabolites such as NADH and flavoproteins
- Application of optical methods for manipulation of neuroglial circuits and vascular architectonics
- Development of novel Magnetic Resonance contrasts for noninvasive imaging of blood flow, volume, and oxygen consumption.
- Application of imaging tools for studying of neurovascular dysfunctions such as stroke, vascular dementia and Alzheimer's Disease
- Hypotheses, Perspectives, Commentaries and Opinions with regards to the body of recent publications that utilize imaging tools for investigation of neurogliovascular communication and the regulation of cerebral blood flow

Table of Contents

frontiers in
NEUROENERGETICS

EDITORIAL
published: 18 January 2012
doi: 10.3389/fnene.2012.00001

Neurovascular imaging

***Anna Devor*[1]* and David Boas*[2]**

[1] *Neurovascular Imaging Laboratory, University of California San Diego, San Diego, CA, USA*
[2] *Martinos Center for Biomedical Imaging, Massachusetts General Hospital, Charlestown, MA, USA*
**Correspondence: adevor@ucsd.edu*

In this e-book we present a collection of papers submitted to *Frontiers in Neuroenergetics* in response to the "Special topic" initiative titled "Neurovascular Imaging." Advances in imaging technology, both optical and MRI based methods, traditionally have played (and continue playing) a major role in the advancement of neuroscience in general and in the understanding of cerebral blood flow and metabolism in particular. Therefore, our initial intent was to highlight the technological advances and impact they had on neurovascular/neurometabolic research, including description of the key biological results. However, it was the last aspect of our proposal – the biological results – that was met with the most overwhelming enthusiasm. Thus, while improvements of imaging technology are featured in the majority of the included articles, the main focus is on using those technological advances to better understand neurovascular and neurometabolic coupling.

So, what does it take to make significant progress in understanding of this coupling? First, as in every study in this e-book, it requires a team of investigators armed with state-of-the-art measurement tools and a novel ("transformative") approach, a.k.a. *imagination*. Second, one has to recognize the limitations of their measurement tools and consider the *measurement theory* – the relationship between the experimental "observables" and the underlying physiological parameters (Harris et al., 2010; Lindauer et al., 2010; Logothetis, 2010; Vanzetta and Slovin, 2010). For example, although BOLD fMRI measures deoxyhemoglobin, one has to consider both intra- and extravascular contributions to the signal and effects of vessel size, which vary as a function of the magnetic field of an MRI scanner. Likewise, one has to account for specific experimental conditions producing a biological behavior that might or might not translate to the intact brain situation (Filosa, 2010). Finally, merely the number of physiological parameters, which interact to produce a biological behavior, necessitates the use of computational modeling (Buxton, 2010). In particular, a solid theoretical framework is required to bridge between micro- and macroscopic levels of description – a critical step for translation of basic science observations in healthy brain (Cauli and Hamel, 2010; Hamilton et al., 2010; Saka et al., 2010; Sirotin and Das, 2010; Vazquez et al., 2010; Kleinfeld et al., 2011) and in experimental disorders (Luckl et al., 2010) to human studies (Koch et al., 2010; Lindauer et al., 2010; Obrig et al., 2010; Lin et al., 2011).

With the continuing development of optical (Akkin et al., 2010; Gregg et al., 2010; Hu and Wang, 2010; Srienc et al., 2010) and MRI (Harel et al., 2010; Hyder et al., 2010; Lin et al., 2011) imaging technology, and the steadily increasing availability of specific fluorescent and MR-visible indicators (Barros, 2010), our ability to probe the biological mechanisms underlying functional hyperemia is on a steep rise. Importantly, new methods allow not only measurement, but also well-controlled manipulations (Allegra Mascaro et al., 2010; Kleinfeld et al., 2011) crucial for testing causality rather than simply establishing a correlation between measurement parameters (that does not automatically imply that one of the parameters drives the other). Moreover, the present collection of papers reaches well beyond the current state of knowledge, defining important questions and roadmaps for future research (Buxton, 2010; Cauli and Hamel, 2010; Hamilton et al., 2010; Vazquez et al., 2010; Kleinfeld et al., 2011; Lin et al., 2011).

For us, *Neurovascular Imaging* is a lifetime-long affair that combines the magic of imaging ("seeing is believing") with the enigma of neurovascular communication waiting to be resolved, and the excitement of basic discovery with satisfaction of the usefulness/medical relevance of the results. We hope that the present collection of papers will be of particular encouragement for the young people in the field. The *Neurovascular Imaging* train is on a fast track toward genuine understanding of neurovascular and neurometabolic mechanisms with outstanding clinical importance.

REFERENCES

Akkin, T., Landowne, D., and Sivaprakasam, A. (2010). Detection of neural action potentials using optical coherence tomography: intensity and phase measurements with and without dyes. *Front. Neuroenergetics* 2:22. doi: 10.3389/fnene.2010.00022

Allegra Mascaro, A. L., Sacconi, L., and Pavone, F. S. (2010). Multi-photon nanosurgery in live brain. *Front. Neuroenergetics* 2:21. doi: 10.3389/fnene.2010.00021

Barros, L. F. (2010). Towards single-cell real-time imaging of energy metabolism in the brain. *Front. Neuroenergetics* 2:4. doi: 10.3389/fnene.2010.00004

Buxton, R. B. (2010). Interpreting oxygenation-based neuroimaging signals: the importance and the challenge of understanding brain oxygen metabolism. *Front. Neuroenergetics* 2:8. doi: 10.3389/fnene.2010.00008

Cauli, B., and Hamel, E. (2010). Revisiting the role of neurons in neurovascular coupling. *Front. Neuroenergetics* 2:9. doi: 10.3389/fnene.2010.00009

Filosa, J. A. (2010). Vascular tone and neurovascular coupling: considerations toward an improved in vitro model. *Front. Neuroenergetics* 2:16. doi: 10.3389/fnene.2010.00016

Gregg, N. M., White, B. R., Zeff, B. W., Berger, A. J., and Culver, J. P. (2010). Brain specificity of diffuse optical imaging: improvements from superficial signal regression and tomography. *Front. Neuroenergetics* 2:14. doi: 10.3389/fnene.2010.00014

Hamilton, N. B., Attwell, D., and Hall, C. N. (2010). Pericyte-mediated regulation of capillary diameter: a component of neurovascular coupling in health and disease. *Front. Neuroenergetics* 2:5. doi: 10.3389/fnene.2010.00005

Harel, N., Bolan, P. J., Turner, R., Ugurbil, K., and Yacoub, E. (2010). Recent advances in high-resolution mr application and its implications for neurovascular coupling research. *Front. Neuroenergetics* 2:130. doi: 10.3389/fnene.2010.00130

Harris, S., Jones, M., Zheng, Y., and Berwick, J. (2010). Does neural input or processing play a greater role in the magnitude of neuroimaging signals? *Front. Neuroenergetics* 2:15. doi: 10.3389/fnene.2010.00015

Hu, S., and Wang, L. V. (2010). Neurovascular photoacoustic tomography. *Front. Neuroenergetics* 2:10. doi: 10.3389/fnene.2010.00010

Hyder, F., Sanganahalli, B. G., Herman, P., Coman, D., Maandag, N. J., Behar, K. L., Blumenfeld, H., and Rothman, D. L. (2010). Neurovascular and neurometabolic couplings in dynamic calibrated fMRI: transient oxidative neuroenergetics for block-design and event-related paradigms. *Front. Neuroenergetics* 2:18. doi: 10.3389/fnene.2010.00018

Kleinfeld, D., Blinder, P., Drew, P. J., Driscoll, J. D., Muller, A., Tsai, P. S., and Shih, A. Y. (2011). A guide to delineate the logic of neurovascular signaling in the brain. *Front. Neuroenergetics* 3:1. doi: 10.3389/fnene.2011.00001

Koch, S. P., Habermehl, C., Mehnert, J., Schmitz, C. H., Holtze, S., Villringer, A., Steinbrink, J., and Obrig, H. (2010). High-resolution optical functional mapping of the human somatosensory cortex. *Front. Neuroenergetics* 2:12. doi: 10.3389/fnene.2010.00012

Lin, A. L., Gao, J. H., Duong, T. Q., and Fox, P. T. (2011). Functional neuroimaging: a physiological perspective. *Front. Neuroenergetics* 2:17. doi: 10.3389/fnene.2010.00017

Lindauer, U., Dirnagl, U., Fuchtemeier, M., Bottiger, C., Offenhauser, N., Leithner, C., and Royl, G. (2010). Pathophysiological interference with neurovascular coupling – when imaging based on hemoglobin might go blind. *Front. Neuroenergetics* 2:25. doi: 10.3389/fnene.2010.00025

Logothetis, N. K. (2010). Neurovascular uncoupling: much ado about nothing. *Front. Neuroenergetics* 2:2. doi: 10.3389/fnene.2010.00002

Luckl, J., Baker, W., Sun, Z. H., Durduran, T., Yodh, A. G., and Greenberg, J. H. (2010). The biological effect of contralateral forepaw stimulation in rat focal cerebral ischemia: a multispectral optical imaging study. *Front. Neuroenergetics* 2:19. doi: 10.3389/fnene.2010.00019

Obrig, H., Rossi, S., Telkemeyer, S., and Wartenburger, I. (2010). From acoustic segmentation to language processing: evidence from optical imaging. *Front. Neuroenergetics* 2:13. doi: 10.3389/fnene.2010.00013

Saka, M., Berwick, J., and Jones, M. (2010). Linear superposition of sensory-evoked and ongoing cortical hemodynamics. *Front. Neuroenergetics* 2:23. doi: 10.3389/fnene.2010.00023

Sirotin, Y. B., and Das, A. (2010). Spatial relationship between flavoprotein fluorescence and the hemodynamic response in the primary visual cortex of alert macaque monkeys. *Front. Neuroenergetics* 2:6. doi: 10.3389/fnene.2010.00006

Srienc, A. I., Kurth-Nelson, Z. L., and Newman, E. A. (2010). Imaging retinal blood flow with laser speckle flowmetry. *Front. Neuroenergetics* 2:128. doi: 10.3389/fnene.2010.00128

Vanzetta, I., and Slovin, H. (2010). A BOLD assumption. *Front. Neuroenergetics* 2:24. doi: 10.3389/fnene.2010.00024

Vazquez, A. L., Masamoto, K., Fukuda, M., and Kim, S. G. (2010). Cerebral oxygen delivery and consumption during evoked neural activity. *Front. Neuroenergetics* 2:11. doi: 10.3389/fnene.2010.00011

Received: 16 December 2011; accepted: 03 January 2012; published online: 18 January 2012. Citation: Devor A and Boas D (2012) Neurovascular imaging. Front. Neuroenerg. ***4****:1. doi: 10.3389/fnene.2012.00001*

frontiers in
NEUROENERGETICS

REVIEW ARTICLE
published: 17 June 2010
doi: 10.3389/fnene.2010.00008

Interpreting oxygenation-based neuroimaging signals: the importance and the challenge of understanding brain oxygen metabolism

Richard B. Buxton*

Center for Functional Magnetic Resonance Imaging, Department of Radiology, University of California, San Diego, La Jolla, CA, USA

Edited by:
Anna Devor, University of California, San Diego, USA

Reviewed by:
Richard Hoge, Université de Montréal, Canada
Daniel Bulte, University of Oxford, UK
Peter Jezzard, University of Oxford, UK

****Correspondence:***
Richard B. Buxton, Center for Functional Magnetic Resonance Imaging, Department of Radiology, University of California, San Diego, W. M. Keck Building, 9500 Gilman Drive, La Jolla, CA 92093-0677, USA.
e-mail: rbuxton@ucsd.edu

Functional magnetic resonance imaging is widely used to map patterns of brain activation based on blood oxygenation level dependent (BOLD) signal changes associated with changes in neural activity. However, because oxygenation changes depend on the relative changes in cerebral blood flow (CBF) and cerebral metabolic rate of oxygen ($CMRO_2$), a quantitative interpretation of BOLD signals, and also other functional neuroimaging signals related to blood or tissue oxygenation, is fundamentally limited until we better understand brain oxygen metabolism and how it is related to blood flow. However, the positive side of the complexity of oxygenation signals is that when combined with dynamic CBF measurements they potentially provide the best tool currently available for investigating the dynamics of $CMRO_2$. This review focuses on the problem of interpreting oxygenation-based signals, the challenges involved in measuring $CMRO_2$ in general, and what is needed to put oxygenation-based estimates of $CMRO_2$ on a firm foundation. The importance of developing a solid theoretical framework is emphasized, both as an essential tool for analyzing oxygenation-based multimodal measurements, and also potentially as a way to better understand the physiological phenomena themselves. The existing data, integrated within a simple theoretical framework of O_2 transport, suggests the hypothesis that an important functional role of the mismatch of CBF and $CMRO_2$ changes with neural activation is to prevent a fall of tissue pO_2. Future directions for better understanding brain oxygen metabolism are discussed.

Keywords: cerebral metabolic rate of oxygen, cerebral blood flow, functional magnetic resonance imaging, blood oxygenation level dependent, tissue oxygenation, positron emission tomography

INTRODUCTION

A brief neural stimulus produces a rapid and robust increase of cerebral blood flow (CBF), as illustrated in **Figure 1A**. Although this phenomenon is the basis for most current functional neuroimaging methods, it is still not clear what physiological function this serves. The CBF response is quite strong, with the fractional CBF change typically ~2–4 times larger than the associated fractional change in the cerebral metabolic rate of oxygen ($CMRO_2$). A useful way of describing this effect is that the oxygen extraction fraction (OEF) – the fraction of delivered oxygen that is extracted from the blood and metabolized – *decreases* with increased neural activity. This counterintuitive result, first reported by Fox and Raichle (1986), is surprising because at rest CBF and $CMRO_2$ appear to be tightly coupled, with a relatively uniform OEF across the brain despite a wide regional variation of blood flow (Gusnard and Raichle, 2001). Fortunately for the field of functional neuroimaging, the increase of local blood oxygenation with activation produces a small increase of the signal measured with functional magnetic resonance imaging (fMRI) because of the magnetic properties of deoxyhemoglobin, with higher deoxyhemoglobin levels tending to reduce the MR signal. Decreased deoxyhemoglobin due to the drop in OEF with activation then leads to an increase of the MR signal, the blood oxygenation level dependent (BOLD) response (Kwong et al., 1992; Ogawa et al., 1992; Buxton, 2009) (**Figure 1B**). Other techniques, including optical methods (Dunn et al., 2005; Grant et al., 2009; Roche-Labarbe et al., 2010) and tissue oxygenation measurements in animal studies (Caesar et al., 2008; Piilgaard and Lauritzen, 2009; Thomsen et al., 2009), also exploit the change in blood or tissue oxygenation due to the mismatch of CBF and $CMRO_2$ changes as a biomarker of altered neural activity.

Because oxygenation changes depend on the relative changes in CBF and $CMRO_2$, a quantitative interpretation of BOLD signals, and also other functional neuroimaging signals related to blood or tissue oxygenation, is fundamentally limited until we better understand brain oxygen metabolism and how it is related to blood flow. While there has been a large research effort focused on the links between neural activity and blood flow, our understanding of oxygen metabolism changes is limited by the intrinsic difficulty of measuring $CMRO_2$. However, the complexity of oxygenation signals also has a positive side: the fact that oxygenation signals are sensitive to both CBF and $CMRO_2$ changes offers the possibility of estimating $CMRO_2$ changes when these measurements are combined with additional measurements of CBF. In fact, a quantitative interpretation of oxygenation-based signals offers the best hope we have for measuring dynamic changes in $CMRO_2$ (Herman et al., 2009). This is intrinsically a multimodal imaging approach, and a key required element to make it work is a theoretical framework that accurately relates our measured signals to the underlying physiology.

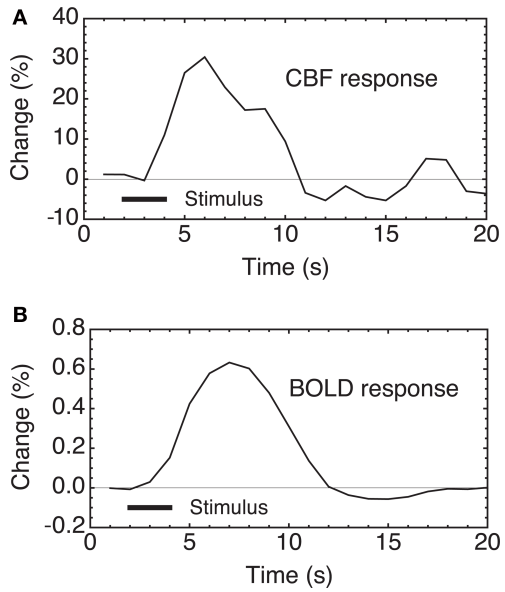

FIGURE 1 | CBF and BOLD responses to a brief stimulus in human subjects. (A) Two seconds of finger tapping evoke a strong CBF change in primary motor cortex, measured here with an arterial spin labeling (ASL) MRI method. **(B)** The CBF change is accompanied by a local increase in blood oxygenation, giving rise to the BOLD response measured with fMRI. Because of the nature of the measurements, BOLD-fMRI has intrinsically higher sensitivity than ASL, despite the small magnitude of the signal changes. Data from Miller et al. (2001).

This review focuses on the problem of interpreting oxygenation-based signals, the challenges involved in measuring $CMRO_2$ in general, and what is needed to put oxygenation-based estimates of $CMRO_2$ on a firm foundation. The importance of developing a solid theoretical framework is emphasized, both as an essential tool for analyzing oxygenation-based multimodal measurements, and also potentially as a way to better understand the physiological phenomenon that lies at the heart of BOLD-fMRI: the mismatch of CBF and $CMRO_2$ changes with activation.

THE PROBLEM: CAN WE INTERPRET OXYGENATION-BASED SIGNALS AS A QUANTITATIVE REFLECTION OF PHYSIOLOGICAL ACTIVITY?

Functional MRI based on mapping the BOLD response has developed into a widely used and sensitive tool for mapping patterns of activation in the human brain. Sophisticated statistical methods have been developed to identify significant signal changes associated with a stimulus, and these detected changes are taken as evidence for a change in neural activity at that location (with the caveat that the changes in deoxyhemoglobin may be dominated by downstream venous vessels that could be displaced from the precise site of neural activity change). This robust mapping approach addresses the basic question: where does activity occur? However, an important challenge facing functional neuroimaging is to move beyond mapping to meaningfully address the question of quantifying the activity change. This is a distinctly different, and much harder, problem than simply identifying where a change has occurred.

The key question is: does the magnitude of the BOLD response quantitatively reflect the magnitude of the underlying physiological changes? There are two primary effects that could alter the BOLD signal even for the same underlying change in neural activity: the baseline CBF state, and the coupling of CBF and $CMRO_2$ changes. The BOLD response has a ceiling, corresponding to complete removal of deoxyhemoglobin, and so the amount of deoxyhemoglobin present in the baseline state sets the possible dynamic range for the BOLD response (Brown et al., 2003). This baseline effect could be an important confounding factor when studying disease populations, where the baseline CBF and $CMRO_2$ may be altered by medications or by chronic aspects of the disease process itself (Fleisher et al., 2009). The second effect, that has received less attention to date, is that the BOLD response is sensitive to the exact coupling of CBF and $CMRO_2$ (Ances et al., 2008; Herman et al., 2009). That is, methods sensitive to blood or tissue oxygenation depend on the *relative balance* of the changes in CBF and $CMRO_2$. Increased neural activity drives increases in both blood flow and oxygen metabolism, but these physiological changes drive blood oxygenation in opposite directions.

The magnitude of the BOLD response thus depends on the CBF/$CMRO_2$ coupling ratio n, defined as the ratio of the fractional change in CBF to the fractional change in $CMRO_2$ for a given stimulus. This would not be a problem for interpreting the BOLD response if n is fixed. For example, a simple picture would be that increased neural activity requires increased energy metabolism, and the increased $CMRO_2$ then drives an increase in CBF in a fixed ratio. However, a large body of evidence supports an alternative view that aspects of neural signaling, such as neurotransmitter release, nitric oxide (NO) generation, extracellular potassium changes, and activation of arachidonic acid pathways, can either dilate or constrict the blood vessels (Attwell and Iadecola, 2002; Hamel, 2006). In particular, the astrocytes, with processes projecting to both neuronal synapses and blood vessels, are thought to play a key role in detecting synaptic activity and modulating blood flow (Iadecola and Nedergaard, 2007; Koehler et al., 2009). In short, it is likely that the rapid control of CBF is driven by fast feed-forward mechanisms related to the neural activity itself, rather than feedback mechanisms related to energy metabolism. In other words, it appears that CBF and $CMRO_2$ changes are driven in parallel by neural activity.

This raises the critical question: which aspects of neural activity drive $CMRO_2$, which drive CBF, and are they always in the same ratio? The energy cost of neural activity is primarily in restoring ionic gradients following neural signaling, fueled by increased ATP consumption, and the ATP is replenished by the oxidative metabolism of glucose (Attwell and Laughlin, 2001). The focus here is on O_2 metabolism, because $CMRO_2$ is the relevant metabolic rate that combines with CBF to alter blood and tissue oxygenation. Clearly, though, $CMRO_2$ requires glucose metabolism, because glucose is the substrate that is oxidized. Positron emission tomography (PET) studies typically find that the fractional change of the cerebral metabolic rate of glucose (CMRGlc) more closely follows the fractional CBF change and is larger than the fractional $CMRO_2$ change (Fox et al., 1988). However, the link between CBF and CMRGlc is not tight, in that CMRGlc changes occur even when the CBF response is blocked (Cholet et al., 1997), and a recent study found

an uncoupling of CBF and CMRGlc related to inhibition (Devor et al., 2008). A larger fractional change in CMRGlc compared to $CMRO_2$ suggests that there is some degree of *aerobic glycolysis* and a corresponding generation of lactate despite an abundance of available oxygen (Prichard et al., 1991). The term aerobic glycolysis emphasizes the distinction to *anaerobic* glycolysis, in which reduced O_2 availability prevents oxidative metabolism of the pyruvate created by glycolysis, and the pyruvate is subsequently converted to lactate. When oxygen is not available, glycolysis can provide a source of ATP. However, glycolysis alone generates less than 1/15 of the ATP generated by full oxidative metabolism, so the additional ATP generated by the aerobic glycolysis in the well-oxygenated healthy brain is a small fraction of the increased ATP generated by the smaller increase of oxidative metabolism. It is still unclear how aerobic glycolysis fits into the metabolic side of neural activation (Paulson et al., 2010), particularly because the contribution to energy metabolism is small. The rest of this review focuses on $CMRO_2$, with the assumption that it is not limited by the availability of glucose.

It is likely that $CMRO_2$ simply responds as needed to match ATP production to ATP consumption, so that the increase of $CMRO_2$ reflects the overall energy cost of the evoked neural activity. In contrast, if the CBF response is driven by feed-forward mechanisms related to the neural signaling itself, this opens the possibility that the coupling index n is not fixed. As discussed below, a number of studies suggest that n varies regionally and even within the same region as the stimulus changes. Typical values are in the range $n \sim 2$–4, and unfortunately this is a range in which the BOLD response magnitude is expected to be sensitive to the exact value of n. For example, theoretical calculations indicate that for the same $CMRO_2$ change (and by assumption the same overall evoked neural activity), the BOLD response magnitude differs by 100% for $n = 2$ compared with $n = 3$ (Ances et al., 2008).

THE CHALLENGING TASK OF MEASURING $CMRO_2$

MEASURING $CMRO_2$ WITH LABELED OXYGEN

In contrast to $CMRO_2$, there are relatively direct and robust ways to measure CBF and CMRGlc. For these measurements, techniques have been developed in which a single agent is injected, allowed to distribute through the brain, and a single measurement of the concentration of the agent then provides a direct measure of the appropriate physiological quantity (CBF or CMRGlc). The accepted standard for CBF measurements is a microsphere experiment, in which labeled microspheres are injected arterially. Because the microspheres are too large to pass through the capillaries, they stick in the tissue, and the local concentration of microspheres then directly reflects the local CBF. With an appropriate measurement of the injected arterial bolus, the local CBF can be quantified in absolute units of ml blood/ml tissue/min. While microspheres are not used in human subjects, microsphere techniques provide the classic "gold standard" for validating other methods for measuring CBF. For human studies with MRI, pulsed arterial spin labeling (ASL) methods approach the ideal microsphere experiment because the delivery of magnetically labeled blood is measured only ~1.5 s after creation of the labeled blood in the arteries, so there is little time for the labeled blood to pass through the capillary bed and clear from tissue (Buxton, 2005).

For measuring CMRGlc there is also an accepted standard based on injection of radioactively labeled deoxyglucose, a chemically modified form of glucose (Sokoloff et al., 1977; Phelps et al., 1981). Deoxyglucose is taken up from the blood like glucose and binds to the enzyme hexokinase, the first step in the glycolysis pathway. However, because of the structural difference between glucose and deoxyglucose, the latter cannot proceed to the later stages of glycolysis, and essentially sticks in the tissue. By waiting sufficiently long for unmetabolized deoxyglucose to diffuse back into blood and clear from the tissue, the remaining radioactive label in tissue directly reflects the local rate of metabolism of deoxyglucose, and can be quantified by also measuring the arterial concentration curve of the agent during delivery. This approach is applied in humans with PET using deoxyglucose labeled with ^{18}F, a positron emitting radionuclide. As with microspheres for CBF measurement, the reason this technique works so well is that a single measurement of the tissue concentration of the agent directly reflects the metabolic rate.

Oxygen dynamics in the tissue can be measured by injecting labeled O_2, either with ^{15}O for PET detection (Mintun et al., 1984) or ^{17}O for NMR detection (Arai et al., 1990, 1991; Fiat and Kang, 1992, 1993). However, deriving $CMRO_2$ from such measurements is surprisingly difficult. The essential problem is that one cannot tell whether the detected oxygen nucleus is in O_2, and thus not metabolized, or in water, and thus metabolized. Imagine measuring tissue concentration as a function of time during and following an injection of labeled O_2. Initially, the labeled oxygen nucleus detected in the tissue will be in the form O_2. Because the solubility of O_2 in extravascular tissue is very low compared to blood due to hemoglobin binding, most of the labeled oxygen is in the blood compartment of the tissue, so that cerebral blood volume (CBV) strongly affects the measured concentration of labeled oxygen. Over time some of the initially delivered O_2 will diffuse back to the blood without being metabolized and clear from the tissue. Another component will enter the mitochondria and be converted to water by oxygen metabolism. The labeled water will eventually diffuse to the blood and clear from the tissue. However, as blood continues to circulate the labeled water will be delivered back to the tissue, at a rate that depends on CBF, so that now the labeled oxygen enters as water as well as O_2. In short, the kinetics of the labeled oxygen nucleus depends strongly on CBF and blood volume in addition to $CMRO_2$, and there is no point in time when the tissue concentration cleanly reflects $CMRO_2$ alone.

For this reason, the current standard method for measuring $CMRO_2$ with PET requires three separate measurements following injection of ^{15}O labeled O_2, water, and carbon monoxide (for blood volume measurement), and analysis of the dynamic tissue concentration curves within a theoretical framework that accounts for the combined effects of $CMRO_2$, CBF and CBV on the observed tracer kinetics (Mintun et al., 1984). In addition, temporal sampling of arterial blood is needed to measure the arterial time course of labeled O_2 and labeled water. Even with these combined measurements it is still necessary to assume that there is no back flux of unmetabolized O_2 from tissue to blood, specifically that all the O_2 that leaves the capillary is metabolized. For both PET and NMR studies a number of ideas have been proposed for simplifying these measurements, but each of these is sensitive to particular

assumptions of the model (Ohta et al., 1992; Zhu et al., 2002, 2005, 2006; Ibaraki et al., 2004; Zhang et al., 2004; Kudomi et al., 2007, 2009). In short, the complexity of these studies reflects the intrinsic difficulty of measuring local O_2 metabolism, and emphasizes the need for an accurate theoretical framework to integrate the different measurements. Furthermore, as with all studies using injected tracers, the assumption is that the physiology is in a steady-state throughout the measurement so that the observed dynamics of the agent reflect the dynamics of the injected bolus and its transport to tissue. For this reason the measurements of $CMRO_2$ are necessarily steady-state rather than dynamic. Despite the complexities of the technique, PET measurement of $CMRO_2$ is now being done at a number of institutions, although usually as a baseline measurement in different clinical conditions. Applications looking at brain activation in healthy subjects are less common (Mintun et al., 2002).

Another NMR approach for measuring $CMRO_2$ exploits a particular magnetic property of ^{17}O: when incorporated into a water molecule, it acts as a relaxation agent, altering the relaxation times of hydrogen nuclei. Furthermore, this effect can be modulated by applying a radiofrequency pulse at the ^{17}O resonance frequency (Ronen and Navon, 1994; Ronen et al., 1997, 1998). In this way the presence of ^{17}O labeled water can be detected with standard proton MRI as a change in relaxation rate. However, when the ^{17}O is incorporated into an O_2 molecule it does not have this relaxation property. This creates the interesting scenario in which ^{17}O inhaled as O_2 is not visible with standard proton MRI until the ^{17}O has been incorporated into water by O_2 metabolism in the mitochondria. The rate of appearance of labeled water is then proportional to local $CMRO_2$. To quantify this, however, requires additional measurement of the arterial input function (concentration of the label in arterial blood), and accounting for recirculation of the labeled water. Despite early interest in this approach, it has not been widely used to date due to the complexity involved in addressing these issues (similar to issues in the PET studies described earlier), combined with the high cost of ^{17}O, although a recent study has extended the method to larger animals (Mellon et al., 2009).

MEASURING $CMRO_2$ FROM BLOOD OR TISSUE OXYGENATION

The alternative to the more classical tracer kinetics approaches described above is to use blood or tissue oxygenation in combination with a measurement of CBF to estimate a change in $CMRO_2$. This section focuses on the calibrated-BOLD approach, the primary method used in human studies, and tissue pO_2 measurements used in animal studies. These two approaches are primarily sensitive to changes in $CMRO_2$. Although these methods are not as sensitive to the baseline $CMRO_2$ value, they provide the best opportunity available to measure the dynamics of $CMRO_2$.

Before discussing these methods, though, it is important to note briefly that two recent alternative MRI approaches have been proposed that potentially could provide estimates of baseline absolute $CMRO_2$. Both focus on the question of estimating the venous oxygenation through its effect on the transverse relaxation rate R_2. With TRUST, the signal in a draining vein such as the sagittal sinus is isolated with an approach similar to ASL, and the transverse relaxation rate R_2 is measured (Lu and Ge, 2008; Xu et al., 2009). From calibration studies in blood samples, R_2 varies with O_2 saturation. Combining this estimate of venous O_2 concentration with a separate measurement of CBF then provides an estimate of baseline $CMRO_2$. When this measurement is done in the sagittal sinus the result is a whole-brain $CMRO_2$ estimate, but if this technique can be adapted for regional measurements it will provide important information on the distribution of baseline $CMRO_2$. Even as a whole-brain measurement, baseline venous oxygenation can account for a significant amount of the variance of the BOLD response between subjects (Lu et al., 2010). The second method exploits a detailed model of how R_2 changes with time as the MR signal decays, with the essential assumption that the additional signal decay in a gradient echo measurement compared with a spin echo measurement is entirely due to the effects of deoxyhemoglobin (Yablonskiy and Haacke, 1994; He and Yablonskiy, 2007; He et al., 2008). With additional assumptions about properties of the tissue compartments, this approach gave estimates of baseline O_2 extraction fraction that are in good agreement with PET measurements. As these methods mature they may provide an important complement to the dynamic methods discussed below by providing the link between fractional and absolute changes in $CMRO_2$.

An essential component of BOLD and tissue pO_2 methods is a theoretical framework that accurately relates CBF and $CMRO_2$ changes to the measured oxygenation signal. Modeling these physiological variables, in terms of how they relate to each other and in terms of how they relate to the imaging signals, is an active area of research (Valabregue et al., 2003; Buxton et al., 2004; Gjedde, 2005a,b; Huppert et al., 2007, 2009; Uludag et al., 2009; Zheng et al., 2010). To clarify how such a theoretical framework can be used to estimate $CMRO_2$ changes, we focus here on the simple theoretical framework defined in **Table 1**, which relates, CBF, $CMRO_2$, the BOLD signal, and tissue pO_2. In this framework, changes in CBF and $CMRO_2$ are related to the BOLD response by Eqs 1,2, and to the tissue pO_2 response by Eqs 1, 3, and 4. In this framework, Eq. 1 is the most solid, essentially just reflecting mass balance. The product of flow and arterial O_2 concentration is the rate of delivery of O_2 to the capillary bed, and multiplying by the fraction of delivered O_2 that is metabolized gives $CMRO_2$. The remaining equations, however, represent specific models.

Modeling the BOLD response

Equation 2 is a model for the BOLD response proposed by Davis et al. (1998), based on physical reasoning and Monte Carlo simulations. This is a simple model of a complex phenomenon, and yet this model has proven to be more robust than one might have thought given the restrictive assumptions that went into its derivation. Although originally derived just from consideration of extravascular signal changes, it captures the basic behavior of more detailed models that include additional effects (discussed below). The model reflects the primary dependence of the BOLD signal on changes in the O_2 extraction fraction, but also includes an additional term in f that is intended to model the effect of blood volume changes on the BOLD signal as a power law relation with CBF, with an empirical exponent $\alpha = 0.4$ (Grubb et al., 1974). The role of blood volume changes in modulating the observed BOLD response is somewhat subtle, and we still do not have a satisfactory understanding. In principle, blood volume changes could influence the BOLD response by changing the local total deoxyhemoglobin in tissue independently of a change in blood oxygenation. That is, blood oxygenation determines the

Table 1 | Simple theoretical framework for estimating $CMRO_2$ from multimodal measurements.

Theoretical Framework

VARIABLES

f = CBF normalized to baseline

r = $CMRO_2$ normalized to baseline

s = BOLD signal normalized to baseline

E = O_2 extraction fraction

p_C = mean blood pO_2 (mmHg)

p_T = mean tissue pO_2 (mmHg)

REQUIRED BASELINE PARAMETERS (TYPICAL VALUES)

E_0 = 0.4

p_{T0} = 25 mmHg

MODEL PARAMETERS

α = 0.4 (blood volume effects)

β = 1.5 (intravascular signal changes, diffusion)

M = local scaling factor, determined by calibration

p_{50} = 26 mmHg (O_2-hemoglobin 50% saturation)

h = 2.8 (Hill exponent)

MODEL EQUATIONS

(1) Mass balance:

$$r = \frac{E}{E_0} f$$

(2) BOLD signal (Davis et al., 1998):

$$s = M\left[1 - f^{\alpha}\left(\frac{E}{E_0}\right)^{\beta}\right]$$

(3) Blood/tissue O_2 gradient:

$$r = \frac{p_C - p_T}{p_{C0} - p_{T0}}$$

(4) Mean blood pO_2 (Gjedde, 2005a,b):

$$p_C = p_{50}\left[\frac{2}{E} - 1\right]^{1/h}$$

The equations describe: (1) Mass balance for O_2, expressed in terms of variables normalized to their baseline values; (2) Davis model for the BOLD signal, with the parameter α describing effects of blood volume changes, and β approximating differential diffusion effects around large and small vessels estimated from Monte Carlo simulations; (3) Assumption that the tissue/blood pO_2 gradient increases to match a change in $CMRO_2$, and that this gradient is determined solely by the difference of the mean O_2 concentrations in blood and tissue (no capillary recruitment); and (4) Expression for mean blood pO_2 assuming the Hill equation for the O_2-hemoglobin saturation curve, with exponent h and half-saturation at a pO_2 of p_{50}, and assuming that the pO_2 corresponding to half of the total extracted O_2 is the mean value for blood.

deoxyhemoglobin concentration in blood, but total deoxyhemoglobin also depends on the volume of the blood compartments that contain partially deoxygenated blood. This is usually thought of as "venous" blood, but really also includes capillary and to some extent arteriolar blood, because it is thought that arteriolar blood is already slightly deoxygenated. Blood volume changes also can affect the measured BOLD response by a pure exchange of volumes, an effect that is not related to blood oxygenation. For example, a blood volume increase on the arterial side should have little effect on total deoxyhemoglobin, but if the increased blood volume occurs at the expense of a reduced extravascular volume, then the measured signal could change due to an intrinsic signal difference between the blood and the extravascular material that is displaced. This basic effect of a signal difference due to an exchange of one volume for another carrying a different signal is amplified in the VASO technique for measuring blood volume changes, by nulling the magnetization of blood to increase the intrinsic signal difference between the intravascular and extravascular spaces (Lu et al., 2003), although the full mechanisms of signal change with VASO are likely more complicated (Donahue et al., 2006, 2009). Although this effect is much weaker in the BOLD response, it is good to remember that the BOLD response is not purely oxygenation-dependent.

The BOLD signal model in Eq. 2 contains two additional parameters, β and M. The exponent β was derived from Monte Carlo simulations of spins diffusing around magnetized cylinders (Boxerman et al., 1995b), and essentially captures the idea that the same amount of deoxyhemoglobin has less of an effect on the BOLD signal change when it is in capillaries compared to when it is in larger veins (Ogawa et al., 1993). The source of this effect is the random movement of water molecules due to diffusion. It happens that the magnitude of motion of a water molecule during an experiment is comparable to the diameter of a capillary, so near the smallest vessels each molecule will sample a range of field offsets. Because all the water molecules are essentially sampling the same range of field offsets, the net phase dispersion when the net signal is measured is not as great as it would be if the molecules had not moved around. The net phase dispersion translates directly into the measured signal change, so the signal change is larger around larger vessels, where diffusion is less important because of the larger spatial scale of the field offsets. From numerical simulations, $\beta = 1.5$ approximately captures these effects for 1.5 T, decreasing to a value near 1 at high fields. Although this simple model ignores several effects, such as intravascular signal changes (Boxerman et al., 1995a) and volume exchange effects, it agrees reasonably well with models that explicitly include these effects (Buxton et al., 1998, 2004; Obata et al., 2004; Leontiev et al., 2007).

The parameter M is an overall scaling factor that essentially depends on the amount of deoxyhemoglobin present in the baseline state, as well as details of the image acquisition method such as the field strength and echo time (Davis et al., 1998; Buxton et al., 2004). This parameter sets the maximum possible BOLD signal amplitude for that region of brain, corresponding to complete removal of deoxyhemoglobin. That is, it is important to remember that the BOLD response has a ceiling, and that ceiling is reflected in M. Unlike the parameters α and β, which are usually assumed to be constant, the parameter M must be measured for each brain location for the particular experimental acquisition. This is done in the *calibrated-BOLD* approach introduced by Davis et al. (1998) by also measuring the BOLD and CBF responses to breathing CO_2. The CBF response is measured with an ASL technique (Detre et al., 1992; Wong et al., 1997) and the essential idea is to exploit the fact that the ASL signal depends just on CBF changes, while the BOLD signal depends on CBF and $CMRO_2$ changes. Mild hypercapnia is thought to produce a large change in CBF without changing $CMRO_2$ (Sicard and Duong, 2005) (although there is still some controversy about this assumption; Zappe et al., 2008), and Eq. 2 is used to calculate M for a particular brain region with the assumption that $r = 1$. With M estimated, the measured CBF and BOLD responses to stimulus activation are used with Eq. 2 to derive an estimate of r, the fractional change in $CMRO_2$.

A useful way to look at the role played by the BOLD model is that it allows us to draw contours of equal BOLD response in a plane defined by the fractional $CMRO_2$ change on the *x*-axis and the fractional CBF change on the *y*-axis. **Figure 2A** shows an example for $M = 0.08$ (i.e., an 8% ceiling on the BOLD response magnitude). If the value of M is not known, these contours would reflect equal but unknown increments of the BOLD response. Note that the non-linearity of the BOLD signal model primarily affects the spacing of the contour lines, while each contour is reasonably linear. If we are willing to assume that Eq. 2 holds for dynamic as well as steady-state changes (more on this question below), a hypothetical trajectory of CBF and $CMRO_2$ responses to a brief stimulus can be plotted in this plane along with the resulting BOLD response. An example is shown in **Figure 2**. Both CBF and $CMRO_2$ are assumed to exhibit a smoothed response, with two features added to illustrate how transients of the BOLD response could occur. The first feature is that the $CMRO_2$ response has a slightly faster rise time than the CBF response, producing an initial dip of the BOLD response. The second feature is a slight undershoot of the CBF response after the stimulus before it returns to baseline, producing a more pronounced undershoot of the BOLD response. This is just a simulated example, but it illustrates that the modeling framework predicts that relatively subtle differences in the CBF and $CMRO_2$ responses can produce transient features of the BOLD response that are similar to those that often have been reported (Perthen et al., 2008).

Modeling tissue pO_2 changes

In addition to signals related to blood oxygenation there is growing interest in using signals related to tissue oxygenation in animal models, including traditional microelectrode methods as well as newer methods (Ndubuizu and LaManna, 2007). Interestingly, though, blood and tissue oxygenation signals are not equivalent, and the theoretical framework helps to clarify the differences. The simple theoretical framework for interpreting tissue pO_2 shown in **Table 1** is adapted from the work of Gjedde (2005a), although framed in a slightly different way (discussed below). The model is based on three key assumptions: (1) With increased activity there is no capillary recruitment, so the vascular geometry stays the same. Increased $CMRO_2$ requires an increased gradient of O_2 concentration between

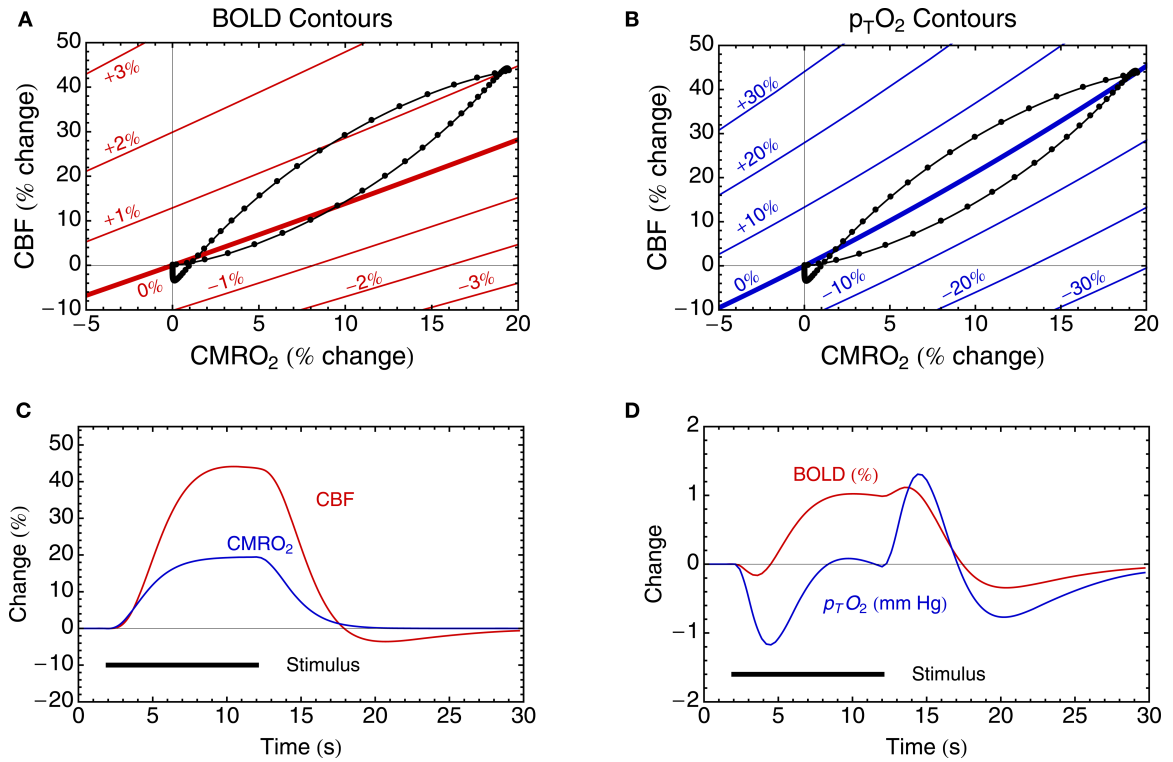

FIGURE 2 | Theoretical curves derived from the theoretical framework in Table 1. (A) Equations 1 and 2 define contours (in red) of equal BOLD signal change in the CBF/$CMRO_2$ plane, here illustrated for $M = 8\%$. The contour of zero BOLD response has a slope slightly greater than 1 because of the way blood volume effects are included. **(B)** Equations 1, 3, and 4 define contours (in blue) of equal tissue pO_2 change, calculated with the assumption that at baseline $p_TO_2 = 25$ mmHg. **(C)** Hypothetical CBF and $CMRO_2$ responses to a simple stimulus are shown. These two responses define a trajectory in the CBF/$CMRO_2$ plane, shown in (**A,B**) as the black curve. The points on the curve represent equal time increments in the evolving CBF and $CMRO_2$ curves in **(C)**. **(D)** The resulting BOLD and tissue pO_2 responses are shown for the CBF and $CMRO_2$ responses in **(C)**. Note that in this example the CBF and $CMRO_2$ responses are approximately in the ratio 2:1 (i.e., $n \sim 2$), and this causes the trajectory to pass over and under the zero change contour of p_TO_2, leading to the complex dynamics in **(D)**. In addition, the CBF response was constructed with a weak post-stimulus undershoot to illustrate that this can create a more pronounced undershoot in the BOLD signal. In this example the ratio of the undershoot to the peak response is only ~8% for CBF, but ~30% for the BOLD response.

blood and tissue, and if the vessel geometry is fixed this increased gradient must be due to an increased difference between blood and tissue pO_2 values, leading to Eq. 3. (2) The O_2 saturation Y of hemoglobin as a function of pO_2 is described by the Hill equation with exponent h and half-saturation value p_{50}, the pO_2 at which hemoglobin is 50% saturated: $Y = 1/[1 + (p_{50}/pO_2)^h]$. The values for h and p_{50} for human blood in **Table 1** are taken from Mintun et al. (2001), but Gjedde (2005a) has suggested using higher values of $p_{50} = 35$ mmHg and $h = 3.5$ to approximate the Bohr effect. (3) The mean blood pO_2 driving diffusion into the tissue is the value derived from the Hill equation when the total O_2 concentration is halfway to the full extraction fraction from the blood given by E. Equations 1, 3, and 4 effectively provide two relationships between the four physiological variables CBF, $CMRO_2$, E and tissue pO_2. In this way measuring any two of these variables allows one to calculate the remaining two from the equations. Specifically, measuring tissue pO_2 and CBF allows calculation of $CMRO_2$ and E.

At first glance the formulation in **Table 1** may seem surprising, because it does not include any of the microscopic parameters that are usually introduced in analyzing O_2 diffusion into tissue (Gjedde, 2005a; Caesar et al., 2008). For example, the classic Krogh cylinder model is framed in terms of parameters such as the O_2 diffusion constant, capillary radius and capillary spacing (Mintun et al., 2001). Instead, the goal here was to define the framework in terms of macroscopic variables, with introduction of as few microscopic variables as possible, because the microscopic parameters may not be well known. For example, the exact value of the O_2 diffusivity does not enter the equations because it is assumed to be constant and effectively cancels out from Eq. 3. Instead of referencing the model parameters to microscopic parameters, the model is anchored by specifying baseline values of the macroscopic variables. In this case, one must specify E and tissue pO_2 in the baseline state, and combined with Eq. 3 this gives the baseline mean blood pO_2. The key difference between the current formulation, and the previous formulation used to interpret pO_2 measurements (Caesar et al., 2008; Piilgaard and Lauritzen, 2009; Thomsen et al., 2009), is that this approach allows one to relate *fractional changes* in $CMRO_2$ to pO_2 without assuming values for microscopic variables, while the previous formulation focused on relating pO_2 to *absolute* $CMRO_2$, which requires accurate knowledge of microscopic O_2 diffusivity.

In short, the formulation in **Table 1** exploits the general phenomenon of levels of description: not all of the variables that need to be specified in a microscopic modeling framework will carry through to affect macroscopic parameters. By anchoring the model to assumptions about the baseline values of the macroscopic parameters we essentially fine-tune the relevant microscopic parameters to produce that baseline state, without ever introducing those microscopic parameters explicitly. Importantly, this approach also effectively allows the model to be adjusted to the human brain without having to assume that microscopic parameters measured in animal models carry through precisely to humans. In this case, there are a number of PET measurements of E in human subjects that suggest a baseline value of 0.4 is reasonable. For baseline tissue pO_2 there is considerable variability in the tissue (discussed further below), and the "typical" value given in **Table 1** is consistent with recent measurements in animal models (Ances et al., 2001; Thompson et al., 2005).

The tissue pO_2 model allows us to draw contours of equal tissue pO_2 in the plane defined by the fractional changes in $CMRO_2$ and CBF (**Figure 2B**). One clear feature of these contour lines is that they are distinctly different from the contours of the BOLD response. Specifically, the line of constant BOLD signal and the line of constant tissue pO_2 have different slopes. This means that there is a range of possible CBF and $CMRO_2$ responses, lying between the two zero change contour lines, where the BOLD response and the tissue pO_2 response will have opposite signs (a negative tissue pO_2 response occurring with a positive BOLD response). Again assuming that this model accurately describes dynamic changes as well as steady-state changes, the predicted variation of tissue pO_2 for the hypothetical CBF and $CMRO_2$ responses is shown in **Figure 2D**. Note that this response is quite complicated, with a more pronounced initial dip compared with the BOLD response, and a positive response that only begins after the end of the stimulus. This complex response shows features similar to the interesting variety of tissue pO_2 responses that have recently been reported for different stimuli in animal models, including relatively simple positive responses to a strong stimulus (Ances et al., 2001), a pronounced initial dip (Offenhauser et al., 2005) and complex wiggles and slow post-stimulus undershoots (Thompson et al., 2003, 2004). The source of the complexity of the pO_2 response is that the simulated CBF and $CMRO_2$ responses have a ratio of about 2:1, and this means that the trajectory of the response passes back and forth across the zero contour of the tissue pO_2 response. This is consistent with the pO_2 measurements of Thompson and colleagues, in which all of the pO_2 fluctuations they reported were less than ~5% of the baseline pO_2. The potentially important implications of this are discussed further below.

IMPROVING AND VALIDATING THE THEORETICAL FRAMEWORK

Validating the accuracy of the models

The discussion above illustrates that an appropriate modeling framework can play two important roles. First, it provides a way to combine multimodal measurements (in this case CBF and BOLD responses, or CBF and tissue pO_2 responses) to make a quantitative estimate of the $CMRO_2$ response. Second, it provides a framework for exploring how different responses (e.g., BOLD and tissue pO_2) will co-vary or diverge under different conditions. In particular, the theoretical framework brings out significant quantitative differences in the BOLD and tissue pO_2 responses that are not intuitively obvious. Examples are the predictions that: (1) a slight post-stimulus undershoot of CBF can produce a much more pronounced undershoot of the BOLD response; (2) there are possible changes in which the BOLD and tissue pO_2 responses will have opposite sign; and (3) the tissue pO_2 response can be significantly more complicated than the underlying CBF and $CMRO_2$ responses or the accompanying BOLD response. However, the theoretical framework outlined here is really just the starting point, and a number of possible limitations have to be tested, and the theoretical framework revised accordingly.

The BOLD signal model has several potentially important limitations. Although it was argued above that the current model is more robust than one might conclude from the restrictive assumptions involved in its derivation, this needs to be further tested. In particular, the most important aspect to nail down is the role

played by blood volume changes (at all levels of the vascular tree) on the observed BOLD response. In applying the Davis model the exponent $\alpha = 0.4$ is almost always used, with the assumption that this captures the volume change of blood compartments containing deoxyhemoglobin (primarily venous). However, this value originally came from whole-brain measurements of *total* blood volume changes in an animal model. A more recent study using PET methods in human subjects found larger values (as high as $\alpha = 0.64$) (Rostrup et al., 2005), and a recent study in humans with the VASO technique also found values as high as $\alpha \sim 0.6$ (Lin et al., 2008, 2009). It should be noted, though, that the VASO technique measures an absolute total blood volume change with activation, and a baseline value for blood volume must be assumed to estimate α. However, these methods measure total blood volume changes, and the primary quantity we need for interpreting the BOLD response is the venous volume change. A recent study using a novel method specifically sensitive to the venous blood found $\alpha \sim 0.2$ (Chen and Pike, 2009a), smaller than the previously reported values for total blood volume but still greater than 0.

A number of investigators are attacking the question of determining the volume changes in different vascular compartments with a variety of techniques in animal models. Two photon microscopy studies, which allow direct visualization of the vessels and accurate measurement of vessel diameters in the upper 0.5 mm of cortex in rats and mice, have found that the volume changes are primarily on the arterial side, with relatively small changes in venous blood volume (Hillman et al., 2007). In addition, a number of MRI techniques have been developed to estimate volume changes in different vascular compartments, but it remains a challenging task to clearly isolate specific compartments from each other and from confounding flow effects. Several of these studies in animal models also found that most of the blood volume change is on the arterial side (Kim and Kim, 2006; Kim et al., 2007). More studies are clearly needed to clarify how blood volume changes with activation, but a working model based on these results is that most of the change is arterial, with smaller fractional changes in the venous and possibly the capillary compartments.

As noted above, the parameter β was initially introduced to approximate the net effect of smaller and larger vessels in describing the extravascular BOLD effect. It turns out fortuitously that this form also gives a reasonable description of the BOLD response when intravascular signal changes and volume exchange effects are included (Buxton et al., 2004; Leontiev et al., 2007). For this reason it may be better to look at β as a parameter that captures multiple effects, and no longer think of it in terms of the original derivation. A more detailed model of the BOLD response including multiple vascular compartments and effects could be used to estimate the value of β that maximizes the accuracy of the Davis model.

Although the concerns about which values of α and β should be used need to be addressed, it turns out that estimates of fractional $CMRO_2$ change in a calibrated-BOLD experiment are relatively robust to uncertainties in α and β. The primary reason for this is that if the same model is used to analyze both the hypercapnia experiment and the activation experiment, the calculation is partially self-correcting (Davis et al., 1998; Ances et al., 2008). However, this robustness is based on the assumption that the relationship between volume changes and flow just depends on the magnitude of the flow change, and not on the details of how the flow change is evoked. A key question that needs to be addressed is whether this relationship is the same for CBF changes induced by hypercapnia and neural activity.

In contrast to α and β, the value of M is critical. In general, the Davis model is robust because many of the physiological variables that could have a strong effect on the BOLD response magnitude are essentially lumped into the parameter M. This includes physiological parameters, such as baseline venous blood volume and hematocrit, but also aspects of the image acquisition, such as echo time and field strength, and even the way that a region of interest is selected for averaging. For this reason, the value of M must be measured in each experiment, and a dangerous pitfall is to assume a value of M reported in the literature and apply it to data collected in a different way (Chiarelli et al., 2007b; Leontiev et al., 2007; Lin et al., 2008).

The tissue pO_2 model also has a number of simplifying assumptions that need to be tested. Clearly this model ignores many of the complexities of O_2 transport in blood, such as a shift of p_{50} as CO_2 diffuses into the blood, although these may be approximated by an appropriate choice of p_{50} and h (Gjedde, 2005a). Perhaps the most important question, though, is: Can the macroscopic effects be described in terms of the average pO_2 values in blood and tissue? That is, even for the simplest microscopic model, the Krogh cylinder, blood and tissue pO_2 values have a large spatial variability (Mintun et al., 2001), and experimental measurements show a wide range of pO_2 values, raising the question of whether it is even meaningful to talk about a mean tissue pO_2 (Ndubuizu and LaManna, 2007). Note, though, that the relevant question is not whether pO_2 is uniform in tissue, which would be a possible assumption that could be used to derive Eq. 3. Instead, the question is whether a much more detailed microscopic description leads to predictions for the macroscopic variables that differ significantly from the predictions of the simpler macroscopic models. A promising avenue for addressing questions like these is to construct detailed models of the vascular tree from animal imaging data and use such realistic geometries to calculate oxygen transport (Fang et al., 2008). These simulations also should include known effects of blood transport, such as the shift of p_{50}, and so need to model CO_2 production and clearance simultaneously with O_2 transport and consumption. In addition, such simulations could also test assumptions of the PET models used for estimation of $CMRO_2$, particularly the significance of the assumption of zero back flux of unmetabolized O_2 from the tissue. While such modeling is computationally demanding, it is not out of reach, and recent studies are encouraging.

Dynamic responses

One of the exciting aspects of oxygenation-based methods, compared with tracer methods, is the possibility of measuring dynamic $CMRO_2$ changes. However, the theoretical framework described in **Table 1** is based on steady-state relationships, and it is an open question whether these equations are accurate for dynamic studies. For example, Eq. 1 is intrinsically a steady-state equation because the net extraction fraction is the result of the full passage of the blood through the vascular bed, which requires a finite time. To deal with this issue, more detailed models are required that carefully take into account the dynamics of different compartments,

or explicitly consider an extended vascular network (Boas et al., 2008). While such models may be too complex for routine use, they would provide a valuable test-bed for validating simpler models, such as the framework described here, and guide the development of more accurate macroscopic models that capture the dynamics. For these reasons, the dynamic curves in **Figure 2** should be considered as suggestive of what the dynamics might look like, because they were calculated by assuming that the steady-state relationships apply at each time point, and this needs to be tested with the more detailed models.

In addition to these basic questions regarding the modeling, it is still an open question whether there are transient physiological changes that are not captured by the simple theoretical framework. There is a reasonable consensus that the initial dip of the BOLD response reflects a faster rise of $CMRO_2$ compared to CBF (Malonek and Grinvald, 1996; Devor et al., 2003), and the current framework captures that possibility (see **Figure 2**). However, there is no consensus on whether the post-stimulus BOLD undershoot is a neural, vascular or metabolic effect. Intriguing recent evidence suggests a neuronal modulation of the undershoot (Sadaghiani et al., 2009), but it has more commonly been hypothesized to be a biomechanical (Buxton et al., 1998; Mandeville et al., 1999; Chen and Pike, 2009b) or metabolic effect (Frahm et al., 1996, 2008; Lu et al., 2004. If the undershoot is due to a mismatch of CBF and $CMRO_2$, then the current framework will capture the effect. For example, the undershoot could be due to a slow recovery of $CMRO_2$ combined with a fast recovery of CBF, or a fast recovery of $CMRO_2$ combined with an undershoot of CBF (the latter possibility is illustrated in **Figure 2**). However, another possibility is that transients of blood volume and blood flow are different, so that blood volume recovers slowly even though CBF and $CMRO_2$, and thus intrinsic blood oxygenation, have returned to baseline. This effect is not captured by the current theoretical framework, because Eq. 2 assumes a fixed relationship between blood flow and blood volume given by a power law. For this reason, it is important to determine empirically whether this effect occurs.

Early MRI studies using MION, a magnetic agent that labels the blood plasma, found a slow recovery of blood volume with a duration that matched the BOLD post-stimulus undershoot and was longer than the recovery time of CBF (Mandeville et al., 1998). This observation prompted two similar models – the balloon model (Buxton et al., 1998) and the delayed compliance model (Mandeville et al., 1999) – hypothesizing that a slow recovery of venous blood volume, elevating total dexoyhemoglobin even though blood oxygenation had returned to baseline, could account for the BOLD post-stimulus undershoot. Later studies with MION and higher spatial resolution found that the slow recovery of blood volume was primarily in the middle layers of cortex (Yacoub et al., 2006; Zhao et al., 2007). Interestingly, though, the BOLD undershoot was present in the upper layers as well as the middle layers. This suggests that while a slow venous volume recovery could be a contributing factor, particularly in the middle layers, it cannot be a general explanation. The presence of a BOLD undershoot in the upper layers without a slow blood volume recovery suggests that there is also an alteration of blood oxygenation, presumably due to a mismatch of CBF and $CMRO_2$ in the post-stimulus period (Yacoub et al., 2006). In contrast to the MION studies, though, other studies using different techniques have not found evidence for a slow recovery of blood volume (Lu et al., 2004; Hillman et al., 2007; Frahm et al., 2008). The BOLD post-stimulus undershoot in the absence of a slow venous recovery could be due a slow recovery of $CMRO_2$ as noted above, although there is no direct evidence for this. Instead, this explanation remains when the possibilities of a slow blood volume recovery or a CBF undershoot are excluded. However, **Figure 2** suggests that a weak undershoot of CBF would be sufficient to explain a more substantial BOLD undershoot, and in practice it may be difficult to exclude such a possibility because of the noise in the measurements. In short, an important physiological question that needs to be resolved in establishing a theoretical framework is whether blood volume changes are being accurately modeled.

CURRENT EXPERIMENTAL MEASUREMENTS OF THE COUPLING OF CBF AND $CMRO_2$

In addition to PET studies of the coupling of CBF and $CMRO_2$ (Fox and Raichle, 1986; Fox et al., 1988; Marrett and Gjedde, 1997; Ito et al., 2005), several groups have adopted the calibrated-BOLD approach and reported values of the CBF/$CMRO_2$ coupling index n in the range of about 2–4 (Davis et al., 1998; Hoge et al., 1999; Kim et al., 1999; Kastrup et al., 2002; St Lawrence et al., 2003; Stefanovic et al., 2004, 2005; Uludag and Buxton, 2004; Fujita et al., 2006; Chiarelli et al., 2007a; Leontiev and Buxton, 2007; Leontiev et al., 2007; Ances et al., 2008, 2009; Perthen et al., 2008; Restom et al., 2008; Lin et al., 2009). Other studies have used the framework of the calibrated-BOLD approach to argue that CBF and $CMRO_2$ are coupled in a similar way in deactivations and activations (Shmuel et al., 2002; Stefanovic et al., 2004, 2005; Uludag et al., 2004; Pasley et al., 2007).

Figure 3 shows a sampling of current data in human subjects using either PET or calibrated-BOLD techniques. The plotted points are representative values from the studies, and the symbols used reflect the brain area and the technique. Also plotted are lines of constant values of n, the ratio of the CBF and $CMRO_2$ changes. Note that the word "coupling" is used here simply to describe the empirical ratio n, and does not necessarily imply a direct mechanistic link between CBF and $CMRO_2$. Instead, current ideas point to CBF and $CMRO_2$ being driven in parallel by neural activity. For reference to **Figure 2**, the contour predicted for constant tissue pO_2 also is plotted.

There is a considerable spread of the coupling ratios, with most measurements lying in the range $n \sim 2$–4. The calibrated-BOLD measurements show the highest changes in CBF and $CMRO_2$, and this could be due to reduced partial volume averaging of gray matter signals with the improved spatial resolution of MRI compared with PET. Overall, though, there does not appear to be a strong difference in the coupling ratio n between calibrated-BOLD and PET measurements. The original observation of the CBF/$CMRO_2$ mismatch by Fox and Raichle is one of the largest values of n found (~6), but later PET studies found $n \sim 2$ in other brain regions. Undoubtedly, some (perhaps most) of the variance in these data is due to the different methods used. However, there is a trend in this data for motor/somatosensory data to have the highest values of n, basal ganglia to have the lowest values, and visual areas to lie in the middle.

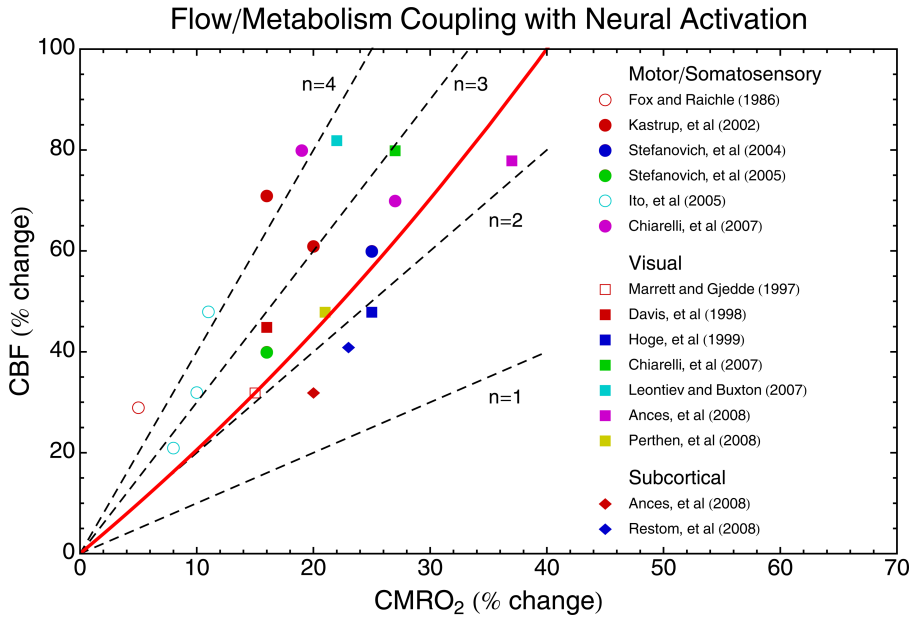

FIGURE 3 | Experimental measurements of CBF/CMRO$_2$ coupling in human brain. PET measurements are indicated by open symbols, and calibrated-BOLD measurements are indicated by filled symbols. Different symbol shapes are used for different brain areas, as indicated. Lines of constant *n* are shown as dashed lines, and the solid red curve is the contour of constant tissue pO$_2$ calculated from the theoretical framework and shown in **Figure 2B**. The fact that the points are all well above the line *n* = 1 produces the BOLD effect with activation. A speculation discussed in the text is that the function served by a large value of *n* is to prevent a fall in tissue pO$_2$ as CMRO$_2$ increases.

In a study specifically comparing simultaneous activation of basal ganglia areas with a motor task and visual areas with a visual stimulus, Ances et al. (2008) found a significantly higher value of *n* in visual cortex ($n \sim 2.3$) compared to basal ganglia ($n \sim 1.7$). At first glance this degree of difference does not sound like it should be too important, but the effect on the BOLD response was striking. The ratio of the BOLD responses for these two tasks was ~7, even though the ratio of the CMRO$_2$ responses was only ~2. Interestingly, this failure of the BOLD response to accurately reflect the underlying CMRO$_2$ change was not due to a difference in the value of the scaling parameter *M* between the two regions, but rather due to the difference in *n*. The CBF response to hypercapnia was also larger in the visual area compared to basal ganglia, in parallel with the larger value of *n* associated with neural activation, suggesting a generally greater responsiveness of the blood vessels in the visual areas. This data, in addition to the other data in **Figure 3**, suggests that the coupling ratio *n* may vary between brain regions within the same subject. In addition, recent experiments suggest that *n* varies within visual cortex with the frequency of a visual stimulus (Lin et al., 2008) and with time for a sustained stimulus (Lin et al., 2009).

Positron emission tomography studies have been reported with a wide variation in the coupling of CBF and CMRO$_2$, including extreme cases of no change in CMRO$_2$ with an activation CBF (Kuwabara et al., 1992), as well as variability with the duration (Mintun et al., 2002) or frequency (Vafaee et al., 1999; Vafaee and Gjedde, 2000) of a visual stimulus. Taken together, the available data suggest that *n* may vary between regions, and even within a region it may vary with stimulus amplitude or other characteristics.

In short, the variability of *n* poses a significant problem for the interpretation of BOLD signals. Specifically, the relative value of BOLD responses cannot be taken as a quantitative reflection of the relative values of the underlying physiological changes. Variability of *n* is consistent with the current idea that neural activity drives CBF and CMRO$_2$ in parallel, and emphasizes the critical importance of understanding exactly which aspects of neural activity drive CBF and which create a demand for higher CMRO$_2$.

OPEN QUESTIONS

The phenomenon that a brief neural stimulus produces a robust, but delayed, increase of CBF (**Figure 1**) lies at the heart of many functional neuroimaging techniques, and yet we still do not have a clear picture of the mechanisms involved, or even of the physiological function served by this response: why is it so large, why is it so fast, and does it have anything to do with oxygen metabolism? The experimental data, integrated within the theoretical framework, may provide a possible explanation. These questions are considered in this section, emphasizing the idea that tissue pO$_2$ may be the key to understanding CBF/CMRO$_2$ coupling.

WHY IS THE CBF CHANGE SO LARGE?

As noted above, recent studies of the tissue pO$_2$ response with neural activation have found interestingly complex wiggles. However, stepping back from these detailed fluctuations, a remarkable finding is that the fluctuations are relatively small. For example, with a visual stimulus in a cat model Thompson et al. (2003, 2004) found pO$_2$ fluctuations that were all less than about 5% of the baseline pO$_2$. Other studies with electrical stimulation in rats have found larger variations of ~20% (Ances et al., 2001; Offenhauser et al., 2005),

but conceivably the stimuli used were exceptionally strong compared to normal physiological stimuli. In parallel to these animal studies, the PET and calibrated-BOLD studies shown in **Figure 3** indicate that the CBF/$CMRO_2$ coupling ratio n is ~2–4. The theoretical framework in **Table 1** shows that these different experimental results are consistent with a simple picture: the observed CBF/$CMRO_2$ coupling ratio is approximately what is required to maintain a constant tissue pO_2 (the contour of constant pO_2 is plotted in **Figure 3**). Furthermore, the theoretical pO_2 curve in **Figure 2** illustrates that complex fluctuations of tissue pO_2, but of small magnitude, can occur as the dynamic curves of CBF and $CMRO_2$ response pass over and under the contour of constant pO_2 in the CBF/$CMRO_2$ plane.

This observation suggests the hypothesis that the existence of the BOLD effect – the apparent mismatch of CBF and $CMRO_2$ changes – could be the result of a homeostatic mechanism acting to prevent a fall of tissue pO_2 despite changes in the metabolic rate. Based on the theoretical framework in **Table 1**, a $CMRO_2$ increase of 20% with no change in CBF would lead to a 30% drop of tissue pO_2, while a CBF change ~2.5 times larger than the $CMRO_2$ change would preserve tissue pO_2 ~25 mmHg. An earlier idea for why n is large was that O_2 delivery is limited at baseline (Gjedde et al., 1991; Buxton and Frank, 1997), motivated by the previous assumption of the PET methods that the pO_2 in tissue is near 0 so that back flux of O_2 from tissue to blood is negligible (Mintun et al., 1984). In that case, because tissue pO_2 cannot drop, and because there is no capillary recruitment, the only way to increase the O_2 gradient from blood to tissue is to increase the blood pO_2 by decreasing E. Valabregue et al. (2003) pointed out that relaxing the assumption of zero tissue pO_2 gave more flexibility for CBF and $CMRO_2$ to vary, and the pO_2 measurements cited above support the idea that tissue pO_2 is reasonably high. The current argument is in a sense an extension of the original oxygen limitation hypothesis, but now in terms of a non-zero tissue pO_2 that is prevented from dropping lower, rather than a zero tissue pO_2 that cannot drop. The required value of n needed to maintain tissue pO_2 decreases for higher values of baseline tissue pO_2.

WHY IS THE CBF CHANGE SO FAST?

The argument above addresses the question of why n is large, but does not necessarily address why the CBF response is so fast. The dynamic example in **Figure 2** essentially assumes that the time constants for adjustments of blood and tissue oxygenation are on the order of 1 s, and this needs to be tested with more detailed models, as discussed above. As a start in this direction, it is useful to estimate the time constants for different aspects of energy metabolism as a guide to whether these components would require a fast CBF response, and whether they could potentially provide a rapid signal to drive the CBF response. It's important to note that these time scales do not describe how quickly the glucose or O_2 metabolic rates could change. Both metabolic rates are likely to be able to change on a very short time scale with no changes in the concentrations of glucose or oxygen, through changes in the activity of rate-limiting enzymes. Instead, these time constants reflect the speed with which an abrupt change in metabolic rate would translate into a change in concentration of the metabolic substrates or products.

One clear function of blood flow is to deliver the substrates of energy metabolism, glucose and oxygen, and clear the waste products, carbon dioxide and heat. Metabolic rates are usually expressed as moles per minute per gram of tissue, but it is useful to consider these rates referenced to a unit volume of tissue, rather than a unit mass, and the metabolic rate is then a concentration divided by time (mM/min). In the adult human brain, a typical glucose metabolic rate is about 0.3 mM/min (Chugani et al., 1987), and a typical concentration of glucose in brain is about 2 mM at normal plasma glucose levels (Gruetter et al., 1998). The time constant for depleting the glucose is thus on the order of several minutes, suggesting that the regulation of blood flow on a time scale of seconds is not required to support glucose metabolism. Furthermore, if the O_2 supply was somehow abruptly stopped but CMRGlc continued at the normal rate, lactate would accumulate at a rate of about 0.6 mM/min, so a change of lactate concentration of only 1 mM would take on the order of 90 s to grow.

The $CMRO_2$ is higher, about 1.6 mM/min (Ito et al., 2004), and the tissue concentration of O_2 is lower. If the tissue pO_2 is ~25 mmHg, a solubility of 0.0013 mM/mmHg gives an extravascular O_2 concentration of only ~0.03 mM. Arterial blood has an O_2 concentration of about 9 mM, so for a typical tissue blood volume fraction of 5% and a roughly 70% average hemoglobin saturation the intravascular O_2 content in tissue is about 0.26 mM. The total O_2 concentration in an element of tissue then is about 0.3 mM, with most of that in the blood compartment. The time constant for depleting the available O_2 is then on the order of 10 s, much shorter than the equivalent time for depletion of glucose. Excluding the O_2 in blood within a tissue element, the O_2 concentration associated with baseline tissue pO_2 would be depleted in ~1 s at the baseline metabolic rate, providing some support for applying the steady-state theoretical framework to dynamic changes.

Blood flow also carries away CO_2 and heat. Because CO_2 rapidly equilibrates with bicarbonate ions, the total pool of CO_2 in the brain is quite large, ~25 mM. The CO_2 production rate is close to the O_2 consumption rate, ~1.6 mM/min, so the time constant for changing total CO_2 is on the order of 10 min. Conceivably, though, pH changes could begin to become important on a shorter time scale, and a possible role for CO_2 in the post-stimulus undershoot has recently been proposed (Yucel et al., 2009). If the heat produced by the metabolic reactions is not dissipated, the temperature of the brain could rise to a level that could impair brain function. About 440 kJ of heat is released per mole of O_2 metabolized, and the heat capacity of water is ~4.2 J/g/°C (Yablonskiy et al., 2000). If the heat of metabolism was not cleared, the temperature would rise only ~0.1°C in 40 s. Thus, while clearance of heat is an important function, it does not appear that this requires the fast CBF response observed with neural stimulation.

In short, if energy metabolism increased without a change in CBF, the time scales for significant changes in the concentrations of glucose, lactate, and CO_2, as well as the temperature rise due to added heat, appear to be too long to require a fast CBF response, or to provide the signal for increasing CBF. On the other hand, the time scale for changes in pO_2 is comparable, although perhaps a bit longer, than the observed CBF response, suggesting that a fast CBF response is necessary to prevent a drop of tissue pO_2.

WHAT DRIVES THE CBF CHANGE?

The arguments above raise two key questions: why does the brain need to preserve tissue pO_2, and what mechanisms could be involved in maintaining it? At first glance, it appears that the normal pO_2 level (~25 mmHg) is much higher than it needs to be, given that the effective K_m for cytochrome oxidase, the O_2 concentration where O_2 availability limits $CMRO_2$, is below 1 mmHg (Gnaiger et al., 1998). That is, it appears that $CMRO_2$ should not be affected by transient dips in tissue pO_2. However, there are two potential reasons why a higher pO_2 may be important for healthy brain function. The first is that there are many other reactions for which O_2 is a substrate, and these have much larger K_m values than cytochrome oxidase (Vanderkooi et al., 1991; Erecinska and Silver, 2001). For these reactions, fluctuations of tissue pO_2 could affect the reaction rate. A second possible reason why maintaining a high tissue pO_2 may be important is related to the thermodynamics of energy metabolism. The Gibbs free energy (ΔG) available from oxidative metabolism of glucose depends on the O_2 concentration. This ΔG must be sufficiently negative to offset the strong positive ΔG required to produce ATP from ADP and Pi. If the ΔG of oxidative metabolism is reduced because of low tissue pO_2, there will be a point where $CMRO_2$ cannot proceed unless the ΔG related to producing ATP also is reduced. This would be a reduction of the phosphorylation potential, the ratio [ATP]/[ADP][Pi]. This phenomenon was observed in cell cultures, where even though the rate of O_2 metabolism could be maintained down to very low levels of pO_2, the phosphorylation potential began to decrease at much higher levels (Wilson et al., 1979).

In the last decade there has been a surge of research on the mechanisms by which cells sense their oxygen level and respond with a wide range of physiological changes, particularly the cascade of events that follows stabilization of hypoxia-inducible factor-1 (HIF-1, Semenza, 2009). While often considered in the context of responses to hypoxia, it is interesting to note that some of the intermediate reactions are sensitive to the pO_2 at higher levels (Ward, 2008), and recent work suggests that these mechanisms may play a role in normoxia as well as hypoxia (Semenza, 2009). While it is conceivable that a pO_2 feedback system may be involved in driving the acute CBF changes with activation, it is not clear that these mechanisms could operate effectively on the time scale of a few seconds. Such mechanisms, like other metabolic influences, may operate on a longer time scale to match CBF with energy demands. For this reason, the immediate trigger for the CBF increase most likely operates in a feed-forward fashion, with aspects of neural activity triggering an initial response that is then modulated by slower feedback responses. A great deal of experimental evidence has supported a role for astrocytes in modulating CBF, acting as both an integrator of local synaptic activity and an effector of blood flow change (Iadecola and Nedergaard, 2007). However, it is still not clear whether astrocyte responses are fast enough to drive CBF changes on a time scale of seconds, as the time scale observed for vascular responses in slice preparations is much longer than what is observed in awake humans (Koehler et al., 2009).

One mechanism that has been observed to respond quickly enough to drive the CBF response is the production of NO (Buerk et al., 2003). While NO is produced by vascular and endothelial mechanisms, it also is produced by neurons. Interestingly, though, the neurons that produce NO have been isolated to a class of inhibitory GABA-ergic interneurons (Estrada and DeFelipe, 1998). This is an example of a mechanism that has an inhibitory effect on the neuronal population, and yet also increases blood flow. Adenosine is another prime example, reducing neuronal excitability while also acting as a vasodilator (Dirnagl et al., 1994; Haydon and Carmignoto, 2006). At first glance, this counterintuitive behavior is puzzling if the goal is to match blood flow to the level of neural activity. However, this combined effect makes sense as a protection against a potentially dangerous drop in tissue pO_2, by both increasing delivery and decreasing demand for O_2. Both effects would serve to raise tissue pO_2. This is consistent with the idea of *oxygen conformance*, that a primary defense of an organism when faced with hypoxia is to reduce the ATP consumption and O_2 metabolic rate (Hochachka et al., 1996).

The existence of mechanisms that drive neural activity down while increasing CBF suggests the possibility that a greater involvement of inhibitory activity could be associated with larger values of n. However, we should be cautious in interpreting these studies: the identification of a particular mechanism in simple preparations does not necessarily mean these mechanisms are dominant or even invoked *in vivo*. For example, interneurons also release neuropeptide Y (Abounader and Hamel, 1997), a vasoconstrictor, and astrocytes can trigger both vessel dilation and constriction (Zonta et al., 2003; Mulligan and MacVicar, 2004; Blanco et al., 2008), and we have no clear picture of how these different potential mechanisms are integrated into a responsive system *in vivo*. Nevertheless, the possibility of significant variations in $CBF/CMRO_2$ coupling related to inhibition is a potentially fruitful direction for future research.

In summary, the data and the theoretical modeling suggest the hypothesis that the underlying function served by $n \sim 2$–3 is to approximately maintain tissue pO_2 at a constant level. However, feed-forward mechanisms driven by the neural activity itself, such as NO production, are likely required to achieve the fast CBF response necessary to prevent a fall in pO_2. Furthermore, the specific interplay of different aspects of the evoked activity, such as the degree of evoked inhibitory activity, could alter the $CBF/CMRO_2$ coupling ratio. This speculative scenario needs to be tested with detailed studies in animal models of the specific aspects of neural activity that drive CBF changes, and how these relate to the overall energy demands of the full evoked activity. Finally, it is interesting to note that the hypothesis that tissue pO_2 is approximately conserved during neural activation is consistent with a broader evolutionary hypothesis. Baseline pO_2 levels in tissue are similar to what is thought to have been the atmospheric level of O_2 two billion years ago, when the machinery of oxidative metabolism evolved. It has been hypothesized that organisms try to preserve this level of O_2 in tissues as a balance between too little, limiting O_2 metabolism, and too much leading to increased generation of reactive oxygen species and potential cellular damage (Massabuau, 2003).

CONCLUSIONS

The basic picture of blood flow and oxygen metabolism being driven in parallel by neural activity – rather than a serial connection with neural activity driving energy metabolism which then drives blood flow changes – creates a significant challenge for interpreting many brain imaging signals in a quantitative way. The central

problem is that methods sensitive to blood or tissue oxygenation depend on the *relative balance* of the changes in blood flow and oxygen metabolism. For this reason, any quantitative interpretation of oxygenation signals such as the BOLD response in terms of the underlying physiological changes is problematic without a better understanding of O_2 metabolism. Because blood flow and glucose metabolism are easier to measure, there has been much more work done relating neural activity to CBF and CMRGlc. However, the positive side of the complexity of oxygenation signals is that they potentially provide the best methods we have for studying the dynamics of $CMRO_2$ when combined with separate CBF measurements. To make this a reality, though, requires a validated theoretical framework that accurately describes how our oxygenation signals (such as BOLD or tissue pO_2 responses) depend on the changes in CBF and $CMRO_2$. The current framework may be sufficient, but this needs to be tested with experimental measurements and more detailed modeling. This goal is within reach, but will require a focused research effort.

In addition, an accurate theoretical framework allows us to explore the physiological consequences of different hypotheses. For example, the existing data integrated within the simple theoretical framework described here suggests the hypothesis that an important functional role of the mismatch of CBF and $CMRO_2$ changes with neural activation is to prevent a fall of tissue pO_2. This hypothesis would explain why the CBF response is as fast and as large as it is, and accounts for the complexity of the observed dynamics of pO_2 when dynamic CBF and $CMRO_2$ responses are not perfectly balanced. However, many basic questions remain unresolved, particularly the mechanisms that control CBF changes in the healthy, awake human brain and, most importantly, how these mechanisms may be altered in disease. Progress in answering these questions will lay a foundation for using oxygenation-dependent neuroimaging signals as a quantitative probe of brain function, rather than simply a mapping tool.

ACKNOWLEDGMENTS

The author would like to thank the following individuals for stimulating discussions on this topic: Beau Ances, Nic Blockley, David Boas, Anders Dale, Anna Devor, David Dubowitz, Valerie Griffeth, Edith Hamel, Thomas Liu, Farshad Moradi, Scott Small, Roger Springett, and Kamil Uludag. This work was supported by NIH grant NS-036722.

REFERENCES

Abounader, R., and Hamel, E. (1997). Associations between neuropeptide Y nerve terminals and intraparenchymal microvessels in rat and human cerebral cortex. *J. Comp. Neurol.* 388, 444–453.

Ances, B. M., Buerk, D. G., Greenberg, J. H., and Detre, J. A. (2001). Temporal dynamics of the partial pressure of brain tissue oxygen during functional forepaw stimulation in rats. *Neurosci. Lett.* 306, 106–110.

Ances, B. M., Leontiev, O., Perthen, J. E., Liang, C., Lansing, A. E., and Buxton, R. B. (2008). Regional differences in the coupling of cerebral blood flow and oxygen metabolism changes in response to activation: implications for BOLD-fMRI. *Neuroimage* 39, 1510–1521.

Ances, B. M., Liang, C. L., Leontiev, O., Perthen, J. E., Fleisher, A. S., Lansing, A. E., and Buxton, R. B. (2009). Effects of aging on cerebral blood flow, oxygen metabolism, and blood oxygenation level dependent responses to visual stimulation. *Hum. Brain Mapp.* 30, 1120–1132.

Arai, T., Mori, K., Nakao, S., Watanabe, K., Kito, K., Aoki, M., Mori, H., Morikawa, S., and Inubushi, T. (1991). In vivo oxygen-17 nuclear magnetic resonance for the estimation of cerebral blood flow and oxygen consumption. *Biochem. Biophys. Res. Commun.* 179, 954–961.

Arai, T., Nakao, S., Mori, K., Ishimori, K., Morishima, I., Miyazawa, T., and Fritz-Zieroth, B. (1990). Cerebral oxygen utilization analyzed by the use of oxygen-17 and its nuclear magnetic resonance. *Biochem. Biophys. Res. Commun.* 169, 153–158.

Attwell, D., and Iadecola, C. (2002). The neural basis of functional brain imaging signals. *Trends Neurosci.* 25, 621–625.

Attwell, D., and Laughlin, S. B. (2001). An energy budget for signaling in the grey matter of the brain. *J. Cereb. Blood Flow Metab.* 21, 1133–1145.

Blanco, V. M., Stern, J. E., and Filosa, J. A. (2008). Tone-dependent vascular responses to astrocyte-derived signals. *Am. J. Physiol. Heart Circ. Physiol.* 294, H2855–H2863.

Boas, D. A., Jones, S. R., Devor, A., Huppert, T. J., and Dale, A. M. (2008). A vascular anatomical network model of the spatio-temporal response to brain activation. *Neuroimage* 40, 1116–1129.

Boxerman, J. L., Bandettini, P. A., Kwong, K. K., Baker, J. R., Davis, T. L., Rosen, B. R., and Weisskoff, R. M. (1995a). The intravascular contribution to fMRI signal change: Monte Carlo modeling and diffusion-weighted studies in vivo. *Magn. Reson. Med.* 34, 4–10.

Boxerman, J. L., Hamberg, L. M., Rosen, B. R., and Weisskoff, R. M. (1995b). MR contrast due to intravascular magnetic susceptibility perturbations. *Magn. Reson. Med.* 34, 555–566.

Brown, G. G., Eyler Zorrilla, L. T., Georgy, B., Kindermann, S. S., Wong, E. C., and Buxton, R. B. (2003). BOLD and perfusion response to finger-thumb apposition after acetazolamide administration: differential relationship to global perfusion. *J. Cereb. Blood Flow Metab.* 23, 829–837.

Buerk, D. G., Ances, B. M., Greenberg, J. H., and Detre, J. A. (2003). Temporal dynamics of brain tissue nitric oxide during functional forepaw stimulation in rats. *Neuroimage* 18, 1–9.

Buxton, R. B. (2005). Quantifying CBF with arterial spin labeling. *J. Magn. Reson. Imaging* 22, 723–726.

Buxton, R. B. (2009). *Introduction to Functional Magnetic Resonance Imaging: Principles and Techniques*. Cambridge: Cambridge University Press.

Buxton, R. B., and Frank, L. R. (1997). A model for the coupling between cerebral blood flow and oxygen metabolism during neural stimulation. *J. Cereb. Blood Flow Metab.* 17, 64–72.

Buxton, R. B., Uludag, K., Dubowitz, D. J., and Liu, T. T. (2004). Modeling the hemodynamic response to brain activation. *Neuroimage* 23(Suppl. 1), S220–S233.

Buxton, R. B., Wong, E. C., and Frank, L. R. (1998). Dynamics of blood flow and oxygenation changes during brain activation: the balloon model. *Magn. Reson. Med.* 39, 855–864.

Caesar, K., Offenhauser, N., and Lauritzen, M. (2008). Gamma-aminobutyric acid modulates local brain oxygen consumption and blood flow in rat cerebellar cortex. *J. Cereb. Blood Flow Metab.* 28, 906–915.

Chen, J. J., and Pike, G. B. (2009a). BOLD-specific cerebral blood volume and blood flow changes during neuronal activation in humans. *NMR Biomed.* 22, 1054–1062.

Chen, J. J., and Pike, G. B. (2009b). Origins of the BOLD post-stimulus undershoot. *Neuroimage* 46, 559–568.

Chiarelli, P. A., Bulte, D. P., Gallichan, D., Piechnik, S. K., Wise, R., and Jezzard, P. (2007a). Flow-metabolism coupling in human visual, motor, and supplementary motor areas assessed by magnetic resonance imaging. *Magn. Reson. Med.* 57, 538–547.

Chiarelli, P. A., Bulte, D. P., Piechnik, S., and Jezzard, P. (2007b). Sources of systematic bias in hypercapnia-calibrated functional MRI estimation of oxygen metabolism. *Neuroimage* 34, 35–43.

Cholet, N., Seylaz, J., Lacombe, P., and Bonvento, G. (1997). Local uncoupling of the cerebrovascular and metabolic responses to somatosensory stimulation after neuronal nitric oxide synthase inhibition. *J. Cereb. Blood Flow Metab.* 17, 1191–1201.

Chugani, H. T., Phelps, M. E., and Mazziotta, J. C. (1987). Positron emission tomography study of human brain functional development. *Ann. Neurol.* 22, 487–497.

Davis, T. L., Kwong, K. K., Weisskoff, R. M., and Rosen, B. R. (1998). Calibrated functional MRI: mapping the dynamics of oxidative metabolism. *Proc. Natl. Acad. Sci. U.S.A.* 95, 1834–1839.

Detre, J. A., Leigh, J. S., WIlliams, D. S., and Koretsky, A. P. (1992). Perfusion imaging. *Magn. Reson. Med.* 23, 37–45.

Devor, A., Dunn, A. K., Andermann, M. L., Ulbert, I., Boas, D. A., and Dale, A. M. (2003). Coupling of total hemoglobin concentration, oxygenation, and neural activity in rat somatosensory cortex. *Neuron* 39, 353–359.

Devor, A., Hillman, E. M., Tian, P., Waeber, C., Teng, I. C., Ruvinskaya, L., Shalinsky, M. H., Zhu, H., Haslinger, R. H., Narayanan, S. N., Ulbert, I., Dunn, A. K., Lo, E. H., Rosen, B. R., Dale, A.

M., Kleinfeld, D., and Boas, D. A. (2008). Stimulus-induced changes in blood flow and 2-deoxyglucose uptake dissociate in ipsilateral somatosensory cortex. *J. Neurosci.* 28, 14347–14357.

Dirnagl, U., Niwa, K., Lindauer, U., and Villringer, A. (1994). Coupling of cerebral blood flow to neuronal activation: role of adenosine and nitric oxide. *Am. J. Physiol.* 267, H296–H301.

Donahue, M. J., Hua, J., Pekar, J. J., and van Zijl, P. C. (2009). Effect of inflow of fresh blood on vascular-space-occupancy (VASO) contrast. *Magn. Reson. Med.* 61, 473–480.

Donahue, M. J., Lu, H., Jones, C. K., Edden, R. A., Pekar, J. J., and van Zijl, P. C. (2006). Theoretical and experimental investigation of the VASO contrast mechanism. *Magn. Reson. Med.* 56, 1261–1273.

Dunn, A. K., Devor, A., Dale, A. M., and Boas, D. A. (2005). Spatial extent of oxygen metabolism and hemodynamic changes during functional activation of the rat somatosensory cortex. *Neuroimage* 27, 279–290.

Erecinska, M., and Silver, I. A. (2001). Tissue oxygen tension and brain sensitivity to hypoxia. *Respir. Physiol.* 128, 263–276.

Estrada, C., and DeFelipe, J. (1998). Nitric oxide-producing neurons in the neocortex: morphological and functional relationship with intraparenchymal microvasculature. *Cereb. Cortex* 8, 193–203.

Fang, Q., Sakadzic, S., Ruvinskaya, L., Devor, A., Dale, A. M., and Boas, D. A. (2008). Oxygen advection and diffusion in a three-dimensional vascular anatomical network. *Opt. Express* 16, 17530–17541.

Fiat, D., and Kang, S. (1992). Determination of the rate of cerebral oxygen consumption and regional cerebral blood flow by non-invasive 17O in vivo NMR spectroscopy and magnetic resonance imaging: Part 1. Theory and data analysis methods. *Neurol. Res.* 14, 303–311.

Fiat, D., and Kang, S. (1993). Determination of the rate of cerebral oxygen consumption and regional cerebral blood flow by non-invasive 17O in vivo NMR spectroscopy and magnetic resonance imaging. Part 2. Determination of CMRO2 for the rat by 17O NMR, and CMRO2, rCBF and the partition coefficient for the cat by 17O MRI. *Neurol. Res.* 15, 7–22.

Fleisher, A. S., Podraza, K. M., Bangen, K. J., Taylor, C., Sherzai, A., Sidhar, K., Liu, T. T., Dale, A. M., and Buxton, R. B. (2009). Cerebral perfusion and oxygenation differences in Alzheimer's disease risk. *Neurobiol. Aging* 30, 1737–1748.

Fox, P. T., and Raichle, M. E. (1986). Focal physiological uncoupling of cerebral blood flow and oxidative metabolism during somatosensory stimulation in human subjects. *Proc. Natl. Acad. Sci. U.S.A.* 83, 1140–1144.

Fox, P. T., Raichle, M. E., Mintun, M. A., and Dence, C. (1988). Nonoxidative glucose consumption during focal physiologic neural activity. *Science* 241, 462–464.

Frahm, J., Baudewig, J., Kallenberg, K., Kastrup, A., Merboldt, K. D., and Dechent, P. (2008). The post-stimulation undershoot in BOLD fMRI of human brain is not caused by elevated cerebral blood volume. *Neuroimage* 40, 473–481.

Frahm, J., Krüger, G., Merboldt, K.-D., and Kleinschmidt, A. (1996). Dynamic uncoupling and recoupling of perfusion and oxidative metabolism during focal activation in man. *Magn. Reson. Med.* 35, 143–148.

Fujita, N., Matsumoto, K., Tanaka, H., Watanabe, Y., and Murase, K. (2006). Quantitative study of changes in oxidative metabolism during visual stimulation using absolute relaxation rates. *NMR. Biomed.* 19, 60–68.

Gjedde, A. (2005a). The pathways of oxygen in brain. I. Delivery and metabolism of oxygen. *Adv. Exp. Med. Biol.* 566, 269–275.

Gjedde, A. (2005b). The pathways of oxygen in brain. II. Competitions for cytochrome c oxidase and NOS are keys to flow-metabolism coupling. *Adv. Exp. Med. Biol.* 566, 277–283.

Gjedde, A., Ohta, S., Kuwabara, H., and Meyer, E. (1991). "Is oxygen diffusion limiting for blood-brain transfer of oxygen?," in *Brain Work and Mental Activity*, eds N. A. Lassen, D. H. Ingvar, M. E. Raichle, and L. Friberg (Copenhagen: Munksgaard), 177–184.

Gnaiger, E., Lassnig, B., Kuznetsov, A., Rieger, G., and Margreiter, R. (1998). Mitochondrial oxygen affinity, respiratory flux control and excess capacity of cytochrome c oxidase. *J. Exp. Biol.* 201, 1129–1139.

Grant, P. E., Roche-Labarbe, N., Surova, A., Themelis, G., Selb, J., Warren, E. K., Krishnamoorthy, K. S., Boas, D. A., and Franceschini, M. A. (2009). Increased cerebral blood volume and oxygen consumption in neonatal brain injury. *J. Cereb. Blood Flow Metab.* 29, 1704–1713.

Grubb, R. L. Jr., Raichle, M. E., Eichling, J. O., and Ter-Pogossian, M. M. (1974). The effects of changes in PaCO2 on cerebral blood volume, blood flow, and vascular mean transit time. *Stroke* 5, 630–639.

Gruetter, R., Ugurbil, K., and Seaquist, E. R. (1998). Steady-state cerebral glucose concentrations and transport in the human brain. *J. Neurochem.* 70, 397–408.

Gusnard, D. A., and Raichle, M. E. (2001). Searching for a baseline: functional imaging and the resting human brain. *Nat. Rev. Neurosci.* 2, 685–694.

Hamel, E. (2006). Perivascular nerves and the regulation of cerebrovascular tone. *J. Appl. Physiol.* 100, 1059–1064.

Haydon, P. G., and Carmignoto, G. (2006). Astrocyte control of synaptic transmission and neurovascular coupling. *Physiol. Rev.* 86, 1009–1031.

He, X., and Yablonskiy, D. A. (2007). Quantitative BOLD: mapping of human cerebral deoxygenated blood volume and oxygen extraction fraction: default state. *Magn. Reson. Med.* 57, 115–126.

He, X., Zhu, M., and Yablonskiy, D. A. (2008). Validation of oxygen extraction fraction measurement by qBOLD technique. *Magn. Reson. Med.* 60, 882–888.

Herman, P., Sanganahalli, B. G., Blumenfeld, H., and Hyder, F. (2009). Cerebral oxygen demand for short-lived and steady-state events. *J. Neurochem.* 109(Suppl. 1), 73–79.

Hillman, E. M., Devor, A., Bouchard, M. B., Dunn, A. K., Krauss, G. W., Skoch, J., Bacskai, B. J., Dale, A. M., and Boas, D. A. (2007). Depth-resolved optical imaging and microscopy of vascular compartment dynamics during somatosensory stimulation. *Neuroimage* 35, 89–104.

Hochachka, P. W., Buck, L. T., Doll, C. J., and Land, S. C. (1996). Unifying theory of hypoxia tolerance: molecular/metabolic defense and rescue mechanisms for surviving oxygen lack. *Proc. Natl. Acad. Sci. U.S.A.* 93, 9493–9498.

Hoge, R. D., Atkinson, J., Gill, B., Crelier, G. R., Marrett, S., and Pike, G. B. (1999). Linear coupling between cerebral blood flow and oxygen consumption in activated human cortex. *Proc. Natl. Acad. Sci. U.S.A.* 96, 9403–9408.

Huppert, T. J., Allen, M. S., Benav, H., Jones, P. B., and Boas, D. A. (2007). A multicompartment vascular model for inferring baseline and functional changes in cerebral oxygen metabolism and arterial dilation. *J. Cereb. Blood Flow Metab.* 27, 1262–1279.

Huppert, T. J., Allen, M. S., Diamond, S. G., and Boas, D. A. (2009). Estimating cerebral oxygen metabolism from fMRI with a dynamic multicompartment Windkessel model. *Hum. Brain Mapp.* 30, 1548–1567.

Iadecola, C., and Nedergaard, M. (2007). Glial regulation of the cerebral microvasculature. *Nat. Neurosci.* 10, 1369–1376.

Ibaraki, M., Shimosegawa, E., Miura, S., Takahashi, K., Ito, H., Kanno, I., and Hatazawa, J. (2004). PET measurements of CBF, OEF, and CMRO2 without arterial sampling in hyperacute ischemic stroke: method and error analysis. *Ann. Nucl. Med.* 18, 35–44.

Ito, H., Ibaraki, M., Kanno, I., Fukuda, H., and Miura, S. (2005). Changes in cerebral blood flow and cerebral oxygen metabolism during neural activation measured by positron emission tomography: comparison with blood oxygenation level-dependent contrast measured by functional magnetic resonance imaging. *J. Cereb. Blood Flow Metab.* 25, 371–377.

Ito, H., Kanno, I., Kato, C., Sasaki, T., Ishii, K., Ouchi, Y., Iida, A., Okazawa, H., Hayashida, K., Tsuyuguchi, N., Ishii, K., Kuwabara, Y., and Senda, M. (2004). Database of normal human cerebral blood flow, cerebral blood volume, cerebral oxygen extraction fraction and cerebral metabolic rate of oxygen measured by positron emission tomography with 15O-labelled carbon dioxide or water, carbon monoxide and oxygen: a multicentre study in Japan. *Eur. J. Nucl. Med. Mol. Imaging* 31, 635–643.

Kastrup, A., Kruger, G., Neumann-Haefelin, T., Glover, G. H., and Moseley, M. E. (2002). Changes of cerebral blood flow, oxygenation, and oxidative metabolism during graded motor activation. *Neuroimage* 15, 74–82.

Kim, S. G., Rostrup, E., Larsson, H. B. W., Ogawa, S., and Paulson, O. B. (1999). Determination of relative CMRO2 from CBF and BOLD changes: significant increase of oxygen consumption rate during visual stimulation. *Magn. Reson. Med.* 41, 1152–1161.

Kim, T., Hendrich, K. S., Masamoto, K., and Kim, S. G. (2007). Arterial versus total blood volume changes during neural activity-induced cerebral blood flow change: implication for BOLD fMRI. *J. Cereb. Blood Flow Metab.* 27, 1235–1247.

Kim, T., and Kim, S. G. (2006). Quantification of cerebral arterial blood volume using arterial spin labeling with intravoxel incoherent motion-sensitive gradients. *Magn. Reson. Med.* 55, 1047–1057.

Koehler, R. C., Roman, R. J., and Harder, D. R. (2009). Astrocytes and the regulation of cerebral blood flow. *Trends Neurosci.* 32, 160–169.

Kudomi, N., Hayashi, T., Watabe, H., Teramoto, N., Piao, R., Ose, T., Koshino, K., Ohta, Y., and Iida, H. (2009). A physiologic model for recirculation water correction in CMRO2 assessment with 15O2 inhalation PET. *J. Cereb. Blood Flow Metab.* 29, 355–364.

Kudomi, N., Watabe, H., Hayashi, T., and Iida, H. (2007). Separation of input function for rapid measurement of quantitative CMRO2 and CBF in a single PET scan with a dual tracer administration method. *Phys. Med. Biol.* 52, 1893–1908.

Kuwabara, H., Ohta, S., Brust, P., Meyer, E., and Gjedde, A. (1992). Density of perfused capillaries in living human brain during functional activation. *Prog. Brain Res.* 91, 209–215.

Kwong, K. K., Belliveau, J. W., Chesler, D.A., Goldberg, I. E., Weisskoff, R.M.,Poncelet, B. P., Kennedy, D. N., Hoppel, B. E., Cohen, M. S., Turner, R., Cheng, H. -M., Brady, T. J., and Rosen, B. R. (1992). Dynamic magnetic resonance imaging of human brain activity during primary sensory stimulation. *Proc. Natl. Acad. Sci. U.S.A.* 89, 5675–5679.

Leontiev, O., and Buxton, R. B. (2007). Reproducibility of BOLD, perfusion, and CMRO(2) measurements with calibrated-BOLD fMRI. *Neuroimage* 35, 175–184.

Leontiev, O., Dubowitz, D. J., and Buxton, R. B. (2007). CBF/CMRO2 coupling measured with calibrated BOLD fMRI: sources of bias. *Neuroimage* 36, 1110–1122.

Lin, A. L., Fox, P. T., Yang, Y., Lu, H., Tan, L. H., and Gao, J. H. (2008). Evaluation of MRI models in the measurement of CMRO2 and its relationship with CBF. *Magn. Reson. Med.* 60, 380–389.

Lin, A. L., Fox, P. T., Yang, Y., Lu, H., Tan, L. H., and Gao, J. H. (2009). Time-dependent correlation of cerebral blood flow with oxygen metabolism in activated human visual cortex as measured by fMRI. *Neuroimage* 44, 16–22.

Lu, H., and Ge, Y. (2008). Quantitative evaluation of oxygenation in venous vessels using T2-Relaxation-Under-Spin-Tagging MRI. *Magn. Reson. Med.* 60, 357–363.

Lu, H., Golay, X., Pekar, J. J., and Van Zijl, P. C. (2003). Functional magnetic resonance imaging based on changes in vascular space occupancy. *Magn. Reson. Med.* 50, 263–274.

Lu, H., Golay, X., Pekar, J. J., and Van Zijl, P. C. (2004). Sustained poststimulus elevation in cerebral oxygen utilization after vascular recovery. *J. Cereb. Blood Flow Metab.* 24, 764–770.

Lu, H., Yezhuvath, U. S., and Xiao, G. (2010). Improving fMRI sensitivity by normalization of basal physiologic state. *Hum. Brain Mapp.* 31, 80–87.

Malonek, D., and Grinvald, A. (1996). Interactions between electrical activity and cortical microcirculation revealed by imaging spectroscopy: implications for functional brain mapping. *Science* 272, 551–554.

Mandeville, J. B., Marota, J. J. A., Ayata, C., Zaharchuk, G., Moskowitz, M. A., Rosen, B. R., and Weisskoff, R. M. (1999). Evidence of a cerebrovascular post-arteriole Windkessel with delayed compliance. *J. Cereb. Blood Flow Metab.* 19, 679–689.

Mandeville, J. B., Marota, J. J. A., Kosofsky, B. E., Keltner, J. R., Weissleder, R., Rosen, B. R., and Weisskoff, R. M. (1998). Dynamic functional imaging of relative cerebral blood volume during rat forepaw stimulation. *Magn. Reson. Med.* 39, 615–624.

Marrett, S., and Gjedde, A. (1997). Changes of blood flow and oxygen consumption in visual cortex of living humans. *Adv. Exp. Med. Biol.* 413, 205–208.

Massabuau, J. C. (2003). Primitive, and protective, our cellular oxygenation status? *Mech. Ageing Dev.* 124, 857–863.

Mellon, E. A., Beesam, R. S., Baumgardner, J. E., Borthakur, A., Witschey, W. R. II, and Reddy, R. (2009). Estimation of the regional cerebral metabolic rate of oxygen consumption with proton detected 17O MRI during precision 17O2 inhalation in swine. *J. Neurosci. Methods* 179, 29–39.

Miller, K. L., Luh, W. M., Liu, T. T., Martinez, A., Obata, T., Wong, E. C., Frank, L. R., and Buxton, R. B. (2001). Nonlinear temporal dynamics of the cerebral blood flow response. *Hum. Brain Mapp.* 13, 1–12.

Mintun, M. A., Lundstrom, B. N., Snyder, A. Z., Vlassenko, A. G., Shulman, G. L., and Raichle, M. E. (2001). Blood flow and oxygen delivery to human brain during functional activity: theoretical modeling and experimental data. *Proc. Natl. Acad. Sci. U.S.A.* 98, 6859–6864.

Mintun, M. A., Raichle, M. E., Martin, W. R. W., and Herscovitch, P. (1984). Brain oxygen utilization measured with O-15 radiotracers and positron emission tomography. *J. Nucl. Med.* 25, 177–187.

Mintun, M. A., Vlassenko, A. G., Shulman, G. L., and Snyder, A. Z. (2002). Time-related increase of oxygen utilization in continuously activated human visual cortex. *Neuroimage* 16, 531–537.

Mulligan, S. J., and MacVicar, B. A. (2004). Calcium transients in astrocyte endfeet cause cerebrovascular constrictions. *Nature* 431, 195–199.

Ndubuizu, O., and LaManna, J. C. (2007). Brain tissue oxygen concentration measurements. *Antioxid. Redox Signal.* 9, 1207–1219.

Obata, T., Liu, T. T., Miller, K. L., Luh, W. M., Wong, E. C., Frank, L. R., and Buxton, R. B. (2004). Discrepancies between BOLD and flow dynamics in primary and supplementary motor areas: application of the balloon model to the interpretation of BOLD transients. *Neuroimage* 21, 144–153.

Offenhauser, N., Thomsen, K., Caesar, K., and Lauritzen, M. (2005). Activity-induced tissue oxygenation changes in rat cerebellar cortex: interplay of postsynaptic activation and blood flow. *J. Physiol.* 565, 279–294.

Ogawa, S., Menon, R. S., Tank, D. W., Kim, S.-G., Merkle, H., Ellerman, J. M., and Ugurbil, K. (1993). Functional brain mapping by blood oxygenation level-dependent contrast magnetic resonance imaging: a comparison of signal characteristics with a biophysical model. *Biophys. J.* 64, 803–812.

Ogawa, S., Tank, D. W., Menon, R., Ellermann, J. M., Kim, S.-G., Merkle, H., and Ugurbil, K. (1992). Intrinsic signal changes accompanying sensory stimulation: functional brain mapping with magnetic resonance imaging. *Proc. Natl. Acad. Sci. U.S.A.* 89, 5951–5955.

Ohta, S., Meyer, E., Thompson, C. J., and Gjedde, A. (1992). Oxygen consumption of the living human brain measured after a single inhalation of positron emitting oxygen. *J. Cereb. Blood Flow Metab.* 12, 179–192.

Pasley, B. N., Inglis, B. A., and Freeman, R. D. (2007). Analysis of oxygen metabolism implies a neural origin for the negative BOLD response in human visual cortex. *Neuroimage* 36, 269–276.

Paulson, O. B., Hasselbalch, S. G., Rostrup, E., Knudsen, G. M., and Pelligrino, D. (2010). Cerebral blood flow response to functional activation. *J. Cereb. Blood Flow Metab.* 30, 2–14.

Perthen, J. E., Lansing, A. E., Liau, J., Liu, T. T., and Buxton, R. B. (2008). Caffeine-induced uncoupling of cerebral blood flow and oxygen metabolism: a calibrated BOLD fMRI study. *Neuroimage* 40, 237–247.

Phelps, M. E., Kuhl, D. E., and Mazziotta, J. C. (1981). Metabolic mapping of the brain's response to visual stimulation: studies in humans. *Science* 211, 1445–1448.

Piilgaard, H., and Lauritzen, M. (2009). Persistent increase in oxygen consumption and impaired neurovascular coupling after spreading depression in rat neocortex. *J. Cereb. Blood Flow Metab.* 29, 1517–1527.

Prichard, J., Rothman, D., Novotny, E., Petroff, O., Kuwabara, T., Avison, M., Howseman, A., Hanstock, C., and Shulman, R. (1991). Lactate rise detected by 1H NMR in human visual cortex during physiologic stimulation. *Proc. Natl. Acad. Sci. U.S.A.* 88, 5829–5831.

Restom, K., Perthen, J. E., and Liu, T. T. (2008). Calibrated fMRI in the medial temporal lobe during a memory-encoding task. *Neuroimage* 40, 1495–1502.

Roche-Labarbe, N., Carp, S. A., Surova, A., Patel, M., Boas, D. A., Grant, P. E., and Franceschini, M. A. (2010). Noninvasive optical measures of CBV, StO(2), CBF index, and rCMRO(2) in human premature neonates' brains in the first six weeks of life. *Hum. Brain Mapp.* 31, 341–352.

Ronen, I., Lee, J. H., Merkle, H., Ugurbil, K., and Navon, G. (1997). Imaging H2(17)O distribution in a phantom and measurement of metabolically produced H2(17)O in live mice by proton NMR. *NMR Biomed.* 10, 333–340.

Ronen, I., Merkle, H., Ugurbil, K., and Navon, G. (1998). Imaging of H217O distribution in the brain of a live rat by using proton-detected 17O MRI. *Proc. Natl. Acad. Sci. U.S.A.* 95, 12934–12939.

Ronen, I., and Navon, G. (1994). A new method for proton detection of H2(17)O with potential applications for functional MRI. *Magn. Reson. Med.* 32, 789–793.

Rostrup, E., Knudsen, G. M., Law, I., Holm, S., Larsson, H. B., and Paulson, O. B. (2005). The relationship between cerebral blood flow and volume in humans. *Neuroimage* 24, 1–11.

Sadaghiani, S., Ugurbil, K., and Uludag, K. (2009). Neural activity-induced modulation of BOLD poststimulus undershoot independent of the positive signal. *Magn. Reson. Imaging* 27, 1030–1038.

Semenza, G. L. (2009). Regulation of oxygen homeostasis by hypoxia-inducible factor 1. *Physiology (Bethesda)* 24, 97–106.

Shmuel, A., Yacoub, E., Pfeuffer, J., Van de Moortele, P. F., Adriany, G., Hu, X., and Ugurbil, K. (2002). Sustained negative BOLD, blood flow and oxygen consumption response and its coupling to the positive response in the human brain. *Neuron* 36, 1195–1210.

Sicard, K. M., and Duong, T. Q. (2005). Effects of hypoxia, hyperoxia, and hypercapnia on baseline and stimulus-evoked BOLD, CBF, and CMRO2 in spontaneously breathing animals. *Neuroimage* 25, 850–858.

Sokoloff, L., Reivich, M., Kennedy, C., Rosiers, M. H. D., Patlak, C. S., Pettigrew, K. D., Sakurada, O., and Shinohara, M. (1977). The [14-C] deoxyglucose method for the measurement of local cerebral glucose utilization: theory, procedure, and normal values in the conscious and anesthetized albino rat. *J. Neurochem.* 28, 897–916.

Stefanovic, B., Warnking, J. M., Kobayashi, E., Bagshaw, A. P., Hawco, C., Dubeau,

F., Gotman, J., and Pike, G. B. (2005). Hemodynamic and metabolic responses to activation, deactivation and epileptic discharges. *Neuroimage* 28, 205–215.

Stefanovic, B., Warnking, J. M., and Pike, G. B. (2004). Hemodynamic and metabolic responses to neuronal inhibition. *Neuroimage* 22, 771–778.

St Lawrence, K. S., Ye, F. Q., Lewis, B. K., Frank, J. A., and McLaughlin, A. C. (2003). Measuring the effects of indomethacin on changes in cerebral oxidative metabolism and cerebral blood flow during sensorimotor activation. *Magn. Reson. Med.* 50, 99–106.

Thompson, J. K., Peterson, M. R., and Freeman, R. D. (2003). Single-neuron activity and tissue oxygenation in the cerebral cortex. *Science* 299, 1070–1072.

Thompson, J. K., Peterson, M. R., and Freeman, R. D. (2004). High-resolution neurometabolic coupling revealed by focal activation of visual neurons. *Nat. Neurosci.* 7, 919–920.

Thompson, J. K., Peterson, M. R., and Freeman, R. D. (2005). Separate spatial scales determine neural activity-dependent changes in tissue oxygen within central visual pathways. *J. Neurosci.* 25, 9046–9058.

Thomsen, K., Piilgaard, H., Gjedde, A., Bonvento, G., and Lauritzen, M. (2009). Principal cell spiking, postsynaptic excitation, and oxygen consumption in the rat cerebellar cortex. *J. Neurophysiol.* 102, 1503–1512.

Uludag, K., and Buxton, R. B. (2004). Measuring the effects of indomethacin on changes in cerebral oxidative metabolism and cerebral blood flow during sensorimotor activation. *Magn. Reson. Med.* 51, 1088–1089; author reply 1090.

Uludag, K., Dubowitz, D. J., Yoder, E. J., Restom, K., Liu, T. T., and Buxton, R. B. (2004). Coupling of cerebral blood flow and oxygen consumption during physiological activation and deactivation measured with fMRI. *Neuroimage* 23, 148–155.

Uludag, K., Muller-Bierl, B., and Ugurbil, K. (2009). An integrative model for neuronal activity-induced signal changes for gradient and spin echo functional imaging. *Neuroimage* 48, 150–165.

Vafaee, M. S., and Gjedde, A. (2000). Model of blood-brain transfer of oxygen explains nonlinear flow-metabolism coupling during stimulation of visual cortex. *J. Cereb. Blood Flow Metab.* 20, 747–754.

Vafaee, M. S., Meyer, E., Marrett, S., Paus, T., Evans, A. C., and Gjedde, A. (1999). Frequency-dependent changes in cerebral metabolic rate of oxygen during activation of human visual cortex. *J. Cereb. Blood Flow Metab.* 19, 272–277.

Valabregue, R., Aubert, A., Burger, J., Bittoun, J., and Costalat, R. (2003). Relation between cerebral blood flow and metabolism explained by a model of oxygen exchange. *J. Cereb. Blood Flow Metab.* 23, 536–545.

Vanderkooi, J. M., Erecinska, M., and Silver, I. A. (1991). Oxygen in mammalian tissue: methods of measurement and affinities of various reactions. *Am. J. Physiol.* 260, C1131–C1150.

Ward, J. P. (2008). Oxygen sensors in context. *Biochim. Biophys. Acta* 1777, 1–14.

Wilson, D. F., Erecinska, M., Drown, C., and Silver, I. A. (1979). The oxygen dependence of cellular energy metabolism. *Arch. Biochem. Biophys.* 195, 485–493.

Wong, E. C., Buxton, R. B., and Frank, L. R. (1997). Implementation of quantitative perfusion imaging techniques for functional brain mapping using pulsed arterial spin labeling. *NMR Biomed.* 10, 237–249.

Xu, F., Ge, Y., and Lu, H. (2009). Noninvasive quantification of whole-brain cerebral metabolic rate of oxygen (CMRO(2)) by MRI. *Magn. Reson. Med.* 62, 141–148.

Yablonskiy, D. A., Ackerman, J. J., and Raichle, M. E. (2000). Coupling between changes in human brain temperature and oxidative metabolism during prolonged visual stimulation. *Proc. Natl. Acad. Sci. U.S.A.* 97, 7603–7608.

Yablonskiy, D. A., and Haacke, E. M. (1994). Theory of NMR signal behavior in magnetically inhomogeneous tissues: the static dephasing regime. *Magn. Reson. Med.* 32, 749–763.

Yacoub, E., Ugurbil, K., and Harel, N. (2006). The spatial dependence of the poststimulus undershoot as revealed by high-resolution BOLD- and CBV-weighted fMRI. *J. Cereb. Blood Flow Metab.* 26, 634–644.

Yucel, M. A., Devor, A., Akin, A., and Boas, D. A. (2009). The possible role of CO_2 in producing a post-stimulus CBF and BOLD undershoot. *Front Neuroenerg.* 1:7. doi: 10.3389/neuro.14.007.2009.

Zappe, A. C., Uludag, K., Oeltermann, A., Ugurbil, K., and Logothetis, N. K. (2008). The influence of moderate hypercapnia on neural activity in the anesthetized nonhuman primate. *Cereb. Cortex* 18, 2666–2673.

Zhang, N., Zhu, X. H., Lei, H., Ugurbil, K., and Chen, W. (2004). Simplified methods for calculating cerebral metabolic rate of oxygen based on ^{17}O magnetic resonance spectroscopic imaging measurement during a short $^{17}O_2$ inhalation. *J. Cereb. Blood Flow Metab.* 24, 840–848.

Zhao, F., Jin, T., Wang, P., and Kim, S. G. (2007). Improved spatial localization of post-stimulus BOLD undershoot relative to positive BOLD. *Neuroimage* 34, 1084–1092.

Zheng, Y., Pan, Y., Harris, S., Billings, S., Coca, D., Berwick, J., Jones, M., Kennerley, A., Johnston, D., Martin, C., Devonshire, I. M., and Mayhew, J. (2010). A dynamic model of neurovascular coupling: Implications for blood vessel dilation and constriction. *Neuroimage*. (in press).

Zhu, X. H., Zhang, N., Zhang, Y., Zhang, X., Ugurbil, K., and Chen, W. (2005). In vivo ^{17}O NMR approaches for brain study at high field. *NMR Biomed.* 18, 83–103.

Zhu, X. H., Zhang, X., Zhang, N., Zhang, Y., Strupp, J., Ugurbil, K., and Chen, W. (2006). "High-field ^{17}O study of 3D CMRO2 imaging in human visual cortex," in *ISMRM 14th Annual Meeting*, Seattle, p. 409.

Zhu, X. H., Zhang, Y., Tian, R. X., Lei, H., Zhang, N., Zhang, X., Merkle, H., Ugurbil, K., and Chen, W. (2002). Development of (17)O NMR approach for fast imaging of cerebral metabolic rate of oxygen in rat brain at high field. *Proc. Natl. Acad. Sci. U.S.A.* 99, 13194–13199.

Zonta, M., Angulo, M. C., Gobbo, S., Rosengarten, B., Hossmann, K. A., Pozzan, T., and Carmignoto, G. (2003). Neuron-to-astrocyte signaling is central to the dynamic control of brain microcirculation. *Nat. Neurosci.* 6, 43–50.

Conflict of Interest Statement: The author declares that the research was conducted in the absence of any commercial or financial relationships that could be construed as a potential conflict of interest.

Received: 16 March 2010; paper pending published: 15 April 2010; accepted: 21 May 2010; published online: 17 June 2010.

Citation: Buxton RB (2010) Interpreting oxygenation-based neuroimaging signals: the importance and the challenge of understanding brain oxygen metabolism. Front. Neuroenerg. ***2****:8. doi: 10.3389/fnene.2010.00008*

frontiers in
NEUROENERGETICS

REVIEW ARTICLE
published: 17 June 2010
doi: 10.3389/fnene.2010.00010

Neurovascular photoacoustic tomography

Song Hu and Lihong V. Wang*

Department of Biomedical Engineering, Optical Imaging Laboratory, Washington University in St. Louis, St. Louis, MO, USA

Edited by:
David Boas, Massachusetts General Hospital, USA; Massachusetts Institute of Technology, USA; Harvard Medical School, USA

Reviewed by:
Sava Sakadzic, Harvard University, USA; Myles Jones, University of Sheffield, UK

****Correspondence:***
Lihong V. Wang, Department of Biomedical Engineering, Optical Imaging Laboratory, Washington University in St. Louis, One Brookings Drive, St. Louis, MO 63130-4899, USA. e-mail: lhwang@biomed.wustl.edu

Neurovascular coupling refers to the relationship between neuronal activities and downstream hemodynamic responses. Photoacoustic tomography (PAT), enabling comprehensive label-free imaging of hemodynamic activities with highly scalable penetration and spatial resolution, has great potential in the study of neurovascular coupling. In this review, we first introduce the technical basis of hemodynamic PAT – including label-free quantification of total hemoglobin concentration, blood oxygenation, and blood flow – as well as its applications in hemodynamic monitoring. Then, we demonstrate the potential application of PAT in neurovascular imaging by highlighting representative studies on cerebral vascular responses to whisker stimulation and Alzheimer's disease. Finally, potential research directions and associated technical challenges are discussed.

Keywords: photoacoustic tomography, neurovascular coupling, hemodynamics, whisker stimulation, Alzheimer's disease

BACKGROUND AND MOTIVATION

Advances in brain imaging and sensing have greatly facilitated the understanding of neuronal activity and energetics. One classic technique is to use a microelectrode to directly record the activity of cortical neurons. However, this procedure is invasive, thereby limiting the number of recordings and discouraging chronic studies. Alternatively, the relationship between local neuronal activities and subsequent changes in cerebral hemodynamics, which is referred to as neurovascular coupling, has been widely used as a non-invasive pathway to study brain functions (Malonek and Grinvald, 1996; Wang et al., 2003). Clinical neuroimaging modalities (Girouard and Iadecola, 2006) [such as magnetic resonance imaging (MRI) and positron emission tomography (PET)] and high-resolution optical microscopy technologies (Devor et al., 2007; Srinivasan et al., 2009) [such as two-photon microscopy (TPM) and optical coherence tomography (OCT)] provide insights into neurovascular coupling at two distinct spatial scales. Photoacoustic tomography (PAT), a fast-growing technology capable of multi-scale imaging (Wang, 2009), is able to bridge the resolution and penetration gaps between clinical modalities at the organ level and optical microscopy technologies at the cellular level. Utilizing diffraction-limited optical focusing, optical-resolution photoacoustic microscopy (OR-PAM), a new embodiment of PAT, has achieved cellular (Hu et al., 2010) and even subcellular resolution (Maslov et al., 2010) *in vivo*. With more relaxed acoustic focusing, millimeter penetration with a tissue level resolution and centimeter penetration with an organ level resolution have been demonstrated by acoustic-resolution photoacoustic microscopy (AR-PAM) and macroscopy (AR-PAMac), respectively (Zhang et al., 2006; Song and Wang, 2007). Despite higher economic and computational expenses, ultrasound array based photoacoustic computed tomography (PACT) (Gamelin et al., 2008; Zemp et al., 2008) can improve the temporal resolution enough to enable real-time monitoring of acute hemodynamics while maintaining a similar penetration-to-resolution ratio. **Figure 1** illustrates the high scalability of PAT, from the subcellular to the organ level. "Resolution" in the horizontal axis represents both the lateral and the axial resolutions. The axial resolution of PAT depends on time-resolved ultrasonic detection. It is directly related to the transducer bandwidth, which is usually linearly proportional to the center frequency of the transducer, f_0. Thus, better axial resolution is achieved with greater f_0, i.e., the axial resolution is inversely proportional to f_0. The maximum penetration depth is also inversely proportional to f_0 because the acoustic attenuation is approximately linearly proportional to f_0. Within the optical penetration limit, the relative axial resolution – defined as the ratio of the penetration depth to the axial resolution – is roughly a constant of 200 (the slope of the red line in **Figure 1**), considered high enough to provide good-quality images (Wang, 2009). The lateral resolution of PAT is from optical or ultrasonic focusing, which depends on the center wavelength of the optical illumination or the acoustic detection and can deteriorate in the presence of strong optical or acoustic scattering of biological tissues. Besides the capability of multi-scale imaging with a single modality, PAT enables label-free vascular imaging with a high signal-to-noise ratio (SNR) by capitalizing on the optical absorption of endogenous hemoglobin, the primary carrier of oxygen in the blood. This unique feature allows PAT to avoid possible alterations to the intrinsic hemodynamics caused by exogenous angiographic agents (Hu and Wang, 2010) and, more importantly, to delineate vascular networks perfused with red blood cells (RBC), the functional vascular subset supporting neuronal activities and tissue metabolism (Hu et al., 2010). This article is mainly focused on the technical advantages of PAT for neurovascular imaging, supported with pilot studies. Potential prospects and associated technical challenges are also presented.

TECHNICAL BASIS OF PAT FOR NEUROVASCULAR IMAGING

THREE MAJOR EMBODIMENTS

Similar to most of biomedical imaging modalities, PAT is an excitation-probing process. The typical photoacoustic excitation source is a nanosecond short-pulsed laser, although an intensity-modulated continuous-wave laser can also be used to produce photoacoustic signals (Maslov and Wang, 2008). Endogenous or exogenous optical

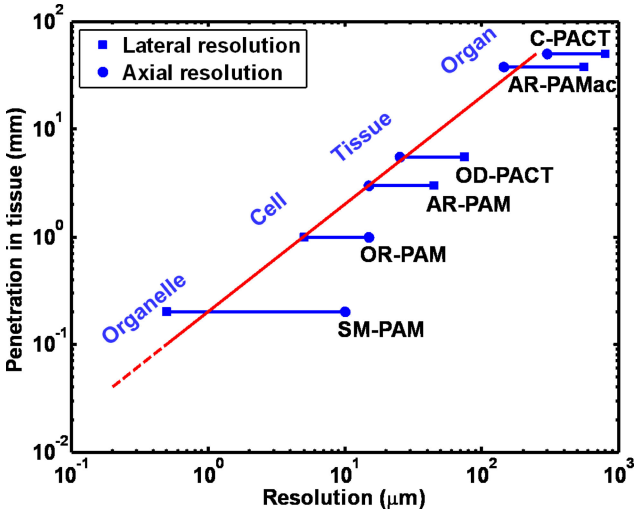

FIGURE 1 | Multi-scale photoacoustic tomography with consistent imaging contrasts. SM-PAM: sub-micron photoacoustic microscopy (Maslov et al., 2010); OR-PAM: optical-resolution photoacoustic microscopy (Maslov et al., 2008); AR-PAM: acoustic-resolution photoacoustic microscopy (Zhang et al., 2006); OD-PACT: optical-detection-based photoacoustic computed tomography (Zhang et al., 2008a); AR-PAMac: acoustic-resolution photoacoustic macroscopy (Song and Wang, 2007); C-PACT: circular photoacoustic computed tomography (Ku and Wang, 2005).

absorbers (i.e., pigments or chromophores) in biological tissues are excited by the deposited photons, inducing thermal expansion. Consequently, these photoacoustic sources emit ultrasonic waves (referred to as photoacoustic waves). The photoacoustic waves are then detected by a high-frequency ultrasonic transducer to form a volumetric mapping of the spatially distributed photoacoustic sources, which are related to the optical absorption or molecular properties of the tissue (Wang, 2008b).

According to the mechanisms of optical illumination and ultrasonic detection, PAT for neurovascular imaging can be classified into three major embodiments: PACT, AR-PAM and OR-PAM. **Figure 2** shows their schematics, along with representative label-free cerebral vascular images acquired by each embodiment. In PACT (**Figure 2A-1**), a pulsed laser beam from a wavelength-tunable laser system is expanded and homogenized to provide uniform illumination covering the entire region of interest (ROI). A circular-scanning single-element ultrasonic transducer (Wang et al., 2003) or a stationary transducer array (Li et al., 2010) is placed around the tissue to receive photoacoustic waves. With a generalized inverse spherical Radon transform, the spatial distribution of the photoacoustic sources can be reconstructed within the limits of acoustic resolution (Xu and Wang, 2006). Alternatively, the computational reconstruction can be avoided by point-scanning the dual foci of optical illumination and ultrasonic detection, which is referred to as photoacoustic microscopy (PAM). In PAM, the optical and

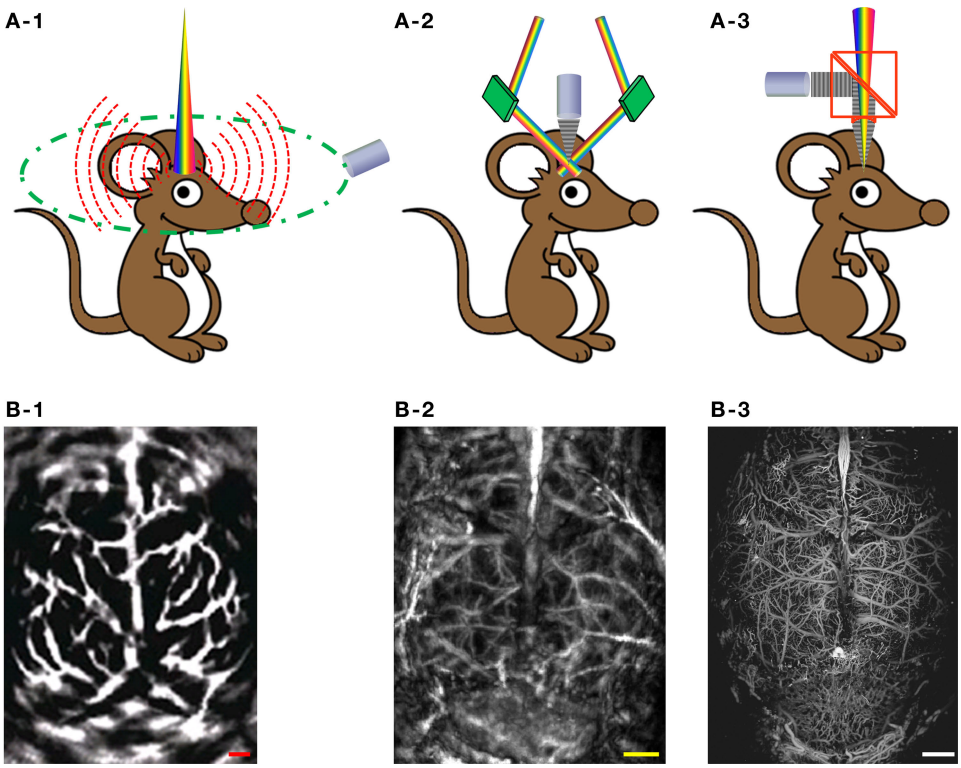

FIGURE 2 | Three major embodiments of PAT for label-free cerebral vascular imaging. (A-1) Schematic of PACT. **(A-2)** Schematic of dark-field AR-PAM. **(A-3)** Schematic of OR-PAM. **(B-1)** PACT image of the cortical vasculature in a living adult rat with both the scalp and the skull intact. Excerpted from (Wang et al., 2003). **(B-2)** Dark-field AR-PAM image of the cortical vasculature in a living adult mouse with both the scalp and the skull intact. Excerpted from (Stein et al., 2008). **(B-3)** OR-PAM image of the cortical vasculature in a living adult mouse with the scalp removed and the skull intact. All scale bars are 1 mm.

ultrasonic foci are configured coaxially and confocally, and the lateral resolution is dominated by the more tightly focused part. In AR-PAM, ultrasound detection is tightly focused to achieve a relatively high spatial resolution in the optical diffusive regime (Wang and Wu, 2007). **Figure 2A-2** illustrates the most mature version of AR-PAM with dark-field optical illumination (Zhang et al., 2006). In the dark-field system, a pulsed laser beam is reshaped by a conical lens to form a ring pattern and then is weakly focused beneath the tissue to overlap the tight ultrasonic focus. The optical focus is 2 mm in diameter, which is much wider than the 50-μm ultrasonic focus; moreover, the optically dark zone above the tissue surface is ideal for placing the ultrasonic transducer in the acoustic/optical confocal configuration. To provide more detailed insight into neurovascular coupling, we can further refine the spatial resolution of PAT down to the capillary level, where the PAM technology is referred to as OR-PAM (Hu et al., 2009a). In **Figure 2A-3**, a diffraction-limited bright-field optical illumination, which is ten times smaller in diameter than the acoustic focus, is adopted to achieve optical resolution. A home-made acoustic-optical beam splitter, consisting of two right-angle prisms and a thin layer of silicone oil in between, aligns the optical illumination and the acoustic detection (Maslov et al., 2008). With OR-PAM, cortical microvasculature as small as single capillaries can be clearly resolved in a living adult mouse through the intact skull (**Figure 2B-3**). However, the tissue penetration of OR-PAM is restricted to ~1 mm due to the high optical scattering, and therefore the scalp needs to be removed. Taking advantage of the tissue property that ultrasonic scattering per unit path length is 100–1000 times weaker than optical scattering, AR-PAM is able to penetrate both the scalp and the skull of an adult mouse, at the expense of spatial resolution (**Figure 2B-2**) (Stein et al., 2008). With a reduced ultrasonic frequency, PACT can even penetrate through the scalp and skull of an adult rat (**Figure 2B-1**) (Wang et al., 2003).

LABEL-FREE PHOTOACOUSTIC IMAGING AND MONITORING OF HEMODYNAMICS

For label-free vascular imaging, PAT senses the two major endogenous chromophores in the blood stream, oxyhemoglobin (HbO_2) and deoxyhemoglobin (HbR). Taking advantage of the oxygenation dependence in the optical absorption spectrum of hemoglobin, PAT at multiple (at least two) optical wavelengths can quantify the relative concentrations of HbO_2 and HbR within single blood vessels, and subsequently the oxygen saturation (sO_2) and the total relative concentration (HbT) of hemoglobin (Hu et al., 2009a; Hu and Wang, 2010). Alternatively, relative HbT can also be directly measured by using a single isosbestic point in the hemoglobin absorption spectra, where the molar extinction coefficients of HbR and HbO_2 are equal and thus the photoacoustic signal reflects the HbT but not the sO_2. Among the mainstream neuroimaging modalities, only near-infrared spectroscopy (NIRS) and blood-oxygen-level-dependent (BOLD) MRI can assess sO_2 with endogenous contrasts. However, NIRS suffers from poor spatial resolution, and BOLD MRI is sensitive only to HbR (Ogawa et al., 1990; Bunce et al., 2006).

Figures 3A–C show non-invasive AR-PAM monitoring of blood-oxygenation dynamics in a living mouse cortex under hypoxic challenge (both the scalp and the skull were kept intact). The initial state of the experimental animal was hyperoxia, which served as a baseline. Then, the animal was subjected to three isolated hypoxic challenges by switching the inhalation gas from pure oxygen to hypoxic gas (5% O_2, 5% CO_2, and 90% N_2). According to the mouse cortex image (**Figure 3A**), a cross section containing five major vessels (**Figure 3B**) was selected for hemodynamic imaging. A pixelwise normalization of the cross-sectional image acquired at a HbR-dominant wavelength (561 nm) to the oxygen-insensitive reference image acquired at an isosbestic wavelength (570 nm) was used to measure the hemodynamic response (Stein et al., 2009). The normalized dynamic oxygenation profile for each of the five vessels (**Figure 3C**) clearly shows a dramatic increase (13–28%) in the ratiometric photoacoustic signal in response to each hypoxic challenge, which indicates the deoxygenation of hemoglobin.

Taking advantage of the single-RBC resolution and sensitivity of OR-PAM, we can also accurately trace hemodynamic changes in microvessel diameter, such as vasomotion and vasodilation in response to tissue oxygen variation **(Figures 3D–G)** (Hu et al., 2009b). Similar to the oxygenation dynamic monitoring experiment, a cross section containing an arteriole–venule pair was selected according to the sO_2 mapping acquired using dual-wavelength OR-PAM measurements (A1 and V1 in **Figure 3E**) for a 70-min monitoring. During the cross-sectional monitoring, the physiological state of the animal was switched between hyperoxia and hypoxia (indicated by the red and blue time segments, respectively, in **Figure 3F**) by alternating the inhalation gas between pure oxygen and hypoxic gas (5% O_2, 5% CO_2, and 90% N_2). Vasomotion under hyperoxia and vasodilation under hypoxia are clearly represented by the diameter oscillation and expansion of the vessel cross section, respectively (**Figure 3F**). Compared with arteriole A1, venule V1 had a much weaker vasomotion but a similar oscillation frequency (**Figure 3G**).

Besides the above two important hemodynamic parameters that are closely associated with neuronal metabolism, blood flow is also a key parameter in the study of neurovascular physiology and diseases, such as stroke. Recently, blood flow measurement using Doppler photoacoustics has been actively studied (Brunker and Beard, 2010; Fang et al., 2007a,b; Fang and Wang, 2009; Yao and Wang, 2010). The photoacoustic Doppler effect was first observed in small light-absorbing particles flowing in clear media (Fang et al., 2007a) and later extended to tissue-mimicking phantoms (Brunker and Beard, 2010; Fang et al., 2007b; Fang and Wang, 2009) and *in vivo* (Yao and Wang, 2010). Doppler photoacoustics, similar to traditional photoacoustics, involves both optics and ultrasound. Whenever there is a relative motion between the photoacoustic source and the ultrasonic transducer, the detected photoacoustic signal undergoes a Doppler frequency shift. Doppler photoacoustics bridges the spatial gap between Doppler optics and Doppler ultrasound. Because RBCs have a much higher optical absorption than the extravascular background (Wang, 2008a) it also can potentially lower background noise and increase detection sensitivity.

The cerebral metabolic rate of oxygen consumption ($CMRO_2$) is essential for investigating brain functions and visualizing neuronal activities. Combining the currently available photoacoustic measurements of HbT, sO_2, vessel diameter, and blood flow, PAT

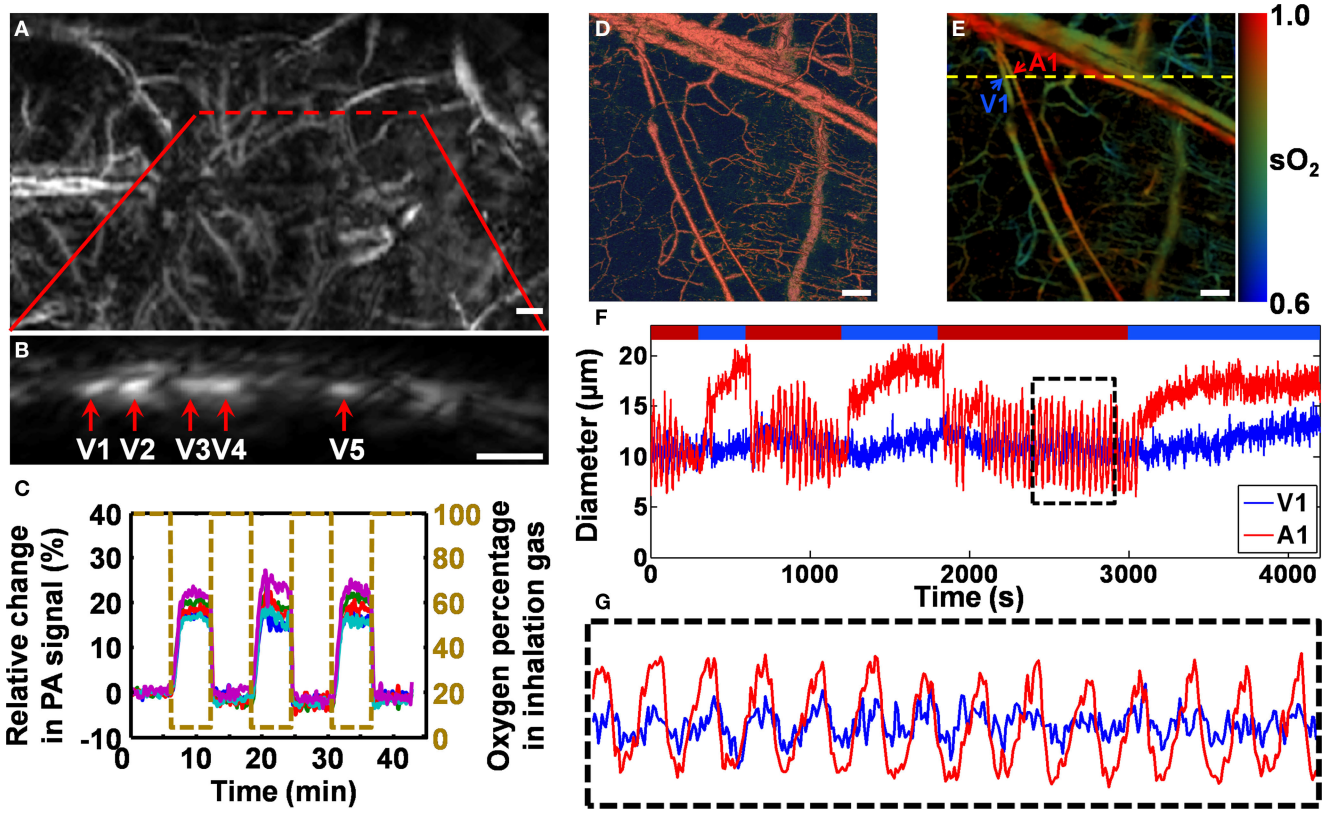

FIGURE 3 | *In vivo* label-free photoacoustic monitoring of hemodynamics in rodent models. (A–C) AR-PAM monitoring of blood-oxygenation dynamics in a living mouse cortex under hypoxic challenge. Excerpted from (Stein et al., 2009). **(A)** Photoacoustic image of the mouse cortex vasculature through the intact scalp and skull. The red dashed line indicates the area over which the cross-sectional scanning was performed. **(B)** A representative cross-sectional image along the red dashed line in **(A)**. **(C)** Ratiometric photoacoustic signals generated by a pixelwise normalization of the HbR data acquired at 561 nm to the oxygen-insensitive reference data acquired at 570 nm. **(D–G)** OR-PAM monitoring of vasomotion and vasodilation in response to switching the physiological state between hyperoxia and hypoxia. Excerpted from (Hu et al., 2009b). **(D)** Structural image of a nude mouse ear *in vivo* acquired at 570 nm. **(E)** Vessel-by-vessel sO_2 mapping of the same region using dual-wavelength measurements at 570 and 578 nm. The calculated sO_2 values are shown in the color bar. A1 indicates a representative arteriole; V1 indicates a representative venule; the yellow dashed line shows the position of the cross-sectional scan. **(F)** Changes in the arteriolar and venular diameters in response to switching the physiological state. **(G)** Close-up of the boxed region in **(F)**. Scale bars are 500 μm in **(A)** and **(B)**, and 50 μm in **(D)** and **(E)**.

has the potential to become the first single modality that enables independent quantification of $CMRO_2$ at high spatial resolution without the use of an exogenous contrast agent (Wang, 2008a).

PILOT STUDIES

CEREBRAL VASCULAR RESPONSES TO WHISKER STIMULATION

In rodent models, barrels of the somatosensory cortex are spatially and functionally discrete, each corresponding to a single contralateral whisker, forming an ideal system for the study of neurovascular coupling. In one of the very first neurovascular studies using photoacoustics, Wang et al. (2003) used a single-element transducer based PACT system to observe the hemodynamic counterparts of neuronal activities in response to mechanical stimulation of the whisker pad of a rat.

As shown in **Figure 4**, to maximize the hemodynamic response due to whisker stimulation, all whiskers on the right side of the rat snout were deflected simultaneously at a distance of 10 mm from the whisker pad, with a stimulation frequency of 10 Hz and an oscillation amplitude of 8 mm. The whisker stimulation started 0.5 s before the photoacoustic data collection at each scanning position and lasted for 4.5 s. Subtracting the control image without whisker stimulation from the functional image with whisker stimulation produced a functional map of the vascular response evoked by the whisker stimulation. The PACT-imaged vascular patterns (in gray in **Figure 4**) in the activated regions match well with the functional differential signals (in blue and red in **Figure 4**), indicating that the functional signals detected by PACT did represent the hemodynamic changes induced by whisker stimulation. It is worth pointing out that with higher-resolution systems, such as OR-PAM, the activity of individual barrels may be visualized.

INTRAVITAL IMAGING OF AMYLOID PLAQUES

Amyloid plaques are hypothesized to play a major role in the pathogenesis of Alzheimer's disease (AD), but the underlying mechanisms are still elusive and need extensive animal studies. Although clinical neuroimaging technologies such as PET have improved the diagnosis of AD (Klunk et al., 2004), their spatial resolutions are inadequate for imaging subtle microscopic changes due to AD progression or treatment. OR-PAM, capable of detecting

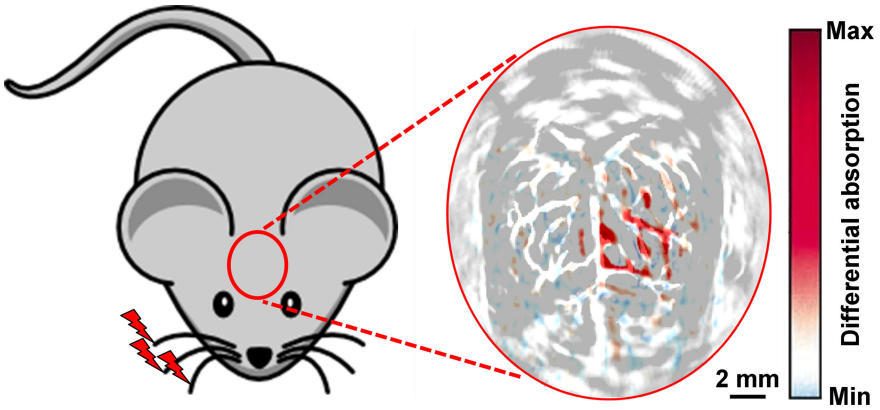

FIGURE 4 | *In vivo* PACT image of the cerebral vascular response to right-side whisker stimulation in an adult rat model, acquired with both the scalp and the skull intact. The hemodynamic response due to whisker stimulation is shown in blue and red and is superimposed on the cortical vascular image shown in gray. Excerpted from (Wang et al., 2003).

not only endogenous but also exogenous optical absorption contrasts with superb sensitivity and cellular level resolution, provides a potential solution.

Recently, we validated OR-PAM imaging of amyloid plaques with established fluorescence microscopy and TPM (Hu et al., 2009c). For *in vitro* validation, a Congo red-stained brain section from a 10-month-old APPswe/PS1dE9 (APP/PS1) mouse was first imaged using conventional fluorescence microscopy (**Figure 5A**). Then, a 1×1 mm^2 ROI (enclosed by a red dashed box in **Figure 5A**) was imaged by OR-PAM for comparison (inset, **Figure 5A**). All the amyloid plaques visualized using fluorescence microscopy were also observed with OR-PAM, suggesting that OR-PAM has the sensitivity and spatial resolution required to image amyloid plaques. For *in vivo* validation, a 10-month-old APP/PS1 mouse was injected with Congo red through the cisterna magna. Twenty-four hours after injection, an open-skull cranial window was created over the parietal cortex, and dye labeling was confirmed by fluorescence microscopy (**Figure 5B**). A ROI (enclosed by a yellow dashed box in **Figure 5B**) containing a variety of amyloid plaques and blood vessels was selected for dual-wavelength (523 and 570 nm) imaging with OR-PAM, followed by imaging with TPM. Images acquired using OR-PAM and TPM were directly compared, revealing excellent correlation in plaque distribution (arrows in **Figures 5C,D**). It should be noted that the imaged plaque sizes are slightly different in the two imaging modalities, which is likely due to the differences in imaging contrast and sensitivity between the two techniques. However, since each plaque can serve as its own reference, measures of relative plaque growth are expected to be similar.

Some other photoacoustic studies on neurovascular disease and physiology, such as epilepsy and hindpaw stimulation in rodent models, are not covered here (Stein et al., 2008; Zhang et al., 2008b).

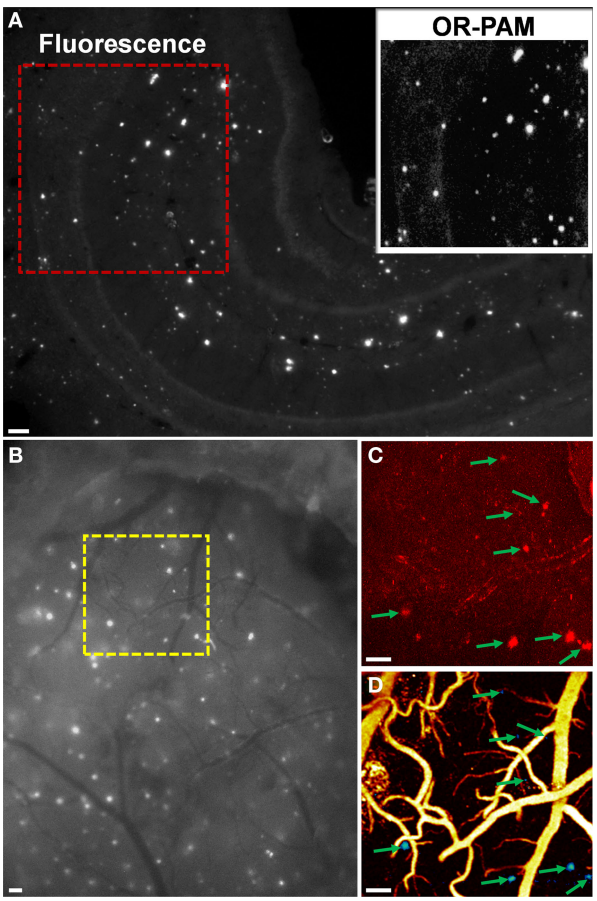

FIGURE 5 | (A) Entire hippocampus of a Congo red-stained brain section from a 10-month-old APP/PS1 mouse imaged using conventional fluorescence microscopy. Inset: OR-PAM image of the red-boxed region for comparison. **(B)** Exposed cortical region of a Congo red-injected 10-month-old APP/PS1 mouse imaged using conventional fluorescence microscopy through a cranial window. The region of interest marked by the yellow dashed box was imaged by TPM in **(C)** and dual-wavelength OR-PAM in **(D)**, respectively. In **(D)**, amyloid plaques are colored blue and blood vessels are colored yellow. Arrows indicate plaques. All scale bars are 100 μm. Excerpted from (Hu et al., 2009c).

PROSPECTS AND CHALLENGES

Providing high-sensitivity label-free vascular imaging and characterization at multiple spatial scales, PAT holds the potential to play an important role in neurovascular studies. Several future prospects and associated challenges are envisaged.

(i) Real-time PAT. Potential methods include galvanometer based optical-scanning OR-PAM (Xie et al., 2009), voice coil based mechanical-scanning AR-PAM (Harrison et al., 2009), and ultrasound array based non-scanning PACT (Gamelin et al., 2008; Li et al., 2010). Although the temporal resolution of PAT has been advanced to as fast as ~1 frame/s (Li et al., 2010), it is still not fast enough to catch some fast neurovascular responses. Two major bottlenecks are the rates of data acquisition and laser repetition (Hu and Wang, 2010).

(ii) $CMRO_2$ quantification. For a localized vascular system, we can estimate the relative $CMRO_2$ using

$$CMRO_2 \propto sO_2^{in} \cdot [HbT]_{in} \cdot A_{in} \cdot v_{in} - sO_2^{out} \cdot [HbT]_{out} \cdot A_{out} \cdot v_{out}, \quad (1)$$

where $sO_2^{in/out}$, $[HbT]^{in/out}$, $A_{in/out}$, and $v_{in/out}$ are the sO_2, relative HbT, cross-sectional area, and flow velocity of the feeder/draining vessels of the local system, respectively (Wang, 2008a). As discussed in Section "Technical basis of PAT for neurovascular imaging", all the above parameters are measurable via PAT. A major technical challenge in $CMRO_2$ quantification is the fluence compensation in the sO_2 calculation (Hu and Wang, 2010). In PAT, the detected signal amplitude is proportional to the product of local optical absorption coefficient and optical fluence. The wavelength dependences of optical fluence must be compensated for before we can apply the known optical absorption spectra of HbR and HbO_2 to calculate sO_2. Poor fluence compensation can lead to inaccuracy (Stein et al., 2009).

(iii) Multimodal imaging. Established neuroimaging technologies, such as TPM and MRI, provide fruitful anatomical, functional, or molecular information that is highly complementary to photoacoustic contrasts. Taking advantage of the high scalability of PAT, it would be convenient and powerful to fuse PAT and the existing neuroimaging technologies into a multi-contrast system.

(iv) Effective absorption contrast agents. Although low-quantum-yield fluorochromes can be used as photoacoustic contrast agents for molecular imaging (Razansky et al., 2007), SNR is usually presented as a limiting factor due to the unoptimized optical absorption property. For instance, although OR-PAM has demonstrated *in vivo* transcranial imaging of single capillaries (Hu et al., 2009a), which are similar to or even smaller than the size of amyloid plaques in rodent models, transcranial imaging of amyloid plaques still requires further improvements in the optical absorption of amyloid-specific dyes (Hu et al., 2009c). To extend the scope of PAT from neurovascular coupling to more general neuronal activities, we must develop more effective absorption contrast agents.

In conclusion, PAT bridges the spatial gap between biological microscopy and clinical imaging. Both the spatial resolution and the tissue penetration of PAT are highly scalable. The combination of scalability and endogenous hemoglobin contrast enables label-free, multi-scale, multi-parameter vascular imaging, making PAT a promising tool for neurovascular study.

ACKNOWLEDGMENTS

The authors appreciate Prof. James Ballard's close reading of the manuscript. This work was sponsored by National Institutes of Health Grants R01 EB000712, EB000712A2S1, R01 EB00071207S2, R01 EB008085, R01 CA113453901, U54 CA136398, and 5P60 DK02057933. L.V.W. has a financial interest in Microphotoacoustics, Inc. and Endra, Inc., which, however, did not support this work.

REFERENCES

Brunker, J., and Beard, P. (2010). *Pulsed Photoacoustic Doppler Flowmetry Using a Cross Correlation Method.* Proceedings of SPIE 7564, San Francisco.

Bunce, S. C., Izzetoglu, M., Izzetoglu, K., Onaral, B., and Pourrezaei, K. (2006). Functional near-infrared spectroscopy. *IEEE Eng. Med. Biol. Mag.* 25, 54–62.

Devor, A., Tian, P., Nishimura, N., Teng, I. C., Hillman, E. M., Narayanan, S. N., Ulbert, I., Boas, D. A., Kleinfeld, D., and Dale, A. M. (2007). Suppressed neuronal activity and concurrent arteriolar vasoconstriction may explain negative blood oxygenation level-dependent signal. *J. Neurosci.* 27, 4452–4459.

Fang, H., Maslov, K., and Wang, L. V. (2007a). Photoacoustic Doppler effect from flowing small light-absorbing particles. *Phys. Rev. Lett.* 99, 184501.

Fang, H., Maslov, K., and Wang, L. V. (2007b). Photoacoustic Doppler flow measurement in optically scattering media. *Appl. Phys. Lett.* 91, 3.

Fang, H., and Wang, L. V. (2009). M-mode photoacoustic particle flow imaging. *Opt. Lett.* 34, 671–673.

Gamelin, J., Aguirre, A., Maurudis, A., Huang, F., Castillo, D., Wang, L.V., and Zhu, Q. (2008). Curved array photoacoustic tomographic system for small animal imaging. *J. Biomed. Opt.* 13, 024007.

Girouard, H., and Iadecola, C. (2006). Neurovascular coupling in the normal brain and in hypertension, stroke, and Alzheimer disease. *J. Appl. Physiol.* 100, 328–335.

Harrison, T., Ranasinghesagara, J. C., Lu, H., Mathewson, K., Walsh, A., and Zemp, R. J. (2009). Combined photoacoustic and ultrasound biomicroscopy. *Opt. Express* 17, 22041–22046.

Hu, S., Maslov, K., Tsytsarev, V., and Wang, L. V. (2009a). Functional transcranial brain imaging by optical-resolution photoacoustic microscopy. *J. Biomed. Opt.* 14, 040503.

Hu, S., Maslov, K., and Wang, L. V. (2009b). Noninvasive label-free imaging of microhemodynamics by optical-resolution photoacoustic microscopy. *Opt. Express* 17, 7688–7693.

Hu, S., Rao, B., Maslov, K., and Wang, L. V. (2010). Label-free photoacoustic ophthalmic angiography. *Opt. Lett.* 35, 1–3.

Hu, S., Yan, P., Maslov, K., Lee, J.-M., and Wang, L. V. (2009c). Intravital imaging of amyloid plaques in a transgenic mouse model using optical-resolution photoacoustic microscopy. *Opt. Lett.* 34, 3899–3901.

Hu, S., and Wang, L.V. (2010). Photoacoustic imaging and characterization of the microvasculature. *J. Biomed. Opt.* 15, 011101.

Klunk, W. E., Engler, H., Nordberg, A., Wang, Y., Blomqvist, G., Holt, D. P., Bergstrom, M., Savitcheva, I., Huang, G. F., Estrada, S., Ausen, B., Debnath, M. L., Barletta, J., Price, J. C., Sandell, J., Lopresti, B. J., Wall, A., Koivisto, P., Antoni, G., Mathis, C. A., and Langstrom, B. (2004). Imaging brain amyloid in Alzheimer's disease with Pittsburgh Compound-B. *Ann. Neurol.* 55, 306–319.

Ku, G., and Wang, L. V. (2005). Deeply penetrating photoacoustic tomography in biological tissues enhanced with an optical contrast agent. *Opt. Lett.* 30, 507–509.

Li, C., Aguirre, A., Gamelin, J., Maurudis, A., Zhu, Q., and Wang, L. V. (2010). Real-time photoacoustic tomography of cortical hemodynamics in small animals. *J. Biomed. Opt.* 15, 010509.

Malonek, D., and Grinvald, A. (1996). Interactions between electrical activity and cortical microcirculation revealed by imaging spectroscopy: implications for functional brain mapping. *Science* 272, 551–554.

Maslov, K., Ku, G., and Wang, L. V. (2010). *Photoacoustic Microscopy with Submicron Resolution.* Proceedings of SPIE 7564, San Francisco.

Maslov, K., and Wang, L. V. (2008). Photoacoustic imaging of biological tissue with intensity-modulated continuous-wave laser. *J. Biomed. Opt.* 13, 024006.

Maslov, K., Zhang, H. F., Hu, S., and Wang, L. V. (2008). Optical-resolution photoacoustic microscopy for *in vivo* imaging of single capillaries. *Opt. Lett.* 33, 929–931.

Ogawa, S., Lee, T. M., Nayak, A. S., and Glynn, P. (1990). Oxygenation-sensitive contrast in magnetic resonance image of rodent brain at high magnetic fields. *Magn. Reson. Med.* 14, 68–78.

Razansky, D., Vinegoni, C., and Ntziachristos, V. (2007). Multispectral photoacoustic imaging of fluorochromes in small animals. *Opt. Lett.* 32, 2891–2893.

Song, K. H., and Wang, L. V. (2007). Deep reflection-mode photoacoustic

imaging of biological tissue. *J. Biomed. Opt.* 12, 060503.

Srinivasan, V. J., Sakadzic, S., Gorczynska, I., Ruvinskaya, S., Wu, W., Fujimoto, J. G., and Boas, D. A. (2009). Depth-resolved microscopy of cortical hemodynamics with optical coherence tomography. *Opt. Lett.* 34, 3086–3088.

Stein, E. W., Maslov, K., and Wang, L. V. (2008). Noninvasive mapping of the electrically stimulated mouse brain using photoacoustic microscopy. *Proc. SPIE* 6856.

Stein, E. W., Maslov, K., and Wang, L. V. (2009). Noninvasive, *in vivo* imaging of blood-oxygenation dynamics within the mouse brain using photoacoustic microscopy. *J. Biomed. Opt.* 14, 020502.

Wang, L. V. (2008a). Prospects of photoacoustic tomography. *Med. Phys.* 35, 5758–5767.

Wang, L. V. (2008b). Tutorial on photoacoustic microscopy and computed tomography. *IEEE J. Sel. Top. Quantum Electron.* 14, 171–179.

Wang, L. V. (2009). Multiscale photoacoustic microscopy and computed tomography. *Nat. Photon* 3, 503–509.

Wang, L. V., and Wu, H. (2007). *Biomedical Optics: Principles and Imaging.* Hoboken, NJ: Wiley.

Wang, X., Pang, Y., Ku, G., Xie, X., Stoica, G., and Wang, L. V. (2003). Noninvasive laser-induced photoacoustic tomography for structural and functional *in vivo* imaging of the brain. *Nat. Biotechnol.* 21, 803–806.

Xie, Z., Jiao, S., Zhang, H. F., and Puliafito, C. A. (2009). Laser-scanning optical-resolution photoacoustic microscopy. *Opt. Lett.* 34, 1771–1773.

Xu, M., and Wang, L. V. (2006). Photoacoustic imaging in biomedicine. *Rev. Sci. Instrum.* 77, 041101.

Yao, J., and Wang, L. V. (2010). *Transverse Flow Velocity Measurement with Photoacoustic Doppler Bandwidth Broadening.* Proceedings of SPIE 7564, San Francisco.

Zemp, R. J., Song, L., Bitton, R., Shung, K. K., and Wang, L. V. (2008). Realtime photoacoustic microscopy in vivo with a 30-MHz ultrasound array transducer. *Opt. Express.* 16, 7915–7928.

Zhang, E., Laufer, J., and Beard, P. (2008a). Backward-mode multiwavelength photoacoustic scanner using a planar Fabry-Perot polymer film ultrasound sensor for high-resolution three-dimensional imaging of biological tissues. *Appl. Opt.* 47, 561–577.

Zhang, Q., Liu, Z., Carney, P. R., Yuan, Z., Chen, H., Roper, S. N., and Jiang, H. (2008b). Non-invasive imaging of epileptic seizures *in vivo* using photoacoustic tomography. *Phys. Med. Biol.* 53, 1921–1931.

Zhang, H. F., Maslov, K., Stoica, G., and Wang, L. V. (2006). Functional photoacoustic microscopy for high-resolution and noninvasive *in vivo* imaging. *Nat. Biotechnol.* 24, 848–851.

Conflict of Interest Statement: L. V. Wang has a financial interest in Microphotoacoustics, Inc. and Endra, Inc., which, however, did not support this work.

Received: 02 March 2010; paper pending published: 30 March 2010; accepted: 26 May 2010; published online: 17 June 2010.

Citation: Hu S and Wang LV (2010) Neurovascular photoacoustic tomography. Front. Neuroenerg. ***2****:10. doi: 10.3389/fnene.2010.00010*

frontiers in
NEUROENERGETICS

REVIEW ARTICLE
published: 18 June 2010
doi: 10.3389/fnene.2010.00011

Cerebral oxygen delivery and consumption during evoked neural activity

Alberto L. Vazquez[1]*, Kazuto Masamoto[2], Mitsuhiro Fukuda[1] and Seong-Gi Kim[1,3]

[1] *Department of Radiology, University of Pittsburgh, Pittsburgh, PA, USA*
[2] *Center for Science and Engineering, University of Electro-communications, Tokyo, Japan*
[3] *Department of Neurobiology, University of Pittsburgh, Pittsburgh, PA, USA*

Edited by:
David Boas, Massachusetts General Hospital, USA; Massachusetts Institute of Technology, USA; Harvard Medical School, USA

Reviewed by:
Fahmeed Hyder, Yale University, USA
Abbas Yaseen, Harvard University, USA

***Correspondence:**
Alberto L. Vazquez, 3025 E Carson St, McGowan Institute Room 159 BIRC, Pittsburgh, PA 15203, USA.
e-mail: alv15@pitt.edu

Increases in neural activity evoke increases in the delivery and consumption of oxygen. Beyond observations of cerebral tissue and blood oxygen, the role and properties of cerebral oxygen delivery and consumption during changes in brain function are not well understood. This work overviews the current knowledge of functional oxygen delivery and consumption and introduces recent and preliminary findings to explore the mechanisms by which oxygen is delivered to tissue as well as the temporal dynamics of oxygen metabolism. Vascular oxygen tension measurements have shown that a relatively large amount of oxygen exits pial arterioles prior to capillaries. Additionally, increases in cerebral blood flow (CBF) induced by evoked neural activation are accompanied by arterial vasodilation and also by increases in arteriolar oxygenation. This increase contributes not only to the down-stream delivery of oxygen to tissue, but also to delivery of additional oxygen to extra-vascular spaces surrounding the arterioles. On the other hand, the changes in tissue oxygen tension due to functional increases in oxygen consumption have been investigated using a method to suppress the evoked CBF response. The functional decreases in tissue oxygen tension induced by increases in oxygen consumption are slow to evoked changes in CBF under control conditions. Preliminary findings obtained using flavoprotein autofluorescence imaging suggest cellular oxidative metabolism changes at a faster rate than the average changes in tissue oxygen. These issues are important in the determination of the dynamic changes in tissue oxygen metabolism from hemoglobin-based imaging techniques such as blood oxygenation-level dependent functional magnetic resonance imaging **(fMRI)**.

Keywords: P_{O_2}, oxygen, hemoglobin, CBF, CMR_{O_2}, flavoprotein, fMRI

INTRODUCTION

The wide-spread use of imaging methods that are sensitive to the cerebral oxygenation level of blood, such as blood oxygenation-level dependent functional magnetic resonance imaging (BOLD fMRI), has sparked significant interest in the properties and role of oxygen delivery and consumption in the brain, particularly during changes in brain function. In general, oxygen is transported to the brain by blood and it is delivered to tissue at the capillary level by diffusion. In tissue, oxygen diffuses until it is used up in cellular mitochondria. With increases in neural activity, the cerebral metabolic rate of oxygen consumption (CMR_{O_2}) increases (Herscovitch et al., 1985; Fox et al., 1988; Fiat et al., 1993; Davis et al., 1998; Kim et al., 1999; Mayhew et al., 2000; Hyder et al., 2001; Shulman et al., 2001; Boas et al., 2003). In addition, the delivery (or supply) of oxygen to tissue also increases through increases in cerebral blood flow (CBF) (Buxton and Frank, 1997; Davis et al., 1998; Hyder et al., 1998; Kim et al., 1999; Lauritzen, 2001; Zheng et al., 2002). The increase in CBF is produced at least in part by the dilation of feeding arteries, and hence, increases in cerebral blood volume (CBV) have also been observed (Berwick et al., 2005; Vanzetta et al., 2005; Hillman et al., 2007; Kim et al., 2007). This general picture appears to be coherent because it is expected that increases in neural activity (e.g., synaptic transmission and firing rate) require additional energy, which is supplied by increases in oxidative metabolism. As a result, blood flow increases to satisfy the consumption (or demand) of tissue oxygen. However, the role and properties of oxygen delivery and consumption have remained unclear. For instance, steady-state increases in oxygen delivery have been consistently observed to exceed the state-state increases in oxygen consumption by a ratio between 2 and 3 (Uludag et al., 2004). It is this disproportionate ratio that is exploited to image brain function in humans and animals using methods like BOLD fMRI. Fueling our lack of understanding is the fact that neural activity is a highly dynamic process and dynamic measurements of oxygen consumption (and delivery) have been largely unavailable. As a result, the use of blood oxygenation methods to interpret and quantify brain function remains uncertain. Because these processes are not simple and many important variables are not routinely measured, models have been employed to explore, interpret and quantify the dynamics of this process (Zheng et al., 2002; Valabregue et al., 2003; Huppert et al., 2007; Boas et al., 2008). However, the dynamic properties of tissue oxygen consumption with changes in brain function have been difficult to measure, leaving this portion of the model to educated assumptions.

A thorough understanding of cerebral oxygen delivery and consumption is important not only to understand this fundamental metabolic process but also for the quantification of the changes in blood oxygen saturation which are then used to calculate the changes in tissue oxygen metabolism. This physiological parameter can be very useful in research and clinical studies to assess the functional state of tissue. In this work, we will overview the current

knowledge of functional oxygen delivery and consumption and introduce recent findings to explore the role of the large delivery of oxygen to tissue and the temporal dynamics of oxygen consumption. Specifically, previously reported data from our group (Vazquez et al., 2010) will be used in combination with a model of the transport of oxygen to aid in the investigation of these questions. These data will also be used to explore the impact of vascular wall P_{O_2} measurements on the longitudinal gradient of oxygen along the cerebro-vascular tree. Preliminary findings of the functional changes in tissue P_{O_2} as a function of depth over superficial layers will also be explored. Lastly, preliminary findings of the dynamic changes in cellular oxidative metabolism with evoked function obtained using flavoprotein autofluorescence imaging (FAI) are also presented.

BACKGROUND

The mammalian brain is very sensitive to the amount of oxygen. This is exemplified by the disruption of brain function within minutes after discontinuing oxygen supply (e.g., respiratory arrest). Oxygen in air is present at a concentration of 20.9% under standard temperature and pressure (i.e., 25°C and 1 atm). It is transported from air to the lungs by respiration and it dissolves in blood where it mostly binds hemoglobin in red blood cells. The ability of a medium such as blood (plasma) to dissolve oxygen is described by Henry's Law and the solubility coefficient (α), which has been determined to be 1.39×10^{-3} mM/mmHg (Popel, 1989). In the lungs, the inspired oxygen tension is about 150 mmHg under standard body temperature and pressure (i.e., 37°C and fully saturated water vapor gas), setting an upper bound for the oxygen tension of blood. A single hemoglobin molecule is able to bind four oxygen molecules such that the total concentration of oxygen in blood depends mostly on the concentration of hemoglobin, although free oxygen dissolved in blood plasma, reported as the partial pressure or tension of oxygen in blood, also contributes a small amount. The affinity of oxygen to hemoglobin depends on the blood oxygen tension and it is described by the oxygen dissociation curve (ODC) (Popel, 1989; Jensen, 2004). It is worth noting that the ODC is influenced by temperature, pH and carbon dioxide tension (the latter two compose the Bohr effect). A common expression for the ODC is the Hill equation (Eq. 1) which is parametrized by the P_{50} (the oxygen tension at which blood hemoglobin is 50% saturated by oxygen) and the Hill coefficient (h). The kinetics of the association and dissociation of oxygen from hemoglobin have been determined to take tens of milliseconds under normal conditions (Gibson et al., 1955; Popel, 1989). Hence, if an instantaneous equilibrium is assumed, the total concentration of blood concentration can be described by Eq. 1 as the sum of the oxygen dissolved in plasma (C_p) and the oxygen bound to hemoglobin, where [Hb] is the concentration of hemoglobin in blood. Using the values in **Table 1**, an arterial oxygen tension of 100 mmHg would correspond to a dissolved oxygen concentration (C_p) of 0.14 mM and a total oxygen concentration (C_c) of 6.56 mM.

$$C_c = C_p + \frac{4[\mathrm{Hb}]}{1+\left(\frac{\alpha P_{50}}{C_p}\right)^h} \quad (1)$$

Table 1 | Parameter values used for the model described in Eqs 1–3.

Parameter	Value	Remarks
[Hb]	1.72 mM	Vazquez et al. (2010)
α	1.39×10^{-3} mM/ mmHg	Popel (1989)
P_{50}	38 mmHg	Gray et al. (1964)
h	2.73	Valabregue et al. (2003)
CBF_0	150 ml/min	Kim et al. (2007)
PS_c	612 ml/min	Medium-to-small arterial vessel compartment

A relatively simple model can be used to describe the transport of oxygen by conservation of mass assuming that a single vascular compartment with a linear axial and radial oxygen gradient is a reasonable approximation (Eq. 2 and **Figure 1**) (Valabregue et al., 2003). In this fashion, the average amount of oxygen (represented by the product of the compartment's volume V_c and the average oxygen concentration C_c) is described by the average amount of oxygen entering the compartment upstream (CBF C_a), the amount of oxygen leaving the compartment down-stream (CBF C_v) and the amount of oxygen delivered to tissue (represented by the right-most term in Eq. 2). In the latter term, the transport of oxygen out of the vascular space (orthogonal to the direction of flow) is related to the product of the oxygen permeability and surface area of exchange (PS_c) (see **Table 1**). Similarly, the average amount of oxygen in a tissue compartment (represented by the product of the tissue compartment volume V_t and the average tissue oxygen concentration C_t) can be simply described by the difference between the amount entering the tissue compartment and the amount of oxygen consumed (CMR_{O_2}) (Eq. 3). A more in-depth description of this model (Eqs 1–3) and its assumptions can be found in (Popel, 1989; Valabregue et al., 2003).

$$\text{Vessel: } V_c \frac{dC_c(t)}{dt} = \mathrm{CBF}(t)\left(C_a(t) - C_v(t)\right) - PS_c\left(C_p(t) - C_t(t)\right) \quad (2)$$

$$\text{Tissue: } V_t \frac{dC_t(t)}{dt} = PS_c\left(C_p(t) - C_t(t)\right) - \mathrm{CMR}_{O_2}(t) \quad (3)$$

Cerebral oxygen tension is classically measured using polarographic oxygen microelectrodes (Fatt, 1976; Siesjö, 1978). A significant advantage of this method is that it can quantify the absolute tension of free dissolved oxygen with good spatial resolution (typical volumes of about 10 μm in radius or greater). A significant disadvantage of this method is its single point measurement and invasiveness since the electrode must be physically placed at the desired sampling location. In addition, the measurement of intra-vascular P_{O_2} is generally limited to the surface of blood vessels which may not necessarily indicate the intra-vascular P_{O_2}, especially for larger arteries where the vascular wall is thick (a promising new method might overcome some of these shortcomings (Yaseen, et al., 2009)). Although other methods can be used to measure oxygen tension (e.g., phosphorescence quenching), most reports overviewed below used oxygen microelectrodes to measure oxygen tension in blood vessels and tissue.

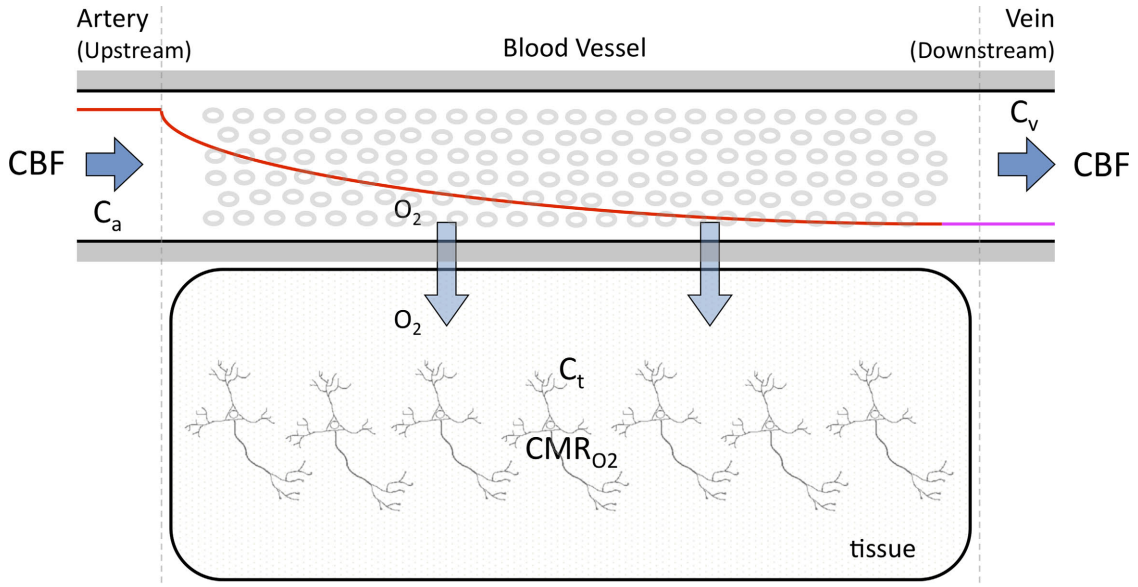

FIGURE 1 | Simplified diagram of the transport of oxygen from blood to tissue. The model in Eqs 2 and 3 consists of a vessel compartment and a tissue compartment, respectively, where the amount of oxygen per unit time is conserved in each compartment. The model implemented in this work assumed a linear intra-vascular oxygen gradient to be a reasonable approximation.

OXYGEN DELIVERY

Oxygen is transported to the brain by the arterial vasculature and most of the blood oxygen is exchanged into tissue in cerebral capillaries by diffusion. Therefore, a longitudinal or axial oxygen concentration gradient exists between cerebral arteries and veins. In addition, the venous (or down-stream) concentration of oxygen directly depends on the flow rate. A few reports of the arterial and venous cerebral oxygen tension in the literature show that the largest drop in vascular P_{O_2} occurs in tissue across capillaries (17 mmHg) (Vovenko, 1999) and between pre-penetrating pial arterioles and post-emerging pial venules (44 mmHg; **Figure 2**, Small Artery to Small Vein locations, or SmArt to SmVen, respectively).

Interestingly, the gradient of oxygen is decreasing along the traversal of blood within the arterial tree becoming significantly lower in small pre-penetrating pial arterioles (Vovenko, 1999; Vazquez et al., 2010). Specifically, in a report by Vovenko (1999) the resting arterial oxygen tension dropped by 23 mmHg prior to entering the capillaries. In a recent study by our group (Vazquez et al., 2010), the arterial oxygen tension dropped by 11 mmHg in the pial surface prior to the arteries penetrating into the cortex (**Figure 2**, medium to small artery locations). Similar measurements in other tissues (e.g., muscle) have also shown a similar efflux of oxygen from arterial vessels (Duling and Berne, 1970). In many studies, vascular P_{O_2} measurements are made at the vessel wall, which underestimates the intra-luminal vascular P_{O_2}. A conventional correction to P_{O_2} measurements at the vessel wall considers the wall thickness and the gradient of oxygen across the wall (Ivanov et al., 1999). In a study by Duling and Berne (1970) these two parameters were measured in cerebral arteries and they found an average P_{O_2} gradient of about 1 mmHg/μm and an average wall thickness of 15% of the intra-luminal diameter. These findings were used to perform a zero-order correction of our arterial

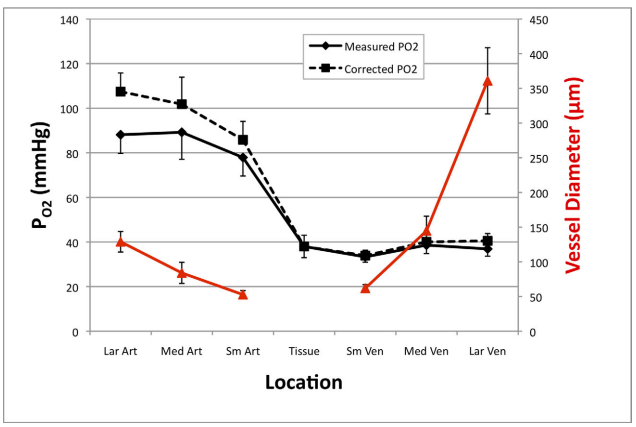

FIGURE 2 | Average resting cerebral P_{O_2} gradient in tissue and pial vasculature (solid black line). P_{O_2} measurements were obtained from the vessel wall and the intra-vascular P_{O_2} (corrected) was estimated using oxygen gradient and wall thickness estimates from the literature (dashed black line). The average vessel diameter is also presented (solid red line) with its corresponding axis on the right. In the horizontal axis, "Lar" was used to denote the largest visible branch of the targeted pial artery ("Art") and vein ("Ven"). These locations are also referred to as large artery and large vein, respectively. "Sm" was used to denote the targeted pre-penetrating arterial branch (also called small artery) and post-emerging venous branch (small vein). "Med" was used to denote the branch location of measurement between the "Lar" and "Sm" locations in each artery and vein (also referred to as medium artery and medium vein). Error bars indicate the standard error (n = 6, 6, 9, 9, 9, 6, and 6 for LarArt, MedArt, SmArt, Tissue, SmVen, MedVen, and LarVen, respectively). This data was adapted from Vazquez et al. (2010).

P_{O_2} measurements obtained at the vessel wall and, as a result, the longitudinal P_{O_2} gradient along the arterial tree slightly steepened to 16 mmHg (from 101.8 to 85.8 mmHg, **Figure 2**). In addition,

the study by Vovenko, was performed under a microscope at high magnification using sharp microelectrodes that were carefully positioned inside the vessel wall in close proximity to the luminal space to avoid this potential source of error. In both studies a significant decrease in arterial P_{O_2} was observed, hence showing that, similar to other tissues, cerebral arteries are indeed permeable to oxygen. The significance of this arterial oxygen gradient is that it allows for the control of the delivery of oxygen to down-stream vasculature through increases in blood flow.

It has been long hypothesized that this delivery of oxygen by the arterial vasculature serves to satisfy the metabolic demands of vascular cells and also the demands of surrounding tissue (Tsai et al., 2003). However, recall that the total efflux of oxygen depends on that bound to hemoglobin and the ODC. In arteries, P_{O_2} is relatively high but the total amount of oxygen transported to tissue is not as large as that in capillaries. Nonetheless, measurements of the radial arterial P_{O_2} gradient beyond the vascular wall have shown that the oxygen tension in tissue surrounding arteries is significantly larger than the P_{O_2} in capillaries (Duling et al., 1979; Sharan et al., 2008). This gradient was observed to take tens of micrometers to equilibrate with the average tissue oxygen tension. These findings indicate that sufficient oxygen escapes arterial blood and reaches surrounding tissue for consumption and that capillaries are not the sole source of oxygen delivery. However, the functional role of this source of oxygen is unclear.

Lastly, after the passage of blood through arteries and capillaries, it enters the venous vasculature where it continually pools with blood from other cortical areas as the branching order decreases. In contrast to the arterial vasculature, no significant differences in oxygen tension were reported along the venous tree although significant variability in the oxygen tension within the draining venous tree was reported (Vovenko, 1999; Vazquez et al., 2010). Interestingly, both studies by Vovenko and our group reported a larger average P_{O_2} in the largest sampled venous location compared to the smallest sampled venous location (by 3–5 mmHg) although these differences were not statistically significant. To account for potential errors stemming from vascular wall measurements, the radial oxygen gradient in veins was measured to be 0.1 mmHg/μm (Vovenko, 1999; Tsai et al., 2003). In addition, the venous vascular wall is thinner than that of arteries (about 10% of the venous lumen diameter) (Burton, 1954). These values were also used to perform a zero-order correction of the venous P_{O_2} measurements and small increases in the venous P_{O_2} were obtained (**Figure 2**). Such increases in venous P_{O_2} have also been reported in other tissues (Tsai et al., 2003). In the brain, this increase in venous P_{O_2} has been attributed to the presence of arterio-venous shunts and the draining of blood from other parts of the brain with different metabolic demands (Tsai et al., 2003).

ARTERIAL P_{O_2} CHANGES DURING INCREASED NEURAL ACTIVITY

It is well-known that increases in neural activity induce increases in CBF and that this dynamic process is responsible for the hyper-oxygenation of both tissue and the down-stream venous vasculature. However, changes in arterial oxygenation with increases in neural activity had not been investigated. To this end, our group investigated the impact of evoked neural activity on arterial, tissue and venous P_{O_2} in the isoflurane-anesthetized rat (Vazquez et al., 2010). The neural stimulus consisted of electrical stimulation of the rat's forelimb with the following parameters: 1 ms pulses at a frequency of 3 Hz, amplitude of 1.5 mA, total duration of 20 s, repeated every 80 s. These parameters have been shown to produce consistent neural responses and robust hemodynamic responses (Masamoto et al., 2009). CBF was measured using a laser Doppler flowmeter (LDF) and it was observed to increase by 44 ± 12% ($n = 9$; standard error reported unless otherwise stated) over the last 10 s of the stimulation period, in part due to increases in the vascular diameter of arteries of about 5%. More importantly, P_{O_2} was measured in pial arteries, pial veins and tissue locations using oxygen microelectrodes and, upon stimulation, vascular P_{O_2} was observed to increase in pial arteries and veins at all the locations sampled (**Figure 3**). The average arterial oxygen tension was observed to increase by 4 ± 1 ($n = 6$), 5 ± 1 ($n = 6$) and 11 ± 2 mmHg ($n = 9$) at the large, medium and small pial artery locations, respectively, during the last 10 s of the stimulation period. Note that the arterial longitudinal gradient decreased on average from 16 mmHg at rest to 10 mmHg during stimulation conditions. The average venous P_{O_2} was observed to increase by 7 ± 2 ($n = 9$), 7 ± 2 ($n = 6$) and 5 ± 2 mmHg ($n = 6$) at the small, medium and large pial vein locations, respectively. Temporally, the earliest average increase in vascular P_{O_2} was observed in medium and small pial arteries.

In summary, the longitudinal arterial P_{O_2} gradient was observed to decrease with increase in function. This is due, at least in part, to the functional increase in CBF. In general, an increase in arterial oxygen tension will also increase the extra-vascular oxygen tension (**Figure 1**). To investigate the mechanism(s) behind the decrease in the longitudinal arterial P_{O_2} gradient, our experimental data were used in combination with the model in Eqs 1 and 2 to estimate the required increases in extra-vascular P_{O_2} to describe the data. For this exercise, the LDF data was assumed to represent CBF, the medium artery P_{O_2} was used to represent the input P_{O_2} of the vascular compartment (C_a) and the tissue P_{O_2} was used as an estimate of the extra-vascular P_{O_2} (C_t). The model was then used to compare the predicted output P_{O_2} (C_v) with the measured small artery P_{O_2} data (**Figure 1**). The values considered for the parameters of the model are listed in **Table 1**. Considering only the steady-state changes, it was calculated that a large increase in the extra-vascular P_{O_2} is necessary to describe the small artery P_{O_2} data (output) and lower resting extra-vascular P_{O_2} levels. Recall that the tissue P_{O_2} level was measured in these experiments at a depth of 300 μm which includes capillary exchange (**Figure 4**, top panel, and **Table 1**). The change in the extra-vascular P_{O_2} was calculated to decrease as the resting extra-vascular P_{O_2} level increased.

Another possibility is that the extra-vascular P_{O_2} level does not change and that the increases in CBF (i.e., blood velocity) impact the permeability of oxygen. Under these assumptions, the relative change in *PS* was calculated to significantly drop with increases in CBF and this decrease grows as the resting extra-vascular P_{O_2} level increases (**Figure 4**, bottom panel). Decreases in oxygen permeability with increases in blood flow have been reported (Tsai et al., 2003; Lamkin-Kennard et al., 2004; Chen et al., 2006), though not of this magnitude. To determine which mechanism(s) contribute to significant hyper-oxygenation in arteries, it is necessary to assess the baseline P_{O_2} at the pial surface as well as the magnitude of superficial tissue P_{O_2} changes with increased brain activity, if any. The P_{O_2} of tissue is known to be heterogeneous, including that of the pial surface. This has been attributed to the relative heterogeneous

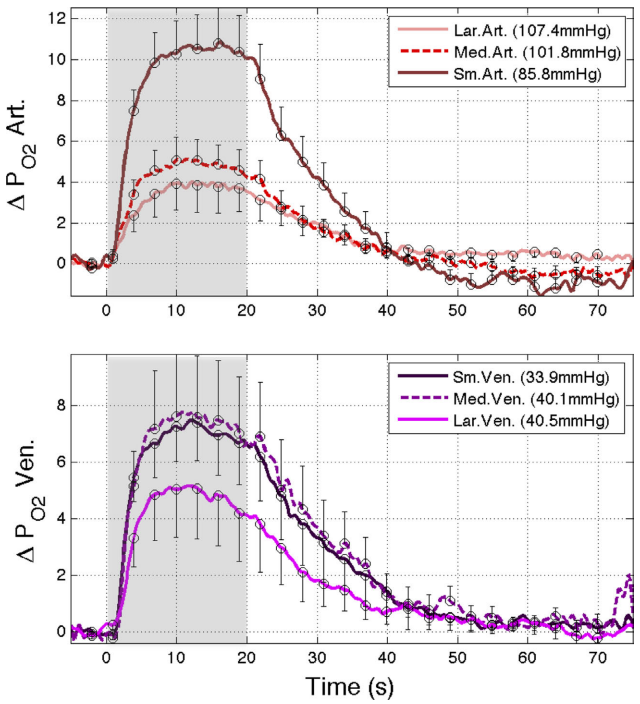

FIGURE 3 | (Top) Change in oxygen tension at sampled large, medium and small pial arteries (labeled LarArt, MedArt, and SmArt, respectively) due to evoked somato-sensory stimulation (gray bars) relative to their respective pre-stimulation level. The small pial artery measured consisted of a pre-penetrating arterial branch just prior to its intra-cortical penetrating location over the activate area. The medium and large locations sampled consisted of the parent branches of the sample small artery sampled. (Bottom) Change in oxygen tension at the vessel wall of sampled small, medium and large pial veins (labeled SmVen, MedVen, and LarVen, respectively) relative to their respective pre-stimulation level. Similar to the small artery location, the small pial vein location was selected just after its intra-cortical emerging location over the active area and the medium and large vein locations corresponded to parent branches. The corresponding baseline P_{O_2} for each location sampled is reported in the legend. Error bars indicate the standard error (n = 6, 6, 9, 9, 9, 6, and 6 for LarArt, MedArt, SmArt, Tissue, SmVen, MedVen, and LarVen, respectively). This data was adapted from Vazquez et al. (2010).

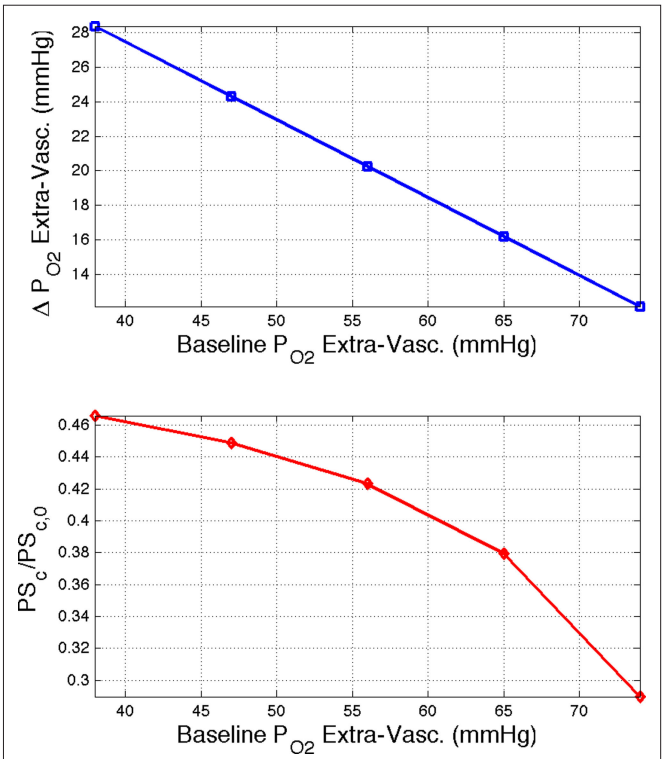

FIGURE 4 | (Top) Model prediction of the increase in the extra-vascular P_{O_2} (C_t) necessary to represent the increase in medium artery P_{O_2} (input, C_a) and small artery P_{O_2} (output, C_v) considering the measured increase in CBF and a constant PS_c (Eq. 2, Figure 1). A higher extra-vascular P_{O_2} level requires a smaller activation-evoked increase in extra-vascular P_{O_2} to describe the data (i.e., small artery P_{O_2}). (Bottom) Model prediction of the decrease in PS_c (i.e., oxygen permeability) necessary to describe the increase in medium and small artery P_{O_2} during increased neural activity while maintaining the extra-vascular P_{O_2} level constant.

distribution of capillaries, arteries and veins in the brain (Popel, 1989; Tsai et al., 2003). Nonetheless, preliminary tissue P_{O_2} measurements at the pial surface and deeper in tissue performed in our laboratory have shown that the surface P_{O_2} level is higher than that at 300 μm in depth, but the functional increase in tissue P_{O_2} is somewhat smaller at the surface compared to deeper in tissue (**Figure 5**). Other reports in the literature have also found a higher tissue P_{O_2} near or at the pial surface (Masamoto et al., 2004; Sharan et al., 2008). Therefore, we conclude that the increase in arterial P_{O_2} requires a decrease in the arterial permeability of oxygen in addition to the increase in CBF which contribute to the hyper-oxygenation of surrounding tissue.

TISSUE OXYGEN DELIVERY DURING INCREASED NEURAL ACTIVITY

The increase in arterial oxygen tension supplies the sub-serving tissues with a relatively large amount of oxygen. Computer simulation work performed by our group determined that, given an estimate of the tissue CMR_{O_2} response, both the upstream arterial P_{O_2} and the intra-cortical area of exchange (by way of an increase in CBV) need to increase in order to fully describe the measured changes in tissue P_{O_2} (Vazquez et al., 2008). The data and simulation work in that study found that the delivery of oxygen required a peak increase of 14 mmHg in tissue P_{O_2} to describe the data. The increase in oxygen delivery can be allocated as contributions from CBF increases alone (6 mmHg for a constant input oxygenation), increases in the input arterial oxygenation (4 mmHg for an increase of 10 mmHg in arterial P_{O_2}) and other mechanisms (4 mmHg), such as an increase in exchange area. The data in **Figure 3** shows similar increases in arterial oxygenation and the residual increase in oxygen delivery can be attributed to increases in exchange area (CBV). In fact, functional increases in intra-cortical blood volume have been measured using MRI in similar experiments (Kim et al., 2007). Alternatively, another mechanism to increase the delivery of oxygen can be through a shift in the ODC due to pH increases and the binding of CO_2 to hemoglobin (i.e., the Bohr effect). To examine this mechanism, our previous simulation work was expanded to consider the possibility of shifts in the blood P_{50} (Eq. 1) as the sole source of the increases in tissue oxygen delivery (i.e., no arterial P_{O_2} or exchange

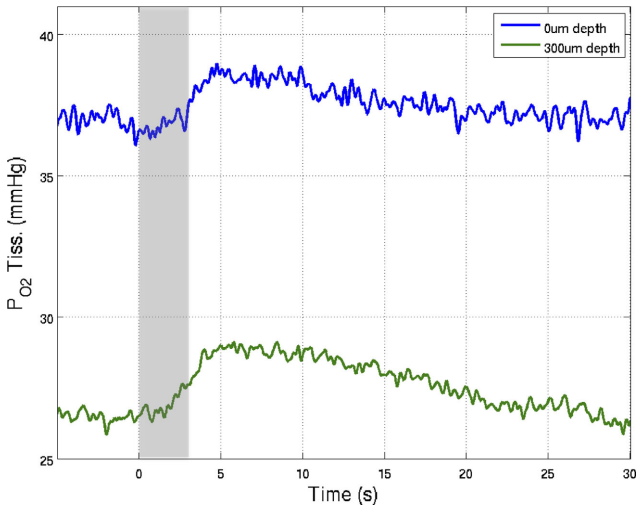

FIGURE 5 | Preliminary measurements of the increase in tissue P_{O_2} that result from increases in somato-sensory stimulation at two different depth locations: at the cortical surface (0 μm, blue line) and 300 μm below the surface (green line). In this experiment, the stimulation period was significantly shorter (3 s), hence the changes in P_{O_2} were not as large as those in **Figure 3**. Although these functional responses were not obtained simultaneously, CBF changes were recorded at both depths using LDF and the evoked CBF responses were essentially the same. The P_{O_2} at the surface was about 10 mmHg larger than that at 300 μm depth.

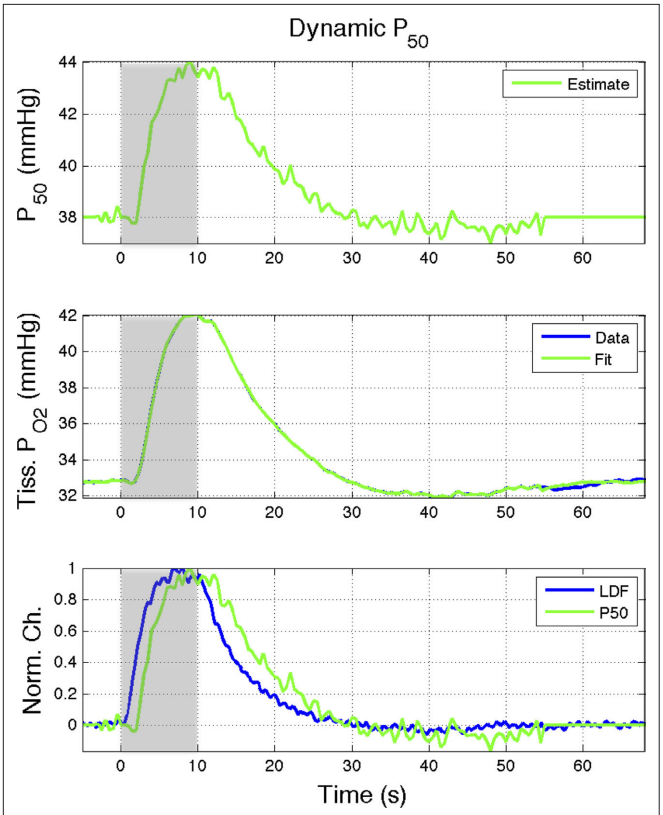

FIGURE 6 | Effect of the blood P_{50} (Eq 1) on the delivery of oxygen to tissue. A 15% increase in P_{50} (top panel) was found to represent the tissue P_{O_2} data (middle panel; Vazquez et al., 2008). (Bottom panel) The estimated changes in P_{50} were temporally similar to the changes in CBF measured in that study although lagged the CBF response (measured using LDF) by about 1.5 s at 50% amplitude. Increases of this magnitude are not likely to be physiological; however, this mechanism may contribute to the hyper-oxygenation of tissue during increases in neural activity.

area increases). The results from this simulation show that an average increase in P_{50} from 38 to 43.7 mmHg was necessary to fully describe the measured changes in tissue P_{O_2} (**Figure 6**). Under resting conditions, arterio-venous differences in blood pH and P_{CO_2} are about −0.05 and 6 mmHg, respectively (Vovenko, 1999), which would in turn increase the P_{50} of blood by about 1.5 mmHg (Severinghaus, 1979). Measurements of the changes in cerebral pH and/or P_{CO_2} with function are necessary to determine if this mechanism contributes to the delivery of oxygen to tissue. Interestingly, this mechanism has also been proposed as that responsible for the slight increases in the venous P_{O_2} longitudinal gradient (Tsai et al., 2003).

OXYGEN CONSUMPTION

Oxygen in tissue is consumed in mitochondria as part of oxidative metabolism. Although this metabolic pathway yields much more energy than glycolysis, the role of oxidative metabolism in satisfying the energetic needs of neural tissue during increased function has been extensively debated (Shulman et al., 2001). This is partly due to the lack of adequate methods to directly measure oxidative metabolism. For example, methods such as O^{15}-PET and O^{17}-NMR are directly sensitive to CMR_{O_2} but require a steady-state of exogenous label to reach tissue (Herscovitch et al., 1985; Fiat et al., 1993). Nonetheless, these and similar techniques have been used to show measurable increases in oxidative metabolism with increases in neural activity (Hyder et al., 2001; Rothman et al., 2003). Much of the scientific interest to measure functional changes in cerebral metabolism stem not only from its physiologically relevant role in maintaining function, but also in part due to its sensitivity to spiking activity. Thompson et al. (2003) measured the changes in tissue oxygen tension and spiking activity with visual stimulation in the primary visual cortex of cats. They showed that increases in spiking activity to preferred-oriented visual stimuli were accompanied by decreases in tissue oxygen tension due to a dominant metabolic response. On the other hand, this CMR_{O_2} -driven decrease was not evident during the presentation of non-preferred orientation visual stimuli which did not elicit significant changes in spiking activity.

CHANGES IN TISSUE P_{O_2} INDUCED BY CHANGES IN CMR_{O_2}

The dynamic changes of tissue oxygen tension can be measured using oxygen microelectrodes as done by Thompson and others (Ances et al., 2001; Thompson et al., 2003; Masamoto et al., 2003). However, this method does not directly measure the functional changes in CMR_{O_2} because the tissue oxygen tension is also manipulated by the concomitant CBF response. Because CMR_{O_2} and CBF modulate the oxygen tension of tissue in opposite fashion, the dynamics of oxidative metabolism have been difficult to measure even when using oxygen specific methods such as oxygen microelectrodes. One solution to overcome this difficulty is to suppress the evoked CBF

response. For this purpose, our group implemented an experimental condition which relies on the administration of a clinical vasodilator, sodium nitroprusside (sNP) (Fukuda et al., 2006; Nagaoka et al., 2006; Masamoto et al., 2008). This agent dilates the vasculature effectively suppressing evoked increases in CBF (and CBV) due to neural stimulation. However, the delivery of this agent significantly reduces the systemic blood pressure (its intended clinical use). To verify that this agent does not disrupt neural function, measurements of local field potential and spiking activity with evoked stimulation prior to, during and after the administration of the agent were performed. These experiments showed that the evoked spiking and local field potential activity during the agent administration was not significantly different than the activity prior to or after agent administration (Fukuda et al., 2006; Masamoto et al., 2008).

Our group has used this suppressed-CBF condition to investigate the CMR_{O_2} response properties to evoked neural activity. In these experiments, BOLD fMRI and optical imaging of intrinsic signal (OIS) were used to represent the oxygenation of blood, and oxygen microelectrodes to represent the oxygenation of tissue, in anesthetized rats and cats (Fukuda et al., 2006; Nagaoka et al., 2006; Moon et al., 2007; Masamoto et al., 2008). OIS was implemented using 620 nm transmitted light which is sensitive to the absorption of light by deoxygenated hemoglobin and therefore has similar sensitivity to BOLD fMRI. In one of these reports (Masamoto et al., 2008), both tissue P_{O_2} and OIS were measured during evoked somato-sensory stimulation for 10 s under control and suppressed-CBF conditions in the isoflurane-anesthetized rat. Somato-sensory stimulation under control conditions evoked an increase in CBF of $48 \pm 10\%$ ($n = 5$; measured using LDF), while under suppressed-CBF conditions, the magnitude of the CBF response was significantly diminished, showing increases of 3–4% over baseline. More importantly, under suppressed-CBF conditions, the dynamic decreases in tissue P_{O_2} and in blood oxygenation (measured by OIS) induced by increases in CMR_{O_2} were considerably slow, taking over 10 s to peak (blue lines in **Figures 7A,B**). In fact, the CMR_{O_2}-driven decreases in tissue P_{O_2} under suppressed-CBF conditions (blue line in **Figure 7C**) appear to be slower than the evoked CBF response measured by LDF under control conditions (green line in **Figure 7C**). In addition, the magnitude of the decreases in tissue P_{O_2} due to evoked increases in CMR_{O_2} was found to be very well correlated with the field potential responses of individual stimuli (Masamoto et al., 2008). These data were supplied to the model described by Eqs 1–3 to estimate the dynamic changes in CMR_{O_2}. The results obtained showed that the calculated CMR_{O_2} dynamics lagged changes in CBF by 2.2 s (measured as the time-to-50% peak during the response onset) (Vazquez et al., 2008). Collectively, these results suggest that temporal dynamics of the average CMR_{O_2} response are as slow as those of the hemodynamic response, if not slower.

DYNAMICS OF CELLULAR CMR_{O_2} CHANGES MEASURED USING FAI

In general, two methods are known to be sensitive to the cellular oxidative metabolic rate, both of which are light-based and invasive. One relies on the absorption of light by cytochrome-c, a mitochondrial protein responsible for transporting electrons between complexes III and IV in the electron transport chain of the TCA cycle (Chance, 1968). The other relies on the fluorescence of tissue proteins that also participate in cellular metabolism. Much of the intrinsic fluorescence of living tissues, or autofluorescence, stems from the reduced form of the coenzyme nicotinamide adenine dinucleotide (NADH) and the oxidized form of flavin adenine dinucleotide (FAD) (Chance, 1968; Huang et al., 2002). These proteins are directly involved in the TCA cycle as proton carriers for the electron transport chain where NADH and $FADH_2$ are oxidized to NAD and FAD, respectively. While NADH is fluorescent, NAD+ is not, and the metabolic rate could be assessed by decreases in the fluorescence of NADH (Huang et al., 2002; Reinert et al., 2004). Different from NADH, its analog $FADH_2$ is not fluorescent, but its oxidized form (FAD, also called flavoprotein) is fluorescent; hence, increases in

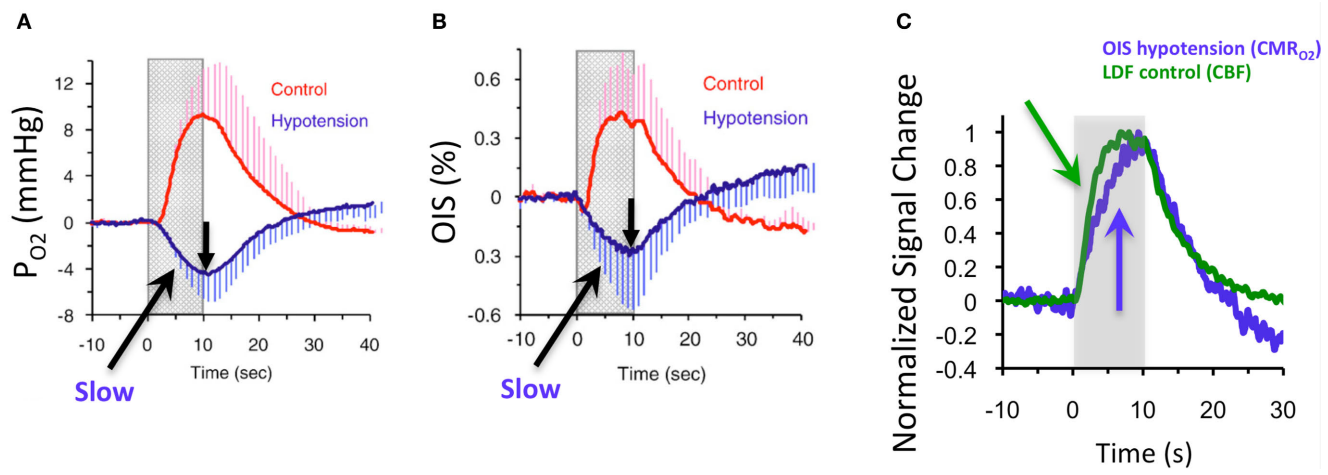

FIGURE 7 | Averaged tissue P_{O_2} (A) and blood oxygenation ((B), OIS) changes to forelimb somato-sensory stimulation (1 ms, 1.2 mA electrical pulses delivered at 6 Hz for 10 s indicated by gray bars) under control (red lines) and suppressed-CBF conditions (blue lines). (C) Normalized time series (baseline to peak) show that the CBF response under control conditions measured by LDF is faster than CMR_{O_2}-induced blood oxygenation (OIS) changes. This data was adapted from Masamoto et al. (2008).

the metabolic rate can be assessed by increases in the fluorescence of FAD (Hassinen and Chance, 1968; Huang et al., 2002; Reinert et al., 2004). More importantly, FAD fluorescence changes *in vivo* are generally larger and easier to detect than that of NADH, although its concentration in tissue is lower (Reinert et al., 2004).

Flavoprotein autofluorescence measurements were pioneered by Dr. Britton Chance and has been extensively used to investigate muscle function and *ex vivo* cellular function in various tissues (Chance et al., 1962, 1979; Garland et al., 1967; Chance, 1968; Shuttleworth et al., 2003; Kasischke et al., 2004; Skala et al., 2007). Recently, FAI was adapted by several groups to image brain functional metabolism *in vivo*. Shibuki et al. (2003) implemented and verified the signal source of this method in rat brain slices and *in vivo*. They stimulated the rat cortex directly with a metal electrode and observed large sub-linear increases in FAD fluorescence as a function of stimulus frequency (as large as 20% for 100 Hz stimuli). They also used a more natural mechanical stimulus of the hind limb (50 Hz vibration) that lasted 1 s and produced increases in FAD fluorescence of about 3% in the somato-sensory cortex. The increase in fluorescence peaked 1 s after stimulation onset and was followed by an equally large decrease in signal that took longer to subside. They hypothesized that the signal decrease was due to the stimulus-evoked CBF (and CBV) response that absorbed the FAD fluorescence emission. To investigate this possibility, they applied a nitric oxide inhibitor (N^G-nitro-L-arginine) topically onto the cortex to reduce the CBF response and this condition indeed reduced the magnitude of the negative portion of the autofluorescence response. In another study, Reinert et al. (2004) studied FAI in the cerebellar cortex of mice using direct electrical stimulation and also found large increases in FAD fluorescence that were followed by a significant and prolonged decrease in fluorescence. They attributed this bi-phasic response to a time-dependent change in the metabolic cascade (a fast initial oxidation of FAD followed by a larger overall reduction in FAD) and to different metabolic contributions from neurons and glial cells. Lastly, Husson et al. (2007) demonstrated the use of FAI to map the orientation domains in the cat visual cortex. In this study, the spatial specificity of the orientation map obtained by FAI was estimated to be about 300 μm while the specificity of the map obtained by OIS (using 610 nm wavelength light) was estimated to be about 450 μm, suggesting that metabolic imaging is more specific to the neuronal activation sites than hemodynamic imaging. Collectively, these studies have demonstrated the sensitivity and feasibility of this method to map functional metabolic responses *in vivo*. This method was recently implemented in our laboratory to investigate the temporal dynamics of the CMR_{O_2} response.

Preliminary FAI experiments have been performed in our laboratory during somato-sensory stimulation in isoflurane-anesthetized rats. The goal of these experiments is to determine the temporal evolution of the functional CMR_{O_2} response with increases in neural activity. Hence, these experiments have been carried out under suppressed-CBF conditions to avoid potential artifacts stemming from the stimulation-evoked vascular (CBF and CBV) response. Images were acquired using an epi-fluorescence microscope with filtered excitation light of 470 ± 20 nm and emission band at 525 ± 25 nm at 10 frames per second. Somato-sensory stimulation at a frequency of 12 Hz for 4 s shows that the FAI signal increase (brightening) is localized to the forelimb somato-sensory area and that it is sustained during the stimulation period (**Figure 8**). More importantly, FAI vascular response artifacts have been mitigated under suppressed-CBF conditions as evidenced by the gray-background intensity of the blood vessels. Therefore, we believe that the data presented, are mostly sensitive to the changes in the cellular oxidative metabolic rate. To further investigate the temporal differences between tissue and blood oxygenation signals driven by changes in CMR_{O_2}, FAI and OIS signals were measured in separate experiments using a longer stimulation period (15 s of forelimb stimulation at a frequency of 3 Hz). The FAI signal showed very fast temporal changes reaching 90% of peak amplitude within 1.5 s of stimulation onset and a rise time constant of 0.5 s for the onset portion of the response (**Figure 9**, left panel). A sustained plateau period was observed in the FAI response followed by a decrease during and after the stimulation period. By contrast, the changes in blood oxygenation measured by OIS showed slower temporal changes, reaching 90% of the peak decrease in 5 s with a rise time constant of 1.9 s (**Figure 9**, right panel). This method and the properties of the measured FAI responses are currently under

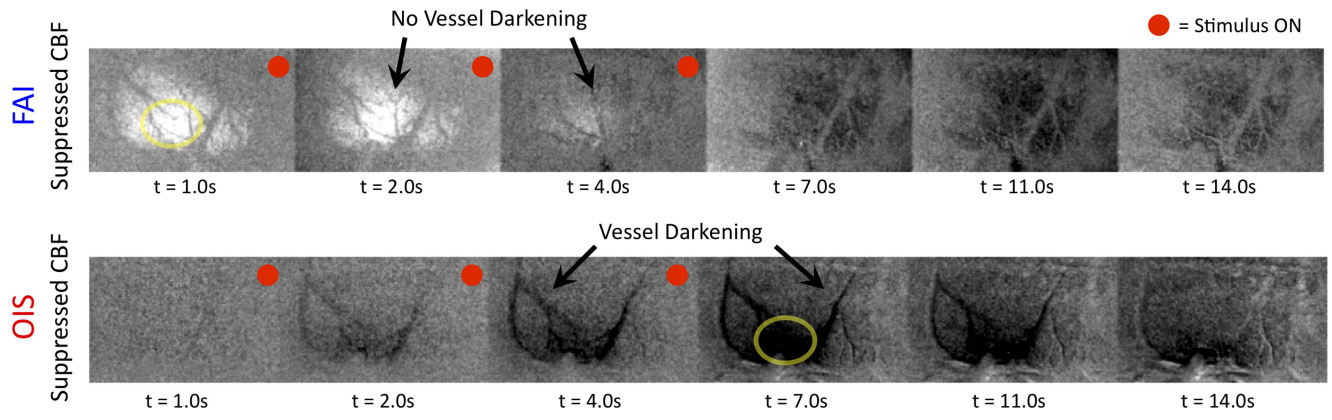

FIGURE 8 | Average FAI and OIS image sequence during somato-sensory stimulation of the rat forelimb (electrical pulses delivered at a frequency of 12 Hz for 4 s) under suppressed-CBF conditions. Each frame shown consists of the average of 10 consecutive images (effective resolution of 1 s; the time of the last image averaged indicated under each image) that have been subtracted from an average pre-stimulation image. Frames with a red-dot on the top-right corner indicate frames acquired during stimulation.

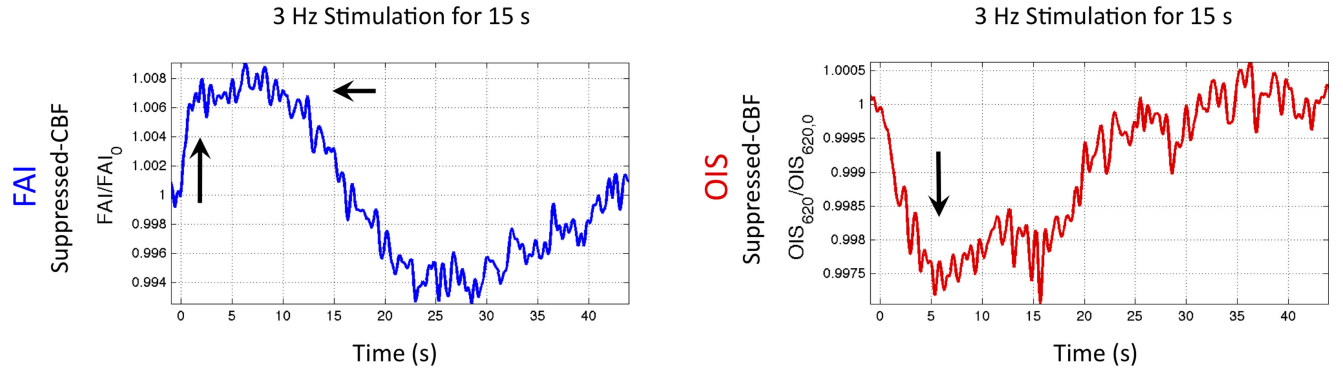

FIGURE 9 | Changes in oxidative metabolism induced by somato-sensory stimulation (3 Hz for 15 s) as detected in tissue and blood oxygenation using FAI (left panel) and OIS (right panel), respectively. These time series were averaged over a ROI covering the forelimb area in one animal. The FAI signal reached 90% peak in less than 2 s, while OIS signal took about 5 s to reach 90% peak.

investigation in our laboratory. To summarize, the temporal evolution of the activation-evoked changes in FAI under suppressed-CBF conditions is significantly faster than that of OIS or tissue P_{O_2} signals (**Figure 7**), indicating that the changes in cellular oxidative metabolism are indeed rapid and take significantly longer to be reflected in the average oxygen tension of tissue and blood.

CONCLUDING REMARKS

Increases in neural activity evoke increases in both CBF and CMR_{O_2}. These increases have been thought to reflect the metabolic demands of tissue. However, in terms of oxidative metabolism, the delivery of oxygen largely exceeds the consumption of oxygen in tissue. The delivery of oxygen is driven by the increases in CBF and its associated increases in CBV, but additional mechanisms are necessary to describe observations of tissue oxygen delivery. Arterial blood is highly saturated with oxygen and measurements of the vascular oxygen tension have shown that a relatively large amount of oxygen diffuses out of arteries prior to capillaries. This oxygen gradient along the arterial vasculature allows the mechanisms regulating CBF to also regulate the delivery of oxygen to sub-serving areas. In addition, neurally-evoked increases in CBF are also accompanied by increases in the arteriolar oxygen tension. This increase in arterial oxygenation contributes not only to the down-stream delivery of oxygen to tissue, but also to delivery of additional oxygen to extra-vascular spaces surrounding the arterioles. The supply of arterial oxygen to tissue has been hypothesized as necessary to homogenize the distribution of tissue oxygen. Nonetheless, other mechanisms beyond the increase in CBF and upstream oxygenation are necessary to fully describe the delivery of oxygen to tissue during evoked neural activity. While measurements of the tissue oxygen tension with increases in neural activity indicate that the role of CBF is not to maintain a constant average tissue oxygen tension, it is possible that the transient increases in tissue oxygen are necessary to maintain a minimum intra-cellular oxygen tension. Further study is necessary to determine the role of oxygen delivery to tissue with changes in neural activity, particularly in combination with the temporal dynamics of CMR_{O_2}.

The dynamics of tissue oxygen consumption have been difficult to measure because CMR_{O_2} and CBF modulate the oxygenation of tissue in opposite fashion. By suppressing the neurally-evoked CBF response, functional decreases in tissue oxygen tension elicited by increases in CMR_{O_2} have been consistently observed. Moreover, the temporal evolution of the tissue P_{O_2} changes are consistently slower than the neurally-evoked changes in CBF elicited by the same stimulus under normal conditions. Preliminary experiments performed using FAI indicate that cellular oxidative metabolism changes at a faster rate than the average changes in tissue and blood oxygenation. This may be due to the small volume occupied by mitochondria, but formal experiments are necessary to determine the relationship between cellular oxidative metabolism and blood oxygenation. Nonetheless, this method shows great promise at elucidating the functional properties and dynamics of CMR_{O_2}.

The findings described in this work have considerable implications for the quantification of the changes in CMR_{O_2} (and blood oxygen saturation) from hemoglobin-based imaging techniques like BOLD fMRI and deoxygenated hemoglobin-weighted OIS. The models used to calculate CMR_{O_2} from blood oxygenation data typically assume that arterial blood is fully saturated with oxygen and that the delivery and consumption of oxygen is rapid such that changes in venous blood oxygen saturation reflect the changes in tissue oxygen consumption. In this review, experimental support is presented for arterial oxygen saturation levels that are high but not 100%, particularly at the level of intra-cortical arteries. It is our opinion that for typical fMRI studies, where voxel sizes span millimeters, an arterial oxygen saturation level near 100% is probably a reasonable assumption. However, for intra-cortical voxels in higher resolution studies (e.g., voxel sizes of hundreds of micrometers), the arterial oxygen saturation level has dropped significantly and the assumption of fully saturated arterial blood may introduce significant errors to the CMR_{O_2} calculation. This can be potentially corrected if the input oxygen saturation is known. Notwithstanding, lower-resolution calibrated fMRI studies or ROI-wide analyses of calibrated fMRI data are not likely to be significantly impacted by this source of error. Another potential issue is that of blood volume changes. Traditionally, arterial blood was thought to be fully saturated with oxygen and does not contribute a BOLD signal change regardless of arterial blood volume changes, such that only changes in venous blood volume and saturation contribute to the BOLD signal (Buxton et al., 2004; Davis et al., 1998; Kim et al., 1999). There is a growing consensus that the changes in arterial volume are significantly larger than those of venous volume (which, like capillary blood volume, appear to be

small) (Lee et al., 2001; Kim et al., 2007; Vazquez et al., 2010). As a result, changes in arterial volume (and saturation) likely contribute a BOLD signal change. The impact and/or necessity of arterial BOLD signal contributions to traditional calibrated fMRI models needs to be investigated. Lastly, the temporal scale of the changes in cellular oxidative metabolism (as indicated by FAI) and blood oxygenation (as indicated by OIS and P_{O_2}) is significantly different, even though the temporal changes between tissue P_{O_2} and blood oxygenation are closer. These findings suggest that calculated CMR_{O_2} values using traditional calibrated fMRI models over transition regions are largely underestimated with respect to cellular oxidative metabolism, but to a lesser extent with respect to the average oxygenation of tissue. At least several models have been published that incorporate an arterial compartment and non-steady CMR_{O_2} dynamics (Zheng et al., 2005; Huppert et al., 2007; Uludag et al., 2009). The error introduced by these assumptions needs to be evaluated to determine appropriate models that can accurately quantify the changes in tissue CMR_{O_2}.

MATERIALS AND METHODS

The experimental methods for the vascular P_{O_2} measurements are reported in Vazquez et al. (2010), and those of the tissue P_{O_2} measurements recorded under control and suppressed-CBF conditions are reported in Masamoto et al. (2008) and Vazquez et al. (2008). Only new, previously unreported studies are described in this section. Five male Sprague-Dawley rats were used in this work ($n = 2$ for the tissue P_{O_2} depth experiments and $n = 3$ for the FAI experiments) following an experimental protocol approved by the University of Pittsburgh Institutional Animal Care and Use Committee. The experimental procedure used was similar to our previous studies (Masamoto et al., 2008; Vazquez et al., 2010). Briefly, the animals were initially anesthetized using isoflurane (5% for induction, 2% for surgery), nitrous oxide (50–65%) and oxygen (35–50%) for intubation and placement of catheters in the femoral artery and femoral vein. The respiration rate and volume were controlled using a ventilator. After intubation, the animals were placed in a stereotaxic frame and the skull was exposed over the somato-sensory area. A well was made using dental acrylic surrounding an area 5 mm × 7 mm on the left side of the skull, centered 3.5 mm lateral and 1.5 mm rostral from Bregma. The skull in this area was then removed using a dental drill. The dura matter was resected and the CSF fluid was released around the fourth ventricle area to minimize herniation. The well and the CSF release areas were then filled with 1.0% agarose gel at body temperature[1]. Two needle electrodes were placed in the right forepaw between digits 2 and 4 for electrical stimulation. The anesthesia and breathing mixture were then changed to isoflurane (1.2–1.4%), oxygen (~10%) and air (~90%) for experimental recording. Rectal temperature was maintained at 37°C throughout with a DC temperature control module. The arterial blood pressure, respiration rate, heart rate, rectal temperature, end-tidal CO_2 tension and isoflurane level were monitored and recorded using a polygraph data acquisition software.

[1]This preparation opens the possibility of oxygen in room air being supplied through the craniotomy. In our experiments, we observed while placing the PO2 probes that the PO2 gradient would settle close to the pial surface PO2 level a few hundred micrometers over the cortical surface. In addition, in placing the PO2 probes over the superior surface of arteries, the PO2 reading would increase prior to the probe reaching an artery. These observations indicated that a significant amount of oxygen is not likely supplied through the craniotomy.

TISSUE Po_2 DEPTH EXPERIMENTS

An optical imaging experiment (620 ± 5 nm transmitted light) was initially performed to map the somato-sensory area for P_{O_2} microelectrode placement (Vazquez et al., 2010). Tissue P_{O_2} measurements were performed using an oxygen microelectrode (APOX, Unisense, Aarhaus, Denmark) with tip diameter of 30 μm. The oxygen microelectrode was penetrated as close as possible to the activation focus location to a depth of 300 μm perpendicular to the cortical surface using a micromanipulator. A LDF probe (Perimed, Stockholm, Sweden) was placed over the cortical surface covering the tissue P_{O_2} probe location. The changes in tissue P_{O_2} and LDF were recorded during somato-sensory stimulation (1 ms pulses at 1.5 mA for 3 s at a frequency of 6 Hz repeated every 35 s, 10 times) at this depth (300 μm) and also at the cortical surface (0 μm). The oxygen microelectrode was calibrated before and after each experiment with 0%, 21%, and 100% oxygen in saline solution at 37°C. In addition, the stability of the current reading was checked before and after each experiment to ensure reliable measurements.

FAI AND OIS EXPERIMENTS

Flavoprotein autofluorescence images were acquired over a 5.5 × 4.1 mm^2 area using an epi-fluorescence macroscope (MVX-10, Olympus, Tokyo, Japan) and a digital cooled-CCD camera (CoolSnap HQ2, Photometrics, Princeton, NJ, USA) during somato-sensory stimulation of the rat forelimb. A mercury lamp light source coupled to a low-noise power supply (Opti-quip, Inc.) was used. The transmitted light was filtered between 450 and 490 nm while the camera recorded the fluorescence emission between 500 and 550 nm at 10 frames per second. Images were acquired under suppressed-CBF conditions, which required the intra-venous infusion of sNP (2 mg/kg in saline) (Masamoto et al., 2008). The infusion rate of the sNP was adjusted to maintain a mean arterial blood pressure between 40 and 45 mmHg over the course of the stimulation experiment. Two different forelimb stimulation experiments were performed: (1) 1 ms, 1.5 mA pulses at a frequency of 12 Hz for 4 s every 16 s repeated 10 times; (2) 1 ms, 1.5 mA pulses every 3 Hz for 15 s every 45 s repeated eight times. The infusion of the agent was terminated after approximately 30 min. FAI experiments were followed by optical imaging OIS experiments. Oblique light guides transmitting filtered red light (620 nm) were used for illumination and a matching barrier filter was placed prior to the camera. Prior to averaging, a ROI was outlined over the skull or dental acrylic to regress out unwanted fluctuations stemming from fluctuations in the light source from all the acquired images. The data from all the trials in an experiment were then averaged and a ROI time series were generated. The activation area ROI was obtained by thresholding a difference image obtained by averaging the images 2 s prior to stimulation onset and the two images obtained 2 s immediately after stimulation onset.

ACKNOWLEDGMENTS

This work was supported by NIH grants F32-NS056682 and RO1-EB003375. The authors would like to thank Dr. Kenneth Reinert and Dr. Timothy Ebner for their help in the implementation of flavoprotein autofluoresncence imaging in our laboratory and Dr. Ping Wang and Ms. Michelle Tasker for their assistance in experimental data collection.

REFERENCES

Ances, B. M., Buerk, D. G., Greenberg, J. H., and Detre, J. A. (2001). Temporal dynamics of the partial pressure of brain tissue oxygen during functional forepaw stimulation in rats. *Neurosci. Lett.* 306, 106–110.

Ances, B. M., Wilson, D. F., Greenberg, J. H., and Detre, J. A. (2001). Dynamic changes in cerebral blood flow, O_2 tension, and calculated cerebral metabolic rate of O_2 during functional activation using oxygen phosphorescence quenching. *J. Cereb. Blood Flow Metab.* 21, 511–516.

Berwick, J., Johnston, D., Jones, M., Martindale, J., Redgrave, P., and McLoughlin, N., Schiessl, I., and Mayhew, J. E. (2005). Neurovascular coupling investigated with two-dimensional optical imaging spectroscopy in rat whisker barrel cortex. *Eur. J. Neurosci.* 22, 1655–1666.

Boas, D. A., Jones, S. R., Devor, A., Huppert, T. J., and Dale, A. M. (2008). A vascular anatomical network model of the spatio-temporal response to brain activation. *Neuroimage* 40, 1116–1129.

Boas, D. A., Strangman, G., Culver, J. P., Hoge, R. D., Jasdzewski, G., and Poldrack, R. A., Rosen, B. R., and Mandeville, J. B. (2003). Can the cerebral metabolic rate of oxygen be estimated with near-infrared spectroscopy? *Phys. Med. Biol.* 48, 2405–2418.

Burton, A. C. (1954). Relation of structure to function of the tissues of the wall of blood vessels. *Physiol. Rev.* 34, 619–642.

Buxton, R. B., and Frank, L. R. (1997). A model for the coupling between cerebral blood flow and oxygen metabolism during neural stimulation. *J. Cereb. Blood Flow Metab.* 17, 64–72.

Buxton, R. B., Uludag, K., Dubowitz, D. J., and Liu, T. T. (2004). Modeling the hemodynamic response to brain activation. *Neuroimage* 23(Suppl. 1), S220–S233.

Chance, B. (1968). Cytochromes: chemical and structural aspects. *Science* 159, 654–658.

Chance, B., Cohen, P., Jobsis, F., and Schoener, B. (1962). Intracellular oxidation-reduction states *in vivo*. *Science* 137, 499–508.

Chance, B., Legallais, V., and Schoener, B. (1962). Metabolically linked changes in fluorescence emission spectra of cortex of rat brain, kidney and adrenal gland. *Nature* 195, 1073–1075.

Chance, B., Schoener, B., Oshino, R., Itshak, F., and Nakase, Y. (1979). Oxidation-reduction ratio studies of mitochondria in freeze-trapped samples. NADH and flavoprotein fluorescence signals. *J. Biol. Chem.* 254, 4764–4771.

Chen, X., Jaron, D., Barbee, K. A., and Buerk, D. G. (2006). The influence of radial RBC distribution, blood velocity profiles, and glycocalyx on coupled NO/O_2 transport. *J. Appl. Physiol.* 100, 482–492.

Davis, T. L., Kwong, K. K., Weisskoff, R. M., and Rosen, B. R. (1998). Calibrated functional MRI: mapping the dynamics of oxidative metabolism. *Proc. Natl. Acad. Sci. U.S.A.* 95, 1834–1839.

Duling, B. R., and Berne, R. M. (1970). Longitudinal gradients in periarteriolar oxygen tension. A possible mechanism for the participation of oxygen in local regulation of blood flow. *Circ. Res.* 27, 669–678.

Duling, B. R., Kuschinsky, W., and Wahl, M. (1979). Measurements of the perivascular P_{O_2} in the vicinity of the pial vessels of the cat. *Pflugers Arch*, 383, 29–34.

Fatt, I. (1976). *The Polarographic Oxygen Sensor: Its Theory of Operation and Its Application in Biology, Medicine, and Technology*. Cleveland, OH: CRC Press.

Fiat, D., Dolinsek, J., Hankiewicz, J., Dujovny, M., and Ausman, J. (1993). Determination of regional cerebral oxygen consumption in the human: 17O natural abundance cerebral magnetic resonance imaging and spectroscopy in a whole body system. *Neurol. Res.* 15, 237–248.

Fox, P. T., Raichle, M. E., Mintun, M. A., and Dence, C. (1988). Nonoxidative glucose consumption during focal physiologic neural activity. *Science* 241, 462–464.

Fukuda, M., Wang, P., Moon, C. H., Tanifuji, M., and Kim, S. G. (2006). Spatial specificity of the enhanced dip inherently induced by prolonged oxygen consumption in cat visual cortex: implication for columnar resolution functional MRI. *Neuroimage* 30, 70–87.

Garland, P. B., Chance, B., Ernster, L., Lee, C. P., and Wong, D. (1967). Flavoproteins of mitochondrial fatty acid oxidation. *Proc. Natl. Acad. Sci. U.S.A.* 58, 1696–1702.

Gibson, Q. H., Kreuzer, F., Meda, E., and Roughton, F. J. (1955). The kinetics of human haemoglobin in solution and in the red cell at 37 degrees C. *J. Physiol. (Lond.)* 129, 65–89.

Gray, L. H., and Steadman, J. M. (1964). Determination of the oxyhaemoglobin dissociation curves for mouse and rat blood. *J. Physiol.* 175, 161–171.

Hassinen, I., and Chance, B. (1968). Oxidation–reduction properties of the mitochondrial flavoprotein chain. *Biochem. Biophys. Res. Commun.* 31, 895–900.

Herscovitch, P., Mintun, M. A., and Raichle, M. E. (1985). Brain oxygen utilization measured with oxygen-15 radiotracers and positron emission tomography: generation of metabolic images. *J. Nucl. Med.* 26, 416–417.

Hillman, E. M., Devor, A., Bouchard, M. B., Dunn, A. K., Krauss, G. W., and Skoch, J., Bacskai, B. J., Dale, A. M., and Boas, D. A. (2007). Depth-resolved optical imaging and microscopy of vascular compartment dynamics during somatosensory stimulation. *Neuroimage* 35, 89–104.

Huang, S., Heikal, A. A., and Webb, W. W. (2002). Two-photon fluorescence spectroscopy and microscopy of NAD(P)H and flavoprotein. *Biophys. J.* 82, 2811–2825.

Huppert, T. J., Allen, M. S., Benav, H., Jones, P. B., and Boas, D. A. (2007). A multicompartment vascular model for inferring baseline and functional changes in cerebral oxygen metabolism and arterial dilation. *J. Cereb. Blood Flow Metab.* 27, 1262–1279.

Husson, T. R., Mallik, A. K., Zhang, J. X., and Issa, N. P. (2007). Functional imaging of primary visual cortex using flavoprotein autofluorescence. *J. Neurosci.* 27, 8665–8675.

Hyder, F., Shulman, R. G., and Rothman, D. L. (1998). A model for the regulation of cerebral oxygen delivery. *J. Appl. Physiol.* 85, 554–564.

Hyder, F., Kida, I., Behar, K. L., Kennan, R. P., Maciejewski, P. K., and Rothman, D. L. (2001). Quantitative functional imaging of the brain: towards mapping neuronal activity by BOLD fMRI. *NMR. Biomed.* 14, 413–431.

Ivanov, K. P., Sokolova, I. B., and Vovenko, E. P. (1999). Oxygen transport in the rat brain cortex at normobaric hyperoxia. *Eur. J. Appl. Physiol. Occup. Physiol.* 80, 582–587.

Jensen, F. B. (2004). Red blood cell pH, the Bohr effect, and other oxygenation-linked phenomena in blood O_2 and CO_2 transport. *Acta Physiol. Scand.* 182, 215–227.

Kasischke, K. A., Vishwasrao, H. D., Fisher, P. J., Zipfel, W. R., and Webb, W. W. (2004). Neural activity triggers neuronal oxidative metabolism followed by astrocytic glycolysis. *Science* 305, 99–103.

Kim, S. G., Rostrup, E., Larsson, H. B., Ogawa, S., and Paulson, O. B. (1999). Determination of relative CMR_{O2} from CBF and BOLD changes: significant increase of oxygen consumption rate during visual stimulation. *Magn. Reson. Med.* 41, 1152–1161.

Kim, T., Hendrich, K. S., Masamoto, K., and Kim, S. G. (2007). Arterial versus total blood volume changes during neural activity-induced cerebral blood flow change: implication for BOLD fMRI. *J. Cereb. Blood Flow Metab.* 27, 1235–1247.

Lamkin-Kennard, K. A., Jaron, D., and Buerk, D. G. (2004). Impact of the Fahraeus effect on NO and O_2 biotransport: a computer model. *Microcirculation* 11, 337–349.

Lauritzen, M. (2001). Relationship of spikes, synaptic activity, and local changes of cerebral blood flow. *J. Cereb. Blood Flow Metab.* 21, 1367–1383.

Lee, S. P., Duong, T. Q., Yang, G., Iadecola, C., and Kim, S. G. (2001). Relative changes of cerebral arterial and venous blood volumes during increased cerebral blood flow: implications for BOLD fMRI. *Magn. Reson. Med.* 45, 791–800.

Masamoto, K., Fukuda, M., Vazquez, A., and Kim, S. G. (2009). Dose-dependent effect of isoflurane on neurovascular coupling in rat cerebral cortex. *Eur. J. Neurosci.* 30, 242–250.

Masamoto, K., Kurachi, T., Takizawa, N., Kobayashi, H., and Tanishita, K. (2004). Successive depth variations in microvascular distribution of rat somatosensory cortex. *Brain Res.* 995, 66–75.

Masamoto, K., Omura, T., Takizawa, N., Kobayashi, H., Katura, T., and Maki, A., Kawaguchi, H., and Tanishita, K. (2003). Biphasic changes in tissue partial pressure of oxygen closely related to localized neural activity in guinea pig auditory cortex. *J. Cereb. Blood Flow Metab.* 23, 1075–1084.

Masamoto, K., Vazquez, A., Wang, P., and Kim, S. G. (2008). Trial-by-trial relationship between neural activity, oxygen consumption, and blood flow responses. *Neuroimage* 40, 442–450.

Mayhew, J., Johnston, D., Berwick, J., Jones, M., Coffey, P., and Zheng, Y. (2000). Spectroscopic analysis of neural activity in brain: increased oxygen consumption following activation of barrel cortex. *Neuroimage* 12, 664–675.

Moon, C. H., Fukuda, M., Park, S. H., and Kim, S. G. (2007). Neural interpretation of blood oxygenation level-dependent fMRI maps at submillimeter columnar resolution. *J. Neurosci.* 27, 6892–6902.

Nagaoka, T., Zhao, F., Wang, P., Harel, N., Kennan, R. P., and Ogawa, S., Kim, S. G. (2006). Increases in oxygen consumption without cerebral blood volume change during visual stimulation under hypotension condition. *J. Cereb. Blood Flow Metab.* 26, 1043–1051.

Popel, A. S. (1989). Theory of oxygen transport to tissue. *Crit. Rev. Biomed. Eng.* 17, 257–321.

Reinert, K. C., Dunbar, R. L., Gao, W., Chen, G., and Ebner, T. J. (2004). Flavoprotein autofluorescence imaging of neuronal activation in the cerebellar cortex in vivo. *J. Neurophysiol.* 92, 199–211.

Rothman, D. L., Behar, K. L., Hyder, F., and Shulman, R. G. (2003). In vivo NMR studies of the glutamate neurotransmitter flux and neuroenergetics: implications for brain function. *Annu. Rev. Physiol.* 65, 401–427.

Severinghaus, J. W. (1979). Simple, accurate equations for human blood O_2 dissociation computations. *J. Appl. Physiol.* 46, 599–602.

Sharan, M., Vovenko, E. P., Vadapalli, A., Popel, A. S., and Pittman, R. N. (2008). Experimental and theoretical studies of oxygen gradients in rat pial microvessels. *J. Cereb. Blood Flow Metab.* 28, 1597–1604.

Shibuki, K., Hishida, R., Murakami, H., Kudoh, M., Kawaguchi, T., and Watanabe, M., Watanabe, S., Kouuchi, T., and Tanaka, R. (2003). Dynamic imaging of somatosensory cortical activity in the rat visualized by flavoprotein autofluorescence. *J. Physiol. (Lond.)* 549(Pt 3), 919–927.

Shulman, R. G., Hyder, F., and Rothman, D. L. (2001). Lactate efflux and the neuroenergetic basis of brain function. *NMR Biomed.* 14, 389–396.

Shuttleworth, C. W., Brennan, A. M., and Connor, J. A. (2003). NAD(P)H fluorescence imaging of postsynaptic neuronal activation in murine hippocampal slices. *J. Neurosci.* 23, 3196–3208.

Siesjö, B. K. (1978). *Brain Energy Metabolism* (0471995150 ed.). Chichester/New York: Wiley.

Skala, M. C., Riching, K. M., Gendron-Fitzpatrick, A., Eickhoff, J., Eliceiri, K. W., White, J. G., and Ramanujam, N. (2007). In vivo multiphoton microscopy of NADH and FAD redox states, fluorescence lifetimes, and cellular morphology in precancerous epithelia. *Proc. Natl. Acad. Sci. U.S.A.* 104, 19494–19499.

Thompson, J. K., Peterson, M. R., and Freeman, R. D. (2003). Single-neuron activity and tissue oxygenation in the cerebral cortex. *Science* 299, 1070–1072.

Tsai, A. G., Johnson, P. C., and Intaglietta, M. (2003). Oxygen gradients in the microcirculation. *Physiol. Rev.* 83, 933–963.

Uludag, K., Dubowitz, D. J., Yoder, E. J., Restom, K., Liu, T. T., and Buxton, R. B. (2004). Coupling of cerebral blood flow and oxygen consumption during physiological activation and deactivation measured with fMRI. *Neuroimage* 23, 148–155.

Uludag, K., Muller-Bierl, B., and Ugurbil, K. (2009). An integrative model for neuronal activity-induced signal changes for gradient and spin echo functional imaging. *Neuroimage* 48, 150–165.

Valabregue, R., Aubert, A., Burger, J., Bittoun, J., and Costalat, R. (2003). Relation between cerebral blood flow and metabolism explained by a model of oxygen exchange. *J. Cereb. Blood Flow Metab.* 23, 536–545.

Vanzetta, I., Hildesheim, R., and Grinvald, A. (2005). Compartment-resolved imaging of activity-dependent dynamics of cortical blood volume and oximetry. *J. Neurosci.* 25, 2233–2244.

Vazquez, A. L., Fukuda, M., Tasker, M. L., Masamoto, K., and Kim, S. G. (2010). Changes in cerebral arterial, tissue and venous oxygenation with evoked neural stimulation: implications for hemoglobin-based functional neuroimaging. *J. Cereb. Blood Flow Metab.* 30, 428–439.

Vazquez, A. L., Masamoto, K., and Kim, S. G. (2008). Dynamics of oxygen delivery and consumption during evoked neural stimulation using a compartment model and CBF and tissue $P(O_2)$ measurements. *Neuroimage* 42, 49–59.

Vovenko, E. (1999). Distribution of oxygen tension on the surface of arterioles, capillaries and venules of brain cortex and in tissue in normoxia: an experimental study on rats. *Pflugers Arch.* 437, 617–623.

Yaseen, M. A., Srinivasan, V. J., Sakadzic, S., Wu, W., Ruvinskaya, S., and Vinogradov, S. A., and Boas, D. A. (2009). Optical monitoring of oxygen tension in cortical microvessels with confocal microscopy. *Opt. Express* 17, 22341–22350.

Zheng, Y., Johnston, D., Berwick, J., Chen, D., Billings, S., and Mayhew, J. (2005). A three-compartment model of the hemodynamic response and oxygen delivery to brain. *Neuroimage* 28, 925–939.

Zheng, Y., Martindale, J., Johnston, D., Jones, M., Berwick, J., and Mayhew, J. (2002). A model of the hemodynamic response and oxygen delivery to brain. *Neuroimage* 16(Pt 1), 617–637.

Conflict of Interest Statement: The authors declare that the research was conducted in the absence of any commercial or financial relationships that could be construed as a potential conflict of interest.

Received: 01 March 2010; paper pending published: 05 April 2010; accepted: 26 May 2010; published online: 18 June 2010.
Citation: Vazquez AL, Masamoto K, Fukuda M and Kim S-G (2010) Cerebral oxygen delivery and consumption during evoked neural activity. Front. Neuroenerg. ***2****:11. doi: 10.3389/fnene.2010.00011*

frontiers in
NEUROENERGETICS

REVIEW ARTICLE
published: 23 June 2010
doi: 10.3389/fnene.2010.00013

From acoustic segmentation to language processing: evidence from optical imaging

Hellmuth Obrig[1,2,3]*, Sonja Rossi[1,3], Silke Telkemeyer[3,4,5] and Isabell Wartenburger[3,4,5]

[1] *Max-Planck-Institute for Cognitive and Brain Sciences, Leipzig, Germany*
[2] *Clinic for Cognitive Neurology, University Clinic Leipzig, University of Leipzig, Leipzig, Germany*
[3] *Department of Neurology, Berlin NeuroImaging Center, Charité Universitätsmedizin Berlin, Berlin, Germany*
[4] *Neurocognition of Language/Neurolinguistics, Department of Linguistics, University of Potsdam, Potsdam, Germany*
[5] *Cluster Languages of Emotion, Freie Universität Berlin, Berlin, Germany*

Edited by:
David Boas, Massachusetts General Hospital, USA; Massachusetts Institute of Technology, USA; Harvard Medical School, USA

Reviewed by:
Heather Bortfeld, University of Connecticut, USA
Sharon Fox, Massachusetts Institute of Technology, USA

****Correspondence:***
Hellmuth Obrig, Max-Planck-Institute for Cognitive and Brain Sciences, Stephanstrasse 1a, 04103 Leipzig, Germany. e-mail: obrig@cbs.mpg.de

During language acquisition in infancy and when learning a foreign language, the segmentation of the auditory stream into words and phrases is a complex process. Intuitively, learners use "anchors" to segment the acoustic speech stream into meaningful units like words and phrases. Regularities on a segmental (e.g., phonological) or suprasegmental (e.g., prosodic) level can provide such anchors. Regarding the neuronal processing of these two kinds of linguistic cues a left-hemispheric dominance for segmental and a right-hemispheric bias for suprasegmental information has been reported in adults. Though lateralization is common in a number of higher cognitive functions, its prominence in language may also be a key to understanding the rapid emergence of the language network in infants and the ease at which we master our language in adulthood. One question here is whether the hemispheric lateralization is driven by linguistic input *per se* or whether non-linguistic, especially acoustic factors, "guide" the lateralization process. Methodologically, functional magnetic resonance imaging provides unsurpassed anatomical detail for such an enquiry. However, instrumental noise, experimental constraints and interference with EEG assessment limit its applicability, pointedly in infants and also when investigating the link between auditory and linguistic processing. Optical methods have the potential to fill this gap. Here we review a number of recent studies using optical imaging to investigate hemispheric differences during segmentation and basic auditory feature analysis in language development.

Keywords: optical imaging, infants, language acquisition, acoustic segmentation, NIRS

INTRODUCTION: ACQUISITION OF LANGUAGE COMPETENCE

Language is considered a specific human faculty, which is universal with respect to features such as compositionality, arbitrariness of signs and recursion (Hauser et al., 2002). Beyond such *universal* features, common to all human languages, competence in a *specific* spoken language requires one to recognize phonological and prosodic features, to have knowledge about lexico-semantic representations, and to master specific syntactic rules (Cutler et al., 1983). In addition, languages are embedded into a social context, and their use is shaped by metalinguistic cultural conventions. Thus the acquisition of language implies that both: (i) humans are biologically endowed with the faculty of language and (ii) the acquisition of their specific native language(s) critically depends on social interaction (Bonatti et al., 2002; Kuhl et al., 2003; Kuhl, 2007). An important input for infants in social interaction is speech. Although language competence goes beyond speech perception, infants can use auditory regularities in speech to find anchors enabling the acquisition of language. Investigating the neuronal underpinnings of speech processing may hence delineate a framework in which both, universal – potentially inborn – prerequisites and specifically acquired regularities mutually shape language competence (Dehaene-Lambertz et al., 2006). Studies from a number of disciplines, including linguistics and psychology but also neuroimaging have highlighted commonalities between the processing of complex auditory stimuli and features of speech (Kushnerenko et al., 2001; Benasich et al., 2006). More specifically, the well established lateralization of language processing has been discussed in the light of a potentially more basic specialization of the respective secondary auditory cortices (Zatorre et al., 2002; Poeppel et al., 2008). In this vein influential theories have been put forward, based on experimental findings which show double dissociations of auditory feature analysis, such as spectral vs. temporal complexity (e.g., Schonwiesner et al., 2005) or slow vs. fast modulations of the auditory input (e.g., Boemio et al., 2005). With regard to the question concerning the contribution of biologically endowed vs. use-dependent shaping of the brain's language network, a close relation between the processing of complex auditory features and speech perception allows for an integrative view: acquisition of language builds on a neurobiological ability to process complex auditory stimuli with high precision while the specific language is environmentally shaped.

We proceed based on the fact that language and auditory processing are interrelated by speech and focus our review on the development of speech perception. Recent studies provide evidence that auditory feature analysis is already highly developed at birth (DeCasper and Prescott, 2009; Sambeth et al., 2009), but

is substantially modified by the specific language exposure within the first months of life. Additionally, there is ample evidence that the language acquisition process is bidirectional, in that language competence shapes the interpretation of ambiguous auditory signals, as has been shown in cases of conflicting visual–auditory input (Campbell, 2008; Bristow et al., 2009). Building on the research of the neuronal underpinnings of language acquisition, the scope of our contribution is to give a comprehensive account of recent work using optical imaging investigating speech processing in infants. Besides the methodological focus on this non-invasive tool we outline studies in the context of *segmentation* based on acoustic features. Generally segmentation denotes the ability to find structure in spoken language, which represents a more or less continuous auditory stream. Segmentation allows the listener to identify single words but also phrases and syntactic structure. While segmentation is relevant for the ease at which the language-competent listener decodes the auditory stream, it is a mandatory first step for the prelinguistic infant. Segmentation is initially based on specific "anchors" provided by auditory cues in the speech signal.

METHODOLOGICAL CONSIDERATIONS: WHY DO WE FOCUS ON OPTICAL IMAGING?

Traditionally neuro- and psycholinguistic research has been dominated by electrophysiological approaches. This stems from two properties of the EEG (and in part MEG) technique: (i) exquisite temporal resolution in the range of milliseconds and (ii) comparatively low experimental constraints (Friederici, 2004; Huotilainen et al., 2008). The former allows for the monitoring of temporally sequential sub-processes in language comprehension, and is therefore essential to construct models of hierarchical and parallel processing steps. The latter can be considered a prerequisite to extend neuro- and psycholinguistic research to developmental issues (Friederici, 2005). As an example, EEG recordings can provide reliable information on whether, a prelinguistic infant is sensitive to linguistically relevant features and can additionally test hypotheses that predict a temporal succession of steps affording linguistic operations (Benasich et al., 2002; Friederici, 2005; Kooijman et al., 2005; Oberecker et al., 2005; Mannel and Friederici, 2009). There are, however, substantial limitations. For instance, localization of the neuronal activity elicited by linguistic contrasts is difficult when relying on EEG recordings. Some components of the event-related potentials are typically seen over the central electrodes, such as the N400, essentially reflecting lexico-semantic access. This is counterintuitive given the broad evidence for a lateralization of the language network (Lau et al., 2008). Hence when using EEG the assignment of a language-specific component to a cortical area is somewhat arbitrary – in some instances even with respect to lateralization. Often topography serves to differentiate components rather than an anatomical ascription. Also while electrophysiological approaches are very powerful in detecting brief processes in the range of 10–1000 ms, the integration over a longer time frame requires less robust analytical approaches such as DC-EEG or the analysis of oscillatory activity in the recorded signal (Hald et al., 2006). Both a better localization of the activation and the integration over longer time frames are features of the vascular based techniques. Hence the advent of functional magnetic resonance imaging (fMRI) using BOLD-contrast has led to an enormous boost in neurolinguistic research (Bookheimer, 2002; Gernsbacher and Kaschak, 2003). The technique allows us to investigate exact functional–anatomical relations in the language network and has successfully demonstrated that part of the ambiguity of EEG-based assumptions may resolve when assuming a much wider network to be activated by the language input (Pulvermuller et al., 2009). With respect to auditory presented tasks, however, instrumental noise of the scanner poses a very different challenge. Surprisingly, the comprehension of speech is quite robust. Competent listeners will extract linguistically relevant information even in very noisy environments and cochlear implant wearers extract almost the full linguistic content of spoken language from a very limited number of spectral bands transmitted to the auditory system by the device (Moore and Shannon, 2009). Nonetheless, interfering scanner noise may well be a crucial factor, especially with respect to studies in which the differentiation of subtle acoustic features such as phoneme discrimination is in the focus of interest. Also, concerning the emergence of language competence, fMRI approaches in infants are limited to a rather small number of research labs, in part due to ethical considerations (Dehaene-Lambertz et al., 2002). It therefore comes by no surprise that alternative methodologies such as non-invasive optical imaging have been used in a number of recent studies investigating language acquisition during infancy (Pena et al., 2003; Bortfeld et al., 2009; Hull et al., 2009).

Optical imaging, relying on the principles of near-infrared spectroscopy (NIRS), requires a comparatively simple set-up, which allows for measurements also in preterm infants, neonates, and infants (Aslin and Mehler, 2005; Lloyd-Fox et al., 2010). For an example see **Figure 2E**. The methodology is completely silent, permitting a near natural presentation of auditory stimuli by the lack of instrumental noise. Additionally, the simultaneous acquisition of EEG without any interference is of specific importance to the field (Koch et al., 2006, 2009; Telkemeyer et al., 2009), since many domains of language processing have been reliably mirrored in differential EEG components.

The assessment of neuronal activity by optical imaging is based on the vascular response much like PET and fMRI (Villringer and Dirnagl, 1995). Compared to fMRI it has a coarse spatial resolution in the range of centimeters (but see Zeff et al., 2007). This is comparable to the estimated lateral resolution of EEG. However, as opposed to EEG, the attribution of the signal to the underlying cortical area is reliable. Spatial depths resolution of optical imaging is limited by physical principles of light propagation in highly scattering media (Obrig and Villringer, 2003). Even novel approaches to enhance topographical resolution are restricted to the cortical surface and provide no information on subcortical signal changes or activations in mesial cortical areas, which are distant from the brain's surface. Optical imaging systems to supply a rough depth resolution using multiple distance measurements or time resolved spectroscopy have been used in infants (Hebden and Austin, 2007) and adults (Liebert et al., 2004, 2005), but have not been applied in cognitive tasks. Optimization of the technology is mandatory to allow for an even broader application in the field (Zeff et al., 2007; White et al., 2009).

For the application in language research, most groups have used monitors, which can detect changes in the concentrations of oxygenated and deoxygenated hemoglobin (ΔHbO, ΔHbR). The sum of both

changes results in changes in total hemoglobin concentration in the sampled volume (ΔHbT = ΔHbO + ΔHbR). Due to their differential absorption spectra in the near-infrared spectrum (600–950 nm) the two hemoglobins can be differentiated when light attenuation is measured at two or more wavelengths. This can be perceived as an extension of the well-known fact that fully oxygenated (arterial), and partially deoxygenated (venous) blood differ in color. By solving a simple equation-system the changes in attenuation at the different wavelengths are transformed into hemoglobin concentration changes based on the Beer-Lambert approach (Cope and Delpy, 1988). Methodologically this is a rather conservative approach (see **Figure 1**).

The translation of the measured quantities into a physiologically meaningful signal needs to be mentioned (see also Lloyd-Fox et al., 2010). In brief, the vascular imaging community has adopted the term "activation" for an increase in regional cerebral blood flow (rCBF). The underlying assumption is that an increase in neuronal activity generates an increased metabolic demand, which is met by the increase in blood flow. It is important to note that this tight neurovascular coupling has been demonstrated in a large number of studies using various techniques both invasively in animals and also non-invasively in adult humans (Lauritzen and Gold, 2003; Iadecola, 2004; Logothetis and Wandell, 2004). For optical imaging, the increase in blood flow is reflected by an increase in oxygenated and total hemoglobin (HbO↑, HbT↑), the latter corresponding to blood volume and a decrease in deoxygenated hemoglobin (HbR↓), resulting from an increase in blood flow velocity. The decrease in HbR is less intuitive, since the consumption of oxygen in an activated area intuitively would yield an increase in HbR. However, it has been demonstrated that in most instances the increase in blood flow overcompensates the oxygen demand (Fox and Raichle, 1986). A focal hyperoxygenation, including a decrease in HbR, is therefore expected in an "activated" area.

There is an on-going discussion regarding whether HbO, HbT, or HbR changes will better reflect "activation" in an optical imaging study. This discussion becomes even more heated when it comes to interpreting the findings in infants and neonates, since a number of reports have suggested that in early infanthood the vascular response may follow substantially different rules due to a different metabolic rate of oxygen in non-myelinated brain tissue (Kusaka et al., 2004; Marcar et al., 2004; but Colonnese et al., 2008). Additionally, the fact that many studies have shown increases in HbO without corresponding decreases in HbR has been used to advocate the methodology's sensitivity to activations which would be "silent" in an fMRI-study (but see **Figures 2A–C**). The comparative study simultaneously assessing optical imaging and BOLD-contrast in infants of different ages is missing. Hence, it seems appropriate to report both compounds irrespective of whether both or only one compound yields the hypothesized effect. In our review we consider studies reporting increases in HbO and HbT and/or decreases in HbR as an indicator of an activation in the underlying cerebral tissue (see **Figure 1**). We mark the parameter on which statistics were performed in brackets. When linking results of optical imaging studies to the much larger body of vascular imaging based on BOLD-contrast fMRI, it should be acknowledged that an area in which HbR does not decrease does not easily correspond to an area showing an activation (increase

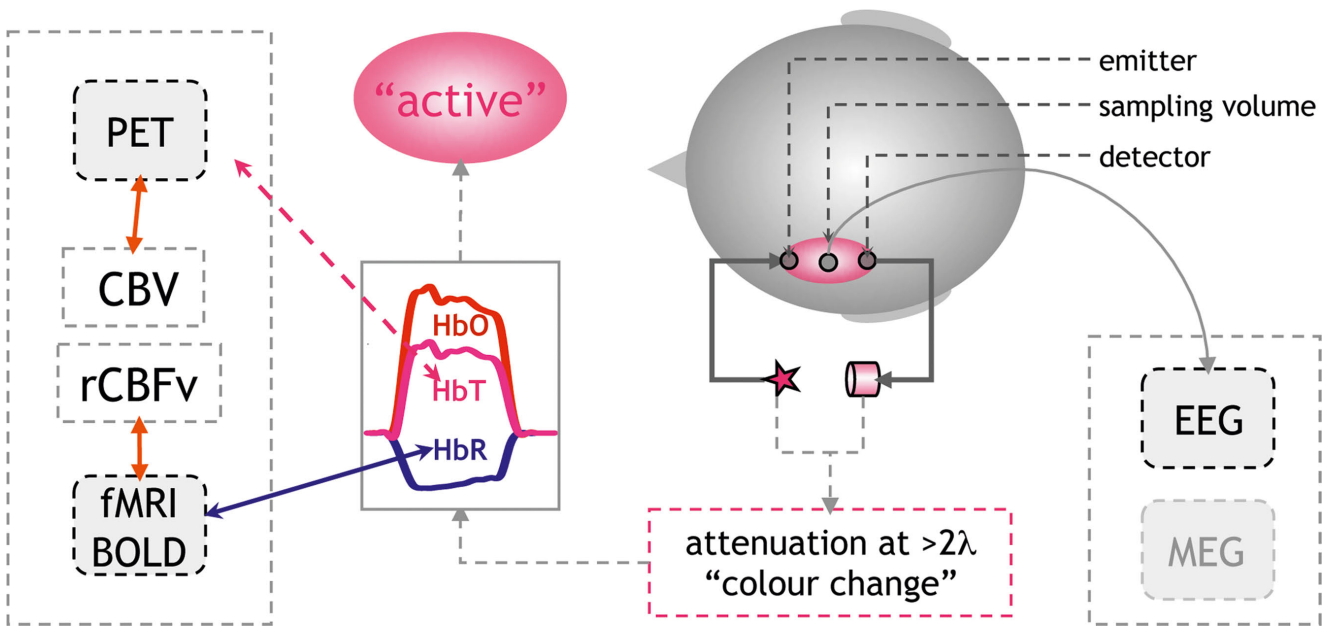

FIGURE 1 | Principles of non-invasive optical imaging: Optical probes are fixed to the head defining the sampling volume (pink ellipse). Measuring changes in attenuation at two or more wavelengths allows to calculate changes in the concentration of HbO, HbR. An increase in HbO and/or a decrease in HbR indicate cerebral activation. Physiologically this pattern results from an increase in regional cerebral blood flow (rCBF) consisting of an increase in blood flow velocity (rCBFv) and volume (rCBV). The increase in rCBF overcompensates the demand in oxygen (Fox and Raichle, 1986). An increased "washout" of HbR results from increased rCBFv. This decrease in HbR is the major source of fMRI BOLD-contrast increases (Steinbrink et al., 2006). The change in total hemoglobin concentration (HbT = HbR + HbO) correlates with blood volume (CBV), which can be assessed by positron emission tomography (PET). Notably the assessment of electrophysiological markers of activation by EEG or MEG (right side of graph) is undemanding as demonstrated in a neonate in **Figure 2E.**

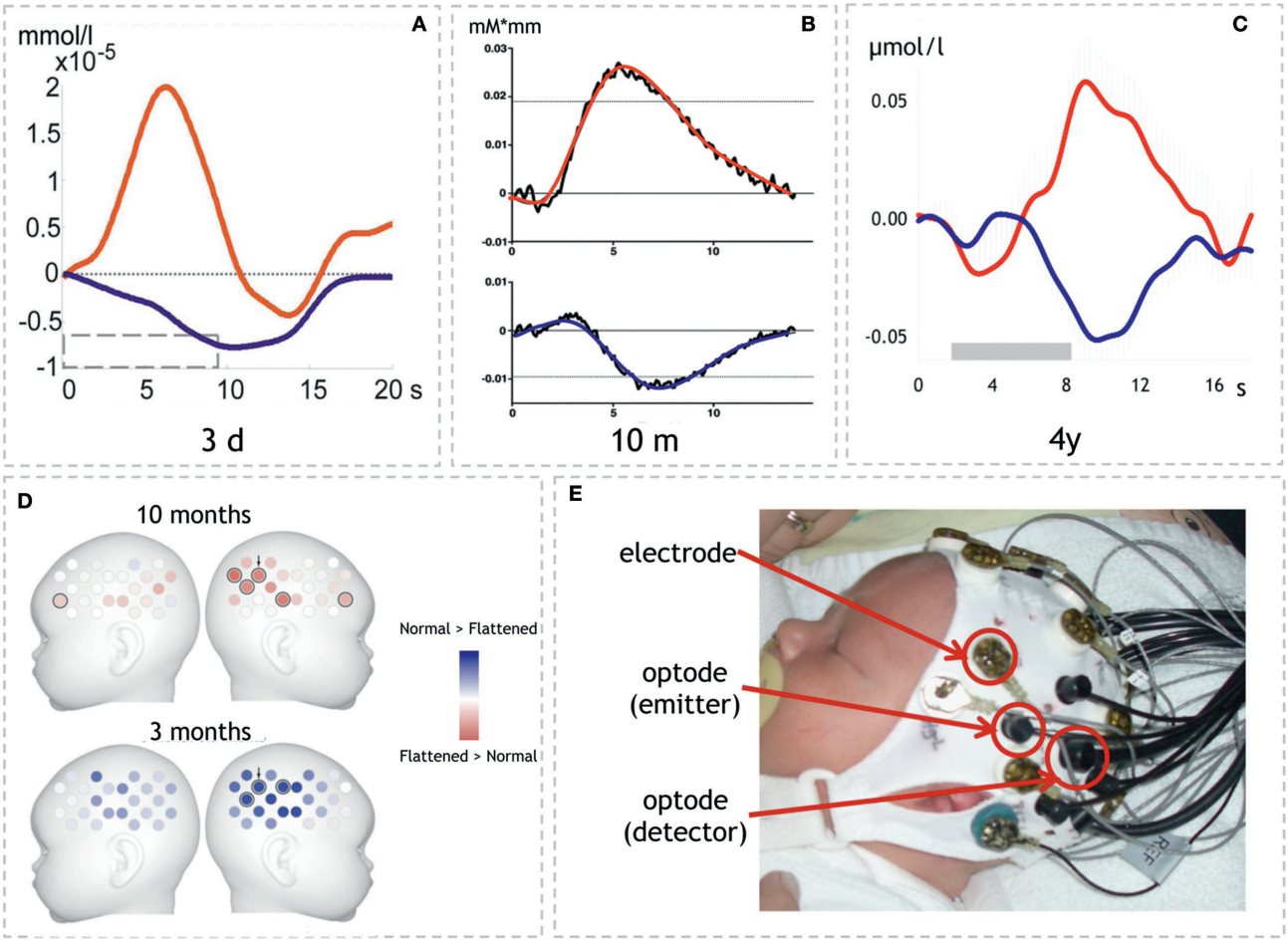

FIGURE 2 | Examples of optical imaging results in infants and neonates. **(A–C)** Time-courses of HbO and HbR in three different age groups. Note that the response pattern is similar in all three studies though magnitude differs. **(A)** Neonates' response to structured noise. Here the statistics on HbR↓ yielded a lateralized response (adapted with permission from Telkemeyer et al., 2009). **(B)** Response to sentences in 10-month-old infants. In this study HbO↑ yielded the effects shown in **(D)** (adapted with permission from Homae et al., 2007). **(C)** Response to hummed sentences in 4-year-old children. HbO↑ *and* HbR↓ showed statistically significant results (adapted with permission from Wartenburger et al., 2007). **(D)** Topographical information is available when using probe arrays (24 volumes over each hemisphere; adapted with permission from Homae et al., 2007). The results show the differential activation to normal vs. flattened speech in two age groups (10 and 3 months). Note that the lateralization changes sides (red: lager response amplitude for flattened speech than normal speech; blue: normal > flattened; results are based on HbO↑). **(E)** Simultaneous assessment of EEG and optical imaging in a neonate as used in (Telkemeyer et al., 2009). (Permission from the infant's parents to show the picture was obtained.)

in BOLD-contrast; Kleinschmidt et al., 1996; Steinbrink et al., 2006)[1]. If HbR increases and HbO decreases this would in most instances yield a decrease in a BOLD-contrast study and would thus be termed "deactivated" or "negative BOLD-contrast" (Wenzel et al., 2000). Increases in both HbO and HbR in response to a stimulus will require a new model for neurovascular coupling. In other words, such a scenario means that a blood-volume based methodology will term the area "activated", while a corresponding BOLD-contrast fMRI study may yield a "deactivation" in the very same area.

The complexity and potential ambiguity of the different response modalities including the vascular response, the electrophysiological response and even the behavioral measure of looking times calls for multimodal approaches. Such approaches may broaden our knowledge on the relation between neuronal, vascular, and behavioral response parameters and will definitely strengthen our confidence in the response seen in either of the methodologies.

[1]BOLD-contrast stems from two major effects. The larger effect is the extra- to intravascular field gradient largely caused by concentration changes of paramagnetic HbR in the vessel. The second effect is due micro-inhomogeneities in the vessel itself. The latter depends on the ratio of HbR and HbO in the vessel, or saturation. Thus, theoretically, an isolated increase in blood volume could yield an increase in BOLD-contrast (i.e., inflow of HbO into the voxel while concentration of HbR remains constant). Such scenarios cannot be easily explained by any of the proposed models of rCBF changes in an activated area. These models describe the complex interplay between blood flow velocity, blood volume, oxygenation, and the BOLD-contrast (Mandeville et al., 1999; Buxton et al., 2004; Stephan et al., 2004). An *increase* in HbR could only elicit a positive BOLD-contrast in scenarios of an extreme increase in blood volume, which is even less compatible with any of these models. In most cases an increase in deoxy-Hb will correspond to a decrease in BOLD, signaling "deactivation" (Wenzel et al., 2000). For a detailed discussion of models to explain the interdependence of BOLD, blood flow, and the local hemoglobin concentrations please refer to Steinbrink et al. (2006).

SEGMENTATION AND ITS RELEVANCE FOR LANGUAGE ACQUISITION

Apart from the methodological focus, why do we focus our review of studies on language acquisition in the context of acoustic segmentation? When we listen to speech we are confronted with a *continuous* auditory stream. On the contrary, all languages follow *hierarchical* principles, which are conventionalized in each language by specific rules. To decode the meaning of speech, it is mandatory to identify single words, phrases, and sentences. During language acquisition this process is initially guided by acoustic cues aiding the segmentation into smaller units. We here differentiate between two levels of such acoustic cues. These two levels differ temporally with respect to the length on which the auditory feature acts (see **Figure 3**). Linguistically, they largely convey cues relevant either for suprasegmental or segmental information (see **Figure 5**).

(i) Sentential prosody – the melodic pitch and durational variation at the sentential level – supplies acoustic cues to chunk the auditory input into sentences and phrases. Since prosodic features act across a number of segments, the linguistic information conveyed is also termed "suprasegmental." Such prosodic grouping of lexical items in a sentence is relevant also for the language-competent adult. However, language-competent listeners will also strongly rely on syntactic rules[2]. On the contrary, during language acquisition in infanthood, prosody plays a critical role for segmentation. It also aids acquisition of syntax as highlighted by the "prosodic bootstrapping account" (Gleitman and Wanner, 1982). The time scale on which prosodic pitch variation conveys auditory cues to segment the speech stream spans over a wide range. While sentential prosody acts over a period of seconds, other cues like stress, also conveying suprasegmental information, may develop in a matter of hundreds of milliseconds (see **Figure 3**). Some aspects of the neuronal correlates of prosodic processing and its development in infancy are discussed in the paragraph "Optical Imaging Studies on the Neural Correlates of Suprasegmental Processing".

(ii) While acoustic cues supplied by prosody segment the speech stream into larger units, the differentiation of single words is also aided by acoustic cues acting on a much shorter time scale. These cues can be based on the specific phonemic inventory of a given language, since it provides constraints of how segments within the auditory stream are ordered to constitute single lexico-semantic entries (i.e., words). Phonemes are the smallest units that distinguish meaning (e.g., */pit/* vs. */bit/* differ only in the initial distinctive phoneme). The linguistic information conveyed by such language-specific regularities is also termed "segmental." As is illustrated in **Figure 3** the duration of such cues is much shorter than those provided by sentential prosody and can reach down to ~10 ms (see **Figure 3**). Studies that deal with such sublexical cues and their relevance for speech processing are discussed in the paragraph "Optical Imaging Studies on the Neural Correlates of Segmental Processing[3]."

[2]As an example the meaning of the sentence "The teacher said the pupil is stupid" depends on how the lexical items are syntactically related ("The teacher said // the pupil is stupid." vs. "The teacher// said the pupil //is stupid."). Typically the ambiguity of this sentence will not occur in spoken language, because sentential prosody will clearly mark boundaries ("//" in the above example). The hierarchical structure of the sentence can also be unambiguously coded by means of syntax (e.g., "The teacher said, *that* the pupil is stupid.").

[3]It should be noted that any acoustic cue that relies on the relation between several phonemes could be considered "suprasegmental." Thereby strictly speaking durational contrasts, pitch accents, and tonal cues could be considered suprasegmental. However, in some languages the relative length of a vowel defines a phonemic boundary, providing segmental information in a specific spoken language (e.g., Minagawa-Kawai et al., 2002). Thus, the terminology may be somewhat misleading in these instances. We discuss here studies on such cues in the context of segmental information as opposed to the studies on sentential prosody, which unambiguously act on a suprasegmental level.

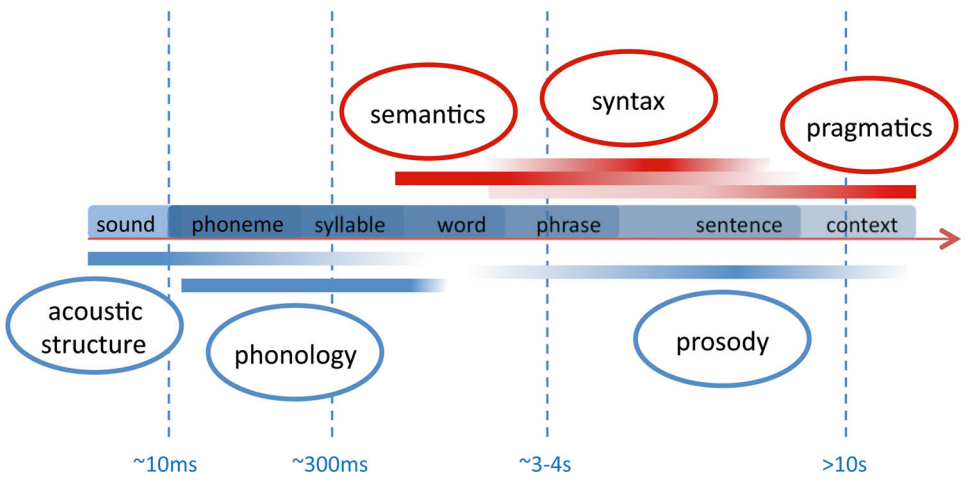

FIGURE 3 | Sketch of temporal frames relevant for speech perception. The smallest *linguistically* relevant segmentation deals with the differentiation of phonemes which rely on transitional differences in the range of 10 ms. Syllables and words form the nucleus of a lexico-semantic decoding of speech. Syntax and prosody act on the level of phrases and sentences which may have a duration of several seconds. The speaker's intention (pragmatics) evolves over largely different temporal frames ranging from single vocalizations to tales and stories. Note that the components below the time line (blue) are available also to the prelinguistic infant due to their acoustic prominence. The other components (red) are fully available only when a certain language competence is reached. In the language-competent adult, all levels strongly interact.

Having sketched some principal issues of segmentation, we next address the question why segmentation issues are essential for language acquisition in infanthood. When newborn infants are confronted with the continuous auditory stream of their environment, they must detect relevant lexical and syntactic units without prior knowledge. Because infants have no or only poorly developed lexical representations and have not yet acquired the syntactic rules, they have to rely on the acoustic structure of the signal in a bottom-up fashion. Infants use auditory markers resulting from phonological regularities and prosodic cues to segment the input (Gervain and Mehler, 2010), because in natural speech the acoustic signal does not contain reliable pauses to indicate word boundaries (Cutler, 1994). The prosodic bootstrapping account assumes that the infant initially recognizes the prosodically marked units of the input to learn the syntactic structure of the language (Gleitman and Wanner, 1982). Thus, prelinguistic infants extract acoustically detectable "anchors" allowing them to segment the input into smaller entities to which meaning will be assigned at a later stage of their development. A number of behavioral findings support an eminent role of auditory feature sensitivity by demonstrating that auditory discrimination starts even before the infant is born. It has been shown that prosodic features and specific speech frequencies are perceived by the fetus (Draganova et al., 2007). This may constitute the fact that newborns can discriminate between the speech of their mother to speech belonging to different rhythmical classes (Mehler et al., 1988). Additionally, they prefer their mother's voice over other female voices (Mehler et al., 1978; DeCasper and Fifer, 1980).

In summary, segmentation is a crucial task to be tackled by the infant even during the early stage of language acquisition. Clearly, for auditory language comprehension adults also have to segment the speech stream. However, while adults can also use the stored lexical and semantic information as well as their pragmatic and contextual knowledge to improve the recognition processes in a top-down fashion, there is converging evidence that infants initially rely on acoustic cues to "tune in" to the language and identify segmental and suprasegmental features of the language, to which they are exposed.

OPTICAL IMAGING STUDIES ON THE NEURAL CORRELATES OF SUPRASEGMENTAL PROCESSING

A number of optical imaging studies have addressed the cerebral oxygenation response to stimuli which differ in suprasegmental properties. Most studies use materials in which prosodic features are varied on a sentential level. On the sentential level prosody segments the speech stream into phrases (Cutler et al., 1997). The prosodic phrase boundary is characterized by three cues: a pitch rise, a pre-boundary lengthening, and a pause. The perception of such a boundary elicits a specific event-related potential in adults (Steinhauer et al., 1999) even if there is no pause between two phrases. This has been discussed with respect to the hypothesis that prosodic properties of a sentence have a primacy for decoding the syntactic structure of a spoken sentence. As pointed out above, the detection of such prosodic cues is especially important in infant language acquisition. We here review optical imaging studies in infants that have addressed two essential questions: (i) whether and at what age prosodic information is processed by an infant and (ii) whether this processing is lateralized.

A recent study addresses the first question in neonates. In their study, Saito et al. (2007b) used two versions of a synthesized reading of a fairy tale. One version included pitch variation at the sentential level while the other did not. The pitch-modulated version elicited a larger activation (HbO↑) over frontal areas, however the expected lateralization to the right hemisphere was not supported by the data. The study is remarkable in showing a very early differentiation between two auditory streams, different only with respect to pitch modulation, during the first days of life. However, the fact that only one (frontal) channel was recorded over both hemispheres and rapid habituation to the modulated speech was seen within 10 s of the stimulation block, may indicate that neonates are sensitive to the different acoustic features rather than to their potential linguistic significance. Interestingly, the same group reported differences between the responses to the mother's and the nurse's voice in premature neonates (Saito et al., 2009). They found an activation (HbO↑) over the left frontal channel in response to both voices. However, only the nurse's voice also elicited an increase over the right frontal area interrogated by the optical probe. Though limited by similar methodological aspects as the earlier study, this difference is interpreted based on the assumption of a stronger familiarization to the nurse's voice, who can be considered the primary care-giver in the highly isolated premature neonate. A stronger activation (HbO↑ bilateral frontal) for infant- vs. adult-directed speech was also seen in a study in healthy full term neonates (Saito et al., 2007a).

The data provides evidence that pitch modulation is detected already from birth. However, the weak lateralization and the very coarse ascription to the frontal lobe raise the question of the relevance to specifically language development. Using a much larger probe array the lateralization of prosodic processing was investigated by Homae et al. (2006). They acoustically presented normal sentences and flattened sentences to 3-month-old infants. For the flattened sentences the pitch contour was digitally replaced by the mean value of the pitch in the normal sentences. Thus the two stimuli differed with respect to the presence of prosodic information. However, they also differed with respect to the "naturalness" of the material as will be discussed below. The results of this optical imaging study using an array of 24 channels over each hemisphere confirm that prosodic information is specifically processed by the infant's brain (**Figure 2D**). While there was a widespread activation (HbO↑and HbR↓) for both conditions, a direct comparison of normal vs. flattened speech yielded a stronger activation (HbO↑) over right temporo-parietal areas. The data thus indicate that a rightward lateralization of suprasegmental, prosodic processing is present already at the age of 3 months. In a follow-up study the same group examined the identical paradigm in 10-month-old infants (Homae et al., 2007). Again, activations over bilateral temporo-parietal areas were seen in response to both stimulus modalities. A direct comparison between flattened vs. normal speech, however, yielded a stronger activation (HbO↑) over the right hemisphere for the flattened material. The authors interpret this – at first glance contradicting – finding by postulating that the processing in 10-month-olds might not only reflect pitch processing *per se* as in 3-month-olds, but that additional processes might play a role here (**Figure 2D**). This is supported by the additional increase in frontal activation in response to the flattened material

in the 10-month-old infants. In other words, 10-month-old infants are assumed to recognize the linguistic input also for the flattened condition, thus no longer solely relying on prosodic cues. The larger activation to the unnaturally aprosodic linguistic input indicates the sensitivity to deviations from normal speech.

A different paradigm was chosen in our optical imaging study investigating lateralization effects in 4-year-old children (Wartenburger et al., 2007). Normally spoken sentences were contrasted with hummed sentences containing solely the prosodic information. Importantly, the hummed condition was naturally performed by the same actor as the normal speech condition. Thus the unnaturalness of digitally modified material was avoided. The results showed a stronger right-hemispheric activation (HbO↑ and HbR↓, see **Figure 2C**) for the hummed in contrast to normal sentences, whereas a stronger left-hemispheric processing was present for normal compared to hummed sentences. Thus, normal sentences containing the full linguistic information and fully accessible to these language-competent children, elicit a lateralization to the language-dominant left hemisphere. In contrast, when all segmental features are omitted, resulting in sentences containing pure suprasegmental prosodic information, the activation is lateralized to right-hemispheric regions. The study explored a third stimulus: a digitally flattened version of the hummed sentences. The naturally hummed material elicited stronger right-hemispheric activations than the flattened version. The finding is in line with the account that no prosodic processing can be expected in the flattened material. Using a different kind of flattened material, Homae et al. (2007) found a stronger rightward lateralization in 10-month-old infants (see above and **Figure 2D**). Notably, while Homae et al. (2006, 2007) used flattened normal sentences whose meaning could be comprehended – at least by adults – in our material the flattened stimuli did not contain segmental features (hummed stimuli were flattened, thus only rhythmic features were preserved). We suggest that in our study the older, language-competent children discarded the flattened material without segmental content as non-linguistic material, thus, not eliciting a sufficient activation of the language network. A rightward lateralization of a prosodic contrast (/itt**a**/ vs. /itt**a?**/) was also reported by Sato et al. (2003) as quoted in Minagawa-Kawai et al. (2008) using a habituation/dishabituation paradigm in different age groups (7 months to 5 years). Interestingly the lateralization was only seen in infants older than 11–12 months of age. In infants aged 7–10 months no lateralization was present. This is in contrast to the report on a much earlier sensitivity to prosodic pitch modulation in 3-month-old infants (Homae et al., 2006), most likely due to the difference in stimulus material using pitch alteration on a syllabic vs. sentential level respectively.

In summary, the optical imaging studies have demonstrated that suprasegmental information at a sentential level is processed by infants starting at a very early age. The different studies also suggest that the processing is lateralized. Variable results concerning the role of the right hemisphere have been interpreted to indicate either a stronger response to an unexpected lack in prosodic information or by the actual processing of the suprasegmental information. Similar diverging lateralizations have been reported in adults in BOLD-contrast fMRI studies using flattened and purely prosodic material (Meyer et al., 2002, 2004). To further clarify the issue it will be relevant to perform a longitudinal study, based on identical material across all age groups. Yielding conflicting results for digitally flattened material, the studies also show that a compromise between control of acoustic/linguistic features and "naturalness" of the material may be especially difficult in infants. With respect to methodological issues, it should be noted that vascular techniques like optical imaging are advantageous when investigating the neural correlates of suprasegmental processing on a sentential level. Ideally the assessment of the more slowly evolving features at the sentential level can be complemented by the electrophysiological markers at the phrase boundaries (e.g., closure positive shift, CPS; Mannel and Friederici, 2009).

It should be noted, that suprasegmental cues also act within single words. Indeed one prominent feature of prosody is the stress pattern that characterizes the intonation of syllables within words (Jusczyk, 1999). Additionally prosodic content, like pitch variation, is relevant in tonal languages (Gandour et al., 2003) and serves lexico-semantic differentiation. Since lexico-semantic tasks predominantly activate the left-hemispheric language areas, such suprasegmental contrasts may lateralize to the left hemisphere. An optical imaging study addressing pitch accent in Japanese infants (Sato et al., 2009) highlights this issue and is discussed below in the framework of different models put forward to explain lateralization of speech processing (paragraph How is Segmentation Guided by Auditory Analysis).

OPTICAL IMAGING STUDIES ON THE NEURAL CORRELATES OF SEGMENTAL PROCESSING

On a smaller temporal scale, phonemes and their combinatorial rules define the inventory from which syllables and words are built. Phonemes and their respective combinatorial rules are also specific to a given language. Hence, they also constitute regularities that allow for segmentation based on the auditory features. With respect to the processing of phonological information, the principle has long been established that at birth infants are sensitive to virtually every phonemic contrast in any existing language (Streeter, 1976; Werker and Tees, 1999; Kuhl and Rivera-Gaxiola, 2008). When infants acquire their native language(s) they lose this ability for contrasts that are not relevant in the given native language(s) (Naatanen et al., 1997; Cheour et al., 1998; Winkler et al., 1999). While this may be a hurdle for foreign language acquisition in adult life, the adaptation to the environmental needs can be considered an essential step to establish the high efficiency by which we decode speech signals in our own language(s). Some optical studies reviewed below have addressed this very issue.

PROCESSING OF PHONOTACTIC CUES

Specific languages allow specific phoneme-combinations. The combinatorial rules of different phonemes in a given language are called phonotactic rules. They are not only specific for a language but also with respect to the on- and offset of a word. For example, /fl/ is a possible combination at the onset of an English or German word (such as /*fl*ight/; German: /Flug/), whereas /tl/ is not. Also /ft/ is not present in English and German for the onset of a word, while it occurs at the coda-position (English: /loft/; German: /Luft/ (air)). Evidently such phonotactic regularities are important for the segmentation of speech into smaller units such as words.

In a series of optical imaging studies, we investigated how phonotactic rules are processed. To this end, pseudowords, legal or illegal with respect to the native phonotactic rules, were acoustically

presented to 3- and 6-month-old infants and adults. In adults we find a stronger activation (HbR↓) for the legal compared to the illegal pseudowords with a clear lateralization to the left hemisphere (Rossi et al., 2010). Preliminary results in the infant studies suggest a differential activation pattern for the two kinds of phonotactic rules at both 3 and 6 months of age, which can be interpreted as a preference for native phonotactics. However, in these age groups the observed effect did not show a clear lateralization. Since we simultaneously recorded EEG in all three studies, we also analyzed the respective electrophysiological markers. In the adult group a larger N400 was seen in response to the legal pseudowords. This further supports the hypothesis that these phonotactically legal pseudowords qualify as potential candidates for lexico-semantic analysis, while illegal items are "discarded" at an earlier, prelexical stage. In infants a similar effect for a frontal negativity was seen at 6 months, while at 3 months this ERP-effect was not robust. Neither in infants nor in adults were the ERP-components lateralized. In summary this experimental series suggests that neural correlates of phonotactic processing show an evolution beginning in early infancy. Conceptually the ERPs confirm the differentiation between native and non-native rules at the age of 6 months. Beyond the fact that a differential processing was already seen at the age of 3 months in the optical imaging data, the methodology also demonstrates the evolving lateralization of the processing from a bilateral auditory to a left-lateralized more linguistic analysis of the material (see **Figure 4**).

SENSITIVITY TO PHONEMIC BOUNDARIES

A similar developmental change has been reported in a sequence of optical imaging studies on the discrimination of phonemes specific to Japanese (Minagawa-Kawai et al., 2002, 2004, 2005, 2007). In Japanese the relative duration of a vowel can determine the meaning of a word. Vowels of different lengths with respect to a prior vowel constitute different phonemes. A phonemic boundary is the discrete transition between two phonemes. In the example used by Minagawa-Kawai et al. (2005), the phonemic boundary for the second vowel in the pseudoword */ma-ma/* lies between 184 and 217 ms when the first vowel is kept constant at 110 ms. In adult native Japanese speakers, the durational vowel contrast showed a stronger response (HbO↑) over the left hemisphere only for across-boundary presentations, supporting the notion that the durational contrast is processed as linguistically relevant (Minagawa-Kawai et al., 2002). Interestingly non-native high-proficiency adult speakers did not show this lateralization (Minagawa-Kawai et al., 2004, 2005). Most notable for our focus on developmental issues the material was used in infants of five different age groups (Minagawa-Kawai et al., 2007). In the youngest age group (3–4 months) the authors found identical response amplitudes for across-boundary and within-category comparisons. However, at 6–7 months stronger responses were present for across-category comparisons. Interestingly, this effect disappeared at 10–11 months to be stable for both age groups older than 12 months. Beyond the evidence for the phoneme differentiation, the older infants (>12 months) also showed a left-hemispheric dominance of the effect. The authors interpret these findings as a developmental change from a more auditory mechanism for the discrimination of the different vowel lengths at 6–7 months to a more linguistic processing mechanism after 12 months. A similar evolution of leftward lateralization at ~12 months is reported in Sato et al. (2003) as quoted in Minagawa-Kawai et al. (2008). Beyond the fact that this work is an impressive demonstration of how optical imaging can be applied in longitudinal developmental studies in

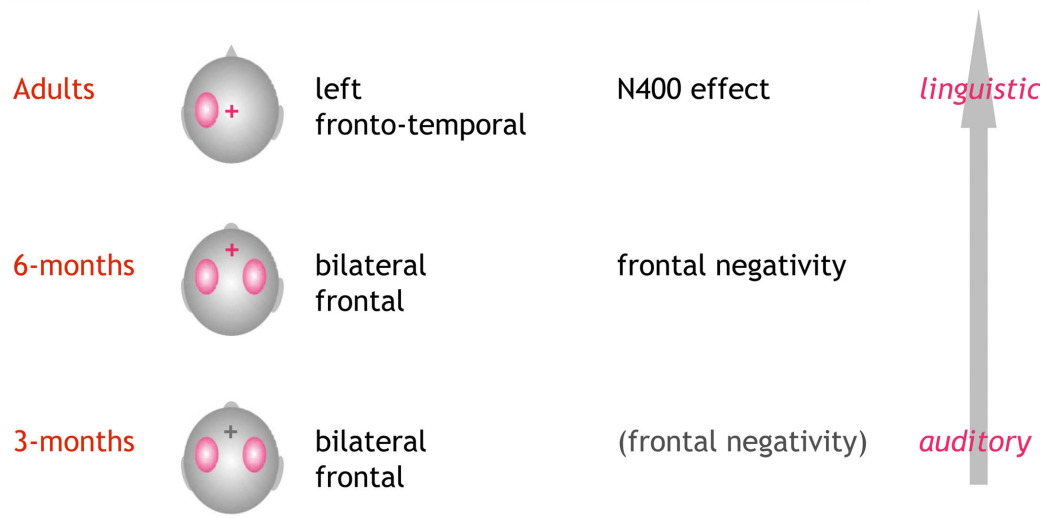

FIGURE 4 | Optical imaging and EEG results from a series of studies on the processing of phonotactics. Phonotactically legal were contrasted to illegal pseudowords (e.g., /**br**op/ vs. /**bz**op/). In adults the EEG showed a characteristic N400-effect mostly at the central electrode positions. Optical imaging showed a clear lateralization of the activation to the left hemisphere (Rossi et al., 2010). Preliminary data in infants suggest that the ERPs (frontal negativity) robustly indicate the tuning into the native phonotactic rules by the age of 6 months. In both 3- and 6-month-old infants, optical imaging showed a bilateral differential activation with respect to the phonotactic legality (Rossi et al., in preparation). The results are in line with a gradual evolution from acoustic change detection to a more linguistic analysis guided by the knowledge on legal word-onsets in the native language.

infants, the elegant design needs mentioning. Using a habituation/dishabituation paradigm, the subjects were first exposed to a period in which no contrast was presented. The actual test phase included a mixture of two durational contrasts, either across or within the phoneme category. Such a design is well suited to identify the "blocked" vascular response supplying spatial information and an integration over all neuronal processing steps involved. By using a combination with an electrophysiological measure of change detection (e.g., mismatch negativity), the response to the individual exemplar of the stimuli could be simultaneously assessed.

HOW IS SEGMENTATION GUIDED BY AUDITORY ANALYSIS?

So far, we can conclude that optical imaging studies have confirmed that segmentation cues at both a supra- and a segmental level lead to specific brain responses at an early age. Additionally an asymmetry for the processing has been consistently shown to evolve during infanthood. How is this related to the more basic principles on auditory analysis? Based on morphological analyses, it has been long established that the planum temporale is larger on the left when compared to the right hemisphere. This has been discussed as a potential reason for the left auditory cortex to have a better capacity to process speech. Thus, when assuming an auditory bottom-up contribution to the evolution of language competence, asymmetry of the auditory core areas may indicate a structural–anatomical disposition partially leading to the strong lateralization of language (for a review of planum temporale asymmetry see for instance Shapleske et al., 1999). Converging evidence from numerous fields including aphasiology and basic research on the auditory system, lead to three partially overlapping theories (see **Figure 5**). Exploring the commonalities and differences between music and language, Zatorre et al. (2002) proceed from a very basic acoustic principle: to precisely temporally analyze rapid modulations within an acoustic object, the sampling must be course with respect to the spectral analysis. Conversely precise spectral information of an auditory object necessitates integration over a longer temporal time frame (Zatorre et al., 2002). The differential relevance of precise temporal resolution for language and the necessity to perceive subtle pitch (spectral) differentiation in music, explains the respective lateralization for these otherwise similarly structured and complex auditory inputs. However, the right-hemispheric mastery of spectral analysis and a left-hemispheric specialization for fine temporal decoding is also consistent with the differential lateralization of transitional phonemic contrasts (/bin/ vs. /pin/) vs. the much slower prosodic cues.

The dual pathway model proceeds from a more linguistic perspective (Friederici and Alter, 2004). Assuming parallel pathways for left-lateralized-segmental and more right-lateralized-suprasegmental processing, the model predicts a relevant interaction. With respect to suprasegmental information, the processing will elicit a more rightward activation when presented in isolation. When suprasegmental cues gain more linguistic salience, activation will shift to the left hemisphere. This specification introduces a primacy of the left hemisphere for linguistically guided analysis of the auditory stream. The prediction also accommodates findings in a recent optical imaging study, which investigates pitch accent in Japanese in a habituation design similar to the above studies on the durational contrast (Sato et al., 2009). Investigating 4- and 10-month-old

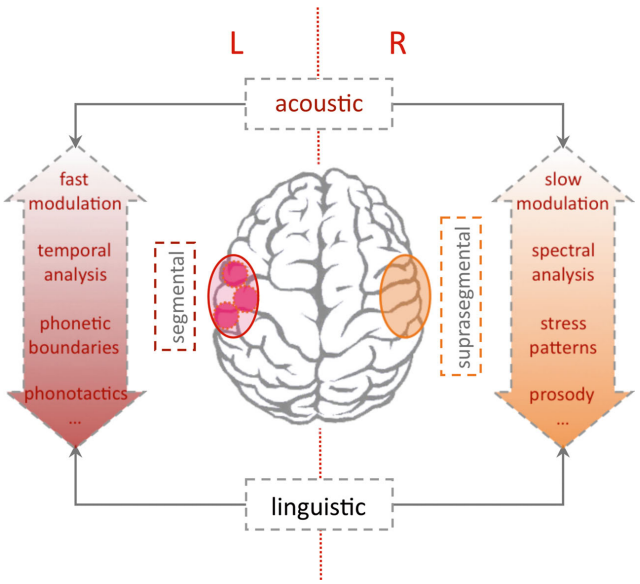

FIGURE 5 | Lateralization of language processing. The "classic" left-hemispheric language areas are essential for syntactic and semantic analysis. The dual pathway model (Friederici and Alter, 2004) predicts a left-lateralized processing of segmental and a right-lateralized analysis of suprasegmental information (e.g., sentential prosody). Since segmental and suprasegmental features develop along different temporal frames (see **Figure 3**) lateralization of auditory analysis with regard to spectral/temporal or fast/slow modulations may constitute some of the lateralization (Poeppel et al., 2008). Note that lateralization is relative and all theories include a close interaction between both hemispheres (Friederici et al., 2007). The stronger engagement of the left hemisphere for syntactic and semantic analysis (also over longer temporal windows) constitutes the critical role of the left hemisphere for intact language functions.

infants, the study reports that both age groups behaviorally differentiated the lexical pitch accent. With respect to lateralization, the lexical pitch accent elicited bilateral activation (HbO↑) at 4 months. On the contrary at 10 months, the infants showed a left-lateralized response (HbO↑) to the lexical pitch contrast, as was described in an earlier study in adults (Sato et al., 2007). Pure tones exhibiting identical pitch variations as the linguistic material, showed a weaker bilateral activation in all age groups. The studies support the model's prediction that with increasing linguistic salience the suprasegmental pitch contrast shifts the activation to the left hemisphere.

A third model assumes an intermediate position. The "multi-time-resolution" hypothesis (Poeppel et al., 2008) postulates at least two temporal integration windows relevant for the processing of speech input. A bilateral activation of auditory cortices is predicted for an integration at a relatively fast rate (20–30 ms window), which is appropriate to decode segment-level information. Slower rate sampling (150–300 ms), which is more relevant for suprasegmental feature analysis, is predicted to elicit a more right-hemispheric activation. The prediction was confirmed by an fMRI study in adults using noise segments that were modulated at different rates according to the predicted windows (Boemio et al., 2005). However in adults, a lateralization may also stem from the primacy of language with respect to

auditory analysis. A recent optical imaging study by our group used the same stimuli in newborns in order to explore whether this lateralization based on the acoustic properties is already present at birth (Telkemeyer et al., 2009). Four different temporal modulations were presented. The four conditions contained segments varying every 12, 25, 160, and 300 ms; the first two kinds of stimuli belong to the fast varying category, whereas the last two stimuli are more slowly modulated. The optical imaging results for 2–6 days old newborns revealed a bilateral activation for the 25 ms fast-modulated stimulus and a right-hemispheric dominance for both slow modulation stimuli (HbR↓). These findings suggest that differences in the acoustic and not the linguistic properties of the auditory input may drive lateralization of speech processing during the first days of life.

BEYOND AUDITORY FEATURES

We have highlighted that analysis of the auditory features in speech is a prerequisite for language acquisition in infancy, since lexico-semantic and syntactic knowledge are not yet developed. Clearly, auditory analysis may segment the speech stream, but it does not allow for the extraction of regularities unless more general cognitive abilities are developed in parallel. This has been the focus of extensive research on artificial grammars, since the demonstration of statistical learning abilities in 8-month-old infants (Saffran et al., 1996). An optical imaging study has recently shown that a precursor of such regularity extraction may be present at birth (Gervain et al., 2008). The authors exposed neonates to different artificial grammars governing the structure of syllable triplets. Adjacent (ABB: e.g., "*mubaba*") and non-adjacent (ABA: e.g., "*bamuba*") repetitions were contrasted to non-structured triplets (ABC: e.g., "*mubage*"). The authors find evidence for a discrimination of ABB, which they interpret as an indicator of a "repetition detector," which may form a nucleus for further structural analysis. Their conclusion rests on the fact that a stronger activation (HbO↑) was seen in frontal and temporal areas for the ABB when compared to ABC structures. Interestingly the activation over left frontal channels showed an increase over the exposure period of ~20 min. Thus, it is evident that very early on, structural, initially "Gestalt-like" features of the auditory stream may aid segmentation. In adults a recent optical imaging study demonstrated that non-linguistic tone sequences which could be segmented due to transitional probabilities, yield a stronger left inferior frontal activation (HbO↑) when compared to random sequences (Abla and Okanoya, 2008). Thus the development from a nucleus of a repetition detector to statistical learning may well be accessible to developmental studies using optical imaging.

In addition, the assumption that no lexico-semantic entries are present until later language development may hold only for very young infants. Bortfeld et al. (2005) were able to show that some very basic lexico-semantic entries may be present already at 6 months ("Mommy and me"). Such lexico-semantic "anchors" may well aid segmentation as discussed in a recent review (Swingley, 2009). It will be interesting to see whether these anchors can also be identified in the activation patterns when relying on optical imaging (Bortfeld et al., 2009).

CONCLUSIONS AND PERSPECTIVE

Non-invasive optical imaging has proven to be especially useful for the research on the neuronal underpinnings of speech perception during language acquisition. This research area greatly profits from the method's clear advantages to supply a silent non-invasive and low-constraint alternative to fMRI. Longitudinal studies tracking the emerging and pre-existing lateralization of auditory and language functions can be considered a solid basis to investigate the rapid unfolding of the cornucopia of linguistic functions during the first years of life. Simultaneous EEG-assessments can converge and extend knowledge along different modalities and time scales. Though fascinating in its broad applicability, it is necessary to also enquire into the somewhat cumbersome topics of technical advances and – not least – questions concerning the physiology of the hemodynamic response. Combined fMRI experiments and careful designs respecting the specific limitations of transcranial optical spectroscopy will decide on the scientific future of this new tool in infant and language research.

ACKNOWLEDGMENTS

Financial support of the EU (NEST 012778, EFRE 20002006 2/6, nEUROpt 201076), BMBF (BNIC, Bernstein Center for Computational Neuroscience, German-Polish cooperation FK: 01GZ0710), and DFG (WA2155) are gratefully acknowledged. Isabell Wartenburger is supported by the Stifterverband für die Deutsche Wissenschaft (Claussen-Simon-Stiftung). We thank Stephen Lapaz for helping to improve the English of the manuscript.

REFERENCES

Abla, D., and Okanoya, K. (2008). Statistical segmentation of tone sequences activates the left inferior frontal cortex: a near-infrared spectroscopy study. *Neuropsychologia* 46, 2787–2795.

Aslin, R. N., and Mehler, J. (2005). Near-infrared spectroscopy for functional studies of brain activity in human infants: promise, prospects, and challenges. *J. Biomed. Opt.* 10, 11009.

Benasich, A. A., Choudhury, N., Friedman, J. T., Realpe-Bonilla, T., Chojnowska, C., and Gou, Z. (2006). The infant as a prelinguistic model for language learning impairments: predicting from event-related potentials to behavior. *Neuropsychologia* 44, 396–411.

Benasich, A. A., Thomas, J. J., Choudhury, N., and Leppanen, P. H. (2002). The importance of rapid auditory processing abilities to early language development: evidence from converging methodologies. *Dev. Psychobiol.* 40, 278–292.

Boemio, A., Fromm, S., Braun, A., and Poeppel, D. (2005). Hierarchical and asymmetric temporal sensitivity in human auditory cortices. *Nat. Neurosci.* 8, 389–395.

Bonatti, L., Frot, E., Zangl, R., and Mehler, J. (2002). The human first hypothesis: identification of conspecifics and individuation of objects in the young infant. *Cogn. Psychol.* 44, 388–426.

Bookheimer, S. (2002). Functional MRI of language: new approaches to understanding the cortical organization of semantic processing. *Annu. Rev. Neurosci.* 25, 151–188.

Bortfeld, H., Fava, E., and Boas, D. A. (2009). Identifying cortical lateralization of speech processing in infants using near-infrared spectroscopy. *Dev. Neuropsychol.* 34, 52–65.

Bortfeld, H., Morgan, J. L., Golinkoff, R. M., and Rathbun, K. (2005). Mommy and me: familiar names help launch babies into speech-stream segmentation. *Psychol. Sci.* 16, 298–304.

Bristow, D., Dehaene-Lambertz, G., Mattout, J., Soares, C., Gliga, T., Baillet, S., and Mangin, J. F. (2009). Hearing faces: how the infant brain matches the face it sees with the speech it hears. *J. Cogn. Neurosci.* 21, 905–921.

Buxton, R. B., Uludağ K., Dubowitz, D. J., and Liu, T. T. (2004). Modeling the hemodynamic response to brain activation. *Neuroimage* 23(Suppl. 1):S220–S233.

Campbell, R. (2008). The processing of audio-visual speech: empirical and

neural bases. *Philos. Trans. R. Soc. Lond., B, Biol. Sci.* 363, 1001–1010.
Cheour, M., Ceponiene, R., Lehtokoski, A., Luuk, A., Allik, J., Alho, K., and Naatanen, R. (1998). Development of language-specific phoneme representations in the infant brain. *Nat. Neurosci.* 1, 351–353.
Colonnese, M. T., Phillips, M. A., Constantine-Paton, M., Kaila, K., and Jasanoff, A. (2008). Development of hemodynamic responses and functional connectivity in rat somatosensory cortex. *Nat. Neurosci.* 11, 72–79.
Cope, M., and Delpy, D. T. (1988). System for long-term measurement of cerebral blood and tissue oxygenation on newborn infants by near infra-red transillumination. *Med. Biol. Eng. Comput.* 26, 289–294.
Cutler, A. (1994). The perception of rhythm in language. *Cognition* 50, 79–81.
Cutler, A., Dahan, D., and van Donselaar, W. (1997). Prosody in the comprehension of spoken language: a literature review. *Lang. Speech* 40 (Pt 2), 141–201.
Cutler, A., Mehler, J., Norris, D., and Segui, J. (1983). A language-specific comprehension strategy. *Nature* 304, 159–160.
DeCasper, A. J., and Fifer, W. P. (1980). Of human bonding: newborns prefer their mothers' voices. *Science* 208, 1174–1176.
DeCasper, A. J., and Prescott, P. (2009). Lateralized processes constrain auditory reinforcement in human newborns. *Hear. Res.* 255, 135–141.
Dehaene-Lambertz, G., Dehaene, S., and Hertz-Pannier, L. (2002). Functional neuroimaging of speech perception in infants. *Science* 298, 2013–2015.
Dehaene-Lambertz, G., Hertz-Pannier, L., and Dubois, J. (2006). Nature and nurture in language acquisition: anatomical and functional brain-imaging studies in infants. *Trends Neurosci.* 29, 367–373.
Draganova, R., Eswaran, H., Murphy, P., Lowery, C., and Preissl, H. (2007). Serial magnetoencephalographic study of fetal and newborn auditory discriminative evoked responses. *Early Hum. Dev.* 83, 199–207.
Fox, P. T., and Raichle, M. E. (1986). Focal physiological uncoupling of cerebral blood flow and oxidative metabolism during somatosensory stimulation in human subjects. *Proc. Natl. Acad. Sci. U.S.A.* 83, 1140–1144.
Friederici, A. D. (2004). Event-related brain potential studies in language. *Curr. Neurol. Neurosci. Rep.* 4, 466–470.
Friederici, A. D. (2005). Neurophysiological markers of early language acquisition: from syllables to sentences. *Trends Cogn. Sci.* 9, 481–488.
Friederici, A. D., and Alter, K. (2004). Lateralization of auditory language functions: a dynamic dual pathway model. *Brain Lang.* 89, 267–276.
Friederici, A. D., von Cramon, D. Y., and Kotz, S. A. (2007). Role of the corpus callosum in speech comprehension: interfacing syntax and prosody. *Neuron* 53, 135–145.
Gandour, J., Dzemidzic, M., Wong, D., Lowe, M., Tong, Y., Hsieh, L., Satthamnuwong, N., and Lurito, J. (2003). Temporal integration of speech prosody is shaped by language experience: an fMRI study. *Brain Lang.* 84, 318–336.
Gernsbacher, M. A., and Kaschak, M. P. (2003). Neuroimaging studies of language production and comprehension. *Annu. Rev. Psychol.* 54, 91–114.
Gervain, J., Macagno, F., Cogoi, S., Pena, M., and Mehler, J. (2008). The neonate brain detects speech structure. *Proc. Natl. Acad. Sci. U.S.A.* 105, 14222–14227.
Gervain, J., and Mehler, J. (2010). Speech perception and language acquisition in the first year of life. *Annu. Rev. Psychol.* 61, 191–218.
Gleitman, L., and Wanner, E. (1982). "Language acquisition: the state of the art," in *Language Acquisition: The State of the Art*, eds E. Wanner and L. Gleitman (Cambridge, MA: Cambridge University Press), 3–48.
Hald, L. A., Bastiaansen, M. C., and Hagoort, P. (2006). EEG theta and gamma responses to semantic violations in online sentence processing. *Brain Lang.* 96, 90–105.
Hauser, M. D., Chomsky, N., and Fitch, W. T. (2002). The faculty of language: what is it, who has it, and how did it evolve? *Science* 298, 1569–1579.
Hebden, J. C., and Austin, T. (2007). Optical tomography of the neonatal brain. *Eur. Radiol.* 17, 2926–2933.
Homae, F., Watanabe, H., Nakano, T., Asakawa, K., and Taga, G. (2006). The right hemisphere of sleeping infant perceives sentential prosody. *Neurosci. Res.* 54, 276–280.
Homae, F., Watanabe, H., Nakano, T., and Taga, G. (2007). Prosodic processing in the developing brain. *Neurosci. Res.* 59, 29–39.
Hull, R., Bortfeld, H., and Koons, S. (2009). Near-infrared spectroscopy and cortical responses to speech production. *Open. Neuroimag. J.* 3, 26–30.
Huotilainen, M., Shestakova, A., and Hukki, J. (2008). Using magnetoencephalography in assessing auditory skills in infants and children. *Int. J. Psychophysiol.* 68, 123–129.
Iadecola, C. (2004). Neurovascular regulation in the normal brain and in Alzheimer's disease. *Nat. Rev. Neurosci.* 5, 347–360.
Jusczyk, P. W. (1999). How infants begin to extract words from speech. *Trends Cogn. Sci.* 3, 323–328.
Kleinschmidt, A., Obrig, H., Requardt, M., Merboldt, K. D., Dirnagl, U., Villringer, A., and Frahm, J. (1996). Simultaneous recording of cerebral blood oxygenation changes during human brain activation by magnetic resonance imaging and near-infrared spectroscopy. *J. Cereb. Blood Flow Metab.* 16, 817–826.
Koch, S. P., Steinbrink, J., Villringer, A., and Obrig, H. (2006). Synchronization between background activity and visually evoked potential is not mirrored by focal hyperoxygenation: implications for the interpretation of vascular brain imaging. *J. Neurosci.* 26, 4940–4948.
Koch, S. P., Werner, P., Steinbrink, J., Fries, P., and Obrig, H. (2009). Stimulus-induced and state-dependent sustained gamma activity is tightly coupled to the hemodynamic response in humans. *J. Neurosci.* 29, 13962–13970.
Kooijman, V., Hagoort, P., and Cutler, A. (2005). Electrophysiological evidence for prelinguistic infants' word recognition in continuous speech. *Brain Res. Cogn. Brain Res.* 24, 109–116.
Kuhl, P., and Rivera-Gaxiola, M. (2008). Neural substrates of language acquisition. *Annu. Rev. Neurosci.* 31, 511–534.
Kuhl, P. K. (2007). Is speech learning 'gated' by the social brain? *Dev. Sci.* 10, 110–120.
Kuhl, P. K., Tsao, F. M., and Liu, H. M. (2003). Foreign-language experience in infancy: effects of short-term exposure and social interaction on phonetic learning. *Proc. Natl. Acad. Sci. U.S.A.* 100, 9096–9101.
Kusaka, T., Kawada, K., Okubo, K., Nagano, K., Namba, M., Okada, H., Imai, T., Isobe, K., and Itoh, S. (2004). Noninvasive optical imaging in the visual cortex in young infants. *Hum. Brain Mapp.* 22, 122–132.
Kushnerenko, E., Cheour, M., Ceponiene, R., Fellman, V., Renlund, M., Soininen, K., Alku, P., Koskinen, M., Sainio, K., and Naatanen, R. (2001). Central auditory processing of durational changes in complex speech patterns by newborns: an event-related brain potential study. *Dev. Neuropsychol.* 19, 83–97.
Lau, E. F., Phillips, C., and Poeppel, D. (2008). A cortical network for semantics: (de)constructing the N400. *Nat. Rev. Neurosci.* 9, 920–933.
Lauritzen, M., and Gold, L. (2003). Brain function and neurophysiological correlates of signals used in functional neuroimaging. *J. Neurosci.* 23, 3972–3980.
Liebert, A., Wabnitz, H., Steinbrink, J., Moller, M., Macdonald, R., Rinneberg, H., Villringer, A., and Obrig, H. (2005). Bed-side assessment of cerebral perfusion in stroke patients based on optical monitoring of a dye bolus by time-resolved diffuse reflectance. *Neuroimage* 24, 426–435.
Liebert, A., Wabnitz, H., Steinbrink, J., Obrig, H., Moller, M., Macdonald, R., Villringer, A., and Rinneberg, H. (2004). Time-resolved multidistance near-infrared spectroscopy of the adult head: intracerebral and extracerebral absorption changes from moments of distribution of times of flight of photons. *Appl. Opt.* 43, 3037–3047.
Lloyd-Fox, S., Blasi, A., and Elwell, C. E. (2010). Illuminating the developing brain: the past, present and future of functional near infrared spectroscopy. *Neurosci. Biobehav. Rev.* 34, 269–284.
Logothetis, N. K., and Wandell, B. A. (2004). Interpreting the BOLD signal. *Annu. Rev. Physiol.* 66, 735–769.
Mandeville, J. B., Marota, J. J., Ayata, C., Zaharchuk, G., Moskowitz, M. A., Rosen, B. R., and Weisskoff, R. M. (1999). Evidence of a cerebrovascular postarteriole windkessel with delayed compliance. *J. Cereb. Blood Flow Metab.* 19, 679–689.
Mannel, C., and Friederici, A. D. (2009). Pauses and intonational phrasing: ERP studies in 5-month-old German infants and adults. *J. Cogn. Neurosci.* 21, 1988–2006.
Marcar, V. L., Strassle, A. E., Loenneker, T., Schwarz, U., and Martin, E. (2004). The influence of cortical maturation on the BOLD response: an fMRI study of visual cortex in children. *Pediatr. Res.* 56, 967–974.
Mehler, J., Bertoncini, J., and Barriere, M. (1978). Infant recognition of mother's voice. *Perception* 7, 491–497.
Mehler, J., Jusczyk, P., Lambertz, G., Halsted, N., Bertoncini, J., and Amiel-Tison, C. (1988). A precursor of language acquisition in young infants. *Cognition* 29, 143–178.
Meyer, M., Alter, K., Friederici, A. D., Lohmann, G., and von Cramon, D. Y. (2002). FMRI reveals brain regions mediating slow prosodic modulations in spoken sentences. *Hum. Brain Mapp.* 17, 73–88.
Meyer, M., Steinhauer, K., Alter, K., Friederici, A. D., and von Cramon, D. Y. (2004). Brain activity varies with modulation of dynamic pitch variance in sentence melody. *Brain Lang.* 89, 277–289.
Minagawa-Kawai, Y., Mori, K., Furuya, I., Hayashi, R., and Sato, Y. (2002). Assessing cerebral representations of short and long vowel categories by NIRS. *Neuroreport* 13, 581–584.

Minagawa-Kawai, Y., Mori, K., Hebden, J. C., and Dupoux, E. (2008). Optical imaging of infants' neurocognitive development: recent advances and perspectives. *Dev. Neurobiol.* 68, 712–728.

Minagawa-Kawai, Y., Mori, K., Naoi, N., and Kojima, S. (2007). Neural attunement processes in infants during the acquisition of a language-specific phonemic contrast. *J. Neurosci.* 27, 315–321.

Minagawa-Kawai, Y., Mori, K., and Sato, Y. (2005). Different brain strategies underlie the categorical perception of foreign and native phonemes. *J. Cogn. Neurosci.* 17, 1376–1385.

Minagawa-Kawai, Y., Mori, K., Sato, Y., and Koizumi, T. (2004). Differential cortical responses in second language learners to different vowel contrasts. *Neuroreport* 15, 899–903.

Moore, D. R., and Shannon, R. V. (2009). Beyond cochlear implants: awakening the deafened brain. *Nat. Neurosci.* 12, 686–691.

Naatanen, R., Lehtokoski, A., Lennes, M., Cheour, M., Huotilainen, M., Iivonen, A., Vainio, M., Alku, P., Ilmoniemi, R. J., Luuk, A., Allik, J., Sinkkonen, J., and Alho, K. (1997). Language-specific phoneme representations revealed by electric and magnetic brain responses. *Nature* 385, 432–434.

Oberecker, R., Friedrich, M., and Friederici, A. D. (2005). Neural correlates of syntactic processing in two-year-olds. *J. Cogn. Neurosci.* 17, 1667–1678.

Obrig, H., and Villringer, A. (2003). Beyond the visible – imaging the human brain with light. *J. Cereb. Blood Flow Metab.* 23, 1–18.

Pena, M., Maki, A., Kovacic, D., Dehaene-Lambertz, G., Koizumi, H., Bouquet, F., and Mehler, J. (2003). Sounds and silence: an optical topography study of language recognition at birth. *Proc. Natl. Acad. Sci. U.S.A.* 100, 11702–11705.

Poeppel, D., Idsardi, W. J., and van Wassenhove, V. (2008). Speech perception at the interface of neurobiology and linguistics. *Philos. Trans. R. Soc. Lond., B, Biol. Sci.* 363, 1071–1086.

Pulvermuller, F., Kherif, F., Hauk, O., Mohr, B., and Nimmo-Smith, I. (2009). Distributed cell assemblies for general lexical and category-specific semantic processing as revealed by fMRI cluster analysis. *Hum. Brain Mapp.* 30, 3837–3850.

Rossi, S., Jürgenson, I. B., Hanulíková, A., Telkemeyer, S., Wartenburger, I., and Obrig, H. (2010). Implicit processing of phonotactic cues: evidence from electrophysiological and vascular responses. *J. Cogn. Neurosci.* (in press).

Saffran, J. R., Aslin, R. N., and Newport, E. L. (1996). Statistical learning by 8-month-old infants. *Science* 274, 1926–1928.

Saito, Y., Aoyama, S., Kondo, T., Fukumoto, R., Konishi, N., Nakamura, K., Kobayashi, M., and Toshima, T. (2007a). Frontal cerebral blood flow change associated with infant-directed speech. *Arch. Dis. Child. Fetal Neonatal Ed.* 92, F113–F116.

Saito, Y., Kondo, T., Aoyama, S., Fukumoto, R., Konishi, N., Nakamura, K., Kobayashi, M., and Toshima, T. (2007b). The function of the frontal lobe in neonates for response to a prosodic voice. *Early Hum. Dev.* 83, 225–230.

Saito, Y., Fukuhara, R., Aoyama, S., and Toshima, T. (2009). Frontal brain activation in premature infants' response to auditory stimuli in neonatal intensive care unit. *Early Hum. Dev.* 85, 471–474.

Sambeth, A., Pakarinen, S., Ruohio, K., Fellman, V., van Zuijen, T. L., and Huotilainen, M. (2009). Change detection in newborns using a multiple deviant paradigm: a study using magnetoencephalography. *Clin. Neurophysiol.* 120, 530–538.

Sato, Y., Mori, K., Furuya, I., Hayashi, R., Minagawa-Kawai, Y., and Koizumi, T. (2003). Developmental changes in cerebral lateralization to spoken language in infants: Measured by near-infrared spectroscopy. *Jpn. J. Logoped. Phoniatr.* 44, 165–171.

Sato, Y., Sogabe, Y., and Mazuka, R. (2007). Brain responses in the processing of lexical pitch-accent by Japanese speakers. *Neuroreport* 18, 2001–2004.

Sato, Y., Sogabe, Y., and Mazuka, R. (2009). Development of hemispheric specialization for lexical pitch-accent in Japanese infants. *J. Cogn. Neurosci.* 22, 2503–2513.

Schonwiesner, M., Rubsamen, R., and von Cramon, D. Y. (2005). Spectral and temporal processing in the human auditory cortex – revisited. *Ann. N. Y. Acad. Sci.* 1060, 89–92.

Shapleske, J., Rossell, S. L., Woodruff, P. W., and David, A. S. (1999). The planum temporale: a systematic, quantitative review of its structural, functional and clinical significance. *Brain Res. Brain Res. Rev.* 29, 26–49.

Steinbrink, J., Villringer, A., Kempf, F., Haux, D., Boden, S., and Obrig, H. (2006). Illuminating the BOLD signal: combined fMRI-fNIRS studies. *Magn. Reson. Imaging* 24, 495–505.

Steinhauer, K., Alter, K., and Friederici, A. D. (1999). Brain potentials indicate immediate use of prosodic cues in natural speech processing. *Nat. Neurosci.* 2, 191–196.

Stephan, K. E., Harrison, L. M., Penny, W. D., and Friston, K. J. (2004). Biophysical models of fMRI responses. *Curr. Opin. Neurobiol.* 14, 629–635.

Streeter, L. A. (1976). Language perception of 2-month-old infants shows effects of both innate mechanisms and experience. *Nature* 259, 39–41.

Swingley, D. (2009). Contributions of infant word learning to language development. *Philos. Trans. R. Soc. Lond., B, Biol. Sci.* 364, 3617–3632.

Telkemeyer, S., Rossi, S., Koch, S. P., Nierhaus, T., Steinbrink, J., Poeppel, D., Obrig, H., and Wartenburger, I. (2009). Sensitivity of newborn auditory cortex to the temporal structure of sounds. *J. Neurosci.* 29, 14726–14733.

Villringer, A., and Dirnagl, U. (1995). Coupling of brain activity and cerebral blood flow: basis of functional neuroimaging. *Cerebrovasc. Brain Metab. Rev.* 7, 240–276.

Wartenburger, I., Steinbrink, J., Telkemeyer, S., Friedrich, M., Friederici, A. D., and Obrig, H. (2007). The processing of prosody: evidence of interhemispheric specialization at the age of four. *Neuroimage* 34, 416–425.

Wenzel, R., Wobst, P., Heekeren, H. H., Kwong, K. K., Brandt, S. A., Kohl, M., Obrig, H., Dirnagl, U., and Villringer, A. (2000). Saccadic suppression induces focal hypooxygenation in the occipital cortex. *J. Cereb. Blood Flow Metab.* 20, 1103–1110.

Werker, J. F., and Tees, R. C. (1999). Influences on infant speech processing: toward a new synthesis. *Annu. Rev. Psychol.* 50, 509–535.

White, B. R., Snyder, A. Z., Cohen, A. L., Petersen, S. E., Raichle, M. E., Schlaggar, B. L., and Culver, J. P. (2009). Mapping the human brain at rest with diffuse optical tomography. *Conf. Proc. IEEE Eng. Med. Biol. Soc.* 1, 4070–4072.

Winkler, I., Kujala, T., Tiitinen, H., Sivonen, P., Alku, P., Lehtokoski, A., Czigler, I., Csepe, V., Ilmoniemi, R. J., and Naatanen, R. (1999). Brain responses reveal the learning of foreign language phonemes. *Psychophysiology* 36, 638–642.

Zatorre, R. J., Belin, P., and Penhune, V. B. (2002). Structure and function of auditory cortex: music and speech. *Trends Cogn. Sci.* 6, 37–46.

Zeff, B. W., White, B. R., Dehghani, H., Schlaggar, B. L., and Culver, J. P. (2007). Retinotopic mapping of adult human visual cortex with high-density diffuse optical tomography. *Proc. Natl. Acad. Sci. U.S.A.* 104, 12169–12174.

Conflict of Interest Statement: The authors declare that the research was conducted in the absence of any commercial or financial relationships that could be construed as a potential conflict of interest.

Received: 28 February 2010; paper pending published: 31 March 2010; accepted: 27 May 2010; published online: 23 June 2010.

Citation: Obrig H, Rossi S, Telkemeyer S and Wartenburger I (2010) From acoustic segmentation to language processing: evidence from optical imaging. Front. Neuroenerg. ***2****:13. doi: 10.3389/fnene.2010.00013*

frontiers in
NEUROENERGETICS

REVIEW ARTICLE
published: 30 July 2010
doi: 10.3389/fnene.2010.00021

Multi-photon nanosurgery in live brain

Anna Letizia Allegra Mascaro[1], Leonardo Sacconi[1,2] and Francesco S. Pavone[1,2]*

[1] *European Laboratory for Non-linear Spectroscopy, University of Florence, Florence, Italy*
[2] *Department of Physics, University of Florence, Florence, Italy*

Edited by:
David Boas, Massachusetts General Hospital, USA; Massachusetts Institute of Technology, USA; Harvard Medical School, USA

Reviewed by:
Chris Shaffer, Cornell University, USA
Willy Supatto, National Centre for Scientific Research, France

****Correspondence:***
Francesco S. Pavone, Department of Physics and European Laboratory for Non-linear Spectroscopy, University of Florence, Via Sansone 1 – 50019 Sesto F.no., Florence, Italy.
e-mail: francesco.pavone@unifi.it

In the last few years two-photon microscopy has been used to perform *in vivo* high spatial resolution imaging of neurons, glial cells and vascular structures in the intact neocortex. Recently, in parallel to its applications in imaging, multi-photon absorption has been used as a tool for the selective disruption of neural processes and blood vessels in living animals. In this review we present some basic features of multi-photon nanosurgery and we illustrate the advantages offered by this novel methodology in neuroscience research. We show how the spatial localization of multi-photon excitation can be exploited to perform selective lesions on cortical neurons in living mice expressing fluorescent proteins. This methodology is applied to disrupt a single neuron without causing any visible collateral damage to the surrounding structures. The spatial precision of this method allows to dissect single processes as well as individual dendritic spines, preserving the structural integrity of the main neuronal arbor. The same approach can be used to breach the blood-brain barrier through a targeted photo-disruption of blood vessels walls. We show how the vascular system can be perturbed through laser ablation leading toward two different models of stroke: intravascular clot and extravasation. Following the temporal evolution of the injured system (either a neuron or a blood vessel) through time lapse *in vivo* imaging, the physiological response of the target structure and the rearrangement of the surrounding area can be characterized. Multi-photon nanosurgery in live brain represents a useful tool to produce different models of neurodegenerative disease.

Keywords: laser surgery, laser ablation, laser dissection, *in vivo* imaging, two-photon microscopy

INTRODUCTION

The link between optics and biology has always been extremely strong. In fact, it was through the use of the first optical microscopes in the 17th century that fundamental concepts such as the existence of the cell itself were defined. In the 1960s, the advent of the laser has totally revolutionized biology and medicine. Recently, femtosecond lasers have gained ground due to their versatile application to a large variety of problems. The first application developed for short-pulsed lasers in biology was multi-photon fluorescence microscopy (Denk et al., 1990). The non-linear nature of multi-photon processes provides an absorption volume spatially confined to the focal region (Zipfel et al., 2003). The localization of the excitation is maintained even in strongly scattering tissues, allowing deep, high-resolution *in vivo* microscopy (Helmchen and Denk, 2005; Svoboda and Yasuda, 2006).

In parallel to its application in imaging, multi-photon absorption has also been used as a tool to manipulate the biological sample under investigation; in particular, this technique has been applied to the selective disruption of labeled cells and intracellular structures. The first published report of femtosecond laser subcellular nanosurgery was by König et al. (1999), who demonstrated the potential of this technique by ablating nanometer-sized regions of the genome within the nucleus of living cells. Following this seminal work, laser nanosurgery has been applied in living cells to investigate the biological function of subcellular compartments, like mitochondria or microtubules (Tolić-Nørrelykke et al., 2004; Watanabe and Arakawa, 2004; Sacconi et al., 2005; Shen et al., 2005; Shimada et al., 2005; Kumar et al., 2006).

A similar approach has also been applied in living animals, where two-photon imaging and laser-induced lesions have been combined. For example, femtosecond laser ablations have been applied for studying the complex events associated with embryo development *in vivo* (Supatto et al., 2005; Kohli and Elezzabi, 2008). Other groups have taken advantage of multi-photon absorption to ablate or dissect individual neurons in worms to study axon regeneration (Yanik et al., 2004) and define the role of specific neurons in behavior. As an example, the function of a single neuron can be identified by observing behavioral changes after the surgery, as shown in the study by Chung et al. (2006), on the thermo-tactic behavior of nematodes.

Recently, the potential of this technique has been applied to the mammalian central nervous system (CNS). Thanks to this approach the investigation of many outstanding problems in neurobiology and human neurodegenerative disease appears now more accessible. For example, Sacconi et al., (2007) demonstrated a method for performing laser nanosurgery in the CNS of anesthetized mice. In this work the spatial localization of multi-photon excitation was exploited to perform selective lesions on the processes of cortical neurons in living mice expressing fluorescent proteins. Furthermore, laser-induced lesions have been used to damage the blood-brain barrier, to investigate the role of microglia (Davalos et al., 2005; Nimmerjahn et al., 2005) and also to produce targeted photo-disruptions as a model of stroke (Nishimura et al., 2006). Although acutely silent, small strokes are neurologically important as cortical microinfarcts and microhemorrhages may increase the risk of developing dementia

(Cullen et al., 2005; Gold et al., 2007). Non-linear laser ablation provides a method to induce vascular lesions one vessel at a time and to study cerebral microvascular diseases. Two-photon excited fluorescence microscopy, coupled to micro-vessel occlusion technique, enables to study the impact of microvascular lesions at cellular level, *in vivo*.

In this review we present some basic features of multi-photon nanosurgery and show some examples that illustrate the advantages offered by this novel methodology. In the first part we will review the experimental system used to perform multi-photon nanosurgery, giving detailed information about our custom-made multi-photon nanodissector and defining a method to gain optical access to the brain. In the second part we will show the results of performing imaging and nanosurgery in neural networks and in the vascular system. While illustrating some applications of femtosecond lasers to disrupt cellular structures of the CNS *in vivo*, we will provide a description of the morphological consequences of the injury event. In the end we will discuss the physical mechanisms of neural nanosurgery to help explaining the consequences of femtosecond laser ablation.

The opportunity provided by multi-photon nanosurgery for interacting with neural networks offers great potential to the investigation of brain remodeling. The nanosurgery technique applied to the nervous system *in vivo* can reveal detailed insight of the dynamic rearrangements of the mammalian CNS. *In vivo* time lapse imaging of cerebral fine structures in the days that follow a point disruption may represent an optimal tool to characterize the network response to injury and mimic a neurodegenerative pathology.

EXPERIMENTAL METHODS

OPTICAL WINDOW PREPARATION

The optical penetration of two-photon microscopy in live brain is limited by the opacity of the intact skull of adult mice. One way to obtain optical access to the neural and vascular network requires a craniotomy surgery; this method, called "open skull" technique (see **Figure 1**), implies the permanent removal of a circular portion of skull (leaving the dura mater unperturbed) and the replacement of this isle of bone with a cover glass (Lendvai et al., 2000; Trachtenberg et al., 2002; Holtmaat et al., 2006).

Alternatively, a small bone area (0.1–0.3 mm^2) can be thinned down to a 20 μm layer ("thinned skull" technique, see Grutzendler et al., 2002; Zuo et al., 2005). While the thinned skull preparation requires bone thinning at every experimental session, the permanent cranial window allows repeated imaging at arbitrary time intervals. Furthermore the open skull provides a larger field of view (0.8–12 mm^2) as well as an excellent optical access for weeks to months.

The experimental protocol of the open skull technique, recently illustrated by Holtmaat et al. (2009), will be described briefly. GFP-M line mice aged 3–5 months are deeply anesthetized by intraperitoneal injection of ketamine (90 mg/kg) and xylazine (9 mg/kg). A small dose of dexamethasone (0.04 ml at 2 mg/ml) is administered prior to surgery to minimize brain swelling. The mouse head is fixed in a stereotactic frame. The eyes are protected from dehydration through application of eye drops. After cutting out a strip of skin, the periosteum is removed by scraping the skull with a scalpel blade. Then, a circular portion of the skull is thinned out with a dental drill. The skull island is lifted up and removed, carefully avoiding to touch the meninges with the tweezers. The optical chamber is constructed by laying a cover glass upon the intact dura, as shown in **Figure 1**. A mixture of dental acrylic and cyanoacrylate glue is used to seal the cranial window. A metal bar is fixed above the skull to stabilize the animal for subsequent imaging sessions. To minimize the inflammatory phenomena that may take place after the surgery, the mice are treated with an anti-inflammatory drug, Carprofen (5 mg/kg), administered daily through subcutaneous injection. The apical dendrites of pyramidal neurons are imaged every 1–2 days to detect and study the remodeling events of the neural network up to more than 1 month after the surgery. Recently, a useful video showing this methodology has been posted on the Journal of Visualized Experiment (Mostany and Portera-Cailliau, 2008).

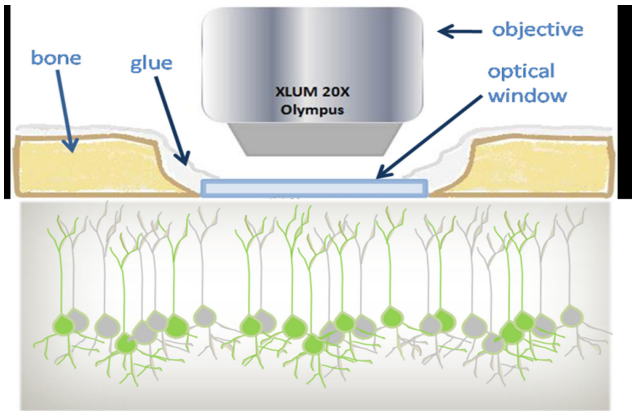

FIGURE 1 | Schematic view of the optical window preparation for *in vivo* imaging. In the craniotomy technique a piece of bone (light brown) is removed and replaced by a thin cover glass (light blue). The chronically implanted glass window replaces the skull and gives optical access to the GFP-labeled cortical neurons. Imaging is performed using 20× long-working-distance water immersion dipping objective.

While the neuronal network is partially labeled in the GFP-M mice, the injection of a vital dye is required to image and manipulate the vascular structures. To this end, blood plasma was labeled through tail vein injection of a 0.2 ml bolus of 5% (w/v) Texas Red dextran (70 kDa) (D-1830, Invitrogen) in physiological saline (Kleinfeld et al., 1998; Zhang et al., 2005; Nishimura et al., 2006; Schaffer et al., 2006). This high molecular weight dye provides stable labeling (typically 3 h).

OPTICAL NANOSURGERY SETUP

In this section we describe a typical experimental setup that combines multi-photon imaging and nanosurgery. This particular experimental system was used in our laboratory to perform *in vivo* multi-photon nanosurgery on cortical neurons (Sacconi et al., 2007). The setup, shown in **Figure 2**, is a custom-made upright two-photon microscope.

A mode-locked Ti:Sapphire laser (Chameleon, Coherent Inc) provides the excitation light (120 fs width pulses at 90 MHz repetition rate). A λ/4 waveplate coupled to a rotatable polarizer finely

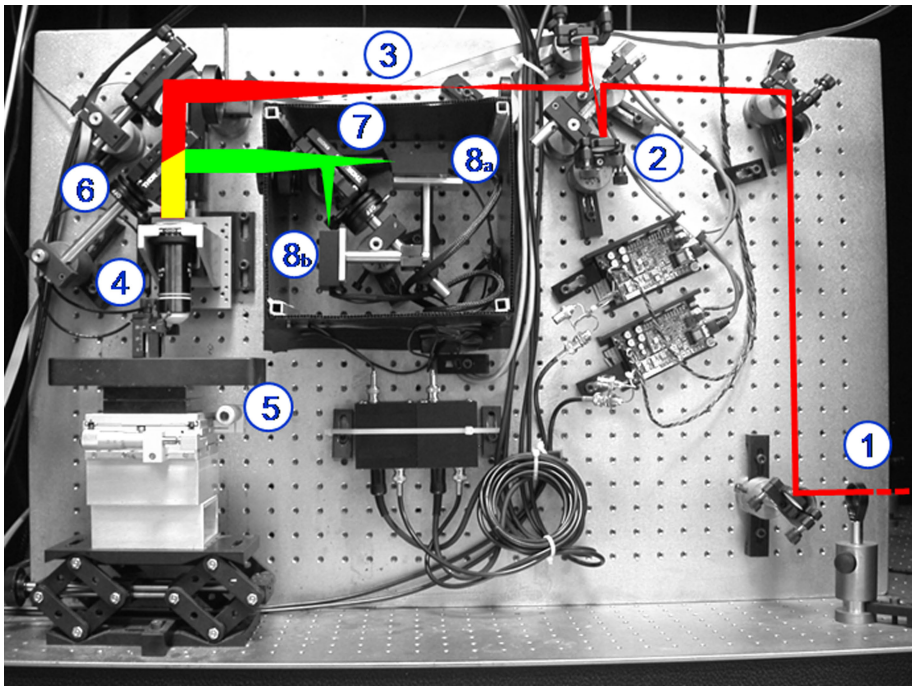

FIGURE 2 | Custom-made two photon apparatus. The figure shows the laser beam [in red, coming from the bottom right side of the panel (1)] that is first scanned by two galvanometric mirrors (2), then expanded by a telescope (3), and finally focused by the objective (4) onto the specimen (5). The emitted light (yellow) is separated from the exciting beam by a first dichroic mirror (6) and then split by a second dichroic mirror (7) in the red and green components. Two photomultipliers detect the split fluorescence emissions (8a,b).

moved by a stepper motor provides a tunable beam intensity control. The laser beam is scanned in the xy-plane by a non-resonant scanning head. The scanning system consists of two closed-loop feedback galvanometer mirrors (VM500, GSI Lumonics), rotated about orthogonal pivots and coupled by a pair of spherical mirrors. The laser beam is then expanded by a telescope composed by a scanning lens and a microscope tube lens. Finally an objective lens (XLUM 20X, NA 0.95, WD 2 mm, Olympus) focuses the beam onto the specimen. The anesthetized mouse is positioned in the stereotactic holder screwing a metal bar placed on the mouse head (see above); in this way the same cerebral region of interest can be found in every imaging session through fixed coordinates with high precision. The stereotactic holder is fixed on a stage through a magnetic platform laying upon a lab jack that allows rough axial positioning of the optical window under the objective. Fine xy-displacement is accomplished through two independent micromanipulators on the magnetic stage. A closed-loop piezoelectric stage (P-721, Physik Instrumente) allows axial displacements of the objective up to 400 μm with nanometric precision. Fluorescence light is separated from the laser optical path by a first dichroic beam splitter (685DCXRU, Chroma Technology) positioned as close as possible to the objective lens (non-de-scanning mode). A two-photon florescence cut-off filter (E700SP-2P, Chroma Technology) eliminates reflected laser light. A second dichroic mirror (FF562-Di02-25 × 36, Semrock) is used to split the two spectral components of the fluorescence signal, the red (570–685 nm) and the green (400–560 nm) emission light. The fluorescence signals are finally collected by two photomultiplier modules (H7710-13, Hamamatsu Photonics). All the microscope optics are fixed onto a custom vertical honeycomb steel breadboard. The electronic components of the setup are computer-controlled during microscopy and nanosurgery experiments. Custom-made software has been developed in LabVIEW 7.1 (National Instruments).

The key requisites for the experimental setup to perform laser nanosurgery are the maximum stability and reproducibility (≈ 0.1 μm) of beam positioning in the *x*, *y* and *z* axes. This condition is fulfilled by closed-loop feedback systems on the piezoelectric stage and on the galvo mirrors. On the other hand, motorized z positioning systems and resonant galvo mirrors, sometimes present in commercial systems, do not fit the requirements for nanosurgery. However, commercial multi-photon setups provided with high stability positioning system can be used to perform both imaging and nanosurgery in the low-density plasma regime, as previously shown (Supatto et al., 2008). Other technical requirements involve, for example, laser pulse dispersion and maximum power deliverable on the sample. Due to the large variety of commercially available systems these parameters should be evaluated on a case-by-case basis.

OPTICAL NANOSURGERY PROCEDURE

The nanosurgery experiment starts with an *in vivo* imaging session of the exposed mouse brain under the optical window. Z-stacks are acquired to obtain 3D-reconstructions of the labeled sample. During the imaging session, the excitation wavelength (λ) is chosen to maximize the multi-photon cross-section of the labeled structures (in our experiment λ = 935 nm). After selecting

the *xyz* coordinates for the desired lesion site, laser dissection is performed by irradiating the selected point with a high energy dose of Ti:Sapphire laser at the same wavelength used for imaging. In a typical experiment, the laser power is increased 5–10 times more than the power used for imaging and the shutter is opened for a period of the order of hundreds of millisecond. The increase of energy dose delivered on the sample in the dissection with respect to imaging arises largely from an increase in exposure time, with a lower contribution from the increase in laser power itself. In fact, the pixel dwell time is ≈5 μs during imaging, whereas it is increased to hundreds of millisecond to perform the nanosurgery. As a consequence, the number of pulses (and the associated energy dose) delivered per unit area is drastically increased (five orders of magnitude). After performing the nanosurgery, the laser power is decreased back and a 3D-image of the sample is acquired to visualize the effects on the irradiated structure.

It is worth mentioning that the experimental parameters for the nanosurgery (laser power and exposure time) critically depend on the target. For example, the depth, the fluorescence level and the dimension of the target structure remarkably affect the energy dose threshold to perform the nanosurgery. Furthermore, the anesthetic levels and the optical window preparation critically affect the stability of the sample and, thus, the outcome of the irradiation. Practically, the laser power is set close to the maximum available value (≈ 300 mW, measured after the objective lens) and an exposure time of 100 ms is tested to induce ablation. Then an imaging session is performed to observe the effects of the laser irradiation. If no morphological changes were induced, the laser surgery is repeated with an increased exposure time. This procedure is performed iteratively, until a detectable structural modification is observed. In a typical experiment the exposure time ranges from 100 to 1000 ms.

NANOSURGERY IN LIVE BRAIN

NEURAL ABLATION

The optical nanosurgery setup, in combination with the optical window preparation, has been used to perform *in vivo* imaging and ablation of fine neural structures in the cortex of live animals. The spatial localization of multi-photon excitation is exploited to perform *in vivo* selective lesions on small subsets of neurons in the somatosensory cortex of mice genetically expressing fluorescent proteins (GFP-M) without causing any visible collateral damage to the surrounding neuronal structures (Sacconi et al., 2007). Neurons are irradiated with a focused, controlled femtosecond energy dose and then the morphological consequences are characterized with time lapse 3D two-photon imaging. The potential of this method is such that different compartments of the CNS can be perturbed by either ablating a neural cell body (see **Figure 3A**) or disrupting the distal portion of a dendrite (see **Figure 3B**), or even providing the selectivity for the ablation of a single spine (see **Figure 3C**).

The possibility of dissecting selected structures depends, to a first approximation, on the depth of the structure and on its fluorescence emission intensity. Although two-photon microscopy allows imaging of layer-5 pyramidal neurons (600–800 μm below the pia), the nanosurgery is more limited in depth because of the loss of energy density along the beam path across the brain. Interneuronal somas placed in the layer-2/3 (200–450 μm below the pia) can be easily disrupted by laser nanosurgery. **Figure 3A** shows the time course of the ablation of a GFP-labeled interneuronal cell body. The interneuron was irradiated in proximity of the red lightning symbol just after the acquisition of the first image. The merge of the neuron before (red) and after (green) injury (right panel in **Figure 3A**) shows the disappearance of the cellular body after laser mediated ablation, while the surrounding network is negligibly affected. Laser nanosurgery can be also applied to apical dendrites of a layer-5 pyramidal neuron. **Figure 3B** shows the time course of a point disruption of a single pyramidal dendrite. The effect of the ablation is the selective degeneration of the distal portion of the neurite, indicating that this may be an active process and not a passive deterioration (see Discussion in the next paragraph). The right panel in **Figure 3B** highlights the integrity of the remaining structure after dissection. Furthermore, the continued expression of fluorescent proteins indicates that the neuron is alive. Finally, the high spatial precision of this method was demonstrated by ablating individual dendritic spines, while sparing the adjacent spines and the structural integrity of the dendrite. **Figure 3C** shows a portion of a GFP-labeled pyramidal dendrite where several spines are present. The right panel of **Figure 3C** highlights the disappearance of a single spine after laser-induced lesion and emphasizes both the stability of the surrounding dendritic spines (indicated by yellow arrowheads) and the absence of any swelling in the dendrite.

This micro-scale model of neural degeneration allows to characterize the remodeling properties of the network after injury. In comparison with other models of neural ablation, e.g., massive neural depletion through 3-acetyl pyridine treatment (Hicks, 1955; Desclina and Escubia, 1974; Balaban, 1985), nanosurgery is highly specific and can be finely tuned to a single neuron, leaving the surrounding structures unaltered.

BLOOD VESSELS DISRUPTION

Another important application of multi-photon microscopy is imaging of blood flow through cortical blood vessels labeled with a vital dye. The nanosurgery technique applied to the vascular system leads to subsurface blood vessel disruption in living animals (Nishimura et al., 2006). This model of stroke allows to reproduce different ischemic conditions and, at the same time, to investigate with day-by-day detail the reactive capabilities of the system. Femtosecond laser pulses are focused on a blood vessel to achieve two different forms of vascular insult; the irradiation may lead either to vessel rupture, which provides a model of hemorrhage (see **Figure 4A**), or to formation of a blood clot (**Figure 4B**).

Two-photon real time imaging of blood flow through the surrounding vessels before and after the laser-induced vascular lesion permits to characterize the dynamics of the degenerative event. In the first example the complete rupture of a blood vessel leads to the release of blood plasma and red blood cells in the surrounding tissue, while flow is left intact in nearby vessels. The formation of a clot, on the other hand, determines a complete blockage of the flow in the targeted blood vessel. Recent studies show that a

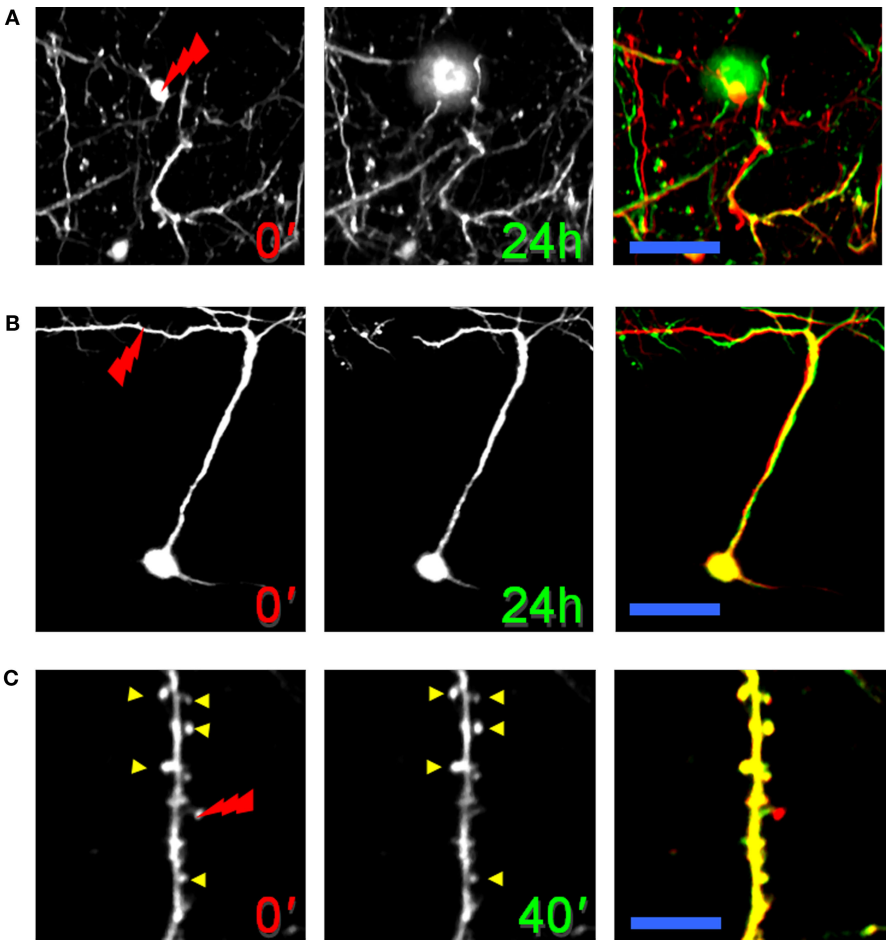

FIGURE 3 | Neural nanosurgery in GFP-M transgenic mice. (A) Laser dissection of an interneuron cell body. Each image is a maximum-intensity projection of a set of 20 optical sections acquired at 2 µm z-step (at 150 µm depth). The tip of the red lightning symbol represents the laser irradiation point. The first panel was acquired just before the laser irradiation. The middle panel was acquired 24 h after the laser irradiation. The last panel shows an overlay of the neuron before (red) and after (green) laser irradiation. Scale bar, 25 µm. **(B)** Laser-induced lesion of a single dendrite. Maximum-intensity z projection (from 100 to 500 µm) of a pyramidal neuron before and 24 h after dendritic dissection. Scale bar, 60 µm. **(C)** Laser ablation of a single dendritic spine. Images of a portion of a dendrite before and 40 min after spine ablation. Scale bar, 15 µm. **(B)** and **(C)** are modified with permission from Sacconi et al. (2007).

single micro-vessel lesion determines the disruption of flow at the nearby downstream vessels, but the presence of loops within the network may partially compensate for the lost vascular afference (Nishimura et al., 2006). The response of the neural network to this local blood deprivation is characterized through the days that follow the vascular insult. Time-lapse observation of the adjacent labeled neurons reveals a relatively high stability of the network in case of a confined damage, while loss of dendritic spines and degeneration of dendrites can be observed if the injury is more widespread (Zhang and Murphy, 2007).

While conventional methods allowed to create mainly large-scale occlusions that destroyed extended areas of brain vasculature (Chen et al., 1986; Ping et al., 2008), the nanosurgery technique can finely tune the injury toward a single blood microvessel (Nishimura et al., 2006; Kleinfeld et al., 2008). The possibility of monitoring blood flow before and after an occlusion discloses a great potential for this technique, that may be applicable to the investigation of interventional therapies for micro-strokes.

MECHANISM OF MULTI-PHOTON NANOSURGERY

In order to explore the mechanism of multi-photon nanosurgery, we analyzed the morphological rearrangements of an apical pyramidal dendrite after the irradiation with a high energy dose of femtosecond pulsed laser. Based on the biological response, the morphological consequences of irradiating a single dendrite can be grouped into two categories: transient swelling with recovery, and complete dendritic dissection. **Figure 5** shows the time course of the laser-induced degeneration of an apical dendrite in GFP-M transgenic somatosensory cortex. In the first case (see **Figure 5A**) we observe a transient swelling of the dendrite extending several micrometers from the point of irradiation along the dendrite in both directions. The irradiated dendrite temporarily modifies its shape but recovers its original features after a period of hours. While in this example the nanosurgery does not lead to dendritic dissection, in a second class of response the dendrite undergoes a degenerative process. As shown in **Figure 5B**, after laser irradiation, the terminal end of the dendrite distal to the dissection point followed a sequence of

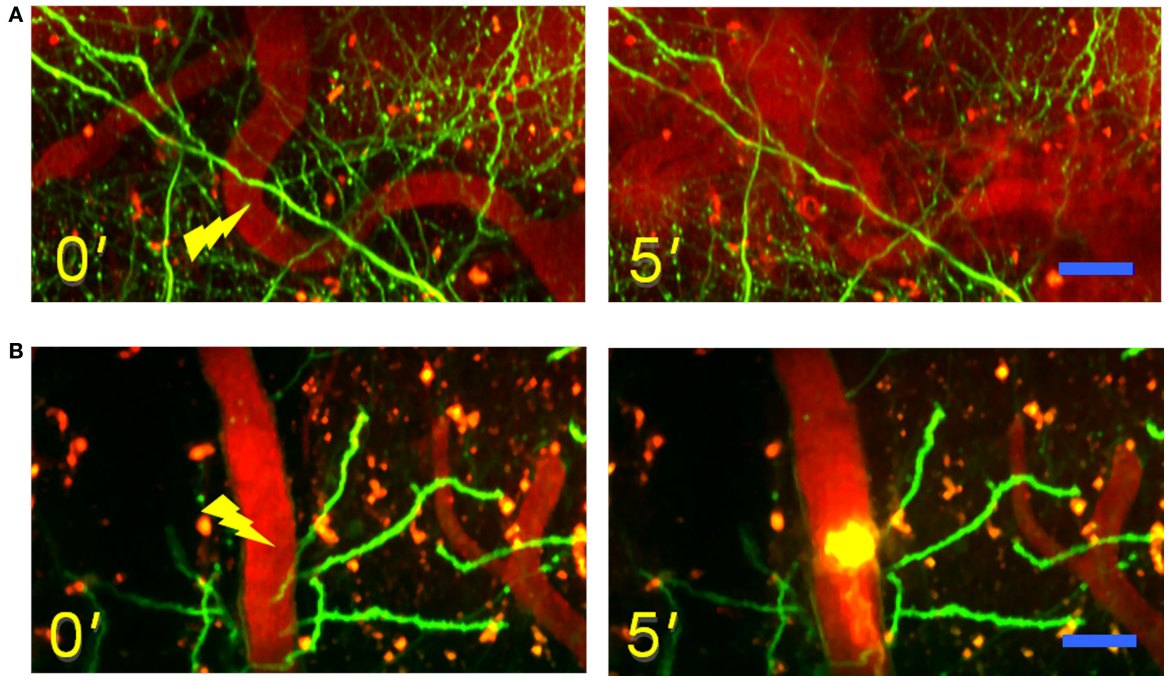

FIGURE 4 | Models of laser-induced vascular lesion. (A) Time lapse images of maximum intensity z-projections (from 20 to 60 μm) before (left) and after (right) the laser-induced ischemic hemorrhage. The figures show in green the GFP-labeled neuron in a GFP-M mouse and in red the vascular network labeled with Texas-red dextran dye. The tip of the yellow lightning symbol represents the laser irradiation point. The first image was acquired just before the laser irradiation. Scale bar, 20 μm. **(B)** Time lapse images of maximum intensity z-projections (from 20 to 100 μm) before (left) and after (right) the laser induction of an intravascular clot. Scale bar, 20 μm.

swelling, degeneration, and disappearance. The energy dose necessary to produce these outcomes (swelling with recovery or neural ablation) cannot be established *a priori*. In fact, the same energy dose can determine the two different biological responses.

These irradiation outcomes may be interpreted on the basis of the physical mechanism underlying the nanosurgery technique. For simplicity, two regimes can be established for nanosurgery (Vogel and Venugopalan, 2003; Vogel et al., 2005). The low-density plasma regime uses long series of pulses from femtosecond oscillators with repetition rates of the order of 80 MHz and pulse energies well below the optical breakdown threshold (König et al., 1999, 2001; Oehring et al., 2000; Smith et al., 2001; Tirlapur and König, 2002; Zeira et al., 2003; Sacconi et al., 2005, 2007; Supatto et al., 2005). The low repetition rate regime, instead, uses amplified series of pulses at repetition rates of kilohertz and pulse energies slightly above the optical breakdown threshold (Watanabe and Arakawa, 2004; Yanik et al., 2004; Heisterkamp et al., 2005; Shen et al., 2005). The mechanisms on which these two regimes rely are quite different. The low repetition rate regime effects are related to thermoelastically-induced formation of transient cavities. An extensive review focused on this regime has been recently published by Tsai et al. (2009). On the other hand, in our work we present several examples in which the dissection is performed in the low-density plasma regime. In this case the dissection is mediated by free-electron-induced chemical decomposition. The chemical decomposition can be induced through two different mechanisms: (1) the fragmentation of the biomolecule derives from its resonant interaction with quasi-free electrons: the capture of a quasi-free electron in an antibonding molecular orbital causes the rupture of a chemical bond and determines the degradation of the molecule; (2) the fragmentation of the biomolecule derives from its interaction with reactive oxygen species (ROS, i.e., free radicals that contain the oxygen atom), originated from laser-induced ionization and dissociation of water molecules.

Following this description, the outcome of the nanosurgery on apical dendrites can be interpreted by an alteration of membrane permeability due to chemical decomposition of the plasma membrane components. The laser-induced transient breach in the cell membrane leads to the dendritical swelling shown in **Figure 5**. Now, if the laser perturbation is small enough, the neuron may re-establish the physiological osmotic equilibrium and recover after a transient swelling, as shown in **Figure 5A**. Otherwise, the membrane disruption may lead to the formation of bead-like structures, followed by degeneration of the distal portion of the dendrite (see **Figure 5B**). This process, called Wallerian degeneration (Waller, 1850), occurs after axonal injury at the distal stump of the site of injury and usually begins within 24 h of a lesion. As recently reported in Kerschensteiner et al. (2005), axonal injuries initially lead to acute axonal degeneration, which is the rapid separation of the proximal and distal ends within 30 min after an injury. Degeneration follows with swelling of the axolemma, and eventually leads to bead-like formations. After axon degradation, granular disintegration of the axonal cytoskeleton and inner organelles occurs. This anterograde deterioration, elicited by the

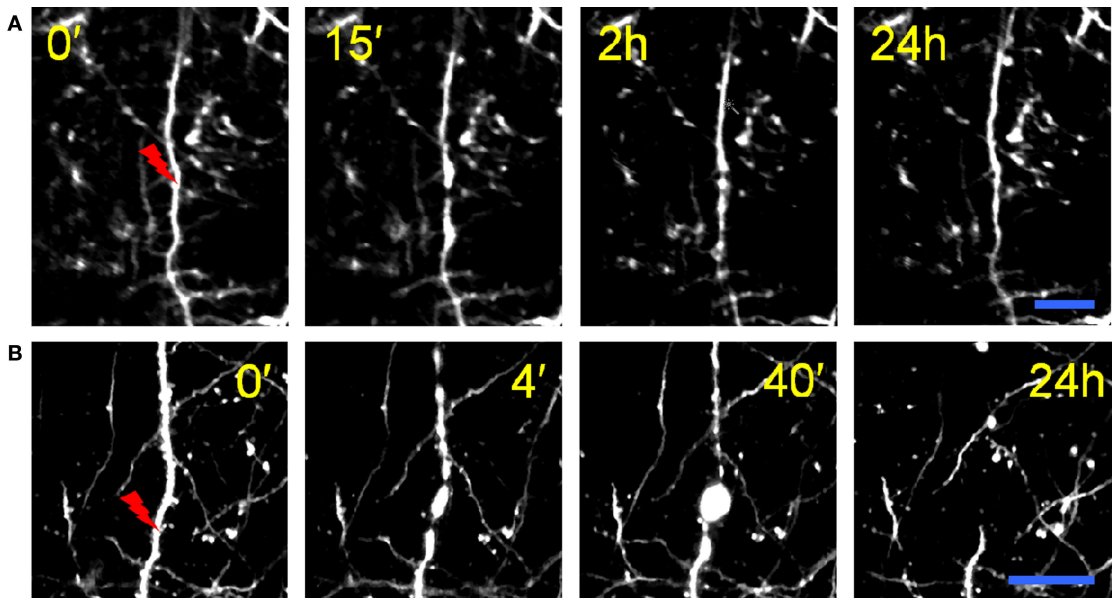

FIGURE 5 | Effects of the nanosurgery on apical dendrites. (A) Laser-induced dendritic swelling. Time-lapse of maximum intensity z-projections (from 140 to 160 µm) of irradiated dendrite in GFP-M transgenic mouse. The tip of the red lightning symbol represents the laser irradiation point. The first panel was acquired just before the laser irradiation. Scale bar, 10 µm. **(B)** Laser-induced lesion of a single dendrite. Time-lapse of maximum intensity z-projections (from 90 to 110 µm) of irradiated dendrite. Scale bar, 25 µm. **(B)** is modified from Sacconi et al. (2007).

calcium influx (George and Griffin, 1994), is dependent on ubiquitin and calpain proteases, suggesting that axonal degeneration is an active process rather than a passive lack of support from the cell body (Zimmerman and Schlaepfer, 1984).

CONCLUSIONS

In the last years laser absorption has been exploited to interfere with biological processes and, thus, to define the effective mechanism of specific events. Multi-photon nanosurgery, applied to the CNS of living mammals, represents the ideal platform to setup different models of cortical injury. *In vivo* two-photon fluorescence imaging coupled to laser-induced nanosurgery, is a promising tool to study the reparative properties of the adult CNS, as it gives an insight of the real dynamics of the neural network plastic properties, in physiological as well as injured conditions. Through multi-photon nanosurgery, we can reproduce interesting models of neural degeneration and finely characterize the evolution of the neural network *in vivo* after those injury events.

ACKNOWLEDGMENTS

The authors thank Francesco Vanzi for useful discussion about the manuscript. This research project has been supported by the European Community's Sixth Framework Program (Marie Curie Transfer of Knowledge Fellowship MTKD-CT-2004-BICAL-509761), by "Consorzio Nazionale Interuniversitario per le Scienze Fisiche della Materia" (CNISM), the PRIN Program 2007, by the "Ente Cassa di Risparmio di Firenze" (private foundation), and by ASI project MoMa.

REFERENCES

Balaban, C. D. (1985). Central neurotoxic effects of intraperitoneally administered 3-acetylpyridine, harmaline and niacinamide in Sprague-Dawley and Long-Evans rats: a critical review of central 3-acetylpyridine neurotoxicity. *Brain Res.* 356, 21–42.

Chen, S. T., Hsu, C. Y., Hogan, E. L., Maricq, H., and Balentine, J. D. (1986). A model of focal ischemic stroke in the rat: reproducible extensive cortical infarction. *Stroke* 17, 738–743.

Chung, S. H., Clark, D. A., Gabel, C. V., Mazur, E., and Samuel, A. D. (2006). The role of the AFD neuron in *C. elegans* thermotaxis analyzed using femtosecond laser ablation. *BMC Neurosci.* 7, 30.

Cullen, K. M., Kócsi, Z., and Stone, J. (2005). Pericapillary haem-rich deposits: evidence for microhaemorrhages in aging human cerebral cortex. *J. Cereb. Blood Flow Metab.* 25, 1656–1667.

Davalos, D., Grutzendler, J., Yang, G., Kim, J. V., Zuo, Y., Jung, S., Littman, D. R., Dustin, M. L., and Gan, W. B. (2005). ATP mediates rapid microglial response to local brain injury *in vivo*. *Nat. Neurosci.* 8, 752 – 758.

Denk, W., Strickler, H. J., and Webb, W. W. (1990). Two-photon laser scanning fluorescence microscopy. *Science* 248, 73–76.

Desclina, J. C., and Escubia J. (1974). Effects of 3-acetylpyridine on the central nervous system of the rat, as demonstrated by silver methods. *Brain Res.* 77, 349–364.

George, R., and Griffin, J. W. (1994). Delayed macrophage responses and myelin clearance during Wallerian degeneration in the central nervous system: the dorsal radiculotomy model. *Exp. Neurol.* 129, 225–236.

Gold, G., Giannakopoulos, P., Herrmann, F. R., Bouras, C., and Kövari, E. (2007). Identification of Alzheimer and vascular lesion thresholds for mixed dementia. *Brain* 130, 2830.

Grutzendler, J., Kasthuri, N., and Gan, W. B. (2002). Long-term dendritic spine stability in the adult cortex. *Nature* 420, 812–816.

Heisterkamp, A., Maxwell, I. Z., Mazur, E., Underwood, J. M., Nickerson, J. A., Kumar, S., and Ingber, D. E. (2005). Pulse energy dependence of subcellular dissection by femtosecond laser pulses. *Opt. Express* 13, 3690–3696.

Helmchen, F., and Denk, W. (2005). Deep tissue two-photon microscopy. *Nat. Methods* 2, 932–940.

Hicks S. P. (1955). Pathologic effects of antimetabolites. I. Acute lesions in the hypothalamus, peripheral ganglia, and adrenal medulla caused by 3-acetyl pyridine and prevented by nicotinamide. *Am. J. Pathol.* 31,189–199.

Holtmaat, A., Bonhoeffer, T., Chow, D. K., Chuckowree, J., De Paola, V., Hofer, S. B., Hübener, M., Keck, T., Knott, G., Lee, W. C., Mostany, R., Mrsic-Flogel, T. D., Nedivi, E.,

Portera-Cailliau, C., Svoboda, K., Trachtenberg, J. T., and Wilbrecht, L. (2009). Long-term, high-resolution imaging in the mouse neocortex through a chronic cranial window. *Nat. Protoc.* 4, 1128–1144.

Holtmaat, A., Wilbrecht, L., Knott, G. W., Welker, E., and Svoboda, K. (2006). Experience dependent and cell-type-specific spine growth in the neocortex. *Nature* 441, 979–983.

Kerschensteiner, M., Schwab, M. E., Lichtman, J. W., and Misgeld, T. (2005). *In vivo* imaging of axonal degeneration and regeneration in the injured spinal cord. *Nat. Med.* 11, 572–577.

Kleinfeld, D., Friedman, B., Lyden, P. D., and Shih, A. Y. (2008). "Targeted occlusion to surface and deep vessels in neocortex via linear and nonlinear optical absorption," in *Animal Models of acute Neurological Injuries*, eds J. Chen, Z. Xu, X.-M. Xu, and J. Zhang (New York: The Humana Press Inc), pp. 169–185.

Kleinfeld, D., Mitra, P. P., Helmchen, F., and Denk, W. (1998). Fluctuations and stimulus-induced changes in blood flow observed in individual capillaries in layers 2 through 4 of rat neocortex. *Proc. Natl. Acad. Sci. U.S.A.* 95, 15741–15746.

Kohli, V., and Elezzabi, A. Y. (2008). Laser surgery of zebrafish (Danio rerio) embryos using femtosecond laser pulses: Optimal parameters for exogenous material delivery, and the laser's effect on short- and long-term development. *BMC Biotechnol.* 8, 7.

König, K., Riemann, I., and Fritzsche, W. (2001). Nanodissection of human chromosomes with near-infrared femtosecond laser pulses. *Opt. Lett.* 26, 819–821.

König, K., Riemann, I., Fischer, P., and Halbhuber, K. H. (1999). Intracellular nanosurgery with near infrared femtosecond laser pulses. *Cell. Mol. Biol.* 45, 195–201.

Kumar, S., Maxwell, I. Z., Heisterkamp, A., Polte, T. R., Lele, T., Salanga, M., Mazur, E., and Ingber, D. E. (2006). Viscoelastic retraction of single living stress fibers and its impact on cell shape, cytoskeletal organization, and extracellular matrix mechanics. *Biophys. J.* 90, 3762–3773.

Lendvai, B., Stern, E., Chen, B., and Svoboda, K. (2000). Experience-dependent plasticity of dendritic spines in the developing rat barrel cortex *in vivo*. *Nature* 404, 876–881.

Li, P., and Murphy, T. H. (2008). Two-Photon Imaging during Prolonged Middle Cerebral Artery Occlusion in Mice Reveals Recovery of Dendritic Structure after Reperfusion. *J. Neurosci.* 28, 11970 –11979.

Mostany, R., and Portera-Cailliau, C. (2008). A craniotomy surgery procedure for chronic brain imaging. JoVE. (2008) Available at: http://www.jove.com/index/details.stp?id=680, doi: 10.3791/680.

Nimmerjahn, A., Kirchhoff, F., and Helmchen, F. (2005). Resting microglial cells are highly dynamic surveillants of brain parenchyma *in vivo*. *Science* 308, 1314–1318.

Nishimura, N., Schaffer, C. B., Friedman, B., Tsai, P. S., Lyden, P. D., and Kleinfeld, D. (2006). Targeted insult to subsurface cortical blood vessels using ultrashort laser pulses: three models of stroke. *Nat. Methods* 3, 99–108.

Oehring, H., Riemann, I., Fischer, P., Halbhuber, K. J., and König, K. (2000). Ultrastructure and reproduction behaviour of single CHO-K1 cells exposed to near infrared femtosecond laser pulses. *Scanning* 22, 263–270.

Sacconi, L., O'Connor, R. P., Jasaitis, A., Masi, A., Buffelli, M., and Pavone, F. S. (2007). *In vivo* multi-photon nanosurgery on cortical neurons. *J. Biomed. Opt.* 12, 050502. doi:10.1117/1.2798723.

Sacconi, L., Tolić-Nørrelykke, I. M., Antolini, R., and Pavone, F. S. (2005). Combined intracellular three-dimensional imaging and selective nanosurgery by a nonlinear microscope. *J. Biomed. Opt.* 10, 014002–014005.

Schaffer, C. B., Friedman, B., Nishimura, N., Schroeder, L. F., Tsai, P. S., Ebner, F. F., Lyden, P. D., and Kleinfeld, D. (2006). Two-photon imaging of cortical surface microvessels reveals a robust redistribution in blood flow after vascular occlusion. *PLoS Biol.* 4, e22. doi:10.1371/journal.pbio.0040022.

Shen, N., Datta, D., Schaffer, C. B., LeDuc, P., Ingber, D. E., and Mazur, E. (2005). Ablation of cytoskeletal filaments and mitochondria in cells using a femtosecond laser nanoscissor. *Mech. Chem. Biosyst.* 2, 17–26.

Shimada, T., Watanabe, W., Matsunaga, S., Higashi, T., Ishii, H., Fukui, K., Isobe, K., and Itoh, K. (2005). Intracellular disruption of mitochondria in a living HeLa cell with a 76-MHz femtosecond laser oscillator. *Opt. Express* 13, 9869–9880.

Smith, N. I., Fujita, K., Kaneko, T., Katoh, K., Nakamura, O., Kawata, S., and Takamatsu, T. (2001). Generation of calcium waves in living cells by pulsed-laser-induced photodisruption. *Appl. Phys. Lett.* 79, 1208–1210.

Supatto, W., Débarre, D., Moulia, B., Brouzés, E., Martin, J., Farge, E., and Beaurepaire, E. (2005). *In vivo* modulation of morphogenetic movements in Drosophila embryos with femtosecond laser pulses. *Proc. Natl. Acad. Sci. U.S.A.* 102, 1047–1052.

Supatto, W., Fraser, S. E., and Vermot, J. (2008). An all-optical approach for probing microscopic flows in living embryos. *Biophys. J.* 95, 4.

Svoboda, K., and Yasuda, R. (2006). Principles of two-photon excitation microscopy and its applications to neuroscience. *Neuron* 50, 823–839.

Tirlapur, U. K., and König, K. (2002). Targeted transfection by femtosecond laser. *Nature* 418, 290–291.

Tolić-Nørrelykke, I. M., Sacconi, L., Thon, G., and Pavone, F. S. (2004). Positioning and elongation of the fission yeast spindle by microtubule-based pushing. *Curr. Biol.* 14, 1181–1186.

Trachtenberg, J. T., Chen, B. E., Knott, G. W., Feng, G., Sanes, J. R., Welker, E., and Svoboda, K. (2002). Long-term *in vivo* imaging of experience-dependent synaptic plasticity in adult cortex. *Nature* 420, 788–794.

Tsai, P. S., Blinder, P., Migliori, B. J., Neev, J., Jin, Y., Squier, J. A., and Kleinfeld, D. (2009). Plasma-mediated ablation: An optical tool for submicrometer surgery on neuronal and vascular systems. *Curr. Opin. Biotechnol.* 20, 1–10.

Vogel, A., Noack, J., Hüttman, G., and Paltauf, G. (2005). Mechanisms of femtosecond laser nanosurgery of cells and tissues. *Appl. Phys. B* 81, 1015–1047.

Vogel, A., and Venugopalan, V. (2003). Mechanisms of pulsed laser ablation of biological tissues. *Chem. Rev.* 103, 577–644.

Waller, A. (1850). Experiments on the section of the glossopharyngeal and hypoglossal nerves of the frog, and observations of the alterations produced thereby in the structure of their primitive fibres. *Philos. Trans. R. Soc. Lond., B, Biol. Sci.* 140, 423–429.

Watanabe, W., and Arakawa, N. (2004). Femtosecond laser disruption of subcellular organelles in a living cell. *Opt. Express* 12, 4203–4213.

Yanik, M. F., Cinar, H., Cinar, H. N., Chisholm, A. D., Jin, Y., and Ben-Yakar, A. (2004). Neurosurgery: functional regeneration after laser axotomy. *Nature* 432, 822.

Zeira, E., Manevitch, A., Khatchatouriants, A., Pappo, O., Hyam, E., Darash-Yahana, M., Tavor, E., Honigman, A., Lewis, A., and Galun, E. (2003). Femtosecond infrared laser an efficient and safe *in vivo* gene delivery system for prolonged expression. *Mol. Ther.* 8, 342–350.

Zhang, S., Boyd, J., Delaney, K., and Murphy, T. H. (2005). Rapid reversible changes in dendritic spine structure *in vivo* gated by the degree of ischemia. *J. Neurosci.* 25, 5333–5338.

Zhang, S., and Murphy, T. H. (2007). Imaging the impact of cortical microcirculation on synaptic structure and sensory-evoked hemodynamic responses *in vivo*. *PLoS Biol.* 5, e119. doi: 10.1371/journal.pbio.0050119.

Zimmerman, U. P., and Schlaepfer, W. W. (1984). Multiple forms of Ca-activated protease from rat brain and muscle. *J. Biol. Chem.* 259, 3210–3218.

Zipfel, W. R., Williams, R. M., and Webb, W. W. (2003). Nonlinear magic: multiphoton microscopy in the biosciences. *Nat. Biotechnol.* 21, 1369–1377.

Zuo, Y., Lin, A., Chang, P., and Gan, W. B. (2005). Development of long-term dendritic spine stability in diverse regions of cerebral cortex. *Neuron* 46, 181–189.

Conflict of Interest Statement: The authors declare that the research was conducted in the absence of any commercial or financial relationships that could be construed as a potential conflict of interest.

Received: 26 February 2010; paper pending published: 30 April 2010; accepted: 05 July 2010; published online: 30 July 2010.
Citation: Allegra Mascaro AL, Sacconi L and Pavone FS (2010) Multi-photon nanosurgery in live brain. Front. Neuroenerg. ***2****:21. doi: 10.3389/fnene.2010.00021*

frontiers in
NEUROENERGETICS

REVIEW ARTICLE
published: 16 August 2010
doi: 10.3389/fnene.2010.00016

Vascular tone and neurovascular coupling: considerations toward an improved *in vitro* model

Jessica A. Filosa*

Department of Physiology, Medical College of Georgia, Augusta, GA, USA

Edited by:
Anna Devor, University of California San Diego, USA

Reviewed by:
Jean Rossier, Ecole Superieure de Physique et de Chimie Industrielles, France
Bruno Cauli, Universite Pierre et Marie Curie, France
Eric Newman, University of Minnesota, USA

****Correspondence:***
Jessica A. Filosa, Medical College of Georgia, CA 2092, 1120 15th Street, Augusta, GA 30912, USA.
e-mail: jfilosa@mcg.edu

Neurovascular research has made significant strides toward understanding how the brain neurovascular unit accomplishes rapid and spatial increases in blood flow following neuronal activation. Among the experimental models used, the *in vitro* brain slice preparation provides unique information revealing the potential signals and cellular mechanisms involved in functional hyperemia. The most crucial limitation of this model, however, is the lack of intraluminal pressure and flow in the vessels being studied. Moreover, differences in basal vascular tone have led to varied interpretations regarding the polarity of vascular responses following neuron-to-glial stimulation. Given the complexity of astrocyte-induced neurovascular responses, we propose the use of a modified *in vitro* brain slice preparation, where intraluminal arteriolar pressure and flow are retained. Throughout this review, we discuss the advantages and disadvantages to be considered when using brain slices for neurovascular studies. Potential ways to overcome the current limitations are proposed.

Keywords: astrocytes, calcium, neurovascular coupling, vascular tone, arteriole, potassium, nitric oxide, brain slice

In this article we review and discuss recent advances in our understanding of neurovascular communication, and address the advantages and disadvantages of using the *in vitro* brain slice preparation as a tool to study neurovascular coupling (NVC) in the brain. A number of groups have used this *in vitro* model, and data obtained from their studies (Fergus et al., 1996; Zonta et al., 2003b; Cauli et al., 2004; Hamel, 2004; Mulligan and MacVicar, 2004; Lovick et al., 2005; Filosa et al., 2006; Metea and Newman, 2006; Blanco et al., 2008) have provided seminal work to the field, highlighting the neuronal and astrocytic signaling pathways underlying NVC. A caveat to the data presented below, is however, that NVC mechanism are brain-region specific and dependent on the constituents forming the neurovascular unit (NVU) under study.

STRUCTURAL CONSIDERATIONS OF THE NEUROVASCULAR UNIT

Blood supply is carried to the brain by extracerebral and intracerebral arteries/arterioles. Extracerebral arteries branch off into pial arterioles that surround the surface of the brain and then penetrate the brain parenchyma at right angles as *penetrating* or *parenchymal arterioles* (Edvinsson and MacKenzie, 2002). Parenchymal arterioles in turn give rise to an extensive capillary network, the distribution of which is associated to the metabolic demands of the neuronal microenvironment (Edvinsson and MacKenzie, 2002). The neurovascular control of the cerebral circulation varies, depending on the location and caliber of the vessels. In general, extracerebral vessels are innervated by peripheral nerves (*extrinsic innervation*) originating from the superior cervical, sphenopalatine, otic, internal carotid, and trigeminal ganglia (Gulbenkian et al., 2001). Intracerebral parenchymal microvessels are primarily regulated by local interneurons and neuronal terminals from a central origin (*intrinsic innervation*) such as the basal forebrain, raphe, and locus coeruleus (Iadecola, 1998; Gulbenkian et al., 2001; Hamel, 2006). These arterioles are also regulated by surrounding glial cells and, to some extent, by peripheral nerves that penetrate the brain parenchyma (Goadsby and Edvinson, 2002).

Much of the brain infrastructure is needed to provide neurons with the proper delivery of oxygen and glucose, given the limited energy reserves of the brain. To accomplish this, the brain possesses two fundamental mechanisms namely, *autoregulation* and *functional hyperemia* (Iadecola and Nedergaard, 2007) which are tightly controlled by the intrinsic properties of the vascular cells and by signals released from the various cell types that make up the NVU. The activation of these mechanisms warrants constant blood flow and increased oxygen and glucose delivery under conditions of intense neuronal stimulation.

At the cellular level, the cells that make up the NVU mainly include vascular cells [endothelial cells (EC), pericytes and vascular smooth muscle cells], neuronal terminals or varicosities, astrocytes with their corresponding specialized endfeet processes, and microglia. The interaction between these various cell types aid in the establishment of the blood brain barrier and the control of cerebral blood flow. Cell-to-cell interactions are futher supported by structural components such as gap junctions (Simard et al., 2003; Figueroa and Duling, 2009) and anchoring proteins (e.g., integrins; del Zoppo, 2010) as well as by the functional activation of various ion channels [e.g., aquaporin 4, K^+ channels, transient receptor potential (TRP) channels (Brayden et al., 2008)] strategically expressed on membranes of the cells of the NVU. These associations are crucial for the structural integrity and functional capacity of the NVU. On a larger scale, further control is provided by networks of cells occupying defined brain regions. For example, specialized gap junctions link astrocytes to one another forming a syncytium (Theis et al., 2005). These glial networks efficiently modulate the activity of neuronal populations (Giaume et al., 2010). In addition, the intimate anatomical association of astrocytic processes

with synapses and blood vessels places them in an ideal position to integrate neuronal activity with changes in vascular dynamics. An example of such a coordinated event was shown by Xu et al. (2008) providing evidence that the glia limitans plays an important role in upstream cerebral vasodilation following neuronal stimulation or hypercapnia-induced pial arteriolar dilation (Xu et al., 2004).

While astrocytic endfeet processes occupy a significant portion of the abluminal surface of the vessel wall (Kacem et al., 1998; Simard et al., 2003), other innervations such as neuronal terminals and varicosities of various origins have also been described, suggesting direct neurovascular regulation. For example, basal forebrain nitric oxide synthase (NOS) neurons (Tong and Hamel, 2000) and dopaminergic neurons have been shown to make close contacts with cerebral microvessels or with astrocytic endfeet (Krimer et al., 1998). Cauli et al. (2004) provided structural and functional evidence for the involvement of GABAergic interneurons containing vasoactive mediators such as NO. Clearly, specialized contact areas such as the space between neuronal terminals or varicosities and astrocytic endfeet with the vascular wall provide structural evidence for the intricacy of the signaling mechanisms underlying NVC in the brain and the dynamic interactions between neuronal, glial and vascular networks. The *in vitro* brain slice preparation constitutes an ideal model to study cell-to-cell communication since it possesses all of the constituents of the NVU with the addition of local circuits that allow for the precise stimulation of discrete neuronal and/or astrocytic targets while simultaneously monitoring the activity of the vascular cells.

SIGNALING MECHANISMS UNDERLYING FUNCTIONAL HYPEREMIA IN THE BRAIN

In addition to the above structural observations, strong functional evidence supports an important role for neurons in NVC. The release of neurotransmitters (e.g., glutamate and GABA) has been associated with vasomotor responses both *in vivo* and *in vitro* (Drake and Iadecola, 2007). A direct vasomotor effect from neuronally derived signals has been suggested for dopaminergic, serotonergic, norepinephrine and acetylcholine fibers as well as for neuronally derived neuropeptides such as substance P, neurotensin, vasoactive intestinal peptide (VIP), somatostatin and neuropeptide Y (for review see, Hamel, 2006; Drake and Iadecola, 2007). For example, in hippocampal slices Fergus et al. (1995) showed evidence that NO contributes to basal vascular tone and that CGRP dilated parenchymal arterioles. Interestingly, the magnitude of the vascular response to CGRP was dependent on the degree of arteriolar tone, suggesting an interplay between these signals (Fergus et al., 1995). In slices perfused with a thromboxane A_2 agonist (U46619) to induce arteriolar tone, NMDA produced vasodilation via an NO-dependent mechanism (Lovick et al., 1999; Brown et al., 2000). Vasodilation of cortical arterioles has also been associated with the activation of cholinergic fibers (Vaucher and Hamel, 1995; Vaucher et al., 1997) and NO-containing neurons (Tong and Hamel, 2000). Tong and Hamel (2000) suggested that the anatomical interaction between the cholinergic and nitrergic systems may serve to potentiate vascular responses via acetylcholine's influence on NO signaling (Tong and Hamel, 2000). Cauli et al. (2004) showed that stimulation of single interneurons expressing VIP or NOS mediated vasodilation, whereas stimulation of interneurons expressing somatostatin and neuropeptide Y produced microvessel constriction. Microinjection of dopamine produced constriction of ~50% of microvessels (Krimer et al., 1998).

As has been the case with neurons, evidence exists that astrocyte-derived signals can also trigger vascular responses and play a pivotal role in the signaling mechanisms involved in NVC (Takano et al., 2006; Carmignoto and Gomez-Gonzalo, 2009). Astrocytic activation results in the release of vasoactive agents (Carmignoto and Gomez-Gonzalo, 2009; Koehler et al., 2009) capable of inducing localized vasodilation (*in vitro* an *in vivo*) and/or vasoconstriction (*in vitro* only) of parenchymal arterioles. Astrocytes respond to an increase in synaptic activity with a rise in intracellular Ca^{2+} (Cornell-Bell et al., 1990; Aguado et al., 2002). If the strength of synaptic activity is high, it triggers the propagation of a Ca^{2+} wave that travels to nearby microvessels (Zonta et al., 2003b; Fellin and Carmignoto, 2004; Filosa et al., 2004). This latter step is critical for astrocyte-induced vasodilation (Zonta et al., 2003b; Filosa et al., 2004). Furthermore, astrocytes synthesize and release a number of vasoactive substances such as NO (Wiencken and Casagrande, 1999; Li et al., 2003), prostacyclins, prostaglandins, epoxyeicosatrienoic acids (EETs), glutamate, adenosine, and ATP (Harder et al., 2002; Li et al., 2003; Simard et al., 2003; Zonta et al., 2003a,b; Anderson et al., 2004; Takano et al., 2006) making them key candidates in NVC.

Despite significant progress in our understanding of the signaling events involved in NVC and the contributing role of neurons and astrocytes, recent findings have raised new challenges to the field. For example, while the physiological significance of neuronal and astrocyte-induced vasodilatory responses is clear, it is still not apparent what is the physiological significance for stimulus-induced vasoconstriction at the site of neuronal activation (Girouard et al.; Cauli et al., 2004; Mulligan and MacVicar, 2004; Metea and Newman, 2006; Rancillac et al., 2006). More importantly, based on functional and structural observations, it has been proposed that vessel-to-glia or vessel-to-neuron signaling may play an important role in brain information processing (Moore and Cao, 2008), highlighting the importance of vascular-derived signals and raising the question as to whether information within the NVU flows in a bi-directional manner (Kozlov et al., 2006; Paton et al., 2007; Moore and Cao, 2008; del Zoppo, 2010).

FACTORS AFFECTING VASCULAR TONE AND VASOMOTOR RESPONSES

Under physiological conditions and in response to intraluminal pressure, arterioles display myogenic tone (i.e., constrictions independent of innervation). The mechanisms for this tone-dependent constriction have been extensively studied, and are underlined by an interplay between ion channels that increase intracellular Ca^{2+} (e.g., VDCC, TRPV4) (Knot and Nelson, 1998; Inoue et al., 2004; Zhang et al., 2009; Ma et al., 2010) as well as opening of K^+ channels (e.g., BK, IK and SK) that oppose Ca^{2+}-dependent mechanisms leading to hyperpolarization and vasodilation (Nelson et al., 1995; Wrzosek, 2009). The expression of these channels varies depending upon the cell type (e.g., EC or VSMC) and the location and caliber of the vessel. In a recent review Dunn and Nelson (2010) discusses the implication that K^+ channel activation/inactivation has on VSMC tone.

In addition to the intrinsic properties of the VSMC, vascular tone is regulated by EC signaling. EC release vasodilating (e.g., NO, endothelium-derived hyperpolarizing factor, prostanoids) and vasoconstricting (e.g., endothelin, TXA_2, prostaglandin) substances (Andresen et al., 2006; Feletou and Vanhoutte, 2009). Moreover, EC express an array of ion channels that, when activated, can directly or indirectly alter the membrane potential (V_m) of the VSMC, establishing EC-to-VSMC coupling. In excised parenchymal arterioles, Cipolla et al. (2009) showed the contribution of SK and IK channel activity (expressed in EC) on vascular tone. Direct interactions between ECs and astrocytes have also been proposed, providing structural and functional evidence for bi-directional communication between these cells (Leybaert et al., 2004). At the capillary level, Peppiat demonstrated pericyte constriction following electrical stimulation, purinergic activation, or GABA blockers, likely exemplifying an additional form of bi-directional communication between pericytes and EC and a form by which pericytes may control blood flow perfusion to capillary beds (Peppiatt and Attwell, 2004). Based on the intrinsic mechanisms controlling vascular tone and the intricate structural arrangement of the NVU, one can say that VSMCs are sandwitched from the luminal and abluminal side by functionally dynamic cells (ECs and astrocytes). Interestingly, many of the pathways described in the endothelium (Feletou et al., 2008; Feletou and Vanhoutte, 2009), that are known to play a major role in vascular tone have been observed in astrocytes. **Figure 1** illustrates the various vasoactive signaling pathways described in the endothelium and also observed in astrocytes. What then would be the physiological consequences of such a structural arrangement?

As is the case in EC-to-VSMC signaling, the close association between astrocytes to VSMCs may relate to the need to maintain or control vascular tone within optimal levels. To achieve this, astrocytes would need to constantly monitor hemodynamic changes and locally release vasoactive factors that adjust vascular diameter and maintain CBF constant. If astrocytes contribute to the tonic regulation of vascular tone, it may explain why functional hyperemia studies do not call for an important role for astrocytes and may provide a new meaning to astrocyte-induced vasoconstriction. While the role for astrocytes in functional hyperemia may be indeed relevant, their vasodilatory actions (Takano et al., 2006) may

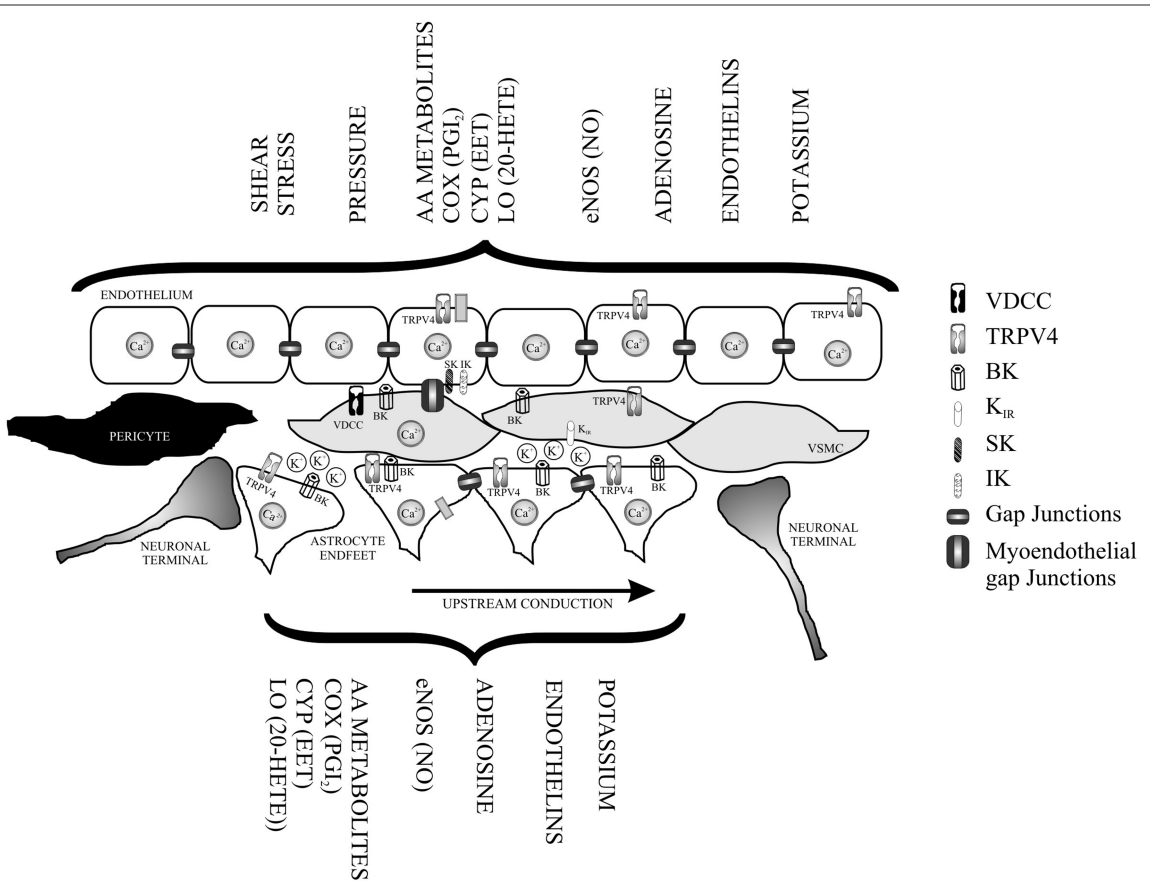

FIGURE 1 | Functional overlapping mechanism from the luminal (endothelium) and abluminal side of a parenchymal arteriole. In addition to direct neuronal-vessel interactions vascular smooth muscle cells (VSMC) are tonically influenced by agonists and/or mechanically activated pathways from the endothelium and from signals released by astrocytic processes also in direct contact with the vessels. The presence of polarized and discrete ion channel types in the layer formed by endothelial cells and astrocytes, provides functional further support for bi-directional communication between these cells and VSMC, as well as, for an electrotonic arrangement capable of modulating vascular tone and conduction of signals over long distances along the microvessel. VDCC (voltage-dependent Ca^{2+} channels), TRPV4 (transient receptor potential vanilloid), BK (Ca^{2+}-activated voltage-dependent K^+ channel), IK (intermediate conductance Ca^{2+} activated K^+ channel), SK (small conductance Ca^{2+} activated K^+ channel), and K_{ir} (inwardly rectifying K^+ channel).

be modulatory depending on the neuronal pathways activated or degree of stimulation. In other words, it is possible that the vasoconstrictive role of astrocytes is primarily linked to their contribution to the re-establishment of vasomotor tone following neuronal stimulation or tone adjustments following hemodynamic-induced vascular responses to sudden blood pressure changes as occurs during autoregulation (Harder et al., 2002).

In an elegant study, Gordon et al. (2008) suggested that the polarity of the vascular response to glia-derived vasoactive signals is coupled to oxygen concentration levels, which in turn determine the metabolic state of the tissue. Oxygen levels modulate extracellular lactate and adenosine concentrations (Gordon et al., 2008). Increased lactate inhibits the activity of prostaglandin E_2 (PGE_2) transporters, raising extracellular PGE_2 levels and thus favoring vasodilatory responses when PO_2 levels are low (Chan et al., 2002). On the other hand, the authors suggested that vasoconstriction responses occur under hyperoxic conditions, where lactate levels are low and extracellular PGE_2 availability is decreased (Gordon et al., 2008). Lindauer et al. (2010) recently challenged these findings by showing that in anesthetized rats, CBF responses to electrical forepaw stimulation or cortical spreading depression under conditions of hyperbaric oxygenation (absence of hemoglobin deoxygenation) were independent of O_2 levels.

Likewise, a study by Metea and Newman (2006) in the retina showed that astrocytes induce both vasodilation and vasoconstriction, but in their case the polarity of the response was dependent on NO availability. While NO inhibition leads to vasodilation, NO availability favored vasoconstriction (Metea and Newman, 2006). The later observation was attributed to NO interactions with arachidonic acid (AA) metabolites favoring vasoconstriction through the potential NO inhibiting effects on cytochrome P450 (Udosen et al., 2003) and decreased downstream formation of the vasodilating metabolites, EETs (Metea and Newman, 2006). In support of these findings, Rancillac et al. (2006) showed that glutamate-induced NO released from cerebellar slices resulted in vasoconstriction of microvessels preconstricted with U46619. The vasoconstriction response was also dependent on the synthesis of prostanoids and endothelin. Given the strong evidence for NO inhibition of 20-HETE formation (Alonso-Galicia et al., 1997) and the ability of the AA metabolites, EETs and 20-HETEs, to modulate the activity of large conductance Ca^{2+}-activated K^+ (BK) channels in vascular cells (Feletou, 2009) and astrocytes (Gebremedhin et al., 2003, 2005) one possibility for NO-mediated constriction could be tonic EET-dependent BK activation in astrocytic endfeet, resulting in K^+ accumulation and VSMC depolarization. A role for K^+ channel-induced vasodilation and vasoconstriction was recently discussed by Girouard et al. (2010) (see below).

In a previous study, we showed that BK channel activation in astrocytic endfeet contributes to vasodilatory responses in parenchymal arterioles (Filosa et al., 2006). Moreover, our group also showed that the magnitude of the K^+-induced vasodilatory response was correlated to the degree of tone of the arteriole, highlighting how changes to the intrinsic properties of the VSMCs alters their sensitivity to a given signal (Blanco et al., 2008). In addition, Girouard et al. (2010) recently showed that at the same level of tone, opposite type vascular responses could be evoked by varying K^+ levels at the gliovascular space. Girouard's study further incorporates the importance of upstream signaling events to vascular responses. The magnitude of the Ca^{2+} change in the astrocyte determined the amount of K^+ efflux from the endfeet. It is suggested that low or modest changes in K^+ levels activate inwardly rectifying (K_{ir}) channels in VSMCs (Filosa et al., 2006) leading to vasodilation whereas high K^+ levels at the gliovascular space cause VSMC depolarization and thus vasoconstriction. These studies suggest that in order to accurately interpret stimulus-induced vascular responses, the cells at the NVU must be close to physiological conditions including the steady-state of the EC and VSMCs, the resting V_m of the VSMCs, and the Ca^{2+} dynamic in all of the cells.

Undoubtedly, NO signaling plays a central role in NVC studies; however, the precise cellular sources and downstream targets for NO are largely unknown. While NO is believed to be the predominant signal in the cerebellum (Yang et al., 1999; Yang et al., 2000), findings from the cortex would suggest NO action in NVC are modulatory (Lindauer et al., 1999). In brain slices, NOS inhibition with L-NNA induced constriction of parenchymal arteriole, suggesting a tonic vasodilatory influence (Fergus et al., 1996), and neuronal stimulation-induced vasodilatory responses are in part mediated by NO derived from a neuronal origin (Lovick et al., 1999; Brown et al., 2000). Kitaura et al. (2007) showed that inhibiton of nNOS significantly decreased vasodilatory responses to stimulation while de Labra et al. (2009) recently suggested that stimulation-induced hemodynamic changes were associated with both eNOS and nNOS activity, depending on the degree of stimulation. In addition, de Labra suggested that NO from a vascular or glial source had a more prominent role in low frequency-induced vascular responses, while NO from a neuronal source played a more prominent role during intense stimulation. Data from these studies would suggest a possible mechanism by which the degree of stimulation may recruit the participation of different elements of the NVU, or networks, in orchestrating vascular responses.

Altogether, the ability of NO to interfere with AA signaling pathways in astrocytes (Metea and Newman, 2006), vascular tone (Feletou et al., 2008), neuronal activity (Ferraro and Sardo, 2004) and signaling events that affect many of the constituents of the NVU (i.e., K^+ channel activity) brings into question whether interference with NO signaling alters the basal activity of the cells making up the NVU, disrupting, in turn, bi-directional steady-state communication pathways that optimize vascular responses to neuronally derived signals. Evidence supporting a role for astrocyte-derived NO in controlling vascular tone was provided by Chisari et al. (2004); co-cultures of basilar artery with activated LPS glia showed changes in vascular tone induced by NO. Moreover, because NO alters Ca^{2+} activity in astrocytes (Bal-Price et al., 2002), it is possible that endothelial-derived NO contributes to basal astrocytic activity. Future studies addressing the dynamic interactions between vascular cells and astrocytes in a bi-directional manner will help elucidate how interfering with these pathways may result in variable vascular responses following neuronal excitability.

ADVANTAGES AND DISADVANTAGES OF THE *IN VITRO* BRAIN SLICE PREPARATION

Albeit these important observations and given confounding differences in the data obtained by various groups, a clearer understanding of NVC mechanisms may be possible if an improved and better standardized brain slice preparation is developed. Ideally, this

preparation should include important hemodynamic variables such as intraluminal pressure and/or flow and take into consideration the levels of cellular activity at rest.

While numerous efforts have been made to maintain neuronal and glial viability in brain slices (Collingridge, 1995; Brahma et al., 2000; Hájos and Mody, 2009), little consideration has been made to ensure penetrating cerebral arterioles are maintained near physiological conditions when using this preparation. To this end, experts in the microcirculation field have provided extensive reports, albeit on excised arterioles, on the criteria needed to obtain proper vascular responses, and how changes to these variables could account for significant alterations in vascular reactivity and function (Ngai and Winn, 1995). However, only one study (Lovick et al., 2005) attempted to mimic these conditions in the brain slice preparation.

In an attempt to mimic physiological conditions, the solutions used to perfuse brain slices have been adjusted to include much of the constituents of the cerebrospinal fluid (CSF) (Reid et al., 1988; Hájos and Mody, 2009). While these solutions have proven to be successful in achieving reliable electrophysiological and imaging recordings from both neurons and astrocytes, a closer look at some of the major constituents of the artificial CSF (aCSF) is needed. For example, glucose concentrations used by most researchers (10–25 mM) far exceed that of the actual CSF (~2.5 mM) (Silver and Erecinska, 1994). In addition, the use of 95% O_2 has also been shown to result in different neuronal excitability levels and in the production of superoxide ($\bullet O_2^-$) and cell death (D'Agostino et al., 2007; Hájos and Mody, 2009). Moreover, based on a study by Gordon et al. (2008), tissue PO_2 levels may also have a crucial impact on the physiological response of vascular cells.

Another important player affected by O_2 levels is NO. Given that NO production is dependent on O_2 availability (Kojima et al., 2001) and its presence influences cell function and NVC outcomes, caution should be taken when interpreting results where these variables are not carefully controlled or monitored. So what would be the ideal aCSF solution when performing NVC experiments in brain slices? While more data is needed to better address this question, perfusing slices with a 20% O_2 solution might be closer to physiological conditions and is unlikely to induce cell death (D'Agostino et al., 2007). In a recent study, Ledo et al. (2010) simultaneously measured NO and O_2 levels 200 μm deep into the slice using an aCSF solution bubbled with 95% O_2–5% CO_2; under these conditions O_2 levels were around 57.3 ± 38.2 μM. To our knowledge the outcome of 20% O_2 levels on NO availability at different depths of the brain slice has not been explored and would need further consideration, given the steep O_2 gradient from the surface of the slice to deeper layers (~200 μm) (Ledo et al., 2005). In addition, an even closer physiological approach would be to perfuse parenchymal arterioles with a solution that mimics blood constituents, establishing suitable PO_2 gradients at the NVU before and during intense neuronal activation protocols are used. A similar approach has been extensively used in the renal physiology field where a renal arteriole is perfused with normal blood and hemodynamic variables are measured under different conditions (Casellas and Navar, 1984; Casellas and Moore, 2003). An approach of this nature would allow the exploration of further questions such as the effect vascular-derived signals have on resting astrocytic and neuronal function.

FUTURE DIRECTIONS TO A BETTER *IN VITRO* MODEL

Altogether, these observations call for a more optimized *in vitro* model to dissect the underlying signaling mechanisms of NVC. While we strongly believe brain slices to be an ideal *in vitro* model, we suggest the inclusion of the following criteria: (1) optimal neuronal and astrocytic viability/activity and (2) optimal physiological conditions for the arteriole under investigation. As previously shown, brain slices should be kept under conditions that prevent cell swelling to maintain the viability of the neurons and astrocytes. In addition, the penetrating cerebral arterioles need to be exposed to an intraluminal solution that maximizes the viability of the vascular cells. Ideally, arterioles should be pressurized to allow for the development of myogenic tone. The presence of myogenic tone should be used as an indication that vascular cells have achieved optimal resting activity, the state at which vascular responses would be comparable to those under *in vivo* conditions. Using an *in vitro* preparation in which all the components of the NVU are brought to a closer physiological condition will provide more reliable interpretations of the dynamic interactions between vascular cells, astrocytes, and neurons in the brain.

Here we highlight previously reported experimental paradigms from which successful arteriolar myogenic tone and flow can be achieved in penetrating cerebral arterioles removed from the brain or from brain slices (Dacey and Duling, 1982; Ngai and Winn, 1995; Cipolla et al., 2004; Lovick et al., 2005). To this end, penetrating arterioles can be cannulated at one end and pressurized under no-flow conditions (Ngai and Winn, 1995). Following a successful cannulation, the arteriole is slowly pressurized in a stepwise manner until an intraluminal pressure between 20 and 40 mmHg is achieved and the vessel shows spontaneous tone (Dacey and Duling, 1982, 1984; Ngai and Winn, 1995). This latter step is typically conducted at 35°C to further stimulate tone (Ngai and Winn, 1995). Arterioles are allowed to equilibrate to their steady-state pressure before experimental protocols are executed. To maintain intraluminal pressure constant, the distal end of the arteriole is clamped and pressure is continuously monitored from a pressure transducer connected to a computer. In addition to intraluminal pressure, using the same cannula approach, flow can be introduced into parenchymal arterioles and its effects incorporated into experimental questions (Lovick et al., 2005). As previously performed in renal tubules, fluorescence recovery after photobleaching can be used to measure mean axial velocity of the intraluminal perfusate (Flamion et al., 1991) within the penetrating arteriole and thus provide a measurement of flow rate, a parameter not well investigated, but likely key in NVC-associated responses. For example, flow rate (shear stress) can induce NO production from the endothelium, changing the steady-state diameter (tone) of the arteriole and possibly vascular reactivity to vasoactive signals released by astrocytes and/or neurons (Ngai and Winn, 1995). Thus, one important question still to be determined is whether, under different hemodynamic conditions, cerebral arterioles would behave similarly to glial/neuronal-derived signals. An additional question, and suggested by the recently proposed hemo-neuronal hypothesis (Moore and Cao, 2008), is whether different hemodynamic conditions can alter neuronal excitability in the brain. Significant advances to this already reliable *in vitro* model will help expand our understanding of the cellular events underlying NVC in the brain.

Contrary to the disadvantages mentioned above, the brain slice preparation offers a number of advantages including: the presence of all of the cellular constituents comprising the NVU, the use of low-dose pharmacological agents to better define the cellular mechanisms underlying NVC, the unlimited access to brain regions of interest, and the simultaneous monitoring of the activity of multiple cell types. Moreover, the brain slice preparation allows for the study of cell-cell communication such as mechanisms underlying intracellular conduction throughout the astrocytic network and/or vascular networks and detailed mechanisms such as the spread of electrical conduction between cells with major emphasis on ECs.

In summary, further consideration and improvements are indeed needed to better address the signaling mechanisms underlying NVC in the brain. While *in vivo* approaches provide the ultimate clues to the understanding of how the brain communicates with the surrounding microcirculation, studies in brain slices have provided seminal observations on the cellular events underlying functional hyperemia in the brain. An optimized *in vitro* model will help address future unexplored questions such as the importance of studying NVC in different brain regions (inaccessible with current *in vivo* techniques) where the microenvironment of the NVC is drastically different.

The above observations also suggest that NVC mechanisms are driven by a multiplicity of signals and conditions. However, among future questions to address is the physiological function of neuronal-induced vs. astrocyte-induced vascular responses. Based on *in vivo* findings, a current suggestion is that increases in CBF in response to neuronal stimulation is mainly driven by neuronal networks (Rossier, 2009) with vasoconstriction distant to the site of activation (Devor et al., 2007). If this were the case, what is the role of astrocytes in NVC signaling? One possibility is that astrocytes contribute to basal CBF regulation or in the spatial spread of stimulus-dependent CBF activation to upstream vessels (Xu et al., 2008). Clearly, astrocytes possess vasoconstrictive and vasodilatory signals; however, *in vivo* studies have only associated their activation to vasodilation (Takano et al., 2006). We suggest that the vasoconstrictive action of these cells may be involved in the local maintenance of vascular tone, which plays an important role in determining the degree and efficiency of vascular responses to neuronally derived signals. Moreover, we predict that under basal conditions, VSMCs are under tonic influences by EC and astrocyte-derived signals, which are overwritten by neuronal signals following increases in neuronal activity. Accordingly, astrocytes may participate in autoregulatory mechanisms and also help re-establish vascular tone following hyperemic responses (Harder et al., 2002; Rossier, 2009).

ACKNOWLEDGMENTS

I thank Drs. Javier Stern and Laura Gonzalez Bosc for their comments on the manuscript. This work was funded by the National Heart, Lung and Blood Institute (R01HL089067) and the American Heart Association (0535231N).

REFERENCES

Aguado, F., Espinosa-Parrilla, J. F., Carmona, M. A., and Soriano, E. (2002). Neuronal activity regulates correlated network properties of spontaneous calcium transients in astrocytes in situ. *J. Neurosci.* 22, 9430–9444.

Alonso-Galicia, M., Drummond, H. A., Reddy, K. K., Falck, J. R., and Roman, R. J. (1997). Inhibition of 20-HETE production contributes to the vascular responses to nitric oxide. *Hypertension* 29, 320–325.

Anderson, C. M., Bergher, J. P., and Swanson, R. A. (2004). ATP-induced ATP release from astrocytes. *J. Neurochem.* 88, 246–256.

Andresen, J., Shafi, N. I., and Bryan, R. M. Jr. (2006). Endothelial influences on cerebrovascular tone. *J. Appl. Physiol.* 100, 318–327.

Bal-Price, A., Moneer, Z., and Brown, G. C. (2002). Nitric oxide induces rapid, calcium-dependent release of vesicular glutamate and ATP from cultured rat astrocytes. *Glia* 40, 312–323.

Blanco, V. M., Stern, J. E., and Filosa, J. A. (2008). Tone-dependent vascular responses to astrocyte-derived signals. *Am. J. Physiol. Heart Circ. Physiol.* 294, H2855–2863.

Brahma, B., Forman, R. E., Stewart, E. E., Nicholson, C., and Rice, M. E. (2000). Ascorbate inhibits edema in brain slices. *J. Neurochem.* 74, 1263–1270.

Brayden, J. E., Earley, S., Nelson, M. T., and Reading, S. (2008). Transient receptor potential (TRP) channels, vascular tone and autoregulation of cerebral blood flow. *Clin. Exp. Pharmacol. Physiol.* 35, 1116–1120.

Brown, L. A., Key, B. J., and Lovick, T. A. (2000). Fluorescent imaging of nitric oxide production in neuronal varicosities associated with intraparenchymal arterioles in rat hippocampal slices. *Neurosci. Lett.* 294, 9–12.

Carmignoto, G., and Gomez-Gonzalo, M. (2009). The contribution of astrocyte signaling to neurovascular coupling. Brain Res Rev.

Casellas, D., and Moore, L. C. (2003). The juxtamedullary nephron preparation. *Methods Mol. Med.* 86, 413–427.

Casellas, D., and Navar, L. G. (1984). In vitro perfusion of juxtamedullary nephrons in rats. *Am. J. Physiol.* 246, F349–F358.

Cauli, B., Tong, X. K., Rancillac, A., Serluca, N., Lambolez, B., Rossier, J., and Hamel, E. (2004). Cortical GABA interneurons in neurovascular coupling: relays for subcortical vasoactive pathways. *J. Neurosci.* 24, 8940–8949.

Chan, B. S., Endo, S., Kanai, N., and Schuster, V. L. (2002). Identification of lactate as a driving force for prostanoid transport by prostaglandin transporter PGT. *Am. J. Physiol. Renal Physiol.* 282, F1097–F1102.

Chisari, M., Salomone, S., Laureanti, F., Copani, A., and Sortino, M. A. (2004). Modulation of cerebral vascular tone by activated glia: involvement of nitric oxide. *J. Neurochem.* 91, 1171–1179.

Cipolla, M. J., Li, R., and Vitullo, L. (2004). Perivascular innervation of penetrating brain parenchymal arterioles. *J. Cardiovasc. Pharmacol.* 44, 1–8.

Cipolla, M. J., Smith, J., Kohlmeyer, M. M., and Godfrey, J. A. (2009). SKCa and IKCa channels, myogenic tone, and vasodilator responses in middle cerebral arteries and parenchymal arterioles: effect of ischemia and reperfusion. *Stroke* 40, 1451–1457.

Collingridge, G. L. (1995). The brain slice preparation: a tribute to the pioneer Henry McIlwain. *J. Neurosci. Methods* 59, 5–9.

Cornell-Bell, A. H., Finkbeiner, S. M., Cooper, M. S., and Smith, S. J. (1990). Glutamate induces calcium waves in cultured astrocytes: long-range glial signaling. *Science* 247, 470–473.

D'Agostino, D. P., Putnam, R. W., and Dean, J. B. (2007). Superoxide (*O2–) production in CA1 neurons of rat hippocampal slices exposed to graded levels of oxygen. *J. Neurophysiol.* 98, 1030–1041.

Dacey, R. G. Jr., and Duling, B. R. (1982). A study of rat intracerebral arterioles: methods, morphology, and reactivity. *Am. J. Physiol.* 243, H598–H606.

Dacey, R. G. Jr., and Duling, B. R. (1984). Effect of norepinephrine on penetrating arterioles of rat cerebral cortex. *Am. J. Physiol.* 246, H380–H385.

de Labra, C., Rivadulla, C., Espinosa, N., Dasilva, M., Cao, R., and Cudeiro, J. (2009). Different sources of nitric oxide mediate neurovascular coupling in the lateral geniculate nucleus of the cat. *Front. Syst. Neurosci.* 3, 9.

del Zoppo, G. J. (2010). The neurovascular unit in the setting of stroke. *J. Intern. Med.* 267, 156–171.

Devor, A., Tian, P., Nishimura, N., Teng, I. C., Hillman, E. M., Narayanan, S. N., Ulbert, I., Boas, D. A., Kleinfeld, D., and Dale, A. M. (2007). Suppressed neuronal activity and concurrent arteriolar vasoconstriction may explain negative blood oxygenation level-dependent signal. *J. Neurosci.* 27, 4452–4459.

Drake, C. T., and Iadecola, C. (2007). The role of neuronal signaling in controlling cerebral blood flow. *Brain Lang.* 102, 141–152.

Dunn, K. M., and Nelson, M. T. (2010). Potassium channels and neurovascular coupling. *Circ. J.* 74, 608–616.

Edvinsson, L. M., and MacKenzie, E. T. (2002). *General and Comparative Anatomy of the Cerebral Circulation*, 2nd Edn. New York: Lippincott Williams and Wilkins.

Feletou, M. (2009). Calcium-activated potassium channels and endothelial

dysfunction: therapeutic options? *Br. J. Pharmacol.* 156, 545–562.

Feletou, M., Tang, E. H., and Vanhoutte, P. M. (2008). Nitric oxide the gatekeeper of endothelial vasomotor control. *Front. Biosci.* 13, 4198–4217.

Feletou, M., and Vanhoutte, P. M. (2009). EDHF: an update. *Clin. Sci.* 117, 139–155.

Fellin, T., and Carmignoto, G. (2004). Neurone-to-astrocyte signalling in the brain represents a distinct multifunctional unit. *J. Physiol. (Lond.)* 559, 3–15.

Fergus, A., Jin, Y., Thai, Q. A., Kassell, N. F., and Lee, K. S. (1995). Vasodilatory actions of calcitonin gene-related peptide and nitric oxide in parenchymal microvessels of the rat hippocampus. *Brain Res.* 694, 78–84.

Fergus, A., Jin, Y., Thai, Q. A., Kassell, N. F., and Lee, K. S. (1996). Tonic protein kinase C-mediated vasoconstriction is unmasked when nitric oxide synthase is inhibited in cerebral microvessels. *Neuroscience* 74, 927–934.

Ferraro, G., and Sardo, P. (2004). Nitric oxide and brain hyperexcitability. *In Vivo* 18, 357–366.

Figueroa, X. F., and Duling, B. R. (2009). Gap junctions in the control of vascular function. *Antioxid. Redox Signal.* 11, 251–266.

Filosa, J. A., Bonev, A. D., and Nelson, M. T. (2004). Calcium dynamics in cortical astrocytes and arterioles during neurovascular coupling. *Circ. Res.* 95, e73–e81.

Filosa, J. A., Bonev, A. D., Straub, S. V., Meredith, A. L., Wilkerson, M. K., Aldrich, R. W., and Nelson, M. T. (2006). Local potassium signaling couples neuronal activity to vasodilation in the brain. *Nat. Neurosci.* 9, 1397–1403.

Flamion, B., Bungay, P. M., Gibson, C. C., and Spring, K. R. (1991). Flow rate measurements in isolated perfused kidney tubules by fluorescence photobleaching recovery. *Biophys. J.* 60, 1229–1242.

Gebremedhin, D., Narayanan, J., and Harder, D. R. (2005). Role of astrocytic KCa channel openings in the glutamate receptor mediated release of EETs from rat brain astrocytes. *FASEB J.* 19, A1257.

Gebremedhin, D., Yamaura, K., Zhang, C., Bylund, J., Koehler, R. C., and Harder, D. R. (2003). Metabotropic glutamate receptor activation enhances the activities of two types of Ca^{2+}-activated K^+ channels in rat hippocampal astrocytes. *J. Neurosci.* 23, 1678–1687.

Giaume, C., Koulakoff, A., Roux, L., Holcman, D., and Rouach, N. (2010). Astroglial networks: a step further in neuroglial and gliovascular interactions. *Nat. Rev. Neurosci.* 11, 87–99.

Girouard, H., Bonev, A. D., Hannah, R. M., Meredith, A., Aldrich, R. W., and Nelson, M. T. (2010). Astrocytic endfoot Ca^{2+} and BK channels determine both arteriolar dilation and constriction. *Proc. Natl. Acad. Sci. U.S.A.* 107, 3811–3816.

Goadsby, P. J., and Edvinson, L. (2002). *Neurovascular Control of the Cerebral Circulation*, 2nd Edn. New York: Lippincott Williams and Wilkins.

Gordon, G. R., Choi, H. B., Rungta, R. L., Ellis-Davies, G. C., and MacVicar, B. A. (2008). Brain metabolism dictates the polarity of astrocyte control over arterioles. *Nature* 456, 745–749.

Gulbenkian, S., Uddman, R., and Edvinsson, L. (2001). Neuronal messengers in the human cerebral circulation. *Peptides* 22, 995–1007.

Hájos, N., and Mody, I. (2009). Establishing a physiological environment for visualized in vitro brain slice recordings by increasing oxygen supply and modifying aCSF content. *J. Neurosci. Methods* 183, 107–113.

Hamel, E. (2004). Cholinergic modulation of the cortical microvascular bed. *Prog. Brain Res.* 145, 171–178.

Hamel, E. (2006). Perivascular nerves and the regulation of cerebrovascular tone. *J. Appl. Physiol.* 100, 1059–1064.

Harder, D. R., Zhang, C., and Gebremedhin, D. (2002). Astrocytes function in matching blood flow to metabolic activity. *News Physiol. Sci.* 17, 27–31.

Iadecola, C. (1998). Neurogenic control of the cerebral microcirculation: is dopamine minding the store? *Nat. Neurosci.* 1, 263–265.

Iadecola, C., and Nedergaard, M. (2007). Glial regulation of the cerebral microvasculature. *Nat. Neurosci.* 10, 1369–1376.

Inoue, R., Morita, H., and Ito, Y. (2004). Newly emerging Ca^{2+} entry channel molecules that regulate the vascular tone. *Expert Opin. Ther. Targets* 8, 321–334.

Kacem, K., Lacombe, P., Seylaz, J., and Bonvento, G. (1998). Structural organization of the perivascular astrocyte endfeet and their relationship with the endothelial glucose transporter: a confocal microscopy study. *Glia* 23, 1–10.

Kitaura, H., Uozumi, N., Tohmi, M., Yamazaki, M., Sakimura, K., Kudoh, M., Shimizu, T., and Shibuki, K. (2007). Roles of nitric oxide as a vasodilator in neurovascular coupling of mouse somatosensory cortex. *Neurosci. Res.* 59, 160–171.

Knot, H. J., and Nelson, M. T. (1998). Regulation of arterial diameter and wall $[Ca^{2+}]$ in cerebral arteries of rat by membrane potential and intravascular pressure. *J. Physiol. (Lond.)* 508(Pt 1), 199–209.

Koehler, R. C., Roman, R. J., and Harder, D. R. (2009). Astrocytes and the regulation of cerebral blood flow. *Trends Neurosci.* 32, 160–169.

Kojima, H., Hirata, M., Kudo, Y., Kikuchi, K., and Nagano, T. (2001). Visualization of oxygen-concentration-dependent production of nitric oxide in rat hippocampal slices during aglycemia. *J. Neurochem.* 76, 1404–1410.

Kozlov, A. S., Angulo, M. C., Audinat, E., and Charpak, S. (2006). Target cell-specific modulation of neuronal activity by astrocytes. *Proc. Natl. Acad. Sci. U.S.A.* 103, 10058–10063.

Krimer, L. S., Muly, E. C. 3rd, Williams, G. V., and Goldman-Rakic, P. S. (1998). Dopaminergic regulation of cerebral cortical microcirculation. *Nat. Neurosci.* 1, 286–289.

Ledo, A., Barbosa, R., Cadenas, E., and Laranjinha, J. (2010). Dynamic and interacting profiles of *NO and O2 in rat hippocampal slices. *Free Radic. Biol. Med.* 48, 1044–1050.

Ledo, A., Barbosa, R. M., Gerhardt, G. A., Cadenas, E., and Laranjinha, J. (2005). Concentration dynamics of nitric oxide in rat hippocampal subregions evoked by stimulation of the NMDA glutamate receptor. *Proc. Natl. Acad. Sci. U.S.A.* 102, 17483–17488.

Leybaert, L., Cabooter, L., and Braet, K. (2004). Calcium signal communication between glial and vascular brain cells. *Acta Neurol. Belg.* 104, 51–56.

Li, N., Sul, J. Y., and Haydon, P. G. (2003). A calcium-induced calcium influx factor, nitric oxide, modulates the refilling of calcium stores in astrocytes. *J. Neurosci.* 23, 10302–10310.

Lindauer, U., Leithner, C., Kaasch, H., Rohrer, B., Foddis, M., Fuchtemeier, M., Offenhauser, N., Steinbrink, J., Royl, G., Kohl-Bareis, M., and Dirnagl, U. (2010). Neurovascular coupling in rat brain operates independent of hemoglobin deoxygenation. *J. Cereb. Blood Flow Metab.* 30, 757–768.

Lindauer, U., Megow, D., Matsuda, H., and Dirnagl, U. (1999). Nitric oxide: a modulator, but not a mediator, of neurovascular coupling in rat somatosensory cortex. *Am. J. Physiol.* 277, H799–H811.

Lovick, T. A., Brown, L. A., and Key, B. J. (1999). Neurovascular relationships in hippocampal slices: physiological and anatomical studies of mechanisms underlying flow-metabolism coupling in intraparenchymal microvessels. *Neuroscience* 92, 47–60.

Lovick, T. A., Brown, L. A., and Key, B. J. (2005). Neuronal activity-related coupling in cortical arterioles: involvement of astrocyte-derived factors. *Exp. Physiol.* 90, 131–140.

Ma, X., Qiu, S., Luo, J., Ma, Y., Ngai, C. Y., Shen, B., Wong, C. O., Huang, Y., and Yao, X. (2010) Functional role of vanilloid transient receptor potential 4-canonical transient receptor potential 1 complex in flow-induced Ca^{2+} influx. *Arterioscler. Thromb. Vasc. Biol.* 30, 851–858.

Metea, M. R., and Newman, E. A. (2006). Glial cells dilate and constrict blood vessels: a mechanism of neurovascular coupling. *J. Neurosci.* 26, 2862–2870.

Moore, C. I., and Cao, R. (2008). The hemo-neural hypothesis: on the role of blood flow in information processing. *J. Neurophysiol.* 99, 2035–2047.

Mulligan, S. J., and MacVicar, B. A. (2004). Calcium transients in astrocyte endfeet cause cerebrovascular constrictions. *Nature* 431, 195–199.

Nelson, M. T., Cheng, H., Rubart, M., Santana, L. F., Bonev, A. D., Knot, H. J., and Lederer, W. J. (1995). Relaxation of arterial smooth muscle by calcium sparks. *Science* 270, 633–637.

Ngai, A. C., and Winn, H. R. (1995). Modulation of cerebral arteriolar diameter by intraluminal flow and pressure. *Circ. Res.* 77, 832–840.

Paton, J. F., Waki, H., Abdala, A. P., Dickinson, J., and Kasparov, S. (2007). Vascular-brain signaling in hypertension: role of angiotensin II and nitric oxide. *Curr. Hypertens. Rep.* 9, 242–247.

Peppiatt, C., and Attwell, D. (2004). Neurobiology: feeding the brain. *Nature* 431, 137–138.

Rancillac, A., Rossier, J., Guille, M., Tong, X. K., Geoffroy, H., Amatore, C., Arbault, S., Hamel, E., and Cauli, B. (2006). Glutamatergic control of microvascular tone by distinct GABA neurons in the cerebellum. *J. Neurosci.* 26, 6997–7006.

Reid, K. H., Edmonds, H. L. Jr., Schurr, A., Tseng, M. T., and West, C. A. (1988). Pitfalls in the use of brain slices. *Prog. Neurobiol.* 31, 1–18.

Rossier, J. (2009). Wiring and plumbing in the brain. *Front. Hum. Neurosci.* 3, 2.

Silver, I. A., and Erecinska, M. (1994). Extracellular glucose concentration in mammalian brain: continuous monitoring of changes during increased neuronal activity and upon limitation in oxygen supply in normo-, hypo-, and hyperglycemic animals. *J. Neurosci.* 14, 5068–5076.

Simard, M., Arcuino, G., Takano, T., Liu, Q. S., and Nedergaard, M. (2003). Signaling at the gliovascular interface. *J. Neurosci.* 23, 9254–9262.

Takano, T., Tian, G. F., Peng, W., Lou, N., Libionka, W., Han, X., and Nedergaard, M. (2006). Astrocyte-mediated control of cerebral blood flow. *Nat. Neurosci.* 9, 260–267.

Theis, M., Sohl, G., Eiberger, J., and Willecke, K. (2005). Emerging complexities in identity and function of

glial connexins. *Trends Neurosci.* 28, 188–195.

Tong, X. K., and Hamel, E. (2000). Basal forebrain nitric oxide synthase (NOS)-containing neurons project to microvessels and NOS neurons in the rat neocortex: cellular basis for cortical blood flow regulation. *Eur. J. Neurosci.* 12, 2769–2780.

Udosen, I. T., Jiang, H., Hercule, H. C., and Oyekan, A. O. (2003). Nitric oxide-epoxygenase interactions and arachidonate-induced dilation of rat renal microvessels. *Am. J. Physiol. Heart Circ. Physiol.* 285, H2054–H2063.

Vaucher, E., and Hamel, E. (1995). Cholinergic basal forebrain neurons project to cortical microvessels in the rat: electron microscopic study with anterogradely transported Phaseolus vulgaris leucoagglutinin and choline acetyltransferase immunocytochemistry. *J. Neurosci.* 15, 7427–7441.

Vaucher, E., Linville, D., and Hamel, E. (1997). Cholinergic basal forebrain projections to nitric oxide synthase-containing neurons in the rat cerebral cortex. *Neuroscience* 79, 827–836.

Wiencken, A. E., and Casagrande, V. A. (1999). Endothelial nitric oxide synthetase (eNOS) in astrocytes: another source of nitric oxide in neocortex. *Glia* 26, 280–290.

Wrzosek, A. (2009). Endothelium as target for large-conductance calcium-activated potassium channel openers. *Acta Biochim. Pol.* 56, 393–404.

Xu, H. L., Koenig, H. M., Ye, S., Feinstein, D. L., and Pelligrino, D. A. (2004). Influence of the glia limitans on pial arteriolar relaxation in the rat. *Am. J. Physiol. Heart Circ. Physiol.* 287, H331–H339.

Xu, H. L., Mao, L., Ye, S., Paisansathan, C., Vetri, F., and Pelligrino, D. A. (2008). Astrocytes are a key conduit for upstream signaling of vasodilation during cerebral cortical neuronal activation in vivo. *Am. J. Physiol. Heart Circ. Physiol.* 294, H622–H632.

Yang, G., Chen, G., Ebner, T. J., and Iadecola, C. (1999). Nitric oxide is the predominant mediator of cerebellar hyperemia during somatosensory activation in rats. *Am. J. Physiol.* 277, R1760–R1770.

Yang, G., Huard, J. M., Beitz, A. J., Ross, M. E., and Iadecola, C. (2000). Stellate neurons mediate functional hyperemia in the cerebellar molecular layer. *J. Neurosci.* 20, 6968–6973.

Zhang, D. X., Mendoza, S. A., Bubolz, A. H., Mizuno, A., Ge, Z. D., Li, R., Warltier, D. C., Suzuki, M., and Gutterman, D. D. (2009). Transient receptor potential vanilloid type 4-deficient mice exhibit impaired endothelium-dependent relaxation induced by acetylcholine in vitro and in vivo. *Hypertension* 53, 532–538.

Zonta, M., Sebelin, A., Gobbo, S., Fellin, T., Pozzan, T., and Carmignoto, G. (2003a). Glutamate-mediated cytosolic calcium oscillations regulate a pulsatile prostaglandin release from cultured rat astrocytes. *J. Physiol. (Lond.)* 553, 407–414.

Zonta, M., Angulo, M. C., Gobbo, S., Rosengarten, B., Hossmann, K. A., Pozzan, T., and Carmignoto, G. (2003b). Neuron-to-astrocyte signaling is central to the dynamic control of brain microcirculation. *Nat. Neurosci.* 6, 43–50.

Conflict of Interest Statement: The author declares that the research was conducted in the absence of any commercial or financial relationships that could be construed as a potential conflict of interest.

Received: 01 March 2010; paper pending published: 08 April 2010; accepted: 28 June 2010; published online: 16 August 2010.

Citation: Filosa JA (2010) Vascular tone and neurovascular coupling: considerations toward an improved in vitro model. Front. Neuroenerg. ***2****:16. doi: 10.3389/fnene.2010.00016*

frontiers in
NEUROENERGETICS

REVIEW ARTICLE
published: 19 August 2010
doi: 10.3389/fnene.2010.00018

Neurovascular and neurometabolic couplings in dynamic calibrated fMRI: transient oxidative neuroenergetics for block-design and event-related paradigms

Fahmeed Hyder[1,2,3,4]*, Basavaraju G. Sanganahalli[1,2,3], Peter Herman[1,2,3], Daniel Coman[1,2,3], Natasja J. G. Maandag[1,3†], Kevin L. Behar[1,2,5], Hal Blumenfeld[6,7,8] and Douglas L. Rothman[1,2,3,4]

[1] *Magnetic Resonance Research Center, School of Medicine, Yale University, New Haven, CT, USA*
[2] *Core Center for Quantitative Neuroscience with Magnetic Resonance, School of Medicine, Yale University, New Haven, CT, USA*
[3] *Department of Diagnostic Radiology, School of Medicine, Yale University, New Haven, CT, USA*
[4] *Department of Biomedical Engineering, School of Engineering and Applied Science, Yale University, New Haven, CT, USA*
[5] *Department of Psychiatry, School of Medicine, Yale University, New Haven, CT, USA*
[6] *Department of Neurology, School of Medicine, Yale University, New Haven, CT, USA*
[7] *Department of Neurosurgery, School of Medicine, Yale University, New Haven, CT, USA*
[8] *Department of Neurobiology, School of Medicine, Yale University, New Haven, CT, USA*

Edited by:
David Boas, Massachusetts General Hospital, USA; Massachusetts Institute of Technology, USA; Harvard Medical School, USA

Reviewed by:
Richard Buxton, University of California San Diego, USA
Alberto L. Vazquez, University of Pittsburgh, USA

****Correspondence:***
D. S. Fahmeed Hyder, N143 TAC (Magnetic Resonance Research Center), 300 Cedar Street, Yale University, New Haven, CT 06520, USA.
e-mail: fahmeed.hyder@yale.edu

†Current address:
Natasja J. G. Maandag, Sint Maartenskliniek, Hengstdal 3, 6522 JV Nijmegen, Netherlands

Functional magnetic resonance imaging (fMRI) with blood-oxygenation level dependent (BOLD) contrast is an important tool for mapping brain activity. Interest in quantitative fMRI has renewed awareness in importance of oxidative neuroenergetics, as reflected by cerebral metabolic rate of oxygen consumption (CMR_{O_2}), for supporting brain function. Relationships between BOLD signal and the underlying neurophysiological parameters have been elucidated to allow determination of dynamic changes in CMR_{O_2} by "calibrated fMRI," which require multi-modal measurements of BOLD signal along with cerebral blood flow (CBF) and volume (CBV). But how do CMR_{O_2} changes, steady-state or transient, derived from calibrated fMRI compare with neural activity recordings of local field potential (LFP) and/or multi-unit activity (MUA)? Here we discuss recent findings primarily from animal studies which allow high magnetic fields studies for superior BOLD sensitivity as well as multi-modal CBV and CBF measurements in conjunction with LFP and MUA recordings from activated sites. A key observation is that while relationships between neural activity and sensory stimulus features range from linear to non-linear, associations between hyperemic components (BOLD, CBF, CBV) and neural activity (LFP, MUA) are almost always linear. More importantly, the results demonstrate good agreement between the changes in CMR_{O_2} and independent measures of LFP or MUA. The tight neurovascular and neurometabolic couplings, observed from steady-state conditions to events separated by <200 ms, suggest rapid oxygen equilibration between blood and tissue pools and thus calibrated fMRI at high magnetic fields can provide high spatiotemporal mapping of CMR_{O_2} changes.

Keywords: glia, glucose, glutamate, mitochondria, neuron, oxygen transport

INTRODUCTION

In the adult mammalian brain glucose oxidation provides majority of the ATP needed to support normal function of neurons and astrocytes (Shulman et al., 2004). Since endogenous energy reserves are at μM to mM levels (Hyder, 2009), timely delivery of energy substrates (i.e., glucose and oxygen) from blood to support neural activity is essential (Paulson et al., 2010). Variations in neural activity trigger a cascade of responses that collectively adjust delivery of energy substrates to meet the local ATP demand (Riera et al., 2008). "Neurovascular coupling" relates local changes in neural activity and constriction/dilation of blood vessels to decrease/increase cerebral blood flow (CBF) and/or volume (CBV) to a region, whereas "neurometabolic coupling" relates focal alterations in neural activity to cerebral metabolic rate of oxygen consumption (CMR_{O_2}) to keep pace with cellular ATP demand.

Recently there has been renewed interest in CMR_{O_2} mapping as a close approximation for brain work (Hyder et al., 2002). Positron emission tomography (PET) measures CMR_{O_2} non-invasively, but requires use of multiple radioactive tracers (Ito et al., 2005). Magnetic resonance spectroscopy (MRS) utilizing detection of non-radioactive ^{17}O isotope can also measure CMR_{O_2} non-invasively (Zhu et al., 2009), whereas ^{13}C MRS used in conjunction with different ^{13}C-labeled substrates (e.g., glucose or acetate) can distinguish between energetics of neurons and astrocytes (Hyder et al., 2006). Both of these MRS techniques, however, have lower spatial resolution compared to magnetic resonance imaging (MRI) and PET, whereas all of these techniques have relatively poor temporal resolution. Measurements of tissue oxygen tension (pO_2) can be used to infer local dynamics of uncoupling between oxygen delivery (i.e., CBF) and its subsequent utilization (i.e., CMR_{O_2}) (Ances et al., 2001), but its invasiveness limits translation to humans.

Because functional MRI (fMRI) has good spatiotemporal resolution and allows non-invasive imaging of almost the entire brain, it has great translational possibilities (Matthews et al., 2006). The blood-oxygenation level dependent (BOLD) signal, however, reports indirectly on neural activity because it measures the hyperemic response (Ogawa et al., 1993). But it is feasible to calculate CMR_{O_2} from the BOLD signal (S) provided that it is calibrated by combining CBF and CBV measurements (Hoge and Pike, 2001; Hyder et al., 2001) according to the relationship

$$\Delta S/S = A\left(\frac{\Delta CBF/CBF - \Delta CMR_{O_2}/CMR_{O_2}}{1+\Delta CBF/CBF} - \Delta CBV/CBV\right). \quad (1)$$

The basis for ΔCMR_{O_2} mapping with "calibrated fMRI" is that it reflects the oxidative ATP demanded for neural work (Davis et al., 1998; Hoge et al., 1999). Recent non-human studies report that magnitudes of ΔCMR_{O_2} derived from calibrated fMRI are commensurate with changes in neural firing under steady-state conditions (Smith et al., 2002; Kida et al., 2006; Maandag et al., 2007). However *both* the neurovascular and neurometabolic couplings remain to be established for Eq. 1.

The first and second terms on the right-hand side of Eq. 1 reflect changes in oxygenation and volume, respectively, where for $\Delta S/S > 0$ the first term has to exceed the second term. Because arterial blood is almost fully oxygenated, functional hyperemia – and thus, by inference, BOLD signal – manifests oxygenation and volume changes primarily at the venous end (Hoge and Pike, 2001; Hyder et al., 2001). Although magnitudes of the two terms on the right-hand side of Eq. 1 are typically on the order of 0.1–0.2 for functional studies (Hoge and Pike, 2001; Hyder et al., 2001), the metabolic ($\Delta CMR_{O_2}/CMR_{O_2}$) and hemodynamic ($\Delta CBF/CBF$) factors which together contribute to the first term can be much larger.

For increased oxygenation $\Delta CBF/CBF$ has to be greater than $\Delta CMR_{O_2}/CMR_{O_2}$. Because increased blood oxygenation is proportional to decreased tissue oxygen extraction at steady-state according to Fick's principle, an embedded assumption in ΔCMR_{O_2} time courses derived from calibrated fMRI is that oxygen is equilibrated between blood and tissue pools (Hyder et al., 1998). To date, steady-state assumptions of Eq. 1 are extended into the dynamic regime without experimental evidence of rapid oxygen equilibration between blood and tissue pools. For dynamic ΔCMR_{O_2} modeling from calibrated fMRI, *both* neurometabolic and neurovascular couplings have to be examined to establish if the same linearity of terms in Eq. 1 vs. neural activity can be used for event-related paradigms all the way up to block-design paradigms.

The second term of Eq. 1, which reflects changes in venous blood volume ($\Delta CBV/CBV$), is typically much smaller than changes in the metabolic ($\Delta CMR_{O_2}/CMR_{O_2}$) and hemodynamic ($\Delta CBF/CBF$) terms (Hoge and Pike, 2001; Hyder et al., 2001). Despite the small magnitude of this term, independent measurement is important because its dynamic evolution is significantly different from measured time courses of CBF and BOLD signal (Kida et al., 2007; Shen et al., 2008). In non-human studies ΔCBV is usually measured independently (Hyder et al., 2001), whereas in human studies ΔCBV is usually estimated from an assumed relationship with ΔCBF (Hoge and Pike, 2001). To date, changes in hematocrit are either neglected and/or lumped into the second term (Hyder et al., 2001), an assumption which needs further testing (Herman et al., 2009b).

The parameter A in Eq. 1, as originally described by Ogawa et al. (1993) in describing the BOLD model (and similar to the parameter M in other calibrated fMRI reports; see Hoge and Pike, 2001 for details), is a magnetic field dependent constant. It has been reported to be 0.1–0.2 for gray matter at 1.5T and 0.3–0.4 at 7.0T, respectively, where human and animal calibrated fMRI studies are typically conducted (Hoge and Pike, 2001; Hyder et al., 2001). Because the parameter A (or M) may vary regionally, and also depends on the echo time used in gradient-echo or spin-echo fMRI experiments, independent measurements are required for different experimental conditions (Chiarelli et al., 2007; Leontiev et al., 2007; Ances et al., 2009b).

Early calibrated fMRI studies, both in humans (Davis et al., 1998; Kim et al., 1999; Hoge and Pike, 2001; Restom et al., 2008; Ances et al., 2009a) and animals (Kida et al., 1999, 2000; Hyder et al., 2001; Shen et al., 2008), focused on high resolution ΔCMR_{O_2} maps. Because neural activity measurements were not available, these reports excluded assessment of neurovascular and neurometabolic couplings which are embedded in the interpretation of calibrated fMRI results. A critical issue in estimating ΔCMR_{O_2} derived from calibrated fMRI to represent changes in neural activity, especially in a dynamic manner, is whether changes in oxygen extraction affect the observed neurovascular and neurometabolic couplings differently for transient and steady-state events. This issue is particularly important for calculating the temporal evolution of CMR_{O_2} with *dynamic* calibrated fMRI because it is unclear whether couplings of the different parameters in Eq. 1 vs. neural activity can be assumed to be the same for event-related and block-design paradigms. To address this unresolved issue in the interpretation of calibrated fMRI results, we conducted calibrated fMRI studies at high magnetic field (11.7T) for superior BOLD sensitivity and included extracellular measurements of local field potential (LFP) and multi-unit activity (MUA) from the activated sites. Our findings lend confidence in the measurement of CMR_{O_2} transients with *dynamic* calibrated fMRI at high magnetic fields (Herman et al., 2009a; Sanganahalli et al., 2009).

MULTI-MODAL METHODS FOR CALIBRATED fMRI AND NEURAL ACTIVITY

Today, MRI can be used to measure CBF, CBV, and the BOLD signal in the same session with relatively high spatiotemporal resolution (Kida and Hyder, 2006). Of these methods, BOLD is the easiest to implement and apply because it requires no exogenous MRI contrast agent. CBV requires an exogenous MRI contrast agent, whereas CBF needs additional radio frequency (RF) hardware to selectively label arterial blood water. The temporal resolution of BOLD and CBV can be increased with marginal sensitivity losses (Kida et al., 2007; Shen et al., 2008), but dynamic measurements of CBF experience significant loss in signal-to-noise ratio (SNR) with fast imaging (Silva and Kim, 1999; Kida et al., 2004). Each method is generally believed to have superior SNR at higher magnetic field strengths, whereas the intravascular component of BOLD signal is reduced at higher magnetic fields (Ugurbil et al., 2000).

Oxyhemoglobin is diamagnetic and deoxyhemoglobin is paramagnetic, allowing BOLD image-contrast to be generated by conventional spin-echo or gradient-echo images which are sensitive to magnetic properties of blood (Kennan et al., 1994; Weisskoff et al., 1994). Deoxyhemoglobin in blood behaves as an endogenous MRI contrast agent, creating local magnetic field gradients which extend into the surrounding tissue and dephase magnetization of tissue water protons. Local gradients outside blood vessels enhance dephasing of tissue water protons which is detected by decreased signals in both spin-echo or gradient-echo images due to attenuation of transverse relaxation rates of tissue water protons ($1/T_2$).

The CBV image-contrast by MRI is similar to BOLD in the sense that it is also based on magnetic susceptibility (Kennan et al., 1998; Mandeville et al., 1998). In non-human subjects changes in CBV are usually measured by utilizing plasma-borne intravascular paramagnetic MRI contrast agents, which are nanoparticles composed of oxides of iron or other metals, that affect the transverse relaxation rates of tissue water protons. If the MRI contrast agent is uniformly distributed in the vascular system and has a long half-life of elimination, then changes in spin-echo or gradient-echo images acquired before and after the MRI agent injection can be interpreted straightforwardly as CBV changes within the entire vascular network (CBV_t).

However, because the volume term in Eq. 1 is localized to the venous compartment (CBV_v) the use of ΔCBV_t in place of ΔCBV_v in Eq. 1 may over represent contributions of the volume term to some extent, thus causing a slight underestimation of ΔCMR_{O_2} from calibrated fMRI. Using slightly different MRI methods to separate arterial (CBV_a) and venous (CBV_v) compartments (Kim and Kim, 2005), recent studies in non-human subjects show that changes in CBV_a may dominate (Kim et al., 2007). However it is yet unclear how to incorporate changes of ΔCBV_a vs. ΔCBV_v into Eq. 1 for calibrated fMRI.

The CBF sensitivity by MRI is achieved by arterial spin labeling (ASL), where magnetic labeling by RF pulses of flowing spins in arterial blood water (e.g., by inversion or saturation) functions as an endogenous tracer (Detre et al., 1992; Williams et al., 1992). The labeled spins of blood water mix with unlabeled stationary spins of tissue water to attenuate the apparent longitudinal relaxation time of tissue water. Although ASL techniques suffer from poor temporal resolution because of the waiting period required for exchange of labeled and unlabeled spins, alternative labeling methods can be used to improve CBF temporal resolution, albeit with some sensitivity losses (Silva and Kim, 1999; Kida et al., 2004).

ΔCMR_{O_2} estimated from calibrated fMRI requires measurements of BOLD signal, CBF, and CBV in the same subject and preferably in the same session. BOLD and CBF methods do not differ when applied to human and non-human subjects. However CBV methods vary significantly between human (e.g., see Stefanovic and Pike, 2005) and non-human (e.g., see Lu et al., 2005) subjects because MRI contrast agents cannot be repeatedly injected into humans. When changes in BOLD signal, CBF, and CBV are measured in the same session in non-human subjects, CBV is measured last because injection of the MRI contrast agent affects the other imaging signals. Because of difficulties with the CBV measurement in human subjects, Grubb's relationship (Grubb et al., 1974) is usually used to estimate this component from measured CBF changes, where $CBV = CBF^{\phi}$. While a high Φ value (e.g., 0.4 as in Grubb's original observation with hypercapnia challenge in primates; Grubb et al., 1974) has been typically assumed in some calibrated fMRI studies (Davis et al., 1998; Hoge et al., 1999; Chiarelli et al., 2007; Leontiev et al., 2007; Ances et al., 2009b), measured Φ values during functional activation are typically much smaller (Kida et al., 2007; Jin and Kim, 2008; Shen et al., 2008).

To estimate ΔCMR_{O_2} from calibrated fMRI in relation to dynamic changes in neural activity, it is necessary to examine neurovascular and neurometabolic couplings for transient and steady-state events. If oxygen equilibrates rapidly between blood and tissue pools, then the same linearity of terms in Eq. 1 vs. neural activity can be used for event-related paradigms all the way up to block-design paradigms. Thus, for event-related and block-design paradigms, we measured high SNR hyperemic (BOLD, CBV, CBF) responses from the rat somatosensory cortex and related these imaging signals to neural activity (LFP, MUA) (**Figure 1**). The forepaw stimulation model in the α-chloralose anesthetized rat is extensively used because the time-dependent stimulus parameters (duration, frequency, etc.) can be easily and reproducibly manipulated (Van Camp et al., 2006; Sanganahalli et al., 2008) to compare activation responses in a dynamic manner (Herman et al., 2009a; Sanganahalli et al., 2009). To examine dynamic variations of neurometabolic and neurovascular couplings both the number of stimulus pulses (i.e., single event to steady-state) and the stimulus interval between pulses (i.e., low to high frequency) were varied. Because the ASL measurement of CBF dynamics lacks sensitivity compared with the BOLD and CBV measurements, we employed laser-Doppler flowmetry to measure red blood cell flux (Silva and Kim, 1999; Kida et al., 2004) and which can be easily combined with electrical measurements in rat brain (Trubel et al., 2006; Schridde et al., 2008).

In our laboratory we use a dual-sensor device consisting of adjacent but isolated electrical and optical probes to simultaneously measure neural and CBF signals, respectively (Herman

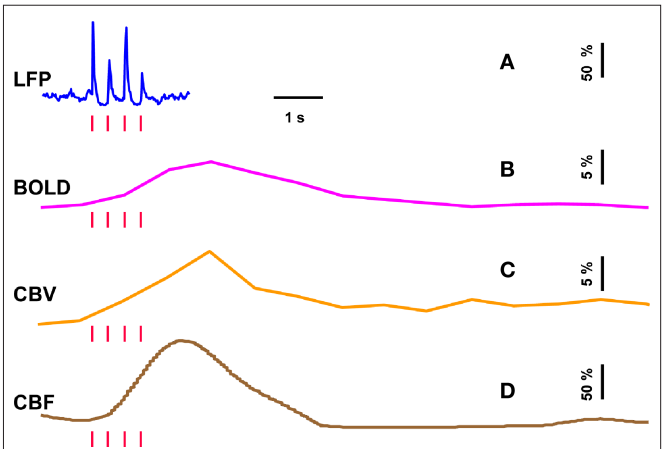

FIGURE 1 | Single trial multi-modal data. Representative neural [**(A)**; LFP] and imaging [**(B–D)**; BOLD, CBV, CBF] signals for short forepaw stimuli (vertical bars). While there was an evoked LFP for each stimulus pulse, alternate LFP's were not identical. A similar trend was observed for MUA (data not shown). Modified from results published in Herman et al. (2009a).

et al., 2009a; Sanganahalli et al., 2009). LFP and MUA, measured simultaneously with a high impedance microelectrode (>2 MΩ), are obtained by splitting the extracellular signal into low (<150 Hz) and high (0.4–10 kHz) frequency bands. Laser-Doppler signals are measured with respect to the pre-stimulus baseline, where the intensity of the optical signal (with 3 Hz forepaw stimulation) was calibrated to CBF data collected with the ASL technique (3 Hz, 2 mA, 0.3 ms, 96 pulses) as previously described (Kida et al., 2004). The high temporal resolution neural signals were integrated into 0.02 s running bins (equivalent to 50 Hz sampling of the laser-Doppler signal for CBF) allowing comparison with the lower temporal resolution BOLD and CBV data. All fMRI data were obtained on an 11.7T horizontal-bore spectrometer using a ^{1}H surface coil RF probe and high SNR gradient-echo contrast pulse sequence with repetition and echo time of 1000 and 15 ms, respectively (Herman et al., 2009a; Sanganahalli et al., 2009).

The basis of using calibrated fMRI to represent neuronal transients with dynamic ΔCMR_{O_2} is to test the temporal relationships between hyperemic components (BOLD, CBV, CBF) and neural activity (LFP, MUA), *both* for transient and steady-state events. If these relationships are linear within the stimuli ranges examined, then the respective transfer functions (of BOLD, CBV, CBF) would be considered time invariant (Boynton et al., 1996; Ances et al., 2000). Convolution theory states that the input signal, $i(t)$, when convolved with a transfer function, $h(t)$, produces an output signal, $r(t)$. In our experiments we measure both $i(t)$ and $r(t)$ with high spatiotemporal resolution (Herman et al., 2009a; Sanganahalli et al., 2009). LFP or MUA were used as the neural signal, whereas BOLD, CBV, and CBF represented the independent hyperemic responses. The transfer function, $h(t)$, can be achieved by a deconvolution between $r(t)$ and $i(t)$. If the frequency domain representations of $i(t)$, $r(t)$, and $h(t)$ are given by $I(\omega)$, $R(\omega)$, and $H(\omega)$, respectively, then it can be shown that:

$$\begin{aligned} i(t) \otimes h(t) &= r(t) \\ I(\omega) \times H(\omega) &= R(\omega) \end{aligned} \qquad (2)$$

where t and ω are time and frequency domains, respectively, and inverse Fourier transform of $H(\omega)$ gives $h(t)$. The gamma variate function is widely used for transfer function modeling. We used a slightly different form of the original equation (Madsen, 1992) so that the fitting parameters are independent from each other (Herman et al., 2009a; Sanganahalli et al., 2009). To find the best applicable transfer function we used a least-square mean Gauss–Newton fitting method which has three steps: (i) a transfer function is created with initial parameters; (ii) a transfer function is convolved with the input; (iii) a residual signal is created by differencing the predicted and measured signals. If the predicted signal is significantly different from the measured signal, then the parameters of the transfer function are changed and the process is continued from the first step. The fitting process is typically completed within a few hundred iterations and the last applied parameters are used to define the transfer function. Residuals are found acceptable if all of their values are within the range of uncertainty of the corresponding measured signal, as represented by the standard deviation (SD) about the mean.

RELATIONSHIP BETWEEN NEURAL AND HYPEREMIC RESPONSES

Trends of electrophysiological recordings of LFP and MUA from the contralateral somatosensory cortex averaged across six subjects are shown in **Figure 2A**. The patterns of the LFP and MUA data were generally similar and in both cases the evoked neural responses to multiple stimuli were normalized to the response of the first stimulus pulse. At the lowest stimulation frequency of 1.5 Hz, each evoked neural response for individual stimulus pulses was quite similar to the prior ones with minimal neural response attenuation for additional stimulus pulses.

In contrast, at the highest stimulation frequency of 6.0 Hz there were small or negligible evoked neural responses detected for multiple stimulus pulses (i.e., there was mainly one large evoked response with the first stimulus pulse). For the intermediate stimulus frequency of 3.0 Hz, alternate evoked neural responses to subsequent stimulus pulses were significantly attenuated compared to the neural response of the previous stimulus pulse. Stimulus frequency dependent variations in neural activity are consistent with studies using various anesthetics (Nemoto et al., 2004; Ureshi et al., 2004) including α-chloralose (Matsuura and Kanno, 2001; Sheth et al., 2004). In summary, at a stimulus frequency of 6.0 Hz increasing the stimulus number changed the evoked response very little (from the response with a single stimulus pulse), whereas at lower stimulus frequencies increasing the stimulus number augmented the evoked responses linearly (Herman et al., 2009a; Sanganahalli et al., 2009).

Trends of hyperemic responses (BOLD, CBV, CBF) from the contralateral somatosensory cortex averaged across eight subjects are shown in **Figures 2B–D**. Although the BOLD, CBV, and CBF data generally behaved similarly (e.g., augmentation with higher stimulus number or attenuation with higher stimulus frequency), the temporal patterns of each varied indicating their dissimilar physiologic origins. Both the intensity and width of each hyperemic response augmented with increasing stimulus number (Herman et al., 2009a; Sanganahalli et al., 2009). For stimulus frequencies of 1.5 and 3.0 Hz, the hyperemic response grew linearly with increasing number of stimulus pulses, whereas for the same number of stimulus pulses the hyperemic response decreased with higher stimulus frequency (Herman et al., 2009a; Sanganahalli et al., 2009). At stimulus frequencies of 1.5 and 3.0 Hz, enhancement of the response with increase in stimulus number is correlated with the increase in neural activity. For a stimulus frequency of 6.0 Hz, the responses were nearly identical for different numbers of stimulus pulses, similar to the neural data.

Each hyperemic response was measured with respect to the pre-stimulus baseline. The mean time-to-peak in BOLD responses was ~3.9 s, peaking at ~8%, ~5%, and ~4%, respectively, for stimulation frequencies of 1.5, 3.0, and 6.0 Hz. This is due to the stimulus frequency tuning responses under α-chloralose anesthesia (Sanganahalli et al., 2008). The mean time-to-peak in CBV responses was ~3.3 s, peaking at 11%, 10%, and 4%, respectively, for stimulation frequencies of 1.5, 3.0, and 6.0 Hz. Optical studies using the combination of oxy- and deoxyhemoglobin signals to estimate CBV changes demonstrate similar dependencies with variations in stimulus frequency and duration (Sheth et al., 2003; Nemoto et al., 2004). The mean time-to-peak in CBF responses

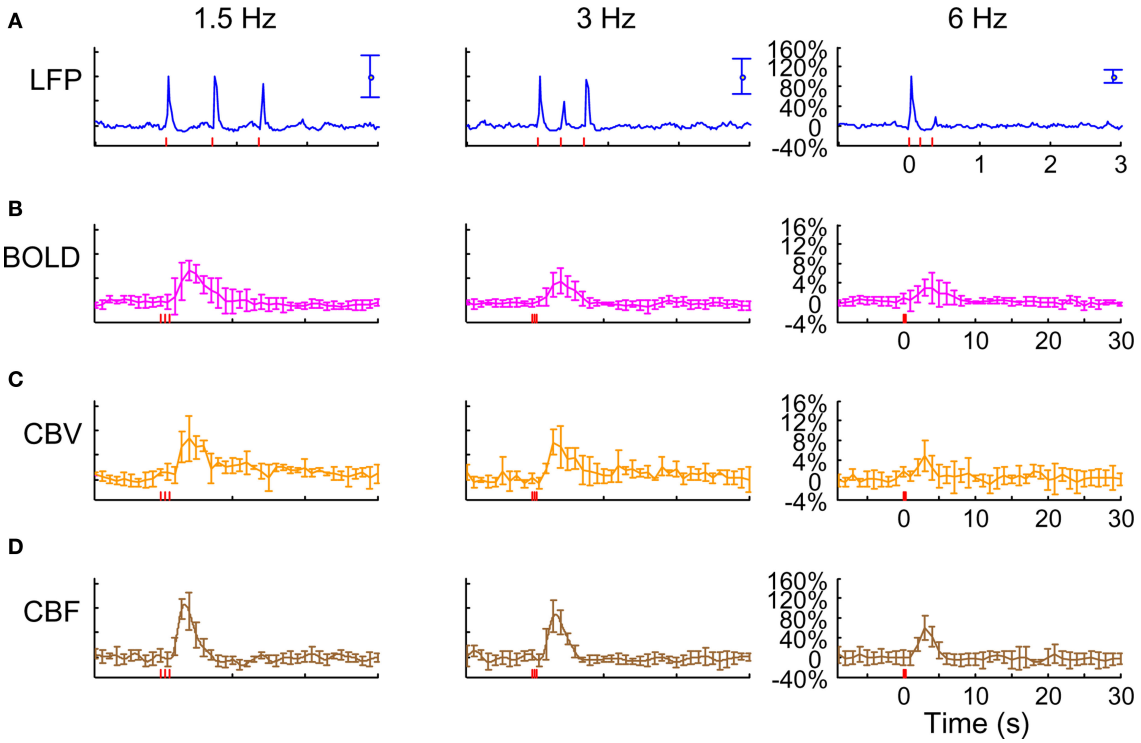

FIGURE 2 | Neural and hyperemic responses to varying transient stimuli. LFP **(A)** simultaneously recorded with MUA (data not shown) from the contralateral somatosensory cortex. Responses to subsequent stimuli were normalized to the response of the first stimulus pulse. At stimulation frequency of 1.5 Hz, each evoked response for individual stimulus pulses was quite similar to the prior ones. At stimulation frequency of 3.0 Hz, alternate responses to subsequent stimuli were significantly attenuated compared to the response of the first stimulus pulse. At stimulation frequency of 6.0 Hz, the responses to subsequent stimuli were significantly attenuated. As the number of stimulus pulses increased, the responses were augmented for stimulation frequencies of 1.5 and 3.0 Hz but not for 6.0 Hz (data not shown). BOLD **(B)**, CBV **(C)**, and CBF **(D)** recorded from the contralateral somatosensory cortex. The CBF data were obtained simultaneously with the LFP (and MUA) data. In correspondence with the neural data, as stimulation frequency increased the hyperemic responses became attenuated. However the degree of attenuation was different for each modality. The vertical bars represent the stimuli ± SD from the mean. All data shown for three stimulus pulses indicated by red vertical bars. Neural and hyperemic traces are in 4 and 40 s duration, respectively. Modified from results published in Sanganahalli et al. (2009).

was ~3 s, peaking at ~100%, ~101%, and ~53%, respectively, for stimulation frequencies of 1.5, 3.0, and 6.0 Hz. Our observation of the CBF trends with variations in stimulus duration and frequency is in agreement with prior observations (Ances et al., 2000; Martindale et al., 2003). The time course of cessation of the hyperemic response was different for each modality, with CBV having the slowest decay to pre-stimulation baseline values. Generally, the characteristics of CBF responses (intensity, width) were similar to the BOLD and CBV data, but with some caveats. For example, the non-linearity of the CBF response (vs. stimulus number with different stimulus frequency) was different than that observed with BOLD or CBV.

Since each signal is a function of varying amplitude over time, we measured response strength as the integral of the signal over the entire neural and hyperemic responses (**Figure 3**). We plotted normalized responses to quantify the relationships between hyperemic components (BOLD, CBV, CBF) and neural activity (LFP, MUA). Since neural and hyperemic signals at stimulus frequency of 6 Hz showed very little change with increasing stimulus number, this analysis was omitted here. **Figures 3A,B** show the relationships between LFP and MUA vs. hyperemic responses (at stimulation frequencies of 1.5 and 3.0 Hz). Because the comparisons in **Figure 3** are of signal integrals (i.e., intensity and width) between the hyperemic components (BOLD, CBV, CBF) and neural activity (LFP, MUA) – which occur over quite dissimilar time scales (e.g., see **Figure 1**) – the intercepts on the vertical and horizontal axes are slightly different. While these findings are generally consistent with other reports (Sheth et al., 2004; Ureshi et al., 2004; Van Camp et al., 2006), the current results are unique in that the relationship for all components of neurovascular and neurometabolic couplings were investigated for very small temporal changes of the stimuli.

CMR_{O_2} TRANSIENTS WITH DYNAMIC CALIBRATED fMRI

We used convolution analysis to find a transfer function that connects the neural signal to each hyperemic component, the effectiveness of which was characterized by the residual signal as given by the difference between the measured and predicted signals. If temporal fluctuations of the residual signal were smaller than the uncertainty of the measured signal over time (i.e., SD of the experimental measurement), the convolution process would produce a universal impulse response function. This is extremely

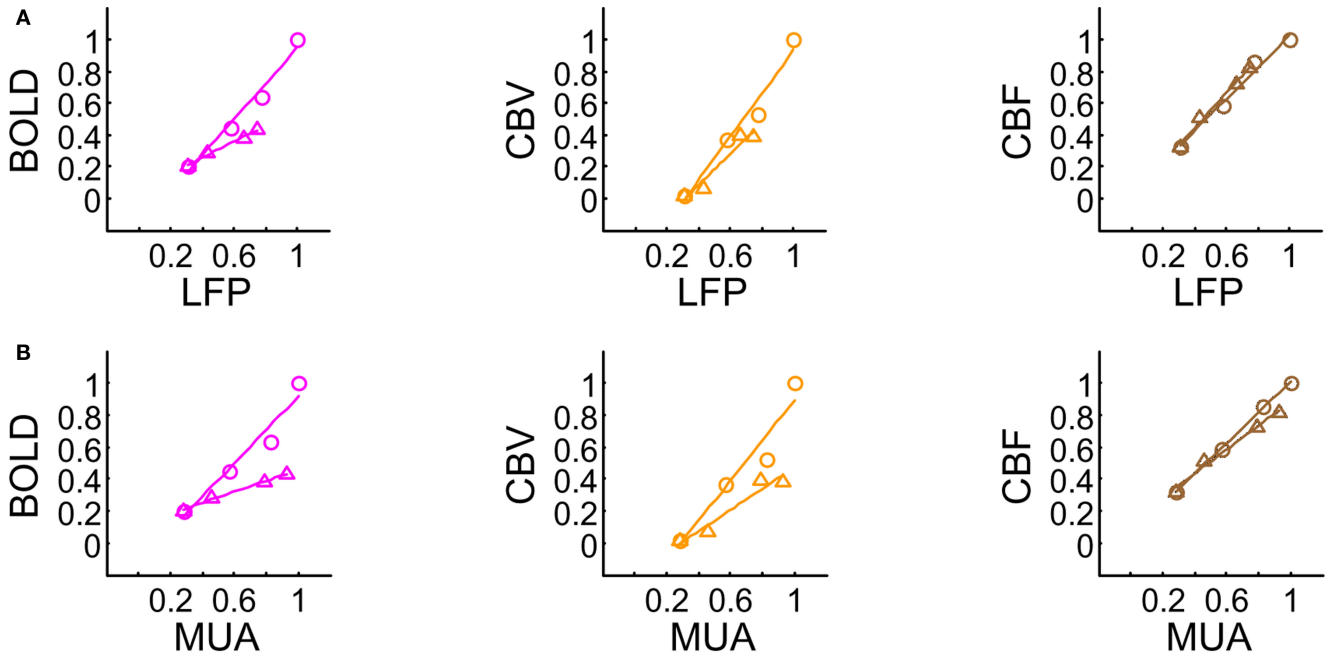

FIGURE 3 | Relationships between multi-modal imaging signals vs. LFP (A) and MUA **(B)**. For a stimulus frequency of 6.0 Hz the hyperemic responses changed minimally with increasing number of stimulus pulses (data not shown), whereas linear trends were observed for stimulus frequencies of 1.5 Hz (O) and 3.0 Hz (Δ). These linear trends resulted in universal transfer functions for each of the hyperemic responses. For each signal type (i.e., BOLD, CBV, CBF), because the same transfer function was successfully able to simulate the raw signal for various temporal events, the results and their analysis verified that the measured hyperemic responses were linear for the applied stimuli. All of the transfer functions were described with one (BOLD, CBF) or two (CBV) gamma variate functions. The scale of the CBF transfer function was a magnitude greater than the other transfer functions. CBF *h*(t) peaks the earliest (1.83 s), whereas BOLD *h*(t) peaks the latest (2.57 s). Both of these transfer functions have shorter tails to reach baselines (within ~4 and ~8 s, respectively, after peaking), whereas CBV *h*(t) has a very long tail (requiring ~1 min to reach baseline). CBV *h*(t) peaks about the same time as the CBF *h*(t) (2.16 s). Modified from results published in Sanganahalli et al. (2009) and Herman et al. (2009a).

important as it suggests that the respective transfer function should be time invariant within the temporal regime of the stimulus parameters.

We parameterized the transfer function with a gamma variate for each hyperemic component (Herman et al., 2009a; Sanganahalli et al., 2009). Briefly, the transfer functions generated by convolution analysis with LFP and MUA were quite similar in shape and the time-to-peak for BOLD, CBV, and CBF impulses were ~2.6, ~2.1, and ~1.8 s, respectively. The systematic difference between the time-to-peak of each measured response and each transfer function is consistent with prior observations (Ances et al., 2000; Buracas and Boynton, 2002; Silva et al., 2007), but prior studies did not include neural data or used *interpolated* neural data for deconvolution. We used the *strength* of the neural data to specifically target the delicate non-linear trends of neural data over time and their impact on the impulse response function.

Past studies applied convolution analysis with the BOLD response to report either linearity (Boynton et al., 1996) or non-linearity (Vazquez and Noll, 1998), but these studies used the stimulus itself as the input due to lack of neural activity recordings. Recent studies which include neural activity measurements reveal specific trends that agree with our observations (Matsuura and Kanno, 2001; Sheth et al., 2004), but only a few have applied convolution analysis with CBF and CBV (Ances et al., 2001; Martin et al., 2006; Silva et al., 2007). In general, the transfer functions generated for BOLD, CBV, and CBF are in good agreement with literature reports. Since a detailed discussion of each transfer function is not the goal here, the general observations are as follows: the CBF impulse peaks the earliest whereas the BOLD and CBF impulses are different in shape compared to the CBV impulse which has a very long tail.

While results from prior studies are insightful about convolution theory, they should be interpreted with caution because of the use of an *interpolation* procedure between consecutive evoked neural signals (Ances et al., 2000; Mathiesen et al., 2000), whereas we used the signal *strength*. Interpolating between separate neural events creates the impression of a more weighted neural signal. For long stimulus durations this process may have minimal impact on deconvolution because smoothing changes the signal envelope (or shape) very little. In contrast, however, for brief stimuli this approach could generate non-linearity from deconvolution because smoothing creates a signal that is quite different from the actual response. In our studies, treatment of *each* evoked neural response was a key feature utilized in both linearity assessments across different measurements and demonstration of the time invariance of the transfer functions.

Demonstration of time invariance of the transfer function was based on two different systematic comparisons of the predicted and measured signals (Herman et al., 2009a; Sanganahalli et al., 2009). In one comparison, the root-mean-square (RMS) of the residual signal was compared with the SD of the measurement.

The RMS of the residual signal was averaged across the entire data set and compared with the average of the measurement SD over the same duration. In each case, the comparison showed that the residual "noise" in modeling was smaller than the measurement uncertainty. In another comparison, only the hyperemic phase (i.e., the first 10 s of data after stimulation onset) was compared. This representation, similar to the RMS vs. SD comparison, showed that the predicted and measured signals were well correlated in each case, thereby suggesting time invariance of transfer functions.

The electrical and imaging data (**Figure 2**) revealed linear relationships between neural activity and each of the hyperemic components (**Figure 3**). A comprehensive convolution analysis revealed that the respective transfer functions (of BOLD, CBV, CBF) are time invariant for extremely brief events (separated by less than 200 ms) and all the way up to steady-state events (Herman et al., 2009a; Sanganahalli et al., 2009). These results enable calibrated fMRI to be utilized in a dynamic manner for calculating CMR_{O_2} transients (**Figure 4,** upper panel). To estimate ΔCMR_{O_2} from our multi-modal data we used a value of 0.5 for *A* in Eq. 1, which is expected based on prior observations of rat cerebral cortex at magnetic fields higher than 7.0T (Kida et al., 1999, 2000; Hyder et al., 2001; Englot et al., 2008; Schridde et al., 2008).

Relaxation measurements in different brain regions suggest that the T_2 nearly halves from 4.0T to 11.7T (de Graaf et al., 2006) – from about 65 ms to about 35 ms – thereby suggesting that the *A* value in Eq. 1 may vary significantly at lower and higher magnetic fields. Using the data acquired at 11.7T, when the *A* value is halved from 0.5 then the ΔCMR_{O_2} is reduced by nearly the same magnitude, whereas when the *A* value is doubled from 0.5 then the ΔCMR_{O_2} is only marginally increased. Employing a lower value for A (e.g., 0.10–0.15, gray matter at 1.5T) with the current 11.7T data leads to a reduction in ΔCMR_{O_2} to a very low values, which would be in clear disagreement with steady-state ^{13}C MRS data for the same rat model where significant changes in CMR_{O_2} have been reported with forepaw stimulation (Hyder et al., 1996, 2000). Furthermore, the energetic changes measured with ^{13}C MRS are in agreement with neural firing at steady-state (Smith et al., 2002; Kida et al., 2006; Maandag et al., 2007).

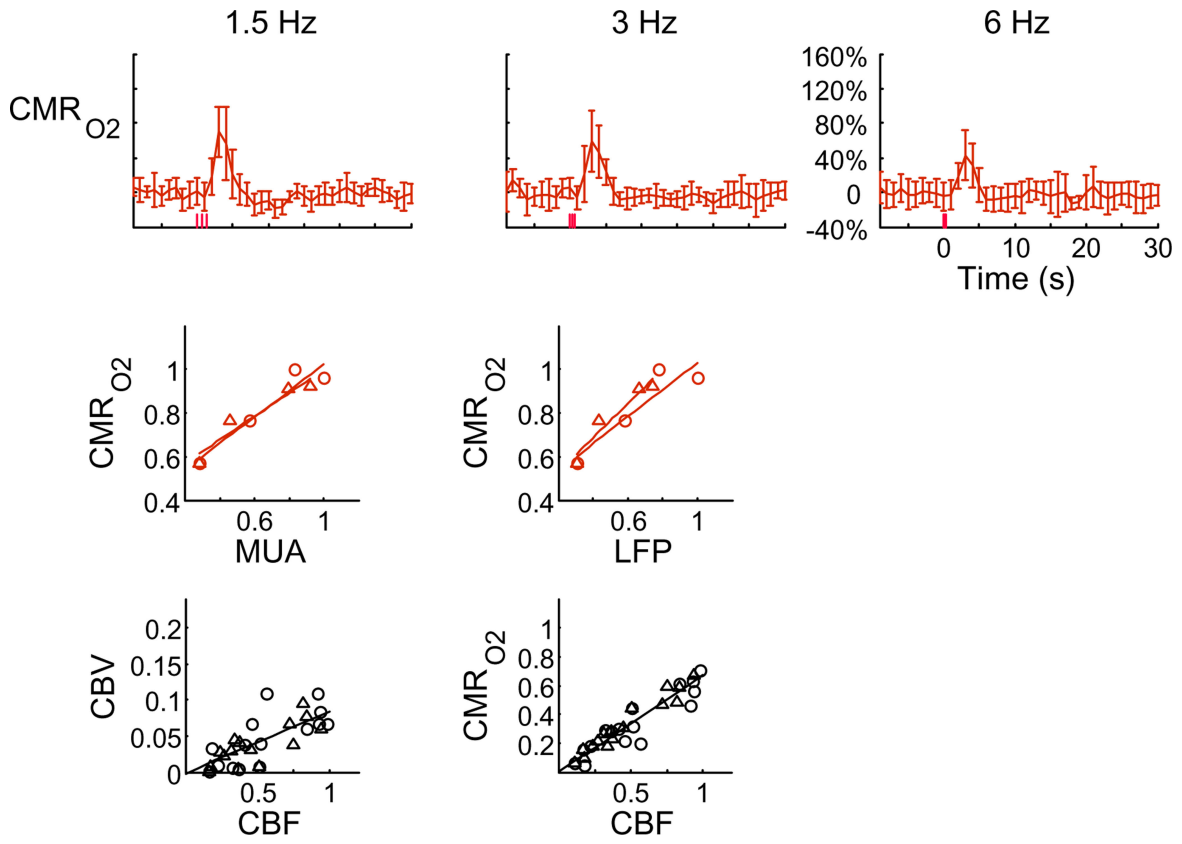

FIGURE 4 | Dynamic calibrated fMRI. CMR_{O_2} dynamics (top) and relationships with neural (middle) and hemodynamic (bottom) responses. Time courses of CMR_{O_2} responses (top) from the contralateral somatosensory cortex during variation of stimulation frequency (with three stimulus pulses indicated by red vertical bars). In correspondence with the neural data, as stimulation frequency increased the energetic responses were attenuated. For stimulus frequencies of 1.5 and 3.0 Hz the energetic responses increased linearly with higher number of stimulus pulses, whereas for stimulus frequency of 6.0 Hz the energetic responses were nearly identical for different number of stimulus pulses (data not shown). Each trace is 40 s in duration. CMR_{O_2} values were calculated using Eq. 1. Relationships between CMR_{O_2} vs. neural (middle) and CMR_{O_2} vs. hemodynamic (bottom) data. Modified from results published in Sanganahalli et al. (2009) and Herman et al. (2009a).

Human calibrated fMRI experiments use a brief hypercapnia challenge to estimate the *A* value in Eq. 1 (Davis et al., 1998; Hoge et al., 1999). If $\Delta CMR_{O_2} \approx 0$ is assumed with hypercapnia, then the *A* value can be estimated by measurements of BOLD signal and CBF with hypercapnia where CBV is assumed from CBF based on Grubb's relationship (Grubb et al., 1974). In non-human subjects, however, the *A* value can be measured in conjunction with independent assessment of the CMR_{O_2} with ^{13}C MRS (see Shulman et al., 2002 for details), bypassing the need for hypercapnia (Kida et al., 2000; Hyder et al., 2001). Measurements of BOLD signal, CBF, CBV, and CMR_{O_2} (by ^{13}C MRS) at different physiological conditions allow the *A* value to be validated. This latter approach, however, is limited by the spatial resolution of MRS at high magnetic fields, which for the rat currently enables calibrated fMRI to the more homogenous cerebral cortex.

Figure 4 shows the ΔCMR_{O_2} time courses obtained from group averaged data (upper panel), as well as the relationships of ΔCMR_{O_2} with neural (middle panel) and hemodynamic (lower panel) responses. For stimulus frequencies of 1.5 and 3.0 Hz, the CMR_{O_2} response (intensity, width) increased linearly with higher number of stimulus pulses, whereas for the same number of stimulus pulses the CMR_{O_2} response decreased with higher stimulus frequency (Herman et al., 2009a; Sanganahalli et al., 2009). For a stimulus frequency of 6.0 Hz, the CMR_{O_2} responses were nearly identical for different numbers of stimulus pulses. The mean time-to-peak in CMR_{O_2} responses was ~3.5 s, which is slightly delayed in comparison to CBF. CMR_{O_2} responses for four stimulus pulses were largest at a stimulus frequency of 1.5 Hz (63 ± 38%) and 3.0 Hz (68 ± 39%), as compared to 6.0 Hz (38 ± 27%). Because existing pO_2, PET, and other MRS methods do not provide high temporal resolution CMR_{O_2} data, the good agreement between CMR_{O_2} vs. neural activity (middle panel) provides the best validation available, although still indirect, of the use of dynamic calibrated fMRI for calculating ΔCMR_{O_2} (Hyder et al., 2002).

All hyperemic (BOLD, CBV, CBF) and neural (LFP, MUA) relationships used integrated (i.e., intensity and width) values (**Figure 3**). Since we do not know the nominal SNR of each of these measured signals, it is difficult to discuss linearity or non-linearity trends in the integral plots beyond the applied stimuli. Therefore linearity or non-linearity trends from these plots should be limited to the range of stimuli conditions examined. However the slightly different intercepts for hyperemic vs. neural (**Figure 3**) and CMR_{O_2} vs. neural plots (**Figure 4,** middle panel) correspond to larger experimental error in CMR_{O_2} prediction, which can be described by error propagation (Herman et al., 2009a; Sanganahalli et al., 2009). If we assume all hyperemic and neural signals have the same SNR for stimuli shorter than what we applied, it would suggest that CMR_{O_2} experimental accuracy is insufficient to predict a response for such short stimuli. However it is also possible that CMR_{O_2} vs. neural plot may indicate a slight non-linearity for shorter events than our current single event.

Overall, linear relationships were observed for CMR_{O_2} vs. neural activity, with either LFP or MUA. Recent studies in primates imply that LFP and MUA respectively correspond to the neural input (pre-synaptic) and output (post-synaptic) signaling (Logothetis et al., 2001), which roughly approximates pre-synaptic and post-synaptic signaling. As stated earlier, LFP and MUA generally behaved similarly as a function of stimulus number within the range of stimulus frequencies tested. Therefore, the linear relationships between CMR_{O_2} vs. neural activity depicted in **Figure 4** (middle panel) suggest that the coupled pre-synaptic and post-synaptic activities corresponding to the forepaw stimuli are roughly equally weighted for the rat somatosensory cortex, which is in good agreement with theoretical predictions (Attwell and Laughlin, 2001). Moreover, the commonality of relationships between hyperemic components (BOLD, CBV, CBF) and neural activity (LFP, MUA), with either LFP or MUA, depicted in **Figure 3** using the signal *strength* (not the signal *amplitude*) in each case suggests that LFP and MUA are equally well correlated with the neuroimaging signals. This finding in rat brain (Herman et al., 2009a; Sanganahalli et al., 2009) stands in contrast to prior findings in primate brain (Logothetis et al., 2001).

The impacts of CB V and CBF on the calculated values of CMR_{O_2} (Eq. 1) are important because they have different dynamic relationships to the BOLD signal (**Figure 2**). The Grubb relationship (Grubb et al., 1974), defined as $CBV = CBF^{\phi}$, shows that the value of the exponent,Φ as calculated for the entire hyperemic phase was approximately 0.15 (**Figure 4**, lower left panel). This value is in close agreement with recent animal studies (Jin and Kim, 2008; Shen et al., 2008) but is far smaller than what is typically assumed in human calibrated fMRI experiments (Davis et al., 1998; Hoge et al., 1999). However, we note that the value of Φ was allowed to vary over time for the dynamic CMR_{O_2} calculation (Kida et al., 2007). A tight CBF–CMR_{O_2} dynamic coupling, ranging between 3:2 and 5:2 (**Figure 4**, lower right panel), was also observed. The CBF–CMR_{O_2} coupling of about 2:1 is in agreement with predictions of oxygen transport models (Hyder et al., 1998; Herman et al., 2006; Huppert et al., 2007) and results from steady-state calibrated fMRI studies (Hoge et al., 1999; Uludag et al., 2004; Chiarelli et al., 2007). Although the characteristics of CBF dynamics appear to be quite similar to CMR_{O_2} transients, careful examination of these two impulse response functions shows that oxygen delivery is fitted by a gamma variate (CBF), whereas oxygen use is not (CMR_{O_2}). The CMR_{O_2} transfer functions were parameterized by a constrained non-linear half-order rational equation, where CMR_{O_2} transients generated with LFP or MUA as the input were indistinguishable (Herman et al., 2009a; Sanganahalli et al., 2009).

LIMITATIONS OF DYNAMIC CALIBRATED fMRI

To consolidate measurements from a single probe (e.g., electrical, optical) with high resolution fMRI data, it is important to realize that results pertain mainly to these focal sites. Because sampling from larger spatial regions with microelectrodes is not practical, our electrical data were confined to the middle cortical layers, which were then related to fMRI voxels located in similar cortical regions. Preliminary electrophysiology work (data not shown) suggests that the current results may be extended to layers above, but not necessarily layers below. Moreover, these cortical results should not be extrapolated to sub-cortical regions without additional experimental evidence of the neurometabolic and neurovascular couplings. Our results provide *temporal* transfer functions, although studies are underway to obtain the *spatial* transfer functions which span the somatosensory cortex tangentially in a specific cortical layer.

An important issue for estimating ΔCMR_{O_2} transients from calibrated fMRI is whether changes in oxygen extraction affect the observed neurovascular and neurometabolic couplings differently

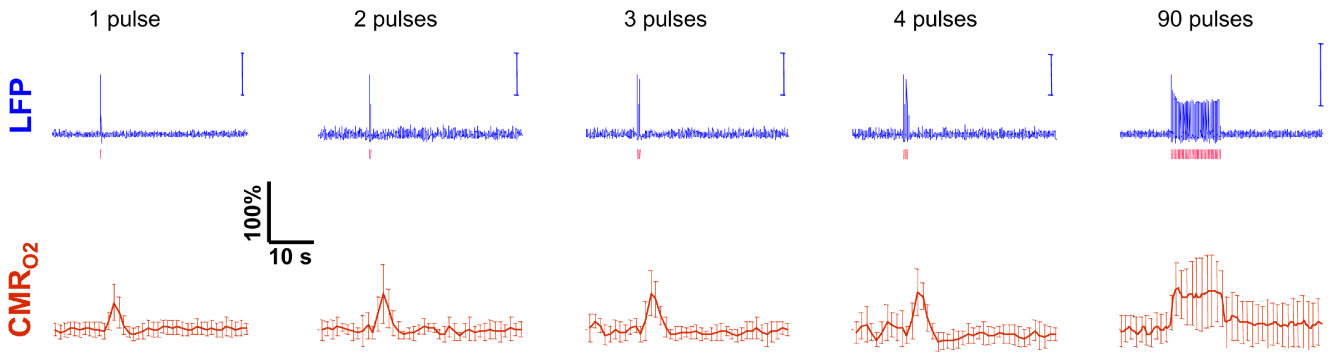

FIGURE 5 | Measured LFP and calculated CMR_{O_2} signals for short- and long-lasting stimuli. Convolution analysis of the universal transfer functions suggests linearity of the hyperemic responses with neural activity. Similar trends were observed with MUA (data not shown). Modified from results published in Sanganahalli et al. (2009) and Herman et al. (2009a).

for transient and steady-state events. The different components of Eq. 1 were linearly correlated with neural activity and furthermore the transfer functions of each of the components of Eq. 1 were time invariant. Together, these findings imply that oxygen equilibrates quickly between tissue and blood pools and thus all points of the hyperemic phase carry nearly the *same* calibration in Eq. 1 in relation to neural activity. First, we had to experimentally assess if linearity exists between each hyperemic component and neural activity. Here we used the *strength* of each signal type. Second, we tested the universality of the respective transfer functions to accurately predict the measured responses. With linearity and time invariance demonstrated from the multi-modal data, we identified a BOLD component for transient CMR_{O_2} changes, from single events to steady-state (**Figure 5**). The transfer functions (for BOLD, CBV, CBF) generated for short-lasting events accurately predicted the response to long-lasting events.

These findings for CMR_{O_2} transients raise the issue of the early dip observed with a variety of methods, including recordings of tissue pO_2, optical imaging of deoxyhemoglobin, and/or BOLD signal. The prior studies suggest the possibility of even an earlier CMR_{O_2} increase (within the first 500–700 ms after stimulation onset). The early tissue pO_2 dip has been observed in anesthetized rats and cats (Ances et al., 2001; Thompson et al., 2003). Although optical imaging of deoxyhemoglobin have reported the early dip (Malonek and Grinvald, 1996), some inconsistencies remain about its visibility (Jones et al., 2001; Lindauer et al., 2001). The early dip in the BOLD signal has been noted primarily in some human studies (Menon et al., 1995; Hu et al., 1997), but it remains unclear whether this observation is specific to humans because no rat (Silva et al., 2000) or monkey (Logothetis et al., 2001) studies have reported the early dip, whereas some cat studies have reported the dip (Kim et al., 2000) and others have not (Jezzard et al., 1997). Moreover the early BOLD signal dip may be sensitive to blood pCO_2 (Harel et al., 2002). Despite the fact that the magnitude of the dip is near detection threshold of most techniques, its observation remains a very important topic of research (Ances, 2004). Future fMRI sensitivity improvements (e.g., better RF coils) may allow measurement of the early BOLD signal dip and earlier CMR_{O_2} increases to be assessed.

Of the many factors that affect the BOLD signal in Eq. 1, the common approach in calibrated fMRI has been not to include hematocrit (Buxton et al., 1998). At steady-state, CMR_{O_2} calculation by calibrated fMRI assumes that volume (or discharge) hematocrit is unchanged, an assumption which has been partly confirmed by comparing kinetics of red blood cell and plasma volume changes (Herman et al., 2009b). However, dynamically different velocities of red blood cell and plasma compartments may become exaggerated in capillaries, which in turn could affect the flow (or tube) hematocrit (Pries et al., 1986). Thus, an important consideration for future calibrated fMRI studies is the possible involvement of transient hematocrit changes (Fahraeus, 1929) on the dynamic BOLD contrast, and which in turn may account for small deviations in the residual signals that have been observed.

CONCLUSION

The results discussed above show that comparing signal *strength* of measured neural (LFP, MUA) and hyperemic (BOLD, CBV, CBF) components, over a wide range of stimuli time epochs, shows strong neurometabolic and neurovascular couplings that subsequently lead to dynamic calibrated fMRI to be performed. In the rat brain, CMR_{O_2} increases within 1 s of stimulus onset and even for single event the energy demand peaks to nearly the same value as that obtained for steady-state stimuli. The early increase in CMR_{O_2} suggests that the energy expended by neural activity is primarily generated through oxidative metabolism. Thus, we find no significant mismatch between oxidative and non-oxidative energy consumption at early times during dynamic changes in neural activity. Although CMR_{O_2} transients appear slower than the actual neural responses, their coupling for events separated by less than 200 ms highlights the sensitivity of high magnetic field dynamic calibrated fMRI for high resolution mapping of oxidative energetics.

ACKNOWLEDGMENTS

The authors thank scientists and engineers at MRRC (mrrc.yale.edu), and QNMR (qnmr.yale.edu). This work was supported by grants from National Institutes of Health (R01 MH-067528, R01 CA-140102, R01 EB-011968, R01 NS-049307, R01 NS-055829, R01 NS-051854, R01 AG-034953, P30 NS-52519, P01 NS-062686) and Juvenile Diabetes Research Foundation (Pilot Award 42004807).

REFERENCES

Ances, B. M. (2004). Coupling of changes in cerebral blood flow with neural activity: what must initially dip must come back up. *J. Cereb. Blood Flow Metab.* 24, 1–6.

Ances, B. M., Buerk, D. G., Greenberg, J. H., and Detre, J. A. (2001). Temporal dynamics of the partial pressure of brain tissue oxygen during functional forepaw stimulation in rats. *Neurosci. Lett.* 306, 106–110.

Ances, B. M., Liang, C. L., Leontiev, O., Perthen, J. E., Fleisher, A. S., Lansing, A. E., and Buxton, R. B. (2009a). Effects of aging on cerebral blood flow, oxygen metabolism, and blood oxygenation level dependent responses to visual stimulation. *Hum. Brain Mapp.* 30, 1120–1132.

Ances, B. M., Sisti, D., Vaida, F., Liang, C. L., Leontiev, O., Perthen, J. E., Buxton, R. B., Benson, D., Smith, D. M., Little, S. J., Richman, D. D., Moore, D. J., and Ellis, R. J. (2009b). Resting cerebral blood flow: a potential biomarker of the effects of HIV in the brain. *Neurology* 73, 702–708.

Ances, B. M., Zarahn, E., Greenberg, J. H., and Detre, J. A. (2000). Coupling of neural activation to blood flow in the somatosensory cortex of rats is time-intensity separable, but not linear. *J. Cereb. Blood Flow Metab.* 20, 921–930.

Attwell, D., and Laughlin, S. B. (2001). An energy budget for signaling in the grey matter of the brain. *J. Cereb. Blood Flow Metab.* 21, 1133–1145.

Boynton, G. M., Engel, S. A., Glover, G. H., and Heeger, D. J. (1996). Linear systems analysis of functional magnetic resonance imaging in human V1. *J. Neurosci.* 16, 4207–4221.

Buracas, G. T., and Boynton, G. M. (2002). Efficient design of event-related fMRI experiments using M-sequences. *Neuroimage* 16, 801–813.

Buxton, R. B., Wong, E. C., and Frank, L. R. (1998). Dynamics of blood flow and oxygenation changes during brain activation: the balloon model. *Magn. Reson. Med.* 39, 855–864.

Chiarelli, P. A., Bulte, D. P., Gallichan, D., Piechnik, S. K., Wise, R., and Jezzard, P. (2007). Flow-metabolism coupling in human visual, motor, and supplementary motor areas assessed by magnetic resonance imaging. *Magn. Reson. Med.* 57, 538–547.

Davis, T. L., Kwong, K. K., Weisskoff, R. M., and Rosen, B. R. (1998). Calibrated functional MRI: mapping the dynamics of oxidative metabolism. *Proc. Natl. Acad. Sci. U.S.A.* 95, 1834–1839.

de Graaf, R. A., Brown, P. B., McIntyre, S., Nixon, T. W., Behar, K. L., and Rothman, D. L. (2006). High magnetic field water and metabolite proton T1 and T2 relaxation in rat brain in vivo. *Magn. Reson. Med.* 56, 386–394.

Detre, J. A., Leigh, J. S., Williams, D. S., and Koretsky, A. P. (1992). Perfusion imaging. *Magn. Reson. Med.* 23, 37–45.

Englot, D. J., Mishra, A. M., Mansuripur, P. K., Herman, P., Hyder, F., and Blumenfeld, H. (2008). Remote effects of focal hippocampal seizures on the rat neocortex. *J. Neurosci.* 28, 9066–9081.

Fahraeus, R. (1929). The suspension stability of the blood. *Physiol. Rev.* 9, 241–274.

Grubb, R. L. Jr., Raichle, M. E., Eichling, J. O., and Ter-Pogossian, M. M. (1974). The effects of changes in PaCO2 on cerebral blood volume, blood flow, and vascular mean transit time. *Stroke* 5, 630–639.

Harel, N., Lee, S. P., Nagaoka, T., Kim, D. S., and Kim, S. G. (2002). Origin of negative blood oxygenation level-dependent fMRI signals. *J. Cereb. Blood Flow Metab.* 22, 908–917.

Herman, P., Sanganahalli, B. G., Blumenfeld, H., and Hyder, F. (2009a). Cerebral oxygen demand for short-lived and steady-state events. *J. Neurochem.* 109(Suppl. 1), 73–79.

Herman, P., Sanganahalli, B. G., and Hyder, F. (2009b). Multimodal measurements of blood plasma and red blood cell volumes during functional brain activation. *J. Cereb. Blood Flow Metab.* 29, 19–24.

Herman, P., Trubel, H. K., and Hyder, F. (2006). A multiparametric assessment of oxygen efflux from the brain. *J. Cereb. Blood Flow Metab.* 26, 79–91.

Hoge, R. D., Atkinson, J., Gill, B., Crelier, G. R., Marrett, S., and Pike, G. B. (1999). Linear coupling between cerebral blood flow and oxygen consumption in activated human cortex. *Proc. Natl. Acad. Sci. U.S.A.* 96, 9403–9408.

Hoge, R. D., and Pike, G. B. (2001). Oxidative metabolism and the detection of neuronal activation via imaging. *J. Chem. Neuroanat.* 22, 43–52.

Hu, X., Le, T. H., and Ugurbil, K. (1997). Evaluation of the early response in fMRI in individual subjects using short stimulus duration. *Magn. Reson. Med.* 37, 877–884.

Huppert, T. J., Allen, M. S., Benav, H., Jones, P. B., and Boas, D. A. (2007). A multicompartment vascular model for inferring baseline and functional changes in cerebral oxygen metabolism and arterial dilation. *J. Cereb. Blood Flow Metab.* 27, 1262–1279.

Hyder, F. (2009). Dynamic imaging of brain function. *Methods Mol. Biol.* 489, 3–22.

Hyder, F., Chase, J. R., Behar, K. L., Mason, G. F., Siddeek, M., Rothman, D. L., and Shulman, R. G. (1996). Increased tricarboxylic acid cycle flux in rat brain during forepaw stimulation detected with 1H[13C]NMR. *Proc. Natl. Acad. Sci. U.S.A.* 93, 7612–7617.

Hyder, F., Kennan, R. P., Kida, I., Mason, G. F., Behar, K. L., and Rothman, D. (2000). Dependence of oxygen delivery on blood flow in rat brain: a 7 tesla nuclear magnetic resonance study. *J. Cereb. Blood Flow Metab.* 20, 485–498.

Hyder, F., Kida, I., Behar, K. L., Kennan, R. P., Maciejewski, P. K., and Rothman, D. L. (2001). Quantitative functional imaging of the brain: towards mapping neuronal activity by BOLD fMRI. *NMR. Biomed.* 14, 413–431.

Hyder, F., Patel, A. B., Gjedde, A., Rothman, D. L., Behar, K. L., and Shulman, R. G. (2006). Neuronal-glial glucose oxidation and glutamatergic-GABAergic function. *J. Cereb. Blood Flow Metab.* 26, 865–877.

Hyder, F., Rothman, D. L., and Shulman, R. G. (2002). Total neuroenergetics support localized brain activity: implications for the interpretation of fMRI. *Proc. Natl. Acad. Sci. U.S.A.* 99, 10771–10776.

Hyder, F., Shulman, R. G., and Rothman, D. L. (1998). A model for the regulation of cerebral oxygen delivery. *J. Appl. Physiol.* 85, 554–564.

Ito, H., Ibaraki, M., Kanno, I., Fukuda, H., and Miura, S. (2005). Changes in cerebral blood flow and cerebral oxygen metabolism during neural activation measured by positron emission tomography: comparison with blood oxygenation level-dependent contrast measured by functional magnetic resonance imaging. *J. Cereb. Blood Flow Metab.* 25, 371–377.

Jezzard, P., Rauschecker, J. P., and Malonek, D. (1997). An in vivo model for functional MRI in cat visual cortex. *Magn. Reson. Med.* 38, 699–705.

Jin, T., and Kim, S. G. (2008). Improved cortical-layer specificity of vascular space occupancy fMRI with slab inversion relative to spin-echo BOLD at 9.4 T. *Neuroimage* 40, 59–67.

Jones, M., Berwick, J., Johnston, D., and Mayhew, J. (2001). Concurrent optical imaging spectroscopy and laser-Doppler flowmetry: the relationship between blood flow, oxygenation, and volume in rodent barrel cortex. *Neuroimage* 13, 1002–1015.

Kennan, R. P., Scanley, B. E., Innis, R. B., and Gore, J. C. (1998). Physiological basis for BOLD MR signal changes due to neuronal stimulation: separation of blood volume and magnetic susceptibility effects. *Magn. Reson. Med.* 40, 840–846.

Kennan, R. P., Zhong, J., and Gore, J. C. (1994). Intravascular susceptibility contrast mechanisms in tissues. *Magn. Reson. Med.* 31, 9–21.

Kida, I., and Hyder, F. (2006). Physiology of functional magnetic resonance imaging: energetics and function. *Methods Mol. Med.* 124, 175–195.

Kida, I., Hyder, F., Kennan, R. P., and Behar, K. L. (1999). Toward absolute quantitation of bold functional MRI. *Adv. Exp. Med. Biol.* 471, 681–689.

Kida, I., Kennan, R. P., Rothman, D. L., Behar, K. L., and Hyder, F. (2000). High-resolution CMR(O2) mapping in rat cortex: a multiparametric approach to calibration of BOLD image contrast at 7 Tesla. *J. Cereb. Blood Flow Metab.* 20, 847–860.

Kida, I., Maciejewski, P. K., and Hyder, F. (2004). Dynamic imaging of perfusion and oxygenation by functional magnetic resonance imaging. *J. Cereb. Blood Flow Metab.* 24, 1369–1381.

Kida, I., Rothman, D. L., and Hyder, F. (2007). Dynamics of changes in blood flow, volume, and oxygenation: implications for dynamic functional magnetic resonance imaging calibration. *J. Cereb. Blood Flow Metab.* 27, 690–696.

Kida, I., Smith, A. J., Blumenfeld, H., Behar, K. L., and Hyder, F. (2006). Lamotrigine suppresses neurophysiological responses to somatosensory stimulation in the rodent. *Neuroimage* 29, 216–224.

Kim, D. S., Duong, T. Q., and Kim, S. G. (2000). High-resolution mapping of iso-orientation columns by fMRI. *Nat. Neurosci.* 3, 164–169.

Kim, S. G., Rostrup, E., Larsson, H. B., Ogawa, S., and Paulson, O. B. (1999). Determination of relative CMRO2 from CBF and BOLD changes: significant increase of oxygen consumption rate during visual stimulation. *Magn. Reson. Med.* 41, 1152–1161.

Kim, T., Hendrich, K. S., Masamoto, K., and Kim, S. G. (2007). Arterial versus total blood volume changes during neural activity-induced cerebral blood flow change: implication for BOLD fMRI. *J. Cereb. Blood Flow Metab.* 27, 1235–1247.

Kim, T., and Kim, S. G. (2005). Quantification of cerebral arterial blood volume and cerebral blood flow using MRI with modulation of tissue and vessel (MOTIVE) signals. *Magn. Reson. Med.* 54, 333–342.

Leontiev, O., Dubowitz, D. J., and Buxton, R. B. (2007). CBF/CMRO2 coupling measured with calibrated BOLD fMRI: sources of bias. *Neuroimage* 36, 1110–1122.

Lindauer, U., Royl, G., Leithner, C., Kuhl, M., Gold, L., Gethmann, J., Kohl-Bareis, M., Villringer, A., and Dirnagl, U. (2001). No evidence for early decrease in blood oxygenation in rat whisker cortex in response to

functional activation. *Neuroimage* 13, 988–1001.

Logothetis, N. K., Pauls, J., Augath, M., Trinath, T., and Oeltermann, A. (2001). Neurophysiological investigation of the basis of the fMRI signal. *Nature* 412, 150–157.

Lu, H., Soltysik, D. A., Ward, B. D., and Hyde, J. S. (2005). Temporal evolution of the CBV-fMRI signal to rat whisker stimulation of variable duration and intensity: a linearity analysis. *Neuroimage* 26, 432–440.

Maandag, N. J., Coman, D., Sanganahalli, B. G., Herman, P., Smith, A. J., Blumenfeld, H., Shulman, R. G., and Hyder, F. (2007). Energetics of neuronal signaling and fMRI activity. *Proc. Natl. Acad. Sci. U.S.A.* 104, 20546–20551.

Madsen, M. (1992). A simplified formulation of the gamma variate function. *Phys. Med. Biol.* 37, 1597–1600.

Malonek, D., and Grinvald, A. (1996). Interactions between electrical activity and cortical microcirculation revealed by imaging spectroscopy: implications for functional brain mapping. *Science* 272, 551–554.

Mandeville, J. B., Marota, J. J., Kosofsky, B. E., Keltner, J. R., Weissleder, R., Rosen, B. R., and Weisskoff, R. M. (1998). Dynamic functional imaging of relative cerebral blood volume during rat forepaw stimulation. *Magn. Reson. Med.* 39, 615–624.

Martin, C., Martindale, J., Berwick, J., and Mayhew, J. (2006). Investigating neural-hemodynamic coupling and the hemodynamic response function in the awake rat. *Neuroimage* 32, 33–48.

Martindale, J., Mayhew, J., Berwick, J., Jones, M., Martin, C., Johnston, D., Redgrave, P., and Zheng, Y. (2003). The hemodynamic impulse response to a single neural event. *J. Cereb. Blood Flow Metab.* 23, 546–555.

Mathiesen, C., Caesar, K., and Lauritzen, M. (2000). Temporal coupling between neuronal activity and blood flow in rat cerebellar cortex as indicated by field potential analysis. *J. Physiol. (Lond.)* 523(Pt 1), 235–246.

Matsuura, T., and Kanno, I. (2001). Quantitative and temporal relationship between local cerebral blood flow and neuronal activation induced by somatosensory stimulation in rats. *Neurosci. Res.* 40, 281–290.

Matthews, P. M., Honey, G. D., and Bullmore, E. T. (2006). Applications of fMRI in translational medicine and clinical practice. *Nat. Rev. Neurosci.* 7, 732–744.

Menon, R. S., Ogawa, S., Hu, X., Strupp, J. P., Anderson, P., and Ugurbil, K. (1995). BOLD based functional MRI at 4 Tesla includes a capillary bed contribution: echo-planar imaging correlates with previous optical imaging using intrinsic signals. *Magn. Reson. Med.* 33, 453–459.

Nemoto, M., Sheth, S., Guiou, M., Pouratian, N., Chen, J. W., and Toga, A. W. (2004). Functional signal- and paradigm-dependent linear relationships between synaptic activity and hemodynamic responses in rat somatosensory cortex. *J. Neurosci.* 24, 3850–3861.

Ogawa, S., Menon, R. S., Tank, D. W., Kim, S. G., Merkle, H., Ellermann, J. M., and Ugurbil, K. (1993). Functional brain mapping by blood oxygenation level-dependent contrast magnetic resonance imaging. A comparison of signal characteristics with a biophysical model. *Biophys. J.* 64, 803–812.

Paulson, O. B., Hasselbalch, S. G., Rostrup, E., Knudsen, G. M., and Pelligrino, D. (2010). Cerebral blood flow response to functional activation. *J. Cereb. Blood Flow Metab.* 30, 2–14.

Pries, A. R., Ley, K., and Gaehtgens, P. (1986). Generalization of the Fahraeus principle for microvessel networks. *Am. J. Physiol.* 251, H1324–H1332.

Restom, K., Perthen, J. E., and Liu, T. T. (2008). Calibrated fMRI in the medial temporal lobe during a memory-encoding task. *Neuroimage* 40, 1495–1502.

Riera, J. J., Schousboe, A., Waagepetersen, H. S., Howarth, C., and Hyder, F. (2008). The microarchitecture of the cerebral cortex: functional neuroimaging models and metabolism. *Neuroimage* 40, 1436–1459.

Sanganahalli, B. G., Herman, P., Blumenfeld, H., and Hyder, F. (2009). Oxidative neuroenergetics in event-related paradigms. *J. Neurosci.* 29, 1707–1718.

Sanganahalli, B. G., Herman, P., and Hyder, F. (2008). Frequency-dependent tactile responses in rat brain measured by functional MRI. *NMR. Biomed.* 21, 410–416.

Schridde, U., Khubchandani, M., Motelow, J. E., Sanganahalli, B. G., Hyder, F., and Blumenfeld, H. (2008). Negative BOLD with large increases in neuronal activity. *Cereb. Cortex* 18, 1814–1827.

Shen, Q., Ren, H., and Duong, T. Q. (2008). CBF, BOLD, CBV, and CMRO2 fMRI signal temporal dynamics at 500-msec resolution. *J. Magn. Reson. Imaging* 27, 599–606.

Sheth, S., Nemoto, M., Guiou, M., Walker, M., Pouratian, N., and Toga, A. W. (2003). Evaluation of coupling between optical intrinsic signals and neuronal activity in rat somatosensory cortex. *Neuroimage* 19, 884–894.

Sheth, S. A., Nemoto, M., Guiou, M., Walker, M., Pouratian, N., and Toga, A. W. (2004). Linear and nonlinear relationships between neuronal activity, oxygen metabolism, and hemodynamic responses. *Neuron* 42, 347–355.

Shulman, R. G., Hyder, F., and Rothman, D. L. (2002). Biophysical basis of brain activity: implications for neuroimaging. *Q. Rev. Biophys.* 35, 287–325.

Shulman, R. G., Rothman, D. L., Behar, K. L., and Hyder, F. (2004). Energetic basis of brain activity: implications for neuroimaging. *Trends Neurosci.* 27, 489–495.

Silva, A. C., and Kim, S. G. (1999). Pseudo-continuous arterial spin labeling technique for measuring CBF dynamics with high temporal resolution. *Magn. Reson. Med.* 42, 425–429.

Silva, A. C., Koretsky, A. P., and Duyn, J. H. (2007). Functional MRI impulse response for BOLD and CBV contrast in rat somatosensory cortex. *Magn. Reson. Med.* 57, 1110–1118.

Silva, A. C., Lee, S. P., Iadecola, C., and Kim, S. G. (2000). Early temporal characteristics of cerebral blood flow and deoxyhemoglobin changes during somatosensory stimulation. *J. Cereb. Blood Flow Metab.* 20, 201–206.

Smith, A. J., Blumenfeld, H., Behar, K. L., Rothman, D. L., Shulman, R. G., and Hyder, F. (2002). Cerebral energetics and spiking frequency: the neurophysiological basis of fMRI. *Proc. Natl. Acad. Sci. U.S.A.* 99, 10765–10770.

Stefanovic, B., and Pike, G. B. (2005). Venous refocusing for volume estimation: VERVE functional magnetic resonance imaging. *Magn. Reson. Med.* 53, 339–347.

Thompson, J. K., Peterson, M. R., and Freeman, R. D. (2003). Single-neuron activity and tissue oxygenation in the cerebral cortex. *Science* 299, 1070–1072.

Trubel, H. K., Sacolick, L. I., and Hyder, F. (2006). Regional temperature changes in the brain during somatosensory stimulation. *J. Cereb. Blood Flow Metab.* 26, 68–78.

Ugurbil, K., Adriany, G., Andersen, P., Chen, W., Gruetter, R., Hu, X., Merkle, H., Kim, D. S., Kim, S. G., Strupp, J., Zhu, X. H., and Ogawa, S. (2000). Magnetic resonance studies of brain function and neurochemistry. *Annu. Rev. Biomed. Eng.* 2, 633–660.

Uludag, K., Dubowitz, D. J., Yoder, E. J., Restom, K., Liu, T. T., and Buxton, R. B. (2004). Coupling of cerebral blood flow and oxygen consumption during physiological activation and deactivation measured with fMRI. *Neuroimage* 23, 148–155.

Ureshi, M., Matsuura, T., and Kanno, I. (2004). Stimulus frequency dependence of the linear relationship between local cerebral blood flow and field potential evoked by activation of rat somatosensory cortex. *Neurosci. Res.* 48, 147–153.

Van Camp, N., Verhoye, M., and Van der Linden, A. (2006). Stimulation of the rat somatosensory cortex at different frequencies and pulse widths. *NMR. Biomed.* 19, 10–17.

Vazquez, A. L., and Noll, D. C. (1998). Nonlinear aspects of the BOLD response in functional MRI. *Neuroimage* 7, 108–118.

Weisskoff, R. M., Zuo, C. S., Boxerman, J. L., and Rosen, B. R. (1994). Microscopic susceptibility variation and transverse relaxation: theory and experiment. *Magn. Reson. Med.* 31, 601–610.

Williams, D. S., Detre, J. A., Leigh, J. S., and Koretsky, A. P. (1992). Magnetic resonance imaging of perfusion using spin inversion of arterial water. *Proc. Natl. Acad. Sci. U.S.A.* 89, 212–216.

Zhu, X. H., Du, F., Zhang, N., Zhang, Y., Lei, H., Zhang, X., Qiao, H., Ugurbil, K., and Chen, W. (2009). Advanced in vivo heteronuclear MRS approaches for studying brain bioenergetics driven by mitochondria. *Methods Mol. Biol.* 489, 317–357.

Conflict of Interest Statement: The authors declare that the research was conducted in the absence of any commercial or financial relationships that could be construed as a potential conflict of interest.

Received: 04 March 2010; paper pending published: 19 April 2010; accepted: 02 July 2010; published online: 19 August 2010.
Citation: Hyder F, Sanganahalli BG, Herman P, Coman D, Maandag NJG, Behar KL, Blumenfeld H and Rothman DL (2010) Neurovascular and neurometabolic couplings in dynamic calibrated fMRI: transient oxidative neuroenergetics for block-design and event-related paradigms. Front. Neuroenerg. ***2****:18. doi: 10.3389/fnene.2010.00018*

frontiers in
NEUROENERGETICS

REVIEW ARTICLE
published: 25 April 2011
doi: 10.3389/fnene.2011.00001

A guide to delineate the logic of neurovascular signaling in the brain

***David Kleinfeld*[1,2,3]*, *Pablo Blinder*[1], *Patrick J. Drew*[1], *Jonathan D. Driscoll*[1], *Arnaud Muller*[1], *Philbert S. Tsai*[1] *and Andy Y. Shih*[1]**

[1] *Department of Physics, University of California San Diego, La Jolla, CA, USA*
[2] *Section of Neurobiology, University of California San Diego, La Jolla, CA, USA*
[3] *Center for Neural Circuits and Behavior, University of California San Diego, La Jolla, CA, USA*

Edited by:
Anna Devor, University of California San Diego, USA

Reviewed by:
Christopher I. Moore, Massachusetts Institute of Technology, USA
Samuel S.-H Wang, Princeton University, USA

****Correspondence:***
David Kleinfeld, Department of Physics, University of California, 9500 Gilman Drive, La Jolla, CA 92093-0374, USA.
e-mail: dk@physics.ucsd.edu

The neurovascular system may be viewed as a distributed nervous system within the brain. It transforms local neuronal activity into a change in the tone of smooth muscle that lines the walls of arterioles and microvessels. We review the current state of neurovascular coupling, with an emphasis on signaling molecules that convey information from neurons to neighboring vessels. At the level of neocortex, this coupling is mediated by: (i) a likely direct interaction with inhibitory neurons, (ii) indirect interaction, via astrocytes, with excitatory neurons, and (iii) fiber tracts from subcortical layers. Substantial evidence shows that control involves competition between signals that promote vasoconstriction versus vasodilation. Consistent with this picture is evidence that, under certain circumstances, increased neuronal activity can lead to vasoconstriction rather than vasodilation. This confounds naïve interpretations of functional brain images. We discuss experimental approaches to detect signaling molecules *in vivo* with the goal of formulating an empirical basis for the observed logic of neurovascular control.

Keywords: astrocytes, blood flow, channelrhodopsin, interneurons, neurotransmitter, two-photon

Blood is a vital and limited resource in the brain. All aspects of neuronal and non-neuronal activity require a supply of oxygen and glucose – a need that constantly evolves with changes in brain activity (Fox and Raichle, 1986; Leybaert, 2005). How is the distribution of blood controlled relative to these changing needs? More basically, what are the signals that different classes of cells use to communicate changes in their metabolic load? How are these signals integrated to change the flow in the blood vessels that intercalate cortical neurons and glia (**Figure 1**)?

An understanding of neurovascular signaling bears directly on the limit to cortical function and, more generally, on resource management by the central nervous system. From a clinical perspective, understanding the relation of neuronal activity to changes in blood oxygen and flow is an essential step toward addressing the role of vascular dysfunction and disease in dementia (Paulson et al., 1990; Kövari et al., 2007). From the perspective of cognitive science, a quantitative understanding of neurovascular signaling is crucial for the interpretation of functional brain images (LeDoux et al., 1983) – especially those obtained with blood oxygenation level dependent functional magnetic resonance imaging (BOLD fMRI). Magnetic resonance imaging and other macroscopic diagnostic techniques have provided a "window" into the brain from which modulation of macroscopic blood by neuronal activity may be assessed (Belliveau et al., 1991; Ogawa et al., 1992). These techniques are likely to evolve into essential tools for judging cognitive capabilities in a clinical setting and may be critical for the early identification and hopefully containment of dementia.

We view neurovascular control in terms of the net action of a tractable number of signaling molecules that arrive via one global and two local pathways (**Figure 2**). All of these function in a push–pull manner, i.e., one set of signals induces vasodilation through relaxation of arteriole smooth muscle, while a second set induces vasoconstriction (Cauli et al., 2004). The first local pathway involves local inhibitory interneurons that act directly on smooth muscle. Different subclasses of interneurons co-release different transmitters that act to either dilate vessels, including nitric oxide (NO) and vasoactive intestinal peptide (VIP), or to constrict vessels, including the neuropeptides somatostatin (SOM) and neuropeptide Y (NPY). In some cases the same interneuron can cause both effects; e.g., some SOM-expressing cells further express nitric oxide synthetase (Kawaguchi, 2001). Additional evidence for a role of interneurons in the modulation of blood flow comes from an increase in flow concurrent with γ-band oscillations in inhibitory networks (Niessing et al., 2005). Increases in flow correlate with such global rhythms. It is thus natural to hypothesize that the competition between dilation and constriction depends on the relative activation of different inhibitory networks (Gibson et al., 1999); this hypothesis may be tested with cell-specific markers of neuronal activity.

The second local pathway for the control of blood flow originates with excitatory neurons and acts via astrocytes (Filosa et al., 2004; Iadecola and Nedergaard, 2007). Volume conduction of the excitatory transmitter glutamate can cause an increase in intracellular Ca^{2+} in astrocytes, which in turn initiates the conversion of arachidonic acid to the dilators prostaglandin E (PG_E) and epoxyeicosatrienoic acid (EET) or the constrictor 20-hydroxyeicosatetraenoic acid (20-HETE). Recent work shows that the competition between dilation and constriction depends on the partial pressure of oxygen (pO_2) (Gordon et al., 2008); dilation dominates at low pO_2.

Lastly, global pathways involve the vasodilator acetylcholine (ACh) and the constrictor serotonin (5HT), released from their respective subcortical nuclei, i.e., nucleus basalis magnocellularis

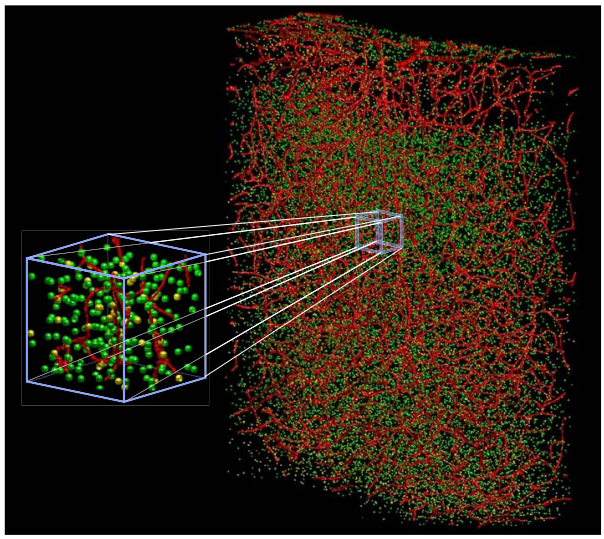

FIGURE 1 | Three dimensional vectorized reconstruction of all of the cell soma and blood vessels in a slab of mouse cerebral cortex. Features in the raw data are analyzed and transformed into a digital map that represents them as cylinders and spheres with vector coordinates and associated radii. The vascular network is in red, the neuronal nuclei are in green, and non-neuronal nuclei are in yellow. The total volume is a 600-μm × 900-μm × 250-μm. Derived from Tsai et al. (2003, 2009).

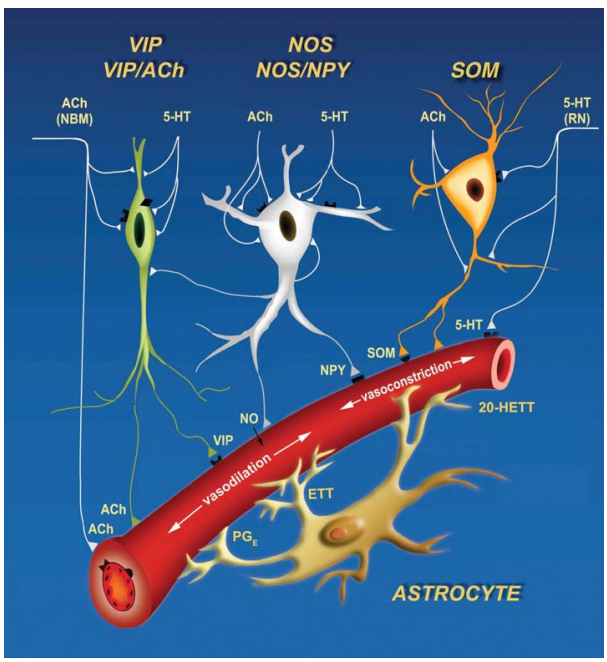

FIGURE 2 | Cartoon of three signaling pathways, two local and one global, that can both constrict and dilate the arteriole vasculature. Inhibitory interneurons can drive dilation via nitric oxide (NO), catalyzed by nitric oxide synthetase (NOS), and vasoactive intestinal peptide (VIP), and drive constriction via somatostatin (SOM) and neuropeptide Y (NPY). Astrocytes can dilate via protoglandin E (PG_E) and epoxyeicosatrienoic acid (EET) and constrict via 20-Hydroxyeicosatetraenoic acid (20-HETE). Lastly, extrinsic input of acetylcholine (ACh) will dilate while serotonin (5HT) will constrict. Derived from Cauli et al. (2004).

and the dorsal raphe nucleus (Hamel, 2004, 2006). An additional neural pathway for the modulation of cortical blood flow occurs via the rostral ventrolateral medulla (RVLM; Golanov and Reis, 1996), whose projections to cortex are relayed by the interlaminar thalamic nucleus. Neurons in the RVLM are sensitive to oxygen levels. Their activation causes bilateral increase in cortical blood flow via thalamic intermediates. This raises the possibility that changes in cortical blood flow and activity are slaved to fluctuations in breathing and blood oxygenation (Wise et al., 2004; Shmueli et al., 2007; Drew et al., 2008). Blood flow is further driven by cortical state (Jones et al., 2008); this mode of control may well lie in changes in the patterns of activation of excitatory cells and subpopulations of inhibitory cells (**Figure 2**) that may involve modulatory control via Ach and 5HT pathways, as well as noradrenergic inputs (NA) from locus coeruleus (Cohen et al., 1997).

POTENTIAL FOCUS OF AN EXPERIMENTAL PROGRAM

We consider competition among vasoactive pathway that predominantly effect parenchymal microvessels. We hypothesize that microvascular tone may be defined as a function of the local concentration of specific signaling molecules, such as EET, 20-HETE, NO, NPY, PG_E, SOM, and VIP. The driving term is neuronal activity, which may be a one-to-one function of the neuronal stimulus for primary sensory areas. Formally, we seek a relation of the form

$$\text{Smooth muscle tension} \equiv f\begin{pmatrix} \text{SOM}^+ \text{ inhibitory interneuron activation} \\ \text{VIP}^+ \text{ inhibitory interneuron activation} \\ \vdots \\ \text{Astrocyte activation} = f\,(\text{excitatory cell activation}) \\ \text{Extracortical and endothelial contributions} \\ [\text{O}_2]_{\text{tissue}} \end{pmatrix} \quad (1)$$

and

$$\text{Vascular output} \equiv f\begin{pmatrix} \text{Smooth muscle tension} \\ \vdots \\ \text{Vascular architecture} \end{pmatrix} \quad (2)$$

where the functionalities, denoted *f*, are yet to be determined. Nonetheless, this general formalism emphasizes the need to study muscle tension on a cell type-by-type or transmitter-by-transmitter basis. It further reinforces the need to map the geometry of the vasculature (**Figure 1**) and the location of neuronal control regions (**Figure 2**).

The greatest uncertainty in the hypothesis that the control of cortical blood flow depends on the balance of neurotransmitters that lead to vasoconstriction versus dilation is that much of our understanding of signaling comes from experiments with brain slice preparations. Not only is vascular pressurization absent, but responses take place on tens of seconds (Cauli et al., 2004; Gordon et al., 2008), while the vasculature responds to changes in neuronal activity on the 0.5-s time-scale *in vivo*. It remains an open issue if signaling is faster *in vivo*, although such long times are observed when astrocytic Ca^{2+} levels are directly excited *in vivo* (Wang et al., 2006; **Figure 3**).

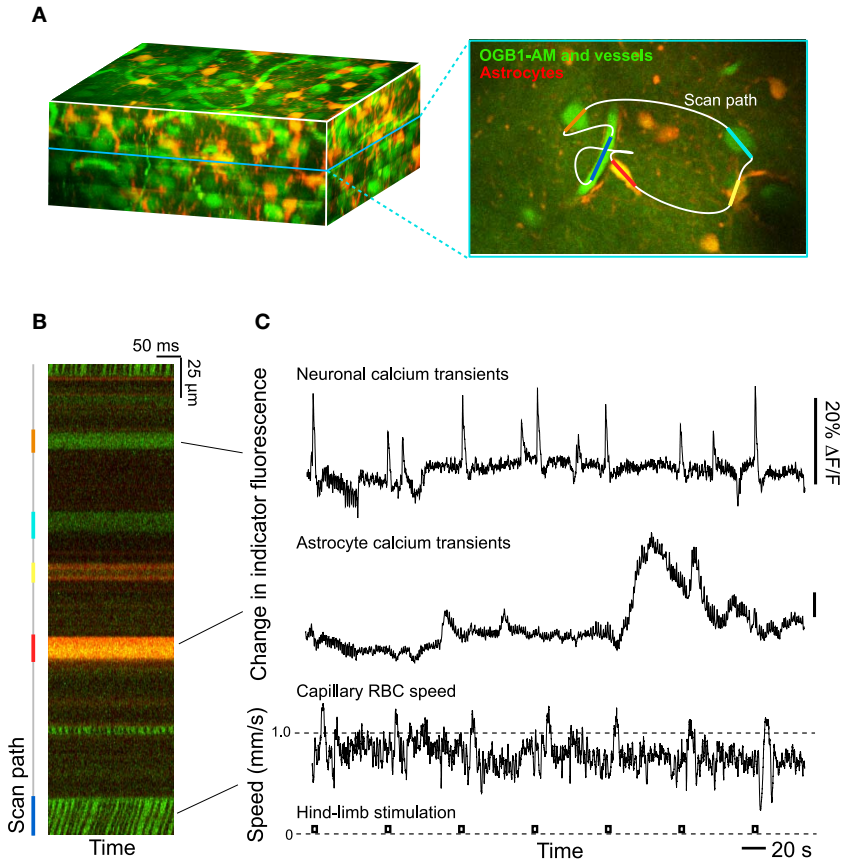

FIGURE 3 | Two-photon laser scanning microscopy with arbitrary scan pathways to record from functionally labeled cells and vessels. **(A)** Neurons and glia are labeled with the Ca^{2+} reporter Oregon Green BAPTA-1 AM and glia have sulforhodamine 101 as an additional label. Blood plasma is stained with fluorescein so that blood cell motion is measured. **(B)** Intensity along the scan path records Ca^{2+} signals and blood cell movement. **(C)** Traces of functional changes in intracellular Ca^{2+} and flood flow; note flow changes concurrent with stimulation. Algorithms from Helmchen and Kleinfeld (2008), Drew et al. (2010), Driscoll et al. (2011).

A first approach to define the inputs and output to a model of neurovascular coupling is to measure the activity of identified cell types concurrent with blood flow in a neighboring microvessel. The activity of neurons and glia in cortex may be established by measuring their internal calcium levels with optical contrast agents (Garaschuk et al., 2006; **Figure 3**) and *in vivo* two-photon laser scanning microscopy (TPLSM; Svoboda et al., 1997; **Figure 3**). Similarly, both the speed of blood cells and vascular tone may be concurrently established with two-photon microscopy (Helmchen and Kleinfeld, 2008; **Figure 3**). The clarity of these measurements depends on the ability to record from specific cell types and the specificity of co-release of different neuropeptides by interneurons. This implies the need to use transgenic animals that either express a functional indicator in specific cell types or, as a more general approach, to use mice that express Cre recombinase in specific cell types (Luo et al., 2008; Bernard et al., 2009; **Table 1**). Cre recombinase drives the labeling of these cells types by crossing these mouse lines with fluorescent reporter mice (Madisen et al., 2010), in which a member of the fluorescent protein (FP) family (Tsien, 1998; Shaner et al., 2004) and/or a genetically encoded functional indicator is coded between lox-sites (Wallace et al., 2008; **Table 2**); Cre recombinase activates sequences between these sites (Mallo, 2006). A complementary and common method is to infect cells that express Cre recombinase with a virus whose genetic material is modified to code a fluorescent indicator between lox-sites (**Table 2**). As a technical issue, a construct with double lox-sites improves specificity of Cre recombinase targeting strategies (Atasoy et al., 2008).

A second, albeit related approach is to manipulate the output of the neurons and astrocytes that release signaling factors and measure the volume concentration of signaling molecules, particularly under conditions of changing vascular dilation versus constriction. The activity of neurons and glia may be manipulated with photoexcitation of caged molecules, with ectopic expression of chemical receptors modified to have unnatural affinities to a specific drug (Alexander et al., 2009), with ectopic expression of receptors with native binding sites (Arenkiel et al., 2008), and with optogenetic agents that are targeted to specific cell types (Cardin et al., 2009, 2010; Sohal et al., 2009). The latter strategy includes the use of channelrhodopsin (ChR2) to depolarize cells (Boyden et al., 2005; Arenkiel et al., 2007; Gradinaru et al., 2009) and halorhodopsin (NpHR; Zhang et al., 2007) or archaerhodopsin-3 (Arch; Chow et al., 2010) to inactivate cells. Other agents act directly on specific G-protein coupled pathways (Airan et al., 2009). All of these agents are typically delivered

by viral injection in combination with Cre recombinase labeled animals, as described above (**Tables 1 and 2**). A complementary strategy is the use of short hairpin RNA (shRNAs) to silence specific cell signaling pathways (**Table 3**).

The presence of multiple sources for the different signaling molecules suggests the additional need to measure receptor activation by these molecules directly. Receptor activation via the volume conduction of vasoactive signaling molecules may be observed with new cell-based indicators, CNiFERs, that can be made sensitive to any molecule that has a G-coupled protein receptor (**Figures 4A,B**). In a first realization with ACh sensing as the task, HEK cells were transfected with the muscarinic (M1) G_q-protein receptor along with the $[Ca^{2+}]_{int}$ reporter TN-XXL (Heim and Griesbeck, 2004). These show a strong response to the release of endogenous ACh

Table 1 | Mice that express fluorescent proteins or Cre recombinase in cell-types relevant to neurovascular regulation.

Promotor	Expression	Goal	Jax number	References
hGFAP	eGFP	Visualization of cortical astrocytes		Nolte et al. (2001)
GAD67	GFP	Visualization of parvalbumin, calretinin, or somatostatin-positive interneurons	003718, 007677, 006334	Oliva Jr. et al. (2000), Tamamaki et al. (2003), Chattopadhyaya et al. (2004), Ma et al. (2006)
Camk2a	tdTomato (a red FP)	Visualization of cortical excitatory neurons		Madisen et al. (2010)
Camk2a	Cre recombinase	Gene targeting to cortical excitatory neurons	005359	Tsien et al. (1996)
hGFAP	Cre recombinase	Gene targeting to cortical astrocytes	004600	Brenner et al. (1994), Zhuo et al. (2001)
Parvalbumin	Cre recombinase	Gene targeting of parvalbumin-positive cortical interneurons	008069	Wulff et al. (2008)
Smooth muscle myosin heavy chain	Cre recombinase and GFP	Gene targeting and visualization of pial vascular smooth muscle	007742	Xin et al. (2002a,b)

Table 2 | Viral expression cassettes for *in vivo* manipulation and detection of astrocyte and interneuronal signaling.

Protein expressed	Goal	Targeting strategies	References
Channelrhodopsin 2	Light-mediated cell depolarization		Arenkiel et al. (2007), Gradinaru et al. (2009)
Halorhodopsin	Light-mediated cell hyperpolarization	(i) Cre-lox	Zhang et al. (2007), Chow et al. (2010)
Archaerhodopsin-3		(ii) Cell type – specific promoters	
hM3Dq (G-coupled protein receptor for cell activation)	Drug-based (clozapine-N-oxide) regulation of activity	(iii) Cell type – trophic viruses	Alexander et al. (2009)
TRPV1	Ligand-based (capsaicin) regulation of activity		Arenkiel et al. (2008)
Tn-XXL or GCaMP3 (Fluorescent protein based Ca^{2+} sensors)	Cell-specific detection of intracellular calcium increases		Mank et al. (2008), Tian et al. (2009)

Table 3 | Viral expression cassettes for *in vivo* genetic manipulation of astrocyte and interneuronal signaling.

shRNA target	Pathway	Targeting strategies	References
mGluR	Astrocyte glutamate signaling pathway		Zonta et al. (2003)
phospholipase A_2, cyclo-oxygenase-1, or cytochrome p450	Astrocyte arachidonic acid metabolism		Zonta et al. (2003), Mulligan and MacVicar (2004)
Ca^{2+} sensitive large conductance BK channels	Astrocytic potassium release		Filosa et al. (2006), Weaver et al. (2006), Girouard et al. (2010)
VIP or vascular receptor VPAC1	Interneuron VIP release	Cre-lox	Fahrenkrug et al. (2000), Cauli et al. (2004)
NOS	Interneuron NO release		Cauli et al. (2004), Enager et al. (2008)
SOM or vascular receptor SSTR	Interneuron SOM release		Cauli et al. (2004), Enager et al. (2008), Kocharyan et al. (2008)
NPY or vascular receptor NPY-Y1	Interneuron NPY release		Cauli et al. (2004)

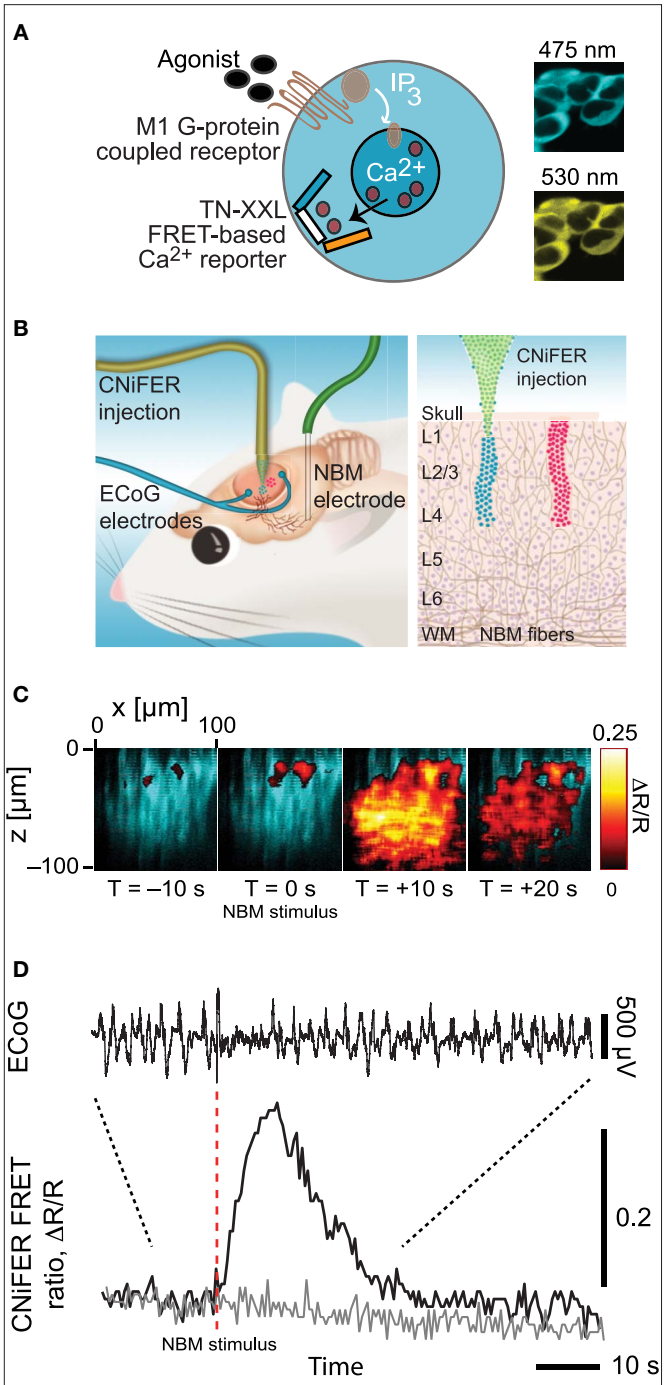

FIGURE 4 | Overview of CNiFER methodology. (A) Schematic of the cell-based sensors with a Gq family, G-protein coupled receptor for acetylcholine and the TN-XXL genetically expressible calcium reporter. **(B)**. Cartoon of the injection of CNiFERs and the placement of microelectrodes in rat frontal cortex. **(C)** *In vivo* response of M1-CNiFERs to cholinergic input after electrical activation of nucleus basalis (NBM). The X–Z scan was obtained with TPLSM through the depth of cortex before and after activation of cholinergic neurons in NBM. **(D)** Time dependence of the M1-CNiFER response, together with control data from CNiFERs without the M1 receptor, and the electrocorticogram (ECoG). The decrease in amplitude of the ECoG after stimulation, as expected for cholinergic activation of cortex. Adapted from Nguyen et al. (2010).

(**Figures 4C,D**). CNiFER technology may be extended, by the use of $G_{i/o}$- and G_s-protein receptors and chimeric Gα-q proteins (Coward et al., 1999), to sense neuropeptides such as VIP and SOM.

In toto, the combination of many *in vivo* tools, including electrophysiology, *in vivo* two-photon imaging, intracellular ion measurements (**Figure 3**), neurotransmitter receptor activation measurements (**Figure 4**), microdialysis measurements, single vessel blood flow measurements (**Figure 3**) as well as direct measurement of the activation of smooth muscle (**Figure 5**), and measurement of tissue oxygen levels (Sakadzic´ et al., 2010), can allow one to assess the influence of single neurons and networks of neurons on vascular control. These can be further supported by optical and chemical activation of specific cell types, as illustrated by the optical activation of astrocytes to increase blood flow in neighboring capillaries (**Figure 6**) in a manner similar to that seen with caged compounds (Takano et al., 2006). Lastly, automated reconstruction techniques allow one to map local architectonics (**Figure 1**). In all such endeavors, it important to realize that one may conceive new

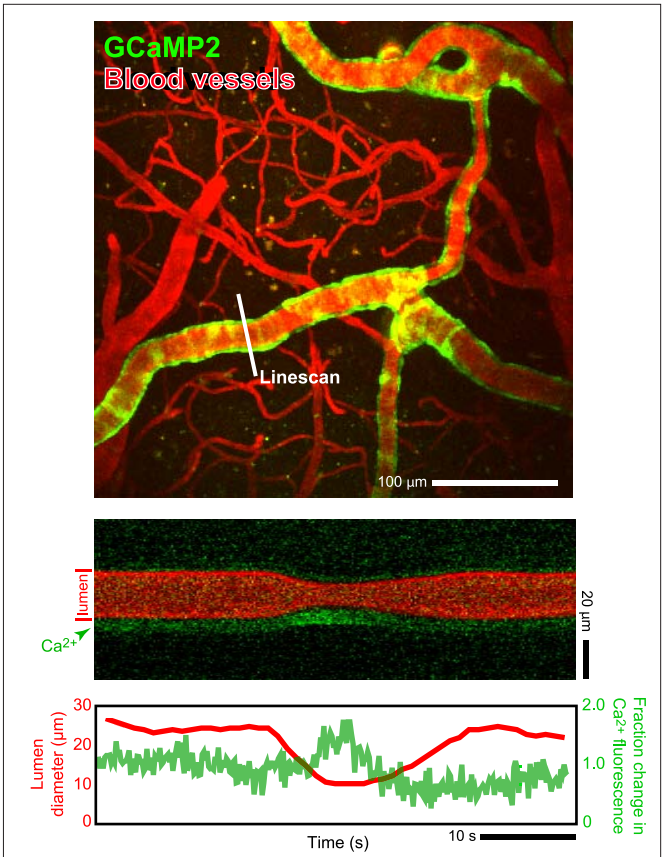

FIGURE 5 | *In vivo* measurements of arteriole smooth muscle activation concomitant with changes in blood flow in a neighboring microvessel. We made use of α-actin-BAC-GCaMP2 mice that expressed the genetically encoded Ca^{2+} indicator GCaMP2 in smooth muscle (Ji et al., 2004). Two-photon laser scanning microscopy was used to measure both calcium concentration and blood flow. The change in vessel diameter in the bottom line-scan data is a vasomotor event. In these transgenic animals the observable changes in $[Ca^{2+}]$ are limited to large contractile events; thus the present data must be considered as preliminary. Algorithms from Helmchen and Kleinfeld (2008).

tools as they are required. One anticipated need is a calcium-clamp to control smooth muscle tension, possibly realized with caged molecules and optical indicators, as a means to fix the flow in a region and observe changes in signaling molecule concentration.

EXAMPLE PROPOSED EXPERIMENT

Somatosensory input leads to neuronal activation in ipsilateral parietal cortex as well as contralateral cortex, albeit with a reduced amplitude (**Figures 7A,B**). Unexpectedly, contralateral sensory input leads to net dilation of vessels, while ipsilateral input has the paradoxical effect of net constriction (Devor et al., 2008; **Figure 7**). One possible explanation is that contralateral input leads to rapid release of VIP while ipsilateral input preferentially excites SOM+ interneurons more slowly. One can make use of microdialysis, or for greater spatial localization an extension of CNiFER technology to form VPAC1-CNiFERs to detect vasoactive intestinal peptide and SST1-CNiFERs to detect somatostatin. We predict that the ratio of VPAC1-CNiFER to SST1-CNiFER signals will be greater for contralateral versus ipsilateral stimulation (**Figure 8**).

PARADIGM-SHIFT TO CONSIDERING NEUROVASCULAR COUPLING IN TERMS OF SIGNALING MOLECULES

The conventional view is that neuronal spiking leads to an increase in local metabolism, and that metabolism leads to increased oxygen extraction from the blood as well as an increase in blood speed (Fox and Raichle, 1986; Leybaert, 2005). Thus neuronal activity is mirrored by changes in blood oxygenation. This paradigm is the accepted view for the interpretation of BOLD fMRI (Logothetis et al., 2001). But this causal relation breaks down, as shown by a multiplicity of recent experiments (Metea and Newman, 2006; Devor et al., 2008; Gordon et al., 2008; Sirotin and Das, 2008; Girouard et al., 2010; Lindauer et al., 2010; **Figure 7C**). We envision a model of neurovascular control that maps the activity of different neuronal subtypes to changes in vascular tone (Eqs 1 and 2). In our hypothesized paradigm, neuronal activity forms the inputs, the dynamics of the underlying signaling molecules form the internal state variables, and the vascular tone is the output state variable. This is not unlike the case of neuronal dynamics, where the input is derived from synaptic activity, the opening probabilities of channels form the internal state variables, and voltage is the output.

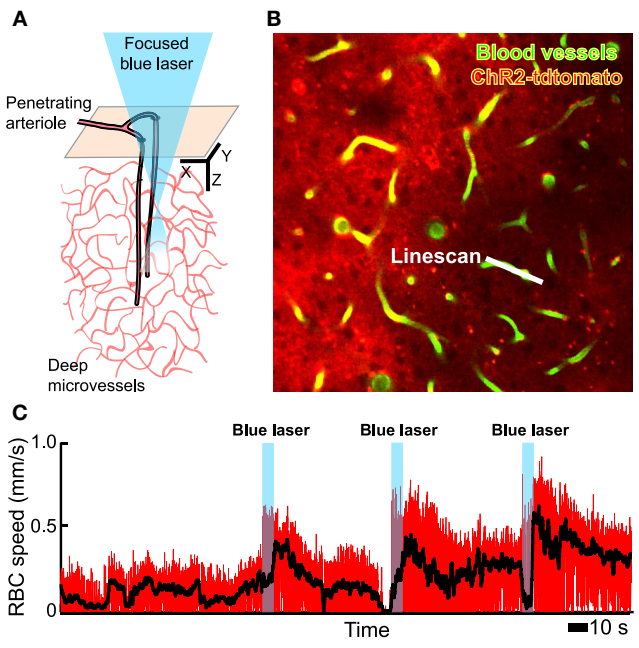

FIGURE 6 | *In vivo* focal photoexcitation of channelrhodopsin-labeled astrocytes leads an increase in capillary blood flow. We used GFAP-Cre+/– mice with an injection of adeno-associated virus serotype 2/5 with a FLEX-ChR2-tdtomato construct (Zhuo et al., 2001). Histological analysis shows that these animals have weak, non-specific expression of Cre recombinase in cortical neurons during adulthood, when the viral injection was made; thus the present data must be considered as preliminary. **(A)** Schematic of measurement region. **(B)** Planar image from layer 2/3, obtained with TPLSM, that includes a scanned capillary. **(C)** Change in capillary red blood cell speed upon activation of ChR2; the black line is a running average to remove heart rate contributions.

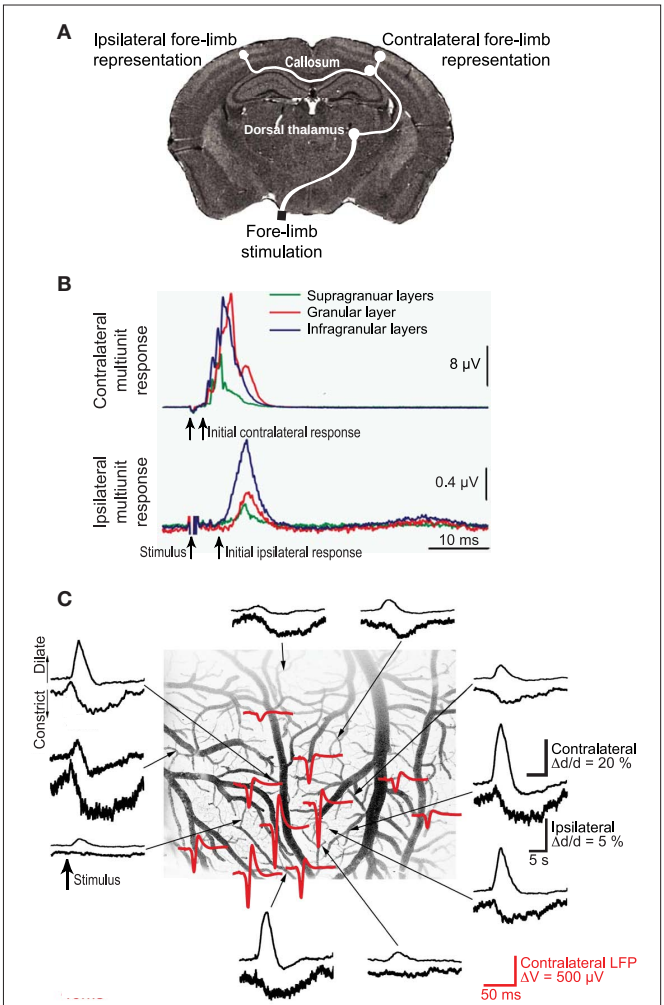

FIGURE 7 | Ipsilateral versus contralateral electrophysiological and neurovascular responses to sensory input. (A) Schematic of neuronal pathways. The contralateral cortex receives input via brainstem (not shown) and thalamic relays. This input is further relayed to ipsilateral cortex via collosal projections. **(B)** Measured multiunit responses to electrical stimulation of the fore-limb; 500 stimulation trials were averaged. **(C).** Net vasodilation in surface cortical arterioles in response to somatotopic stimulation on the contralateral side (upper traces in each pair) but vasoconstriction in response to ipsilateral stimulation (lower traces). The stimulus-induced ECoG (red) identifies the locus of the electrical response. Adapted from Devor et al. (2008).

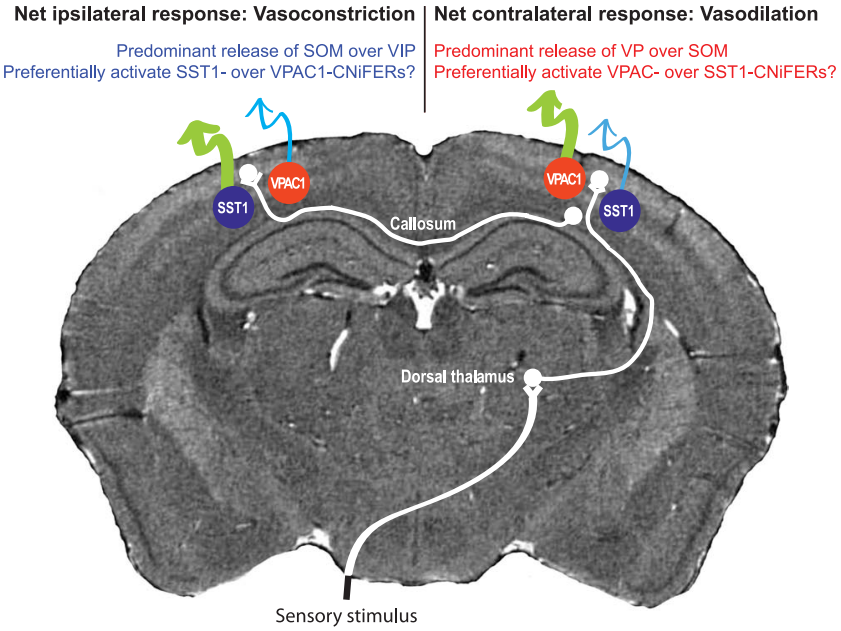

FIGURE 8 | Proposal for observing opposing vascular changes via competition of vasoactive neuropeptides. This proposal builds on the results in **Figure 6**, where the same sensory input leads to vasodilation at the epicenter of cortical activation in the contralateral hemisphere by vasoconstriction in the ipsilateral hemisphere. We predict that co-release of the dilator VIP dominates In the contralateral hemisphere while the constrictor SOM dominates in the ipsilateral hemisphere.

ACKNOWLEDGMENTS

We thank Costantino Iadacola, Patrick D. Lyden, and Jean Rossier for discussions and Edith Hamel for sharing artwork. This work was supported by grants from the NIH (EB003832, MH085499, NS059832, and OD006831 to David Kleinfeld and AG029681 to Gert Cauwenberghs), and fellowships from the Israeli Science Foundation (to Pablo Blinder), Canadian Institutes of Health Research (to Andy Y. Shih), and American Heart Association (to Andy Y. Shih).

REFERENCES

Airan, R. D., Thompson, K. R., Fenno, L. E., Bernstein, H., and Deisseroth, K. (2009). Temporally precise in vivo control of intracellular signalling. *Nat. Methods* 458, 1025–1029.

Alexander, G. M., Rogan, S. C., Abbas, A. I., Armbruster, B. N., Pei, Y., Allen, J. A., Nonneman, R. J., Hartmann, J., Moy, S. S., Nicolelis, M. A., McNamara, J. O., and Roth, B. L. (2009). Remote control of neuronal activity in transgenic mice expressing evolved G protein-coupled receptors. *Neuron* 63, 27–39.

Arenkiel, B. R., Klein, M. E., Davison, I. G., Katz, L. C., and Ehlers, M. D. (2008). Genetic control of neuronal activity in mice conditionally expressing TRPV1. *Nat. Methods* 5, 299–302.

Arenkiel, B. R., Peca, J., Davison, I. G., Feliciano, C., Deisseroth, K., Augustine, G. J., Ehlers, M. D., and Feng, G. (2007). In vivo light-induced activation of neural circuitry in transgenic mice expressing channelrhodopsin-2. *Neuron* 54, 205–218.

Atasoy, D., Aponte, Y., Su, H. H., and Sternson, S. M. (2008). A FLEX switch targets channelrhodopsin-2 to multiple cell types for imaging and long-range circuit mapping. *J. Neurosci.* 28, 7025–7030.

Belliveau, J. W., Kennedy, D. N., McKinstry, R. C., Buchbinder, B. R., Weisskoff, R. M., Cohen, M. S., Vevea, J. M., Brady, T. J., and Rosen, B. R. (1991). Functional mapping of the human cortex using magnetic resonance imaging. *Science* 254, 716–719.

Bernard, A., Sorensen, S. A., and Lein, E. S. (2009). Shifting the paradigm: new approaches for characterizing and classifying neurons. *Curr. Opin. Neurobiol.* 19, 530–536.

Boyden, E. S., Zhang, F., Bamberg, E., Nagel, G., and Deisseroth, K. (2005). Millisecond-timescale, genetically targeted optical control of neural activity. *Nat. Neurosci.* 8, 1263–1268.

Brenner, M., Kisseberth, W. C., Su, Y., Besnard, F., and Messing, A. (1994). GFAP promotor directs astrocyte-specific expression in transgenic mice. *J. Neurosci.* 14, 1030–1037.

Cardin, J. A., Carlén, M., Meletis, K., Knoblich, U., Zhang, F., Deisseroth, K., Tsai, L. H., and Moore, C. I. (2009). Driving fast-spiking cells induces gamma rhythm and controls sensory responses. *Nat. Methods* 459, 663–667.

Cardin, J. A., Carlén, M., Meletis, K., Knoblich, U., Zhang, F., Deisseroth, K., Tsai, L. H., and Moore, C. I. (2010). Targeted optogenetic stimulation and recording of neurons in vivo using cell-type-specific expression of Channelrhodopsin-2. *Nat. Protoc.* 5, 247–254.

Cauli, B., Tong, X. K., Rancillac, A., Serluca, N., Lambolez, B., Rossier, J., and Hamel, E. (2004). Cortical GABA interneurons in neurovascular coupling: relays for subcortical vasoactive pathways. *J. Neurosci.* 24, 8940–8949.

Chattopadhyaya, B., Cristo, G. D., Higashiyama, H., Knott, G. W., Kuhlman, S. J., Welker, E., and Huang, Z. J. (2004). Experience and activity-dependent maturation of perisomatic GABAergic innervation in primary visual cortex during a postnatal critical period. *J. Neurosci.* 24, 9498–9611.

Chow, B. Y., Han, X., Dobry, A. S., Qian, X., Chuong, A. S., Li, M., Henninger, M. A., Belfort, G. M., Lin, Y., Monahan, P. E., and Boyden, E. S. (2010). High-performance genetically targetable optical neural silencing by light-driven proton pumps. *Nature* 463, 98–102.

Cohen, Z., Molinatti, G., and Hamel, E. (1997). Astroglial and vascular interactions of noradrenaline terminals in the rat cerebral cortex. *J. Cereb. Blood Flow Metab.* 17, 894–904.

Coward, P., Chan, S. D., Wada, H. G., Humphries, G. M., and Conklin, B. R. (1999). Chimeric G proteins allow a high-throughput signaling assay of Gi-coupled receptors. *Anal. Biochem.* 270, 242–248.

Devor, A., Hillman, E. M., Tian, P., Waeber, C., Teng, I. C., Ruvinskaya, L., Shalinsky, M. H., Zhu, H., Haslinger, R. H., Narayanan, S. N., Ulbert, I., Dunn, A. K., Lo, E. H., Rosen, B. R., Dale, A. M., Kleinfeld, D., and Boas, D. A. (2008). Stimulus-induced changes in blood flow and 2-deoxyglucose uptake dissociate in ipsilateral somatosensory cortex. *J. Neurosci.* 28, 14347–14357.

Drew, P. J., Blinder, P., Cauwenberghs, G., Shih, A. Y., and Kleinfeld, D. (2010). Rapid determination of particle velocity from space-time images using the Radon transform. *J. Comput. Neurosci.* 29, 5–11.

Drew, P. J., Duyn, J. H., Galanov, E., and Kleinfeld, D. (2008). Finding

coherence in spontaneous oscillations. *Nat. Neurosci.* 11, 991–993.

Driscoll, J. D., Shih, A. Y., Drew, P. J., and Kleinfeld, D. (2011). "Quantitative two-photon imaging of blood flow in cortex," in *Imaging in Neuroscience and Development*, ed. R. Yuste (New York: Cold Spring Harbor Laboratory Press), in press.

Enager, P., Piilgaard, H., Offenhauser, N., Kocharyan, A., Fernandes, P., Hamel, E., and Lauritzen, M. (2008). Pathway-specific variations in neurovascular and neurometabolic coupling in rat primary somatosensory cortex. *J. Cereb. Blood Flow Metab.* 29, 976–986.

Fahrenkrug, J., Hannibal, J., Tams, J., and Georg, B. (2000). Immunohistochemical localization of the VIP1 receptor (VPAC1R) in rat cerebral blood vessels: relation to PACAP and VIP containing nerves. *J. Cereb. Blood Flow Metab.* 20, 1205–1214.

Filosa, J. A., Bonev, A. D., and Nelson, M. T. (2004). Calcium dynamics in cortical astrocytes and arterioles during neurovascular coupling. *Circ. Res.* 95, 73–81.

Filosa, J. A., Bonev, A. D., Straub, S. V., Meredith, A. L., Wilkerson, M. K., Aldrich, R., and Nelson, M. T. (2006). Local potassium signaling couples neuronal activity to vasodilation in the brain. *Nat. Neurosci.* 9, 1397–1403.

Fox, P. T., and Raichle, M. E. (1986). Focal physiological uncoupling of cerebral blood flow and oxidative metabolism during domatosensory stimulation in human subjects. *Proc. Natl. Acad. Sci. U.S.A.* 83, 1140–1144.

Garaschuk, O., Milos, R. I., and Konnerth, A. (2006). Targeted bulk-loading of fluorescent indicators for two-photon brain imaging in vivo. *Nat. Protoc.* 1, 380–386.

Gibson, J. R., Beierlein, M., and Connors, B. W. (1999). Two networks of electrically coupled inhibitory neurons in neocortex. *Nature* 4, 75–79.

Girouard, H., Bonev, A. D., Hannah, R. M., Meredith, A., Aldrich, R. W., and Nelson, M. T. (2010). Astrocytic endfoot $Ca2^{+}$ and BK channels determine both arteriolar dilation and constriction. *Proc. Natl. Acad. Sci. U.S.A.* 107, 3811–3816.

Golanov, E. V., and Reis, D. J. (1996). Contribution of oxygen-sensitive neurons of the rostral ventrolateral medulla to hypoxic cerebral vasodilatation in the rat. *J. Physiol.* 495, 201–216.

Gordon, G. R. C., Choi, H. B., Rungta, R. L., Ellis-Davies, G. C. R., and MacVicar, B. A. (2008). Brain metabolism dictates the polarity of astrocyte control over arterioles. *Nature* 456, 745–750.

Gradinaru, V., Mogri, M., Thompson, K. R., Henderson, J. M., and Deisseroth, K. (2009). Optical deconstruction of Parkinsonian neural circuitry. *Science* 324, 354–359.

Hamel, E. (2004). Cholinergic modulation of the cortical microvascular bed. *Prog. Brain Res.* 145, 171–178.

Hamel, E. (2006). Perivascular nerves and the regulation of cerebrovascular tone. *J. Appl. Physiol.* 100, 1059–1064.

Heim, N., and Griesbeck, O. (2004). Genetically encoded indicators of cellular calcium dynamics based on troponin C and green fluorescent protein. *J. Biol. Chem.* 279, 14280–14286.

Helmchen, F., and Kleinfeld, D. (2008). In vivo measurements of blood flow and glial cell function with two-photon laser scanning microscopy. *Methods Enzymol.* 444, 231–254.

Iadecola, C., and Nedergaard, M. (2007). Glial regulation of the cerebral microvasculature. *Nat. Neurosci.* 10, 1369–1376.

Ji, G., Feldman, M. E., Deng, K. Y., Greene, K. S., Wilson, J., Lee, J. C., Johnston, R. C., Rishniw, M., Tallini, Y., Zhang, J., Wier, W. G., Blaustein, M. P., Xin, H. B., Nakai, J., and Kotlikoff, M. I. (2004). Ca2+-sensing transgenic mice: postsynaptic signaling in smooth muscle. *J. Biol. Chem.* 279, 21461–21468.

Jones, M., Devonshire, I. M., Berwick, J., Martin, C., Redgrave, P., and Mayhew, J. (2008). Altered neurovascular coupling during information-processing states. *Eur. J. Neurosci.* 27, 2758–2772.

Kawaguchi, Y. (2001). Distinct firing patterns of neuronal subtypes in cortical synchronized activities. *J. Neurosci.* 21, 7261–7272.

Kocharyan, A., Fernandes, P., Tong, X. K., Vaucher, E., and Hamel, E. (2008). Specific subtypes of cortical GABA interneurons contribute to the neurovascular coupling response to basal forebrain stimulation. *J. Cereb. Blood Flow Metab.* 28, 221–231.

Kövari, E., Gold, G., Herrmann, F. R., Canuto, A., Hof, P. R., Bouras, C., and Giannakopoulos, P. (2007). Cortical microinfarcts and demyelination affect cognition in cases at high risk for dementia. *Neurology* 66, 927–931.

LeDoux, J. E., Thompson, M. E., Iadecola, C., Tucker, L. W., and Reis, D. J. (1983). Local cerebral blood flow increases during auditory and emotional processing in the conscious rat. *Science* 221, 573–578.

Leybaert, L. (2005). Neurobarrier coupling in the brain: a partner of neurovascular and neurometabolic coupling? *J. Cereb. Blood Flow Metab.* 25, 2–16.

Lindauer, U., Leithner, C., Kaasch, H., Rohrer, B., Foddis, M., Füchtemeier, M., Offenhauser, N., Steinbrink, J., Royl, G., Kohl-Bareis, M., and Dirnagl, U. (2010). Neurovascular coupling in rat brain operates independent of hemoglobin deoxygenation. *J. Cereb. Blood Flow Metab.* 30, 757–768.

Logothetis, N. K., Pauls, J., Augath, M., Trinath, T., and Oeltermann, A. (2001). Neurophysiological investigation of the basis of the fMRI signal. *Nature* 412, 150–157.

Luo, L., Callaway, E. M., and Svoboda, K. (2008). Genetic dissection of neural circuits. *Neuron* 57, 634–660.

Ma, Y., Hu, H., Berrebi, A. S., Mathers, P. H., and Agmon, A. (2006). Distinct subtypes of somatostatin-containing neocortical interneurons revealed in transgenic mice. *J. Neurosci.* 26, 5069–5082.

Madisen, L., Zwingman, T. A., Sunkin, S. M., Oh, S. W., Zariwala, H. A., Gu, H., Ng, L. L., Palmiter, R. D., Hawrylycz, M. J., Jones, A. R., Lein, E. S., and Zeng, H. (2010). A robust and high-throughput Cre reporting and characterization system for the whole mouse brain. *Nat. Neurosci.* 13, 133–140.

Mallo, M. (2006). Controlled gene activation and inactivation in the mouse. *Front. Biosci.* 11, 313–327.

Mank, M., Santos, A. F., Direnberger, S., Mrsic-Flogel, T. D., Hofer, S. B., Stein, V., Hendel, T., Reiff, D. F., Levelt, C., Borst, A., Bonhoeffer, T., Hübener, M., and Griesbeck, O. (2008). A genetically encoded calcium indicator for chronic in vivo two-photon imaging. *Nat. Methods* 5, 805–811.

Metea, M. R., and Newman, E. A. (2006). Glial cells dilate and constrict blood vessels: a mechanism of neurovascular coupling. *J. Neurosci.* 26, 2862–2870.

Mulligan, S. J., and MacVicar, B. A. (2004). Calcium transients in astrocyte endfeet cause cerebrovascular constrictions. *Nature* 431, 195–199.

Nguyen, Q.-T., Schroeder, L. F., Mank, M., Muller, A., Taylor, P. W., Griesbeck, O., and Kleinfeld, D. (2010). An in vivo biosensor for neurotransmitter release and in situ receptor activity. *Nat. Neurosci.* 13, 127–132.

Niessing, J., Ebisch, B., Schmidt, K. E., Niessing, M., Singer, W., and Galuske, R. A. (2005). Hemodynamic signals correlate tightly with synchronized gamma oscillations. *Science* 309, 948–951.

Nolte, C., Matyash, M., Pivneva, T., Schipke, C. G., Ohlemeyer, C., Hanisch, U. K., Kirchhoff, F., and Kettenmann, H. (2001). GFAP promoter-controlled EGFP-expressing transgenic mice: a tool to visualize astrocytes and astrogliosis in living brain tissue. *Glia* 33, 72–86.

Ogawa, S., Tank, D. W., Menon, R., Ellermann, J. M., Kim, S.-G., Merkle, H., and Ugurbil, K. (1992). Intrinsic signal changes accompanying sensory stimulation: functional brain mapping with magnetic resonance imaging. *Proc. Natl. Acad. Sci. U.S.A.* 89, 5951–5955.

Oliva, A. A. Jr., Jiang, M., Lam, T., Smith, T. L., and Swann, J. W. (2000). Novel hippocampal interneuronal subtypes identified using transgenic mice that express green fluorescent protein in GABAergic interneurons. *J. Neurosci.* 20, 3354–3368.

Paulson, O. B., Strandgaard, S., and Edvinsson, L. (1990). Cerebral autoregulation. *Cerebrovasc. Brain Metab. Rev.* 2, 161–192.

Sakadzić, S., Roussakis, E., Yaseen, M. A., Mandeville, E. T., Srinivasan, V. J., Arai, K., Ruvinskaya, S., Devor, A., Lo, E. H., Vinogradov, S. A., and Boas, D. A. (2010). Two-photon high-resolution measurement of partial pressure of oxygen in cerebral vasculature and tissue. *Nat. Methods* 7, 755–759.

Shaner, N. C., Campbell, R. E., Steinbach, P. A., Giepmans, B. N., Palmer, A. E., and Tsien, R. Y. (2004). Improved monomeric red, orange and yellow fluorescent proteins derived from *Discosoma* sp. red fluorescent protein. *Nat. Biotechnol.* 22, 1567–1572.

Shmueli, K., van Gelderen, P., de Zwart, J. A., Horovitz, S. G., Fukunaga, M., Jansma, J. M., and Duyn, J. H. (2007). Low-frequency fluctuations in the cardiac rate as a source of variance in the resting-state fMRI BOLD signal. *Neuroimage* 38, 306–320.

Sirotin, Y. B., and Das, A. (2008). Anticipatory haemodynamic signals in sensory cortex not predicted by local neuronal activity. *Nature* 457, 475–479.

Sohal, V. S., Zhang, F., Yizhar, O., and Deisseroth, K. (2009). Parvalbumin neurons and gamma rhythms enhance cortical circuit performance. *Nature* 459, 698–702.

Svoboda, K., Denk, W., Kleinfeld, D., and Tank, D. W. (1997). *In vivo* dendritic calcium dynamics in neocortical pyramidal neurons. *Nature* 385, 161–165.

Takano, T., Tian, G. F., Peng, W., Lou, N., Libionka, W., Han, X., and Nedergaard, M. (2006). Astrocyte-mediated control of cerebral blood flow. *Nat. Neurosci.* 9, 260–267.

Tamamaki, N., Yanagawa, T., Tomioka, R., Miyazaki, J., Obata, K., and Kaneko, T. (2003). Green fluorescence protein expression and colocalization with calretinin, parvalbumin, and somatostatin in the GAD67-GFP knock-in mouse. *J. Comp. Neurol.* 40, 60–79.

Tian, L., Hires, S. A., Mao, T., Huber, D., Chiappe, M. E., Chalasani, S. H., Petreanu, L., Akerboom, J., McKinney, S. A., Schreiter, E. R., Bargmann, C. I., Jayaraman, V., Svoboda, K., and Looger, L. L. (2009). Imaging neural activity in worms, flies and mice with improved GCaMP calcium indicators. *Nat. Methods* 6, 875–881.

Tsai, P. S., Friedman, B., Ifarraguerri, A. I., Thompson, B. D., Lev-Ram, V., Schaffer, C. B., Xiong, Q., Tsien, R. Y., Squier, J. A., and Kleinfeld, D. (2003). All-optical histology using ultrashort laser pulses. *Neuron* 39, 27–41.

Tsai, P. S., Kaufhold, J., Blinder, P., Friedman, B., Drew, P., Karten, H. J., Lyden, P. D., and Kleinfeld, D. (2009). Correlations of neuronal and microvascular densities in murine cortex revealed by direct counting and colocalization of cell nuclei and microvessels. *J. Neurosci.* 18, 14553–14570.

Tsien, J. Z., Chen, D. F., Gerber, D., Tom, C., Mercer, E. H., Anderson, D. J., Mayford, M., Kandel, E. R., and Tonegawa, S. (1996). Subregion- and cell type-restricted gene knockout in mouse brain. *Cell* 87, 1317–1326.

Tsien, R. Y. (1998). The green fluorescent protein. *Annu. Rev. Biochem.* 67, 509–544.

Wallace, D. J., Borgloh, S. M. Z. A., Astori, S., Yang, Y., Bausen, M., Kügler, S., Palmer, A. E., Tsien, R. Y., Sprengel, R., Kerr, J. N., Denk, W., and Hasan, M. T. (2008). Single-spike detection in vitro and in vivo with a genetic Ca2+ sensor. *Nat. Methods* 5, 797–804.

Wang, X., Lou, N., Xu, Q., Tian, G. F., Peng, W. G., Han, X., Kang, J., Takano, T., and Nedergaard, M. (2006). Astrocytic $Ca2^{+}$ signaling evoked by sensory stimulation in vivo. *Nat. Neurosci.* 9, 816–823.

Weaver, A. K., Bomben, V. C., and Sontheimer, H. (2006). Expression and function of calcium-activated potassium channels in human glioma cells. *Glia* 54, 223–233.

Wise, R. G., Ide, K., Poulin, M. J., and Tracey, I. (2004). Resting fluctuations in arterial carbon dioxide induce significant low frequency variations in BOLD signal. *Neuroimage* 21, 1652–1664.

Wulff, P., Ponomarenko, A. A., Bartos, M., Korotkova, T. M., Fuchs, E. C., Bahner, F., Both, M., Tort, A. B. L., Kopell, N. J., Wisden, W., and Monyer, H. (2008). Hippocampal theta rhythm and its coupling with gamma oscillations require fast inhibition onto paralbumin-positive interneuron. *Proc. Natl. Acad. Sci. U.S.A.* 106, 3561–3566.

Xin, H. B., Deng, K. Y., Rishniw, M., Ji, G., and Kotlikoff, M. I. (2002a). Smooth muscle expression of Cre recombinase and eGFP in transgenic mice. *Physiol. Genomics* 10, 211–219.

Xin, H. B., Deng, K. Y., Rishniw, M., Ji, G., and Kotlikoff, M. I. (2002b). Smooth muscle expression of Cre recombinase and eGFP in transgenic mice. *Physiol. Genomics* 10, 211–215.

Zhang, F., Wang, L.-P., Brauner, M., Liewald, J. F., Ka, K., Watzke, N., Wood, P. G., Bamberg, E., Nagel, G., Gottschalk, A., and Deisseroth, K. (2007). Multimodal fast optical interrogation of neural circuitry. *Nature* 446, 633–641.

Zhuo, L., Theis, M., Alvarez-Maya, I., Brenner, M., Willecke, K., and Messing, A. (2001). hGFAP-cre transgenic mice for the manipulation of glial and neuronal function in vivo. *Genesis* 31, 85–94.

Zonta, M., Angulo, M. C., Gobbo, S., Rosengarten, B., Hossmann, K. A., Pozzan, T., and Carmignoto, G. (2003). Neuron-to-astrocyte signaling is central to the dynamic control of brain microcirculation. *Nat. Neurosci.* 6, 43–50.

Conflict of Interest Statement: The authors declare that the research was conducted in the absence of any commercial or financial relationships that could be construed as a potential conflict of interest.

Received: 08 March 2010; paper pending published: 08 March 2010; accepted: 11 April 2011; published online: 25 April 2011. Citation: Kleinfeld D, Blinder P, Drew PJ, Driscoll JD, Muller A, Tsai PS and Shih AY (2011) A guide to delineate the logic of neurovascular signaling in the brain. Front. Neuroenerg. ***3****:1. doi: 10.3389/fnene.2011.00001*

frontiers in
NEUROENERGETICS

PERSPECTIVE ARTICLE
published: 23 June 2010
doi: 10.3389/fnene.2010.00009

Revisiting the role of neurons in neurovascular coupling

Bruno Cauli[1] and Edith Hamel[2]*

[1] *Laboratoire de Neurobiologie des Processus Adaptatifs, Université Pierre et Marie Curie, Paris, France*
[2] *Laboratory of Cerebrovascular Research, Montreal Neurological Institute, Montréal, QC, Canada*

Edited by:
Anna Devor, University of California San Diego, USA

Reviewed by:
Karl A. Kasischke, University of Rochester Medical Center, USA; Rochester University, USA
Bruno Weber, University of Zurich, Switzerland

***Correspondence:**
Edith Hamel, Laboratory of Cerebrovascular Research, Montreal Neurological Institute, 3801 University Street, Montréal, QC H3A 2B4, Canada.
e-mail:edith.hamel@mcgill.ca

In this article, we will review molecular, anatomical, physiological and pharmacological data in an attempt to better understand how excitatory and inhibitory neurons recruited by distinct afferent inputs to the cerebral cortex contribute to the coupled hemodynamic response, and how astrocytes can act as intermediaries to these neuronal populations. We aim at providing the pros and cons to the following statements that, depending on the nature of the afferent input to the neocortex, (*i*) different neuronal or astroglial messengers, likely acting in sequence, mediate the hemodynamic changes, (*ii*) some recruited neurons release messengers that directly alter blood vessel tone, (*iii*) others act by modulating neuronal and astroglial activity, and (*iv*) astrocytes act as intermediaries for both excitatory and inhibitory neurotransmitters. We will stress that a given afferent signal activates a precise neuronal circuitry that determines the mediators of the hemodynamic response as well as the level of interaction with surrounding astrocytes.

Keywords: neuronal network, inhibitory interneuron, excitatory pathways, astrocytes, cerebral blood flow

ACTIVITY IN NEURONAL NETWORKS UNDERLIES ACTIVITY-DEPENDENT CHANGES IN HEMODYNAMIC SIGNALS

The temporal and spatial coupling between increased neuronal activity and cerebral blood flow (CBF), known as functional hyperemia or neurovascular coupling, is a highly regulated phenomenon that ensures adequate supply of oxygen and glucose to the neurons at work during a given task. Although intuitively appealing, a direct link between energy state and blood flow is not universally accepted, and the physiological basis of neurovascular coupling still remains uncertain. Indeed, neither the lack of glucose or oxygen appears to fully justify the hemodynamic response (Powers et al., 1996; Wolf et al., 1997; Lindauer et al., 2010), which may serve as a safety measure for substrate delivery during functional activation (Leithner et al., 2010). Despite these limitations, the changes in hemodynamic signals (BOLD response, CBF or cerebral blood volume, CBV) are commonly used as surrogate markers to map changes in neural activity in brain imaging procedures, such as functional magnetic resonance (fMRI), positron emission tomography (PET), or diffuse optical imaging (DOI) under both physiological and pathological conditions. Accordingly, an adequate interpretation of imaging data imperatively requires understanding of the cellular basis of the activated neurocircuitry and its interaction with astrocytic and vascular targets. In contrast to the innervation of large cerebral arteries by ganglia from the peripheral nervous system, which is mainly involved in autoregulation (for a review, Hamel, 2006), the neuronal circuitry at play here refers to pathways of the central nervous system that interact with the brain microcirculation.

As such, it is known that the changes in activity are triggered by the incoming afferents, but that it is their local processing by the targeted cells that drives the perfusion changes (Logothetis et al., 2001; Lauritzen and Gold, 2003; Lauritzen, 2005). These hemodynamic changes are mainly, if not exclusively, achieved by the control of the vasculature at the arteriolar level (Hillman et al., 2007), from the pial surface down to the precapillary level where vascular pericytes stand (Jones, 1970), the latter contractile elements being likely involved in a localized control of capillary tone (Peppiatt et al., 2006). Additionally, it has been shown that the hemodynamic response correlates with synchronized synaptic activity, a highly energy consuming process (Arthurs et al., 2000), and that it is controlled by signaling molecules released during increased synaptic activity (Devor et al., 2007). Recently, using the neurovascular coupling response to various sensory stimuli (whisker, forepaw or hindpaw, visual), elegant experiments demonstrated that the spread of the hemodynamic activity accurately reflects the neural response (Berwick et al., 2008), that it is driven by synaptic activity generated by intracortical processing (Franceschini et al., 2008), and that the latter reflected the balance between excitatory and inhibitory signals (Devor et al., 2005, 2007; Shmuel et al., 2006). Particularly, suppressed neuronal activity or functional neuronal inhibition has been associated with decrease in blood oxygenation and perfusion, which could explain the negative BOLD signals (Shmuel et al., 2002, 2006) as it occurred concurrently with arteriolar constriction (Devor et al., 2007).

IDENTIFICATION OF THE UNDERLYING NEURONAL CIRCUITRY

As an attempt to identify the underlying neuronal circuitry, an interesting study by Lu et al. (2004) showed that laminar BOLD and CBV responses to rat whisker stimulation spatially correlated with increased neuronal activity evaluated by c-Fos upregulation. In an unrelated study in rats treated with the serotonin releasing drug m-chlorophenylpiperazine, positive BOLD signals and c-Fos immunoreactivity correlated in areas of increased activity, but not in those that displayed diminished BOLD signals, presumably due to decreased neuronal signaling (Stark et al., 2006). Recently, it was shown that stimulation of corticocortical and thalamocortical inputs to the same area of the somatosensory cortex induced completely distinct frequency-dependent changes in CBF and oxygen consumption, and evoked activity in different populations of

cortical excitatory pyramidal cells and inhibitory GABA interneurons (Enager et al., 2009). Stimulation intensity increases occurred with the silencing or recruitment of distinct inhibitory interneurons, indicating that neural network activation is both stimulus- and frequency-dependent. Particularly, the hemodynamic responses were attributed to activation of cyclooxygenase-2 (COX-2) pyramidal cells and somatostatin (SOM)/nitric oxide synthase (NOS) inhibitory interneurons, consistent with pharmacological studies that implicated COX-2- and NOS-derived vasodilator messengers in these neurovascular pathways (Niwa et al., 2000; Gotoh et al., 2001; Hoffmeyer et al., 2007). Moreover, increased activity in inhibitory interneurons has been associated with the initiation of the hemodynamic response triggered by synchronized cortical activity, as induced by activation of the basal forebrain (Niessing et al., 2005). Stimulation of this basalocortical afferent input further indicated selective activation of cholinoceptive layers II to VI SOM and neuropeptide Y (NPY) interneurons, as well as layer I GABA interneurons, with widespread activation of pyramidal cells, including those that contain COX-2 (Kocharyan et al., 2008; Lecrux et al., 2009). Although it was demonstrated that the CBF response was triggered by cholinergic afferents, its full expression required $GABA_A$-mediated transmission on neuronal, vascular and/or astrocytic targets (Kocharyan et al., 2008). Together these anatomical, neurochemical and functional studies demonstrate the importance of identifying the cellular ensemble that underlies hemodynamic signals, highlighting that specific subsets of neurons are activated by a given stimulus, depending on the afferent input they receive and integrate.

PERIVASCULAR ASTROCYTES AS INTERMEDIARIES TO BOTH GLUTAMATE AND GABA PATHWAYS

In addition to the difficulty in identifying the exact contribution of excitatory and inhibitory neurotransmissions in the evoked hemodynamic response, the effect of these neurotransmitter systems on perivascular astrocytes needs to be considered (for a detailed review, Carmignoto and Gomez-Gonzalo, 2009). The enwrapping of synapses and blood vessels (Kacem et al., 1998) by glial processes and, particularly, their intervening endfeet in multiple neurovascular appositions identified at the ultrastructural level led to the concept of a neuronal-astrocytic-vascular tripartite functional unit (Vaucher and Hamel, 1995; Cohen et al., 1996; Paspalas and Papadopoulos, 1996; Vaucher et al., 2000). The significance of these interactions in the regulation of CBF was first substantiated by the demonstration that astrocytes could synthesize vasodilatory messengers (**Table 1**), particularly epoxyeicosatrienoic acids (EETs) generated from P450 arachidonic acid epoxygenase activity (Alkayed et al., 1996) that were involved in the CBF response to glutamate (Alkayed et al., 1997; Harder et al., 1998). Soon after came the first *in vitro* (in cortical slices) and *in vivo* demonstrations for a role of astrocytes, through metabo-

Table 1 | Summary of neuronal and gial mediators of functional hyperemia.

			Mechanisms of release			Targets on VSMC	
	Vasodilators (*in vivo*)	Cellular origin	Transmitter	Receptors	2nd messenger	Receptor	signalling
neuronal	NO (Northington et al., 1992)	NOS/NPY interneurons (Dawson et al., 1991)	Glutamate	NMDA-R	↗ Ca^{2+}	sGC	↗ cGMP
	VIP (Yaksh et al., 1987)	VIP interneurons (Morrison et al., 1984)		iGluRs mGluR1/5 ?		VPAC1	↗ cAMP
	PGE_2 (Niwa et al., 2000)	COX-2 pyramids (Breder et al., 1995)		NMDA-R		EP	↗ cAMP
glial	PGE_2 (Takano et al., 2006)	COX-1 astrocytes (Takano et al., 2006)	Glutamate / GABA	mGluR5 / $GABA_{A/B}$			
	EETs (Peng et al., 2002)	astrocytes (Alkayed et al., 1996)				K_{Ca} GPCR ?	↗ g K_{Ca}
	K^+ (Girouard et al., 2010)	astrocytes (Filosa et al., 2006)				K_{ir}	↗ g K_{Ir}

Only cortical mediators identified in vivo are listed. Neuronal and glial metabolism by-products (e.g., CO_2, H^+, adenosine…) are not included. NO, nitric oxide; VIP, vasoactive intestinal polypeptide; PgE_2, prostaglandin E_2; EETs, epoxyeicosatrienoic acids; NOS, nitric oxide synthase; NPY, neuropeptide Y; COX, cyclooxygenase, NMDA-R, N-methyl D aspartate receptors, iGluRs; ionotropic glutamate receptors, mGluR, metabotropic glutamate receptors; VSMC, vascular smooth muscle cell, sGC, soluble guanylate cyclase, VPAC1, VIP/PACAP receptor type 1; EP, prostaglandin E_2 receptors; GPCR, G protein coupled receptor. K_{Ca}, Ca^{2+}-activated K^+ channels; K_{ir}, inward rectifier K^+ channels; g, conductance. References can be found in the main list.

tropic glutamate receptor (mGluRs)-induced Ca^{2+} transients, in microarteriolar dilation and the increase blood flow to forepaw stimulation, a response mediated by arachidonic acid products, possibly prostaglandin E_2 (PGE_2) (Zonta et al., 2003). Since this pioneer study, a role for astrocytes in neurovascular coupling has been reaffirmed in various paradigms (Carmignoto and Gomez-Gonzalo, 2009).

Another pathway activated in astrocytic endfeet following Ca^{2+} increases is the large-conductance, calcium-sensitive potassium (BK) channels that induce K^+ release (**Table 1**), activation of smooth muscle Kir channels and relaxation (Filosa et al., 2006). Recently, it was shown that the extent of the Ca^{2+} increases in astrocytic endfeet determined the dilatory or contractile nature of the vascular response, both mediated by extracellular K^+ (Girouard et al., 2010). This novel mechanism would reunify previous "apparently" contradictory findings, in brain slices or in retina, of dilation and constriction being induced by increased Ca^{2+} signaling in astrocytes, and explained by the levels of NO (Mulligan and MacVicar, 2004; Metea and Newman, 2006), oxygen (Gordon et al., 2008), or the pre-existing tone of the vessels (Blanco et al., 2008). Further, the study by Girouard et al. (2010) showed that neuronal activation *in vitro* (electrical field stimulation) similarly acted through serial activation of astrocytic BK and smooth muscle Kir channels. Considering that GABA (Nilsson et al., 1993; Serrano et al., 2006; Meier et al., 2008) and peptides such as SOM that colocalize with GABA (Somogyi et al., 1984; Cauli et al., 2000) in interneurons also increase Ca^{2+} signaling in astrocytes, (Straub et al., 2006), the latter could act as intermediaries to GABA in neurovascular coupling (**Table 1**). Whether or not the astrocytic/smooth muscle BK and Kir channel activation cascade is involved still remains to be determined. Similarly, it would be interesting to evaluate if the latter, or other contractile mechanisms of neuronal (Cauli et al., 2004; Rancillac et al., 2006) or vascular origins (Mulligan and MacVicar, 2004) could explain the dilatory and constrictive phases seen in the central core of neuronal depolarization and surround region of hyperpolarization, respectively, after somatosensory stimulation (Devor et al., 2007). To date the cellular and molecular mechanisms or even the functional significance of this response remains unknown.

NEURALLY-DERIVED VASOACTIVE MESSENGERS

In addition to the astrocyte-derived vasodilatory messengers PGE_2 (Zonta et al., 2003), EETs (Alkayed et al., 1996), or K^+ ions (Filosa et al., 2006), some vasodilators are chiefly synthesized by distinct neuronal populations (**Table 1**). These include COX-2-derived prostanoids (Niwa et al., 2000) produced by some Layer II–III pyramidal cells (Yamagata et al., 1993; Breder et al., 1995), nitric oxide (NO) (Gotoh et al., 2001) whose synthetic enzyme is expressed by discrete subpopulations of cortical GABA interneurones (Kubota et al., 1994), VIP (Yaksh et al., 1987), acetylcholine (Scremin et al., 1973) and corticotropin-releasing factor (De Michele et al., 2005) synthesized by bipolar/bitufted GABA interneurones (Morrison et al., 1984; Chédotal et al., 1994a; Cauli et al., 1997; Gallopin et al., 2006). As for astrocyte-derived messengers, their release is stimulated by glutamatergic neurotransmission (Wang et al., 1986; Faraci and Breese, 1993; Pepicelli et al., 2005). For instance the highly Ca^{2+} permeable NMDA receptors, expressed by cortical neurons (Monyer et al., 1994; Cauli et al., 2000), promote the release of PGE_2 (Pepicelli et al., 2005) and NO (Faraci and Breese, 1993).

Alike astrocytes, some GABA interneurons produce substances with vasocontractile properties, namely NPY (Abounader et al., 1995; Cauli et al., 2004) and SOM (Long et al., 1992; Cauli et al., 2004). Cortical neurons producing these vasoactive peptides are intimately associated with blood vessels through neuronal-astrocytic-vascular appositions described above (Chédotal et al., 1994b; Abounader and Hamel, 1997; Estrada and DeFelipe, 1998; Vaucher et al., 2000; Wang et al., 2005), and their receptors are expressed by smooth muscle cells and astrocytes (Chalmers et al., 1995; Bao et al., 1997; Abounader et al., 1999; Fahrenkrug et al., 2000; Cauli et al., 2004; Straub et al., 2006; Cahoy et al., 2008). This raises the intriguing question of whether or not astrocytes are intermediaries for neuron-derived vasoactive messengers or, alternatively, if the latter exert direct effects on the microcirculation.

TEMPORAL SEQUENCES IN THE RECRUITMENT OF NEURONS AND ASTROCYTES

It is widely admitted that an increase in intracellular Ca^{2+} (**Table 1**) is a required early event for the production and/or release of vasoactive messengers from neurons (Lauritzen, 2005) and astrocytes (Straub and Nelson, 2007). Examination of Ca^{2+} dynamics in these cell types could provide a clue to decipher their relative and temporal contribution to functional hyperemia. The general view is that rapid Ca^{2+} events reflect an entry following fast (10–12 ms) spiking response of neurons (Petersen et al., 2003) and/or activation of Ca^{2+} permeable ionotropic receptors, whereas slower dynamics are mainly driven by activation of metabotropic receptors leading to the release of Ca^{2+} from intracellular stores (Perea and Araque, 2005). Hence, cortical neurons, which express more frequently and abundantly ionotropic glutamate receptors (Monyer et al., 1994; Cauli et al., 2000) than astrocytes (Conti et al., 1997; Cahoy et al., 2008), are likely to be responsible for the majority of fast Ca^{2+} responses. In contrast, group I mGluRs ubiquitously expressed by cortical neurons (Baude et al., 1993; Cauli et al., 2000) and astrocytes (Porter and McCarthy, 1996) would be responsible for slower Ca^{2+} dynamics in both cell types. Consistent with this, in somatosensory or visual cortex, evoked Ca^{2+} events in neurons are virtually locked with sensory stimulations and precede those in astrocytes by a few seconds (Stosiek et al., 2003; Ohki et al., 2005; Wang et al., 2006; Schummers et al., 2008; Murayama et al., 2009), although a small proportion (~5%) of astrocytes can exhibit Ca^{2+} responses as fast as neurons (Winship et al., 2007).

Calcium uncaging in astrocytic endfeet *in vivo* showed that arterioles start to dilate ~500 ms after the onset of Ca^{2+} increase (Takano et al., 2006) indicating that synthesis, release and effects of vasodilatory messengers must be achieved within this time window. Since hemodynamic responses initiate ~600 ms after the onset of sensory stimulations (Kleinfeld et al., 1998; Devor et al., 2003), it appears that only cell types exhibiting fast evoked Ca^{2+} events (i.e., less than 100 ms) can account for the early phase of the hemodynamic response. Therefore, vasoactive messengers produced by neurons and, possibly, also by astrocytes with fast Ca^{2+} events, could explain this response (**Figure 1**).

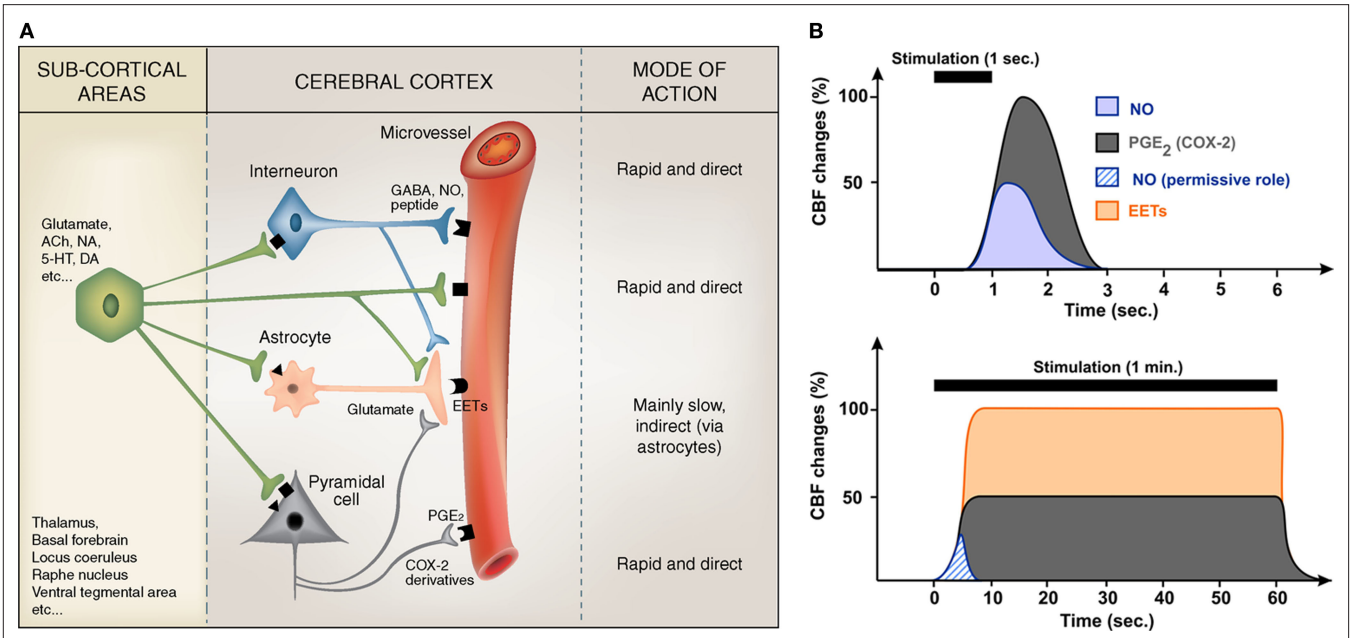

FIGURE 1 | Summary of the proposed regulation of cortical microvessels by pyramidal cells, GABA interneurons and astrocytes (A), and how their respective effects can temporally regulate CBF changes (B). (A) Subcortical afferents from a variety of brain areas target distinct populations of neurons in the cerebral cortex. These activated neuronal networks can either directly act on local microvessels, which are endowed with receptors (geometric forms on the vessel wall) for most neurotransmitters/neuromediators, or indirectly via astrocytes that act as intermediaries to both pyramidal cells and interneurons. Known direct vasoactive mediators released from pyramidal cells and interneurons correspond respectively to COX-2 derivatives like prostaglandin E2 (PGE2) and NO and, possibly, GABA, whereas astrocytes act chiefly by releasing dilatory EETs, an effect comparatively slow as opposed to that of NO and PGE2 (or other neurally released vasoactive molecules or peptides). The possibility that sub-cortical afferents directly contact and act upon cortical astrocytes or microvessels also has to be taken into consideration. Modified from Figure 3 in Hamel (2006). **(B)** Schematic representation of the relative and temporal contributions of selected vasoactive mediators produced by pyramidal cells (PGE2), interneurons (NO) and astrocytes (EETs), to the CBF response evoked by sensory stimulation (see **Table 1** for a more complete list). Brief stimulations (1 s) are more likely to involve neurally-derived mediators whereas sustained stimulation (1 min) are more susceptible to recruit astrocyte-derived messengers. NO being transiently released its contribution to CBF response during sustained stimulation is minor and could account for its permissive role.

MULTIPLICITY OF VASOACTIVE MESSENGERS: ARE THEY ALL REQUIRED?

In the cerebral cortex, none of the vasoactive messengers implicated in neurovascular coupling (Girouard and Iadecola, 2006), whether of neuronal or astroglial origin, can individually account for the hemodynamic response, as demonstrated by genetic invalidation (Ma et al., 1996; Niwa et al., 2000, 2001; Kitaura et al., 2007) or synthesis inhibition (Lindauer et al., 1999; Peng et al., 2002; Hoffmeyer et al., 2007; Leithner et al., 2010). When individually summed the inhibition of these messengers largely exceeds the expected value of 100% (Iadecola, 2004), which suggests that their kinetics of action, temporal and spatial recruitment must be carefully considered to elucidate their relative contributions. Alternatively, this may suggest that the activated pathways do not obligatorily operate independently from each other, and that, under certain circumstances, some may act like modulator rather than mediator of the perfusion responses, as documented for NO in the somatosensory cortex (Lindauer et al., 1999).

NO, one of the fastest diffusible (Wood and Garthwaite, 1994) vasodilator produced by a subset NPY-expressing interneurons (Dawson et al., 1991) is likely to represent an immediate early messenger of neurovascular coupling. Correspondingly, Shibuki's group showed that neuronal NO can account for up to 50% of the CBF response evoked by a brief (1 s) sensory stimulation (Kitaura et al., 2007). In contrast, others only found a permissive role for NO when long (1 min) stimulations were used (Lindauer et al., 1999; Liu et al., 2008). These differences likely reflect the fact that NO release is transient (Buerk et al., 2003) which can be explained by the NO scavenging effect of hemoglobin and/or by the adaptation of NO producing interneurons (Karagiannis et al., 2009). In contrast, vasodilatory prostanoids produced by COX-2, which is chiefly expressed by pyramidal cells (Yamagata et al., 1993; Breder et al., 1995), account for ~50% of the CBF response evoked by both sustained (Niwa et al., 2000) and brief stimulations (Kitaura et al., 2007). Consistent with an involvement of neuron-derived messengers in the early phase of neurovascular coupling, blockade of prostanoids and NO synthesis almost completely abolished hemodynamic responses evoked by brief sensory stimulations (Kitaura et al., 2007). During long lasting sensory stimulation, blockade of EETs synthesis (Peng et al., 2002) or their receptors (Liu et al., 2008) blocked about 50% of the blood flow response, demonstrating that EETs produced by astrocytes (Alkayed et al., 1996) are released during sustained neuronal activity.

Similarly, the local release of K^+ from astrocytic endfeet (Filosa et al., 2006) accounts for up to 50% of the CBF increase evoked by long lasting sensory stimulations (Girouard et al., 2010; Leithner et al., 2010) Surprisingly, combined blockade of NOS, COXs, p450 epoxygenase, BK channels and adenosine receptors (Leithner

et al., 2010) did not reach a total inhibition of the late phase of the hemodynamic response as expected from individual blockades (see above). This suggests that either multiple inhibition was incomplete or that other long lasting vasodilatory messengers are involved (Cauli et al., 2004), possibly VIP, which is contained within GABA interneurons targeted by thalamocortical afferents (Staiger et al., 1996) and released during sensory stimulation (Wang et al., 1985). Similarly vasodilatory messengers derived from the endothelium (Rosenblum, 1986) such as NO, prostacyclin (Faraci and Heistad, 1998) but also EETs (Campbell and Fleming, 2010), might be recruited under certain circumstances as it was reported for endothelial NO after muscarinic m5 receptor activation (Elhusseiny and Hamel, 2000; Yamada et al., 2001).

CURRENT UNDERSTANDING, FUTURE DIRECTIONS AND CLINICAL IMPLICATIONS

Current evidence suggests that neuronal and astroglial signals that transduce changes in neuronal activity into an integrated vascular response are highly dependent upon the neurotransmitter released by the incoming afferents, and strictly determined by the target neurons within the activated area. Particularly, depending on the nature of the afferent input (*i*) different neuronal or astroglial messengers, likely acting in sequence, mediate the hemodynamic changes, (*ii*) some recruited neurons release messengers that can directly alter blood vessel tone, (*iii*) others act by modulating neuronal and astroglial activity, and (*iv*) astrocytes may act as intermediaries for both excitatory and inhibitory neurotransmitters (**Figure 1**).

Probably due to the large diversity of cortical neurons (Ascoli et al., 2008), to our knowledge, no *in vivo* study has yet investigated Ca^{2+} dynamics in identified neurons producing vasoactive substances or the vascular effects of their stimulation. The growing development of transgenic mice expressing genetically encoded fluorescent reporters and/or optogenetic tools (Cardin et al., 2009; Sohal et al., 2009) in discrete subsets of cortical neurons (Heintz, 2001) together with the emergence of ultrafast multispectral imaging systems (Bouchard et al., 2009) that allow simultaneous monitoring of Ca^{2+} events and hemodynamics should help evaluate the contribution of specific neuronal types in neurovascular coupling. This should provide decisive conclusions on the temporal, spatial and extent of the neurally-driven hemodynamic alterations and how the latter can be interpreted in the context of brain imaging of normal or pathological physiology.

Indeed, since astrocytes appear as intermediary effectors in conveying signals for sustained hemodynamic responses, their alteration – primarily expressed by a state of chronic activation – in several chronic diseases of the central nervous system such as Alzheimer's disease or epilepsy, has to be seriously considered. Altered perfusion signals detected by fMRI, PET or DOI may represent astroglial dysfunction and not necessary impaired neuronal activity. Extending such thinking to the microcirculation itself, the functional endpoint in the intricate cascade of neuronal-astrocytic-vascular events evoked by increased brain activity, any diseases of the blood vessels themselves or alterations in their physical capacity to dilate or constrict, as seen in pathologies such as hypertension, diabetes, hypercholesterolemia and, even Alzheimer's disease (Iadecola, 2004; Zlokovic, 2008) would hinder the correct vascular response to totally normal neuronal activities. This further highlights that extreme caution should be applied to perfusion signals when making direct inference to altered neural activity (Schleim and Roiser, 2009; Ekstrom, 2010). Hence, a careful understanding of the neuronal circuitry at work will need to be interpreted in the context of a healthy or sick brain taking neuroinflammation and vascular diseases as possible confound factors.

ACKNOWLEDGMENTS

Bruno Cauli was supported by grants from the Human Frontier Science Program (HFSP) and the Centre National de la Recherche Scientifique (CNRS), and Edith Hamel from the Canadian Institutes of Health Research (CIHR).

REFERENCES

Abounader, R., Elhusseiny, A., Cohen, Z., Olivier, A., Stanimirovic, D., Quirion, R., and Hamel, E. (1999). Expression of neuropeptide Y receptors mRNA and protein in human brain vessels and cerebromicrovascular cells in culture. *J. Cereb. Blood Flow Metab.* 19, 155–163.

Abounader, R., and Hamel, E. (1997). Associations between neuropeptide Y nerve terminals and intraparenchymal microvessels in rat and human cerebral cortex. *J. Comp. Neurol.* 388, 444–453.

Abounader, R., Villemure, J. G., and Hamel, E. (1995). Characterization of neuropeptide Y (NPY) receptors in human cerebral arteries with selective agonists and the new Y1 antagonist BIBP 3226. *Br. J. Pharmacol.* 116, 2245–2250.

Alkayed, N. J., Birks, E. K., Narayanan, J., Petrie, K. A., Kohler-Cabot, A. E., and Harder, D. R. (1997). Role of P-450 arachidonic acid epoxygenase in the response of cerebral blood flow to glutamate in rats. *Stroke* 28, 1066–1072.

Alkayed, N. J., Narayanan, J., Gebremedhin, D., Medhora, M., Roman, R. J., and Harder, D. R. (1996). Molecular characterization of an arachidonic acid epoxygenase in rat brain astrocytes. *Stroke* 27, 971–979.

Arthurs, O. J., Williams, E. J., Carpenter, T. A., Pickard, J. D., and Boniface, S. J. (2000). Linear coupling between functional magnetic resonance imaging and evoked potential amplitude in human somatosensory cortex. *Neuroscience* 101, 803–806.

Ascoli, G. A., Alonso-Nanclares, L., Anderson, S. A., Barrionuevo, G., Benavides-Piccione, R., Burkhalter, A., Buzsáki, G., Cauli, B., Defelipe, J., Fairén, A., Feldmeyer, D., Fishell, G., Fregnac, Y., Freund, T. F., Gardner, D., Gardner, E. P., Goldberg, J. H., Helmstaedter, M., Hestrin, S., Karube, F., Kisvárday, Z. F., Lambolez, B., Lewis, D. A., Marin, O., Markram, H., Muñoz, A., Packer, A., Petersen, C. C., Rockland, K. S., Rossier, J., Rudy, B., Somogyi, P., Staiger, J. F., Tamas, G., Thomson, A. M., Toledo-Rodriguez, M., Wang, Y., West, D. C., and Yuste, R. (2008). Petilla terminology: nomenclature of features of GABAergic interneurons of the cerebral cortex. *Nat. Rev. Neurosci.* 9, 557–568.

Bao, L., Kopp, J., Zhang, X., Xu, Z. Q., Zhang, L. F., Wong, H., Walsh, J., and Hokfelt, T. (1997). Localization of neuropeptide Y Y1 receptors in cerebral blood vessels. *Proc. Natl. Acad. Sci. U.S.A.* 94, 12661–12666.

Baude, A., Nusser, Z., Roberts, J. D., Mulvihill, E., McIlhinney, R. A., and Somogyi, P. (1993). The metabotropic glutamate receptor (mGluR1 alpha) is concentrated at perisynaptic membrane of neuronal subpopulations as detected by immunogold reaction. *Neuron* 11, 771–787.

Berwick, J., Johnston, D., Jones, M., Martindale, J., Martin, C., Kennerley, A. J., Redgrave, P., and Mayhew, J. E. (2008). Fine detail of neurovascular coupling revealed by spatiotemporal analysis of the hemodynamic response to single whisker stimulation in rat barrel cortex. *J. Neurophysiol.* 99, 787–798.

Blanco, V. M., Stern, J. E., and Filosa, J. A. (2008). Tone-dependent vascular responses to astrocyte-derived signals. *Am. J. Physiol. Heart Circ. Physiol.* 294, H2855–H2863.

Bouchard, M. B., Chen, B. R., Burgess, S. A., and Hillman, E. M. (2009). Ultrafast multispectral optical imaging of cortical oxygenation, blood flow, and intracellular calcium dynamics. *Opt. Express* 17, 15670–15678.

Breder, C. D., Dewitt, D., and Kraig, R. P. (1995). Characterization of inducible

cyclooxygenase in rat brain. *J. Comp. Neurol.* 355, 296–315.

Buerk, D. G., Ances, B. M., Greenberg, J. H., and Detre, J. A. (2003). Temporal dynamics of brain tissue nitric oxide during functional forepaw stimulation in rats. *Neuroimage* 18, 1–9.

Cahoy, J. D., Emery, B., Kaushal, A., Foo, L. C., Zamanian, J. L., Christopherson, K. S., Xing, Y., Lubischer, J. L., Krieg, P. A., Krupenko, S. A., Thompson, W. J., and Barres, B. A. (2008). A transcriptome database for astrocytes, neurons, and oligodendrocytes: a new resource for understanding brain development and function. *J. Neurosci.* 28, 264–278.

Campbell, W. B., and Fleming, I. (2010). Epoxyeicosatrienoic acids and endothelium-dependent responses. *Pflugers Arch.* 459, 881–895.

Cardin, J. A., Carlen, M., Meletis, K., Knoblich, U., Zhang, F., Deisseroth, K., Tsai, L. H., and Moore, C. I. (2009). Driving fast-spiking cells induces gamma rhythm and controls sensory responses. *Nature* 459, 663–667.

Carmignoto, G., and Gomez-Gonzalo, M. (2009). The contribution of astrocyte signalling to neurovascular coupling. *Brain Res. Rev.* 63, 138–148.

Cauli, B., Audinat, E., Lambolez, B., Angulo, M. C., Ropert, N., Tsuzuki, K., Hestrin, S., and Rossier, J. (1997). Molecular and physiological diversity of cortical nonpyramidal cells. *J. Neurosci.* 17, 3894–3906.

Cauli, B., Porter, J. T., Tsuzuki, K., Lambolez, B., Rossier, J., Quenet, B., and Audinat, E. (2000). Classification of fusiform neocortical interneurons based on unsupervised clustering. *Proc. Natl. Acad. Sci. U.S.A.* 97, 6144–6149.

Cauli, B., Tong, X. K., Rancillac, A., Serluca, N., Lambolez, B., Rossier, J., and Hamel, E. (2004). Cortical GABA interneurons in neurovascular coupling: relays for subcortical vasoactive pathways. *J. Neurosci.* 24, 8940–8949.

Chalmers, D. T., Lovenberg, T. W., and De Souza, E. B. (1995). Localization of novel corticotropin-releasing factor receptor (CRF2) mRNA expression to specific subcortical nuclei in rat brain: comparison with CRF1 receptor mRNA expression. *J. Neurosci.* 15, 6340–6350.

Chédotal, A., Cozzari, C., Faure, M. P., Hartman, B. K., and Hamel, E. (1994a). Distinct choline acetyltransferase (ChAT) and vasoactive intestinal polypeptide (VIP) bipolar neurons project to local blood vessels in the rat cerebral cortex. *Brain Res.* 646, 181–193.

Chédotal, A., Umbriaco, D., Descarries, L., Hartman, B. K., and Hamel, E. (1994b). Light and electron microscopic immunocytochemical analysis of the neurovascular relationships of choline acetyltransferase and vasoactive intestinal polypeptide nerve terminals in the rat cerebral cortex. *J. Comp. Neurol.* 343, 57–71.

Cohen, Z., Bonvento, G., Lacombe, P., and Hamel, E. (1996). Serotonin in the regulation of brain microcirculation. *Prog. Neurobiol.* 50, 335–362.

Conti, F., Minelli, A., DeBiasi, S., and Melone, M. (1997). Neuronal and glial localization of NMDA receptors in the cerebral cortex. *Mol. Neurobiol.* 14, 1–18.

Dawson, T. M., Bredt, D. S., Fotuhi, M., Hwang, P. M., and Snyder, S. H. (1991). Nitric oxide synthase and neuronal NADPH diaphorase are identical in brain and peripheral tissues. *Proc. Natl. Acad. Sci. U.S.A.* 88, 7797–7801.

De Michele, M., Touzani, O., Foster, A. C., Fieschi, C., Sette, G., and McCulloch, J. (2005). Corticotropin-releasing factor: effect on cerebral blood flow in physiologic and ischaemic conditions. *Exp. Brain Res.* 165, 375–382.

Devor, A., Dunn, A. K., Andermann, M. L., Ulbert, I., Boas, D. A., and Dale, A. M. (2003). Coupling of total hemoglobin concentration, oxygenation, and neural activity in rat somatosensory cortex. *Neuron* 39, 353–359.

Devor, A., Tian, P., Nishimura, N., Teng, I. C., Hillman, E. M., Narayanan, S. N., Ulbert, I., Boas, D. A., Kleinfeld, D., and Dale, A. M. (2007). Suppressed neuronal activity and concurrent arteriolar vasoconstriction may explain negative blood oxygenation level-dependent signal. *J. Neurosci.* 27, 4452–4459.

Devor, A., Ulbert, I., Dunn, A. K., Narayanan, S. N., Jones, S. R., Andermann, M. L., Boas, D. A., and Dale, A. M. (2005). Coupling of the cortical hemodynamic response to cortical and thalamic neuronal activity. *Proc. Natl. Acad. Sci. U.S.A.* 102, 3822–3827.

Ekstrom, A. (2010). How and when the fMRI BOLD signal relates to underlying neural activity: the danger in dissociation. *Brain Res. Rev.* 62, 233–244.

Elhusseiny, A., and Hamel, E. (2000). Muscarinic–but not nicotinic–acetylcholine receptors mediate a nitric oxide-dependent dilation in brain cortical arterioles: a possible role for the M5 receptor subtype. *J. Cereb. Blood Flow Metab.* 20, 298–305.

Enager, P., Piilgaard, H., Offenhauser, N., Kocharyan, A., Fernandes, P., Hamel, E., and Lauritzen, M. (2009). Pathway-specific variations in neurovascular and neurometabolic coupling in rat primary somatosensory cortex. *J. Cereb. Blood Flow Metab.* 29, 976–986.

Estrada, C., and DeFelipe, J. (1998). Nitric oxide-producing neurons in the neocortex: morphological and functional relationship with intraparenchymal microvasculature. *Cereb. Cortex* 8, 193–203.

Fahrenkrug, J., Hannibal, J., Tams, J., and Georg, B. (2000). Immunohistochemical localization of the VIP1 receptor (VPAC1R) in rat cerebral blood vessels: relation to PACAP and VIP containing nerves. *J. Cereb. Blood Flow Metab.* 20, 1205–1214.

Faraci, F. M., and Breese, K. R. (1993). Nitric oxide mediates vasodilatation in response to activation of N-methyl-D-aspartate receptors in brain. *Circ. Res.* 72, 476–480.

Faraci, F. M., and Heistad, D. D. (1998). Regulation of the cerebral circulation: role of endothelium and potassium channels. *Physiol. Rev.* 78, 53–97.

Filosa, J. A., Bonev, A. D., Straub, S. V., Meredith, A. L., Wilkerson, M. K., Aldrich, R. W., and Nelson, M. T. (2006). Local potassium signaling couples neuronal activity to vasodilation in the brain. *Nat. Neurosci.* 9, 1397–1403.

Franceschini, M. A., Nissila, I., Wu, W., Diamond, S. G., Bonmassar, G., and Boas, D. A. (2008). Coupling between somatosensory evoked potentials and hemodynamic response in the rat. *Neuroimage* 41, 189–203.

Gallopin, T., Geoffroy, H., Rossier, J., and Lambolez, B. (2006). Cortical sources of CRF, NKB, and CCK and their effects on pyramidal cells in the neocortex. *Cereb. Cortex* 16, 1440–1452.

Girouard, H., Bonev, A. D., Hannah, R. M., Meredith, A., Aldrich, R. W., and Nelson, M. T. (2010). Astrocytic endfoot Ca2+ and BK channels determine both arteriolar dilation and constriction. *Proc. Natl. Acad. Sci. U.S.A.* 107, 3811–3816.

Girouard, H., and Iadecola, C. (2006). Neurovascular coupling in the normal brain and in hypertension, stroke, and Alzheimer disease. *J. Appl. Physiol.* 100, 328–335.

Gordon, G. R., Choi, H. B., Rungta, R. L., Ellis-Davies, G. C., and MacVicar, B. A. (2008). Brain metabolism dictates the polarity of astrocyte control over arterioles. *Nature*. 456, 745–749.

Gotoh, J., Kuang, T. Y., Nakao, Y., Cohen, D. M., Melzer, P., Itoh, Y., Pak, H., Pettigrew, K., and Sokoloff, L. (2001). Regional differences in mechanisms of cerebral circulatory response to neuronal activation. *Am. J. Physiol. Heart Circ. Physiol.* 280, H821–H829.

Hamel, E. (2006). Perivascular nerves and the regulation of cerebrovascular tone. *J. Appl. Physiol.* 100, 1059–1064.

Harder, D. R., Alkayed, N. J., Lange, A. R., Gebremedhin, D., and Roman, R. J. (1998). Functional hyperemia in the brain: hypothesis for astrocyte-derived vasodilator metabolites. *Stroke* 29, 229–234.

Heintz, N. (2001). BAC to the future: the use of bac transgenic mice for neuroscience research. *Nat. Rev. Neurosci.* 2, 861–870.

Hillman, E. M., Devor, A., Bouchard, M. B., Dunn, A. K., Krauss, G. W., Skoch, J., Bacskai, B. J., Dale, A. M., and Boas, D. A. (2007). Depth-resolved optical imaging and microscopy of vascular compartment dynamics during somatosensory stimulation. *Neuroimage* 35, 89–104.

Hoffmeyer, H. W., Enager, P., Thomsen, K. J., and Lauritzen, M. J. (2007). Nonlinear neurovascular coupling in rat sensory cortex by activation of transcallosal fibers. *J. Cereb. Blood Flow Metab.* 27, 575–587.

Iadecola, C. (2004). Neurovascular regulation in the normal brain and in Alzheimer's disease. *Nat. Rev. Neurosci.* 5, 347–360.

Jones, E. G. (1970). On the mode of entry of blood vessels into the cerebral cortex. *J. Anat.* 106, 507–520.

Kacem, K., Lacombe, P., Seylaz, J., and Bonvento, G. (1998). Structural organization of the perivascular astrocyte endfeet and their relationship with the endothelial glucose transporter: a confocal microscopy study. *Glia* 23, 1–10.

Karagiannis, A., Gallopin, T., David, C., Battaglia, D., Geoffroy, H., Rossier, J., Hillman, E. M., Staiger, J. F., and Cauli, B. (2009). Classification of NPY-expressing neocortical interneurons. *J. Neurosci.* 29, 3642–3659.

Kitaura, H., Uozumi, N., Tohmi, M., Yamazaki, M., Sakimura, K., Kudoh, M., Shimizu, T., and Shibuki, K. (2007). Roles of nitric oxide as a vasodilator in neurovascular coupling of mouse somatosensory cortex. *Neurosci. Res.* 59, 160–171.

Kleinfeld, D., Mitra, P. P., Helmchen, F., and Denk, W. (1998). Fluctuations and stimulus-induced changes in blood flow observed in individual capillaries in layers 2 through 4 of rat neocortex. *Proc. Natl. Acad. Sci. U.S.A.* 95, 15741–15746.

Kocharyan, A., Fernandes, P., Tong, X. K., Vaucher, E., and Hamel, E. (2008). Specific subtypes of cortical GABA interneurons contribute to the neurovascular coupling response to basal forebrain stimulation. *J. Cereb. Blood Flow Metab.* 28, 221–231.

Kubota, Y., Hattori, R., and Yui, Y. (1994). Three distinct subpopulations of GABAergic neurons in rat frontal

agranular cortex. *Brain Res.* 649, 159–173.

Lauritzen, M. (2005). Reading vascular changes in brain imaging: is dendritic calcium the key? *Nat. Rev. Neurosci.* 6, 77–85.

Lauritzen, M., and Gold, L. (2003). Brain function and neurophysiological correlates of signals used in functional neuroimaging. *J. Neurosci.* 23, 3972–3980.

Lecrux, C., Kocharyan, A., Fernandes, P., Vaucher, E., and Hamel, E. (2009). "GABA, glutamate and astroglial mediators in the cortical neurovascular coupling response to basal forebrain cholinergic input," in *Brain'09*, Chicago. June 29–July 3, 2009. Abstract # 59.

Leithner, C., Royl, G., Offenhauser, N., Fuchtemeier, M., Kohl-Bareis, M., Villringer, A., Dirnagl, U., and Lindauer, U. (2010). Pharmacological uncoupling of activation induced increases in CBF and CMRO(2). *J. Cereb. Blood Flow Metab.* 30, 311–322.

Lindauer, U., Leithner, C., Kaasch, H., Rohrer, B., Foddis, M., Fuchtemeier, M., Offenhauser, N., Steinbrink, J., Royl, G., Kohl-Bareis, M., and Dirnagl, U. (2010). Neurovascular coupling in rat brain operates independent of hemoglobin deoxygenation. *J. Cereb. Blood Flow Metab.* 30, 757–768.

Lindauer, U., Megow, D., Matsuda, H., and Dirnagl, U. (1999). Nitric oxide: a modulator, but not a mediator, of neurovascular coupling in rat somatosensory cortex. *Am. J. Physiol.* 277, H799–H811.

Liu, X., Li, C., Falck, J. R., Roman, R. J., Harder, D. R., and Koehler, R. C. (2008). Interaction of nitric oxide, 20-HETE, and EETs during functional hyperemia in whisker barrel cortex. *Am. J. Physiol. Heart Circ. Physiol.* 295, H619–H631.

Logothetis, N. K., Pauls, J., Augath, M., Trinath, T., and Oeltermann, A. (2001). Neurophysiological investigation of the basis of the fMRI signal. *Nature* 412, 150–157.

Long, J. B., Rigamonti, D. D., Dosaka, K., Kraimer, J. M., and Martinez-Arizala, A. (1992). Somatostatin causes vasoconstriction, reduces blood flow and increases vascular permeability in the rat central nervous system. *J. Pharmacol. Exp. Ther.* 260, 1425–1432.

Lu, H., Patel, S., Luo, F., Li, S. J., Hillard, C. J., Ward, B. D., and Hyde, J. S. (2004). Spatial correlations of laminar BOLD and CBV responses to rat whisker stimulation with neuronal activity localized by Fos expression. *Magn. Reson. Med.* 52, 1060–1068.

Ma, J., Ayata, C., Huang, P. L., Fishman, M. C., and Moskowitz, M. A. (1996). Regional cerebral blood flow response to vibrissal stimulation in mice lacking type I NOS gene expression. *Am. J. Physiol.* 270, H1085–H1090.

Meier, S. D., Kafitz, K. W., and Rose, C. R. (2008). Developmental profile and mechanisms of GABA-induced calcium signaling in hippocampal astrocytes. *Glia* 56, 1127–1137.

Metea, M. R., and Newman, E. A. (2006). Glial cells dilate and constrict blood vessels: a mechanism of neurovascular coupling. *J. Neurosci.* 26, 2862–2870.

Monyer, H., Burnashev, N., Laurie, D. J., Sakmann, B., and Seeburg, P. H. (1994). Developmental and regional expression in the rat brain and functional properties of four NMDA receptors. *Neuron* 12, 529–540.

Morrison, J. H., Magistretti, P. J., Benoit, R., and Bloom, F. E. (1984). The distribution and morphological characteristics of the intracortical VIP-positive cell: an immunohistochemical analysis. *Brain Res.* 292, 269–282.

Mulligan, S. J., and MacVicar, B. A. (2004). Calcium transients in astrocyte endfeet cause cerebrovascular constrictions. *Nature* 431, 195–199.

Murayama, M., Perez-Garci, E., Nevian, T., Bock, T., Senn, W., and Larkum, M. E. (2009). Dendritic encoding of sensory stimuli controlled by deep cortical interneurons. *Nature* 457, 1137–1141.

Niessing, J., Ebisch, B., Schmidt, K. E., Niessing, M., Singer, W., and Galuske, R. A. (2005). Hemodynamic signals correlate tightly with synchronized gamma oscillations. *Science* 309, 948–951.

Nilsson, M., Eriksson, P. S., Ronnback, L., and Hansson, E. (1993). GABA induces Ca2+ transients in astrocytes. *Neuroscience* 54, 605–614.

Niwa, K., Araki, E., Morham, S. G., Ross, M. E., and Iadecola, C. (2000). Cyclooxygenase-2 contributes to functional hyperemia in whisker-barrel cortex. *J. Neurosci.* 20, 763–770.

Niwa, K., Haensel, C., Ross, M. E., and Iadecola, C. (2001). Cyclooxygenase-1 participates in selected vasodilator responses of the cerebral circulation. *Circ. Res.* 88, 600–608.

Northington, F. J., Matherne, G. P., and Berne, R. M. (1992). Competitive inhibition of nitric oxide synthase prevents the cortical hyperemia associated with peripheral nerve stimulation. *Proc. Natl. Acad. Sci. U.S.A.* 89, 6649–6652.

Ohki, K., Chung, S., Ch'ng, Y. H., Kara, P., and Reid, R. C. (2005). Functional imaging with cellular resolution reveals precise micro-architecture in visual cortex. *Nature* 433, 597–603.

Paspalas, C. D., and Papadopoulos, G. C. (1996). Ultrastructural relationships between noradrenergic nerve fibers and non-neuronal elements in the rat cerebral cortex. *Glia* 17, 133–146.

Peng, X., Carhuapoma, J. R., Bhardwaj, A., Alkayed, N. J., Falck, J. R., Harder, D. R., Traystman, R. J., and Koehler, R. C. (2002). Suppression of cortical functional hyperemia to vibrissal stimulation in the rat by epoxygenase inhibitors. *Am. J. Physiol. Heart Circ. Physiol.* 283, H2029–H2037.

Pepicelli, O., Fedele, E., Berardi, M., Raiteri, M., Levi, G., Greco, A., jmone-Cat, M. A., and Minghetti, L. (2005). Cyclo-oxygenase-1 and -2 differently contribute to prostaglandin E2 synthesis and lipid peroxidation after *in vivo* activation of N-methyl-D-aspartate receptors in rat hippocampus. *J. Neurochem.* 93, 1561–1567.

Peppiatt, C. M., Howarth, C., Mobbs, P., and Attwell, D. (2006). Bidirectional control of CNS capillary diameter by pericytes. *Nature* 443, 700–704.

Perea, G., and Araque, A. (2005). Properties of synaptically evoked astrocyte calcium signal reveal synaptic information processing by astrocytes. *J. Neurosci.* 25, 2192–2203.

Petersen, C. C., Grinvald, A., and Sakmann, B. (2003). Spatiotemporal dynamics of sensory responses in layer 2/3 of rat barrel cortex measured *in vivo* by voltage-sensitive dye imaging combined with whole-cell voltage recordings and neuron reconstructions. *J. Neurosci.* 23, 1298–1309.

Porter, J. T., and McCarthy, K. D. (1996). Hippocampal astrocytes in situ respond to glutamate released from synaptic terminals. *J. Neurosci.* 16, 5073–5081.

Powers, W. J., Hirsch, I. B., and Cryer, P. E. (1996). Effect of stepped hypoglycemia on regional cerebral blood flow response to physiological brain activation. *Am. J. Physiol.* 270, H554–H559.

Rancillac, A., Rossier, J., Guille, M., Tong, X. K., Geoffroy, H., Amatore, C., Arbault, S., Hamel, E., and Cauli, B. (2006). Glutamatergic control of microvascular tone by distinct gaba neurons in the cerebellum. *J. Neurosci.* 26, 6997–7006.

Rosenblum, W. I. (1986). Endothelial dependent relaxation demonstrated *in vivo* in cerebral arterioles. *Stroke* 17, 494–497.

Schleim, S., and Roiser, J. P. (2009). FMRI in translation: the challenges facing real-world applications. *Front. Hum. Neurosci.* 3:63. doi: 10.3389/neuro.09.063.2009

Schummers, J., Yu, H., and Sur, M. (2008). Tuned responses of astrocytes and their influence on hemodynamic signals in the visual cortex. *Science* 320, 1638–1643.

Scremin, O. U., Rovere, A. A., Raynald, A. C., and Giardini, A. (1973). Cholinergic control of blood flow in the cerebral cortex of the rat. *Stroke* 4, 233–239.

Serrano, A., Haddjeri, N., Lacaille, J. C., and Robitaille, R. (2006). GABAergic network activation of glial cells underlies hippocampal heterosynaptic depression. *J. Neurosci.* 26, 5370–5382.

Shmuel, A., Augath, M., Oeltermann, A., and Logothetis, N. K. (2006). Negative functional MRI response correlates with decreases in neuronal activity in monkey visual area V1. *Nat. Neurosci.* 9, 569–577.

Shmuel, A., Yacoub, E., Pfeuffer, J., Van de Moortele, P. F., Adriany, G., Hu, X., and Ugurbil, K. (2002). Sustained negative BOLD, blood flow and oxygen consumption response and its coupling to the positive response in the human brain. *Neuron* 36, 1195–1210.

Sohal, V. S., Zhang, F., Yizhar, O., and Deisseroth, K. (2009). Parvalbumin neurons and gamma rhythms enhance cortical circuit performance. *Nature* 459, 698–702.

Somogyi, P., Hodgson, A. J., Smith, A. D., Nunzi, M. G., Gorio, A., and Wu, J. Y. (1984). Different populations of GABAergic neurons in the visual cortex and hippocampus of cat contain somatostatin- or cholecystokinin-immunoreactive material. *J. Neurosci.* 4, 2590–2603.

Staiger, J. F., Zilles, K., and Freund, T. F. (1996). Innervation of VIP-immunoreactive neurons by the ventroposteromedial thalamic nucleus in the barrel cortex of the rat. *J. Comp. Neurol.* 367, 194–204.

Stark, J. A., Davies, K. E., Williams, S. R., and Luckman, S. M. (2006). Functional magnetic resonance imaging and c-Fos mapping in rats following an anorectic dose of m-chlorophenylpiperazine. *Neuroimage* 31, 1228–1237.

Stosiek, C., Garaschuk, O., Holthoff, K., and Konnerth, A. (2003). *In vivo* two-photon calcium imaging of neuronal networks. *Proc. Natl. Acad. Sci. U.S.A.* 100, 7319–7324.

Straub, S. V., Bonev, A. D., Wilkerson, M. K., and Nelson, M. T. (2006). Dynamic inositol trisphosphate-mediated calcium signals within astrocytic endfeet underlie vasodilation of cerebral arterioles. *J. Gen. Physiol.* 128, 659–669.

Straub, S. V., and Nelson, M. T. (2007). Astrocytic calcium signaling: the information currency coupling neu-

ronal activity to the cerebral microcirculation. *Trends Cardiovasc. Med.* 17, 183–190.

Takano, T., Tian, G. F., Peng, W., Lou, N., Libionka, W., Han, X., and Nedergaard, M. (2006). Astrocyte-mediated control of cerebral blood flow. *Nat. Neurosci.* 9, 260–267.

Vaucher, E., and Hamel, E. (1995). Cholinergic basal forebrain neurons project to cortical microvessels in the rat: electron microscopic study with anterogradely transported *Phaseolus vulgaris* leucoagglutinin and choline acetyltransferase immunocytochemistry. *J. Neurosci.* 15, 7427–7441.

Vaucher, E., Tong, X. K., Cholet, N., Lantin, S., and Hamel, E. (2000). GABA neurons provide a rich input to microvessels but not nitric oxide neurons in the rat cerebral cortex: a means for direct regulation of local cerebral blood flow. *J. Comp. Neurol.* 421, 161–171.

Wang, H., Hitron, I. M., Iadecola, C., and Pickel, V. M. (2005). Synaptic and vascular associations of neurons containing cyclooxygenase-2 and nitric oxide synthase in rat somatosensory cortex. *Cereb. Cortex* 15, 1250–1260.

Wang, J. Y., Yaksh, T. L., and Go, V. L. (1985). Studies on the *in vivo* release of vasoactive intestinal polypeptide (VIP) from the cerebral cortex: effects of cortical, brainstem and somatic stimuli. *Brain Res.* 326, 317–334.

Wang, J. Y., Yaksh, T. L., Harty, G. J., and Go, V. L. (1986). Neurotransmitter modulation of VIP release from cat cerebral cortex. *Am. J. Physiol.* 250, R104–R111.

Wang, X., Lou, N., Xu, Q., Tian, G. F., Peng, W. G., Han, X., Kang, J., Takano, T., and Nedergaard, M. (2006). Astrocytic Ca(2+) signaling evoked by sensory stimulation *in vivo*. *Nat. Neurosci.* 9, 816–823.

Winship, I. R., Plaa, N., and Murphy, T. H. (2007). Rapid astrocyte calcium signals correlate with neuronal activity and onset of the hemodynamic response *in vivo*. *J. Neurosci.* 27, 6268–6272.

Wolf, T., Lindauer, U., Villringer, A., and Dirnagl, U. (1997). Excessive oxygen or glucose supply does not alter the blood flow response to somatosensory stimulation or spreading depression in rats. *Brain Res.* 761, 290–299.

Wood, J., and Garthwaite, J. (1994). Models of the diffusional spread of nitric oxide: implications for neural nitric oxide signalling and its pharmacological properties. *Neuropharmacology* 33, 1235–1244.

Yaksh, T. L., Wang, J. Y., and Go, V. L. (1987). Cortical vasodilatation produced by vasoactive intestinal polypeptide (VIP) and by physiological stimuli in the cat. *J. Cereb. Blood Flow Metab.* 7, 315–326.

Yamada, M., Lamping, K. G., Duttaroy, A., Zhang, W., Cui, Y., Bymaster, F. P., McKinzie, D. L., Felder, C. C., Deng, C. X., Faraci, F. M., and Wess, J. (2001). Cholinergic dilation of cerebral blood vessels is abolished in M(5) muscarinic acetylcholine receptor knockout mice. *Proc. Natl. Acad. Sci. U.S.A.* 98, 14096–14101.

Yamagata, K., Andreasson, K. I., Kaufmann, W. E., Barnes, C. A., and Worley, P. F. (1993). Expression of a mitogen-inducible cyclooxygenase in brain neurons: regulation by synaptic activity and glucocorticoids. *Neuron* 11, 371–386.

Zlokovic, B. V. (2008). The blood-brain barrier in health and chronic neurodegenerative disorders. *Neuron* 57, 178–201.

Zonta, M., Angulo, M. C., Gobbo, S., Rosengarten, B., Hossmann, K. A., Pozzan, T., and Carmignoto, G. (2003). Neuron-to-astrocyte signaling is central to the dynamic control of brain microcirculation. *Nat. Neurosci.* 6, 43–50.

Conflict of Interest Statement: The authors declare that the research was conducted in the absence of any commercial or financial relationships that could be construed as a potential conflict of interest.

Received: 18 March 2010; paper pending published: 15 April 2010; accepted: 26 May 2010; published online: 23 June 2010.

Citation: Cauli B and Hamel E (2010) Revisiting the role of neurons in neurovascular coupling. Front. Neuroenerg. ***2****:9. doi: 10.3389/fnene.2010.00009*

frontiers in
NEUROENERGETICS

PERSPECTIVE ARTICLE
published: 21 July 2010
doi: 10.3389/fnene.2010.00017

Functional neuroimaging: a physiological perspective

Ai-Ling Lin[1,2]*, Jia-Hong Gao[3], Timonthy Q. Duong[1,4,5,6,7] and Peter T. Fox[1,2,4,6,7]

[1] Research Imaging Institute, University of Texas Health Science Center, San Antonio, TX, USA
[2] Department of Psychiatry, University of Texas Health Science Center, San Antonio, TX, USA
[3] Department of Psychiatry and Behavioral Neuroscience, and Brain Research Imaging Center, University of Chicago, Chicago, IL, USA
[4] Department of Physiology, University of Texas Health Science Center, San Antonio, TX, USA
[5] Department of Ophthalmology, University of Texas Health Science Center, San Antonio, TX, USA
[6] South Texas Veterans Health Care System, Department of Veterans Affairs, San Antonio, TX, USA
[7] Department of Radiology, University of Texas Health Science Center, San Antonio, TX, USA

Edited by:
Anna Devor,
University of California San Diego, USA

Reviewed by:
Richard Buxton,
University of California San Diego, USA
Joseph Mandeville, Massachusetts General Hospital, USA
David Boas, Massachusetts General Hospital, USA; Massachusetts Institute of Technology, USA; Harvard Medical School, USA

***Correspondence:**
Ai-Ling Lin, Research Imaging Center, School of Medicine, The University of Texas Health Science Center, 7703 Floyd Curl Drive, San Antonio, TX 78229, USA.
e-mail: lina3@uthscsa.edu

Metabolic physiology and functional neuroimaging have played important and complementary roles over the past two decades. In particular, investigations of the mechanisms underlying functional neuroimaging signals have produced fundamental new insights into hemodynamic and metabolic regulation. However, controversies were also raised as regards the metabolic pathways (oxidative vs. non-oxidative) for meeting the energy demand and driving the increases in cerebral blood flow (CBF) during brain activation. In a recent study, with the concurrent functional MRI-MRS measurements, we found that task-evoked energy demand was predominately met through oxidative metabolism (approximately 98%), despite a small increase in cerebral metabolic rate of oxygen (12–17%). In addition, the task-induced increases in CBF were most likely mediated by anaerobic glycolysis rather than oxygen demand. These observations and others from functional neuroimaging support the activation-induced neuron-astrocyte interactions portrayed by the astrocyte-neuron lactate shuttle model. The concurrent developments of neuroimaging methods and metabolic physiology will also pave the way for the future investigation of cerebral hemodynamics and metabolism in disease states.

Keywords: functional neuroimaging, CBF, $CMRO_2$, ANLS model, neurodegenerative disorders

The quest to understand the functional organization of the brain has occupied mankind for more than a century. The close relationship between cerebral blood flow (CBF) and brain function was first observed in the late nineteenth century by the Italian physiologist, Mosso (1881). Mosso recorded pulsations from the forearm and the brain, showing stronger brain pulsations during cognitive events, such as hearing the bells from his church and performing mental arithmetic (Posner and Raichle, 1994). These studies suggested that measurement of CBF might be an important way to assess brain function during mental activity. Roy and Sherrington (1890), two distinguished British physiologists, further characterized the close relationship between brain function and CBF. They attributed task-induced vasodilation to an increased demand for cerebral metabolism in response to neuronal activity. The Roy–Sherrington principle has been interpreted to mean that CBF changes reflect a tight coupling between cellular energy requirements and vascular delivery of glucose and oxygen. Roy and Sherrington's observation of focally increased blood flow during brain functional activation has been replicated thousands of times by a myriad of techniques, beginning early in the last century (Fulton, 1928).

Whole-brain measurements of CBF, oxygen metabolism (cerebral metabolic rate of oxygen, $CMRO_2$) and glucose metabolism (CMR_{Glc}) also began appearing in the early part of the twentieth century (Schmidt and Kety, 1947; Landau et al., 1955; Sokoloff et al., 1977). Collectively, these studies demonstrated that: the brain's resting-state energy demand is high (although the human brain is only 2% of body's weight, it consumes 20% of the body's oxygen and 25% body's glucose; Sokoloff et al., 1977); resting-state brain energy production is provided almost exclusively by glucose oxidation (approximately 90%; Siesjo, 1978); and, basal CBF and $CMRO_2$ are tightly coupled across brain regions (A linear CBF-$CMRO_2$ relationship was observed with a slope of approximately 0.97; Fox and Raichle, 1986).

Studies using emerging, pre-imaging radiotracer techniques convincingly demonstrated that brain blood flow is dramatically increased by increased partial pressure of carbon dioxide ($PaCO_2$) and by decreased partial pressure of oxygen (PaO_2), a form of cerebrovascular autoregulation (Kety and Schmidt, 1948). These observations provided strong support for the Roy and Sherrington hypothesis, as CO_2 is the primary "chemical product" of glucose oxidation, and extended the hypothesis to include substrate ($[O_2]$) availability as a potent vascular regulator. With the advent of autoradiographic methods (Schmidt and Kety, 1947; Landau et al., 1955; Sokoloff et al., 1977) and non-invasive radiotracer imaging methods (Reivich et al., 1979; Raichle et al., 1983), blood flow and glucose consumption could be measured regionally, allowing the Roy and Sherrington hypothesis to be further explored. As expected, task performance reliably elicited large, highly focal increases in CBF (Fox et al., 1988) and CMR_{Glc} (Phelps and Mazziotta, 1985; Fox et al., 1988). The observed increases in CBF and CMR_{Glc} were similar in magnitude, typically in the range of 30–50%, apparently supporting the Roy and Sherrington hypothesis that neural activity focally increased metabolic rate and thereby increased blood flow.

The first imaging-based measurements of $CMRO_2$ during task performance were reported in the early 1980s, using 15-O positron emission tomography (PET) (Frackowiak et al., 1980; Mintun et al., 1984). In two different brain systems (visual and somatosensory), Fox et al., observed that task-induced increases in $CMRO_2$ were much lower than those in CBF or CMR_{Glc} (Fox and Raichle, 1986; Fox et al., 1988). The $CMRO_2$ shortfall during focal neuronal activation, in fact, caused a local oxygen surplus, with the oxygen extraction fraction (OEF) falling from a resting value of approximately 40% to a task-state value of approximately 20%. These findings clearly contradicted the Roy and Sherrington hypothesis. Since glucose can be metabolized by either oxidative or non-oxidative (i.e, lactate-producing) pathways and since the increase of $CMRO_2$ was minimal, Fox and colleagues suggested that: (i) the glucose is predominately metabolized by anaerobic glycolysis; (ii) the energy demand associated with neuronal activation is small (as opposed to resting-state demand) and glycolysis alone may provide the energy needed for the transient changes in brain activity; and (iii) CBF response must be regulated by factors other than oxidative metabolism and total energy demand. The observation that the stimulus-evoked increase in glucose consumption observed with PET is at least partially non-oxidative has been confirmed with ^{1}H NMR spectroscopic (MRS) measurements of tissue lactate concentration [Lac] (Prichard et al., 1991; Frahm et al., 1996). The increase in lactate production (i.e., non-oxidative metabolism) was found in later studies to be a modulator of CBF increase (Mintun et al., 2004). Such uncoupling of CBF and $CMRO_2$ is the basis for the blood oxygenation level-dependent (BOLD) functional MRI (fMRI) contrast (Kwong et al., 1992; Ogawa et al., 1992). These PET and MRS observations raise a general question: does the evoked neuronal activity drive oxidative or non-oxidative metabolism?

To further clarify this issue, we performed concurrent fMRI and ^{1}H MRS measurements to identify the relationship between task-evoked increases in CBF, $CMRO_2$, [Lac] and ATP production (J_{ATP}) during graded visual stimulation (4, 8, and 16 Hz; 4 min for each condition) (Lin et al., 2010). Percent changes (%Δ) in CBF, $CMRO_2$ and [Lac] varied with frequency, with %ΔCBF and %Δ[Lac] peaking at 8 Hz, while %Δ$CMRO_2$ reached a maximum at 4 Hz (Vafaee and Gjedde, 2000; Lin et al., 2008). The magnitude of %ΔCBF (57.1–65.1%) and %Δ[Lac] (31.3–50.0%) were much larger than that of %Δ$CMRO_2$ (12.2–17.0%). As a result, %ΔCBF was tightly coupled with lactate production rate (J_{Lac}; [Lac] divided by stimulation period; $r = 0.91$, $P < 0.001$) (Gjedde, 1997; Lin et al., 2010), but negatively correlated with %Δ$CMRO_2$ ($r = -0.64$, $P = 0.024$). J_{ATP}, determined with changes in $CMRO_2$ and J_{Lac} by a stoichiometric relationship, was found predominately contributed by oxidative metabolism (approximately 98%) at each stimulus condition. Consequently, %ΔJ_{ATP} was linearly correlated to %Δ$CMRO_2$ ($r = 1.00$, $P < 0.001$). Similar findings were also reported by PET studies (Gjedde, 1997). The fMRI-MRS observations confirm that (i) CBF response to neuronal activity is driven more by anaerobic glycolysis, rather than oxygen demand, and (ii) energy demand is predominately met through oxidative metabolic pathway regardless the $CMRO_2$ increases are much lower than those of [Lac].

The collective evidence from the functional imaging literature (PET, fMRI, and MRS) has forced the development of alternatives to the Roy–Sherrington hypothesis. Of these, the astrocyte-neuron lactate shuttle (ANLS) model is the most conceptually evolved and widely accepted (Pellerin and Magistretti, 1994). The ANLS model posits a cooperation between neurons and astrocytes in meeting the activation-induced needs both for energy production and for neurotransmitter production. Upon neuronal firing, glucose is taken up by both neurons and astrocytes. The majority of the glucose is taken up by the astrocytes and the remainder by neurons. Glucose metabolism in neurons is small but entirely aerobic, to support neurotransmission (Brand, 2005; Hyder et al., 2006). Astrocytic glucose consumption, on the other hand, is large but much less energetically efficient by virtue of being predominately anaerobic. Astrocytic glycolysis (2 ATP) is used to support Na^+/K^+ ion pumping and glutamate(Glu)-glutamine(Gln) conversion. Lactate generated by astrocytic glycolysis is eventually transported to neurons as fuel, but with some loss into the circulation, which increases hyperemia (Mintun et al., 2004; Hyder et al., 2006).

The fMRI-MRS observations, described above (Lin et al., 2010), are in line with the ANLS model. First, CBF increases are not regulated by oxidative metabolism. %ΔCBF and %Δ$CMRO_2$ are negatively correlated. In contrast, non-oxidative metabolism is a more likely candidate. %ΔCBF and %ΔJ_{Lac} are positively correlated. But other factors (e.g., Ca^{2+}, K^+ and adenosine signaling pathway) may also play a role. Second, the increases in CMR_{Glc} are for purposes other than energy demand, e.g., for astrocyte-mediated neurotransmitter recycling, with the evidence being that increases in [Lac] are far more than that of $CMRO_2$. Third, the two metabolic pathways (oxidative and non-oxidative) are co-existent, dissociable, and serve different purposes in maintaining neuronal functions during visual stimulation. Oxidative metabolism is predominately neuronal and supports ATP production for the release of neurotransmitters; with the evidence being that the energy demand (J_{ATP}) was predominately (approximately 98%) met through oxidative metabolism in all stimulus conditions. Non-oxidative metabolism, on the other hand, mainly occurs in astrocytes to support the Glu-Gln conversion and lactogenesis-mediated hyperemia. Since astrocytic lactate is eventually taken up into the tricarboxylic acid cycle as a fuel substrate by neurons, it has to be pointed out that oxidative metabolism is expected to increase as neuronal activation continues. In support of this formulation, prolonged visual stimulation (>20 min) has been reported to induce gradually rising levels of $CMRO_2$ and gradually decreasing CMR_{Glc}, J_{Lac} and CBF under a high-frequency stimulation (e.g., 8 Hz) (Prichard et al., 1991; Gjedde and Marrett, 2001; Mintun et al., 2002; Vlassenko et al., 2006; Lin et al., 2009). Consequently, %ΔCBF and %Δ$CMRO_2$ were re-coupled (the coupling ratio, n = %ΔCBF/%Δ$CMRO_2$, decreased from 8 to 2) as stimulation continued. However, inconsistent observations have also been reported in prior fMRI studies (Hoge et al., 1999) that the coupling ratio already reached to 2–3 during acute, transient visual stimulation (approximately 20–60 s). The discrepancy could be due to the stimulation frequency or to the modeling strategy used in the studies. For example, a low coupling ratio (2–3) was observed with low frequencies (e.g., 1–4 Hz), while a high ratio (6–10) was observed with high frequencies, during short-term visual stimulation (20 s to 6 min) (Lin et al., 2008). As a result, ratio of 2–3 is

expected if low frequencies are used. Details of the discrepancy regarding modeling strategy can be found in our previous publication (Lin et al., 2009).

Metabolic physiology and functional neuroimaging are highly complementary fields of inquiry. An in-depth understanding of neuronal metabolic physiology will enhance the interpretation of functional neuroimaging research, and vice versa. The evidence above addressed the cooperation of functional neuroimaging and metabolic physiology in understanding the coordination between neurovasculature, neurons and astrocytes during *steady-state*. For future studies, more effort should be invested in exploring their coordination during *transient state*. For instance, the dynamic mechanism of the BOLD signal may be explained by the asynchrony of task-induced neuronal and glial responses, as follows. Because neuronal responses precede those of astrocytes (approximately 4 s; Schummers et al., 2008), the increase in oxidative metabolism precedes that of non-oxidative metabolism (Kasischke et al., 2004) and, consequently, the CBF response. $CMRO_2$ increases that precede CBF increases result in the "initial dip" of the BOLD signal (Menon et al., 1995; Malonek and Grinvald, 1996). Astrocytic activity, following the neuronal activity, results in a significant increase in CBF and, consequently, the increase in BOLD signal. On the other hand, the post-stimulus "undershoot" phenomenon (the negative signal following the cessation of stimulation; Buxton et al., 1998; Mandeville et al., 1999; Lu et al., 2004) observed in BOLD and CBF signals contradicts the notion of "watering the entire garden for the sake of one thirsty flower" (Malonek and Grinvald, 1996), but may pave a way for further understanding the temporal relationship between the neuronal and astrocytic activities after the stimulus termination.

Further developments in neuroimaging techniques and metabolic theories are crucial for future research. As regards neuroimaging techniques, it would be important to determine quantitative ATP production, $CMRO_2$ and CMR_{Glc} using other MR methods, such as Phosphorous-31, Oxygen-17 and Carbon-13 MRS, respectively. In addition, direct observations of the differential roles of neurons and astrocytes associated with ATP-$CMRO_2$ and CBF-lactate couples would be significant. Concurrent MRI, MRS and optical imaging measurements may help achieve this goal. As regards metabolic physiology, theories of neurovascular and neurometabolic mechanisms are evolving. Some issues proposed by the ANLS model need further investigation. For example, whether the lactate transferred to neurons as a fuel substrate is from astrocytic or neuronal activity, and whether lactate is the preferential substrates of neurons for neurotransmission-related energy needs is still under debate. Further, whether the small increase in $CMRO_2$ during neuronal activation is due to the small fraction of glucose undergoing oxidative phosphorylation or due to other reasons is controversial. Brand proposed that ATP can be synthesized by means of deactivation of mitochondrial uncoupling protein (UCP) to elevate oxidative phosphorylation without raising oxygen consumption, which may provide an alternative explanation for relative low levels of $CMRO_2$ changes during brain activation (Brand, 2005).

The concurrent developments of neuroimaging methods and physiological theories will also pave the way for the investigation of cerebral hemodynamics and metabolism in disease states. For example, the most well-documented example of a mitochondrial-failure-based neurodegenerative disorder is Huntington's disease (HD) (Jenkins et al., 1993; Koroshetz et al., 1997). Nonetheless, Powers et al. (2007) recently reported PET evidence that the well-documented regional decreases in CMR_{Glc} associated with HD are not accompanied by comparable decreases in $CMRO_2$, which led them to conclude that HD is not a mitochondrial disorder. (We would argue, however, that this conclusion is not yet warranted, as Powers' study did not include a challenge, in which neuronal activation was used to elevate MRO_2 above resting levels). Similar neuroimaging approaches may apply to other neurodegenerative disorders, including Alzheimer's disease (AD), Down's Syndrome-related AD and Parkinson's disease (PD), to investigate possible underlying metabolic dysfunctions of those diseases. In addition to human studies, animal models also play an essential role since they allow more flexibility for neurovascular-metabolic coupling investigations of both normal and disease states. For example, treatments of rapamycin (a drug developed as an immunosuppressant) and calorie restriction are currently only available for animals in aging and AD studies (Van Remmen et al., 2001; Richardson, 2009; Spilman et al., 2010). Neuroimaging methods can help clarify the pathophysiology of these diseases and identify the mechanism of action of these effective treatments (in aging and AD) by defining the correlation between changes in CBF, $CMRO_2$, CMR_{Glc} and ATP.

In summary, we addressed our perspective on the interplay of metabolic physiology and functional neuroimaging over the past century; the replacement of the Roy–Sherrington principle by the ANLS model; and, the future direction of the developments of neuroimaging techniques and physiological theories. These developments should provide the bases for predicting causes and consequences of deregulation in neurological diseases, including neurodegenerative disorders, in the near future.

ACKNOWLEDGMENTS

This work was supported by National Institute of Health (NIH) and UTHSCSA General Clinical Research Center (GCRC) grants M01 RR01346.

REFERENCES

Brand, M. D. (2005). The efficiency and plasticity of mitochondrial energy transduction. *Biochem. Soc. Trans.* 33, 897–904.

Buxton, R. B., Wong, E. C., and Frank, L. R. (1998). Dynamics of blood flow and oxygen metabolism during brain activation: the balloon model. *Magn. Reson. Med.* 39, 855–864.

Fox, P. T., and Raichle, M. E. (1986). Focal physiological uncoupling of cerebral blood flow and oxidative metabolism during somatosensory stimulation in human subjects. *Proc. Natl. Acad. Sci. U.S.A.* 83, 1140–1144.

Fox, P. T., Raichle, M. E., Mintun, M. A., and Dence, C. (1988). Nonoxidative glucose consumption during focal physiologic neural activity. *Science* 241, 462–464.

Frackowiak, R. S., Lenzi, G. L., Jones, T., and Heather, J. D. (1980). Quantitative measurement of regional cerebral blood flow and oxygen metabolism in man using 15O and positron emission tomography: theory, procedure, and normal values. *J. Comput. Assist. Tomogr.* 4, 727–736.

Frahm, J., Kruger, G., Merboldt, K. D., and Kleinschmidt, A. (1996). Dynamic uncoupling and recoupling of perfusion and oxidative metabolism during focal brain activation in man. *Magn. Reson. Med.* 35, 143–148.

Fulton, J. (1928). Observation upon the vascularity of the human occipital lobe during visual activity. *Brain* 51, 310–320.

Gjedde, A. (1997). "The relation between brain function and cerebral blood flow

and metabolism," in *Cerebrovascular Disease*, eds H. Bajter and L. Caplan (Philadelphia, PA: Lippincott-Raven Publishers), 23–40.

Gjedde, A., and Marrett, S. (2001). Glycolysis in neurons, not astrocytes, delays oxidative metabolism of human visual cortex during sustained checkerboard stimulation in vivo. *J. Cereb. Blood Flow Metab.* 21, 1384–1392.

Hoge, R. D., Atkinson, J., Gill, B., Crelier, G. R., Marrett, S., and Pike, G. B. (1999). Investigation of BOLD signal dependence on cerebral blood flow and oxygen consumption: the deoxyhemoglobin dilution model. *Magn. Reson. Med.* 42, 849–863.

Hyder, F., Patel, A. B., Gjedde, A., Rothman, D. L., Behar, K. L., and Shulman, R. G. (2006). Neuronal-glial glucose oxidation and glutamatergic-GABAergic function. *J. Cereb. Blood Flow Metab.* 26, 865–877.

Jenkins, B. G., Koroshetz, W. J., Beal, M. F., and Rosen, B. R. (1993). Evidence for impairment of energy metabolism in vivo in Huntington's disease using localized 1H NMR spectroscopy. *Neurology* 43, 2689–2695.

Kasischke, K. A., Vishwasrao, H. D., Fisher, P. J., Zipfel, W. R., and Webb, W. W. (2004). Neural activity triggers neuronal oxidative metabolism followed by astrocytic glycolysis. *Science* 305, 99–103.

Kety, S. S., and Schmidt, C. F. (1948). The effects of altered arterial tensions of carbon dioxide and oxygen on cerebral blood flow and cerebral oxygen consumption of normal young men. *J. Clin. Invest.* 27, 484–492.

Koroshetz, W. J., Jenkins, B. G., Rosen, B. R., and Beal, M. F. (1997). Energy metabolism defects in Huntington's disease and effects of coenzyme Q10. *Ann. Neurol.* 41, 160–165.

Kwong, K. K., Belliveau, J. W., Chesler, D. A., Goldberg, I. E., Weisskoff, R. M., Poncelet, B. P., Kennedy, D. N., Hoppel, B. E., Cohen, M. S., Turner, R., Cheng, H. M., Brady, T. J., and Rosen, B. R. (1992). Dynamic magnetic resonance imaging of human brain activity during primary sensory stimulation. *Proc. Natl. Acad. Sci. U.S.A.* 89, 5675–5679.

Landau, W. M., Freygang, W. H. J., Roland, L. P., Sokoloff, L., and Kety, S. S. (1955). The local circulation of the living brain: values in the unanesthetized and anesthetized cat. *Trans. Am. Neurol. Assoc.* 80, 125–129.

Lin, A.-L., Fox, P. T., Hardies, J., Duong, T. Q., and Gao, J.-H. (2010). Nonlinear coupling between cerebral blood flow, oxygen consumption, and ATP production in human visual cortex. *Proc. Natl. Acad. Sci. U.S.A.* 107, 8446–8451.

Lin, A.-L., Fox, P. T., Yang, Y., Lu, H., Tan, L.-H., and Gao, J.-H. (2009). Time-dependent correlation of cerebral blood flow with oxygen metabolism in activated human visual cortex as measured by fMRI. *Neuroimage* 44, 16–22.

Lin, A.-L., Fox, P. T., Yang, Y., Lu, H., Tan, L.-H., and Gao, J.-H. (2008). Evaluation of MRI models in the measurement of CMRO2 and its relationship with CBF. *Magn. Reson. Med.* 60, 380–389.

Lu, H., Golay, X., Pekar, J. J., and Van Zijl, P. C. (2004). Sustained poststimulus elevation in cerebral oxygen utilization after vascular recovery. *J. Cereb. Blood Flow Metab.* 24, 764–770.

Malonek, D., and Grinvald, A. (1996). Interactions between electrical activity and cortical microcirculation revealed by imaging spectroscopy: implications for functional brain mapping. *Science* 272, 551–554.

Mandeville, J. B., Marota, J. J., Ayata, C., Zaharchuk, G., Moskowitz, M. A., Rosen, B. R., and Weisskoff, R. M. (1999). Evidence of a cerebrovascular postarteriole windkessel with delayed compliance. *J. Cereb. Blood Flow Metab.* 19, 679–689.

Menon, R. S., Ogawa, S., Hu, X., Strupp, J. P., Anderson, P., and Ugurbil, K. (1995). BOLD based functional MRI at 4 Tesla includes a capillary bed contribution: echo-planar imaging correlates with previous optical imaging using intrinsic signals. *Magn. Reson. Med.* 33, 453–459.

Mintun, M. A., Raichle, M. E., Martin, W. R., and Herscovitch, P. (1984). Brain oxygen utilization measured with O-15 radiotracers and positron emission tomography. *J. Nucl. Med.* 25, 177–187.

Mintun, M. A., Vlassenko, A. G., Rundle, M. M., and Raichle, M. E. (2004). Increased lactate/pyruvate ratio augments blood flow in physiologically activated human brain. *Proc. Natl. Acad. Sci. U.S.A.* 101, 659–664.

Mintun, M. A., Vlassenko, A. G., Shulman, G. L., and Snyder, A. Z. (2002). Time-related increase of oxygen utilization in continuously activated human visual cortex. *Neuroimage* 16, 531–537.

Mosso, A. (1881). *Ueber den Kreislauf des Blutes im menschlichen Gehirn*. Leipzig: Verlag von Veit.

Ogawa, S., Tank, D. W., Menon, R., Ellermann, J. M., Kim, S. G., Merkle, H., and Ugurbil, K. (1992). Intrinsic signal changes accompanying sensory stimulation: functional brain mapping with magnetic resonance imaging. *Proc. Natl. Acad. Sci. U.S.A.* 89, 5951–5955.

Pellerin, L., and Magistretti, P. J. (1994). Glutamate uptake into astrocytes stimulates aerobic glycolysis: a mechanism coupling neuronal activity to glucose utilization. *Proc. Natl. Acad. Sci. U.S.A.* 91, 10625–10629.

Phelps, M. E., and Mazziotta, J. C. (1985). Positron emission tomography: human brain function and biochemistry. *Science* 228, 799–809.

Posner, M. I., and Raichle, M. E. (1994). *Images of Mind*. New York: Scientific American Library.

Powers, W. J., Videen, T. O., Markham, J., McGee-Minnich, L., Antenor-Dorsey, J. V., Hershey, T., and Perlmutter, J. S. (2007). Selective defect of in vivo glycolysis in early huntington's disease striatum. *Proc. Natl. Acad. Sci. U.S.A.* 104, 2945–2949.

Prichard, J., Rothman, D., Novotny, E., Petroff, O., Kuwabara, T., Avison, M., Howseman, A., Hanstock, C., and Shulman, R. (1991). Lactate rise detected by 1H NMR in human visual cortex during physiologic stimulation. *Proc. Natl. Acad. Sci. U.S.A.* 88, 5829–5831.

Raichle, M. E., Martin, W. R., Herscovitch, P., Mintun, M. A., and Markham, J. (1983). Brain blood flow measured with intravenous H2(15)O. II. Implementation and validation. *J. Nucl. Med.* 24, 790–798.

Reivich, M., Kuhl, D., Wolf, A., Greenberg, J., Phelps, M., Ido, T., Casella, V., Fowler, J., Hoffman, E., Alavi, A., Som, P., and Sokoloff, L. (1979). The [18F]fluorodeoxyglucose method for the measurement of local cerebral glucose utilization in man. *Circ. Res.* 44, 127–137.

Richardson, R. B. (2009). Ionizing radiation and aging: rejuvenating an old idea. *Aging* 1, 887–902.

Roy, C. S., and Sherrington, C. S. (1890). On the regulation of the blood-supply of the brain. *J. Physiol. (Lond.)* 11, 85–108.

Schmidt, C. F., and Kety, S. S. (1947). Recent studies of cerebral blood flow and cerebral metabolism in man. *Trans. Assoc. Am. Physicians* 60, 52–58.

Schummers, J., Yu, H., and Sur, M. (2008). Tuned responses of astrocytes and their influence on hemodynamic signals in the visual cortex. *Science* 320, 1638–1643.

Siesjo, B. (1978). *Brain Energy Metabolism*. New York: Wiley, 101–110.

Sokoloff, L., Reivich, M., Kennedy, C., Des Rosiers, M. H., Patlak, C. S., Pettigrew, K. D., Sakurada, O., and Shinohara, M. (1977). The [14C] deoxyglucose method for the measurement of local cerebral glucose utilization: theory, procedure, and normal values in the conscious and anesthetized albino rat. *J. Neurochem.* 28, 897–916.

Spilman, P., Podlutskaya, N., Hart, M. J., Debnath, J., Gorostiza, O., Bredesen, D., Richardson, A., Strong, R., and Galvan, V. (2010). Inhibition of mTOR by rapamycin abolishes cognitive deficits and reduces amyloid-beta levels in a mouse model of Alzheimer's disease. *PLoS ONE* 5, e9979. doi: 10.1371/journal.pone.0009979.

Vafaee, M. S., and Gjedde, A. (2000). Model of blood-brain transfer of oxygen explains nonlinear flow-metabolism coupling during stimulation of visual cortex. *J. Cereb. Blood Flow Metab.* 20, 747–754.

Van Remmen, H., Guo, Z., and Richardson, A. (2001). The anti-ageing action of dietary restriction. *Novartis Found. Symp.* 235, 221–230.

Vlassenko, A. G., Rundle, M. M., Raichle, M. E., and Mintun, M. A. (2006). Regulation of blood flow in activated human brain by cytosolic NADH/NAD + ratio. *Proc. Natl. Acad. Sci. U.S.A.* 103, 1964–1969.

Conflict of Interest Statement: The authors declare that the research was conducted in the absence of any commercial or financial relationships that could be construed as a potential conflict of interest.

Received: 10 February 2010; paper pending published: 15 April 2010; accepted: 01 July 2010; published online: 21 July 2010.
Citation: Lin A-L, Gao J-H, Duong TQ and Fox PT (2010) Functional neuroimaging: a physiological perspective. Front. Neuroenerg. ***2****:17. doi: 10.3389/fnene.2010.00017*

frontiers in
NEUROENERGETICS

HYPOTHESIS AND THEORY ARTICLE
published: 21 May 2010
doi: 10.3389/fnene.2010.00005

Pericyte-mediated regulation of capillary diameter: a component of neurovascular coupling in health and disease

Nicola B. Hamilton, David Attwell and Catherine N. Hall*

Department of Neuroscience, Physiology and Pharmacology, University College London, London, UK

Edited by:
Anna Devor, University of California San Diego, USA

Reviewed by:
Eric Newman, University of Minnesota, USA
Ray Koehler, Johns Hopkins University, USA

****Correspondence:***
Catherine N. Hall, Department of Neuroscience, Physiology and Pharmacology, University College London, Gower St, London, WC1E 6BT, UK.
e-mail: catherine.hall@ucl.ac.uk

Because regional blood flow increases in association with the increased metabolic demand generated by localized increases in neural activity, functional imaging researchers often assume that changes in blood flow are an accurate read-out of changes in underlying neural activity. An understanding of the mechanisms that link changes in neural activity to changes in blood flow is crucial for assessing the validity of this assumption, and for understanding the processes that can go wrong during disease states such as ischaemic stroke. Many studies have investigated the mechanisms of neurovascular regulation in arterioles but other evidence suggests that blood flow regulation can also occur in capillaries, because of the presence of contractile cells, pericytes, on the capillary wall. Here we review the evidence that pericytes can modulate capillary diameter in response to neuronal activity and assess the likely importance of neurovascular regulation at the capillary level for functional imaging experiments. We also discuss evidence suggesting that pericytes are particularly sensitive to damage during pathological insults such as ischaemia, Alzheimer's disease and diabetic retinopathy, and consider the potential impact that pericyte dysfunction might have on the development of therapeutic interventions and on the interpretation of functional imaging data in these disorders.

Keywords: pericyte, capillary, neurovascular coupling, brain

PERICYTES AS CONTRACTILE CELLS

Pericytes are found on almost all capillaries, as well as on small arterioles and venules. They are small cells located on the outside of the vessel, between the endothelial cell layer and the parenchyma. They are separated from the parenchyma by the basal lamina, a thin layer of which also interposes between the pericyte and endothelial cells (red layer in **Figure 1B**; Frank et al., 1987). Pericytes vary morphologically depending on the vascular bed and position along the arterio-venous axis, but in general send out primary projections along the vessel in each direction from the soma, from which secondary and even tertiary processes project around the vessel (**Figure 1A**; Shepro and Morel, 1993). They seem to have important roles in a range of functions, including angiogenesis, vessel stabilization, endothelial cell regulation and maintenance of the blood-brain barrier (Hirschi and D'Amore, 1996; Lai and Kuo, 2005). Pericytes also exhibit macrophage-like activity (Thomas, 1999) and may be multipotent precursors for several different cell types, forming neurons and glia in the CNS and forming liver and skin cells in those tissues (Dore-Duffy et al., 2006, 2008). Long ago, however, the perivascular location and morphology of pericytes led to the suggestion that they might be contractile cells, involved in regulation of capillary blood flow in response to vasoactive agents and neural activity (Dore, 1923). It has taken over 100 years to show that this is indeed the case, and important questions still remain as to the precise role of these cells in the co-ordination of changes in blood flow in response to altered neural activity.

The morphology and location of pericytes provided the first clues that they might have a role in blood flow regulation. Other aspects of CNS pericyte anatomy lend further support to this idea. In the central nervous system, there are more pericytes per endothelial cell than in other areas of the body (Frank et al., 1987; Shepro and Morel, 1993), suggesting that pericytes might play a particularly important role in the nervous system, where regional blood flow control is particularly important. Neuronal terminals which contain dopamine (Favard et al., 1990; Krimer et al., 1998), GABA (Gragera et al., 1993), vasoactive intestinal peptide (VIP; Benagiano et al., 1996), acetylcholine (Arneric et al., 1988) and nitric oxide (NO; Roufail et al., 1995) are closely apposed to capillaries and pericytes suggesting that, as for arterioles (Sato and Sato, 1990; Krimer et al., 1998; Cauli et al., 2004), capillary blood flow could be modulated by neuronal input (**Figure 1B**). For arterioles, glutamate released during neuronal activity plays a critical role in signaling to the blood vessel a requirement for increased local blood flow (Faraci and Breese, 1993; Mathiesen et al., 1998). Astrocytes are a major target for this glutamate signal, metabotropic glutamate receptor activation producing Ca^{2+} rises in their end-feet, which surround arterioles. This stimulates the production of vasoactive metabolites of arachidonic acid [prostaglandin E_2 (PGE_2) and epoxyeicosotrienoic acids (EETs)] which diffuse to the arteriolar smooth muscle and produce vasodilation (Zonta et al., 2003; Metea and Newman, 2006; Gordon et al., 2008). Astrocyte end-feet surround capillaries to a similar extent as they do arterioles (perhaps even more densely; Maynard et al., 1957) and so are in a prime position to transmit signals from neurons to capillaries (**Figure 1B**).

Anatomical evidence also supports the view that pericytes are contractile. Localized constrictions can be observed in corrosion casts of cat spinal cord capillaries, where pericytes express the smooth muscle-specific isoform of actin (αSMA: Toribatake et al., 1997). A subpopulation of retinal and brain pericytes also express αSMA, with stronger expression in pericytes on capillaries which

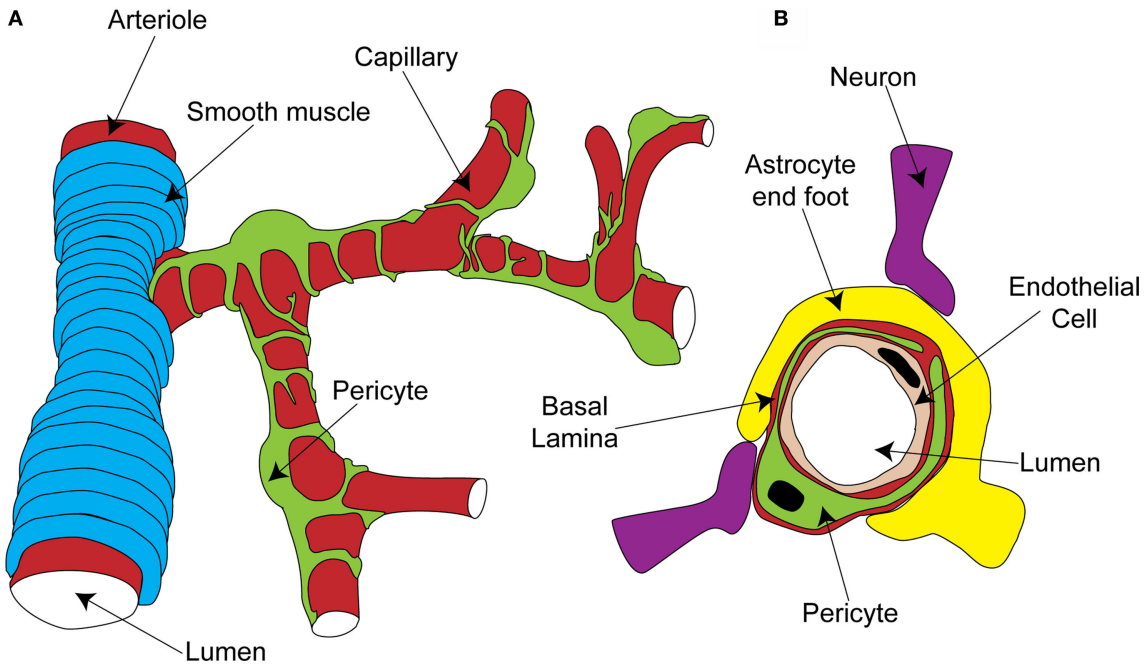

FIGURE 1 | Organisation of the capillary neurovascular unit. (A) Rings of smooth muscle encircle arterioles, while pericytes send processes along and around capillaries, without fully covering the vessel. **(B)** Pericytes are located outside the endothelial cells and are separated from them and the parenchyma by a layer of basal lamina. In the parenchyma, astrocyte end-feet and neuronal terminals are closely associated with the capillary.

branch directly from arterioles and venules, than in pericytes on mid-capillary regions (Nehls and Drenckhahn, 1991), though αSMA is expressed in some of these mid-capillary cells (Bandopadhyay et al., 2001). In peripheral tissues, other contractile proteins such as tropomyosin have been found to follow the same pattern of expression as αSMA (Joyce et al., 1985), suggesting that this will be the case in the brain as well. Electron micrographs of brain pericytes reveal that they contain microfilaments resembling actin- and myosin-containing muscle fibers (Le Beux and Willemot, 1978; Ho, 1985), and immunohistochemistry shows that activation of endothelin-1 (ET-1) receptors to raise the calcium concentration in cultured pericytes produces alignment of F-actin and intermediate filaments, which coincides with constriction (Dehouck et al., 1997). Pericytes do not express exactly the same contractile machinery as smooth muscle, however. For example, they lack the calcium-binding protein calponin, which regulates contractile function in smooth muscle cells (Bandopadhyay et al., 2001).

Much evidence that these pericyte muscle fibers are functional comes from studies of cultured retinal pericytes, in which pericyte surface area or the degree of wrinkling of the silicone surface on which the cells are grown serve as an indication of pericyte tone. Cultured pericytes constrict (or increase wrinkling) in response to some endothelial-derived vasoactive agents, such as ET-1, thromboxane A_2 and angiotensin II (Dodge et al., 1991; Matsugi et al., 1997a), but dilate in response to others, such as prostacyclin (PGI2; Dodge et al., 1991). Consistent with potential neural, as well as endothelial, control of pericyte tone, catecholamines (which are present in neurons innervating capillaries) can modulate cultured pericyte tone, with serotonin, histamine and noradrenaline all constricting cultured pericytes (Kelley et al., 1988; Markhotina et al., 2007). Other vasoactive molecules which are produced in neurons dilate cultured pericytes, such as VIP (Markhotina et al., 2007), NO (Haefliger et al., 1994), which can be produced by neurons or the endothelium, or adenosine (Matsugi et al., 1997b), which is a breakdown product of ATP and is produced during conditions of high metabolic demand. Adenosine dilates arterioles as well and has been proposed as a messenger by which increased blood flow could be directed to areas of increased metabolic demand (Dirnagl et al., 1994). Cultured pericytes also dilate in response to a more acid extracellular pH (Chen and Anderson, 1997), which is another consequence of increased energy use (Chesler and Kaila, 1992), making the pH sensitivity of pericyte tone a further potential mechanism for balancing capillary blood flow with metabolic demand.

Studies on cultured pericytes therefore support a contractile role for these cells, but it seems that expression of contractile proteins may be increased by culturing as *in situ* only a subpopulation of pericytes express αSMA (Nehls and Drenckhahn, 1991; Bandopadhyay et al., 2001), while in culture all pericytes can stain positive for muscle-specific actins (Herman and D'Amore, 1985). Such differences in αSMA expression might be paralleled by changes in expression levels of other proteins, reducing the potential physiological relevance of these studies. However, many of the findings from cultured CNS pericytes have been replicated using acute *ex vivo* preparations (e.g. tissue slices, freshly isolated microvessels or whole mount retinae). For example, angiotensin II and endothelin I both constrict retinal pericytes *in situ* (Schonfelder et al., 1998) and extracellular decreases in pH dilate them (Reber et al., 2003), while noradrenaline constricts pericytes in cerebellar slices (Peppiatt et al., 2006). In addition NO generates hyperpolarizing currents that would be expected to relax pericytes on freshly isolated retinal capillaries

(Sakagami et al., 2001a). Some differences with cultured cells have been observed, however, as histamine dilates rather than constricts retinal pericytes *in situ* (Schonfelder et al., 1998). This study also found that bradykinin and cholinergic agonists dilated retinal pericytes. Other new discoveries from using acute tissue preparations include the constriction of retinal pericytes to GABA antagonists (Peppiatt et al., 2006) and, particularly interestingly, the dilation of cerebellar pericytes to glutamate (Peppiatt et al., 2006). This finding suggests that active neurons could signal to capillaries in the same manner as to arterioles, with glutamate generating vasoactive molecules such as NO, PGE_2 or EETs in neurons or astrocytes which instruct pericytes to dilate capillaries and increase blood flow.

The suggestion from cultured pericytes that the metabolic state of the tissue might be important in their response (Chen and Anderson, 1997; Matsugi et al., 1997b) is backed up by acute preparations, as adenosine, a product of ATP breakdown, generates hyperpolarizing currents that would be expected to relax pericytes (Li and Puro, 2001). Additionally, lactate, the production of which is increased by neuronal activity, produces a constriction of retinal pericytes on isolated capillaries in high oxygen (when presumably there is no need for an increased oxygen supply) but a dilation in low oxygen (Yamanishi et al., 2006), when an increased oxygen supply may be required. Similarly, PDGF-B, the release of which from endothelial cells is critical for pericyte function (Bjarnegard et al., 2004), produces a constriction of retinal pericytes in control conditions but a dilation during ischaemia (Sakagami et al., 2001b). In conditions of metabolic demand, ATP is released from neurons both physiologically and when the energy supply is disrupted during ischaemia (Fields and Burnstock, 2006). In high oxygen, extracellular ATP constricts pericytes on retinal capillaries when *in situ* (Peppiatt et al., 2006) or when vessels are isolated from surrounding neural tissue (Kawamura et al., 2003), but it is not known whether this is switched to a dilation at low oxygen concentrations (as occurs for the effect of glutamate on arterioles: Gordon et al., 2008).

Potentially therefore, pericytes could couple neural activity to increased capillary blood flow *via* two broad mechanisms: either neural activity could directly produce vasoactive molecules (e.g. NO, VIP, PGE_2, noradrenaline) to modulate pericyte tone, or the decrease in oxygen level and increase in lactate and adenosine levels produced by the increased energy use by active neurons could directly dilate pericytes and increase nutrient supply. A recent *in vivo* study suggests, however, that at least changes in oxygen level in the tissue do not directly regulate neurovascular coupling, because when cortex was kept at a high oxygen concentration by perfusion with hyperbaric oxygen, blood flow responses to forepaw stimulation or cortical spreading depression were not affected (Lindauer et al., 2010). If glucose rather than oxygen is limiting for ATP production, however, the metabolic state of the tissue could still feed back to regulate blood flow *via* changes in the levels of metabolites such as lactate or adenosine. Furthermore, oxygen-dependent regulation may still occur in conditions of ischaemia or hypoxia.

MECHANISMS OF REGULATION OF PERICYTE TONE

What are the pathways by which pericytes can respond to neurotransmitters and vasoactive agents with an alteration in their contractile tone?

In general, smooth muscle contraction can be triggered by an elevated intracellular calcium concentration, leading to calcium- and calmodulin-dependent activation of myosin light chain kinase (MLCK, **Figure 2A**). This generates contraction by phosphorylating myosin light chain (MLC) and prompting its interaction with αSMA (Webb, 2003). Conversely, relaxation of smooth muscle is favoured by low calcium levels and decreased MLCK activity, and by the action of myosin light chain phosphatase (MLCP; in its active, unphosphorylated form), which decreases the phosphorylation of MLC and therefore inhibits its interaction with αSMA (Webb, 2003).

PERICYTE CONSTRICTION

Like for vascular smooth muscle cells, pericyte contraction is controlled by the intracellular calcium concentration (Sakagami et al., 1999, 2001a; Sugiyama et al., 2005). For example, the constriction that is produced by electrically stimulating pericytes is blocked by removing extracellular calcium (Peppiatt et al., 2006). Vasoconstrictors and vasodilators such as ET-1 and NO have been used to elucidate, by patch clamp experiments, the electrophysiological changes that control intracellular calcium levels in cultured or freshly isolated retinal pericytes. Some vasoconstrictors are thought to bring about an intracellular calcium rise by depolarizing the cell membrane from the resting voltage, usually between −35 and −60 mV, to a voltage which activates L-type voltage-operated calcium channels (VOCCs; see **Figure 2A**; Sakagami et al., 1999, 2001a). Binding of several vasoconstrictors, such as ET-1 (Kawamura et al., 2002), insulin-like growth factor-1 (IGF-1; Sakagami et al., 1999 and PDGF-B; Sakagami et al., 2001b), to their receptors leads to activation of non-specific cation channels (NSCs) that depolarize the cells and trigger calcium entry through VOCCs (**Figure 2A**). Calcium entry also opens calcium-activated chloride (Cl_{Ca}) channels, which, due to the high intracellular chloride concentration of pericytes, allow chloride to leave the cell, producing a further depolarization allowing further activation of VOCCs (Kawamura et al., 2002). Voltage clamp recordings show that Cl_{Ca} channels in pericytes open transiently and repetitively (Sakagami et al., 1999). This characteristic may help to maximise the calcium influx through VOCCs, as desensitization of the VOCCs is minimized by reducing the time each channel is open (Sakagami et al., 1999). VOCCs are also thought to be activated by the depolarization caused by ATP binding to $P2X_7$ receptors, which are themselves calcium-permeable (**Figure 2A**; Sugiyama et al., 2005). ATP also increases the intracellular calcium concentration *via* $P2Y_4$ receptor activation (Kawamura et al., 2003).

In smooth muscle, vasoactive stimuli (e.g. ET-1) can increase constriction by modifying the phosphorylation state of MLCP, *via* pathways that can include Rho kinase (**Figure 2A**; Hilgers and Webb, 2005). On phosphorylation, MLCP becomes inactive and is unable to remove the phosphate from the MLC (Webb, 2003). This pathway also affects pericyte function as over-expression of Rho-GTPase in pericytes leads to increased constriction (shown by wrinkling of the silicon upon which they were cultured), while inhibition of Rho kinase reduces constriction (Kutcher et al., 2007).

As well as the transient events discussed above, neurons also induce more long-term changes in pericytes by release of glutamate, subsequent activation of astrocyte metabotropic glutamate

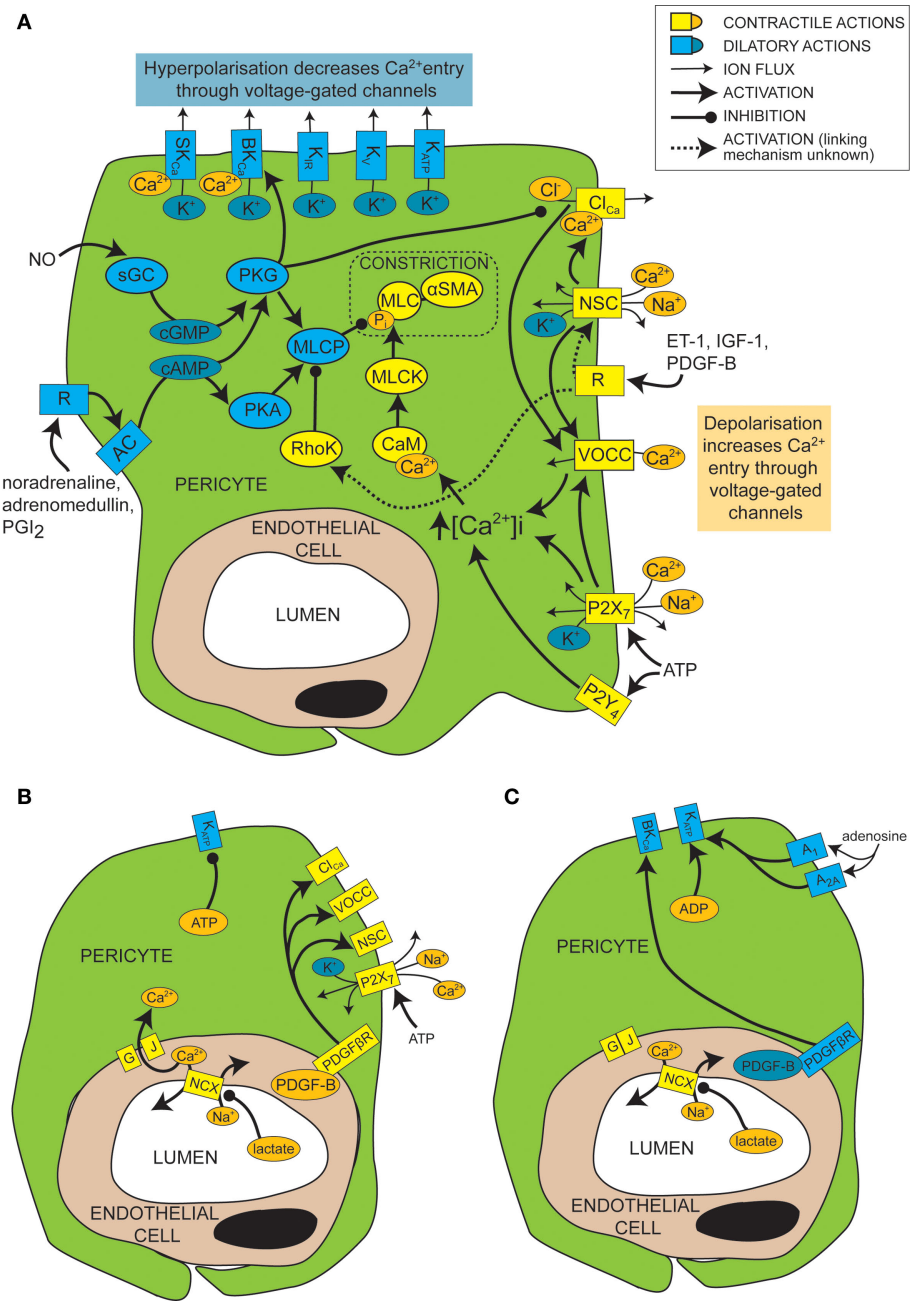

FIGURE 2 | Mechanisms of control of capillary tone. (A) Molecular mechanisms that link vasoactive molecules acting on receptors (labelled "R") to pericyte constriction (yellow and orange shapes) or dilation (blue shapes). Rectangles are membrane proteins, while ovals are cytosolic species. SK_{Ca}, small conductance, calcium-activated potassium channel; BK_{Ca}, large conductance, calcium-activated potassium channel; K_{IR}, inwardly rectifying potassium channel; K_V, voltage-gated potassium channel; K_{ATP}, ATP-sensitive potassium channel; Cl_{Ca}, calcium-activated chloride channel; NSC, non-specific cation channels; R, ligand-binding receptor; VOCC, voltage-operated calcium channel; MLC, myosin light chain; αSMA, alpha smooth muscle actin; MLCK, myosin light chain kinase; CaM, calmodulin; RhoK, Rho kinase; sGC, soluble guanylyl cyclase; PKG, protein kinase G; AC, adenylyl cyclase; PKA, protein kinase A; MLCP, myosin light chain phosphatase; ET-1, endothelin-1; IGF-1, insulin-like growth factor 1; PDGF-B, platelet-derived growth factor-B; PGI_2, prostacyclin. **(B)** When there is a plentiful supply of O_2 and ATP, stimuli such as lactate, PDGF-B and intracellular ATP favour pericyte constriction. GJ, gap junction; PDGFβR, PDGF-B receptor. **(C)** When O_2 and/or ATP are low, lactate, PDGF-B and high intracellular ADP levels favour dilation.

receptors and an increase of NFATc3 nuclear accumulation in pericytes (Filosa et al., 2007). NFAT is a calcium-regulated transcription factor associated with the control of vascular cell contractility (Gonzalez Bosc et al., 2004; Filosa et al., 2007).

PERICYTE DILATION

Just as depolarization and an increase in intracellular calcium level favors constriction of pericytes, so hyperpolarization and a decrease of intracellular calcium level favors dilation. A major pathway which

hyperpolarizes and relaxes vascular smooth muscle cells is activation of potassium channels (Jackson, 2005). It seems that this is also the case for pericytes, as several vasodilators (e.g. PGI_2, adenosine and β-adrenoceptor agonists) produce their actions *via* potassium channel activation (Li and Puro, 2001; Quignard et al., 2003; Hirao et al., 2004; Burnette and White, 2006). Pericytes express potassium channels that are voltage-sensitive, including inward rectifying (K_{IR}) channels (von Beckerath et al., 2000; Cao et al., 2006), voltage-gated potassium channels (von Beckerath et al., 2000) and big and small conductance calcium-activated potassium channels (BK_{Ca} and SK_{Ca}; Wiederholt et al., 1995; Quignard et al., 2003), as well as ATP-sensitive potassium channels (K_{ATP}; Li and Puro, 2001; Hirao et al., 2004), which are not voltage-gated but do exhibit inward rectification at positive potentials (Li and Puro, 2001). Activation of these channels by vasodilators produces vessel relaxation by hyperpolarizing the cell and therefore reducing VOCC activation (**Figure 2A**). An increase in extracellular potassium concentration can also produce dilation by promoting an efflux of potassium at the resting membrane potential, as a result of a raised $[K^+]_o$ increasing the conductance of K_{IR} channels (as shown previously for smooth muscle; Filosa et al., 2006). As well as inducing vasodilation, potassium channel activation in pericytes may also serve to modulate and limit constriction, since serum-derived molecules which constrict pericytes (e.g. IGF-1) also open voltage-dependent potassium channels (Sakagami et al., 1999). Conversely, some vasoconstrictors inhibit potassium channels to increase contractile tone, e.g. ET-1 decreases activity of K_{ATP} channels (Kawamura et al., 2002). Not all vasodilators target potassium channels, however. NO has been found to dilate retinal pericytes at least in part by inhibiting VOCCs and Cl_{Ca} channels, thereby reducing depolarization and calcium entry into the cell and favoring dilation over constriction (**Figure 2A**; Sakagami et al., 2001a).

Cyclic nucleotides are frequently involved in the pathways by which receptor activation on pericytes leads to regulation of ion channels or MLCP (**Figure 2A**). Activation of PGI_2 receptors or β-adrenoceptors, for example, elicits opening of BK_{Ca} channels *via* activation of adenylyl cyclase and production of cAMP (Quignard et al., 2003; Burnette and White, 2006) which, rather than activating protein kinase A (PKA), in this case produces activation of protein kinase G (PKG; Burnette and White, 2006). Even though PKG is more sensitive to cGMP than cAMP, cross-activation can occur as intracellular cAMP levels are generally much higher than cGMP levels, and PKG can become more sensitive to cAMP following autophosphorylation (Smith et al., 1996). Alternatively, cAMP might decrease degradation of cGMP by phosphodiesterase V, boosting cGMP levels and thus PKG activity (Pelligrino and Wang, 1998). In other cell types, PKG activation also occurs in response to NO, because NO activates soluble guanylyl cyclase (sGC) to generate cGMP, which then activates PKG (Garthwaite, 2000). This seems to be the way in which pericytes respond to NO, as pericytes express both sGC (Fessenden and Schacht, 1997) and PKG (Tian et al., 1999) and the dilating effect of NO donors is mimicked by 8-Br-cGMP, a membrane permeable cGMP analog (Sakagami et al., 2001a), and prevented by inhibition of sGC (Haefliger et al., 1994).

Ion channels are not the only target of cyclic nucleotide pathways which evoke relaxation. Adrenomedullin, a vasoactive peptide, which is expressed in CNS endothelial cells and neurons, and is known to increase cerebral blood flow (Serrano et al., 2002) produces an increase in cAMP level in pericytes, activating PKA and decreasing the phosphorylation of MLC, leading to relaxation (Takata et al., 2009). In vascular smooth muscle cells, PKG activation is known to increase the activity of MLCP (Lincoln et al., 2001), which would also produce this effect, so it is possible that the same mechanism is also active in pericytes.

MECHANISMS OF METABOLIC REGULATION OF PERICYTE TONE

As mentioned above, the metabolic state of the tissue can regulate pericyte tone (**Figures 2B,C**). K_{ATP} channels are inherently metabolically regulated, increasing in activity when the intracellular level of ATP falls and that of ADP increases, hyperpolarizing the cell and thus favoring dilation. This effect can be enhanced, as the hyperpolarization closes channels that are activated by depolarization, such as VOCCs and NSCs. This increases the membrane resistance so further current flow through K_{ATP} channels may produce a larger hyperpolarization. Conversely, as the ATP level rises and that of ADP falls, K_{ATP} channels decrease in activity, favoring constriction. An increase in adenosine level, which can occur during hypoxia, activates A_1 and A_{2A} adenosine receptors which then also increase K_{ATP} channel activity (Li and Puro, 2001) and increase capillary blood flow (Hirao et al., 2004). K_{ATP} currents can exert different levels of control over the contractile tone of pericytes, depending on the metabolic state of the tissue. In normoxic conditions, for example, PDGF-B causes a depolarization and constriction of retinal pericytes through activation of NSCs, Cl_{Ca} channels and VOCCs, but in simulated ischaemia, PDGF-B causes dilation by activation of K_{ATP} channels and a subsequent decrease of intracellular calcium concentration (Sakagami et al., 2001b).

Cell-cell communication can also be modulated by the metabolic state of the tissue. Lactate is another bidirectional vasoactive signal, which constricts pericytes in conditions of high oxygen level, but relaxes them when oxygen is scarce (Yamanishi et al., 2006). Constriction in this instance is thought to involve communication with endothelial cells (**Figure 2B**), which express sodium-calcium exchangers that are inhibited by lactate, following a complicated cascade involving activation of monocarboxylate transporters, sodium-hydrogen exchangers and the sodium-potassium ATPase. This results in a decrease in calcium extrusion on lactate application and thus a rise in intracellular calcium concentration that is transmitted through gap junctions to pericytes, producing constriction. Hypoxia apparently closed gap junctions between pericytes and endothelial cells, preventing any calcium rise in endothelial cells from reaching the pericytes, and thus preventing constriction (Yamanishi et al., 2006). The mechanism by which hypoxia alters gap junction coupling is unclear, though agonist induced closure can occur *via* activation of protein kinase C (PKC), for example following prolonged stimulation with ET-1 (Kawamura et al., 2002). It is interesting to note that the closure of gap junctions by hypoxia will increase the membrane resistance of pericytes, so that opening of pericyte ion channels (e.g. K_{ATP} channels as discussed above) will be more able to influence the membrane potential.

PERICYTE REGULATION OF CAPILLARY DIAMETER: *IN VIVO* EVIDENCE AND IMPLICATIONS FOR NEUROIMAGING

Pericytes can modulate capillary diameters *in vitro*, suggesting that they may play a role in the *in vivo* regulation of blood flow. Capillaries are more numerous and densely spaced than

arterioles: in the hippocampus, for example, the average distance between a neuron and a capillary is 8–23 μm, depending on the cell layer, while the average distance between a neuron and an arteriole is 70–160 μm (Lovick et al., 1999). Capillaries therefore seem better placed than arterioles to rapidly detect any increase in neuronal activity and to respond to the requirement for increased blood flow. Of particular relevance to neuroimaging studies, the greater density of capillaries also means that capillary-level regulation of blood flow could potentially allow more spatially-restricted changes in blood flow on occurrence of a localized increase in neuronal activity. Technological advances allowing the use of smaller voxel sizes in imaging techniques that employ blood oxygenation or blood volume as an indicator of neural activation (e.g. the blood-oxygen level dependent (BOLD) signal in functional magnetic resonance imaging, fMRI) may therefore reveal a finer level of spatial detail in the underlying neuronal activity than has previously been observed.

The *in vivo* evidence for regulation of capillary diameter by pericytes is somewhat patchy, however. Optical recordings have allowed comparison of the relative spatial scale of passive vascular changes (i.e. the areas of increased oxygen extraction and deoxyhemoglobin formation due to increased neuronal activity) and active vascular changes, whereby changes in vessel resistance lead to increases in cerebral blood flow and volume. While immediate increases in deoxyhemoglobin level localise well to regions of neuronal activity, suggestive of passive changes in blood oxygenation at the capillary level, later increases in blood flow and volume were originally found to cover much larger areas, suggesting that these occur at the level of arterioles and arteries (Iadecola et al., 1997; Vanzetta and Grinvald, 2008). More recently, however, evidence has been found that changes in cerebral blood flow and volume do occur on a more spatially-restricted scale, consistent with regulation of capillary blood flow. These studies find that when the interfering contribution of large surface vessels is removed, either at the analysis stage (Vanzetta et al., 2004), or by considering only the first (Frostig et al., 1990; Sheth et al., 2004) or last (Berwick et al., 2008) few seconds of the signal, localized increases of cerebral blood volume do occur in the parenchyma (assumed to represent the capillary network), with a spatial resolution of 100–400 μm, corresponding to the areas of cortex activated by whisker stimulation or by a single ocular dominance column in visual cortex (Frostig et al., 1990; Sheth et al., 2004; Vanzetta et al., 2004). From the relative spacing of capillaries and arterioles (see above), each capillary perfuses a tissue volume with a diameter of 15–50 μm, while arterioles perfuse a volume of diameter 140–320 μm. Arterioles could therefore only provide spatially localized perfusion to a single activated column if the arteriole was located directly in the center of a given cortical column, but if blood flow were regulated at the capillary level as well, the capillary network could easily provide this degree of spatial resolution. Indeed, dye injection of penetrating arterioles in rat barrel cortex found that although the area of tissue perfused by a single penetrating arteriole was roughly the same size as a cortical barrel, arteriolar domains did not match barrel domains, so spatial fine tuning by the microvessel network must occur in order to account for the specific change of perfusion in a single cortical barrel (Woolsey et al., 1996).

It is possible that there is a contribution of small arterioles to some of the parenchymal changes that have been assumed to reflect changes in blood volume in capillaries, since the use of increased magnification has shown that some small arterioles may be present, and activity in these vessels may contribute to the localized changes which were earlier attributed to capillaries (Frostig et al., 1990; Berwick et al., 2008). There is, however, further support for a capillary basis for at least some parenchymal blood volume changes, as dilations and constrictions of cerebral capillaries have been observed in rat somatosensory cortex on forepaw stimulation (Stefanovic et al., 2008) and in rat cortex in response to hypercapnia (Hutchinson et al., 2006). Changes in blood volume or diameter in capillaries do not, in themselves, demonstrate active regulation of cerebral blood flow at the capillary level, as upstream arteriolar changes could also produce these effects in capillaries *via* an alteration in perfusion pressure. Nevertheless, tentative evidence for active control of capillary diameter was found by Charpak's group (Chaigneau et al., 2003). If no active regulation occurs at the capillary level, all capillaries in an interconnected network should either dilate or constrict passively in response to an upstream increase or decrease of perfusion pressure. In rat olfactory bulb, however, odour stimulation only produced dilations in those capillaries within an activated olfactory glomerulus (approximate diameter: 200 μm), while capillaries just outside this glomerulus, though closely interconnected, did not respond (Chaigneau et al., 2003). This suggests that active regulation of capillary flow can occur and that changes in capillary flow across the brain can occur on a spatial scale similar to that observed using optical imaging. Furthermore, a simple calculation suggests that, if the change in capillary diameter produced by pericytes in cerebellar slices also occurs *in vivo*, then capillary-level regulation could reduce vascular resistance sufficiently to contribute significantly to the blood flow increase evoked by neural activity (Peppiatt et al., 2006).

Such estimates of the magnitude of the effect on blood flow of altering capillary diameter depend on knowing the relative contributions of arterioles, capillaries and venules to the total vascular resistance, so that the effect of a decrease in resistance in one of these compartments can be assessed. Several models of blood flow through the cerebral vasculature have been formulated which address this issue, which yield estimates for the percentage of vascular resistance at the capillary level ranging from 16%, in a simple multicompartmental model (Lu et al., 2004), to 70% in a more complicated model incorporating branching, parallel vessels, (which assumes that a constant arterial pressure is provided at the upstream end of the penetrating arterioles and a constant venous pressure is maintained downstream of the venules; Boas et al., 2008). Poiseuille's law predicts that flow depends on the fourth power of the vessel radius, and can be used to estimate changes in vessel resistance following diameter changes (though as blood has cells suspended in it that are comparable in size to the capillary diameter, Poiseuille's law is not strictly valid and will actually underestimate the effect of a change in capillary diameter as it neglects the energy required to deform blood cells at very narrow vessel diameters; Secomb, 1987). This means that a 2.1-fold increase in capillary diameter, as is seen after glutamate application to capillaries in vitro (Peppiatt et al., 2006), would decrease capillary resistance by (at least) 20-fold, decrease total vascular resistance by between

15 and 67% and therefore increase blood flow by a factor of 1.18 to 2.98 (for calculation see Peppiatt et al., 2006, Supplementary Material). Clearly experimental evidence is required to assess which of these values is more accurate, but adaptations of these models could be valuable to assess the effect of localized changes in capillary diameter on the spatiotemporal pattern of flow through upstream arterioles, parallel capillaries and downstream venules. Indeed, a recent model simulated capillary dilation over a relatively wide region and predicted spatially-restricted increases in flow that were, nevertheless, not confined to the area of dilation (Reichold et al., 2009). Further modeling using more spatially limited regions of capillary dilation and more anatomically accurate representations of the capillaries will be valuable for generating predictions as to the likely impact of pericyte-mediated capillary diameter regulation.

As well as looking at the spatial patterns of changes in vessel diameters, the relative time courses of haemodynamic changes in parenchymal and arteriolar compartments can also be examined to understand the mechanisms by which changes in vessel resistance are co-ordinated. If capillaries dilate before arterioles, it is likely that they, rather than arterioles, "sense" the requirement for increased blood flow. If, however, capillaries respond later than arterioles, then arterioles are presumably the initial sensor, with capillary dilation occurring as a passive response to increased pressure or via an independent (slower) active dilation pathway. Two studies have found the early parenchymal increase in deoxyhemoglobin concentration in visual cortex, observed after visual stimulation, to be accompanied by a local increase in parenchymal total hemoglobin that is well localized to activated cortical columns (Malonek and Grinvald, 1996, indicating capillary-level regulation) and which occurred before blood flow to the region increased (Malonek et al., 1997). This was interpreted as representing a small degree of capillary dilation, possibly recruiting blood cells from other capillaries, before later upstream increases in blood flow (Malonek and Grinvald, 1996; Malonek et al., 1997). Most studies, however, do not observe this and find that arteriolar flow changes following sensory or electrical stimulation occur at the same time (Matsuura et al., 1999; Li et al., 2003; Hillman et al., 2007), or just before (Vanzetta et al., 2005) changes in capillary perfusion, suggesting that at least the predominant hemodynamic changes originate upstream of capillaries, rather than dilation by capillaries being retrogradely conducted to arterioles.

If retrograde transmission of dilation does not occur, then an important question arises. At what level is increased neuronal activity communicated to the vasculature? Is a local increase in neuronal activity signaled directly to a distant arteriole, e.g. *via* the astrocytic syncytium (Gordon et al., 2007) or does the signal reach the vasculature more directly, at the (nearer) capillary, without necessarily producing a diameter change? In skeletal muscle, local muscle fibre stimulation produces a current and calcium change in local capillary endothelial cells and elicits upstream arteriole dilation (without local capillary dilation; Sarelius et al., 2000; Murrant et al., 2004). It seems this signal is communicated in part, but not exclusively, by electrotonic current spread through endothelial gap junctions (Sarelius et al., 2000). Propagated dilation has been observed from cerebral arterioles to arteries (Iadecola et al., 1997) but has not been observed in cerebral capillaries, though propagated constriction has been reported (Peppiatt et al., 2006) and hyperpolarizations have been shown to propagate via gap junctionally coupled pericytes and endothelial cells in isolated retinal capillaries (Wu et al., 2006), suggesting propagated dilation between pericytes is plausible. As seen above, pericyte hyperpolarization is associated with dilation (Puro, 2007) but often only a fraction of pericytes demonstrate a visible alteration in tone, even when they are all electrophysiologically responsive (e.g. Yamanishi et al., 2006). It may therefore be possible for a neuronal or astrocytic signal to reach capillaries and be signaled upstream to arterioles, as a hyperpolarization of the endothelium and pericytes, without an immediate alteration in capillary diameter. If so, pericytes across the capillary network may exist in different states of rigidity, depending on the vasoactive signals they have received. Their relative tone could therefore dictate which capillaries become most perfused when increased flow arises from the arteriolar level. This would be consistent with increases in red blood cell content in specific capillaries (functional recruitment) which have been observed on electrical stimulation of rat cerebellar and somatosensory cortex (Akgoren and Lauritzen, 1999; Schulte et al., 2003).

In summary, the spatial resolution of changes in cerebral blood volume following sensory stimulation is suggestive of regulation of flow at the capillary level, and dilations and constrictions of capillaries have been observed *in vivo*. Evidence for active regulation of capillary tone *in vivo* is more limited, however, though differential responses in interconnected capillaries suggest that it does occur. Although the limited evidence available points to the initiation of flow increases occurring at the arteriolar level, it remains to be seen whether or not arterioles are the primary site of the neuronal or astrocytic vasoactive signals reaching the vasculature. Further work will doubtless address whether capillaries contribute to upstream transmission of vasodilatory (or vasoconstrictory) signals and how these signals fine tune blood flow through the capillary network.

What are the implications of a possible capillary-level regulation of blood flow for functional imaging studies? The most direct read-out of neuronal activity from the BOLD signal is the increase in deoxyhemoglobin level in capillaries due to increased oxygen extraction by active regions of cortex, but this "initial dip" is not easily detected (Vanzetta and Grinvald, 2008). Indeed it is possible that active capillary-level blood flow regulation could serve to decrease the initial dip, by increasing the amount of oxygenated blood present. As discussed above, blood volume changes with high spatial resolution have been detected optically in primary sensory cortices and the resolution limits are probably set by responses in the capillary network. These spatial resolution limits of 100–400 μm have not been possible previously using magnetic resonance imaging (MRI), but as magnetic field strengths increase (Mangia et al., 2009), and by orienting MRI slices to avoid large blood vessels (Vanzetta and Grinvald, 2008), resolution using the positive phase of the BOLD signal has improved to allow the detection of cortical laminae (Goense and Logothetis, 2006), orientation columns (Yacoub et al., 2008) and olfactory glomeruli (Kida et al., 2002), with voxel diameters reaching 500 μm in humans and 200 μm in animals (Mangia et al., 2009), thus approaching the limits observed using optical techniques. What limits could capillary-level alterations in blood flow therefore impose on the potentially achievable spatial resolution using MRI? In primary sensory cortices, the resolution attainable with optical imaging methods corresponds to a

functional cortical column, and where responses are bigger than a single column, this has been suggested to reflect the underlying spread of neuronal activity, rather than a poorly localized blood flow response (Berwick et al., 2008). In other words, the potential resolution of the vascular response may be significantly greater than is apparent when imaging primary sensory cortices. It would therefore be valuable to compare vascular responses in regions where more spatially localized neuronal firing occurs in response to physiological stimulation, in order to assess whether, in these regions, different stimuli or tasks generate spatially different vascular responses, hopefully reflecting differences in the underlying pattern of neuronal firing. It is conceivable that different vascular responses could occur with a much finer spatial resolution, approximating the spatial density of capillaries (20–40 μm).

PERICYTES AND PATHOPHYSIOLOGY

Pericyte damage has been linked with several different pathological conditions. For example, changes in pericyte morphology at the electron microscope level, suggestive of decreased function and degeneration, have been reported in brain tissue from epilepsy (Liwnicz et al., 1990) and multiple sclerosis (Claudio et al., 1995) patients, while pericyte coverage of capillaries from aged rats is less than in younger controls (Heinsen and Heinsen, 1983). In spontaneously hypertensive rats, conversely, more αSMA-expressing pericytes are found on brain capillaries (Herman and Jacobson, 1988), suggesting that pericytes may be more able to modulate capillary diameter in hypertension, an effect which may either contribute to cardiovascular disease or be adaptive. There is more substantial evidence, however, showing changes in CNS pericytes in three major conditions: Alzheimer's disease, diabetic retinopathy and cerebral ischaemia.

ALZHEIMER'S DISEASE

Amyloid deposits within degenerating pericytes have been observed in the brains of patients with early onset familial (Wisniewski et al., 1992) and normal sporadic Alzheimer's disease (Szpak et al., 2007), and exposure to and internalisation of β-amyloid is toxic to pericytes (Verbeek et al., 1997; Wilhelmus et al., 2007). Accumulation of β-amyloid around capillaries and larger vessels of Alzheimer's disease patients is thought to occur because the perivascular space represents an important clearance pathway for β-amyloid from the interstitial fluid surrounding brain cells (Preston et al., 2003; Carare et al., 2008). Proteins are normally removed from the perivascular space *via* the lymphatic drainage pathways or by transport across the blood-brain barrier (Weller et al., 2008). Indeed, pericytes may be directly involved in β-amyloid clearance across the blood-brain barrier as they express proteins that can act as β-amyloid receptors and can internalise β-amyloid (Wilhelmus et al., 2007). In Alzheimer's disease β-amyloid clearance is insufficient, either due to overproduction of β-amyloid or, as now seems more likely (Zlokovic et al., 2005), due to decreased functioning of the clearance pathways (Weller et al., 2008), so β-amyloid accumulates, forming aggregates or plaques. The presence of β-amyloid produces vasoconstriction, endothelial cell damage and a decrease in cerebral blood flow in larger blood vessels (Thomas et al., 1996; Niwa et al., 2001), and also reduces the reactivity of cerebral blood vessels to neuronal activity or to endothelium-dependent vasodilators (Iadecola et al., 1999; Niwa et al., 2000). The mechanism for these changes seems to involve generation of superoxide by endothelial cells, and, at least in part, a decrease of NO bioavailability (Thomas et al., 1996; Iadecola et al., 1999; Niwa et al., 2001). As pericytes are likely to also be involved in neurovascular coupling it is probable that β-amyloid will have similar effects on the regulation of capillary diameter. Thus, initially low levels of β-amyloid may produce free radicals and hence endothelial damage, capillary constriction and impaired neurovascular coupling (**Figure 3A**). This reduction of the energy supply to the brain may increase neuronal damage, and the decrease in flow may also further impair β-amyloid clearance causing amyloid to accumulate further in a vicious cycle, since blood flow supports protein clearance via the perivascular space and across the blood-brain barrier (Ball et al., 2010). Capillaries may, in fact, be particularly sensitive to β-amyloid-mediated damage, as β-amyloid is more toxic to cultured pericytes than to vascular smooth muscle cells (Verbeek et al., 1997), so alterations in β-amyloid clearance and neurovascular coupling may occur even earlier in capillaries than in larger blood vessels. It is therefore of importance to establish the role of capillaries in impaired vascular function in order to fully understand the pathogenesis of Alzheimer's disease and, hopefully, to identify potential novel drug targets to treat the disease.

Of relevance to functional imaging studies, low levels of β-amyloid disrupt basal CBF and neurovascular coupling before affecting neuronal activity (as assessed by rates of glucose utilisation; Niwa et al., 2000, 2002). Early changes in the BOLD signal related to vascular malfunction are therefore likely to occur in people who will go on to develop Alzheimer's disease, before the onset of neuronal death or cognitive decline. Importantly, as these changes are due to vascular abnormalities, not altered cortical processing, they could confound the interpretation of functional imaging studies on subjects with premorbid Alzheimer's disease. It is therefore important to consider the potential effects of altered neurovascular coupling due to Alzheimer's disease, or other age-related conditions, in the design of studies using older people (D'Esposito et al., 2003).

CEREBRAL ISCHAEMIA

Cerebral ischaemia has long been known to disrupt cerebral blood flow at the capillary level. Following transient focal ischaemia, after a brief period of reactive hyperaemia, cerebral blood flow is reduced, even after removal of arterial occlusion (Leffler et al., 1989), and many cerebral capillaries show poor reperfusion of blood cells (del Zoppo et al., 1991; Mori et al., 1992). This low reflow phenomenon occurs, in part, due to blockade of capillaries by activated polymorphonuclear leukocytes (Mori et al., 1992) and of post-capillaries by activated aggregating platelets and fibrin deposition (del Zoppo, 2008). Activation and increased adherence of these species occurs as a consequence of blood-brain barrier breakdown (del Zoppo, 2008) and is detrimental to the brain, since preventing loss of vessel patency by inhibiting platelet binding to fibrin decreases both microvessel occlusions and infarct volume (Choudhri et al., 1998; Abumiya et al., 2000). Recently, however, pericytes have also been shown to constrict capillaries soon after the onset of simulated retinal ischaemia, and after transient cerebral ischaemia followed by reperfusion (Peppiatt et al., 2006; Yemisci et al., 2009). In the latter study, capillary patency and infarct size was improved by blocking NO synthesis or by scavenging superoxide, and labeling for 3-nitrotyrosine (a product of peroxynitrite-mediated reactions) was

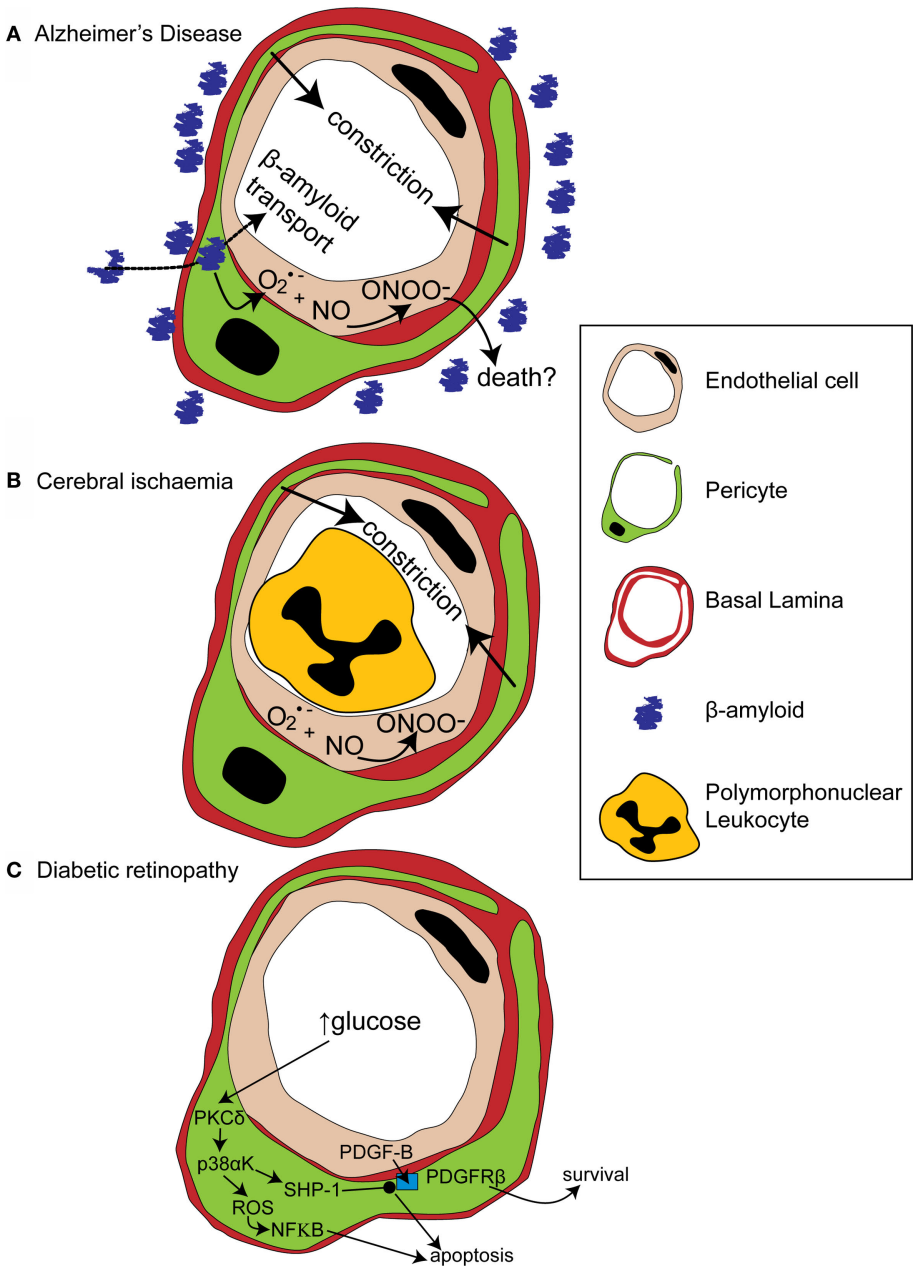

FIGURE 3 | Alterations in pericyte function in disease states. (A) In Alzheimer's disease, β-amyloid removal across the blood-brain barrier slows so β-amyloid aggregates are formed around blood vessels. β-amyloid is toxic to pericytes and produces superoxide ($O_2^{\bullet -}$), which scavenges NO, forming peroxynitrite ($ONOO^-$) and constricting vessels. **(B)** After cerebral ischaemia, the energy supply to an ischaemic region is not fully restored as many capillaries fail to reperfuse due to blockade by polymorphonuclear leukocytes, generation of reactive oxygen species and capillary constriction. **(C)** In diabetic retinopathy, high glucose levels trigger pericyte apoptosis and capillary malfunction *via* activation of protein kinase C δ (PKCδ) and p38α mitogen activated protein kinase (p38αK). Reactive oxygen species (ROS) are generated, producing apoptosis *via* nuclear factor κB (NF-κB) activation and Src homology-2 domain-containing phosphatase-1 (SHP-1) is activated, which inhibits PDGFR-β, decreasing activity of pro-survival pathways and further promoting apoptosis.

found on capillaries, suggesting both that peroxynitrite formation might underlie the constriction of capillaries by pericytes (Yemisci et al., 2009) and that this constriction reduces energy supply to the brain sufficiently to exacerbate neuronal damage. Thus capillary blockade both by activated platelets and leukocytes, and by pericyte constriction, can decrease cerebral blood flow and increase neuronal damage following transient ischaemia (**Figure 3B**).

Interestingly, several electron microscopic studies have observed a migration of pericytes away from the vessel wall following global ischaemia and reperfusion (Takahashi et al., 1997; Gonul et al., 2002; Melgar et al., 2005). This migration began at around the same time as the period of secondary hypoperfusion and continued for at least 12–24 h, by which time pericytes could be observed several microns away from the capillary in the neuropil (Melgar

et al., 2005). The function of pericyte migration is not clear, but in a model of traumatic brain injury, in which pericyte migration was also observed, those pericytes which did not migrate showed cytoplasmic changes consistent with degeneration, suggesting that migration may protect the pericyte from death (Dore-Duffy et al., 2000) (or that pericytes which died rapidly could not migrate). Alternatively, pericytes could be acting as macrophages (Thomas, 1999), to clear up debris from degenerating neurons, or may even be primed to replace dying cells as, in culture at least, pericytes can differentiate into neuronal, astroglial and oligodendrocytic phenotypes (Dore-Duffy et al., 2006). Further study is therefore required to investigate whether pericyte migration is beneficial or damaging to functional recovery from ischaemia, which pathways control this phenomenon and whether any elements of these pathways could potentially be manipulated by therapeutic interventions.

DIABETIC RETINOPATHY

Pericytes are more numerous on retinal capillaries than in any other vascular bed in the body (Frank et al., 1987; Shepro and Morel, 1993). Their loss in the retina occurs at the earliest stages of diabetic retinopathy (Cogan et al., 1961) and is associated with subsequent microaneurysms, haemorrhages, blocked capillaries and changes to the basal lamina. Later, in some patients, blindness can occur as the disease progresses to the proliferative stage, characterized by oedema over the macular region and angiogenesis, which obscures vision and threatens sight (Motiejunaite and Kazlauskas, 2008; Antonetti, 2009). Communication between pericytes and endothelial cells seems to be critically important for maintaining pericytes' presence on retinal capillaries. Platelet-derived growth factor-B (PDGF-B) is produced by endothelial cells, while its receptor, PDGFR-β is expressed on pericytes (**Figure 3C**). Mice in which PDGF-B is knocked out are not viable and die as embryos with an absence of brain pericytes and evidence of lethal haemorrhages (Lindahl et al., 1997). Heterozygotes survive, though with a 30% reduction in the number of retinal pericytes (Hammes et al., 2002). These mice also display retinal microaneurysms and an increased number of acellular capillaries (consisting of tubes of basal lamina empty of endothelial cells and pericytes). The number of pericytes decreases further (in comparison to both diabetic controls and nondiabetic PDGF-$B^{+/-}$ mice) if the mice are made diabetic, and the retinopathy worsens. In addition, in response to hypoxia, they show more *de novo* angiogenesis than do controls (Hammes et al., 2002). Mice with selective endothelial ablation of the PDGF-B gene are also viable and show a wide variation in the number of pericytes present on vessels (Enge et al., 2002). The pericyte density on CNS capillaries turns out to be negatively correlated with the degree of retinopathy, including regressed capillaries and microaneurysms, and proliferative retinopathy was found in all animals where pericyte density on CNS capillaries was decreased by more than 50% (Enge et al., 2002). Together these studies suggest that PDGF-B signaling from endothelial cells to pericytes is important for their association with capillaries and that this association is important for preserving capillary stability, maintaining vessel wall tone (to prevent microaneurysm formation) and preventing both vessel regression and excessive angiogenesis.

A recent paper has cast light on how diabetes may disrupt PDGF-B signaling and thus disrupt pericyte association with retinal capillaries (Geraldes et al., 2009). PKC activity has been previously linked with hyperglycaemia-mediated vascular dysfunction (Koya and King, 1998). Geraldes et al. (2009) showed that levels of PKCδ, a novel PKC isoform (Sampson and Cooper, 2006) which is expressed in retinal pericytes, are increased by high glucose concentrations or by an animal model of diabetes (**Figure 3C**). Conversely, knockout of PKCδ prevents diabetes from inducing pericyte loss and prevents the development of retinopathic features such as acellular capillaries and increased vascular leakage. Using knockout mice and cultured retinal pericytes, PKCδ activation was found to increase p38α MAPK phosphorylation and activation, the effects of which were to increase both reactive oxygen species-mediated activation of NF-κB and expression of Src homology-2 domain–containing phosphatase-1 (SHP-1), a novel target for p38 α MAPK (Geraldes et al., 2009). SHP-1, which inhibits the PDGFR-β (Yu et al., 1998), prevented phosphorylation of the pro-survival targets Akt and ERK in response to endothelial PDGF-B (Geraldes et al., 2009). Both NF-κB activation (Romeo et al., 2002) and decreased phosphorylation of Akt and ERK trigger apoptosis in pericytes and other cell types (Liu et al., 2000; Geraldes et al., 2009). Endothelial cell-pericyte communication *via* PDGF-B is therefore critical for maintaining phosphorylation of pro-survival targets in pericytes and disruption of this pathway by increased activity of PKCδ and its downstream targets, in response to high glucose levels, leads to pericyte loss and the development of retinopathy (**Figure 3C**).

The manner in which pericytes malfunction in disease highlights their importance in roles from controlling vessel tone and capillary perfusion, to maintenance of the blood-brain barrier and stabilising capillary structure. Further understanding of the pathways that are compromised and lead to pericyte death and malfunction in different pathological conditions is likely to be important for the development of new pharmaceutical targets. Equally, the concept that conditions such as stroke and Alzheimer's disease, in addition to producing cognitive impairments, can also alter neurovascular coupling at all levels of the cerebrovascular system, is important not only for understanding disease progression but also when interpreting the BOLD signal in studies using these patient groups.

OVERALL CONCLUSIONS

Pericytes have convincingly been demonstrated to constrict or dilate in response to many different neurotransmitters and vasoactive molecules, and many of the second messenger pathways that lead to constriction or dilation have been elucidated. As yet, however, their behavior following physiological neuronal activity has not been conclusively revealed *in vivo*. It remains to be seen whether pericyte-mediated neurovascular coupling at the capillary level plays an important role in generating the blood flow response to localized neuronal activity, and what the role of pericytes and capillaries is in signaling a requirement for increased flow to upstream arterioles and arteries. As altered pericyte function is associated with several pathological conditions, in terms of their contractile state and other roles such as maintenance of the blood-brain barrier and provision of macrophages or precursors to the neuropil, increased knowledge of pericyte physiology and pathophysiology will be critical for further understanding disease processes, for developing new treatments, and for understanding the contribution of pericytes to functional imaging signals.

ACKNOWLEDGMENTS

Supported by the Fondation Leducq, Wellcome Trust, Medical Research Council UK and the European Research Council.

REFERENCES

Abumiya, T., Fitridge, R., Mazur, C., Copeland, B. R., Koziol, J. A., Tschopp, J. F., Pierschbacher, M. D., and del Zoppo, G. J. (2000). Integrin alpha(IIb)beta(3) inhibitor preserves microvascular patency in experimental acute focal cerebral ischemia. *Stroke* 31, 1402–1409.

Akgoren, N., and Lauritzen, M. (1999). Functional recruitment of red blood cells to rat brain microcirculation accompanying increased neuronal activity in cerebellar cortex. *Neuroreport* 10, 3257–3263.

Antonetti, D. (2009). Eye vessels saved by rescuing their pericyte partners. *Nat. Med.* 15, 1248–1249.

Arneric, S. P., Honig, M. A., Milner, T. A., Greco, S., Iadecola, C., and Reis, D. J. (1988). Neuronal and endothelial sites of acetylcholine synthesis and release associated with microvessels in rat cerebral cortex: ultrastructural and neurochemical studies. *Brain Res.* 454, 11–30.

Ball, K. K., Cruz, N. F., Mrak, R. E., and Dienel, G. A. (2010). Trafficking of glucose, lactate, and amyloid-beta from the inferior colliculus through perivascular routes. *J. Cereb. Blood Flow Metab.* 30, 162–176.

Bandopadhyay, R., Orte, C., Lawrenson, J. G., Reid, A. R., De, S. S., and Allt, G. (2001). Contractile proteins in pericytes at the blood-brain and blood-retinal barriers. *J. Neurocytol.* 30, 35–44.

Benagiano, V., Virgintino, D., Maiorano, E., Rizzi, A., Palombo, S., Roncali, L., and Ambrosi, G. (1996). VIP-like immunoreactivity within neurons and perivascular neuronal processes of the human cerebral cortex. *Eur. J. Histochem.* 40, 53–56.

Berwick, J., Johnston, D., Jones, M., Martindale, J., Martin, C., Kennerley, A. J., Redgrave, P., and Mayhew, J. E. (2008). Fine detail of neurovascular coupling revealed by spatiotemporal analysis of the hemodynamic response to single whisker stimulation in rat barrel cortex. *J. Neurophysiol.* 99, 787–798.

Bjarnegard, M., Enge, M., Norlin, J., Gustafsdottir, S., Fredriksson, S., Abramsson, A., Takemoto, M., Gustafsson, E., Fassler, R., and Betsholtz, C. (2004). Endothelium-specific ablation of PDGFB leads to pericyte loss and glomerular, cardiac and placental abnormalities. *Development* 131, 1847–1857.

Boas, D. A., Jones, S. R., Devor, A., Huppert, T. J., and Dale, A. M. (2008). A vascular anatomical network model of the spatio-temporal response to brain activation. *Neuroimage* 40, 1116–1129.

Burnette, J. O., and White, R. E. (2006). PGI2 opens potassium channels in retinal pericytes by cyclic AMP-stimulated, cross-activation of PKG. *Exp. Eye Res.* 83. 1359–1365.

Cao, C., Goo, J. H., Lee-Kwon, W., and Pallone, T. L. (2006). Vasa recta pericytes express a strong inward rectifier K+ conductance. *Am. J. Physiol. Regul. Integr. Comp. Physiol.* 290, R1601–R1607.

Carare, R. O., Bernardes-Silva, M., Newman, T. A., Page, A. M., Nicoll, J. A., Perry, V. H., and Weller, R. O. (2008). Solutes, but not cells, drain from the brain parenchyma along basement membranes of capillaries and arteries: significance for cerebral amyloid angiopathy and neuroimmunology. *Neuropathol. Appl. Neurobiol.* 34, 131–144.

Cauli, B., Tong, X. K., Rancillac, A., Serluca, N., Lambolez, B., Rossier, J., and Hamel, E. (2004). Cortical GABA interneurons in neurovascular coupling: relays for subcortical vasoactive pathways. *J. Neurosci.* 24, 8940–8949.

Chaigneau, E., Oheim, M., Audinat, E., and Charpak, S. (2003). Two-photon imaging of capillary blood flow in olfactory bulb glomeruli. *Proc. Natl. Acad. Sci. U.S.A.* 100, 13081–13086.

Chen, Q., and Anderson, D. R. (1997). Effect of CO2 on intracellular pH and contraction of retinal capillary pericytes. *Invest Ophthalmol. Vis. Sci.* 38, 643–651.

Chesler, M., and Kaila, K. (1992). Modulation of pH by neuronal activity. *Trends Neurosci.* 15, 396–402.

Choudhri, T. F., Hoh, B. L., Zerwes, H. G., Prestigiacomo, C. J., Kim, S. C., Connolly, E. S. Jr., Kottirsch, G., and Pinsky, D. J. (1998). Reduced microvascular thrombosis and improved outcome in acute murine stroke by inhibiting GP IIb/IIIa receptor-mediated platelet aggregation. *J. Clin. Invest* 102, 1301–1310.

Claudio, L., Raine, C. S., and Brosnan, C. F. (1995). Evidence of persistent blood-brain barrier abnormalities in chronic-progressive multiple sclerosis. *Acta Neuropathol.* 90, 228–238.

Cogan, D. G., Toussaint, D., and Kuwabara, T. (1961). Retinal vascular patterns. IV. Diabetic retinopathy. *Arch. Ophthalmol.* 66, 366–378.

Dehouck, M. P., Vigne, P., Torpier, G., Breittmayer, J. P., Cecchelli, R., and Frelin, C. (1997). Endothelin-1 as a mediator of endothelial cell-pericyte interactions in bovine brain capillaries. *J. Cereb. Blood Flow Metab.* 17, 464–469.

del Zoppo, G. J. (2008). Virchow's triad: the vascular basis of cerebral injury. *Rev. Neurol. Dis.* 5(Suppl. 1), S12–S21.

del Zoppo, G. J., Schmid-Schonbein, G. W., Mori, E., Copeland, B. R., and Chang, C. M. (1991). Polymorphonuclear leukocytes occlude capillaries following middle cerebral artery occlusion and reperfusion in baboons. *Stroke* 22, 1276–1283.

D'Esposito, M., Deouell, L. Y., and Gazzaley, A. (2003). Alterations in the BOLD fMRI signal with ageing and disease: a challenge for neuroimaging. *Nat. Rev. Neurosci.* 4, 863–872.

Dirnagl, U., Niwa, K., Lindauer, U., and Villringer, A. (1994). Coupling of cerebral blood flow to neuronal activation: role of adenosine and nitric oxide. *Am. J. Physiol.* 267, H296–H301.

Dodge, A. B., Hechtman, H. B., and Shepro, D. (1991). Microvascular endothelial-derived autacoids regulate pericyte contractility. *Cell Motil. Cytoskeleton* 18, 180–188.

Dore, S. E. (1923). On the contractility of and nervous supply of capillaries. *Br. J. Dermatol.* 35, 398–404.

Dore-Duffy, P. (2008). Pericytes: pluripotent cells of the blood brain barrier. *Curr. Pharm. Des.* 14, 1581–1593.

Dore-Duffy, P., Katychev, A., Wang, X., and Van, B. E. (2006). CNS microvascular pericytes exhibit multipotential stem cell activity. *J. Cereb. Blood Flow Metab.* 26, 613–624.

Dore-Duffy, P., Owen, C., Balabanov, R., Murphy, S., Beaumont, T., and Rafols, J. A. (2000). Pericyte migration from the vascular wall in response to traumatic brain injury. *Microvasc. Res.* 60, 55–69.

Enge, M., Bjarnegard, M., Gerhardt, H., Gustafsson, E., Kalen, M., Asker, N., Hammes, H. P., Shani, M., Fassler, R., and Betsholtz, C. (2002). Endothelium-specific platelet-derived growth factor-B ablation mimics diabetic retinopathy. *EMBO J.* 21, 4307–4316.

Faraci, F. M., and Breese, K. R. (1993). Nitric oxide mediates vasodilatation in response to activation of N-methyl-D-aspartate receptors in brain. *Circ. Res.* 72, 476–480.

Favard, C., Simon, A., Vigny, A., and Nguyen-Legros, J. (1990). Ultrastructural evidence for a close relationship between dopamine cell processes and blood capillary walls in *Macaca* monkey and rat retina. *Brain Res.* 523, 127–133.

Fessenden, J. D., and Schacht, J. (1997). Localization of soluble guanylate cyclase activity in the guinea pig cochlea suggests involvement in regulation of blood flow and supporting cell physiology. *J. Histochem. Cytochem.* 45, 1401–1408.

Fields, R. D., and Burnstock, G. (2006). Purinergic signalling in neuron-glia interactions. *Nat. Rev. Neurosci.* 7, 423–436.

Filosa, J. A., Bonev, A. D., Straub, S. V., Meredith, A. L., Wilkerson, M. K., Aldrich, R. W., and Nelson, M. T. (2006). Local potassium signaling couples neuronal activity to vasodilation in the brain. *Nat. Neurosci.* 9, 1397–1403.

Filosa, J. A., Nelson, M. T., and Gonzalez Bosc, L. V. (2007). Activity-dependent NFATc3 nuclear accumulation in pericytes from cortical parenchymal microvessels. *Am. J. Physiol., Cell Physiol.* 293, C1797–C1805.

Frank, R. N., Dutta, S., and Mancini, M. A. (1987). Pericyte coverage is greater in the retinal than in the cerebral capillaries of the rat. *Invest Ophthalmol. Vis. Sci.* 28, 1086–1091.

Frostig, R. D., Lieke, E. E., Ts'o, D. Y., and Grinvald, A. (1990). Cortical functional architecture and local coupling between neuronal activity and the microcirculation revealed by *in vivo* high-resolution optical imaging of intrinsic signals. *Proc. Natl. Acad. Sci. U.S.A.* 87, 6082–6086.

Garthwaite, J. (2000). "The physiological roles of nitric oxide in the central nervous system," in Nitric Oxide, ed. B. Mayer (Berlin: Springer-Verlag), 259–275.

Geraldes, P., Hiraoka-Yamamoto, J., Matsumoto, M., Clermont, A., Leitges, M., Marette, A., Aiello, L. P., Kern, T. S., and King, G. L. (2009). Activation of PKC-delta and SHP-1 by hyperglycemia causes vascular cell apoptosis and diabetic retinopathy. *Nat. Med.* 15, 1298–1306.

Goense, J. B., and Logothetis, N. K. (2006). Laminar specificity in monkey V1 using high-resolution SE-fMRI. *Magn. Reson. Imaging* 24, 381–392.

Gonul, E., Duz, B., Kahraman, S., Kayali, H., Kubar, A., and Timurkaynak, E. (2002). Early pericyte response to brain hypoxia in cats: an ultrastructural study. *Microvasc. Res.* 64, 116–119.

Gonzalez Bosc, L. V., Wilkerson, M. K., Bradley, K. N., Eckman, D. M., Hill-Eubanks, D. C., and Nelson, M. T. (2004). Intraluminal pressure is a stimulus for NFATc3 nuclear accumulation: role of calcium, endothelium-derived nitric oxide, and cGMP-dependent protein kinase. *J. Biol. Chem.* 279, 10702–10709.

Gordon, G. R., Choi, H. B., Rungta, R. L., Ellis-Davies, G. C., and MacVicar, B. A. (2008). Brain metabolism dictates the polarity of astrocyte control over arterioles. *Nature* 456, 745–749.

Gordon, G. R., Mulligan, S. J., and MacVicar, B. A. (2007). Astrocyte control of the cerebrovasculature. *Glia* 55, 1214–1221.

Gragera, R. R., Muniz, E., and Martinez-Rodriguez, R. (1993). Electron microscopic immunolocalization of GABA and glutamic acid decarboxylase (GAD) in cerebellar capillaries and their microenvironment. *Cell Mol. Biol. (Noisy-le-grand)* 39, 809–817.

Haefliger, I. O., Zschauer, A., and Anderson, D. R. (1994). Relaxation of retinal pericyte contractile tone through the nitric oxide-cyclic guanosine monophosphate pathway. *Invest Ophthalmol. Vis. Sci.* 35, 991–997.

Hammes, H. P., Lin, J., Renner, O., Shani, M., Lundqvist, A., Betsholtz, C., Brownlee, M., and Deutsch, U. (2002). Pericytes and the pathogenesis of diabetic retinopathy. *Diabetes* 51, 3107–3112.

Heinsen, H., and Heinsen, Y. L. (1983). Cerebellar capillaries. Qualitative and quantitative observations in young and senile rats. *Anat. Embryol.* 168, 101–116.

Herman, I. M., and D'Amore, P. A. (1985). Microvascular pericytes contain muscle and nonmuscle actins. *J. Cell Biol.* 101, 43–52.

Herman, I. M., and Jacobson, S. (1988). In situ analysis of microvascular pericytes in hypertensive rat brains. *Tissue Cell* 20, 1–12.

Hilgers, R. H., and Webb, R. C. (2005). Molecular aspects of arterial smooth muscle contraction: focus on Rho. *Exp. Biol. Med. (Maywood)* 230, 829–835.

Hillman, E. M., Devor, A., Bouchard, M. B., Dunn, A. K., Krauss, G. W., Skoch, J., Bacskai, B. J., Dale, A. M., and Boas, D. A. (2007). Depth-resolved optical imaging and microscopy of vascular compartment dynamics during somatosensory stimulation. *Neuroimage* 35, 89–104.

Hirao, M., Oku, H., Goto, W., Sugiyama, T., Kobayashi, T., and Ikeda, T. (2004). Effects of adenosine on optic nerve head circulation in rabbits. *Exp. Eye Res.* 79, 729–735.

Hirschi, K. K., and D'Amore, P. A. (1996). Pericytes in the microvasculature. *Cardiovasc. Res.* 32, 687–698.

Ho, K. L. (1985). Ultrastructure of cerebellar capillary hemangioblastoma. IV. Pericytes and their relationship to endothelial cells. *Acta Neuropathol.* 67, 254–264.

Hutchinson, E. B., Stefanovic, B., Koretsky, A. P., and Silva, A. C. (2006). Spatial flow-volume dissociation of the cerebral microcirculatory response to mild hypercapnia. *Neuroimage* 32, 520–530.

Iadecola, C., Yang, G., Ebner, T. J., and Chen, G. (1997). Local and propagated vascular responses evoked by focal synaptic activity in cerebellar cortex. *J. Neurophysiol.* 78, 651–659.

Iadecola, C., Zhang, F. Y., Niwa, K., Eckman, C., Turner, S. K., Fischer, E., Younkin, S., Borchelt, D. R., Hsiao, K. K., and Carlson, G. A. (1999). SOD1 rescues cerebral endothelial dysfunction in mice overexpressing amyloid precursor protein. *Nat. Neurosci.* 2, 157–161.

Jackson, W. F. (2005). Potassium channels in the peripheral microcirculation. *Microcirculation* 12, 113–127.

Joyce, N. C., Haire, M. F., and Palade, G. E. (1985). Contractile proteins in pericytes. I. Immunoperoxidase localization of tropomyosin. *J. Cell Biol.* 100, 1379–1386.

Kawamura, H., Oku, H., Li, Q., Sakagami, K., and Puro, D. G. (2002). Endothelin-induced changes in the physiology of retinal pericytes. *Invest Ophthalmol. Vis. Sci.* 43, 882–888.

Kawamura, H., Sugiyama, T., Wu, D. M., Kobayashi, M., Yamanishi, S., Katsumura, K., and Puro, D. G. (2003). ATP: a vasoactive signal in the pericyte-containing microvasculature of the rat retina. *J. Physiol.* 551, 787–799.

Kelley, C., D'Amore, P., Hechtman, H. B., and Shepro, D. (1988). Vasoactive hormones and cAMP affect pericyte contraction and stress fibres *in vitro*. *J. Muscle Res. Cell Motil.* 9, 184–194.

Kida, I., Xu, F., Shulman, R. G., and Hyder, F. (2002). Mapping at glomerular resolution: fMRI of rat olfactory bulb. *Magn Reson. Med*. 48, 570–576.

Koya, D., and King, G. L. (1998). Protein kinase C activation and the development of diabetic complications. *Diabetes* 47, 859–866.

Krimer, L. S., Muly, E. C. III, Williams, G. V., and Goldman-Rakic, P. S. (1998). Dopaminergic regulation of cerebral cortical microcirculation. *Nat. Neurosci.* 1, 286–289.

Kutcher, M. E., Kolyada, A. Y., Surks, H. K., and Herman, I. M. (2007). Pericyte Rho GTPase mediates both pericyte contractile phenotype and capillary endothelial growth state. *Am. J. Pathol.* 171, 693–701.

Lai, C. H., and Kuo, K. H. (2005). The critical component to establish *in vitro* BBB model: Pericyte. *Brain Res. Brain Res. Rev.* 50, 258–265.

Le Beux, Y. J., and Willemot, J. (1978). Actin- and myosin-like filaments in rat brain pericytes. *Anat. Rec.* 190, 811–826.

Leffler, C. W., Busija, D. W., Mirro, R., Armstead, W. M., and Beasley, D. G. (1989). Effects of ischemia on brain blood flow and oxygen consumption of newborn pigs. *Am. J. Physiol.* 257, H1917–H1926.

Li, P., Luo, Q., Luo, W., Chen, S., Cheng, H., and Zeng, S. (2003). Spatiotemporal characteristics of cerebral blood volume changes in rat somatosensory cortex evoked by sciatic nerve stimulation and obtained by optical imaging. *J. Biomed. Opt.* 8, 629–635.

Li, Q., and Puro, D. G. (2001). Adenosine activates ATP-sensitive K+ currents in pericytes of rat retinal microvessels: role of A1 and A2a receptors. *Brain Res.* 907, 93–99.

Lincoln, T. M., Dey, N., and Sellak, H. (2001). Invited review: cGMP-dependent protein kinase signaling mechanisms in smooth muscle: from the regulation of tone to gene expression. *J. Appl. Physiol.* 91, 1421–1430.

Lindahl, P., Johansson, B. R., Leveen, P., and Betsholtz, C. (1997). Pericyte loss and microaneurysm formation in PDGF-B-deficient mice. *Science* 277, 242–245.

Lindauer, U., Leithner, C., Kaasch, H., Rohrer, B., Foddis, M., Fuchtemeier, M., Offenhauser, N., Steinbrink, J., Royl, G., Kohl-Bareis, M., and Dirnagl, U. (2010). Neurovascular coupling in rat brain operates independent of hemoglobin deoxygenation. *J. Cereb. Blood Flow Metab*. 30, 757–768.

Liu, W., Ahmad, S. A., Reinmuth, N., Shaheen, R. M., Jung, Y. D., Fan, F., and Ellis, L. M. (2000). Endothelial cell survival and apoptosis in the tumor vasculature. *Apoptosis* 5, 323–328.

Liwnicz, B. H., Leach, J. L., Yeh, H. S., and Privitera, M. (1990). Pericyte degeneration and thickening of basement membranes of cerebral microvessels in complex partial seizures: electron microscopic study of surgically removed tissue. *Neurosurgery* 26, 409–420.

Lovick, T. A., Brown, L. A., and Key, B. J. (1999). Neurovascular relationships in hippocampal slices: physiological and anatomical studies of mechanisms underlying flow-metabolism coupling in intraparenchymal microvessels. *Neuroscience* 92, 47–60.

Lu, K., Clark, J. W. Jr., Ghorbel, F. H., Robertson, C. S., Ware, D. L., Zwischenberger, J. B., and Bidani, A. (2004). Cerebral autoregulation and gas exchange studied using a human cardiopulmonary model. *Am. J. Physiol. Heart Circ. Physiol.* 286, H584–H601.

Malonek, D., Dirnagl, U., Lindauer, U., Yamada, K., Kanno, I., and Grinvald, A. (1997). Vascular imprints of neuronal activity: relationships between the dynamics of cortical blood flow, oxygenation, and volume changes following sensory stimulation. *Proc. Natl. Acad. Sci. U.S.A.* 94, 14826–14831.

Malonek, D., and Grinvald, A. (1996). Interactions between electrical activity and cortical microcirculation revealed by imaging spectroscopy: implications for functional brain mapping. *Science* 272, 551–554.

Mangia, S., Giove, F., Tkac, I., Logothetis, N. K., Henry, P. G., Olman, C. A., Maraviglia, B., Di, S. F., and Ugurbil, K. (2009). Metabolic and hemodynamic events after changes in neuronal activity: current hypotheses, theoretical predictions and *in vivo* NMR experimental findings. *J. Cereb. Blood Flow Metab.* 29, 441–463.

Markhotina, N., Liu, G. J., and Martin, D. K. (2007). Contractility of retinal pericytes grown on silicone elastomer substrates is through a protein kinase A-mediated intracellular pathway in response to vasoactive peptides. *IET Nanobiotechnol.* 1, 44–51.

Mathiesen, C., Caesar, K., Akgoren, N., and Lauritzen, M. (1998). Modification of activity-dependent increases of cerebral blood flow by excitatory synaptic activity and spikes in rat cerebellar cortex. *J. Physiol.* 512(Pt 2), 555–566.

Matsugi, T., Chen, Q., and Anderson, D. R. (1997a). Contractile responses of cultured bovine retinal pericytes to angiotensin II. *Arch. Ophthalmol.* 115, 1281–1285.

Matsugi, T., Chen, Q., and Anderson, D. R. (1997b). Adenosine-induced relaxation of cultured bovine retinal pericytes. *Invest. Ophthalmol. Vis. Sci.* 38, 2695–2701.

Matsuura, T., Fujita, H., Seki, C., Kashikura, K., and Kanno, I. (1999). Hemodynamics evoked by microelectrical direct stimulation in rat somatosensory cortex. *Comp. Biochem. Physiol., Part A Mol. Integr. Physiol.* 124, 47–52.

Maynard, E. A., Schultz, R. L., and Pease, D. C. (1957). Electron microscopy of the vascular bed of rat cerebral cortex. *Am. J. Anat.* 100, 409–433.

Melgar, M. A., Rafols, J., Gloss, D., and Diaz, F. G. (2005). Postischemic reperfusion: ultrastructural blood-brain barrier and hemodynamic correlative changes in an awake model of transient forebrain ischemia. *Neurosurgery* 56, 571–581.

Metea, M. R., and Newman, E. A. (2006). Glial cells dilate and constrict blood vessels: a mechanism of neurovascular coupling. *J. Neurosci.* 26, 2862–2870.

Mori, E., del Zoppo, G. J., Chambers, J. D., Copeland, B. R., and Arfors, K. E. (1992). Inhibition of polymorphonuclear leukocyte adherence suppresses no-reflow after focal cerebral ischemia in baboons. *Stroke* 23, 712–718.

Motiejunaite, R., and Kazlauskas, A. (2008). Pericytes and ocular diseases. *Exp. Eye Res.* 86, 171–177.

Murrant, C. L., Duza, T., Kim, M. B., Cohen, K. D., and Sarelius, I. H. (2004). Arteriolar dilations induced

by contraction of hamster cremaster muscle are dependent on changes in endothelial cell calcium. *Acta Physiol. Scand.* 180, 231–238.

Nehls, V., and Drenckhahn, D. (1991). Heterogeneity of microvascular pericytes for smooth muscle type alpha-actin. *J. Cell Biol.* 113, 147–154.

Niwa, K., Kazama, K., Younkin, S. G., Carlson, G. A., and Iadecola, C. (2002). Alterations in cerebral blood flow and glucose utilization in mice overexpressing the amyloid precursor protein. *Neurobiol. Dis.* 9, 61–68.

Niwa, K., Porter, V. A., Kazama, K., Cornfield, D., Carlson, G. A., and Iadecola, C. (2001). A beta-peptides enhance vasoconstriction in cerebral circulation. *Am. J. Physiol. Heart Circ. Physiol.* 281, H2417–H2424.

Niwa, K., Younkin, L., Ebeling, C., Turner, S. K., Westaway, D., Younkin, S., Ashe, K. H., Carlson, G. A., and Iadecola, C. (2000). Abeta 1-40-related reduction in functional hyperemia in mouse neocortex during somatosensory activation. *Proc. Natl. Acad. Sci. U.S.A.* 97, 9735–9740.

Pelligrino, D. A., and Wang, Q. (1998). Cyclic nucleotide crosstalk and the regulation of cerebral vasodilation. *Prog. Neurobiol.* 56, 1–18.

Peppiatt, C. M., Howarth, C., Mobbs, P., and Attwell, D. (2006). Bidirectional control of CNS capillary diameter by pericytes. *Nature* 443, 700–704.

Preston, S. D., Steart, P. V., Wilkinson, A., Nicoll, J. A., and Weller, R. O. (2003). Capillary and arterial cerebral amyloid angiopathy in Alzheimer's disease: defining the perivascular route for the elimination of amyloid beta from the human brain. *Neuropathol. Appl. Neurobiol.* 29, 106–117.

Puro, D. G. (2007). Physiology and pathobiology of the pericyte-containing retinal microvasculature: new developments. *Microcirculation* 14, 1–10.

Quignard, J. F., Harley, E. A., Duhault, J., Vanhoutte, P. M., and Feletou, M. (2003). K+ channels in cultured bovine retinal pericytes: effects of beta-adrenergic stimulation. *J. Cardiovasc. Pharmacol.* 42, 379–388.

Reber, F., Gersch, U., and Funk, R. W. (2003). Blockers of carbonic anhydrase can cause increase of retinal capillary diameter, decrease of extracellular and increase of intracellular pH in rat retinal organ culture. *Graefes Arch. Clin. Exp. Ophthalmol.* 241, 140–148.

Reichold, J., Stampanoni, M., Lena, K. A., Buck, A., Jenny, P., and Weber, B. (2009). Vascular graph model to simulate the cerebral blood flow in realistic vascular networks. *J. Cereb. Blood Flow Metab.* 29, 1429–1443.

Romeo, G., Liu, W. H., Asnaghi, V., Kern, T. S., and Lorenzi, M. (2002). Activation of nuclear factor-kappaB induced by diabetes and high glucose regulates a proapoptotic program in retinal pericytes. *Diabetes* 51, 2241–2248.

Roufail, E., Stringer, M., and Rees, S. (1995). Nitric oxide synthase immunoreactivity and NADPH diaphorase staining are co-localised in neurons closely associated with the vasculature in rat and human retina. *Brain Res.* 684, 36–46.

Sakagami, K., Kawamura, H., Wu, D. M., and Puro, D. G. (2001a). Nitric oxide/cGMP-induced inhibition of calcium and chloride currents in retinal pericytes. *Microvasc. Res.* 62, 196–203.

Sakagami, K., Kodama, T., and Puro, D. G. (2001b). PDGF-induced coupling of function with metabolism in microvascular pericytes of the retina. *Invest. Ophthalmol. Vis. Sci.* 42, 1939–1944.

Sakagami, K., Wu, D. M., and Puro, D. G. (1999). Physiology of rat retinal pericytes: modulation of ion channel activity by serum-derived molecules. *J. Physiol.* 521(Pt 3), 637–650.

Sampson, S. R., and Cooper, D. R. (2006). Specific protein kinase C isoforms as transducers and modulators of insulin signaling. *Mol. Genet. Metab.* 89, 32–47.

Sarelius, I. H., Cohen, K. D., and Murrant, C. L. (2000). Role for capillaries in coupling blood flow with metabolism. *Clin. Exp. Pharmacol. Physiol.* 27, 826–829.

Sato, A., and Sato, Y. (1990). Cerebral cortical vasodilatation in response to stimulation of cholinergic fibres originating in the nucleus basalis of Meynert. *J. Auton. Nerv. Syst.* 30(Suppl) S137–S140.

Schonfelder, U., Hofer, A., Paul, M., and Funk, R. H. (1998). *In situ* observation of living pericytes in rat retinal capillaries. *Microvasc. Res.* 56, 22–29.

Schulte, M. L., Wood, J. D., and Hudetz, A. G. (2003). Cortical electrical stimulation alters erythrocyte perfusion pattern in the cerebral capillary network of the rat. *Brain Res.* 963, 81–92.

Secomb, T. W. (1987). Flow-dependent rheological properties of blood in capillaries. *Microvasc. Res.* 34, 46–58.

Serrano, J., Alonso, D., Fernandez, A. P., Encinas, J. M., Lopez, J. C., Castro-Blanco, S., Fernandez-Vizarra, P., Richart, A., Santacana, M., Uttenthal, L. O., Bentura, M. L., Martinez-Murillo, R., Martinez, A., Cuttitta, F., and Rodrigo, J. (2002). Adrenomedullin in the central nervous system. *Microsc. Res. Tech.* 57, 76–90.

Shepro, D., and Morel, N. M. (1993). Pericyte physiology. *FASEB J.* 7, 1031–1038.

Sheth, S. A., Nemoto, M., Guiou, M., Walker, M., Pouratian, N., Hageman, N., and Toga, A. W. (2004). Columnar specificity of microvascular oxygenation and volume responses: implications for functional brain mapping. *J. Neurosci.* 24, 634–641.

Smith, J. A., Francis, S. H., Walsh, K. A., Kumar, S., and Corbin, J. D. (1996). Autophosphorylation of type Ibeta cGMP-dependent protein kinase increases basal catalytic activity and enhances allosteric activation by cGMP or cAMP. *J. Biol. Chem.* 271, 20756–20762.

Stefanovic, B., Hutchinson, E., Yakovleva, V., Schram, V., Russell, J. T., Belluscio, L., Koretsky, A. P., and Silva, A. C. (2008). Functional reactivity of cerebral capillaries. *J. Cereb. Blood Flow Metab.* 28, 961–972.

Sugiyama, T., Kawamura, H., Yamanishi, S., Kobayashi, M., Katsumura, K., and Puro, D. G. (2005). Regulation of P2X7-induced pore formation and cell death in pericyte-containing retinal microvessels. *Am. J. Physiol. Cell Physiol.* 288, C568–C576.

Szpak, G. M., Lewandowska, E., Wierzba-Bobrowicz, T., Bertrand, E., Pasennik, E., Mendel, T., Stepien, T., Leszczynska, A., and Rafalowska, J. (2007). Small cerebral vessel disease in familial amyloid and non-amyloid angiopathies: FAD-PS-1 (P117L) mutation and CADASIL. Immunohistochemical and ultrastructural studies. *Folia Neuropathol.* 45, 192–204.

Takahashi, A., Park, H. K., Melgar, M. A., Alcocer, L., Pinto, J., Lenzi, T., Diaz, F. G., and Rafols, J. A. (1997). Cerebral cortex blood flow and vascular smooth muscle contractility in a rat model of ischemia: a correlative laser Doppler flowmetric and scanning electron microscopic study. *Acta Neuropathol.* 93, 354–368.

Takata, F., Dohgu, S., Nishioku, T., Takahashi, H., Harada, E., Makino, I., Nakashima, M., Yamauchi, A., and Kataoka, Y. (2009). Adrenomedullin-induced relaxation of rat brain pericytes is related to the reduced phosphorylation of myosin light chain through the cAMP/PKA signaling pathway. *Neurosci. Lett.* 449, 71–75.

Thomas, T., Thomas, G., McLendon, C., Sutton, T., and Mullan, M. (1996). beta-Amyloid-mediated vasoactivity and vascular endothelial damage. *Nature* 380, 168–171.

Thomas, W. E. (1999). Brain macrophages: on the role of pericytes and perivascular cells. *Brain Res. Brain Res. Rev.* 31, 42–57.

Tian, F., Fessenden, J. D., and Schacht, J. (1999). Cyclic GMP-dependent protein kinase-I in the guinea pig cochlea. *Hear. Res.* 131. 63–70.

Toribatake, Y., Tomita, K., Kawahara, N., Baba, H., Ohnari, H., and Tanaka, S. (1997). Regulation of vasomotion of arterioles and capillaries in the cat spinal cord: role of alpha actin and endothelin-1. *Spinal Cord* 35, 26–32.

Vanzetta, I., and Grinvald, A. (2008). Coupling between neuronal activity and microcirculation: implications for functional brain imaging. *HFSP J.* 2, 79–98.

Vanzetta, I., Hildesheim, R., and Grinvald, A. (2005). Compartment-resolved imaging of activity-dependent dynamics of cortical blood volume and oximetry. *J. Neurosci.* 25, 2233–2244.

Vanzetta, I., Slovin, H., Omer, D. B., and Grinvald, A. (2004). Columnar resolution of blood volume and oximetry functional maps in the behaving monkey; implications for FMRI. *Neuron* 42, 843–854.

Verbeek, M. M., de Waal, R. M., Schipper, J. J., and Van Nostrand, W. E. (1997). Rapid degeneration of cultured human brain pericytes by amyloid beta protein. *J. Neurochem.* 68, 1135–1141.

von Beckerath, N., Nees, S., Neumann, F. J., Krebs, B., Juchem, G., and Schomig, A. (2000). An inward rectifier and a voltage-dependent K+ current in single, cultured pericytes from bovine heart. *Cardiovasc. Res.* 46, 569–578.

Webb, R. C. (2003). Smooth muscle contraction and relaxation. *Adv. Physiol. Educ.* 27, 201–206.

Weller, R. O., Subash, M., Preston, S. D., Mazanti, I., and Carare, R. O. (2008). Perivascular drainage of amyloid-beta peptides from the brain and its failure in cerebral amyloid angiopathy and Alzheimer's disease. *Brain Pathol.* 18, 253–266.

Wiederholt, M., Berweck, S., and Helbig, H. (1995). Electrophysiological properties of cultured retinal capillary pericytes. *Prog. Retin. Eye Res.* 14, 437–451.

Wilhelmus, M. M., Otte-Holler, I., van Triel, J. J., Veerhuis, R., Maat-Schieman, M. L., Bu, G., de Waal, R. M., and Verbeek, M. M. (2007). Lipoprotein receptor-related protein-1 mediates amyloid-beta-mediated cell death of cerebrovascular cells. *Am. J. Pathol.* 171, 1989–1999.

Wisniewski, H. M., Wegiel, J., Wang, K. C., and Lach, B. (1992). Ultrastructural studies of the cells forming amyloid in the cortical vessel wall in Alzheimer's disease. *Acta Neuropathol.* 84, 117–127.

Woolsey, T. A., Rovainen, C. M., Cox, S. B., Henegar, M. H., Liang, G. E., Liu, D., Moskalenko, Y. E., Sui, J., and Wei, L. (1996). Neuronal units

linked to microvascular modules in cerebral cortex: response elements for imaging the brain. *Cereb. Cortex* 6, 647–660.

Wu, D. M., Minami, M., Kawamura, H., and Puro, D. G. (2006). Electrotonic transmission within pericyte-containing retinal microvessels. *Microcirculation* 13, 353–363.

Yacoub, E., Harel, N., and Ugurbil, K. (2008). High-field fMRI unveils orientation columns in humans. *Proc. Natl. Acad. Sci. U.S.A.* 105, 10607–10612.

Yamanishi, S., Katsumura, K., Kobayashi, T., and Puro, D. G. (2006). Extracellular lactate as a dynamic vasoactive signal in the rat retinal microvasculature. *Am. J. Physiol. Heart Circ. Physiol.* 290: H925–H934.

Yemisci, M., Gursoy-Ozdemir, Y., Vural, A., Can, A., Topalkara, K., and Dalkara, T. (2009). Pericyte contraction induced by oxidative-nitrative stress impairs capillary reflow despite successful opening of an occluded cerebral artery. *Nat. Med.* 15, 1031–1037.

Yu, Z., Su, L., Hoglinger, O., Jaramillo, M. L., Banville, D., and Shen, S. H. (1998). SHP-1 associates with both platelet-derived growth factor receptor and the p85 subunit of phosphatidylinositol 3-kinase. *J. Biol. Chem.* 273, 2694–3687.

Zlokovic, B. V., Deane, R., Sallstrom, J., Chow, N., and Miano, J. M. (2005). Neurovascular pathways and Alzheimer amyloid beta-peptide. *Brain Pathol.* 15, 78–83.

Zonta, M., Angulo, M. C., Gobbo, S., Rosengarten, B., Hossmann, K. A., Pozzan, T., and Carmignoto, G. (2003). Neuron-to-astrocyte signaling is central to the dynamic control of brain microcirculation. *Nat. Neurosci.* 6, 43–50.

Conflict of Interest Statement: The authors declare that the research was conducted in the absence of any commercial or financial relationships that could be construed as a potential conflict of interest.

Received: 11 February 2010; paper pending published: 25 March 2010; accepted: 28 April 2010; published online: 21 May 2010.
Citation: Hamilton NB, Attwell D and Hall CN (2010) Pericyte-mediated regulation of capillary diameter: a component of neurovascular coupling in health and disease. Front. Neuroenerg. ***2****:5. doi: 10.3389/fnene.2010.00005*

frontiers in
NEUROENERGETICS

HYPOTHESIS AND THEORY ARTICLE
published: 27 September 2010
doi: 10.3389/fnene.2010.00130

Recent advances in high-resolution MR application and its implications for neurovascular coupling research

Noam Harel[1]*, Patrick J. Bolan[1], Robert Turner[2], Kamil Ugurbil[1] and Essa Yacoub[1]

[1] *Center for Magnetic Resonance Research, Department of Radiology, School of Medicine, University of Minnesota, Minneapolis, MN, USA*
[2] *Max Planck Institute for Human Cognitive and Brain Sciences, Leipzig, Germany*

Edited by:
David Boas, Massachusetts General Hospital, USA; Massachusetts Institute of Technology, USA; Harvard Medical School, USA

Reviewed by:
Larry Wald, Harvard University, USA

****Correspondence:***
Noam Harel, Center for Magnetic Resonance Research, Department of Radiology, School of Medicine, University of Minnesota, 2021 Sixth Street SE, Minneapolis, MN 55455, USA.
e-mail: noam@cmrr.umn.edu

The current understanding of fMRI, regarding its vascular origins, is based on numerous assumptions and theoretical modeling, but little experimental validation exists to support or challenge these models. The known functional properties of cerebral vasculature are limited mainly to the large pial surface and the small capillary level vessels. However, a significant lack of knowledge exists regarding the cluster of intermediate-sized vessels, mainly the intracortical, connecting these two groups of vessels and where, arguably, key blood flow regulation takes place. In recent years, advances in MR technology and methodology have enabled the probing of the brain, both structurally and functionally, at resolutions and coverage not previously attainable. Functional MRI has been utilized to map functional units down to the levels of cortical columns and lamina. These capabilities open new possibilities for investigating neurovascular coupling and testing hypotheses regarding fundamental cerebral organization. Here, we summarize recent cutting-edge MR applications for studying neurovascular and functional imaging, both in humans as well as in animal models. In light of the described imaging capabilities, we put forward a theory in which a cortical column, an ensemble of neurons involved in a particular neuronal computation is spatially correlated with a specific vascular unit, i.e., a cluster of an emerging principle vein surrounded by a set of diving arteries. If indeed such a correlation between functional (neuronal) and structural (vascular) units exist as a fundamental intrinsic cortical feature, one could conceivably delineate functional domains in cortical areas that are not known or have not been identified.

Keywords: high-resolution, fMRI, cortical vessels, columns, vascular-unit

INTRODUCTION

All hemodynamic mapping techniques are bound by the underlying vascular network. Functional brain imaging techniques such as functional MRI (fMRI) and optical imaging of intrinsic signals rely on the apparent close coupling between neuronal activity and local changes (typically increases) in blood supply (Roy and Sherrington, 1890). Numerous studies have focused on the relationship between neuronal activity and the mechanisms of local blood flow modulation (e.g., Logothetis et al., 2001; Kim et al., 2004). The ultimate spatial resolution of any hemodynamic-based functional mapping technique will rely on the morphology of the underlying vasculature supplying the region and on the controlling mechanisms regulating the flow to the region. The first direct evidence to support such correlation between neuronal activity (as determined by hemodynamic mapping signals) and the fine vascular system was provided by Harrison et al. (2002). In combined optical imaging and corrosion cast preparation in the auditory cortex, it was demonstrated that intrinsic optical signals were spatially associated with a specific capillary bed. However, because optical imaging is recording signals from the cortical surface, the measured signals are a 2-D representation of a 3-D vascular network system, including non-specific surface vessels.

In general terms, the cortical vasculature system can be described by three basic elements: arteries, veins and the fine vascular network, i.e., the capillary bed. A large body of literature exists describing the morphology and functionality of the pial vessels, mainly using optical methods on the exposed cortical surface. At the other end of the vascular tree, the capillary level, there are ample studies exploring their structural nature using a large arsenal of histochemical approaches. Only recently have the functional properties of the capillaries been investigated, using focal and with limited field-of-view (FOV) optical techniques such as Two-Photon imaging (Kleinfeld et al., 1998; Schaffer et al., 2006). Connecting these two groups is a cluster of intracortical vessels, which branch off from large cortical surface vessels, penetrate the cortex at approximately right angles, and extend down to the capillary level deep within the tissue. However, data describing their morphology is limited, and their functional properties are largely a mystery. This is mainly due to technical limitations of accessing these vessels; the intracortical vessels, as their name implies, are embedded within the tissue. While relatively little is known about them, their strategic positioning within the cortical tissue may play a significant role in blood flow regulation at the sub-millimeter scale – the level of fundamental functional units – the cortical columns (Lorente de No, 1938; Mountcastle, 1957).

Furthermore, the current understanding of the vascular origins of the blood oxygenation level dependent (BOLD) mechanism, the most commonly used fMRI contrast, is based on theoretical modeling and assumptions (Boas et al., 2008); little experimental validation exists to support or challenge such models with regard to

its vascular origin (Turner, 2002). Therefore, a better understanding of the vascular system and its spatial correlation with the hemodynamic mapping signal is desperately needed. With the goal of understanding blood flow regulation at the columnar level, we focus our research efforts on these intracortical-level vessels.

In the literature, the intracortical vessels are usually divided into six main groups, following the Duvernoy classification (Duvernoy et al., 1981). Group 1 is composed of vessels which reach layer I (neuronal layer). Group 2 reaches the superficial parts of the pyramidal layers (III). Vessels in group 3 are the most numerous; they penetrate as far down as layer IV, which is also the most heavily vascularized. Group 4 reaches the uniform layer and inner limit of subcortical white matter. Group 5 is comprised of arteries and veins that pass through and vascularize the cortex as well as the adjacent white matter. Group 6 is a special group of arteries including large arteries, which pass through the gray matter without branching and only vascularize the white matter.

The cortical drainage has a surprisingly regular organization (Duvernoy, 1999). The diameters of intracortical veins are, to some extent, less available in the literature than their arterial counterpart. Fixation and embedding the tissue often deform the veins, therefore, diameter measurements taken after sectioning are often lower then those obtained with vascular casting (Roggendorf et al., 1978). The principle intracortical vein (V5) has a diameter of 120–125 μm, where groups 4 (V4), 3 (V3), and 2 (V2) have an average diameter of 65, 45, and 30 μm, respectively (Duvernoy et al., 1981).

Similar to the venous system, the intracortical arteries can be classified into six groups. However, arteries of groups 2 and 3 are by far the most numerous, presumably because these vessels mainly supply the granular layers with the highest metabolic activity. These are followed by arteries in group 4 and then 5 (Duvernoy et al., 1981). Arteries in group 6 are found in relatively low numbers, and those in group 1 are found even less frequently. Arteries, in general, have smaller diameters than their venous counterpart. Arteries in group 6 have a large variability in diameter, ranging from 50 to 240 μm. Arteries of group 5 range from 30 to 75 μm and arteries in groups 2, 3, and 4 have vessels diameters of 15–25, 15–30, and 30–40 μm, respectively (Duvernoy et al., 1981). Within gray matter, capillaries of 3–5 μm diameter (Tieman et al., 2004) and mean length 200 μm drain into venules of 10–20 μm in diameter. In the tangential plane, there are differences in the vascular density according to the cortical layers (Duvernoy et al., 1981; Tieman et al., 2004). Higher capillary density is usually found across the middle layers (layers III/IV). Interestingly, a better correlation was reported between the vascular density and the number of synapses, not the number of neurons (Wolff, 1976).

As described above, our current knowledge of the intracortical vessels are mainly coming from human post-mortem (Duvernoy et al., 1981; Duvernoy, 1991; Reina-De La Torre et al., 1998; Lauwers et al., 2008) or *ex vivo* animals (Woolsey et al., 1996; Harrison et al., 2002) studies. The majority of columnar (Kim et al., 2000; Duong et al., 2001; Zhao et al., 2005) and laminar (Harel et al., 2002; Silva and Koretsky, 2002; Goense and Logothetis, 2006; Harel et al., 2006; Zhao et al., 2006) fMRI studies are currently done in rats, cats and monkeys, where little is known about the intracortical vessels in these species. More specifically, in the cat model, which is being used extensively in electrophysiology, optical imaging, and fMRI studies for understanding neurovascular coupling (Malonek and Grinvald, 1996; Malonek et al., 1997; Thompson et al., 2003), the literature describing these vessels is generally inadequate or non-existent. Thus, since fMRI is currently the chief investigation tool that can resolve hemodynamic changes transversely across the cortical tissue and without depth limitation, it is crucial to relate the fMRI signal changes with the underlying vascular morphology with the goal of a better understanding of blood flow regulation, which may in turn results in tools for improving the spatial specificity of human brain mapping.

METHODS/RESULTS

Here, we describe recent advances in MRI methodology that allows for imaging of the intracortical vessels *in vivo*, at resolutions approaching the macroscopic level. In addition, we describe recent developments in high-resolution fMRI studies in humans that successfully resolved cortical columns.

HIGH-RESOLUTION IMAGING OF INTRACORTICAL VESSELS

Utilizing the advantages of high magnetic field (9.4 T) high-resolution 3D gradient echo images were acquired in the cat visual cortex (**Figure 1**). Using a combination of endogenous BOLD contrast, an exogenous iron-oxide contrast agent and time-of-flight (TOF) micro-angiography we developed an imaging scheme that

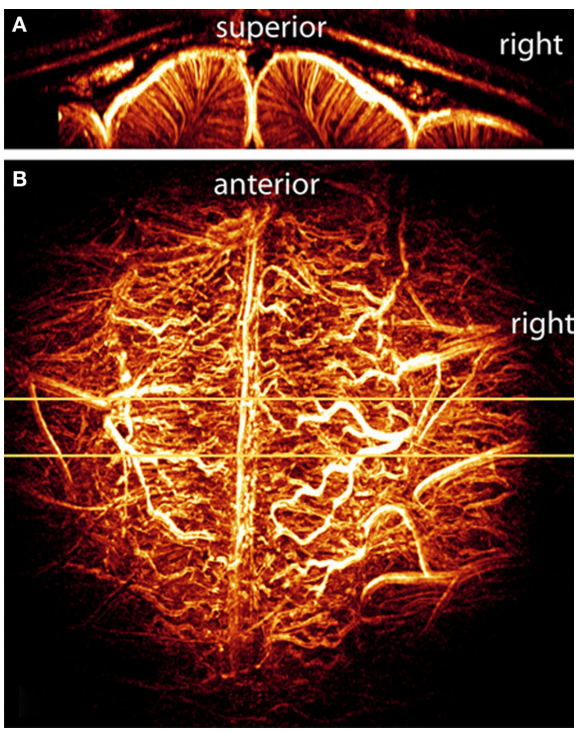

FIGURE 1 | Maximum intensity projections (MIPs) of the 3D volume of a cat brain viewed in (A) coronal and (B) axial orientations. The axial projection **(B)** was performed over the full acquisition volume, whereas the coronal projection **(A)** was produced from a narrow slab indicated by the yellow lines in **(B)**. The coronal view clearly shows the uniform organization of intracortical vessels. The axial view is dominated by the vessels on the pial surface. Figure modified from Bolan et al. (2006).

provided highly detailed image volume with high specificity for distinguishing between arteries and veins within the cortex (see below). The acquisition parameters included: TR/TE = 32.4/5.5 ms, FOV 20 mm × 20 mm × 5 mm, matrix 256 × 256 × 32. The images were reconstructed by windowing with a symmetric Tukey window affecting 20% of pixels on each edge of k-space, zero-filling to twice the native acquisition matrix and Fourier transforming, producing a reconstructed resolution of 39 μm × 39 μm × 78 μm (for more details Bolan et al., 2006).

To further enhance the sensitivity to the microvasculature, a bolus administration of monocrystalline iron oxide (MION), an exogenous contrast agent, was used to delineate smaller cortical vessels that are not visible under normal imaging conditions. MION is an intravascular iron-oxide based contrast agent. It is superparamagnetic with a very high R2 relaxivity which remains in the intravascular space (particle size 22 nm) and has a long blood half-life (Shen et al., 1993). When used in high concentrations, as shown here, the increased intravascular T2 relaxation dominates the signals, causing both arteries and veins to appear dark in gradient echo images (Park et al., 2008). **Figure 1** demonstrates a reconstruction method used to visualize, in great details, the entire vascular network that can be resolved under the current acquisition resolution. An example of a 3-D image using maximum intensity projection (MIP), commonly employed for visualizing MR angiographic data, is shown. The projections were created directly from the volumetric image with no manual modifications. The axial projection (**Figure 1B**) was performed over the full acquisition volume, whereas the coronal projection (**Figure 1A**) was produced from a narrow slab indicated by the yellow lines in (b). These images, particularly the coronal view (**Figure 1A**), give a good overview of the relatively larger surface vasculature and more intriguing, a view of the intracortical vascular architecture.

Most distinctive are the vessels that penetrate into the cortical tissue, i.e., gray matter, nearly perpendicular to the pial surface, and run down to the white matter and beyond. Furthermore, this data is a clear example, and to some extent, a validation of our earlier findings of the largest BOLD signal changes observed at, or adjacent to, the large surface vessels (Harel et al., 2006). Additionally, the coronal view (**Figure 1A**) shows the uniformity and orderly organization of the intracortical vessels found in the cat visual cortex (Bolan et al., 2006).

TIME-OF-FLIGHT SCANS AND VESSEL CLASSIFICATION MAPS

The technique of 3D TOF micro-angiography is used to generate images of the arteries and is demonstrated in **Figure 2**. In the exact setup as the images shown in **Figure 1**, a transverse slab (thickness 2 mm) was positioned in the center of the cortex, so that the superior edge of the slice passed through the sagittal sinus (**Figure 2A**). The vertical position of the slice is critical for producing proper flow weighting in the intracortical arteries running perpendicular to the cortical surface. The flip angle (30°) is greater than the Ernst angle for both blood and cortical gray matter so the spins inside the slice are saturated and show low signal. Blood that flows into the slice is not saturated, and therefore gives a higher signal than blood that has remained inside the slice for one or more excitations. This effect is called the TOF or inflow effect. In **Figure 2A**, the red arrows show an example of a bright vessel in both views. Other bright vessels are evident, particularly in the axial view in which most of the larger intracortical vessels are oriented perpendicular to the image plane. Blue arrows point to veins which are dark due to the BOLD effect (**Figure 2A**). Thus, **Figure 2** demonstrates the ability to first, image the intracortical vessels and second, differentiate and show a clear separation of arteries and veins within the image volume across (tangential) the tissue. **Figure 2B** displays a vessel classification map, a single axial slice across primary

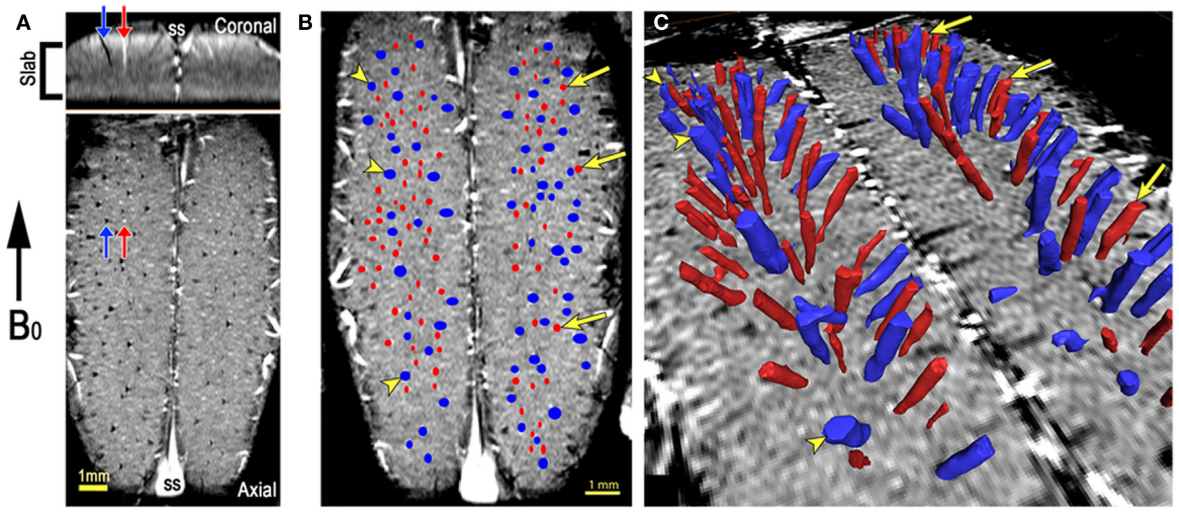

FIGURE 2 | Vascular model of cat visual cortex. (A) An example of 3D time-of-flight (TOF) microangiography in the cat visual cortex. The axial excitation slab (Slab) was positioned so that its superior edge passed through the sagittal sinus (SS), as can be seen in the coronal view. Arteries, indicated by red arrows, are bright due to unsaturated blood flowing into the slab. Veins, indicated by blue arrows, are dark due to their elevated concentration of deoxyhemoglobin (the BOLD effect). **(B)** A dorsal view close up showing in greater details vessels classifications using the TOF and BOLD techniques; Veins: blue, Arteries: red. **(C)** 3D surface rendering of the vessels identified throughout the entire imaged volume. Figure modified from Bolan et al. (2006).

visual cortex of the cat in which intracortical visible vessels were classified as vein or artery, using the TOF and BOLD effect method as described above. A large number of vessels can be identified in a single slice, as shown in **Figure 2A**. By combining several imaging schemes, namely susceptibility-weighted and TOF images, along with 3D image-processing and display methods, we have developed a technique by which we can identify and classify the intracortical vessels as veins or arteries *in vivo*.

With the full 3D information, the extent of each vessel's penetration into the cortex can be determined as is shown by the 3D surface rendering of the vessels (**Figure 2C**). Vessels can then be classified using the method of Duvernoy et al. (1981). It appears that the majority of the arteries visible in these images are of classes A4 and A5, meaning they extend into the deep cortical layers (A4) or continue into the underlying white matter (A5). The veins also vary in their penetration, and fall into the classes V4 and V5 of Duvernoy et al. (1981). The smallest vessels that are reliably detectable with this imaging method, the A4 arteries, are reported to have diameters of 30–40 μm in human subjects (Duvernoy et al., 1981). Smaller vessels (A1-3, V1-3) are visible in the post-MION images, but are not clearly identifiable in the flow-weighted images. Based on this reasoning, the majority of the penetrating vessels seen in these images probably have diameters in the 50–100 μm range.

It is obvious from the data that the distribution of arteries and veins is not completely random. The largest veins oriented perpendicular to the cortical surface are the principle intracortical veins. These are spaced 1–1.5 mm apart, and are surrounded by a network of smaller veins and arteries oriented in the same direction (Bolan et al., 2006). This morphological organization is consistent with previous *ex vivo* studies in cats (McHedlishvili and Kuridze, 1984) and humans (Duvernoy et al., 1981) and is in agreement with the "vascular unit" as was suggested by Duvernoy's model. Thus, the data shown here suggests an orderly structure of the vascular system found in the cat cortex; Furthermore, they demonstrate the capabilities of high-field MRI to identify and resolve these small vascular features *in vivo*.

HIGH-RESOLUTION fMRI AND ITS CORRELATES WITH THE VASCULAR MODEL

In several cats we obtained functional MR images signals from the primary visual cortex following a visual stimulation task. Eight slices with image resolution of 250 μm × 250 μm × 500 μm were acquired. The functional maps were confined to primary visual cortex and followed the expected pattern of activation (Harel et al., 2002, 2006; Zhao et al., 2004). **Figure 3A** shows a BOLD functional map for a single axial slice across primary visual cortex (area 18); in addition, a 3-D surface rendering of the vessels (similar to **Figure 2C**) is displayed (**Figure 3B**). Several interesting features are evident from the data: first, the pattern of the stimulus-induced MR signal changes in the transverse plane had a patchy appearance and was found to be non-uniform across the cortex. As expected from theoretical and modeling studies, it appears that the regions with larger BOLD changes are associated with regions of large principal veins (blue). More intriguingly, these patterns of activations changed as a function of distance from the surface (i.e., deeper into the gray matter) implying the involvement of different

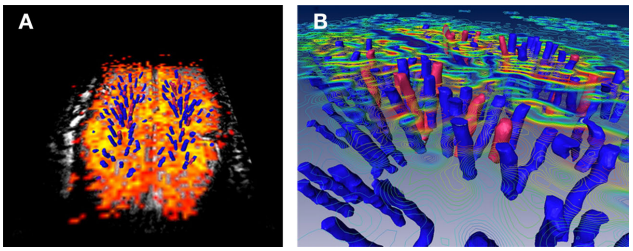

FIGURE 3 | Co-registration of fMRI maps with the underlying vascular model. (A) A representative axial slice across marginal gyrus in the cat primary visual cortex. Orange-to-yellow colors represent voxels that exhibit BOLD signal changes that was correlated with the stimulus paradigm. **(B)** 3D surface rendering of the veins and arteries (blue and red, respectively) within the imaged volume overlaid with iso-amplitude contour lines of the BOLD signals changes.

vascular compartments (Harel et al., 2006). These features are more evident when the fMRI signal changes are plotted as iso-amplitude contour lines and are combined with the vascular model as shown in **Figure 3B**. These preliminary experimental data demonstrate the feasibility of potentially detecting stimulus-induced blood flow changes at extreme high-resolutions and throughout the gray matter volume. Furthermore, these signal changes can now be spatially correlated with the underlying vascular system, relating these blood flow changes to a specific subset of the vascular units within the imaged volume.

FUNCTIONAL MRI REVEALS CORTICAL COLUMNS IN HUMAN

Capitalizing on the advantages of high magnetic fields systems, which offers increases in both the sensitivity as well as the specificity of MR detectable functional signals, the spatial and temporal resolutions of fMRI studies continue to be pushed allowing mapping of smaller and smaller functional properties of cerebral cortex.

A fundamental property of the cerebral cortex is the spatial localization of function. Within a defined cortical region, neurons sharing similar functional properties are often clustered together spanning from the pial surface to the white matter, thus forming a column-like functional unit. Initially, Mountcastle (1957) described the columnar organization of the somatic sensory cortex, which was followed by the work of Hubel and Wiesel (1962, 1965), who mapped the columnar organization of the visual cortex. This functional parcellation extends in the millimeter to sub-millimeter domain. In visual cortex, preference to right or left eye (ocular dominance), direction of motion (Weliky et al., 1996), spatial frequency (Issa et al., 2000), and orientation (Hubel and Wiesel, 1963, 1977; Blasdel and Salama, 1986; Bonhoeffer and Grinvald, 1991) have all been characterized in animals. In humans, the first example of such functional domains to be identified was ocular dominance columns (ODCs). Initially, they were observed using anatomical staining techniques in the post-mortem human brain (Horton and Hedley-Whyte, 1984) followed by functional delineation with fMRI (Menon et al., 1997; Dechent and Frahm, 2000; Cheng et al., 2001; Yacoub et al., 2007). They were found to be about 1 mm in width organized in a periodic layout in primary visual cortex. However, the unique anatomical connections from the lateral geniculate nucleus up to the cortex that give rise to this

unique feature do not exist for other columnar ensembles. Sun et al. (2007) recently have reported on the delineation of much larger temporal frequency domains in human visual cortex.

From years of invasive animal studies, orientation columns in visual cortex are perhaps the best-known example of such a functional organization in the brain. Building on the accomplishments of a long series of theoretical and experimental studies on the underlying mechanisms of fMRI contrast, combined with extensive validation studies using animal models (Fukuda et al., 2006; Harel et al., 2006), our group has recently demonstrated the feasible to map columnar structures in the human brain (Yacoub et al., 2007, 2008) (**Figure 4**). Studies were conducted at 7T using slab selective FOV reduction for spin-echo fMRI (Duong et al., 2003), which was found to have better spatial specificity (Harel et al., 2006). The spatial resolution was: 0.5 mm × 0.5 mm× 3 mm with minimal resolution loss due to EPI blurring along the phase encode direction. TR/TE = 6000/50 ms. To minimize motion effects, subjects used a bite bar. Subjects initially participated in ODC studies (Yacoub et al., 2007) and were brought back to map orientation specific regions using the same anatomical slice.

Striking similarities were found with the known spatial features and spatial relationships between ODC and orientation columns, as was previously described in monkeys and cat studies using the optical imaging method (Bartfeld and Grinvald, 1992; Blasdel, 1992; Hubener et al., 1997; Shoham et al., 1997). These results demonstrate the ability and maturity of high-field MRI to resolve functional units (cortical columns) in humans (Yacoub et al., 2008), features that were previously shown only via invasive approaches in animal studies.

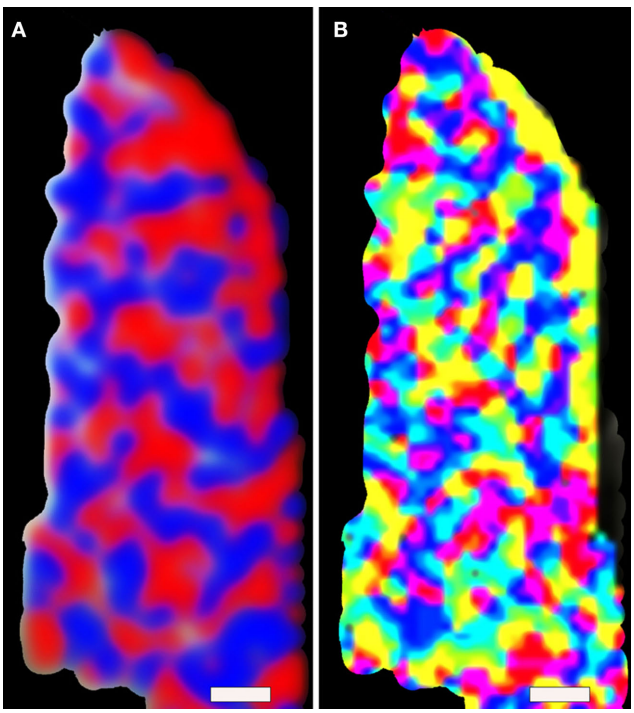

FIGURE 4 | Functional MRI reveals cortical columns in human. An example of ocular dominance **(A)** and orientation **(B)** columns fMRI maps obtain in human at 7 T magnet. The red and blue colors in **(A)** indicate preferences to right or left eye stimulation, whereas the color distribution in **(B)** represents a given voxel's preferred stimulus orientation. (Scale bar: 1.0 mm) Figure modified from Yacoub et al. (2008).

While this achievement was a substantial leap in human fMRI studies, the methodological aspect was not ideal. Due to technical limitations, all the high-resolution, sub-millimeter fMRI studies were limited to single-slice acquisitions and small FOVs, thus the functional maps are a 2-D representation of a complex 3-D brain structure. The use of a single slice requires an "optimal" slice prescription carefully chosen based on a flat imaged plane with minimal curvature of gray matter, ultimately limiting the general application of these methods to pre-screened subjects. Furthermore, with this limited imaging volume, slight motion by the subject is detrimental, as post-processing motion correction algorithms are very limited under these conditions.

Although advantageous due to increases in spatial specificity and functional sensitivity, high magnetic fields have historically been limited because of short relaxation times (T_2*), increased susceptibility artifacts, RF power limits, and non-uniform excitation fields. Thus, the advantages of high fields have been restricted to localized areas in the brain where these problems can be minimized, resulting in highly specific and sensitive fMRI maps. To overcome these limitations, new and more efficient pulse sequences are being developed that will allow mapping these functional domains in 3-D space and over larger volumes, while still maintaining sub-millimeter resolutions (Feinberg et al., 2008). In addition, capitalizing on the advances of gradient hardware, parallel imaging methodology and RF technology, highly accelerated acquisitions (up to 16-fold) (Moeller et al., 2010) have allow for high-resolution imaging of the whole brain on the order of 1 s (see **Figure 5**) with excellent image SNR and minimal distortions. These new developments to expand the benefits and utility of high field fMRI open the possibility to investigate and probe cortical organization and dynamics at spatial and temporal resolutions over large volumes that are not available by any other imaging technique.

HYPOTHESIS: A NEURONAL FUNCTIONAL UNIT IS ASSOCIATED WITH A PARTICULAR VASCULAR UNIT

Building on the advantages of high-field MRI, we have demonstrated the feasibility to image and classify cortical vasculature, *in vivo*, at resolutions approaching the microscopic scale. A vascular model describing the intracortical arterial and venous components was reconstructed and their spatial organization across the cortex was described. From a functional perspective, high-resolution fMRI, at high fields (7 and 9.4 T), allows non-invasive mapping of functional domains down to columnar and laminar levels of cortical organization. New imaging capabilities that allow sub-millimeter mapping of 3D functional units with a larger field of view that approaching whole-brain coverage, are currently being developed by several groups.

Building on these new imaging capabilities demonstrated above, one could explore features of cerebral cortex in several planes. On the neurophysiology/neurovascular research standpoint, the *in vivo* derived vascular model should provide a better understanding of the vascular morphology and its spatial dependency regarding

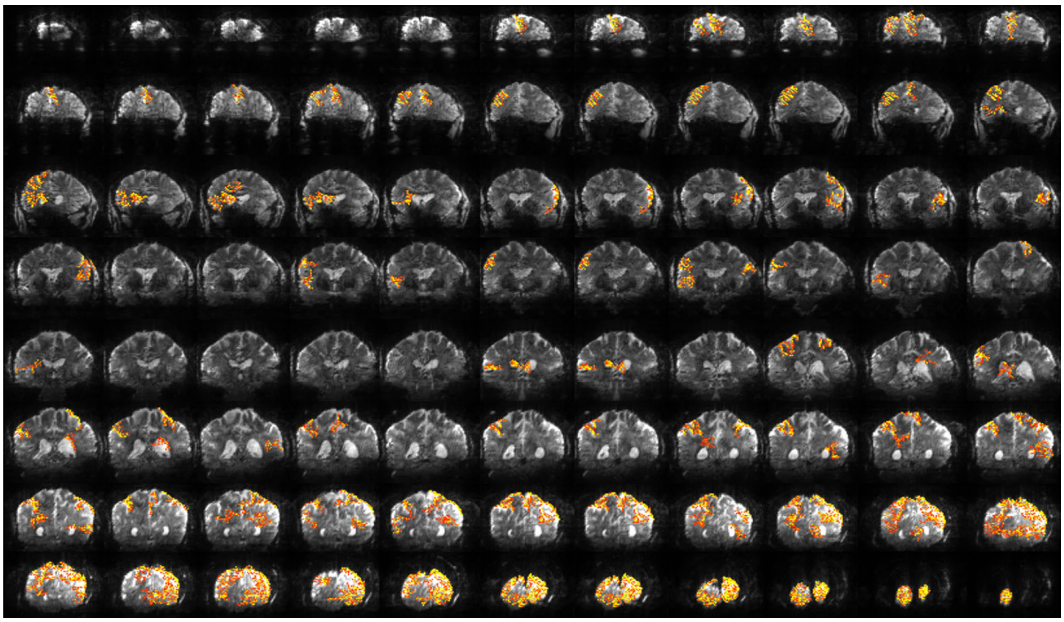

FIGURE 5 | Whole brain fMRI at high resolution. Functional activation maps for a complex visuomotor dissociation task acquired for 88 slices in 1.25 s with 2 mm × 2 mm × 2 mm resolution. Inset: representative coronal slices from a functional scan with 1 mm × 1 mm × 2 mm resolution. Figure modified from Moeller et al. (2010).

the fMRI contrast mechanism. Such new insights should allow for refinements and improvements of the imaging techniques that hopefully will allow better spatial localization and spatial specificity of the fMRI signals to the site of neuronal activity. Clinical applications such as neurosurgery planning, epilepsy, and brain tumor resections will all benefit from increased accuracy.

Historically, our knowledge of brain *function* was based solely on anatomical and lesions studies. When Mountcastle (1957) first described the columnar organization of the somatic sensory cortex on the basis of observations made in single neuron recording experiments, his report was met with disbelief by many neuroanatomists (Mountcastle, 1997). This was because the histological methods available at the time revealed no structural counterpart to match the physiological observations (Mountcastle, 1997, 2003). Since Mountcastle's discovery, followed by many others over the years, cortical columns have been accepted as the basic computational/functional unit of the cortex.

In the whisker barrel cortex of the rat, there is a clear association between the functional unit, in this case the barrel, and the vascular system that supplies and drains the blood with the notion that it optimizes the local interactions between the two (Woolsey et al., 1996). Woolsey summarized his finding as followed: "Matching a functional grouping of neurons with a vascular module is an elegant means of reducing the risk of embarrassment for energy-expensive neuronal activity (ion pumping) while minimizing energy spent for delivery of the energy (cardiac output)" (Woolsey et al., 1996). If Woolsey's theory of the barrel-vascular unit is indeed correct, one should expect to find similar global arrangements, following the same logic across the entire cerebral cortex. Furthermore, it has been shown, using a rat model and chronic hypoxia that plasticity of cortical capillary density can occur on a time scale of several weeks (LaManna et al., 1992, 2004). Also, a high correlation between the distribution of the vascular density with the cytochrome oxidase blobs was found in the monkey primary visual cortex (Zheng et al., 1991). Therefore, if the vascular system has the capacity to adapt to demand, it is highly likely that there will be strong correlations between functional units, i.e., the neurons, and vascularity.

In post-mortem studies in humans a regular organization of vessels within the cortex, which was found to have a circular nature has been reported (Duvernoy et al., 1981); a principal vein (V5) or several smaller veins (V4 or V3) surrounded by an arterial ring containing a larger number (x4) of arteries (see **Figure 6**). Also, there appears to be a relatively uniform distribution of these principle veins (V5) spaced every 0.75–1 mm (Wolff, 1976). Thus, it has been suggested that such vascular organization may manifest as a "vascular unit." Could these vascular units be the equivalent of the vascular units that Woolsey describes in the rat barrel cortex? If so, do they represent a specific functional entity? This "magic" distance in the principal veins, coincidentally or not, is similar to the known sizes and distances between functional cortical columns in visual cortex of cats (Lowel and Singer, 1987; Bonhoeffer and Grinvald, 1993) and humans (Horton et al., 1990; Cheng et al., 2001; Yacoub et al., 2007). Can the spatial arrangement of the vascular system tell us anything about the neuronal properties of the tissue?

We put forward a hypotheses that a cortical column, an ensemble of neurons involved in a particular neuronal computation, is spatially correlated with a specific vascular unit, i.e., a cluster of emerging principal veins surrounded by a set of diving arteries. A "vascular unit" is associated with a known "functional unit" in the cortex. If indeed one can establish a spatial correlation between

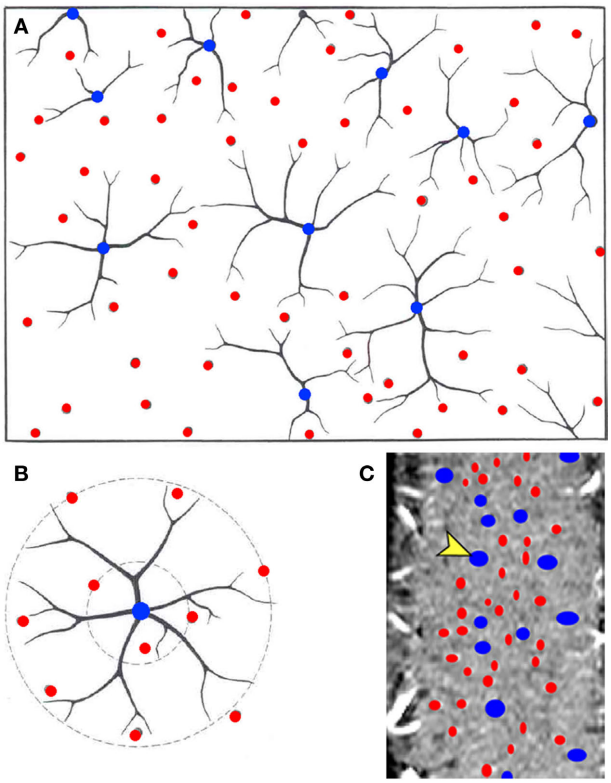

FIGURE 6 | Vascular unit model. A circular nature of the vascular organization. **(A)** A drawing of a cross-section showing the venous units and their arterial rings. **(B)** Duvernoy's proposed spatial organization of the vascular unit; a principle cortical vein (blue) surrounded by several penetrating arteries (red). **(C)** A vessel classification maps in a tangential section in cat visual cortex derived from the MRI data. A and B were modified from Duvernoy et al. (1981).

functional (neuronal) and structural (vascular) units as a basic and fundamental intrinsic cortical feature, this could provide a tool in which one might conceivably delineate functional domains in cortical areas that are not known or have not been identified. For example, columnar structures in V1 are relatively "easy" to resolve using basic stimuli such as eye dominance or drifting bars with altering orientations. However, as one moves to higher visual areas, more complex stimuli are needed to activate functional regions (Tanaka, 1996). Would it be possible in the future to "search" for functional properties based on the vascular layout? Can we use the structural units to foresee the spatial organizations of the functional domains?

Furthermore, what happens in a more "complex" cortical region that processes several computational units? It has been shown in the cat, using optical imaging, that several columnar systems (e.g., ocular dominance, orientation, and spatial frequency) occupy the same cortical tissue. Are each of these functional units associated with their own unique vascular structure? What percent of overlaps exist between units and is there any spatial organization of such overlapping systems?

While these ideas are perhaps hard to comprehend at the present time, the tools and knowledge being developed today will allow us to reach these goals in the future. Perhaps, 1 day, we may even be able to link clinical symptoms of brain disorders (functional properties) with an abnormality of the vascular (structural) unit.

ACKNOWLEDGMENTS

This work was supported, in part, by the NIH grants R01EB008645, P41-RR008079, and P30 NS057091. Instrument acquisition was in part funded by the Keck Foundation. This work was carried out in part using computing resources at the University of Minnesota Supercomputing Institute.

REFERENCES

Bartfeld, E., and Grinvald, A. (1992). Relationships between orientation-preference pinwheels, cytochrome oxidase blobs, and ocular-dominance columns in primate striate cortex. *Proc. Natl. Acad. Sci. U.S.A.* 89, 11905–11909.

Blasdel, G. G. (1992). Differential imaging of ocular dominance and orientation selectivity in monkey striate cortex. *J. Neurosci.* 12, 3115–3138.

Blasdel, G. G., and Salama, G. (1986). Voltage-sensitive dyes reveal a modular organization in monkey striate cortex. *Nature* 321, 579–585.

Boas, D. A., Jones, S. R., Devor, A., Huppert, T. J., and Dale, A. M. (2008). A vascular anatomical network model of the spatio-temporal response to brain activation. *Neuroimage* 40, 1116–1129.

Bolan, P. J., Yacoub, E., Garwood, M., Ugurbil, K., and Harel, N. (2006). In vivo micro-MRI of intracortical neurovasculature. *Neuroimage* 32, 62–69.

Bonhoeffer, T., and Grinvald, A. (1991). Iso-orientation domains in cat visual cortex are arranged in pinwheel-like patterns. *Nature* 353, 429–431.

Bonhoeffer, T., and Grinvald, A. (1993). The layout of iso-orientation domains in area 18 of cat visual cortex: optical imaging reveals a pinwheel-like organization. *J. Neurosci.* 13, 4157–4180.

Cheng, K., Waggoner, R. A., and Tanaka, K. (2001). Human ocular dominance columns as revealed by high-field functional magnetic resonance imaging. *Neuron* 32, 359–374.

Dechent, P., and Frahm, J. (2000). Direct mapping of ocular dominance columns in human primary visual cortex. *Neuroreport* 11, 3247–3249.

Duong, T. Q., Kim, D. S., Ugurbil, K., and Kim, S. G. (2001). Localized cerebral blood flow response at submillimeter columnar resolution. *Proc. Natl. Acad. Sci. U.S.A.* 98, 10904–10909.

Duong, T. Q., Yacoub, E., Adriany, G., Hu, X., Ugurbil, K., and Kim, S. G. (2003). Microvascular BOLD contribution at 4 and 7 T in the human brain: gradient-echo and spin-echo fMRI with suppression of blood effects. *Magn. Reson. Med.* 49, 1019–1027.

Duvernoy, H. M. (1991). *The Human Brain: Surface, Three-Dimensional Sectional Anatomy and MRI*. Wien, Austria: Springer-Verlag.

Duvernoy, H. M. (1999). Vascularization of the cerebral cortex. *Rev. Neurol. (Paris)* 155, 684–687.

Duvernoy, H. M., Delon, S., and Vannson, J. L. (1981). Cortical blood vessels of the human brain. *Brain Res. Bull.* 7, 519–579.

Feinberg, D., Harel, N., Ramanna, S., Ugurbil, K., and Yacoub, E. (2008). "Sub-millimeter single-shot 3D GRASE with inner volume selection for T2 weighted fMRI applications at 7 Tesla," in *Proceedings of the 16th Annual Meeting of the International Society for Magnetic Resonance in Medicine,* Toronto, Abstract 2373.

Fukuda, M., Moon, C. H., Wang, P., and Kim, S. G. (2006). Mapping iso-orientation columns by contrast agent-enhanced functional magnetic resonance imaging: reproducibility, specificity, and evaluation by optical imaging of intrinsic signal. *J. Neurosci.* 26, 11821–11832.

Goense, J. B., and Logothetis, N. K. (2006). Laminar specificity in monkey V1 using high-resolution SE-fMRI. *Magn. Reson. Imaging* 24, 381–392.

Harel, N., Lin, J., Moeller, S., Ugurbil, K., and Yacoub, E. (2006). Combined imaging-histological study of cortical laminar specificity of fMRI signals. *Neuroimage* 29, 879–887.

Harel, N., Zhao, Z., Wang, P., and Kim, S. G. (2002). "Layer specificity of BOLD & CBV fMRI signals at ultra-high resolution," in *8th International Conference on Functional Mapping of the Human Brain*, Sendai Vol. 16, 1221–1223.

Harrison, R. V., Harel, N., Panesar, J., and Mount, R. J. (2002). Blood capillary distribution correlates with hemodynamic-based functional imaging in cerebral cortex. *Cereb. Cortex* 12, 225–233.

Horton, J., and Hedley-Whyte, E. T. (1984). Mapping of cytochrome oxidase patches and ocular dominance columns in human visual cortex. *Philos. Trans. R. Soc. Lond. Biol. B.* 304, 255–272.

Horton, J. C., Dagi, L. R., and McCrane, E. P. (1990). Arrangement of ocular

dominance columns in human visual cortex. *Arch. Opthalmol.* 108, 1025–1031.

Hubel, D., and Wiesel, T. N. (1962). Receptive fields, binocular interaction and functional architecture in the cat's visual cortex. *J. Physiol. (Lond.)* 160, 106–154.

Hubel, D., and Wiesel, T. N. (1965). Receptive fields and functional architecture in two nonstriate visual areas (18 and 19) of the cat. *J. Neurophysiol.* 28, 229–289.

Hubel, D. H., and Wiesel, T. N. (1963). Shape and arrangement of columns in cat's striate cortex. *J. Physiol. (Lond.)* 165, 559–568.

Hubel, D. H., and Wiesel, T. N. (1977). Functional architecture of macaque monkey visual cortex. *Proc. R. Soc. Lond. [Biol.]* 198, 1–59.

Hubener, M., Shoham, D., Grinvald, A., and Bonhoeffer, T. (1997). Spatial relationships among three columnar systems in cat area 17. *J. Neurosci.* 17, 9270–9284.

Issa, N. P., Trepel, C., and Stryker, M. P. (2000). Spatial frequency maps in cat visual cortex. *J. Neurosci.* 20, 8504–8514.

Kim, D. S., Duong, T. Q., and Kim, S. G. (2000). High-resolution mapping of iso-orientation columns by fMRI. *Nat. Neurosci.* 3, 164–169.

Kim, D. S., Ronen, I., Olman, C., Kim, S. G., Ugurbil, K., and Toth, L. J. (2004). Spatial relationship between neuronal activity and BOLD functional MRI. *Neuroimage* 21, 876–885.

Kleinfeld, D., Mitra, P. P., Helmchen, F., and Denk, W. (1998). Fluctuations and stimulus-induced changes in blood flow observed in individual capillaries in layers 2 through 4 of rat neocortex. *Proc. Natl. Acad. Sci. U.S.A.* 95, 15741–15746.

LaManna, J. C., Chavez, J. C., and Pichiule, P. (2004). Structural and functional adaptation to hypoxia in the rat brain. *J. Exp. Biol.* 207, 3163–3169.

LaManna, J. C., Vendel, L. M., and Farrell, R. M. (1992). Brain adaptation to chronic hypobaric hypoxia in rats. *J. Appl. Physiol.* 72, 2238–2243.

Lauwers, F., Cassot, F., Lauwers-Cances, V., Puwanarajah, P., and Duvernoy, H. (2008). Morphometry of the human cerebral cortex microcirculation: general characteristics and space-related profiles. *Neuroimage* 39, 936–948.

Logothetis, N. K., Pauls, J., Augath, M., Trinath, T., and Oeltermann, A. (2001). Neurophysiological investigation of the basis of the fMRI signal. *Nature* 412, 150–157.

Lorente de No, R. (1938). "Architectonics and structure of the cerberal cortex," in *Physiology of the Nervous System*, ed. J. F. Fulton (New York: Oxford University Press), 291–330.

Lowel, S., and Singer, W. (1987). The pattern of ocular dominance columns in flat-mounts of the cat visual cortex. *Exp. Brain Res.* 68, 661–666.

Malonek, D., Dirnagl, U., Lindauer, U., Yamada, K., Kanno, I., and Grinvald, A. (1997). Vascular imprints of neuronal activity: relationships between the dynamics of cortical blood flow, oxygenation, and volume changes following sensory stimulation. *Proc. Natl. Acad. Sci. U.S.A.* 94, 14826–14831.

Malonek, D., and Grinvald, A. (1996). Interactions between electrical activity and cortical microcirculation revealed by imaging spectroscopy: implication for functional brain mapping. *Science* 272, 551–554.

McHedlishvili, G., and Kuridze, N. (1984). The modular organization of the pial arterial system in phylogeny. *J. Cereb. Blood Flow Metab.* 4, 391–396.

Menon, R. S., Ogawa, S., Strupp, J. P., and Ugurbil, K. (1997). Ocular dominance in human V1 demonstrated by functional magnetic resonance imaging. *J. Neurophysiol.* 77, 2780–2787.

Moeller, S., Yacoub, E., Olman, C., Auerbach, E. J., Stupp, J., Harel, N., and Ugurbil, K. (2010). Multiband multislice GE-EPI at 7 tesla, with 16-fold acceleration using partial parallel imaging with application to high spatial and temporal whole-brain fMRI. *Magn. Reson. Med.* 63, 1144–1153.

Mountcastle, V. B. (1957). Modality and topographic properties of single neurons of cat's somatic sensory cortex. *J. Neurophysiol.* 20, 408–434.

Mountcastle, V. B. (1997). The columnar organization of the neocortex. *Brain* 120 (Pt 4), 701–722.

Mountcastle, V. B. (2003). Introduction. Computation in cortical columns. *Cereb. Cortex* 13, 2–4.

Park, S. H., Masamoto, K., Hendrich, K., Kanno, I., and Kim, S. G. (2008). Imaging brain vasculature with BOLD microscopy: MR detection limits determined by in vivo two-photon microscopy. *Magn. Reson. Med.* 59, 855–865.

Reina-De La Torre, F., Rodriguez-Baeza, A., and Sahuquillo-Barris, J. (1998). Morphological characteristics and distribution pattern of the arterial vessels in human cerebral cortex: a scanning electron microscope study. *Anat. Rec.* 251, 87–96.

Roggendorf, W., Cervos-Navarro, J., and Lazaro-Lacalle, M. D. (1978). Ultrastructure of venules in the cat brain. *Cell Tissue Res.* 192, 461–474.

Roy, C., and Sherrington, C. (1890). On the regulation of the blood supply of the brain. *J. Physiol.* 11, 85–108.

Schaffer, C. B., Friedman, B., Nishimura, N., Schroeder, L. F., Tsai, P. S., Ebner, F. F., Lyden, P. D., and Kleinfeld, D. (2006). Two-photon imaging of cortical surface microvessels reveals a robust redistribution in blood flow after vascular occlusion. *PLoS Biol.* 4:e22. doi: 10.1073/pnas.0609551104.

Shen, T., Weissleder, R., Papisov, M., Bogdanov, A. Jr., and Brady, T. J. (1993). Monocrystalline iron oxide nanocompounds (MION): physicochemical properties. *Magn. Reson. Med.* 29, 599–604.

Shoham, D., Hubener, M., Schulze, S., Grinvald, A., and Bonhoeffer, T. (1997). Spatio-temporal frequency domains and their relation to cytochrome oxidase staining in cat visual cortex. *Nature* 385, 529–533.

Silva, A. C., and Koretsky, A. P. (2002). Laminar specificity of functional MRI onset times during somatosensory stimulation in rat. *Proc. Natl. Acad. Sci. U.S.A.* 99, 15182–15187.

Sun, P., Ueno, K., Waggoner, R. A., Gardner, J. L., Tanaka, K., and Cheng, K. (2007). A temporal frequency-dependent functional architecture in human V1 revealed by high-resolution fMRI. *Nat. Neurosci.* 10, 1404–1406.

Tanaka, K. (1996). Inferotemporal cortex and object vision. *Annu. Rev. Neurosci.* 19, 109–139.

Thompson, J. K., Peterson, M. R., and Freeman, R. D. (2003). Single-neuron activity and tissue oxygenation in the cerebral cortex. *Science* 299, 1070–1072.

Tieman, S. B., Mollers, S., Tieman, D. G., and White, J. (2004). The blood supply of the cat's visual cortex and its postnatal development. *Brain Res.* 998, 100–112.

Turner, R. (2002). How much cortex can a vein drain? Downstream dilution of activation-related cerebral blood oxygenation changes. *Neuroimage* 16, 1062–1067.

Weliky, M., Bosking, W. H., and Fitzpatrick, D. (1996). A systematic map of direction preference in primary visual cortex. *Nature* 379, 725–728.

Wolff, J. R. (1976). Proceedings: an ontogenetically defined angi oarchitecture of the neocortex. *Arzneimittelforschung* 26, 1239.

Woolsey, T. A., Rovainen, C. M., Cox, S. B., Henegar, M. H., Liang, G. E., Liu, D., Moskalenko, Y. E., Sui, J., and Wei, L. (1996). Neuronal units linked to microvascular modules in cerebral cortex: response elements for imaging the brain. *Cereb. Cortex* 6, 647–660.

Yacoub, E., Harel, N., and Ugurbil, K. (2008). High-field fMRI unveils orientation columns in humans. *Proc. Natl. Acad. Sci. U.S.A.* 105, 10607–10612.

Yacoub, E., Shmuel, A., Logothetis, N., and Ugurbil, K. (2007). Robust detection of ocular dominance columns in humans using Hahn Spin Echo BOLD functional MRI at 7 Tesla. *Neuroimage* 37, 1161–1177.

Zhao, F., Wang, P., Hendrich, K., and Kim, S. G. (2005). Spatial specificity of cerebral blood volume-weighted fMRI responses at columnar resolution. *Neuroimage* 27, 416–424.

Zhao, F., Wang, P., Hendrich, K., Ugurbil, K., and Kim, S. G. (2006). Cortical layer-dependent BOLD and CBV responses measured by spin-echo and gradient-echo fMRI: insights into hemodynamic regulation. *Neuroimage* 30, 1149–1160.

Zhao, F., Wang, P., and Kim, S. G. (2004). Cortical depth-dependent gradient-echo and spin-echo BOLD fMRI at 9.4T. *Magn. Reson. Med.* 51, 518–524.

Zheng, D., LaMantia, A.-S., and Purves, D. (1991). Specialized vascularization of the primate visual cortex. *J. Neurosci.* 11, 2622–2629.

Conflict of Interest Statement: The authors declare that the research was conducted in the absence of any commercial or financial relationships that could be construed as a potential conflict of interest.

Received: 05 March 2010; paper pending published: 19 March 2010; accepted: 08 September 2010; published online: 27 September 2010.

Citation: Harel N, Bolan PJ, Turner R, Ugurbil K and Yacoub E (2010) Recent advances in high-resolution MR application and its implications for neurovascular coupling research. Front. Neuroenerg. 2:130. doi: 10.3389/fnene.2010.00130

frontiers in
NEUROENERGETICS

HYPOTHESIS AND THEORY ARTICLE
published: 04 October 2010
doi: 10.3389/fnene.2010.00025

Pathophysiological interference with neurovascular coupling – when imaging based on hemoglobin might go blind

Ute Lindauer[1]*, Ulrich Dirnagl[2,3,4], Martina Füchtemeier[2], Caroline Böttiger[2], Nikolas Offenhauser[2], Christoph Leithner[2†] and Georg Royl[2†]

[1] *Department of Neurosurgery, Klinikum rechts der Isar, Technical University, Munich, Germany*
[2] *Departments of Neurology and Experimental Neurology, Charité – Universitätsmedizin Berlin, Berlin, Germany*
[3] *Center for Stroke Research Berlin, Berlin, Germany*
[4] *Neurocure Research Center Berlin, Berlin, Germany*

Edited by:
Anna Devor, University of California San Diego, USA

Reviewed by:
Tom Liu, University of California San Diego, USA
Kamil Uludag, Max Planck Institute, Germany
Noam Harel, University of Minnesota, USA

***Correspondence:**
Ute Lindauer, Departments of Neurosurgery, Experimental Neurosurgery, Klinikum rechts der Isar, Technical University Munich, Ismaninger Str. 22, 81675 Munich, Germany.
e-mail: ute.lindauer@lrz.tum.de

†Christoph Leithner and Georg Royl contributed equally to the manuscript.

Assessing neuronal activity by non-invasive functional brain imaging techniques which are based on the hemodynamic response depends totally on the physiological cascade of metabolism and blood flow. At present, functional brain imaging with near infrared spectroscopy (NIRS) or BOLD-fMRI is widely used in cognitive neuroscience in healthy subjects where neurovascular coupling and cerebrovascular reactivity can be assumed to be intact. Local activation studies as well as studies investigating functional connectivity between brain regions of the resting brain provide a rapidly increasing body of knowledge on brain function in humans and animals. Furthermore, functional NIRS and MRI techniques are increasingly being used in patients with severe brain diseases and this use might gain more and more importance for establishing their use in the clinical routine. However, more and more experimental evidence shows that changes in baseline physiological parameters, pharmacological interventions, or disease-related vascular changes may significantly alter the normal response of blood flow and blood oxygenation and thus may lead to misinterpretation of neuronal activity. In this article we present examples of recent experimental findings on pathophysiological changes of neurovascular coupling parameters in animals and discuss their potential implications for functional imaging based on hemodynamic signals such as fNIRS or BOLD-fMRI. To enable correct interpretation of neuronal activity by vascular signals, future research needs to deepen our understanding of the basic mechanisms of neurovascular coupling and the specific characteristics of disturbed neurovascular coupling in the diseased brain.

Keywords: BOLD-fMRI, cerebral blood flow, cerebral blood oxygenation, cortical spreading depression, deoxy-hemoglobin, functional activation, hemodynamic response, neurovascular coupling

PHYSIOLOGY OF THE HEMODYNAMIC RESPONSE DURING INCREASED NEURONAL ACTIVITY

In the brain, coupling of neuronal activity and metabolism with regional cerebral blood flow (rCBF), and cerebral blood oxygenation (rCBO) is tight ("neurovascular coupling"), so rCBF or rCBO changes can be used to map brain activity with high spatial resolution ("functional neuroimaging"). Considerable progress has been made over the past decades in understanding the physiological mechanisms of neurovascular coupling, but key mechanisms underlying the regulation of brain blood flow and metabolism remain elusive. Tissue factors such as K^+, H^+, NO, or adenosine (Iadecola, 2004) have been center stage ever since 1890, when Roy and Sherrington (1890) first proposed that rCBF is regulated by local metabolites. It has long been suggested that the increase in CBF during neural activation is driven by a need for increased delivery of oxygen or glucose. During functional activation, oxygen metabolism (cerebral metabolic rate of oxygen, $CMRO_2$) increases substantially (Ances et al., 2001b; Gjedde et al., 2002; Dunn et al., 2005), and a regional and transient change in tissue oxygenation occurs. Increased oxygen consumption during neuronal activity results in a decrease in tissue oxygenation which is counteracted by the increase in O_2 supply when CBF increases (Ances et al., 2001a; Thompson et al., 2003; Offenhauser et al., 2005; Enager et al., 2009).

Oxidative metabolism and CBF exert not only counteracting effects on tissue oxygenation but also on hemoglobin oxygenation. On one hand, increased oxygen metabolism drives conversion of oxygenated (oxy-Hb) to deoxygenated hemoglobin (deoxy-Hb). On the other hand, a disproportionately large increase in regional CBF leads to a washout of deoxy-Hb from the activation area, resulting in a decrease of deoxy-Hb and an increase of oxy-Hb (Obrig et al., 1996; Lindauer et al., 2001). CBF increases exceed $CMRO_2$ increases by a factor of 2-10 (Fox et al., 1988; Lin et al., 2008 and references therein). The exact value is still intensely debated. Methodological issues regarding $CMRO_2$ measurement might play a relevant role, especially in fMRI (Lin et al., 2008) and the factor likely varies with stimulation parameters and between brain regions and species. However, consensus exists that the increase in CBF is mostly accompanied by tissue hyperoxygenation. The washout and decrease of deoxy-Hb provides the basis for functional neuroimaging with BOLD-fMRI. The relation of metabolic and vascular events during functional activation is illustrated in **Figure 1**.

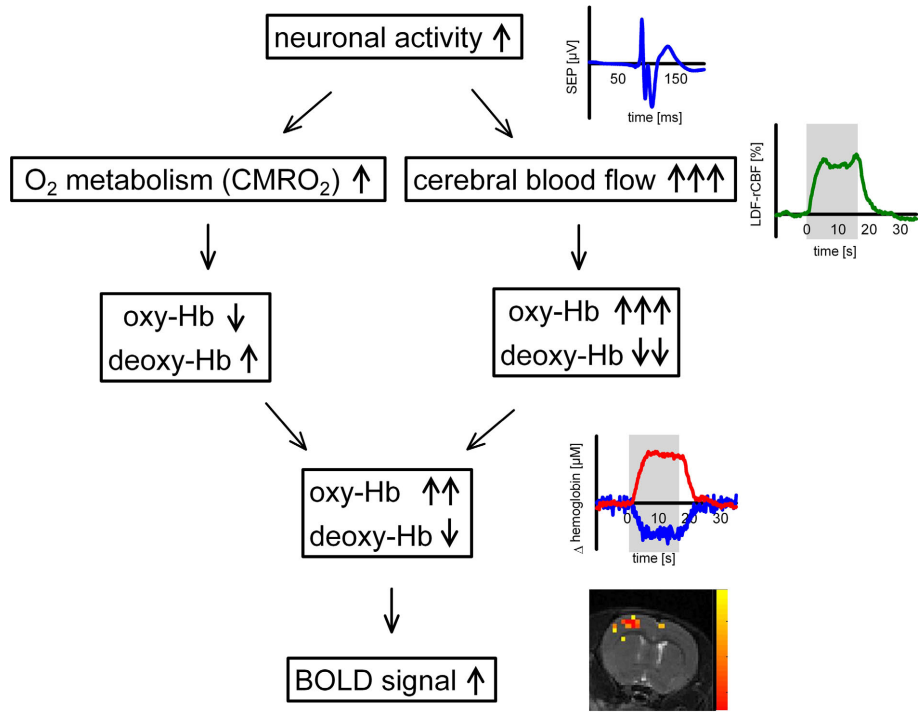

FIGURE 1 | Physiology of the hemodynamic response during increased neuronal activity.

In BOLD-fMRI, the signal transduction of neuronal activity is even more complex and influenced by methodological aspects (e.g., spin echo vs. gradient echo sequences) and field strength (Uludag et al., 2009). However, a close relation between the fMRI-BOLD signal and the deoxy-Hb signal measured with optical imaging has been demonstrated repeatedly, e.g., in a recent study with concurrent measurements by Kennerley et al. (2009). Furthermore, a close correlation has been shown recently between fMRI signal changes and synaptic activity, whereas the correlation with cellular action potentials appears to be weaker (Mathiesen et al., 1998, 2000; Logothetis et al., 2001; Rauch et al., 2008). These findings are congruent with the very recent finding that action potentials are highly energy-efficient, which means that their contribution to activity-dependent metabolism is minimal (Alle et al., 2009).

As described, assessing neuronal activity by non-invasive functional brain imaging techniques which are based on the hemodynamic response depends totally on the physiological cascade of metabolism and blood flow. At present, functional brain imaging with near infrared spectroscopy (fNIRS) or by BOLD-fMRI is widely used in cognitive neuroscience in healthy subjects where neurovascular coupling and cerebrovascular reactivity can be assumed to be intact. Local activation studies as well as studies investigating functional connectivity between brain regions of the resting brain provide a rapidly increasing body of knowledge on brain function in humans and animals (for recent reviews see Obrig and Villringer, 2003; Auer, 2008; Logothetis, 2008; He and Raichle, 2009; Lu et al., 2010). However, more and more experimental evidence shows that changes in baseline physiological parameters, pharmacological interventions, or disease-related vascular changes may significantly alter the normal response of blood flow and blood oxygenation in amplitude as well as time course dynamics and thus may lead to misinterpretation of neuronal activity. Functional MRI techniques are increasingly being used in patients with severe brain diseases, even in patients with vegetative or minimally conscious state (Monti et al., 2010) and this use might increase substantially in the future. To exactly understand the effect of pathophysiology on the mechanisms of neurovascular coupling we need systematic basic research on these interferences. Animal studies on neurovascular coupling are different from human functional activation studies in many aspects. Among others, anesthesia, surgery, small brain size, lack of gyration in rodent brain, and different functional activation systems produce uncertainties when translating the results to the human brain. However, despite this limitation, animal studies deliver important complementary information on blood flow and blood oxygenation changes for human NIRS and fMRI since they allow invasive procedures and multimodal imaging with high signal-to-noise ratio to systematically investigate these pathophysiological influences.

In the following we will therefore summarize examples of recent experimental findings on pathophysiological changes of neurovascular coupling parameters in animals from our group and from others and discuss potential implications for functional imaging based on hemodynamic signals such as NIRS and BOLD-fMRI.

EXAMPLES OF RECENT EXPERIMENTAL FINDINGS

ALTERED BASELINE CONDITIONS: EFFECTS OF CHANGES IN BASELINE BLOOD FLOW, BLOOD OXYGENATION, BODY TEMPERATURE, AND INTRACRANIAL PRESSURE ON HEMODYNAMIC SIGNALS

In studies mapping brain activity, baseline blood flow and baseline blood oxygenation may differ between subjects and between sessions within the same subject. In addition, factors like premedication or anxiety may influence the baseline conditions in patients. Several studies therefore investigated whether baseline cerebral perfusion and oxygenation significantly influence activation induced deoxy-Hb changes and thus the BOLD signal. When modeling the hemodynamic response to brain activation Buxton et al. (2004) predicted a significant reduction of the BOLD response during increased baseline CBF. Their prediction has been confirmed by several experimental studies within the last years. In two recent elegant studies by Jones et al. (2005) and Huppert et al. (2009) using anesthetized animals, hypercapnia was induced to increase baseline perfusion while blood oxygenation and blood flow changes during functional activation were being measured. A perfusion elevation of ~20% during mild hypercapnia (with no change in neuronal activity or $CMRO_2$) resulted in a significantly diminished deoxy-Hb response, whereas the absolute CBF (but not the relative) responses remained constant. When baseline perfusion was increased by up to 100% (stronger hypercapnia), the deoxy-Hb response almost disappeared (Jones et al., 2005). However the notion that $CMRO_2$ and neuronal activity do not change during hypercapnia has recently been questioned (Zappe et al., 2008) and is still matter of a controversial debate (Chen and Pike, 2010).

As long as neuronal activity and $CMRO_2$ remain constant, an increase in baseline blood flow results in blood hyperoxygenation. In our own studies, we therefore addressed the effect of manipulations of baseline blood oxygenation on deoxy-Hb responses. During hyperoxia the deoxy-Hb outwash was significantly reduced under normobaric conditions (Lindauer et al., 2003) or even abolished under hyperbaric conditions of 3 or 4 ATA (Lindauer et al., 2010), while neuronal activity and CBF responses remained unaltered (**Figure 2**).

Induced hypothermia is a routine therapeutic intervention in patients after cardiac arrest (Geocadin et al., 2006) and is currently being investigated as a potential neuroprotective treatment in ischemic stroke (Sacco et al., 2007). It is not clear whether fMRI or fNIRS work under these circumstances. In a recent study we have investigated the effect of hypothermia on neurovascular coupling (Royl et al., 2008). Although hypothermia reduced baseline CBF by almost 50%, neurovascular coupling was preserved. Reduction of functional changes in CBF, deoxy-Hb and $CMRO_2$ followed reductions in neuronal activity during hypothermia (**Figure 3**). Hypothermia therefore seems to be a condition in which functional changes in rCBF and rCBO can still provide a reliable correlate of changes in neuronal activity.

It has long been known that ICP has a strong influence on cerebrovascular dynamics (Kety et al., 1948). The influence of ICP on BOLD-fMRI has not been studied so far. Indirect conclusions can be drawn from studies that report an alteration of BOLD-fMRI in patients with an intracranial tumor, which is often accompanied by an increased ICP. Schreiber et al. (2000) have shown that a glial tumor reduced the ipsilateral BOLD-activity, whereas a non-glial tumor did not cause a significant change. In a recent study, we found that the amplitude of the functional deoxy-Hb decrease in rat somatosensory cortex was reduced when ICP was elevated to 7 mmHg. At an ICP of 14 mmHg the deoxy-Hb response was close to 0 and even reversed at an ICP of 28 mmHg (**Figure 4**). Deoxy-Hb amplitude and ICP were significantly correlated ($r = 0.64$). Time matched control animals without ICP elevation did not show relevant changes in stimulus-induced responses of CBF, CBV, and deoxy-Hb. This data suggests that BOLD-fMRI can be seriously impaired by ICP, e.g., in a patient with a brain tumor and mildly elevated ICP, pre-surgical BOLD-fMRI might not reliably detect functionally eloquent brain areas (Füchtemeier et al., 2010).

ALTERED VASCULAR REACTIVITY: EFFECTS OF REDUCED CBF RESPONSE ON DEOXY-Hb CHANGES DURING FUNCTIONAL ACTIVATION

During aging or vascular dementia and Alzheimer's disease, impaired vascular reactivity may not only reduce the CBF responses during preserved neuronal activation, but may also significantly alter blood oxygenation changes. In a recently published study, we reduced the CBF responses in anesthetized rats by pharmacologically blocking well-known mechanisms of neurovascular coupling. While the CBF response to functional activation was reduced by approximately 70%, the deoxy-Hb response was abolished (**Figure 5**) or even reversed into an increase of deoxy-Hb [see Supplementary Figure 3 in Leithner et al. (2010)] instead of the normal outwash response (Leithner et al., 2010). Importantly, COX-2 inhibitors, a common medication in patients, were part of the pharmacological cocktail used to block the CBF response.

Comparable results of inverted BOLD and tissue oxygenation responses were shown by another group using severe systemic hypotension to abolish the CBF response during functional activation (Nagaoka et al., 2006; Masamoto et al., 2008).

To further address this issue, we are currently investigating whether the well-known impairment of vascular reactivity combined with moderate hypoperfusion within the first 2 h after cortical spreading depression has any impact on blood flow and blood oxygenation responses to somatosensory stimulation in anesthetized rats (Offenhauser et al., 2007). Preliminary and unpublished data from a small pilot study show that within the first 30 min after CSD, the CBF response to whisker hair deflection in anesthetized rats ($n = 5$) was significantly reduced despite restored neuronal responses. In separate animals we found that under these conditions the deoxy-Hb response is considerably altered ($n = 3$) (**Figure 6**). Animals were prepared and CBF and CBO changes assessed as described in Lindauer et al. (2001).

Increased baseline $CMRO_2$ in parallel with reduced CBF during resting and stimulated conditions (transcallosal stimulation) after CSD was recently demonstrated by Piilgaard and Lauritzen (2009), and can be considered as a possible cause for the altered deoxy-Hb response shown in our experiments.

SYNOPSIS OF EXPERIMENTAL DATA

The examples presented show that whereas some changes in baseline conditions such as hypothermia do not alter neurovascular coupling, other alterations in baseline conditions as well as an impairment of vascular function may have a serious impact

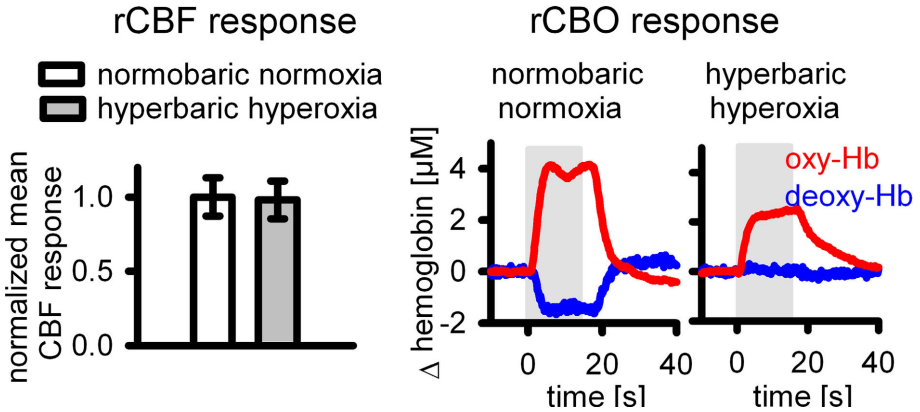

FIGURE 2 | During increased baseline blood oxygenation by hyperbaric hyperoxia, the deoxy-Hb response is abolished (from Lindauer et al., 2010), while the CBF response is unaltered.

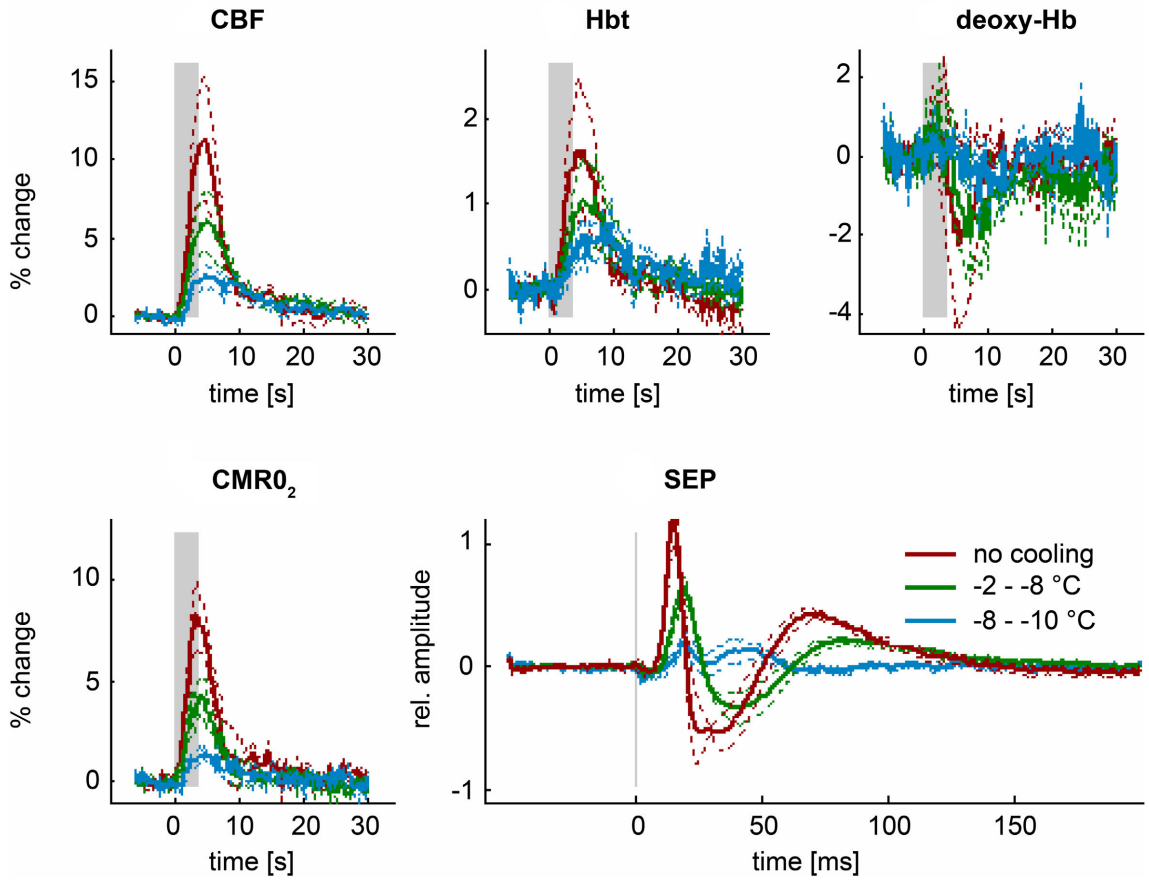

FIGURE 3 | During hypothermia, functional changes in rCBF and rCBO (Hbt and deoxy-Hb) still provide a reliable estimate of neuronal activity and oxygen metabolism (SEP and $CMRO_2$) (from Royl et al., 2008).

on the hemoglobin derived response. In particular, our finding of significantly changed patterns of deoxy-Hb responses to functional activation during pharmacologically or pathophysiologically reduced CBF responses clearly points toward the need for a careful interpretation of neuronal function assessed by methods based on vascular parameters like NIRS and BOLD-fMRI whenever vascular reactivity may be impaired. In conclusion, the neurovascular unit can be seriously disturbed by a variety of interferences, and detailed knowledge of the relationship between oxygen metabolism, blood flow, and blood oxygenation will help us to better understand func-

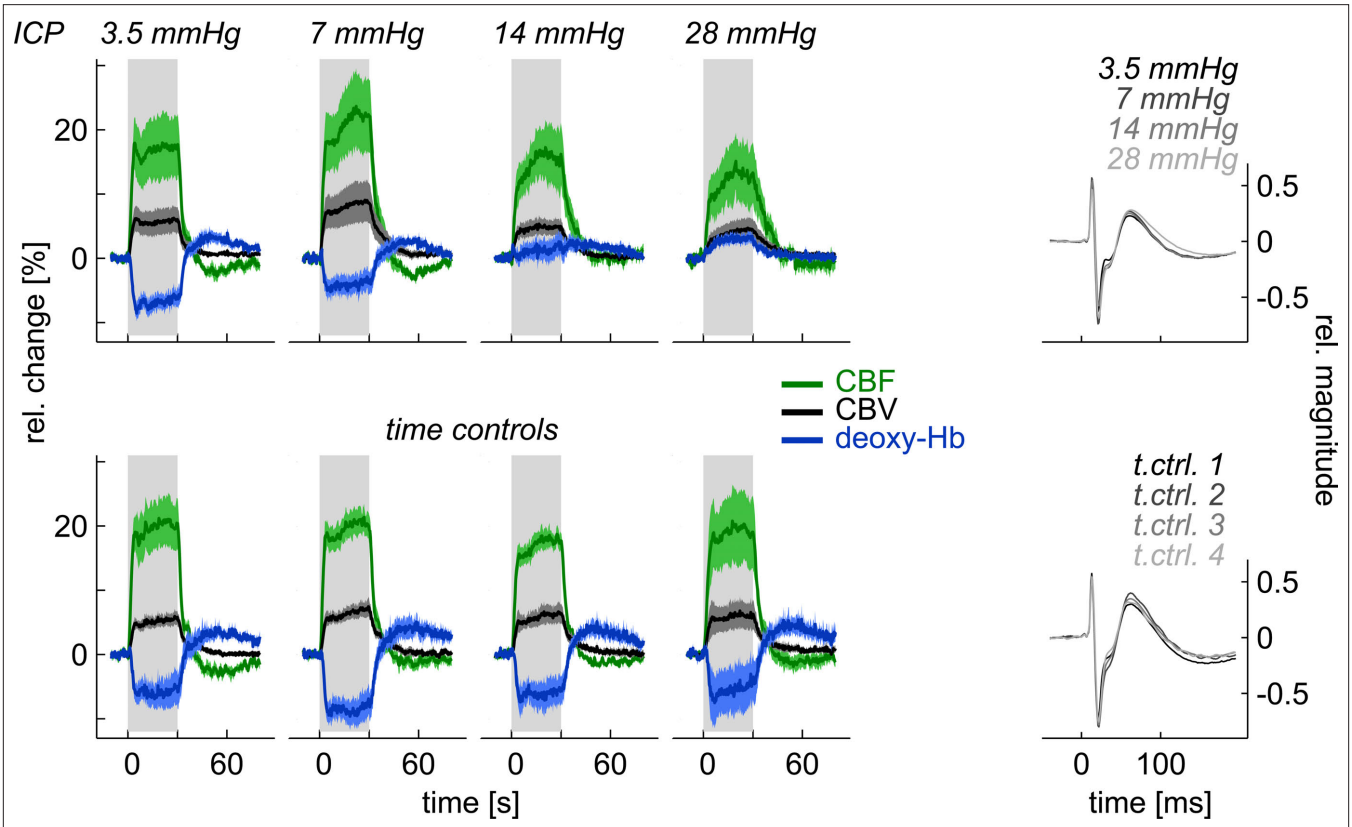

FIGURE 4 | When elevating ICP, functional deoxy-Hb changes can be reduced, leveled out, or reversed, although neuronal activity (SEP) is unchanged and neurovascular coupling persists for CBF and CBV (from Füchtemeier et al., 2010).

tional brain imaging performed on the basis of vascular changes. Further systematic research is needed to achieve this knowledge. Whenever alterations in baseline parameters or vascular reactivity are suspected, it is mandatory that physiological parameters and baseline perfusion be monitored and vascular reactivity tested while using the NIRS or BOLD signal to image brain activation in experimental setups.

POSSIBLE IMPLICATIONS FOR NON-INVASIVE FUNCTIONAL BRAIN IMAGING OF THE DISEASED BRAIN

Our current knowledge of the complex interaction between metabolic and vascular events during neurovascular coupling leads us to anticipate challenges in the quest for a correct interpretation of data by fNIRS or BOLD-fMRI obtained from the diseased brain. Possible pathophysiological effects on the mechanisms or mediators of neurovascular coupling and/or the impairment of the vascular system's ability to react to released mediators are hitherto largely unknown. Pathophysiological events have the potential to interfere with the signal transduction between neural activity and brain hemoglobin oxygenation (i.e., fNIRS and BOLD-fMRI) at many levels.

In the following paragraphs we will discuss potential implications of these studies. We will specifically focus on BOLD-fMRI because it is the most widely used neuroimaging method and the most likely to be applied in patients due to its non-invasiveness and availability. Furthermore, as implementation of fMRI is more standardized than optical imaging, uncritical application of fMRI in situations of disturbed neurovascular coupling might be somewhat more likely and vulnerability for potential confounders is therefore more important for this technique. Notwithstanding the implications equally apply to optical methods that also play an important role in human studies. Particularly fNIRS is suited for investigating psychiatric patients and children since it does not require as much cooperation.

Several studies have been performed so far to better understand the influence of baseline CBF and of drug effects on functional activation induced NIRS and BOLD signal changes in humans. Beside the use of hypercapnia, the influence of caffeine has been investigated in multimodal approaches. A reduction in baseline CBF and baseline BOLD signal accompanied by an increase in the evoked CBF and BOLD response (Chen and Parrish, 2009) as well as reduced measures of resting state BOLD connectivity in the motor cortex (Rack-Gomer et al., 2009) have been described after caffeine intake. For indomethacin, a reduction of the baseline BOLD signal and of stimulation induced BOLD and CBF responses during preserved $CMRO_2$ has been reported, whereas acetylsalicylate, another drug regularly used in patients, had no effect on the BOLD signal (Bruhn et al., 2001; St Lawrence et al., 2003). Furthermore, combined approaches of BOLD signal and CBF measurement are gaining importance to achieve a quantitative interpretation of the magnitude of the BOLD effect in relation to oxygen metabolism under normal conditions (Davis et al., 1998; Leontiev and Buxton, 2007) or to investigate whether the coupling relationship between

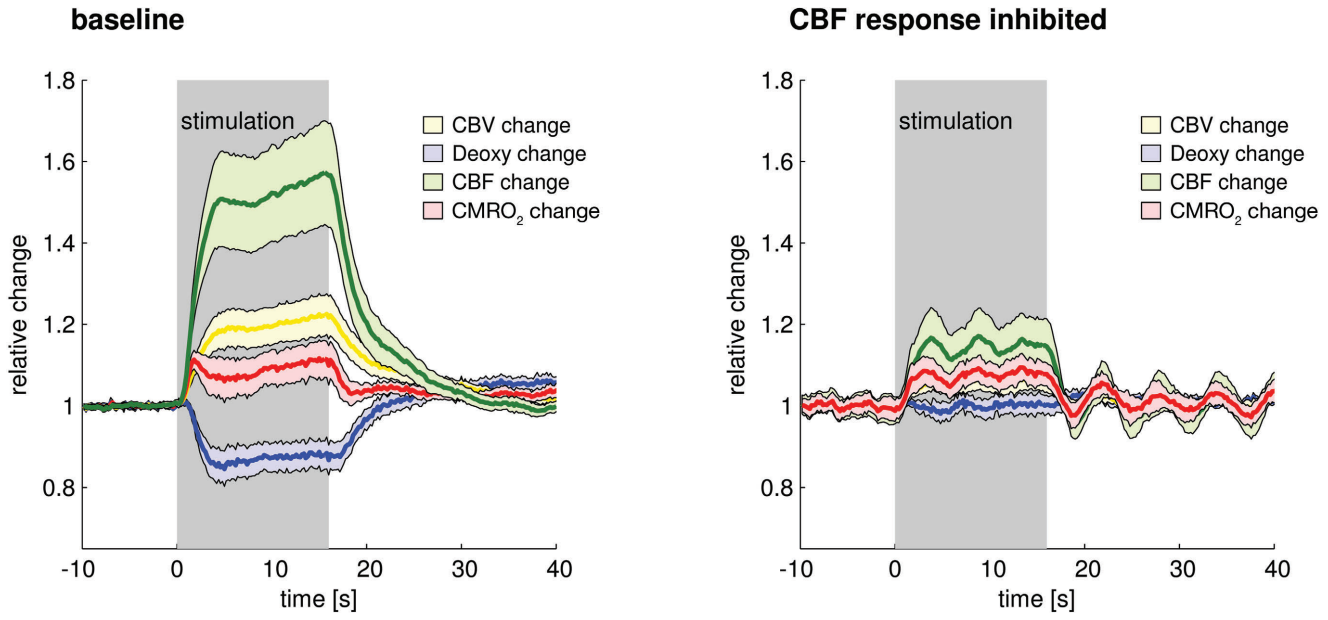

FIGURE 5 | When the CBF response is pharmacologically reduced, the deoxy-Hb response is abolished (from Leithner et al., 2010).

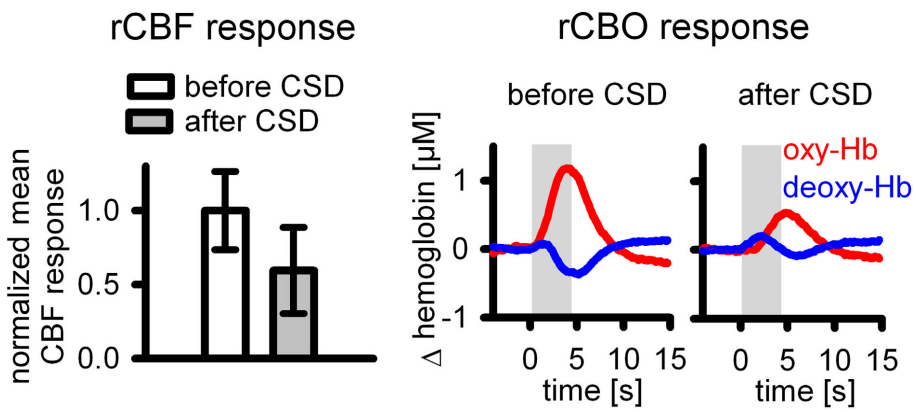

FIGURE 6 | Altered neurovascular coupling within the first hour following CSD in anesthetized rats.

CBF and oxygen metabolism may be altered under conditions of anesthesia, drug intake or disease (calibrated BOLD-fMRI). Only recently, it has been shown that under sevoflurane anesthesia, baseline CBF and the task-induced changes in CBF decreased, whereas a larger change in BOLD was observed (Qiu et al., 2008). While comparing functional activation induced BOLD responses in younger and older subjects, Ances et al. (2009) found a significantly smaller BOLD response for the older age group despite similar fractional CBF and $CMRO_2$ changes and showed that the weaker BOLD response for the older is explained by a reduction in baseline CBF. In another study reduced activation of the frontal cortex has been shown in patients with bipolar disorders performing a cognitive task despite normal vascular responses to hypercapnia (calibrated fNIRS) (Matsuo et al., 2007). In addition, blood flow and blood oxygenation responses may not only be affected in their amplitude but also in their time course dynamics. For example, a study on stroke patients did show a longer time to peak in the BOLD activation time course, presumably reflecting a disturbed cerebral autoregulation (Altamura et al., 2009). Other fMRI studies on human subjects found a prolonged BOLD response in patients with hemodynamically significant stenoses (Roc et al., 2006) or a changed temporal dynamic of the BOLD response under caffeine (Liau et al., 2008). An fNIRS study on patients with cerebral microangiopathy reports a reduced amplitude of the hemodynamic response in tight correlation with behavioral deficits. In addition, an early deoxygenation of hemoglobin right after stimulation onset as well as a delay of the hemodynamic response is described, indicating not only frontal dysfunction but also an impairment of neurovascular coupling in cerebral microangiopathy (Schroeter et al., 2007). Functional MRI-guided neurosurgery is another field of application for BOLD-fMRI

as a non-invasive imaging technique. Despite its attractiveness for presurgical mapping to localize cerebral function in areas within or near tissue intended for neurosurgical resection (for review see Matthews et al., 2006), its reliability and thus applicability in brain tumor patients has been questioned (Fujiwara et al., 2004; Bartoš et al., 2009). In accordance with this critique, a very recent study using a multimodal approach in patients with primary brain tumors shows strong evidence for an impairment of vascular reactivity near meningiomas and high grade gliomas (Jiang et al., 2010). In addition, several studies on patients suffering from cerebrovascular diseases such as stroke or carotid artery stenosis explicitly used BOLD imaging to investigate impaired vascular function during preserved neuronal activity (Hamzei et al., 2003; Rossini et al., 2004; Krainik et al., 2005; Roc et al., 2006). In line with the above mentioned results from animal studies, these examples from human studies provide additional evidence that the deoxy-Hb and the BOLD response alone can result in a misleading interpretation of underlying physiological changes. Therefore they further support the need of knowledge on pathophysiological interferences and the use of controlled methods like calibrated BOLD-fMRI or fNIRS in situations where the normal coupling between CBF and oxygen metabolism in respect to amplitude and time course might be altered.

Despite the numerous studies with data from experimental and clinical studies in animals and humans that critically assess the reliability of vascular parameters to measure neuronal function under altered coupling conditions (Matthews et al., 2006; Iannetti and Wise, 2007; Wierenga and Bondi, 2007; Fleisher et al., 2009), the implementation of this knowledge in clinical studies in patients is still far from being established. Not only prior but also very recent studies on patients with ischemic stroke (Loubinoux et al., 2003; Enzinger et al., 2008), multiple sclerosis (Reddy et al., 2000; White et al., 2009), Parkinson's disease (Schonberg et al., 2010), Alzheimer's disease and dementia (Sauer et al., 2006; Thiyagesh et al., 2009) and schizophrenia (Huang et al., 2010) still do not control for impaired coupling, disturbed vascular reactivity or altered resting levels of blood volume, CBF, CBO, or metabolism as possible confounders to their findings. Therefore, some of these studies may bear the risk of generating a false negative (or false positive) conclusion. Further experimental and clinical studies will help us to identify any involvement of the vascular system, particularly in diseases putatively based on parenchymal alterations.

A number of suggestions for a general improvement of BOLD-fMRI studies during possibly impaired neurovascular coupling have been published by Iannetti and Wise (2007). As more experimental evidence from experimental (animal) studies becomes available, anticipation of changes in amplitude or dynamics of BOLD, CBF, $CMRO_2$, and CBV may be used to optimize imaging protocols. For example, when reduced CBF responses abolish BOLD responses, brain activity may still reliably be measured with CBF based fMRI methods, if reduced amplitudes are accounted for. CBF based neuroimaging also has the advantage of a higher spatial resolution (Duong et al., 2001) since it has been shown to enhance microcirculatory areas (Royl et al., 2006). In addition, it can provide quantitative values (Leithner et al., 2008). On the other hand, if neurovascular coupling is completely blocked and CBF responses are abolished, neuronal activity may lead to an increase in deoxy-Hb and a decrease of the BOLD-signal, which could again be used to detect active brain areas as long as reversed signal characteristics are taken into account. Results of such studies should always be interpreted very carefully. Maximal endeavor should be made to gather complementary data (electrophysiological, baseline physiological parameters, control tasks etc.) to at least partly control for the lack of validation studies linking neuronal activity with vascular parameters in such experiments. In addition to gathering more data from experimental studies, quality standards should be agreed on and established for the publication of functional activation studies performed in the environment of impaired neurovascular coupling.

SUMMARY AND OUTLOOK

Functional MRI may not be reliable in pathological states, as neuronal activity may be preserved but deoxy-Hb changes absent. Alterations in rCBF or arterial blood oxygenation, hyper- or hypocapnia, changes in intracranial pressure, severe decreases of systemic blood pressure, cortical spreading depressions, medication or brain or vascular diseases may alter the relationship between neuronal activity and BOLD-signals, with the risk of false negative findings in brain activation studies. To guarantee correct interpretation of these studies, future research needs to deepen our understanding of the basic mechanisms of neurovascular coupling and the specific characteristics of disturbed neurovascular coupling in the diseased brain.

AUTHORIZATION FOR THE USE OF EXPERIMENTAL ANIMALS

All animal experiments were performed in accordance with institutional and national guidelines and regulations and were approved by the "Landesamt für Arbeitsschutz, Gesundheitsschutz und technische Sicherheit Berlin."

ACKNOWLEDGMENT

This work was supported by the Deutsche Forschungsgemeinschaft, the Hermann and Lilly Schilling Foundation and the European Union (EFRE). We thank Dr. Jörn Gethmann and Marco Foddis for excellent technical assistance.

REFERENCES

Alle, H., Roth, A., and Geiger, J. R. P. (2009). Energy-efficient action potentials in hippocampal mossy fibers. *Science* 325, 1405–1408.

Altamura, C., Reinhard, M., Vry, M. S., Kaller, C. P., Hamzei, F., Vernieri, F., Rossini, P. M., Hetzel, A., Weiller, C., and Saur, D. (2009). The longitudinal changes of BOLD response and cerebral hemodynamics from acute to subacute stroke. A fMRI and TCD study. *BMC Neurosci.* 10, 1–12.

Ances, B. M., Buerk, D. G., Greenberg, J. H., and Detre, J. A. (2001a). Temporal dynamics of the partial pressure of brain tissue oxygen during functional forepaw stimulation in rats. *Neurosci. Lett.* 306, 106–110.

Ances, B. M., Wilson, D. F., Greenberg, J. H., and Detre, J. A. (2001b). Dynamic changes in cerebral blood flow, O_2 tension, and calculated cerebral metabolic rate of O_2 during functional activation using oxygen phosphorescence quenching. *J. Cereb. Blood Flow Metab.* 21, 511–516.

Ances, B. M., Liang, C. L., Leontiev, O., Perthen, J. E., Fleisher, A. S., Lansing, A. E., and Buxton, R. B. (2009). Effects of aging on cerebral blood flow, oxygen metabolism, and blood oxygenation level dependent responses to visual stimulation. *Hum. Brain Mapp.* 30, 1120–1132.

Auer, D. P. (2008). Spontaneous low-frequency blood oxygenation level-dependent fluctuations and functional connectivity analysis of the 'resting' brain. *Magn. Reson. Imaging* 26, 1055–1064.

Bartoš, R., Jech, R., Vymazal, J., Petrovický, P., Vachata, P., Hejčl, A., Zolal, A., and Sameš, M. (2009). Validity of primary

motor area localization with fMRI versus electric cortical stimulation: a comparative study. *Acta Neurochir.* 151, 1071–1080.

Bruhn, H., Fransson, P., and Frahm, J. (2001). Modulation of cerebral blood oxygenation by indomethacin: MRI at rest and functional brain activation. *J. Magn. Reson. Imaging* 13, 325–334.

Buxton, R. B., Uludag, K., Dubowitz, D. J., and Liu, T. T. (2004). Modeling the hemodynamic response to brain activation. *Neuroimage* 23, S220–S233.

Chen, J. J., and Pike, G. B. (2010). Global cerebral oxidative metabolism during hypercapnia and hypocapnia in humans: implications for BOLD fMRI. *J. Cereb. Blood Flow Metab.* 30, 1094–1099.

Chen, Y., and Parrish, T. B. (2009). Caffeine dose effect on activation-induced BOLD and CBF responses. *Neuroimage* 46, 577–583.

Davis, T. L., Kwong, K. K., Weisskoff, R. M., and Rosen, B. R. (1998). Calibrated functional MRI: mapping the dynamics of oxidative metabolism. *Proc. Natl. Acad. Sci. U.S.A.* 95, 1834–1839.

Dunn, A. K., Devor, A., Dale, A. M., and Boas, D. A. (2005). Spatial extent of oxygen metabolism and hemodynamic changes during functional activation of the rat somatosensory cortex. *Neuroimage* 27, 279–290.

Duong, T. Q., Kim, D. S., Ugurbil, K., and Kim, S. G. (2001). Localized cerebral blood flow response at submillimeter columnar resolution. *Proc. Natl. Acad. Sci. U.S.A.* 98, 10904–10909.

Enager, P., Piilgaard, H., Offenhauser, N., Kocharyan, A., Fernandes, P., Hamel, E., and Lauritzen, M. (2009). Pathway-specific variations in neurovascular and neurometabolic coupling in rat primary somatosensory cortex. *J. Cereb. Blood Flow Metab.* 29, 976–986.

Enzinger, C., Johansen-Berg, H., Dawes, H., Bogdanovic, M., Collett, J., Guy, C., Ropele, S., Kischka, U., Wade, D., Fazekas, F., and Matthews, P. M. (2008). Functional MRI correlates of lower limb function in stroke victims with gait impairment. *Stroke* 39, 1507–1513.

Fleisher, A. S., Podraza, K. M., Bangen, K. J., Taylor, C., Sherzai, A., Sidhar, K., Liu, T. T., Dale, A. M., and Buxton, R. B. (2009). Cerebral perfusion and oxygenation differences in Alzheimer's disease risk. *Neurobiol. Aging* 30, 1737–1748.

Fox, P. T., Raichle, M. E., Mintun, M. A., and Dence, C. (1988). Nonoxidative glucose consumption during focal physiologic neural activity. *Science* 241, 462–464.

Füchtemeier, M., Leithner, C., Offenhauser, N., Foddis, M., Kohl-Bareis, M., Dirnagl, U., Lindauer, U., and Royl, G. (2010). Elevating intracranial pressure reverses the decrease in deoxygenated hemoglobin and abolishes the post-stimulus overshoot upon somatosensory activation in rats. *Neuroimage* 52, 445–454.

Fujiwara, N., Sakatani, K., Katayama, Y., Murata, Y., Hoshino, T., Fukaya, C., and Yamamoto, T. (2004). Evoked-cerebral blood oxygenation changes in false-negative activations in BOLD contrast functional MRI of patients with brain tumors. *Neuroimage* 21, 1464–1471.

Geocadin, R. G., Koenig, M. A., Stevens, R. D., and Peberdy, M. A. (2006). Intensive care for brain injury after cardiac arrest: therapeutic hypothermia and related neuroprotective strategies. *Crit. Care Clin.* 22, 619–636.

Gjedde, A., Marrett, S., and Vafaee, M. (2002). Oxidative and nonoxidative metabolism of excited neurons and astrocytes. *J. Cereb. Blood Flow Metab.* 22, 1–14.

Hamzei, F., Knab, R., Weiller, C., and Röther, J. (2003). The influence of extra- and intracranial artery disease on the BOLD signal in FMRI. *Neuroimage* 20, 1393–1399.

He, B. J., and Raichle, M. E. (2009). The fMRI signal, slow cortical potential and consciousness. *Trends Cogn. Sci.* 13, 302–309.

Huang, X. -Q., Lui, S., Deng, W., Chan, R. C. K., Wu, Q. -Z., Jiang, L. -J., Zhang, J. -R., Jia, Z. -Y., Li, X. -L., Li, F., Chen, L., Li, T., and Gong, Q. -Y. (2010). Localization of cerebral functional deficits in treatment-naive, first-episode schizophrenia using resting-state fMRI. *Neuroimage* 49, 2901–2906.

Huppert, T. J., Jones, P. B., Devor, A., Dunn, A. K., Teng, I. C., Dale, A. M., and Boas, D. A. (2009). Sensitivity of neural-hemodynamic coupling to alterations in cerebral blood flow during hypercapnia. *J. Biomed. Opt.* 14, 044038.

Iadecola, C. (2004). Neurovascular regulation in the normal brain and in Alzheimer's disease. *Nat. Rev. Neurosci.* 5, 347–360.

Iannetti, G. D., and Wise, R. G. (2007). BOLD functional MRI in disease and pharmacological studies: room for improvement? *Magn. Reson. Imaging* 25, 978–988.

Jiang, Z., Krainik, A., David, O., Salon, C., Troprès, I., Hoffmann, D., Pannetier, N., Barbier, E. L., Bombìn, E. R., Warnking, J., Pasteris, C., Chabardes, S., Berger, F., Grand, S., Segebarth, C., Gay, E., and Le Bas, J. -F. (2010). Impaired fMRI activation in patients with primary brain tumors. *Neuroimage* 52, 538–548.

Jones, M., Berwick, J., Hewson-Stoate, N., Gias, C., and Mayhew, J. (2005). The effect of hypercapnia on the neural and hemodynamic responses to somatosensory stimulation. *Neuroimage* 27, 609–623.

Kennerley, A. J., Berwick, J., Martindale, J., Johnston, D., Zheng, Y., and Mayhew, J. E. (2009). Refinement of optical imaging spectroscopy algorithms using concurrent BOLD and CBV fMRI. *Neuroimage* 47, 1608–1619.

Kety, S. S., Shenkin, H. A., and Schmidt, C. F. (1948). The effects of increased intracranial pressure on cerebral circulatory functions in man. *J. Clin. Invest.* 27, 493–499.

Krainik, A., Hund-Georgiadis, M., Zysset, S., and von Cramon, D. Y. (2005). Regional impairment of cerebrovascular reactivity and BOLD signal in adults after stroke. *Stroke* 36, 1146–1152.

Leithner, C., Gertz, K., Schröck, H., Priller, J., Prass, K., Steinbrink, J., Villringer, A., Endres, M., Lindauer, U., Dirnagl, U., and Royl, G. (2008). A flow sensitive alternating inversion recovery (FAIR)-MRI protocol to measure hemispheric cerebral blood flow in a mouse stroke model. *Exp. Neurol.* 210, 118–127.

Leithner, C., Royl, G., Offenhauser, N., Füchtemeier, M., Kohl-Bareis, M., Villringer, A., Dirnagl, U., and Lindauer, U. (2010). Pharmacological uncoupling of activation induced increases in CBF and $CMRO_2$. *J. Cereb. Blood Flow Metab.* 30, 311–322.

Leontiev, O., and Buxton, R. B. (2007). Reproducibility of BOLD, perfusion, and $CMRO_2$ measurements with calibrated-BOLD fMRI. *Neuroimage* 35, 175–184.

Liau, J., Perthen, J. E., and Liu, T. T. (2008). Caffeine reduces the activation extent and contrast-to-noise ratio of the functional cerebral blood flow response but not the BOLD response. *Neuroimage* 42, 296–305.

Lin, A. -L., Fox, P. T., Yang, Y., Lu, H., Tan, L. -H., and Gao, J. -H. (2008). Evaluation of MRI models in the measurement of $CMRO_2$ and its relationship with CBF. *Magn. Reson. Med.* 60, 380–389.

Lindauer, U., Gethmann, J., Kühl, M., Kohl-Bareis, M., and Dirnagl, U. (2003). Neuronal activity-induced changes of local cerebral microvascular blood oxygenation in the rat: effect of systemic hyperoxia or hypoxia. *Brain Res.* 975, 135–140.

Lindauer, U., Leithner, C., Kaasch, H., Rohrer, B., Foddis, M., Füchtemeier, M., Offenhauser, N., Steinbrink, J., Royl, G., Kohl-Bareis, M., and Dirnagl, U. (2010). Neurovascular coupling in rat brain operates independent of hemoglobin deoxygenation. *J. Cereb. Blood Flow Metab.* 30, 757–768.

Lindauer, U., Royl, G., Leithner, C., Kühl, M., Gold, L., Gethmann, J., Kohl-Bareis, M., Villringer, A., and Dirnagl, U. (2001). No evidence for early decrease in blood oxygenation in rat whisker cortex in response to functional activation. *Neuroimage* 13, 988–1001.

Logothetis, N. K. (2008). What we can do and what we cannot do with fMRI. *Nature* 453, 869–878.

Logothetis, N. K., Pauls, J., Augath, M., Trinath, T., and Oeltermann, A. (2001). Neurophysiological investigation of the basis of the fMRI signal. *Nature* 412, 150–157.

Loubinoux, I., Carel, C., Pariente, J., Dechaumont, S., Albucher, J. -F., Marque, P., Manelfe, C., and Chollet, F. (2003). Correlation between cerebral reorganization and motor recovery after subcortical infarcts. *Neuroimage* 20, 2166–2180.

Lu, C. -M., Zhang, Y. -J., Biswal, B. B., Zang, Y. -F., Peng, D. -L., and Zhu, C. -Z. (2010). Use of fNIRS to assess resting state functional connectivity. *J. Neurosci. Methods* 186, 242–249.

Masamoto, K., Vazquez, A., Wang, P., and Kim, S. -G. (2008). Trial-by-trial relationship between neural activity, oxygen consumption, and blood flow responses. *Neuroimage* 40, 442–450.

Mathiesen, C., Caesar, K., Akgoren, N., and Lauritzen, M. (1998). Modification of activity-dependent increases of cerebral blood flow by excitatory synaptic activity and spikes in rat cerebellar cortex. *J. Physiol. (Lond.)* 512, 555–566.

Mathiesen, C., Caesar, K., and Lauritzen, M. (2000). Temporal coupling between neuronal activity and blood flow in rat cerebellar cortex as indicated by field potential analysis. *J. Physiol.* 523(Pt 1), 235–246.

Matsuo, K., Kouno, T., Hatch, J. P., Seino, K., Ohtani, T., Kato, N., and Kato, T. (2007). A near-infrared spectroscopy study of prefrontal cortex activation during a verbal fluency task and carbon dioxide inhalation in individuals with bipolar disorder. *Bipolar Disord.* 9, 876–883.

Matthews, P. M., Honey, G. D., and Bullmore, E. T. (2006). Applications of fMRI in translational medicine and clinical practice. *Nat. Rev. Neurosci.* 7, 732–744.

Monti, M. M., Vanhaudenhuyse, A., Coleman, M. R., Boly, M., Pickard, J. D., Tshibanda, L., Owen, A. M., and Laureys, S. (2010). Willful modulation of brain activity in disorders of

consciousness. *N. Engl. J. Med.* 362, 579–589.

Nagaoka, T., Zhao, F., Wang, P., Harel, N., Kennan, R. P., Ogawa, S., and Kim, S. -G. (2006). Increases in oxygen consumption without cerebral blood volume change during visual stimulation under hypotension condition. *J. Cereb. Blood Flow Metab.* 26, 1043–1051.

Obrig, H., Heekeren, H., Ruben, J., Wenzel, R., Ndayisaba, J. P., Dirnagl, U., and Villringer, A. (1996). Continuous spectrum near-infrared spectroscopy approach in functional activation studies in the human adult. *Proc SPIE* 2926, 58–66.

Obrig, H., and Villringer, A. (2003). Beyond the visible – imaging the human brain with light. *J. Cereb. Blood Flow Metab.* 23, 1–18.

Offenhauser, N., Royl, G., Leithner, C., Dirnagl, U., and Lindauer, U. (2007). Sustained alteration of neurometabolic, vascular coupling by cortical spreading depression in rat somatosensory cortex. *J. Cereb. Blood Flow Metab.* 27(Suppl. 1), BO13-07.

Offenhauser, N., Thomsen, K., Caesar, K., and Lauritzen, M. (2005). Activity-induced tissue oxygenation changes in rat cerebellar cortex: interplay of postsynaptic activation and blood flow. *J. Physiol.* 565, 279–294.

Piilgaard, H., and Lauritzen, M. (2009). Persistent increase in oxygen consumption and impaired neurovascular coupling after spreading depression in rat neocortex. *J. Cereb. Blood Flow Metab.* 29, 1517–1527.

Qiu, M., Ramani, R., Swetye, M., Rajeevan, N., and Constable, R. T. (2008). Anesthetic effects on regional CBF, BOLD, and the coupling between task-induced changes in CBF and BOLD: an fMRI study in normal human subjects. *Magn. Reson. Med.* 60, 987–996.

Rack-Gomer, A. L., Liau, J., and Liu, T. T. (2009). Caffeine reduces resting-state BOLD functional connectivity in the motor cortex. *Neuroimage* 46, 56–63.

Rauch, A., Rainer, G., and Logothetis, N. K. (2008). The effect of a serotonin-induced dissociation between spiking and perisynaptic activity on BOLD functional MRI. *Proc. Natl. Acad. Sci. U.S.A.* 105, 6759–6764.

Reddy, H., Narayanan, S., Arnoutelis, R., Jenkinson, M., Antel, J., Matthews, P. M., and Arnold, D. L. (2000). Evidence for adaptive functional changes in the cerebral cortex with axonal injury from multiple sclerosis. *Brain* 123, 2314–2320.

Roc, A. C., Wang, J., Ances, B. M., Liebeskind, D. S., Kasner, S. E., and Detre, J. A. (2006). Altered hemodynamics and regional cerebral blood flow in patients with hemodynamically significant stenoses. *Stroke* 37, 382–387.

Rossini, P. M., Altamura, C., Ferretti, A., Vernieri, F., Zappasodi, F., Caulo, M., Pizzella, V., Del Gratta, C., Romani, G. -L., and Tecchio, F. (2004). Does cerebrovascular disease affect the coupling between neuronal activity and local haemodynamics? *Brain* 127, 99–110.

Roy, C., and Sherrington, C. (1890). On the regulation of the blood supply of the brain. *J. Physiol.* 11, 85–108.

Royl, G., Füchtemeier, M., Leithner, C., Megow, D., Offenhauser, N., Steinbrink, J., Kohl-Bareis, M., Dirnagl, U., and Lindauer, U. (2008). Hypothermia effects on neurovascular coupling and cerebral metabolic rate of oxygen. *Neuroimage* 40, 1523–1532.

Royl, G., Leithner, C., Sellien, H., Müller, J. P., Megow, D., Offenhauser, N., Steinbrink, J., Kohl-Bareis, M., Dirnagl, U., and Lindauer, U. (2006). Functional imaging with Laser Speckle Contrast Analysis: vascular compartment analysis and correlation with Laser Doppler Flowmetry and somatosensory evoked potentials. *Brain Res.* 1121, 95–103.

Sacco, R. L., Chong, J. Y., Prabhakaran, S., and Elkind, M. S. V. (2007). Experimental treatments for acute ischaemic stroke. *Lancet* 369, 331–341.

Sauer, J., ffytche, D. H., Ballard, C., Brown, R. G., and Howard, R. (2006). Differences between Alzheimer's disease and dementia with Lewy bodies: an fMRI study of task-related brain activity. *Brain* 129, 1780–1788.

Schonberg, T., O'Doherty, J. P., Joel, D., Inzelberg, R., Segev, Y., and Daw, N. D. (2010). Selective impairment of prediction error signaling in human dorsolateral but not ventral striatum in Parkinson's disease patients: evidence from a model-based fMRI study. *Neuroimage* 49, 772–781.

Schreiber, A., Hubbe, U., Ziyeh, S., and Hennig, J. (2000). The influence of gliomas and nonglial space-occupying lesions on blood-oxygen-level-dependent contrast enhancement. *AJNR Am. J. Neuroradiol.* 21, 1055–1063.

Schroeter, M. L., Cutini, S., Wahl, M. M., Scheid, R., and Yves von Cramon, D. (2007). Neurovascular coupling is impaired in cerebral microangiopathy – an event-related Stroop study. *Neuroimage* 34, 26–34.

St Lawrence, K. S., Ye, F. Q., Lewis, B. K., Frank, J. A., and McLaughlin, A. C. (2003). Measuring the effects of indomethacin on changes in cerebral oxidative metabolism and cerebral blood flow during sensorimotor activation. *Magn. Reson. Med.* 50, 99–106.

Thiyagesh, S. N., Farrow, T. F. D., Parks, R. W., Accosta-Mesa, H., Young, C., Wilkinson, I. D., Hunter, M. D., and Woodruff, P. W. R. (2009). The neural basis of visuospatial perception in Alzheimer's disease and healthy elderly comparison subjects: an fMRI study. *Psychiatry Res.* 172, 109–116.

Thompson, J. K., Peterson, M. R., and Freeman, R. D. (2003). Single-neuron activity and tissue oxygenation in the cerebral cortex. *Science* 299, 1070–1072.

Uludag, K., Müller-Bierl, B., and Ugurbil, K. (2009). An integrative model for neuronal activity-induced signal changes for gradient and spin echo functional imaging. *Neuroimage* 48, 150–165.

White, A., Lee, J., Light, A., and Light, K. (2009). Brain activation in multiple sclerosis: a BOLD fMRI study of the effects of fatiguing hand exercise. *Mult. Scler.* 15, 580–586.

Wierenga, C., and Bondi, M. (2007). Use of functional magnetic resonance imaging in the early identification of Alzheimer's disease. *Neuropsychol. Rev.* 17, 127–143.

Zappe, A. C., Uludag, K., Oeltermann, A., Ugurbil, K., and Logothetis, N. K. (2008). The influence of moderate hypercapnia on neural activity in the anesthetized nonhuman primate. *Cereb. Cortex* 18, 2666–2673.

Conflict of Interest Statement: The authors declare that the research was conducted in the absence of any commercial or financial relationships that could be construed as a potential conflict of interest.

Received: 22 February 2010; paper pending published: 26 April 2010; accepted: 20 July 2010; published online: 04 October 2010.
Citation: Lindauer U, Dirnagl U, Füchtemeier M, Böttiger C, Offenhauser N, Leithner C and Royl G (2010) Pathophysiological interference with neurovascular coupling – when imaging based on hemoglobin might go blind. Front. Neuroenerg. ***2****:25. doi: 10.3389/fnene.2010.00025*

frontiers in
NEUROENERGETICS

OPINION ARTICLE
published: 02 June 2010
doi: 10.3389/fnene.2010.00002

Neurovascular uncoupling: much ado about nothing

Nikos K. Logothetis*[1,2]

[1] *Max Planck Institute for Biological Cybernetics, Tuebingen, Germany*
[2] *Division of Imaging Science and Biomedical Engineering, University of Manchester, Manchester, UK*
**Correspondence: nikos.logothetis@tuebingen.mpg.de*

The vast majority of human fMRI studies measure Blood-Oxygen-Level-Dependent (BOLD) contrast, which reflects regional changes in cerebral blood flow (CBF), cerebral blood volume (CBV) and blood oxygenation; all three vascular responses reflect local increases in neural activity (Logothetis and Wandell, 2004). Understanding the exact mechanism (often referred to as neurovascular coupling) by means of which changes in neural activity alter hemodynamics is obviously of paramount importance for the meaningful interpretation of fMRI results. Not surprisingly, over the last decade an increasing number of researchers investigated the neurovascular coupling by combining fMRI with electroencephalography (EEG) or magnetoencephalography (MEG) in humans, e.g. (Dale and Halgren, 2001) as well as with intracortical recordings in animals (Logothetis et al., 2001; Goense and Logothetis, 2008; Logothetis, 2008; Rauch et al., 2008). This neurovascular coupling can also be studied with the optical imaging of intrinsic signals (OIS) (Bonhoeffer and Grinvald, 1996), an excellent invasive method of high spatiotemporal resolution that can measure changes in oxygenation and/or blood volume.

Recently, an OIS variant permitting simultaneous measurements of blood volume and oxygenation was used to image the visual cortex of behaving monkeys performing visual or auditory tasks (Sirotin and Das, 2009). Concurrent hemodynamic measurements were performed by rapidly switching between two wavelengths, 530 nm and 605 nm, permitting the measurement of CBV and oxygenation, respectively. During the measurements the monkeys were required to periodically direct their gaze to a point source in order to receive a juice reward. The fixation point remained on continuously, but switched between two equiluminant colors to cue the animal to 'fixate' (green) or 'relax' (red). In one task, the fixation spot was followed by a brief visual stimulus presentation at approximately 2° eccentricity; in a second task only the fixation spot was visible in an otherwise dark room. Finally, in a third control task the animals initiated a trial by pulling a lever. The monkeys were then presented with a tone and were trained to release the lever immediately after a change in tone pitch. Optical imaging was performed in a window covering the V1 representation of visual field eccentricities ranging from about 1° to 5°. The time course of the average hemodynamic response over the full area and the neural signal assessed in extracellular recordings at various locations within the imaging field were used to compare electrical and vascular responses.

Upon imaging V1 while the animals performed the fixation-spot-only task, Sirotin and Das observed robust modulations of the hemodynamic signal at the trial frequency, even though the animals were virtually in total darkness and foveal V1, the only region receiving visual input from the fixation point, lay outside of the imaged area. The authors concluded that in some conditions the hemodynamic responses, and thus fMRI signals, too, bear no relation to the underlying regional neural activity, suggesting that the responses reflect "distal neuromodulatory control of cerebral arteries" (Sirotin and Das, 2009). Not surprisingly, the finding sparked a great deal of controversy [e.g. see discussion in references Raichle, 2009; Zheng et al., 2010, and commentary by Kleinschmidt and Müller (2010)], because it challenges the view that fMRI reflects local neural activity. What follows is a discussion of certain claims and conclusions by Sirotin and Das, as well as some comments on the implications of their findings for how to interpret the relationship between fMRI measures and neural signals.

To begin with, it is worth reiterating that fMRI – just like any other methodology, extracellular recordings being no exception – has serious limitations. There is plenty of evidence (see Logothetis, 2008 and references therein) suggesting that the fMRI signal does not differentiate between function-specific processing and neuromodulation or between bottom-up and top-down signals, and it is likely to confuse excitation and inhibition. In cortical regions in which stimulus- or task-related perceptual or cognitive capacities are instantiated in the activity of a very small number of neurons, volume transmission (Agnati et al., 1992, 2006; Ridet and Privat, 2000; Sykova, 2003) – which probably underlies the altered states of motivation, attention, learning and memory – may affect hemodynamic responses and often make it difficult to deduce the exact role of the area in the task at hand, at least to the extent that this role is thought to be instantiated in the activity of stimulus- or task-selective cortical projection neurons. Even so, the origin of the fMRI signal is at all times neurogenic, and it consistently reflects local changes in overall neural activity.

Interestingly, evidence for the neurogenic basis of the BOLD signal may be found in the same Sirotin-Das (S-D) study that claims to demonstrate a case of neurovascular uncoupling. Specifically, looking at the left spectrogram of **Figure 1** (copied from Figure 2 of Sirotin and Das, 2009) one can discern two dark vertical bars (ca. 50% reduction of the neural signal). The bars are approximately aligned and coextensive with the periods of fixation. The right spectrogram shows the 66- to 130-Hz frequency band, and the superimposed white trace depicts the average of power in this range. This trace was vertically stretched at the bottom of **Figure 1** to allow visualization of the detailed time course of the neural signal. The blue arrow shows a systematic decrease in LFP, perhaps due to a decrease in spontaneous activity, followed by an overshoot (red arrow) after the fixation period. An inspection of the spectrogram might lead one to expect that even greater signal changes may exist in certain subregions of the frequency domain (e.g. 70–75 Hz). The statistical significance of such changes

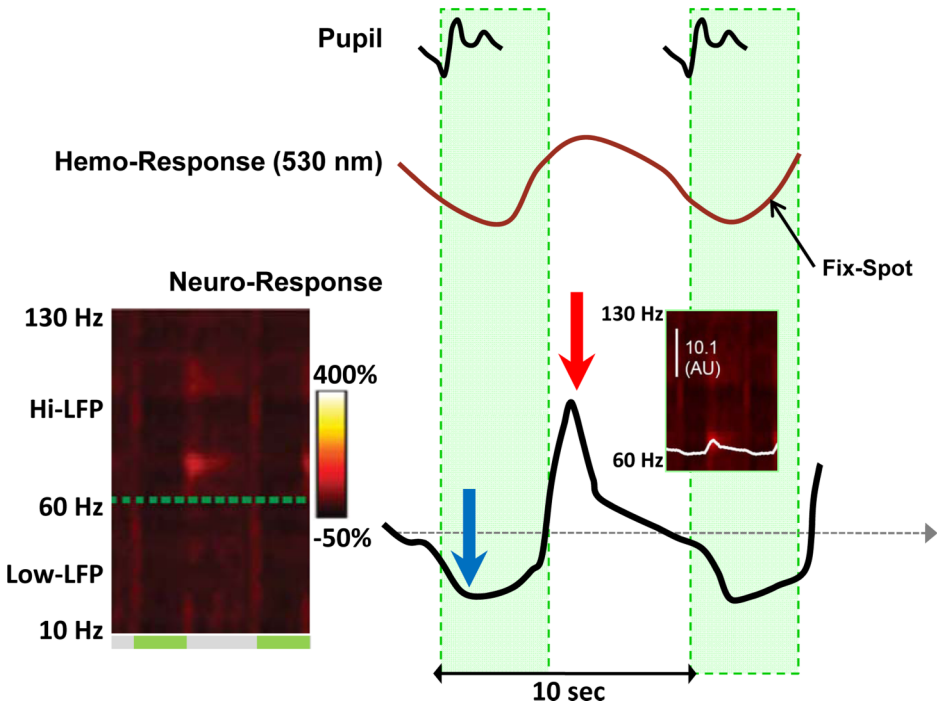

FIGURE 1 | Changes in neural and vascular activity during the performance of the *fix-spot-only* task. The left spectrogram shows the power of the LFP signal in the 10- to 130-Hz range. On the right shown are the trial-triggered papillary (top), hemodynamic (middle), and LFP (bottom) responses (from Figure 2 and Figure S3 in Supplementary Material of the S-D study). An increase in CBV (negative deflection) is evident after the trial onset, followed by an undershoot (positive deflection). The bottom curve is a replica of the white trace shown in the 'Dark' plot of Figure 3A in Supplementary Material of the S-D study (see also inset), but here is vertically stretched to clearly show the activity changes during the task. It represents the trial-triggered power over the hi-LFP frequency range integrated over the 66- to 130-Hz range. The blue arrow shows a clear reduction in LFP (evident in the 'dark' band of the spectrogram over all frequencies during the fixation 'green' periods), followed by a rebound (red arrow) activity most prominent in the 70- to-75-Hz band.

cannot be assessed on the basis of the evidence provided in this study, and they may well be too small to formulate a data-supported hypothesis. Yet a simple qualitative assessment of the figures should be sufficient warning against drawing a conclusion of neurovascular uncoupling, even more so because changes in interneuronal activity might indeed go unnoticed during extracellular recordings.

In multiunit recordings, the electrodes measure changes in the *mean* extracellular field potential (mEFP) that is mostly due to the distribution of current sources in the dendrites (Avitan et al., 2009). The magnitude of the mEFP in such recordings, as well as that of the signals measured in EEG and MEG, is approximately proportional to the magnitude of the population current dipole $\boldsymbol{Q}$, i.e. the average of each cell's current dipole (Barr et al., 1966; Geselowitz, 1967), and it depends critically on both the strength of individual dipoles and the local geometrical arrangements of neurons (Lorente de No, 1947). Neurons with their dendrites facing in one direction and the somata in the other are said to have an *open-field* configuration. Experimental and modeling work has shown that open-field generators produce strong individual current dipoles and, under proper geometrical arrangement (e.g. all dendrites along the longitudinal axis, and neurons forming bundles), also powerful population electrical fields that extend over long distances; typical examples are the neocortical and hippocampal pyramidal cells (Murakami et al., 2002, 2003; Murakami and Okada, 2006). On the other hand, cells with radially symmetric dendrites generate electric fields that are confined within the volume of the cells; they are hence considered to be *closed-field* generators. The small amplitude multiple dipoles, created by action potentials traveling somatofugally in the radially symmetric dendrites tend to diminish, rather than enhance, each other in the extracellular space. Good examples are the aspiny (inhibitory) cortical cells that on average produce $\boldsymbol{Q}$ vectors that are weaker than the supra- and infragranular pyramidal neurons by a factor of up to 8 (Murakami and Okada, 2006). Importantly, the $\boldsymbol{Q}$ of a population of such cells can be much weaker than the linear sum of their individual $\boldsymbol{Q}$ values due to their variable dendritic geometry (Murakami and Okada, 2006). The conclusions drawn from such modeling work are likely to be applicable to the LFPs as well (0.05 through 250 Hz), since the EEG and LFP signals are correlated to each other (Whittingstall and Logothetis, 2009). It is thus possible in principle that selective activation of certain classes of neurons may have weak effects only on certain LFP bands, and even go unnoticed during extracellular recordings. This is simply a limitation of extracellular recordings that must be taken into account in studies of the neurovascular coupling. Moreover, the fact

that increased activity of single inhibitory interneurons likely results in vasomotor responses in neighboring brain microvessels (Hamel, 2006) or that astrocytes may respond selectively to sensory stimuli (Schummers et al., 2008) does not by any means imply a lack of regional stimulus- or task-related, driver or neuromodulatory cortical neural responses (Chance et al., 2002; McCormick et al., 2003; Hasenstaub et al., 2007).

The responses reported by Sirotin and Das are most likely due to site-specific effects of neuromodulatory input on the cortical excitation-inhibition balance. In their experiments, these authors observed task (i.e. visual or auditory discrimination) independent pupillary responses that systematically preceded the trial-locked hemodynamic fluctuations (**Figure 1**). In humans such responses are obtained for a wide variety of cognitive processes ranging from simple sensory-event detection through attention, memory, and language processing (Beatty, 1982). They are mediated almost exclusively via norepinephrine (NE) being released from the locus coeruleus (LC). In fact, LC efferents stimulate the iris dilator muscle both directly and indirectly through the Edinger–Westphal nucleus, which in turn projects to the ciliary ganglion (Yoshitomi et al., 1985; Loewenfeld, 1993). Notably, the LC-induced response is distinct from the pupillary light reflex mediated by acetylcholine (Loewenfeld, 1993), so that under constant low-light conditions such as those used in the S-D study, pupil diameter will be a reliable measure of NE-induced neuromodulation (Koss, 1986; Loewenfeld, 1993; Aston-Jones and Cohen, 2005). In other words, during the Sirotin and Das experiments there was a task-induced, modality-independent periodic activation of the LC of the monkeys.

LC neurons project to most brain regions, including the paleo- and neocortex (Jones et al., 1977), and LC terminals have both nonsynaptic release sites that may provide paracrine-type neurotransmission (Beaudet and Descarries, 1978; Sara, 2009), as well as conventional synapse-like appositions with postsynaptic specializations pointing to the co-existence of wiring transmission (Aston-Jones and Cohen, 2005). NE may increase neural responses by reducing after hyperpolarization (e.g. by blocking Ca^{2+}-dependent K^+ currents) or decrease them by enhancing GABA-induced inhibition (Sara, 2009).

In the S-D study, the monkey was involved in a demanding attentional task which required it to continuously discriminate between two point sources with different spectral energy compositions and make a behavioral decision on the basis of the perceived color. During such a task, the release of NE in V1 that follows LC activation is likely to *augment* the responses induced by the attended fixation spot while *decreasing* spontaneous activity (the excitation-inhibition balance), as has been shown repeatedly by various investigators, e.g. see review by Aston-Jones and Cohen (Aston-Jones and Cohen, 2005). If reduction in spontaneous neural activity in the non-attended foveal and parafoveal regions imaged in the above study is mediated by increases in interneuronal activity via volume transmission, dissociation between "measurable" neural and vascular signals cannot be excluded (see above), and the increase in CBV observed by the authors in the "hitherto unknown signal" (**Figure 1**, middle red trace) may simply reflect increased metabolism due to increases in inhibitory conductance.

An interesting observation in the S-D study is the specificity of V1 neuromodulation. The LC-NE system was initially viewed as having relatively broad and spatially nonspecific effects on cortical information processing. But later studies showed that LC projections, although widespread, exhibit substantial regional and laminar specificity. In monkeys, for instance, the laminar pattern of noradrenergic innervation in primary visual cortex differs fundamentally from that in both prefrontal and primary somatosensory cortices (Morrison et al., 1982; Foote et al., 1983). A large number of studies have demonstrated that the effects of the LC-NE system on target neurons are characterized by temporal and spatial discreteness. In other words, the LC-NE system acts on a discrete, specifiable set of neurons under a particular set of circumstances to produce a defined set of effects (Foote et al., 1983). The regional anatomical-functional specificity is also congruent with the observation that bursts of LC activity are correlated with the outcome of task-related decision processes (see references in the review by Aston-Jones and Cohen, 2005). Interestingly, the S-D study also showed that LC responses, evident via the pupillary response, induce a task- and modality specific change in hemodynamics: no CBV changes in V1 were measured during the auditory control task. By combining broad access and specificity, the massive efferent system of the LC is likely to impose simultaneous internal-state changes on many different brain regions subject to sensory stimulation.

In summary, Sirotin and Das addressed an important question using an outstanding methodology. In agreement with previous studies (see above), they demonstrated that their task selectively modulates neuronal activity in V1, likely reducing spontaneous activity (e.g. for gain control, Chance et al., 2002, but see also alternative observations, McCormick et al., 2003; Hasenstaub et al., 2007). The increased inhibition, visible in their spectrograms, may trigger CBV changes and yield the "anticipatory responses". Yet, the authors' generalizations are unjustified, and I suspect that their conclusions are incorrect.

The fMRI methodology is used extensively in cognitive neuroscience, and as in any advanced field of investigation there are quite a few publications that are senseless and do not enhance our understanding of brain function. The problem, however, is not in the methodology but rather in those investigators who use it without understanding its limitations. Even if neurovascular coupling were well understood, the limitations of fMRI reflecting mass action (Logothetis, 2008) would still require a multimodal approach before we can even begin to fathom the exact neural mechanisms underlying the usual fMRI activations and understand the role of the mapped areas. This having been said, and despite its shortcoming, fMRI is a useful and meaningful tool for the study of brain function, and fMRI signals reflect changes in regional neuronal mass activity.

ACKNOWLEDGMENTS

I thank my colleagues Christoph Kayser, Oxana Eschenko, Ahalya Viswanathan, and Brian Wandell for insightful comments on the final version of the article.

REFERENCES

Agnati, L. F., Bjelke, B., and Fuxe, K. (1992). Volume transmission in the brain. *Am. Sci.* 80, 362–373.

Agnati, L. F., Leo, G., Zanardi, A., Genedani, S., Rivera, A., Fuxe, K., and Guidolin, D. (2006). Volume

transmission and wiring transmission from cellular to molecular networks: history and perspectives. *Acta Psychol. (Amst)* 187, 329–344.

Aston-Jones, G., and Cohen, J. D. (2005). An integrative theory of locus coeruleus-norepinephrine function: adaptive gain and optimal performance. *Annu. Rev. Neurosci.* 28, 403–450.

Avitan, L., Teicher, M., and Abeles, M. (2009). EEG generator-a model of potentials in a volume conductor. *J. Neurophysiol.* 102, 3046–3059.

Barr, R. C., Pilkington, T. C., Boineau, J. P., and Spach, M. S. (1966). Determining surface potentials from current dipoles with application to electrocardiography. *IEEE Trans. Biomed. Eng.* 13, 88–92.

Beatty, J. (1982). Task-evoked pupillary responses, processing load, and the structure of processing resources. *Psychol. Bull.* 91, 276–292.

Beaudet, A., and Descarries, L. (1978). Mono-amine innervation of rat cerebral-cortex – synaptic and non-synaptic axon terminals. *Neuroscience* 3, 851–860.

Bonhoeffer, T., and Grinvald, A. (1996). "Optical imging based on intrinsic signals," in *Brain Mapping, The Methods*, eds A. W. Toga and J. C. Mazziotta (New York: Academic Press), 55–97.

Chance, F. S., Abbott, L. F., and Reyes, A. D. (2002). Gain modulation from background synaptic input. *Neuron* 35, 773–782.

Dale, A. M., and Halgren, E. (2001). Spatiotemporal mapping of brain activity by integration of multiple imaging modalities. *Curr. Opin. Neurobiol.* 11, 202–208.

Foote, S. L., Bloom, F. E., and Astonjones, G. (1983). Nucleus locus ceruleus – new evidence of anatomical and physiological specificity. *Physiol. Rev.* 63, 844–914.

Geselowitz, D. B. (1967). On bioelectric potentials in an inhomogeneous volume conductor. *Biophys. J.* 7, 1–11.

Goense, J. B., and Logothetis, N. K. (2008). Neurophysiology of the BOLD fMRI signal in awake monkeys. *Curr. Biol.* 18, 631–640.

Hamel, E. (2006). Perivascular nerves and the regulation of cerebrovascular tone. *J. Appl. Physiol.* 100, 1059–1064.

Hasenstaub, A., Sachdev, R. N. S., and McCormick, D. A. (2007). State changes rapidly modulate cortical neuronal responsiveness. *J. Neurosci.* 27, 9607–9622.

Jones, B. E., Halaris, A. E., Mcilhany, M., and Moore, R. Y. (1977). Ascending projections of locus coeruleus in rat.1. Axonal-transport in central noradrenaline neurons. *Brain Res.* 127, 1–21.

Kleinschmidt, A., and Müller, N. G. (2010). The blind, the lame, and the poor signals of brain function-a comment on Sirotin and Das (2009). *Neuroimage* 50, 622–625.

Koss, M. C. (1986). Pupillary dilation as an index of central nervous system alpha 2-adrenoceptor activation. *J. Pharmacol. Methods* 15, 1–19.

Loewenfeld, I. (1993). *The Pupil: Anatomy, Physiology, and Clinical Applications*. Detroit: Wayne State University Press.

Logothetis, N. K. (2008). What we can do and what we cannot do with fMRI. *Nature* 453, 869–878.

Logothetis, N. K., Pauls, J., Augath, M., Trinath, T., and Oeltermann, A. (2001). Neurophysiological investigation of the basis of the fMRI signal. *Nature* 412, 150–157.

Logothetis, N. K., and Wandell, B. A. (2004). Interpreting the BOLD signal. *Annu. Rev. Physiol.* 66, 735–769.

Lorente de No, R. (1947). Analysis of the distribution of action currents of nerve in volume conductors. In studies from the Rockefeller Institute Medical Research. *A Study of Nerve Physiology* 132, 384–477.

McCormick, D. A., Shu, Y. S., and Hasenstaub, A. (2003). "Balanced recurrent excitation and inhibition in local cortical networks," in *Excitatory-Inhibitory Balance: Synapses, Circuits, and Systems Plasticity,* ed. T. Hensch (New York: Kluwer Academic Press).

Morrison, J. H., Foote, S. L., Oconnor, D., and Bloom, F. E. (1982). Laminar, tangential and regional organization of the noradrenergic innervation of monkey cortex – dopamine-beta-hydroxylase immunohistochemistry. *Brain Res. Bull.* 9, 309–319.

Murakami, S., Hirose, A., and Okada, Y. C. (2003). Contribution of ionic currents to magnetoencephalography (MEG) and electroencephalography (EEG) signals generated by guinea-pig CA3 slices. *J. Physiol. (Lond.)* 553, 975–985.

Murakami, S., and Okada, Y. (2006). Contributions of principal neocortical neurons to magnetoencephalography and electroencephalography signals. *J. Physiol. (Lond.)* 575, 925–936.

Murakami, S., Zhang, T. S., Hirose, A., and Okada, Y. C. (2002). Physiological origins of evoked magnetic fields and extracellular field potentials produced by guinea-pig CA3 hippocampal slices. *J. Physiol. (Lond.)* 544, 237–251.

Raichle, M. E. (2009). A paradigm shift in functional brain imaging. *J. Neurosci.* 29, 12729–12734.

Rauch, A., Rainer, G., and Logothetis, N. K. (2008). The effect of a serotonin-induced dissociation between spiking and perisynaptic activity on BOLD functional MRI. *Proc. Natl. Acad. Sci. U.S.A.* 105, 6759–6764.

Ridet, J. L., and Privat, A. (2000). Volume transmission. *Trends Neurosci.* 23, 58–59.

Sara, S. J. (2009). The locus coeruleus and noradrenergic modulation of cognition. *Nat. Rev. Neurosci.* 10, 211–223.

Schummers, J., Yu, H. B., and Sur, M. (2008). Tuned responses of astrocytes and their influence on hemodynamic signals in the visual cortex. *Science* 320, 1638–1643.

Sirotin, Y. B., and Das, A. (2009). Anticipatory haemodynamic signals in sensory cortex not predicted by local neuronal activity. *Nature* 457, 475–479.

Sykova, E. (2003). Volume transmission in health and disease: communication via the brain extracellular space. *J. Neurochem.* 85, 2.

Whittingstall, K., and Logothetis, N. K. (2009). Frequency-band coupling in surface EEG reflects spiking activity in monkey visual cortex. *Neuron* 64, 281–289.

Yoshitomi, T., Ito, Y., and Inomata, H. (1985). Adrenergic excitatory and cholinergic inhibitory innervations in the human iris dilator. *Exp. Eye Res.* 40, 453–459.

Zheng, Y., Pan, Y., Harris, S., Billings, S., Coca, D., Berwick, J., Jones, M., Kennerley, A., Johnston, D., Martin, C., Devonshire, I. M., and Mayhew, J. (2010). A dynamic model of neurovascular coupling: implications for blood vessel dilation and constriction. [Epub ahead of print].

Received: 26 March 2010; accepted: 04 April 2010; published online: 02 June 2010.

Citation: Logothetis NK (2010) Neurovascular uncoupling: much ado about nothing. Front. Neuroenerg. ***2****:2. doi: 10.3389/fnene.2010.00002*

frontiers in
NEUROENERGETICS

OPINION ARTICLE
published: 07 June 2010
doi: 10.3389/fnene.2010.00004

Towards single-cell real-time imaging of energy metabolism in the brain

L. Felipe Barros*

Centro de Estudios Científicos, Centro de Ingeniería de la Innovación del, Valdivia, Chile
**Correspondence: fbarros@cecs.cl*

There are hundreds of different neuronal cell types across the brain and perhaps a large variety of astrocytes too. Each one of these cell subtypes is exposed to a different energy load in terms of onset, intensity and duration; from cells that fire at 500 Hz for a few milliseconds, others that sustain 40 Hz for hours and cells that may fire only once in a lifetime. It may be thought therefore that each different cell subtype has evolved a specific way to solve the energy problem, i.e., how to match energy delivery to energy demand. However, most of this rich microscopic detail remains unknown because current techniques to measure metabolite concentrations and metabolic flux have limited spatiotemporal resolution. This Opinion Article discusses how energy metabolism in the brain tissue may appear when looked at the cell level and with resolution of seconds, a task that seems increasingly possible due to the recent introduction of new molecular probes and powerful microscopy techniques.

Picture a 100 meter sprint race. Within seconds of the start signal, the athletes' hearts have increased their metabolic rate by five-fold and even stronger stimulations may be measured in the muscles of their legs. Meanwhile their brains stay unperturbed, for not even the hardest exercise or the most difficult chess move will provoke a significant increase in the overall fuel consumption of the organ. The metabolic rate of the brain does not decrease much either, and even during sleep, despite much diminished sensorial input and lack of movement, it only goes down by 15%. But this boring picture is deceiving, for very interesting things are bound to happen locally. The metabolic rate of individual neurons is highly variable. One moment they are at rest, consuming little energy in housekeeping functions like protein synthesis and intracellular trafficking; the next one they are at full throttle, recovering ion gradients challenged by postsynaptic currents and action potentials. For instance, as our sprinters leave the blocks, several neurons in their striata will have sprinted themselves from quiescence to 40 Hz, a firing rate that may be sustained for hours in a marathon race. Electrical activity means great energy expenditure, and from biophysical data it can be calculated that this level of electrical activity results in a 30-fold rise in fuel demand (Attwell and Laughlin, 2001).

The contrast between cell-level scintillation and organ-level constancy speaks of efficient averaging strategies whose nature we are only beginning to grasp. A first mechanism may be temporal averaging. Auditory neurons can fire at 500 Hz, which translates into a surge in energy demand in excess of 100-fold. However, these high-frequency neurons fire in bursts and the metabolic debt acquired during activity may be paid for during the resting phase. Neurons do not posses energy stores but they do have millimolar concentrations of glucose, lactate and glycolytic intermediaries to last for a short while. Though useful for phasic neurons, temporal averaging is of little use for tonic neurons like those in the striatum, which must sustain high rates of firing indefinitely, thus the need for spatial averaging. If the tissue architecture were arranged in such a way that active cells are surrounded by other cells that remain passive, the energy load may be shared over a larger volume. For instance, if every third neuron in a given area of the striatum were active during the sprint, the rise in regional energy demand would be reduced to more manageable 10-fold. Furthermore, it has been reported that active synapses inhibit their neighbors, a process mediated by purinergic signaling by astrocytes and thought to be instrumental for efficient information processing (Pascual et al., 2005). Given the direct relationship existing between activity and fuel consumption, it seems plausible that this functional contrast-enhancing is accompanied by metabolic inhibition of the neighbors and consequent fuel redistribution, a kind of "metabolic contrast-enhancing." Spatial averaging is conditioned by diffusion, whose effect is dramatically reduced by distance. Over a few micrometers, e.g., the diameter of a neuronal soma, diffusion is highly efficient, mixing molecules much faster than the turnover rates of the transporters and enzymes that produce them (Barros and Martinez, 2007). This means that astrocytes and neuronal somata are essentially homogenous in terms of glucose, lactate, ATP and other metabolites, and that neighboring postsynaptic spines are metabolically coupled. The presence of plasma membranes determines dynamic concentration gradients, between the interstitium, the cytosols of neurons and glial cells and mitochondria, yet we do not know how strong these gradients are and in some cases not even their direction, notably the lactate gradient between neurons and interstitium. Over longer distances, diffusion becomes less effective, giving rise to a second source of compartmentation. The half-time of glucose equilibration between two locations separated by 1 mm is about 20 min, ten times longer than the typical half-time of glucose phosphorylation in the brain tissue (Barros et al., 2007). In other words, there will be no effective spatial averaging of a metabolic load over distances over 1 mm, which sets the maximum size for a metabolic unit in the brain tissue and the spatial resolution of micrometer probes inserted in the interstitium.

The fluctuations in metabolic flux that accompany neuronal activity and the nature of the averaging mechanisms that explain large scale constancy of metabolic flux are almost invisible to current techniques, and as a result we know precious little of how the energy load is handled by the brain tissue. Some of these methods techniques report metabolite concentration and other metabolic flux (**Table 1**).

Arguably the best technique to measure metabolic flux is the 2-deoxyglucose method, introduced by Louis Sokoloff in the 70s, which shows maximum increases of about 30–60% in local glycolytic rate

Table 1 | Resolution of some techniques used in the study of brain energy metabolism.

Metabolite/analyte	Mode of detection	Measured parameter	Spatial resolution	Temporal resolution	References
Glucose/lactate	^{1}H NMR	Concentration	Centimeter	Seconds	Mangia et al. (2009)
Glucose/lactate	Microsensor Microdialysis	Concentration	Millimeter	Seconds	Revised in Barros et al. (2007)
NAD(P)H/flavoproteins	Optical	Concentration	Micrometer	Millisecond	Shuttleworth (2010)
Glucose	Optical	Concentration	Micrometer	Millisecond	Frommer et al. (2009)
Glucose/lactate	^{13}C NMR	Flux	Centimeter	Seconds	Mangia et al. (2009)
2-Deoxyglucose	Auto radiography	Flux	0.3 mm	>20 min	Dienel and Hertz (2001)
F-2-deoxyglucose	PET scanning	Flux	3 mm	>40 min	Kessler (2003)
2-NBDG	Optical	Flux	Micrometer	Minutes	Barros et al. (2009)

in response to physiological activation *in vivo* (Dienel and Hertz, 2001). With a best lateral resolution of 300 μm, a single pixel in a 2-deoxyglucose autoradiograph integrates information from hundreds of cells over 20 min or more; Its non-invasive – though less sensitive – counterpart being Fluorodeoxyglucose PET scanning, of ample use in clinical practice and cognitive studies (Kessler, 2003). Better temporal resolution has been obtained with NMR spectroscopy and also with microprobes inserted in the tissue, which show that synaptic activity is followed within seconds by a decrease in interstitial glucose and an increase in interstitial lactate, changes that suggest local stimulation of glycolysis by a yet to be determined cell type (Barros et al., 2007; Mangia et al., 2009). Even better temporal resolution has been obtained by single photon and multiphoton microscopy recording of NAD(P)H and flavoprotein autofluorescence, reporters of the redox potential of mitochondria (revised in Shuttleworth, 2010), which suggest that synaptic activity is followed within hundreds of milliseconds of changes in mitochondrial metabolism, consistent with sequential activation of NADH usage and NADH production. However, changes in metabolite concentration do not inform unambiguously about flux and it is a given change in concentration may be observed with both increased and decreased flux. Recently, the uptake of fluorescent glucose analogs was measured in cerebellar slices using multiphoton microscopy, showing that Bergmann glial cells transport and metabolize sugars more efficiently than Purkinje cells and granule cells (Barros et al., 2009). This methodology is capable of measuring metabolic flux and can resolve single cells but its temporal resolution is hampered by the slow rate of dye transport into the cell, which precludes the study of acute metabolic modulation. The desired combination of high temporal resolution with high spatial resolution may be attained with genetically encoded nanosensors, which are currently available for an ample range of metabolites (Frommer et al., 2009). Their expression in specific cell types using transgenesis and their detection *in vivo*, perhaps using multiphoton microscopy, should facilitate a new level of understanding of brain energy metabolism.

ACKNOWLEDGMENTS

This work was funded by Fondecyt 10070046. The Centro de Estudios Científicos (CECS) is funded by the Chilean Government through the Millennium Science Initiative and the Centers of Excellence Base Financing Program of CONICYT. CECS is also supported by a group of private companies which at present includes Antofagasta Minerals, Arauco, Empresas CMPC, Indura, Naviera Ultragas and Telefónica del Sur. CIN is funded by Conicyt and the Gobierno Regional de Los Ríos.

REFERENCES

Attwell, D., and Laughlin, S. B. (2001). An energy budget for signaling in the grey matter of the brain. *J. Cereb. Blood Flow Metab.* 21, 1133–1145.

Barros, L. F., Bittner, C. X., Loaiza, A., and Porras, O. H. (2007). A quantitative overview of glucose dynamics in the gliovascular unit. *Glia* 55, 1222–1237.

Barros, L. F., Courjaret, R., Jakoby, P., Loaiza, A., Lohr, C., and Deitmer, J. W. (2009). Preferential transport and metabolism of glucose in Bergmann glia over Purkinje cells: a multiphoton study of cerebellar slices. *Glia* 57, 962–970.

Barros, L. F., and Martinez, C. (2007). An enquiry into metabolite domains. *Biophys. J.* 92, 3878–3884.

Dienel, G. A., and Hertz, L. (2001). Glucose and lactate metabolism during brain activation. *J. Neurosci. Res.* 66, 824–838.

Frommer, W. B., Davidson, M. W., and Campbell, R. E. (2009). Genetically encoded biosensors based on engineered fluorescent proteins. *Chem. Soc. Rev.* 38, 2833–2841.

Kessler, R. M. (2003). Imaging methods for evaluating brain function in man. *Neurobiol. Aging* 24(Suppl. 1), S21–S35.

Mangia, S., Giove, F., Tkac, I., Logothetis, N. K., Henry, P. G., Olman, C. A., Maraviglia, B., Di, S. F., and Ugurbil, K. (2009). Metabolic and hemodynamic events after changes in neuronal activity: current hypotheses, theoretical predictions and in vivo NMR experimental findings. *J. Cereb. Blood Flow Metab.* 29, 441–463.

Pascual, O., Casper, K. B., Kubera, C., Zhang, J., Revilla-Sanchez, R., Sul, J. Y., Takano, H., Moss, S. J., McCarthy, K., and Haydon, P. G. (2005). Astrocytic purinergic signaling coordinates synaptic networks. *Science* 310, 113–116.

Shuttleworth, C. W. (2010). Use of NAD(P)H and flavoprotein autofluorescence transients to probe neuron and astrocyte responses to synaptic activation. *Neurochem. Int.* 56, 379–386.

Received: 27 January 2010; accepted: 04 April 2010; published online: 07 June 2010.

Citation: Barros LF (2010) Towards single-cell real-time imaging of energy metabolism in the brain. Front. Neuroenerg. ***2****:4. doi:10.3389/fnene.2010.00004*

frontiers in
NEUROENERGETICS

GENERAL COMMENTARY
published: 05 August 2010
doi: 10.3389/fnene.2010.00024

A BOLD assumption

Ivo Vanzetta[1]* and Hamutal Slovin[2]

[1] *Institut de Neurosciences Cognitives de la Méditerranée – Centre National de la Recherche Scientifique Unité Mixte de Rechereche 6193, Aix-Marseille Université, Marseille, France*

[2] *Gonda Brain Research Center, Bar-Ilan University, Ramat Gan, Israel*

**Correspondence: ivo.vanzetta@incm.cnrs-mrs.fr*

Interpreting fMRI data relies on the assumption that hemodynamic responses reflect neuronal activity. Some recently reported results seem to suggest that this assumption might be less robust than what has been thought so far. Data by Schummers et al. (2008) suggest that hemodynamic responses depend on functional properties of astrocytes as mediators of neuronal activity to blood vessels, and therefore reflect neuronal tuning properties only indirectly. The question is how much the final outcome differs from a linear integration of the local neuronal responses.

In more specific visual stimulus designs involving perceptual suppression of a physically present visual stimulus (Maier et al., 2008), BOLD responses and neuronal ones have been reported to not always go "hand in hand", suggesting that the relationship between hemodynamic and neuronal responses might depend on stimulus characteristics and behavioral task.

Finally, "anticipatory" hemodynamic responses have been reported (Sirotin and Das, 2009) in V1 of a monkey performing a fixation-on-off task. Importantly, the authors failed to predict the recorded hemodynamic changes from local neuronal activity. But does this rule out the latter as cause for the former? Is it conceivable that complex, modulatory phenomena such as attention involve complex links between neuronal and vascular activity, other than those acting in the case of a salient visual stimulus? What is the relation between eye movements, hemodynamic responses and local neuronal activity? Answers to these questions may help to better understand the main observations in (Sirotin and Das, 2009) and its implications for functional brain imaging.

A central assumption underlying the interpretation of fMRI data is that hemodynamic responses correspond to local neuronal activity and that they reflect its functional properties. Indeed, numerous studies conducted with optical imaging of intrinsic signals and fMRI, and more recently with optogenetic methods (Lee et al., 2010) have permitted remarkable insights into the organization of brain activity and the underlying neuronal mechanisms, suggesting that, within reasonable approximation, this assumption is correct. However, recent reports seem to challenge this assumption. How much?

Schummers et al. (2008) recently reported that hemodynamic responses depend on astrocytic rather than on neuronal activity. The tuning properties of hemodynamic responses would thus reflect those of astrocytic populations rather than of neuronal ones. How different are those? Schummers et al. find that the tuning curves of nearby astrocytes and neurons are centered on the same maximum. Yet, astrocytes are somewhat more narrowly tuned, which would introduce some non-linearity in the translation of the neuronal into the hemodynamic response. More data and extensive simulation work are needed to determine the amplitude of this effect – in particular under anesthesia, which the authors report to affect neurons and astrocytes differently. However, hemodynamic responses integrate over comparatively large neuronal – and thus astrocytic – populations (at least the size of a cortical column). Moreover, both neuronal and astrocytic tuning curves are in most cases symmetric around their maximum. Therefore, at least the spatial bias introduced by the astrocytic filter is likely to be small. In other words, assuming that the hemodynamic responses reflect a linear integration over the neuronal tuning curves of a local population of neurons is probably not such a bad approximation – at least when it comes down to determine what kind of stimulus with respect to another a given patch of cortex is preferably responsive to.

In more specific visual stimulus designs, involving perceptual suppression of a physically present visual stimulus (Maier et al., 2008), BOLD responses and neuronal ones (spikes and LFP, in particular the high frequency range) have been reported to not always go "hand in hand", but to co-vary differently with visual perception. Although a caveat exists here with respect to the lack of detailed knowledge about the local network activity (Nir et al., 2007), these results suggest that hemodynamic responses might be coupled to the different neuronal processes in a stimulus-dependent way. Put differently: the relationship between hemodynamic and neuronal responses is not rigid, but can depend on the specific circumstances and the task.

Finally, in a recent study performed by Sirotin and Das (2009) in awake monkey V1 it has been reported that hemodynamic responses can even anticipate events in the task structure. Importantly, the authors failed to predict those responses from the local neuronal activity recorded by a microelectrode, although they tried a good number of standard approaches to do so. They thus conclude to have found an "exception to the assumption that hemodynamic signals uniformly imply equivalent underlying neuronal activity". Are the hemodynamic signals detected in Sirotin's study to be explained by mechanisms other than local neuronal activity?

Recent commentaries (Tan, 2009; Kleinschmidt and Müller, 2010; Leopold, 2010) took different positions. Kleinschmidt and Müller argue that the measured hemodynamic and electrophysiological signals originated from substantially different sizes of neuronal populations and therefore cannot be compared. They suggest that the fixation task performed by the monkeys in Sirotin's study strongly deploys attention. Its spatial profile would be shaped as a Mexican hat centered on the tiny fixation point – where maximal attentional facilitation takes place – and suppressive in a large off-center part. When passing from facilitation to suppression, the Mexican hat obviously has a "zero crossing" and this gets important when one considers that: (i) on the one

hand, in Sirotin's study the electrical activity (LFP and MUA) was sampled only locally, precisely at about 1.5–2° off fixation, that is, where the zero crossing of the attentional modulation is likely to be (Heinemann et al., 2009). (ii) On the other hand, the hemodynamic signal was averaged over the entire imaged area. Kleinschmidt and Müller therefore suggested that improved spatial sampling of the electrophysiological signal, far from the zero-crossing point of spatial attention, would show the neuronal fingerprint of facilitating or suppressive activity and thus resolve the discrepancies between the two recorded signal modalities.

Alternatively, a recent commentary by Tan (2009) suggests a "dopamine hypothesis" as explanation of the reported anticipatory changes in regional cerebral hemodynamic signal. Indeed, the dopaminergic neurons of the brain stem (substantia nigra and the VTA, ventral tegmental area) exhibit reward-related anticipatory responses that can be adaptively timed (Schultz, 2007). Moreover, it has been suggested that dopamine has a direct effect on the microvasculature, mediated through dopamine receptors (Choi et al., 2006). Given the existence of dopaminergic innervations of the visual cortex arising from the VTA (Phillipson et al., 1987), Tan suggests that regional anticipatory hemodynamic changes in the target area, i.e., the visual cortex, may actually result from anticipatory dopaminergic responses.

We would like to point out another possible effect that might have contributed to the hemodynamic signals recorded in Sirotin and Das's study. Figures 1C,D of their paper shows an intriguing correlation between eye movements (fixation break and acquire but also smaller movements) and the hemodynamic signals: the temporal pattern of acquiring and breaking fixation signal appears to be closely related to the temporal pattern of the hemodynamic signal. This relationship being nearly one-to-one in the shown example, the question arises of whether the recorded hemodynamic signals might not be evoked by one or more neuronal events linked to eye movements. Admittedly, hemodynamic responses in correspondence to several, temporally close, eye movements are less clearly defined. Also, the true time-lag of the intrinsic signal onset with respect to the putative corresponding eye movement is some cases difficult to determine. For instance, one might argue that especially at 605 nm, in some cases, the time course appears to begin its downwards deflection very (if not too) early to be traced back to an oculomotor event (e.g., in the first and the fifth cycle in Figures 1C,D). However, it must be kept in mind that there are well known difficulties in determining the exact timing of the hemodynamic signal in such cyclic protocols (see, e.g., Kleinschmidt and Müller, 2010). Since eye movements tend to align to the trial structure, also here, interactions between two subsequent hemodynamic responses are likely, making it difficult to determine their exact onset. Some insights on this issue, including on the unusually large amplitude of the 605 nm signal (Figure 1D in Sirotin and Das, 2009: 2–5 times larger than usually, see Vanzetta et al., 2004), might be obtained from analyzing the eye movement patterns corresponding to the hemodynamic responses recorded during protocols that used different timings of trials. Unfortunately those are not provided. In any case, it would be interesting to look at the correlation between eye movements and hemodynamic responses, as well as to see whether the time-series of the former could predict the latter in the non-stimulated trials.

A last issue concerns the related (or unrelated) neuronal activity. In Sirotin's study, eye movements could in principle induce neuronal activity by shifting the fixation point over the retina, and specifically through the receptive fields of cells located in the imaged area. Indeed, we have previously shown that the dislocation of small visual stimuli on the retina, induced by large saccadic eye movements, evokes population activity in V1 (Slovin et al., 2002, Figure 11). Alternatively, it is possible that eye movements by themselves contribute to neuronal activation in V1 by extra-retinal modulation (Kagan et al. 2008). Indeed, fixation onset initiated by an eye movement, induces neural modulation in V1 as shown by our own data in Figure 1 below. Whatever is the case, the question arises why this was not seen in the electrophysiological recordings.

First, cortical activation induced by eye movements due to retinal stimulation is limited to the trajectory traced by the small fixation point stimulating over V1, which might not have crossed the receptive fields of the neurons sampled by the recording electrode – at least not in every trial – but which might be visible when integrating over a much larger area, as is done in the case of the hemodynamic signals.

A second explanation appears possible when looking at the low frequency part of the LFP (lo-LFP) measurements presented in Sirotin and Das's paper. The authors note that the lo-LFP band is a poor predictor not only of trial-related hemodynamics, but also of visually evoked one. This result is somewhat surprising given that: (i) other studies (Siegel and König, 2003; Henrie and Shapley, 2005) reported that visual stimuli induce large increase in power over both high and low frequency bands of the LFP and that (ii) the study of Maier et al. (2008) reported lo-LFP band (<30 Hz) to be the only neuronal parameter correlated with the BOLD signal during perceptual suppression in the GFS paradigm. In this latter study, the weak predictive power of the high frequency LFP (hi-LFP) is somewhat surprising but might be attributed to the specific cortical layers from which the signals were recorded. Conversely, the question of why in Sirotin and Das' study neither the high- nor (and especially not) the low-LFP band could be used as a reliable predictor – even for the stimulated condition – might find an answer by a careful inspection of the recorded LFP patterns:

First, the trial-averaged LFP response in their Figure 2A (bottom left panel) shows large activity in the low frequency band in the stimulated trials already before stimulus onset, at or even before the onset of the "acquire fixation" instruction (the red–yellow "flame" during the left half of the green bar), followed by a much smaller rebound just after the onset of the stimulus (the small yellow "spike" right above the leftmost quarter of the red bar). Second, this large activity is absent in the dark trials (Figure 2A, bottom right panel).

The first observation suggests that, in stimulated trials, the hemodynamic response function (HRF) is actually the response to a combination of neuronal responses to (at least) two events, which could have some temporal overlap and which are not necessarily coupled with the same strength to the hemodynamic response. Importantly, at the single trial level, the relative amplitude and timing of these neuronal responses might well be different from one trial to another, therefore eliciting different hemodynamic responses – even if the LFP power integrated

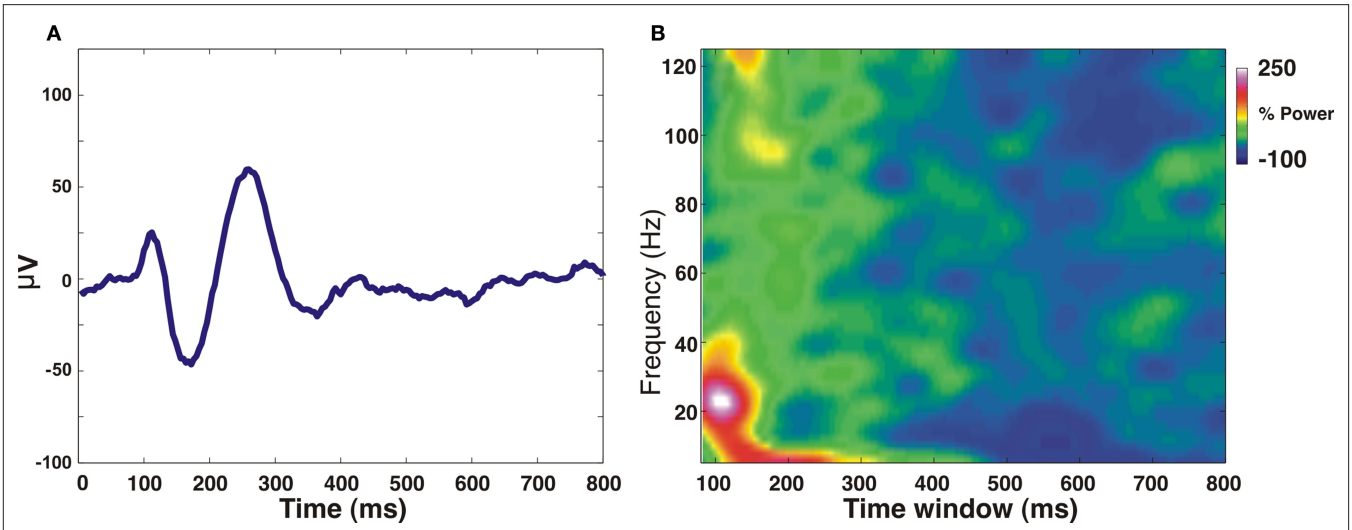

FIGURE 1 | Trial-averaged Local field potential (LFP) changes as a result of "fixation acquire" eye movement, measured in awake monkey V1. LFP was measured using a microelectrode inserted into the upper layers of V1, eccentricity: 1° below the horizontal meridian and 0.5° from the vertical meridian. In each trial, data acquisition started at the very moment ("fixation acquire": $t = 0$) when the monkey begun fixating on the fixation dot displayed on an otherwise black CRT screen. **(A)** The trial-averaged LFP signal (baseline value has been subtracted) shows a clear transient locked to the "fixation acquire" event ($t = 0$). **(B)** Time-dependent Fourier transform (spectrogram) analysis of the LFP signal shown in **(A)**. The analysis was done using a sliding hamming window of 160 ms (very similar results were obtained using a sliding window of 80-ms width); LFP power was normalized to baseline activity ($t = 1200$–1600 ms after acquiring fixation). A clear increase of power can be observed in the low-LFP band (8–50 Hz), much larger than the increase in the high-LFP band (60–120 Hz). Note that, typically, the onset of a visual stimulus induces a substantial gamma band (25-100 Hz) activity (Siegel and König, 2003; Henrie and Shapley, 2005), whereas here this activity is comparatively low, supporting the concept that the measured LFP signals are not (purely) visually evoked.

over a given time interval (e.g., the duration of the stimulus) remains the same. This would question the applicability of the "best neuro-to-hemo fit", according to which the HRF is obtained (their Supplementary Figure S2) and could explain the low predictive power of the lo-LFP for stimulated trials. The second observation then leads to speculate that – somehow in analogy to Maier's study, this HRF obtained from stimulated trials is even less applicable to predict hemodynamic responses in the dark, because the neuronal responses are qualitatively different even for the "fixation-only" part, as can be seen by their average (Figure 2A: compare the two bottom panels).

As compared to lo-LFP, in hi-LFP the ratio between fixation-only and stimulus-on activity appears to be much smaller, which would mean that the HRF is more accurate in agreement with the better predictive power of the high part of the LFP frequency spectrum. However, also for hi-LFP, differences can be seen between stimulated and dark trials during the fixation-only part. Although smaller than in the case of lo-LFP, these differences might again explain why predicting the hemodynamic signals in dark trials from HRFs derived from stimulated trials did not work using hi-LFP, either.

What about the dark-fitted HRFs? At the single trial level, it is hard to see any clear change in either spiking activity nor in the power of any of the two considered large LFP bands that could explain the corresponding hemodynamic response. Might some of those such changes become visible upon careful, more narrow band selection of the LFP? Whatever the answer, at the average level, a periodic activity change in the LFP (both in high and low frequencies) during dark trials clearly exists (e.g., the vertical bands in the time-frequency plane in Figure 2A, bottom right). Since also the average hemodynamic responses show the same periodicity, the two signals must be correlated above chance level. Nevertheless, the attempt to predict the hemodynamic responses from these neuronal signals results in a fairly inaccurate hemodynamic time-series (their Supplementary Figures S3 and S7). The most straightforward explanation is a low information content of the electrical recordings, which could result from small spatial sampling and an unfortunate positioning of the microelectrode as suggested by Kleinschmidt and Müller. These hypotheses can be checked directly by careful analysis of the hemodynamic maps, or by measuring, at the same spatial sites, both the neuronal and hemodynamic responses locally (Vanzetta et al., 2010). It should also be kept in mind that neuronal activity in itself is not to be identified with its measurement, which, depending on the method used, can emphasizes certain aspects while missing others. For instance, voltage-sensitive dye (VSD) signals have been obtained at cortical locations from which clear LFP responses were absent (Devor et al., 2007), possibly because VSD signals are very sensitive to polarization changes in layer 1, and, in contrast to LFP, they do not have constrains related to the geometry of currents.

Another – more speculative – possibility is that instantaneous firing rate, LFP activity power and the like might not always be the correct neuronal counterpart to a hemodynamic response, in particular in the presence of complex modulatory phenomena involving enhancement and suppression, such as attention. It might be possible that a different, more specific selection of LFP bands would allow to better capture such phenomena (e.g., could the LFP power suppression observed between 10 and 20 Hz both in stimulated and dark trials predict a brightening of the cortex? See Figure 2 in Sirotin and Das' paper, as well as the comments by Kleinschmidt and Müller, 2010).

Importantly, inhibitory and excitatory neurons might be coupled differently to hemodynamics, and the relative weight of excitatory and inhibitory neurons might even be different in each trial – in particular in attention-involving tasks, from which some degree of intrinsic variability is difficult to eliminate. If this should turn out to be true, correctly selecting the "elementary" neuronal event from which to extract an HRF able to predict a measured hemodynamic time-series might be very difficult, if not impossible. Yet, this would still not suffice to invalidate the long-standing assumption of coupling between hemodynamic responses and local electrical activity. For instance, the neuronal correlates to the trial-related hemodynamic signal might be found in neuronal correlations (as was suggested by Nir et al., 2007) or in other more complex encoding of neuronal activity (firing patterns, coherence, etc.). Innovative technologies such as optogenetics (Gunaydin et al., 2010), which has recently been coupled with fMRI (Lee et al., 2010), might turn out to be very valuable to provide evidence for the existence or not of such specific links between the hemodynamic response and activation of specific neuronal populations – including that of remote monoaminergic ones (Attwell and Iadecola, 2002).

ACKNOWLEDGMENTS

We thank Hadar Edelman and Ariel Gilad for sharing their data, and Drs. Christian G. Bénar, Guillaume S. Masson and Rafael Malach for discussions and feedback on the manuscript.

REFERENCES

Attwell, D., and Iadecola, C. (2002). The neural basis of functional brain imaging signals. *Trends Neurosci.* 25, 621–625.

Choi, J. K., Chen, Y. I., Hamel, E., and Jenkins, B. G. (2006). Brain hemodynamic changes mediated by dopamine receptors: role of the cerebral microvasculature in dopamine-mediated neurovascular coupling. *Neuroimage* 30, 700–712.

Devor, A., Tian, P., Nishimura, N., Teng, I. C., Hillman, E. M., Narayanan, S. N., Ulbert, I., Boas, D. A., Kleinfeld, D., and Dale, A. M. (2007). Suppressed neuronal activity and concurrent arteriolar vasoconstriction may explain negative blood oxygenation level-dependent signal. *J. Neurosci.* 27, 4452–4459.

Gunaydin, L. A., Yizhar, O., Berndt, A., Sohal, V. S., Deisseroth, K., and Hegemann, P. (2010). Ultrafast optogenetic control. *Nat. Neurosci.* 13, 387–392.

Heinemann, L., Kleinschmidt, A., and Müller, N. G. (2009). Exploring BOLD changes during spatial attention in non-stimulated visual cortex. *PLoS One* 4, e5560. doi: 10.1371/journal.pone.0005560.

Henrie, J. A., and Shapley, R. (2005). LFP power spectra in V1 cortex: the graded effect of stimulus contrast. *J. Neurophysiol.* 94, 479–490.

Kagan, I., Gur, M., and Snodderly, D. M. (2008). Saccades and drifts differentially modulate neuronal activity in V1: effects of retinal image motion, position, and extraretinal influences. *J. Vis.* 8, 1–25.

Kleinschmidt, A., and Müller, N. G. (2010). The blind, the lame, and the poor signals of brain function–a comment on Sirotin and Das (2009). *Neuroimage* 50, 622–625.

Lee, J. H., Durand, R., Gradinaru, V., Zhang, F., Goshen, I., Kim, D. S., Fenno, L. E., Ramakrishnan, C., and Deisseroth, K. (2010). Global and local fMRI signals driven by neurons defined optogenetically by type and wiring. *Nature* 465, 788–792.

Leopold, D. A. (2010). Neuroscience: fMRI under the spotlight. *Nature* 465, 700–701.

Maier, A., Wilke, M., Aura, C., Zhu, C., Ye, F. Q., and Leopold, D. A. (2008). Divergence of fMRI and neural signals in V1 during perceptual suppression in the awake monkey. *Nat. Neurosci.* 11, 1193–1200.

Nir, Y., Fisch, L., Mukamel, R., Gelbard-Sagiv, H., Arieli, A., Fried, I., and Malach, R. (2007). Coupling betwee -neuronal firing rate, gamma LFP, and BOLD fMRI is related to interneuronal correlations. *Curr. Biol.* 17, 1275–1285.

Phillipson, O. T., Kilpatrick, I. C., and Jones, M. W. (1987). Dopaminergic innervation of the primary visual cortex in the rat, and some correlations with human cortex. *Brain Res. Bull.* 18, 621–633.

Schultz, W. (2007). Multiple dopamine functions at different time courses. *Annu. Rev. Neurosci.* 30, 259–288.

Schummers, J., Yu, H., and Sur, M. (2008). Tuned responses of astrocytes and their influence on hemodynamic signals in the visual cortex. *Science* 320, 1638–1643.

Siegel, M., and König, P. (2003). A functional gamma-band defined by stimulus-dependent synchronization in area 18 of awake behaving cats. *J. Neurosci.* 23, 4251–4260.

Sirotin, Y. B., and Das, A. (2009). Anticipatory haemodynamic signals in sensory cortex not predicted by local neuronal activity. *Nature* 457, 475–479.

Slovin, H., Arieli, A., Hildesheim, R., and Grinvald, A. (2002). Long-term voltage-sensitive dye imaging reveals cortical dynamics in behaving monkeys. *J. Neurophysiol.* 88, 3421–3438.

Tan, C. O. (2009). Anticipatory changes in regional cerebral hemodynamics: a new role for dopamine? *J. Neurophysiol.* 101, 2738–2740.

Vanzetta, I., Flynn, C., Ivanov, A. I., Bernard, C., and Bénar, C. G. (2010). Investigation of linear coupling between single-event blood flow responses and interictal discharges in a model of experimental epilepsy. *J. Neurophysiol.* 103, 3139–3152.

Vanzetta, I., Slovin, H., Omer, D. B., and Grinvald, A. (2004). Columnar resolution of blood volume and oximetry functional maps in the behaving monkey; implications for fMRI. *Neuron* 42, 843–854.

Received: 01 July 2010; accepted: 16 July 2010; published online: 05 August 2010.

Citation: Vanzetta I and Slovin H (2010) A BOLD assumption. Front. Neuroenerg. ***2****:24. doi: 10.3389/fnene.2010.00024*

frontiers in
NEUROENERGETICS

ORIGINAL RESEARCH ARTICLE
published: 03 June 2010
doi: 10.3389/fnene.2010.00006

Spatial relationship between flavoprotein fluorescence and the hemodynamic response in the primary visual cortex of alert macaque monkeys

Yevgeniy B. Sirotin* and Aniruddha Das

Department of Neuroscience, Columbia University, New York, NY, USA

Edited by:
Anna Devor,
University of California San Diego, USA

Reviewed by:
Anna W. Roe,
Vanderbilt University, USA
Timothy J. Ebner,
University of Minnesota, USA

****Correspondence:***
Yevgeniy Sirotin,
Department of Neuroscience,
Columbia University, 1051 Riverside
Drive, New York, NY, 10027, USA.
e-mail: ybs2101@columbia.edu

Flavoprotein fluorescence imaging (FFI) is a novel intrinsic optical signal that is steadily gaining ground as a valuable imaging tool in neuroscience research due to its closer relationship with local metabolism relative to the more commonly used hemodynamic signals. We have developed a technique for FFI imaging in the primary visual cortex (V1) of alert monkeys. Due to the nature of neurovascular coupling, hemodynamic signals are known to spread beyond the locus of metabolic activity. To determine whether FFI signals could provide a more focal measure of cortical activity in alert animals, we compared FFI and hemodynamic point spreads (i.e. responses to a minimal visual stimulus) and functional mapping signals over V1 in macaques performing simple fixation tasks. FFI responses were biphasic, with an early and focal fluorescence increase followed by a delayed and spatially broader fluorescence decrease. As expected, the early fluorescence increase, indicating increased local oxidative metabolism, was somewhat narrower than the simultaneously observed hemodynamic response. However, the later FFI decrease was broader than the hemodynamic response and started prior to the cessation of visual stimulation suggesting different mechanisms underlying the two phases of the fluorescence signal. FFI mapping signals were free of vascular artifacts and comparable in amplitude to hemodynamic mapping signals. These results indicate that the FFI response may be a more local and direct indicator of cortical metabolism than the hemodynamic response in alert animals.

Keywords: flavoprotein, visual cortex, monkeys, imaging, fluorescence, hemodynamics

INTRODUCTION

Flavoprotein fluorescence imaging (FFI) is a new method for visualizing cortical activity based on imaging changes in the redox state of mitochondrial flavoproteins, primarily flavin adenine dinucleotide (FAD). It utilizes the fact that the oxidized form of this enzyme, FAD+, is more fluorescent than the reduced form, FADH2 (Chance et al., 1979). In the brain, increases in neuronal activity and the associated local increase in oxidative metabolism are marked by increased FAD fluorescence (Shibuki et al., 2003; Reinert et al., 2004; Husson et al., 2007). Thus this fluorescence signal shows promise as a non-invasive, intrinsic measure of local neuronal activity, free of the complications associated with extrinsic activity markers such as voltage sensitive dyes or calcium indicators. Since the FFI signal derives from local mitochondria, it is likely to give a truer measure of local neural activity than available from the commonly used hemodynamics-based intrinsic-signal brain imaging, which are strongly influenced by non-local inputs (Hamel, 2006; Iadecola and Nedergaard, 2007; Bartels et al., 2008; Sirotin and Das, 2009). Because of their potentially tight link with local neural activity, understanding FFI signals is of tremendous importance for the imaging community. Due to the relative newness of this technique, however, there have been very few studies directly comparing FFI with more conventional hemodynamics-based imaging (Frostig et al., 1990; Vanzetta and Grinvald, 2008; Sirotin et al., 2009).

Several important issues must be addressed in considering FFI as an alternative tool to hemodynamics-based techniques. First, though studies have successfully used FFI imaging signals in anesthetized animals, there have been few comparisons made between the spatiotemporal properties of FFI and hemodynamics-based signals. One study in the primary visual cortex (V1) of cats has compared orientation maps generated with FFI to those generated using standard hemodynamics techniques (Husson et al., 2007). They found that FFI signals appeared to produce better maps of orientation with fewer vascular artifacts. However, the clarity of such maps depends on the difference signal between activation patterns to two orthogonal gratings and does not reflect directly the spatial properties of the overall fluorescence response. Recently, we showed that imaging the V1 point spread to a minimal visual stimulus provides valuable and direct spatiotemporal information about the imaging signal; we used this method to successfully compare stimulus-evoked hemoglobin concentration and oxygenation signals in V1 (Sirotin et al., 2009). A similar analysis comparing the hemodynamic response with FFI signals would determine whether FFI signals have a relative advantage over hemodynamics-based imaging techniques.

Next, much of what we know about the properties of FFI signals comes from only the first phase of the fluorescence response. However, *in vitro* work has shown that FFI signals have a complex timecourse with an early oxidation phase (fluorescence increase) followed by a

prolonged reduction phase (fluorescence decrease) (Duchen, 1992; Kosterin et al., 2005). The two phases of the fluorescence signal are thought to be due to distinct cellular processes and are possibly not even localized within the same cells (Kasischke et al., 2004). Thus, interpretation of *in vivo* FFI signals would benefit from a firm understanding of the interaction between these two phases and how they shape the observed FFI response. However, imaging the full FFI signal *in vivo* has been difficult because of distortions by the hemodynamic response. Both the excitation wavelength (blue) and emission (green) for FAD fluorescence are strongly absorbed by hemoglobin. Thus any changes in the local tissue concentrations of hemoglobin – in particular, the large stimulus-evoked hemodynamic response in the same tissue – severely contaminate the FFI signal, sharply reducing and even reversing its amplitude and adding large vascular artifacts (Shibuki et al., 2003; Weber et al., 2004; Kitaura et al., 2007). Classical studies measuring *in vivo* cortical fluorescence have corrected for simultaneous changes in tissue absorption at the same wavelengths by measuring light reflected off the tissue (Rosenthal and Jobsis, 1971; O'Connor et al., 1972; Harbig et al., 1976; Kramer and Pearlstein, 1979). However, no such correction has yet been implemented for the imaging signals and thus their interpretation remains problematic.

The final issue in assessing the utility of FFI signals is that they have not yet been well characterized in the cerebral cortex of alert animals. Characterizing and understanding FFI signals in alert animals is crucial because many aspects of brain function, including the neural basis of behavior, can only be studied in alert animals. Developing this technique in the alert animal is thus a critical step towards proposing a broader use of FFI as a neuroimaging tool (e.g. Chen et al., 2009). However, FFI imaging in alert animals could involve its own unique problems, which could require approaches different from those used in the anesthetized preparation. The stimulus-evoked hemodynamic response is significantly larger in alert animals and may reach larger values faster, contaminating even early fluorescence signals (Shtoyerman et al., 2000; Berwick et al., 2002; Martin et al., 2002). In addition, we have recently demonstrated the existence of dramatic, stimulus-independent, task-linked fluctuations in cortical hemodynamic signals in V1 of alert monkeys performing simple fixation tasks (Sirotin and Das, 2009). These task-linked fluctuations can strongly modify or even dominate the reflectance signals used for conventional hemodynamics-based intrinsic optical imaging. The strong absorption of the FFI signal by hemoglobin makes it unclear whether FFI signals could be detected in alert animals amongst the large ongoing hemodynamic signals which may similarly contaminate any changes in fluorescence. This issue is especially important for mapping of cortical columns as these signals are significantly smaller than the full imaging signal (Frostig et al., 1990; Bonhoeffer and Grinvald, 1996; Vanzetta et al., 2004).

We have developed a dual-wavelength imaging technique that corrects the FFI signal for simultaneous brain hemodynamics, using a modification of the technique that we used earlier to image local cerebral blood volume concurrently with oxygenation in the alert macaque monkey V1 (Sirotin et al., 2009). We image the cortical surface at two wavelengths in rapid alternation synchronized with the frame rate of our camera. Here, one wavelength is an excitation wavelength for FAD, while the other is an isosbestic wavelength for hemoglobin, absorbed equally by oxy- and deoxyhemoglobin and thus measuring changes in total hemoglobin concentration in tissue, that is, local blood volume[1]. This latter 'blood volume' wavelength was selected to lie within the emission range for FAD fluorescence, and is also in the wavelength range used for monitoring FAD fluorescence; the 'blood volume' signal thus obtained is used to correct the FAD fluorescence signal for distortion by the brain hemodynamic response, revealing the true timecourse of FAD fluorescence. Using this technique, which is similar to the techniques previously employed in measurements of bulk cortical fluorescence (Rosenthal and Jobsis, 1971; O'Connor et al., 1972; Harbig et al., 1976; Kramer and Pearlstein, 1979), we found that significant FFI signals could be detected reliably in the alert macaque cortex. This enabled us to study both the early and late phases of the FFI response and compare their spatiotemporal properties with the simultaneously measured changes in cortical reflectance that we have previously characterized under similar conditions (Sirotin et al., 2009).

MATERIALS AND METHODS

All experimental procedures were performed in accordance with the NIH Guide for the Care and Use of Laboratory Animals and were approved by the Institutional Animal Care and Use Committees (IACUC) of Columbia University and the New York State Psychiatric Institute.

BEHAVIORAL TASK

We trained two macaque monkeys ('T' and 'Y') on a periodic fixation task similar to that used in recent publications from our lab (Sirotin and Das, 2009; Sirotin et al., 2009). The animal was required to maintain passive binocular fixation during 'fixation on' (cued by fixation point color) for juice reward (Fixation window: 0.5° radius, 20" Sony Trinitron monitor, 100 Hz refresh, distance: 133 cm; fix duration: 4 s). We tracked the monkeys' eye position using an infra-red eye tracker and custom software (Matsuda et al., 2000) and aborted trials with premature eye movement. Stimuli were presented for 1 or 2 s during the fixation period. We set the inter-trial interval to 20 s to ensure that the long-lived stimulus-evoked hemodynamic signal decayed to baseline, and to minimize any bleaching of the flavoprotein fluorescence. The experiment continued until the monkey received enough juice and stopped working.

VISUAL STIMULI

Stimuli for measuring point spreads were short bars of light (measuring 0.25×0.04 degrees of visual angle) generated as bitmaps in MATLAB (Mathworks, Natick, MA, USA) flashed on for 2 s on a dark background at maximum contrast using the VSG2/5 graphics card (Cambridge Research Systems, UK). To measure and correct for stimulus-independent trial-related imaging signals (Sirotin and Das, 2009), some of the trials carried no stimulus, but were otherwise identical in their timing ('blank trials'). For orientation mapping, we presented full-field drifting gratings at a spatial frequency of two cycles per degree and maximal contrast. Grating stimuli were presented for 1 s. The orientation of the gratings was randomly selected on each trial from the set: 0, 45, 90, and 135°.

[1]Our measure of blood volume is largely equivalent to cerebral blood volume (CBV) as measured in fMRI for fixed hematocrit. Because CBV in MR studies often measures plasma volume (e.g. via a contrast agent) the two differ if the hematocrit changes.

IMAGING CHAMBERS

Surgery, recording chambers, artificial dura: After the monkeys were trained on visual fixation tasks, craniotomies were performed over the animals' V1 and glass-windowed stainless steel recording chambers were implanted, under surgical anesthesia, using standard sterile procedures. The exposed dura was resected and replaced with a soft, clear silicone artificial dura. After the animals had recovered from the surgery, cortical activity from their V1 was optically imaged, routinely, while the animals engaged in relevant behavioral tasks. Recording chambers and artificial dura were fabricated in our lab using published methods (Shtoyerman et al., 2000).

IMAGING: OPTICS

Images were acquired using a CCD camera (Dalsa 1M30, resolution 256 × 256 pixels, 15 frames/s) through an Optical PCI Bus Digital Frame Grabber (Coreco Imaging, Boston, MA, USA). Imaging software was developed in our lab based on a system by V. Kalatsky (Kalatsky and Stryker, 2003). The camera was coupled to a back-to-back lens combination macroscope (two 55 mm Nikon lenses; 1:1 magnification, numerical aperture = 0.4) and focused on the cortical surface.

IMAGING: ILLUMINATION WAVELENGTHS

The fluorescence of FAD was imaged simultaneously with changes in total tissue hemoglobin concentration ('cerebral blood volume': Sirotin et al., 2009) using a modification of the custom made dual-wavelength system previously used by us to simultaneously image cortical blood volume and oxygenation (Sirotin and Das, 2009; Sirotin et al., 2009). On alternate frames of the camera, the cortex was illuminated by either an excitation wavelength for FAD (blue) or an isosbestic wavelength for hemoglobin (green: absorbed equally by oxy- and deoxyhemoglobin). This gave the effective sampling rate of 7.5 Hz. Our fluorescence filter configuration is similar to the configuration previously used for imaging V1 of anesthetized cats (Husson et al., 2007). The light was provided by appropriate high power LEDs (LEDENGIN, 776 mW) passed through a 415–485 nm interference filter for blue (Chroma D455_70X) or 523–533 nm for green (Omega Optics 528BP10). Light was collected off the cortical surface after passing through a long-pass interference filter (Chroma HQ520LP; cutoff = 520 nm). Thus, using a single filter, we simultaneously measured changes in cortical reflectance using green light and any emitted fluorescence from the blue light. The fluorescence excitation/emission filter pair was selected to have minimal cross-talk with an OD = 6 (i.e. a 10^{-6} attenuation). The entire imaging assembly was covered by light proof baffles that blocked any stray illumination. To avoid photobleaching we turned off the blue LED for the duration of the inter-trial-interval. The LED was turned on one second prior to stimulus onset and kept on for 6 s to measure the evoked response.

OVERALL SIGNAL PROCESSING

The following steps were carried out separately for the blood volume and the FAD fluorescence signals: All images were first 'shift-corrected' to correct for any residual movement of the cortical surface that remained despite the specially designed camera mount, animal head post and overall structural framework (NOTE: most of the residual movements were due to the brain moving relative to the animal's head, when the animal shifted body position, etc.). This 'shift-correction' consisted of aligning each image frame to the first frame of a given experimental session, using the imaged blood vessels as references. Each image frame was cross-correlated with the reference frame, and a gradient descent method used to maximize this correlation value as a function of lateral shifts in the image position, frame by frame. After shift correction, we computed stimulus-triggered average movies of the cortical response for both stimulus-driven and blank trials. To correct for any trial-related signals unrelated to visual stimulation, we divided the stimulus-driven responses by the responses observed on 'blank' trials (Sirotin et al., 2009) and subtracted the average pre-stimulus image (1–5 frames pre-stimulus). These shift-corrected and blank-corrected signals were then used in all subsequent analyses.

To correct the FAD fluorescence signals for distortions due to the stimulus-evoked blood volume changes we divided the observed fractional changes in fluorescence by the simultaneously measured blood volume signal scaled by an appropriate correction factor. The details of our correction method are described in detail in an upcoming paper from our lab. This corrected fluorescence signal was then compared with the imaged blood volume signal.

MEASURING TIMECOURSES

To measure the timecourse of the fluorescence and reflectance point spread signals, we drew regions of interest around the peak of the activation and subtracted any signals well outside the activated area. This served to attenuate or remove common signal fluctuations arising due to pulse and breathing. For measuring the mapping signal [i.e. the signal fraction that is tuned to a given functional property, e.g. orientation (Frostig et al., 1990)], we computed ROIs around orthogonal orientation domains. Fluorescence maps averaged between 1 and 2 s after grating onset were mean subtracted and normalized by their standard deviation. A pair of complementary ROIs marking orthogonal orientation columns was selected as all domains falling one standard deviation below zero and those domains falling one standard deviation above zero. We used the same ROIs, identified from the FFI signal images, to measure the mapping signal for both the fluorescence and reflectance signals.

RESULTS

SIMULTANEOUS IMAGING OF FLAVOPROTEIN FLUORESCENCE AND HEMODYNAMICS

By using FFI we visualized stimulus-evoked cortical responses in V1 of alert behaving macaque monkeys (two animals, 'T' and 'Y'). We then compared these FFI images with more conventional intrinsic-signal images of the same cortical responses as measured concurrently using the blood volume signal, that is, the cortical reflectance signal at a standard blood volume wavelength (see 'Methods'). Specifically, we compared the spatiotemporal properties of cortical point spread responses to a minimal visual stimulus, a 0.25° bar flashed briefly while the animal held its gaze steady in a periodic fixation task (Sirotin et al., 2009). The reflectance signals were used, moreover, to correct the FFI image for any distortions due to changes in local blood volume.

We found that fluorescence signals were highly reproducible across trials and were readily observed on a trial-by-trial basis in our awake animals. **Figure 1** shows the typical pattern of imaged fluorescence and blood volume responses.

SPATIOTEMPORAL PROPERTIES OF BLOOD VOLUME SIGNALS

The V1 point spread images obtained with the blood volume signal (**Figures 1A,B**) closely matched the images we had published earlier using the same method (Sirotin et al., 2009). The signal was monophasic with a latency of ~600 ms, rising to a peak in about 3.5 s, and then decaying back to baseline by 15 s. Even though the signal amplitude varied by more than an order of magnitude over its timecourse, the signal profile changed relatively little during this time. To quantify the spatial spread of the signals, we fitted the profiles measured on each trial with Gaussian functions of the form: $y = ae^{-R^2/\sigma^2} + b$, where R is the radial distance from the response center (see **Figure 3A**). The fitted σ values were on average 2.3 mm during the initial 1.6 s and 1.95 mm at 3–4 s post-stimulus onset. The difference between these values was not significant in any of the experiments in either animal. Thus, the blood volume signal remained largely invariant throughout its full duration.

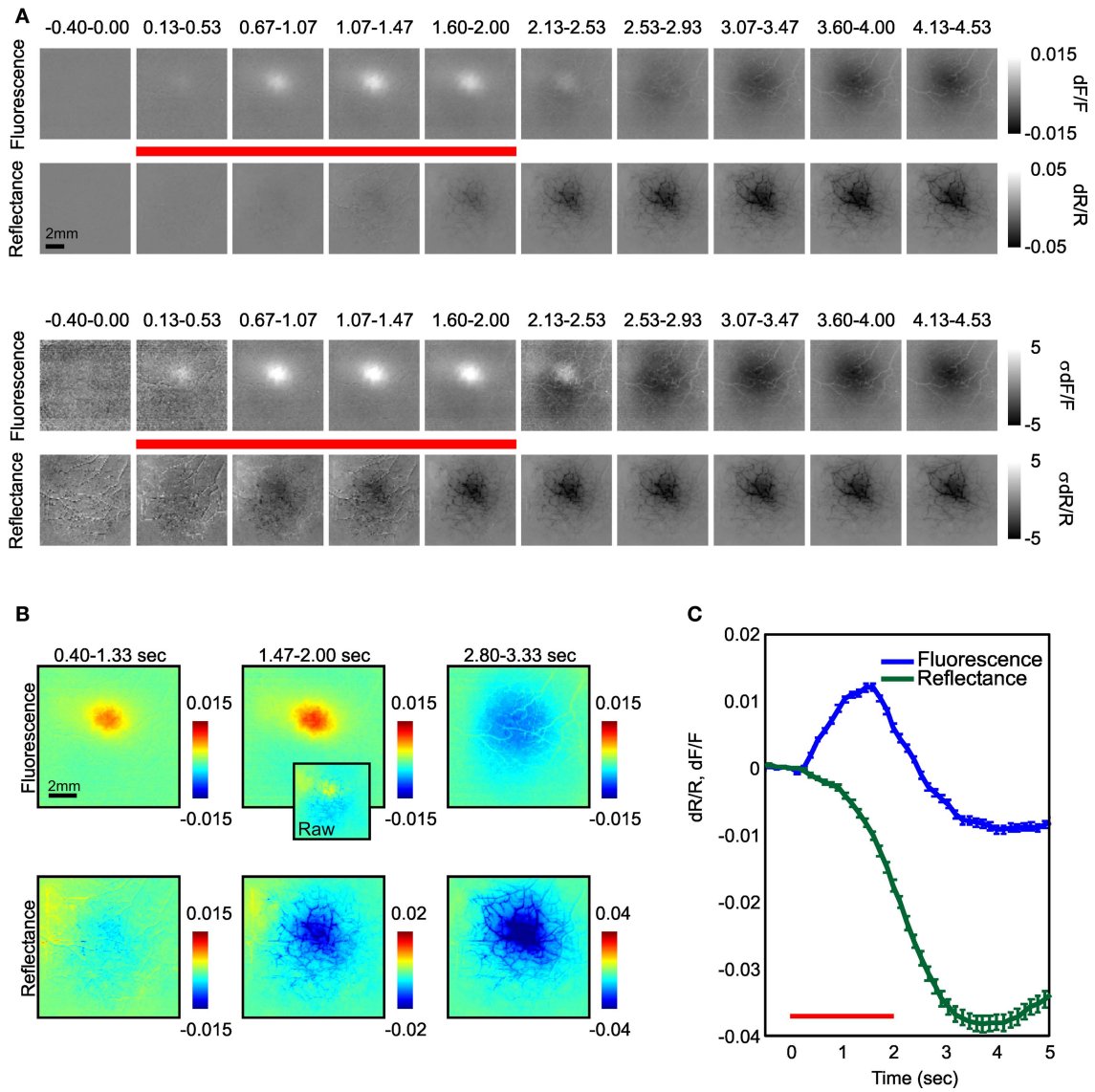

FIGURE 1 | Timecourse of fluorescence and reflectance ('blood volume') changes following visual stimulation. (A) Top: Fluorescence and reflectance changes over V1 following presentation of a 0.25° bar with a fixed scale (see scale bar on right). Bottom: Same as top, but scaled by the standard deviation of the images to compare signal shapes. **(B)** Early, middle, and late fluorescence and reflectance images enlarged to show detail. Inset in middle column shows uncorrected fluorescence signals at this timepoint. Note the presence of significant vascular artifacts in uncorrected image. **(C)** The computed timecourse of fluorescence (blue) and reflectance (green) signals measured about the center of the response in **(A)**. Red bar denotes stimulus presentation period. Note rapid onset of positive fluorescence signals followed by reversal starting prior to stimulus offset. Error bars are standard error of the mean (SEM). Note: All fluorescence signals shown in this paper have been corrected for absorption by hemoglobin. Figure depicts an average of 40 trials.

SPATIOTEMPORAL PROPERTIES OF FLUORESCENCE SIGNALS

The FFI signals were very different in their timecourse than the blood volume signal. These signals were biphasic with an early positive phase consisting of an increase in fluorescence and a delayed negative phase with decreased fluorescence (**Figure 1C**). Neither phase showed any apparent vascular artifacts (**Figure 1B**). As expected, fluorescence increases were faster than the simultaneously measured change in the blood volume signal (we defined the signal latency as the first significant inflection in the slope of the signal, post-stimulus onset (Sirotin et al., 2009); fluorescence: 267–400 ms; reflectance: 533–667 ms, **Figure 2**). However, fluorescence did not continue to increase throughout the stimulation period. Despite continued stimulation, fluorescence began decreasing ~1.5 s after stimulus onset and then reversed polarity (**Figure 1**). We noticed that the early and late phase fluorescence changes appeared to have distinct spatial properties. We therefore examined separately the early positive and late negative fluorescence point spreads and compared them to the simultaneously measured changes in reflectance.

EARLY POSITIVE FLUORESCENCE PHASE

We first examined the spatial spread of the early fluorescence and reflectance signals averaged between 0.67 and 1.60 s after stimulus onset. **Figure 3B** shows the average spatial profile of the responses measured as a function of distance from the response center for monkey 'T'. Consistent with prior work using anesthetized rodents (Weber et al., 2004), we found that the early fluorescence increases were spatially narrower than the simultaneously measured changes in reflectance suggesting that fluorescence increases may be tighter markers of neural activation than hemodynamics (Monkey 'T': fluorescence $\sigma = 1.42$ (0.07), reflectance $\sigma = 2.20$ (0.15), $p < 0.05$; Monkey 'Y': fluorescence $\sigma = 1.90$ (0.17), reflectance $\sigma = 2.37$ (0.30), n.s. $p = 0.37$; **Figure 4**).

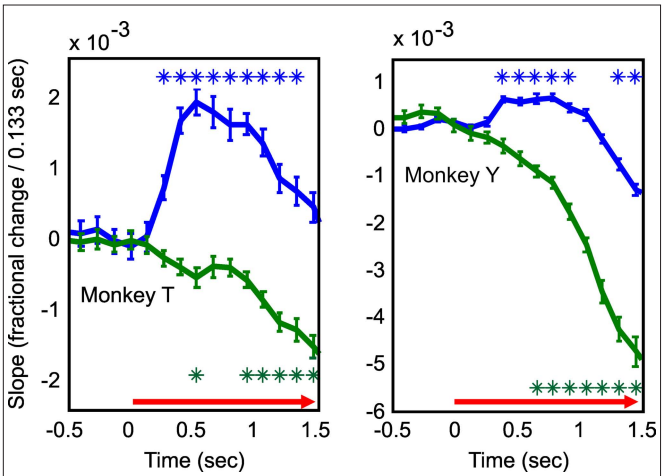

FIGURE 2 | Fluorescence signals begin faster than simultaneously measured changes in reflectance. The slopes of fluorescence (blue) and reflectance (green) signals following stimulus onset. These slopes were calculated by taking trial-by-trial time derivatives of the d*F*/*F* and d*R*/*R* signals (**Figure 1B**) and averaging them for the two animals separately. Asterisks denote significant changes in slope relative to baseline ($p < 0.05$; rank sum test corrected for multiple comparisons). Left and right show results for Monkey T and Monkey Y respectively. Note fluorescence signals reach significance earlier in both animals. Error bars are SEM. Figure depicts an average of 40 trials for monkey 'T' and 16 trials for monkey 'Y'.

LATE NEGATIVE FLUORESCENCE PHASE

We next examined the spatial spread of the late negative phase of the fluorescence signals (3.33–4.00 s) and compared them to the simultaneously measured changes in reflectance (**Figure 3C**). These late fluorescence decreases were significantly wider in spatial spread compared with early positive fluorescence changes (Monkey 'T': $\sigma = 2.92$ (0.12); Monkey 'Y': $\sigma = 2.62$ (0.13); **Figure 4**). Indeed, these late fluorescence signals were also significantly wider than the simultaneously measured changes in blood volume (Monkey 'T': $\sigma = 2.09$ (0.05); Monkey 'Y': $\sigma = 1.81$ (0.05); **Figure 4**). We observed this dramatic difference (40–100%) between the early and late fluorescence signals even though we saw no significant changes in the spatial spread of the blood volume signal between these two timepoints in either monkey (Fig 4).

FFI MAPPING SIGNALS IN ALERT ANIMALS

To determine whether FFI signals are useful for mapping in alert animals we performed orientation mapping in one animal with strong fluorescence responses (**Figure 5**; Monkey T). **Figure 5A** shows the timecourse of FFI and volumetric mapping signals obtained by comparing responses to two orthogonal gratings. FFI orientation maps peaked by about 1 s after stimulus onset and then progressively weakened. By comparison, volumetric maps developed more slowly, reaching a steady level by 2 s after stimulus onset. We found that the spatial location of columns identified by FFI and volumetric signals were comparable (**Figure 5B**), however, volumetric signals were more susceptible to vascular artifacts. To examine the temporal development of the maps, we quantified the mapping signal as the difference in activity between orthogonal orientation domains (**Figure 5C**). Both FFI and volumetric signals appeared to initiate immediately after stimulus onset, however, fluorescence increased at a much faster rate. Consistent with the timecourse of the overall FFI signal, the FFI mapping signal began to decay prior to the end of visual stimulation. However, despite a large undershoot in the overall signal, the FFI mapping signal did not reverse into a negative phase, but remained elevated at a modest level for the full measured duration of the response, even after the end of visual stimulation (**Figures 5C,D**).

DISCUSSION

The ultimate goal of functional brain imaging should be not only to localize neural signals, but to provide a quantitative measure of the neural activity involved. From this standpoint, FFI imaging provides an exciting candidate signal and offers a number of advantages over the commonly used imaging signals based on cerebral hemodynamics. The hemodynamic signal is known to be influenced strongly by neuromodulatory inputs, for example, from subcortical nuclei such as locus coeruleus or the basal forebrain (reviewed by Hamel, 2006). Thus, hemodynamics-based imaging signals likely consist of a complex combination of components, with some that are driven by local neural activity and others reflecting distal neuromodulatory control. For example, we showed recently that the V1 hemodynamic signal recorded in

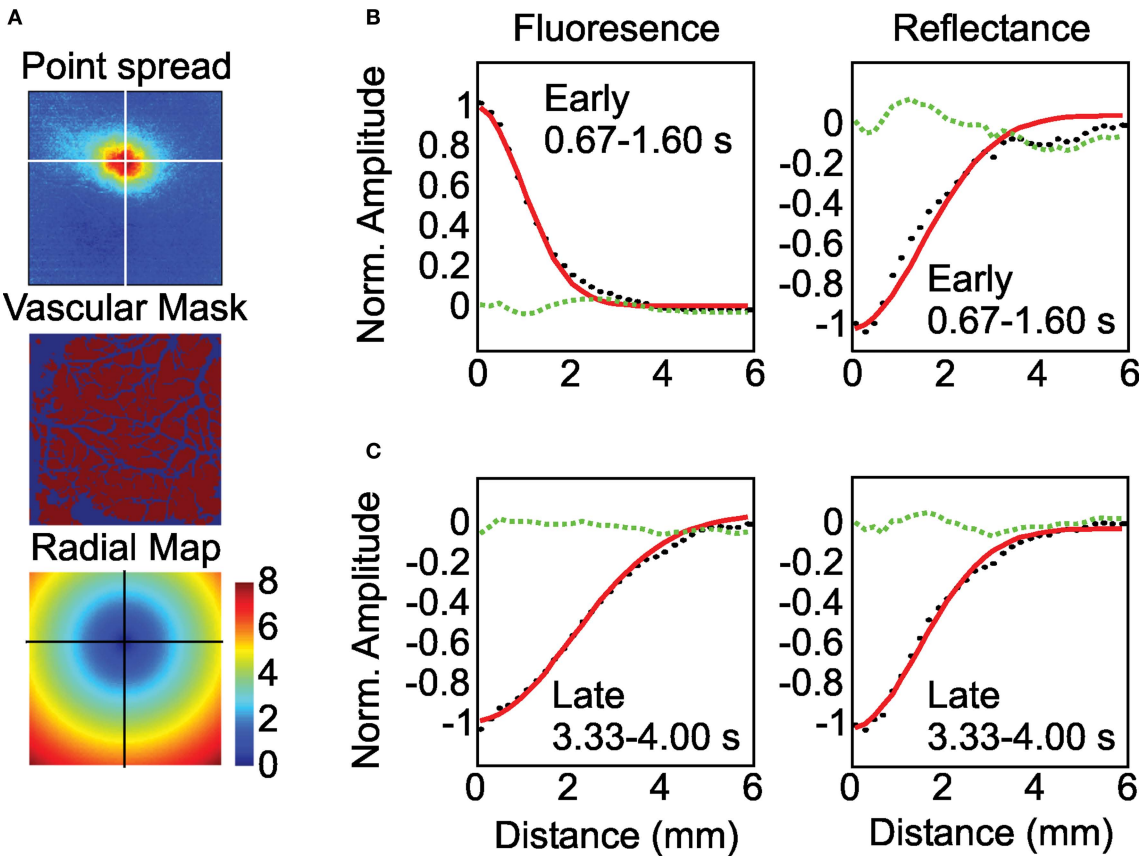

FIGURE 3 | Early and late fluorescence signals have distinct point spreads. **(A)** Schematic of radial profile analysis. From top to bottom: activation center determined from the early fluorescence image; binary mask used to exclude fluorescence and reflectance changes near around large blood vessels; radial map of distance away from response center. Crosshairs mark the response center. Pixels with at the same distance were averaged together to create the radial profiles in **(B)** and **(C)**. **(B)** Computed radial profiles during the early portion of the response (black dots) and the best fitting Gaussian function (red). Dotted green line is the residual of the fit. Note somewhat wider spread of reflectance relative to fluorescence signals. **(C)** Same as **(B)**, but for late fluorescence and reflectance. Note broader late fluorescence signals relative to reflectance. Figure depicts an average of 40 trials.

alert monkeys performing a periodic visual task had a prominent component at trial period that was not predictable by concurrently recorded neural activity and was evident even in the absence of visual stimulation. By contrast, FFI signals are entirely local in origin and can be linked to specific cellular processes (Chance et al., 1979; Duchen, 1992; Shibuki et al., 2003; Reinert et al., 2004; Kosterin et al., 2005). Thus the FFI signal likely offers a reliable quantitative measure of local metabolic changes and hence local neural activity.

An additional advantage of FFI is that these signals are largely free of vascular artifacts (compare the fluorescence and reflectance signals in **Figure 1**). This is because the FFI signal depends on a chromophore (FAD/FADH2) that is local to neural tissue (bound to mitochondrial membranes) as opposed to the one (hemoglobin) contained in passing blood vessels. Even though hemodynamics-based signals are large and clearly indicate the overall locus of neural activity, they are strongly biased toward large pial vessels. It is noteworthy that the space constants observed in the early fluorescence and reflectance images are comparable (**Figure 4**); this is because both signals likely reflect the net point spread of neural activity across cortex (as imaged using voltage sensitive dyes; Grinvald et al., 1994; Chen et al., 2006). However, the vascular patterns observed in hemodynamics-based signals obscure the actual spatial profile of neural activity over cortex. Even though early hemodynamic signals are also free of large vascular patterns (Sheth et al., 2004; Sirotin et al., 2009), at such early timepoints they are typically of smaller amplitude than the peak FFI signals which remain free of vascular artifacts throughout their timecourse. Further, as previously demonstrated in anesthetized cats (Husson et al., 2007), FFI may also be more useful for mapping. We found that, despite a smaller global signal, the FFI mapping signal appears comparable to that observed using hemodynamics. Thus, a larger fraction of the FFI signal is tuned for the functional properties of the underlying neural activity. Taken together, these observations suggest that FFI is likely a better indicator of the exact spatial profile of neural activity than hemodynamics-based measures.

Despite these advantages, measuring fluorescence signals is more technically challenging than the more commonly used reflectance signals and it was unclear whether FFI signals would be reliably measurable in alert animals. Thus, for FFI signals to be useful for neuroimaging, the relative benefits of using these signals

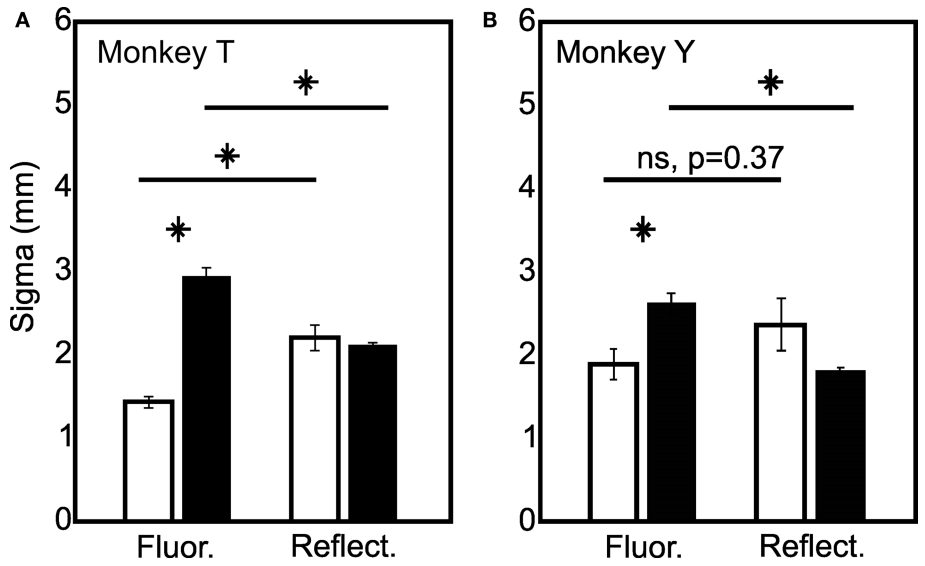

FIGURE 4 | Quantification of the spatial spread of fluorescence and reflectance signals. Early (0.67–1.60 s, white bars) and late (3.33–4.00 s, black bars) response widths are plotted for fluorescence and reflectance signals. Asterisks denote significant differences between point spreads (rank sum test corrected for multiple comparisons). **(A)** and **(B)** show results from monkey T and monkey Y respectively. Error bars are SEM. Note no difference between reflectance point spreads early and late despite clear increases in the fluorescence point spread from early to late. $N = 40$ for monkey 'T' and $N = 16$ for monkey 'Y'.

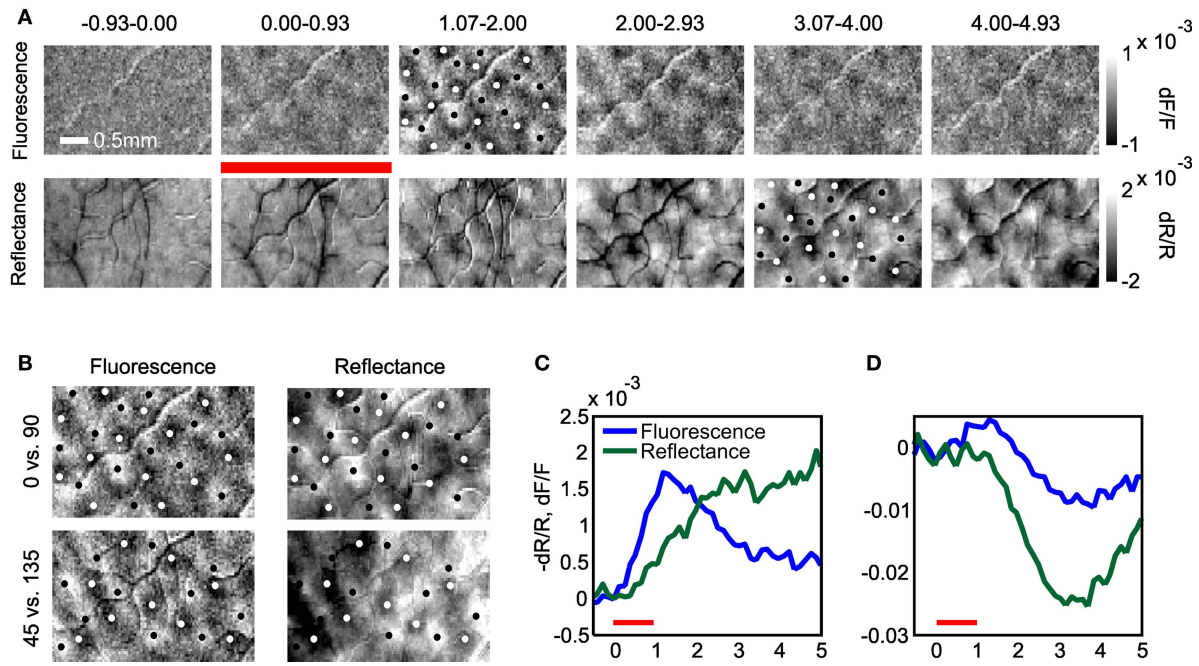

FIGURE 5 | Fluorescence-based functional maps in alert monkeys peak earlier and have fewer vascular artifacts. (A) Development of the fluorescence and reflectance maps during response. Images show the difference in response to full-field drifting gratings of orthogonal orientations (0 vs. 90°). Red bar denotes stimulus presentation period. White and black column marker points show approximate centers of orientation domains. Note opposite sign of fluorescence and reflectance signals. Column markers on fluorescence and reflectance images are the same, but inverted in color for visibility. **(B)** Orientation maps obtained with fluorescence and reflectance signals show the same pattern of columnar activity for maps obtained with cardinal or oblique orientations. Note that the reflectance signals have been inverted for ease of comparison with the fluorescence signals. **(C)** The timecourse of fluorescence (blue) and reflectance (green) mapping signals measured as the difference in activity between orthogonal columns. Note earlier peak and similar amplitudes of fluorescence and reflectance mapping signals. The reflectance signal is flipped in sign for easier comparison with the fluorescence signal. **(D)** The timecourse of the global fluorescence and reflectance signals evoked by grating stimulation for comparison with **(C)**. Note reversal of the net fluorescence signal is absent from the mapping signal in **(C)**. Figure depicts average of 19 trials for each orientation.

over hemodynamics-based signals must outweigh the additional experimental complexity. This requires a detailed understanding of the spatiotemporal properties of cortical FFI signals from alert animals.

FEASIBILITY OF FFI IMAGING IN ALERT ANIMALS

Here we have demonstrated that FFI point spreads and mapping signals can be routinely obtained from the primary visual cortex of monkeys performing simple visual tasks. Prior work showed that early FFI signals measured in cortex of anesthetized preparations appeared to be free of artifacts due to changes in cortical reflectance (Shibuki et al., 2003; Weber et al., 2004). However, these signals were quickly contaminated by the stimulus-evoked hemodynamic response. Because the hemodynamic response starts with latencies as short as 600 ms (Weber et al., 2004; Sirotin et al., 2009), it begins to contaminate the fluorescence signal even within the first second of the response. Additionally, we have previously found that reflectance signals in V1 of alert primates are modulated significantly by large trial-related hemodynamic signals unrelated to visual stimulation (Sirotin and Das, 2009). Such trial-related hemodynamic activity in alert animals contaminates all portions of the fluorescence response. To remove this confound, we corrected the raw FFI signals for changes in reflectance. Though, classical investigations measuring fluorescence *in vivo* have corrected their signals for simultaneously measured changes in reflectance (Rosenthal and Jobsis, 1971; O'Connor et al., 1972; Harbig et al., 1976; Kramer and Pearlstein, 1979), no such correction was performed in any of the imaging studies to date. Our corrected FFI signals were free of vascular artifacts for the full duration of the imaged response (e.g. compare our **Figure 1** with Figure 5 in Shibuki et al., 2003) and we could therefore examine both the early and later phases of the FFI signal. We believe that such correction will be of general benefit for all future studies measuring cortical fluorescence responses.

THE BIPHASIC FLUORESCENCE SIGNAL

The *in vitro* FFI response to stimulation is typically biphasic, with an early increase (oxidation phase) followed by a prolonged decrease (reduction phase) (Duchen, 1992; Kosterin et al., 2005). The onset of the reduction phase may start prior to the cessation of stimulation and different mechanisms have been proposed for the two phases of this metabolic response. The oxidation phase is due to fast Ca^{2+} and ADP evoked increases in the rate of FADH2 utilization in the electron transport chain. The reduction phase is thought to be due to a somewhat more delayed increase in tricarboxylic acid (TCA) cycle activity that replenishes FADH2 at a faster rate than it can be utilized by the electron transport chain (Turner et al., 2007).

We found that cortical FFI signals corrected for simultaneous changes in reflectance were largely consistent with the *in vitro* results (Duchen, 1992; Kosterin et al., 2005) and with *in vivo* signals measured in the cerebellum (Reinert et al., 2004, 2007; Gao et al., 2006) which are largely uncontaminated by changes in reflectance. FFI signals were biphasic (**Figures 1C and 5D**), with a spatially narrow fluorescence increase, declining prior to the end of stimulation, and followed by a fluorescence decrease. Interestingly, we found that even as the net fluorescence signal reversed polarity, the functionally tuned FFI mapping signal remained positive (**Figures 5C,D**). Taken together, these results suggest that the cortical FFI signal, rather than being an index of absolute cortical metabolism, is a difference signal reflecting the overall balance between tuned increases in FADH2 utilization in the electron transport chain and its replenishing by a possibly untuned increase in TCA cycle activity (Turner et al., 2007). Still, it is possible that the early increase in FFI signal may still be a linear indicator of neural activity (Tohmi et al., 2006). To clarify this point, future studies must therefore carefully explore the relationship between neural activity and the full timecourse of the FFI signal.

RELATIONSHIP OF EARLY FLUORESCENCE SIGNALS WITH HEMODYNAMICS

In agreement with previous studies in cortex (Weber et al., 2004; Husson et al., 2007), we observed that early fluorescence increases are faster and somewhat narrower spatially than the simultaneously imaged reflectance changes. At our isosbestic imaging wavelength (528 nm), the reflectance signal is insensitive to blood oxygenation and, for small signal changes, is roughly proportional to changes in the concentration of hemoglobin (Kohl et al., 2000; Sheth et al., 2004; Prahl, 2008; Sirotin et al., 2009). We found that the spatial spread of FFI signals was 25–50% narrower that of the simultaneously measured hemodynamic response. This is comparable to the previously conducted comparison between laser speckle imaging signals and FFI in rodent barrel cortex (Weber et al., 2004). It is very likely that the difference between the FFI and hemodynamic signals at these early timepoints reflects a tighter coupling of the FFI signal with increases in cortical metabolism (driven primarily by local neural activity; Attwell and Laughlin, 2001; Attwell and Iadecola, 2002) than the coupling of the hemodynamic response to cortical metabolism. It is important to point out that, at these early timepoints (0.67–1.60 s), the hemodynamic signal is confined to small vessels (below our camera resolution of 36 μm; **Figure 1**) so the difference between the signals is unlikely to be due to vascular overspill into larger vessels (Sheth et al., 2004, 2005).

As previously observed in anesthetized cats, we found that functional maps obtained using FFI peaked earlier and were relatively unaffected by vascular artifacts as compared to volumetric signals (Husson et al., 2007). The overall pattern of orientation columns was not different between FFI and hemodynamic signals. Further, the amplitude of the mapping signal was comparable between FFI and volumetric signals. Indeed, the relatively large amplitude of these signals is significantly better than mapping signal amplitudes observed at commonly used red imaging wavelengths (i.e. >605 nm; Husson et al., 2007), which are typically only half as large as the volumetric mapping signal (Vanzetta et al., 2004). Thus, FFI signals appear to be particularly useful for mapping fine-scale cortical architecture in alert behaving animals.

THE WIDE POINT SPREAD OF THE LATE FLUORESCENCE SIGNALS

To our knowledge, no study to date has examined the spatial profile of the late cortical fluorescence signal *in vivo*. Surprisingly, we found that the spatial extent of late fluorescence decreases were significantly wider than both the early fluorescence increases and the simultaneously measured hemodynamic signals (**Figure 4**). In the cerebellum, Gao et al. (2006) have shown that lateral inhibition between adjacent cortical regions can lead to negative fluorescence signals *in vivo*. Unlike the cerebellum, visual cortex has both

excitatory and inhibitory lateral connections. Thus, it is possible that the exact spatiotemporal dynamics of FFI signals are shaped by the properties of lateral connectivity in cortex.

FUTURE DIRECTIONS IN DEVELOPING THE FFI SIGNAL AS AN IMAGING TOOL IN ALERT ANIMALS

Two issues must be addressed to further develop FFI as an imaging tool in alert animals. First, in order for FFI to be advantageous over the more easily measured hemodynamic signals, its spatiotemporal properties must be more readily interpretable in terms of neural activity. Future work must therefore investigate how the spatial spreads of the early and late FFI signals compare to the underlying spread of neural activity and whether FFI signals are indeed better measures of local neural activation than hemodynamics. Of special importance is whether FFI signals are temporally linear. The two phases of the FFI signal are likely driven by different underlying processes with different temporal properties (Duchen, 1992; Brennan et al., 2007). The FFI responses to extended stimulation may, therefore, not be linearly related to their responses to brief stimuli. Hence, a better understanding of the relationship between neural activity and the two phases of the fluorescence response would be fundamental for correctly interpreting FFI.

Second, though we were able to routinely image FFI signals, we did observe significant bleaching of fluorescence across our experimental session (Shibuki et al., 2003; Weber et al., 2004). We therefore minimized the cortical exposure to the excitation wavelength. Reflectance changes, on the other hand, can be measured continuously without any detrimental effects to the animal (Sirotin and Das, 2009). This technical limitation currently precludes the use FFI signals to investigate any slow fluctuations in cortical state which may have significant behavioral relevance (Aston-Jones and Cohen, 2005; Raichle and Snyder, 2007; Sirotin and Das, 2009). However, using more sensitive optics, together with lower intensities of excitation light and temporally sparse sampling may overcome this limitation in the future.

ACKNOWLEDGMENTS

We thank: M.E. Goldberg for supporting a dedicated machine shop. B. Thomas for manufacturing the LED driving circuits. J. Caban for machining the optical hardware. M. Bucklin, E. Glushenkova, S. Levine, and J. Ordinario for excellent technical assistance. Mariana Cardoso for helpful scientific discussions. The work was supported by National Institutes of Health (NIH) Grants R01 EY013759 and R01 EY019500 (to Aniruddha Das), and R24 EY015634 (to Dr. M.E. Goldberg), as well as the Columbia Research Initiatives in Science and Engineering, the Gatsby Initiative in Brain Circuitry, The Dana Foundation Program in Brain and Immuno Imaging and the Esther and Joseph Klingenstein Foundation, Fellowship in the Neurosciences (to Aniruddha Das).

REFERENCES

Aston-Jones, G., and Cohen, J. D. (2005). An integrative theory of locus coeruleus-norepinephrine function: adaptive gain and optimal performance. *Annu. Rev. Neurosci.* 28, 403–450.

Attwell, D., and Iadecola, C. (2002). The neural basis of functional brain imaging signals. *Trends Neurosci.* 25, 621–625.

Attwell, D., and Laughlin, S. B. (2001). An energy budget for signaling in the grey matter of the brain. *J. Cereb. Blood Flow Metab.* 21, 1133–1145.

Bartels, A., Logothetis, N. K., and Moutoussis, K. (2008). fMRI and its interpretations: an illustration on directional selectivity in area V5/MT. *Trends Neurosci.* 31, 444–453.

Berwick, J., Martin, C., Martindale, J., Jones, M., Johnston, D., Zheng, Y., Redgrave, P., and Mayhew, J. (2002). Hemodynamic response in the unanesthetized rat: intrinsic optical imaging and spectroscopy of the barrel cortex. *J. Cereb. Blood Flow Metab.* 22, 670–679.

Bonhoeffer, T., and Grinvald, A. (1996). "Optical imaging base on intrinsic signals: the methodology," in *Brain Mapping. The Methods,* eds A. W. Toga and J. C. Mazziota (San Diego: Academic Press), 55–87.

Brennan, A. M., Connor, J. A., and Shuttleworth, C. W. (2007). Modulation of the amplitude of NAD(P)H fluorescence transients after synaptic stimulation. *J. Neurosci. Res.* 85, 3233–3243.

Chance, B., Schoener, B., Oshino, R., Itshak, F., and Nakase, Y. (1979). Oxidation-reduction ratio studies of mitochondria in freeze-trapped samples. NADH and flavoprotein fluorescence signals. *J. Biol. Chem.* 254, 4764–4771.

Chen, G., Popa, L. S., Wang, X., Gao, W., Barnes, J., Hendrix, C. M., Hess, E. J., and Ebner, T. J. (2009). Low-frequency oscillations in the cerebellar cortex of the tottering mouse. *J. Neurophysiol.* 101, 234–245.

Chen, Y., Geisler, W. S., and Seidemann, E. (2006). Optimal decoding of correlated neural population responses in the primate visual cortex. *Nat. Neurosci.* 9, 1412–1420.

Duchen, M. R. (1992). Ca(2+)-dependent changes in the mitochondrial energetics in single dissociated mouse sensory neurons. *Biochem. J.* 283(Pt 1): 41–50.

Frostig, R. D., Lieke, E. E., Ts'o, D. Y., and Grinvald, A. (1990). Cortical functional architecture and local coupling between neuronal activity and the microcirculation revealed by in vivo high-resolution optical imaging of intrinsic signals. *Proc. Natl. Acad. Sci. USA* 87, 6082–6086.

Gao, W., Chen, G., Reinert, K. C., and Ebner, T. J. (2006). Cerebellar cortical molecular layer inhibition is organized in parasagittal zones. *J. Neurosci.* 26, 8377–8387.

Grinvald, A., Lieke, E. E., Frostig, R. D., and Hildesheim, R. (1994). Cortical point-spread function and long-range lateral interactions revealed by real-time optical imaging of macaque monkey primary visual cortex. *J. Neurosci.* 14, 2545–2568.

Hamel, E. (2006). Perivascular nerves and the regulation of cerebrovascular tone. *J. Appl. Physiol.* 100, 1059–1064.

Harbig, K., Chance, B., Kovach, A. G., and Reivich, M. (1976). *In vivo* measurement of pyridine nucleotide fluorescence from cat brain cortex. *J. Appl. Physiol.* 41, 480–488.

Husson, T. R., Mallik, A. K., Zhang, J. X., and Issa, N. P. (2007). Functional imaging of primary visual cortex using flavoprotein autofluorescence. *J. Neurosci.* 27, 8665–8675.

Iadecola, C., and Nedergaard, M. (2007). Glial regulation of the cerebral microvasculature. *Nat. Neurosci.* 10, 1369–1376.

Kalatsky, V. A., and Stryker, M. P. (2003). New paradigm for optical imaging: temporally encoded maps of intrinsic signal. *Neuron* 38, 529–545.

Kasischke, K. A., Vishwasrao, H. D., Fisher, P. J., Zipfel, W. R., and Webb, W. W. (2004). Neural activity triggers neuronal oxidative metabolism followed by astrocytic glycolysis. *Science* 305, 99–103.

Kitaura, H., Uozumi, N., Tohmi, M., Yamazaki, M., Sakimura, K., Kudoh, M., Shimizu, T., and Shibuki, K. (2007). Roles of nitric oxide as a vasodilator in neurovascular coupling of mouse somatosensory cortex. *Neurosci. Res.* 59, 160–171.

Kohl, M., Lindauer, U., Royl, G., Kuhl, M., Gold, L., Villringer, A., and Dirnagl, U. (2000). Physical model for the spectroscopic analysis of cortical intrinsic optical signals. *Phys. Med. Biol.* 45, 3749–3764.

Kosterin, P., Kim, G. H., Muschol, M., Obaid, A. L., and Salzberg, B. M. (2005). Changes in FAD and NADH fluorescence in neurosecretory terminals are triggered by calcium entry and by ADP production. *J. Membr. Biol.* 208, 113–124.

Kramer, R. S., and Pearlstein, R. D. (1979). Cerebral cortical microfluorometry at isosbestic wavelengths for correction of vascular artifact. *Science* 205, 693–696.

Martin, C., Berwick, J., Johnston, D., Zheng, Y., Martindale, J., Port, M., Redgrave, P., and Mayhew, J. (2002). Optical imaging spectroscopy in the unanaesthetised rat. *J. Neurosci. Methods* 120, 25–34.

Matsuda, K., Nagami, T., Kawano, K., and Yamane, S. (2000). *A New System for Measuring Eye Position on a Personal Computer.* Program No. 744.2 Neuroscience 2000 Abstracts. New Orlean, LA. Society for Neuroscience.

O'Connor, M. J., Herman, C. J., Rosenthal, M., and Jobsis, F. F. (1972). Intracellular

redox changes preceding onset of epileptiform activity in intact cat hippocampus. *J. Neurophysiol.* 35, 471–483.

Prahl, S. (2008). *Tabulated Molar Extinction Coefficient for Hemoglobin in Water*. Available at: http://omlc.ogi.edu/spectra/hemoglobin/summary.html/

Raichle, M. E., and Snyder, A. Z. (2007). A default mode of brain function: a brief history of an evolving idea. *Neuroimage* 37, 1083–1090; discussion 1097–1089.

Reinert, K. C., Dunbar, R. L., Gao, W., Chen, G., and Ebner, T. J. (2004). Flavoprotein autofluorescence imaging of neuronal activation in the cerebellar cortex in vivo. *J. Neurophysiol.* 92, 199–211.

Reinert, K. C., Gao, W., Chen, G., and Ebner, T. J. (2007). Flavoprotein autofluorescence imaging in the cerebellar cortex *in vivo*. *J. Neurosci. Res.* 85, 3221–3232.

Rosenthal, M., and Jobsis, F. F. (1971). Intracellular redox changes in functioning cerebral cortex. II. Effects of direct cortical stimulation. *J. Neurophysiol.* 34, 750–762.

Sheth, S. A., Nemoto, M., Guiou, M., Walker, M., Pouratian, N., Hageman, N., and Toga, A. W. (2004). Columnar specificity of microvascular oxygenation and volume responses: implications for functional brain mapping. *J. Neurosci.* 24, 634–641.

Sheth, S. A., Nemoto, M., Guiou, M. W., Walker, M. A., and Toga, A. W. (2005). Spatiotemporal evolution of functional hemodynamic changes and their relationship to neuronal activity. *J. Cereb. Blood Flow Metab.* 25, 830–841.

Shibuki, K., Hishida, R., Murakami, H., Kudoh, M., Kawaguchi, T., Watanabe, M., Watanabe, S., Kouuchi, T., and Tanaka, R. (2003). Dynamic imaging of somatosensory cortical activity in the rat visualized by flavoprotein autofluorescence. *J. Physiol. (Lond.)* 549, 919–927.

Shtoyerman, E., Arieli, A., Slovin, H., Vanzetta, I., and Grinvald, A. (2000). Long-term optical imaging and spectroscopy reveal mechanisms underlying the intrinsic signal and stability of cortical maps in V1 of behaving monkeys. *J. Neurosci.* 20, 8111–8121.

Sirotin, Y. B., and Das, A. (2009). Anticipatory haemodynamic signals in sensory cortex not predicted by local neuronal activity. *Nature* 457, 475–479.

Sirotin, Y. B., Hillman, E. M., Bordier, C., and Das, A. (2009). Spatiotemporal precision and hemodynamic mechanism of optical point spreads in alert primates. *Proc. Natl. Acad. Sci. USA* 106, 18390–18395.

Tohmi, M., Kitaura, H., Komagata, S., Kudoh, M., and Shibuki, K. (2006). Enduring critical period plasticity visualized by transcranial flavoprotein imaging in mouse primary visual cortex. *J. Neurosci.* 26, 11775–11785.

Turner, D. A., Foster, K. A., Galeffi, F., and Somjen, G. G. (2007). Differences in O_2 availability resolve the apparent discrepancies in metabolic intrinsic optical signals in vivo and in vitro. *Trends Neurosci.* 30, 390–398.

Vanzetta, I., and Grinvald, A. (2008). Coupling between neuronal activity and microcirculation: implications for functional brain imaging. *HFSP J.* 2, 79–98.

Vanzetta, I., Slovin, H., Omer, D. B., and Grinvald, A. (2004). Columnar resolution of blood volume and oximetry functional maps in the behaving monkey; implications for FMRI. *Neuron* 42, 843–854.

Weber, B., Burger, C., Wyss, M. T., von Schulthess, G. K., Scheffold, F., and Buck, A. (2004). Optical imaging of the spatiotemporal dynamics of cerebral blood flow and oxidative metabolism in the rat barrel cortex. *Eur. J. Neurosci.* 20, 2664–2670.

Conflict of Interest Statement: The authors declare that the research was conducted in the absence of any commercial or financial relationships that could be construed as a potential conflict of interest.

Received: 04 March 2010; paper pending published: 04 April 2010; accepted: 10 May 2010; published online: 03 June 2010.

Citation: Sirotin YB and Das A (2010) Spatial relationship between flavoprotein fluorescence and the hemodynamic response in the primary visual cortex of alert macaque monkeys. Front. Neuroenerg. ***2****:6. doi: 10.3389/fnene.2010.00006*

frontiers in
NEUROENERGETICS

ORIGINAL RESEARCH ARTICLE
published: 14 June 2010
doi: 10.3389/fnene.2010.00012

High-resolution optical functional mapping of the human somatosensory cortex

Stefan P. Koch[1]*, Christina Habermehl[1], Jan Mehnert[1,2], Christoph H. Schmitz[1,3], Susanne Holtze[1,2], Arno Villringer[1,2,4,5], Jens Steinbrink[1,6] and Hellmuth Obrig[1,2,4,5]

[1] *Berlin NeuroImaging Center, Charité Universitätsmedizin Berlin, Berlin, Germany*
[2] *Max Planck Institute for Human Cognitive and Brain Sciences, Leipzig, Germany*
[3] *NIRx Medizintechnik GmbH, Berlin, Germany*
[4] *Day Care Clinic for Cognitive Neurology, University Hospital Leipzig, Leipzig, Germany*
[5] *Berlin School of Mind and Brain, Humboldt University Berlin, Germany*
[6] *Center for Stroke Research Berlin, Universitätsmedizin Berlin, Germany*

Edited by:
David Boas, Massachusetts General Hospital, USA; Massachusetts Institute of Technology, USA; Harvard Medical School, USA

Reviewed by:
Theodore Huppert, University of Pittsburgh Medical Center, USA; Joseph P. Culver, Harvard Medical School, USA

****Correspondence:***
Stefan P. Koch, Berlin NeuroImaging Center, Department of Neurology, Charité University Hospital, Chariteplatz 1, 10117 Berlin, Germany. e-mail: stefan.koch@charite.de

Non-invasive optical imaging of brain function has been promoted in a number of fields in which functional magnetic resonance imaging (fMRI) is limited due to constraints induced by the scanning environment. Beyond physiological and psychological research, bedside monitoring and neurorehabilitation may be relevant clinical applications that are yet little explored. A major obstacle to advocate the tool in clinical research is insufficient spatial resolution. Based on a multi-distance high-density optical imaging setup, we here demonstrate a dramatic increase in sensitivity of the method. We show that optical imaging allows for the differentiation between activations of single finger representations in the primary somatosensory cortex (SI). Methodologically our findings confirm results in a pioneering study by Zeff et al. (2007) and extend them to the homuncular organization of SI. After performing a motor task, eight subjects underwent vibrotactile stimulation of the little finger and the thumb. We used a high-density diffuse-optical sensing array in conjunction with optical tomographic reconstruction. Optical imaging disclosed three discrete activation foci one for motor and two discrete foci for vibrotactile stimulation of the first and fifth finger, respectively. The results were co-registered to the individual anatomical brain anatomy (MRI) which confirmed the localization in the expected cortical gyri in four subjects. This advance in spatial resolution opens new perspectives to apply optical imaging in the research on plasticity notably in patients undergoing neurorehabilitation.

Keywords: near-infrared spectroscopy, optical imaging, optical tomography, somatotopy, somatosensory system, vibrotactile stimulation

INTRODUCTION

Imaging techniques such as BOLD-contrast magnetic resonance imaging (fMRI) and positron emission tomography (PET) offer the possibility to assess brain activity on the basis of the vascular–metabolic response and localize such activation with a resolution of millimeters. Optical imaging (OI) has been successfully advocated to also non-invasively assess changes in cortical hemodynamics in response to functional stimulation. The methodology is especially suited for experimental designs in which the constraints of an MR-scanner environment limit performance of a specific task or are not suited for the specific group of subjects. This applies to infants but also to patients, who may need continuous monitoring or direct interaction with the examiner to be motivated to perform a task. Furthermore, the low methodological constraints render OI an ideal tool for some tasks, for instance when complex motor tasks or straight posture are required (Miyai et al., 2001). Not least the advantages enable long-term measurements as, e.g., in sleep (Olopade et al., 2007) or applications in field research (Grocott et al., 2007). Beyond that, optical imaging operates interference-free with other modalities, therefore a simultaneous approach, with electrophysiological techniques such as electroencephalography (EEG) and magnetoencephalography (MEG) is easily feasible and allows investigating neurovascular coupling. In sum, its non-invasiveness requiring no exposure to radiation, magnetic fields or contrast agents and device portability allow a flexible handling in a clinical diagnostic, prognostic, and rehabilitative environment (Miyai et al., 2001).

One major methodological shortcoming of OI is spatial resolution. Typically in the range of few centimeters, topographical assignment of the activations is hampered by a sparse spatial sampling over the scalp. In the most commonly used next-neighbor approach, the individual measurement channels are defined by a pair of light-emitting and light-detecting probe separated by an inter-optode distance (IOD) of 2–4 cm. These discrete measurement points are then interpolated into a topographic map of functional activation, which is superimposed onto the brain area covered by the probe array. To enhance the spatial resolution a multi-distance approach using several sources and detectors has been proposed. Since light attenuation of multiple neighbors with different IODs is assessed, this approach yields measurements of overlapping photon paths with different sampled target depths (Barbour et al., 2001; Boas et al., 2004). The differential sensitivity of the volumes interrogated by light, leads to a rough depth discrimination and facilitates the separation of signals from superficial

and deeper layers. Thus sensitivity to the cerebro-cortical signal is augmented. Also such an approach enhances lateral resolution. A pioneering study (Zeff et al., 2007) recently demonstrated the feasibility of retinotopic mapping of the primary visual cortex, based on eccentricity and angular stimulation (see also White and Culver, 2010). The study proves that state-of-the-art technology and advanced analytical tools enhance spatial resolution dramatically in non-invasive optical imaging, opening an entirely new perspective for the application in basic and clinical research.

Here, we extend the use of high-density optical imaging to another sensory system and test whether this technique is sensitive enough to functionally map the somatotopic organization of the somatosensory cortex. The somatosensory system consists of two major cortical representations, the primary (SI) and the secondary somatosensory cortex (SII), both of which have been shown to be somatotopically organized. While SII is located in the deeper part of the inferior parietal cortex, which is not accessible to non-invasive optical techniques, the SI hand area can be regarded an ideal candidate for optical imaging access, due to its superficial location at the posterior wall of the central sulcus. The idea of somatotopy has long been established. Based on the observation that motor convulsion or dysesthesia 'march' along typical routes over the body in some simple focal epileptic seizures and that these 'routes' are highly reproducible within and between patients, Jackson postulated a somatotopic organization of the somatosensory and motor cortex already in the 19th century (Jackson, 1863). In 1931, cortical somatotopic organization was first experimentally proven in humans by applying electrical stimulation to precentral and postcentral cortices (Foerster, 1931). Finally, the term "somatotopy" was introduced by Penfield (Penfield and Boldrey, 1937). With respect to somatosensation, he applied electrical stimulation to the surface of the postcentral gyrus in patients undergoing brain surgery. Based on the patients' reports of thereby elicited sensations, the idea of the sensory homunculus was established (Penfield and Boldrey, 1937; Penfield and Rasmussen, 1950). The gross anatomy (head, arm, trunk, and leg) is clearly differentially represented by areas of contralateral sensory (SI) and primary motor (M1) cortices. The representations follow a latero-medial sequence along the precentral and postcentral gyri, respectively. The representational organization within the hand sub-division is more complex and still partly controversial. In SI a basic somatotopic arrangement was found using MEG (Baumgartner et al., 1991; Hari et al., 1993; Nakamura et al., 1998), EEG (Buchner et al., 1995) and fMRI studies differing in type of stimulation, number of fingers stimulated and spatial resolution (Sakai et al., 1995; Wolf et al., 1996; Gelnar et al., 1998; Kurth et al., 1998; Stippich et al., 1999; Francis et al., 2000; Nelson and Chen, 2008; Schweizer et al., 2008; Weibull et al., 2008). The few studies covering the entire SI finger area at a high spatial resolution found a map similar to that described by Penfield. The thumb is represented in the most lateral, anterior, and inferior position, followed by the other fingers ordered along the central sulcus in a superior to medial direction (Maldjian et al., 1999; Kurth et al., 2000; van Westen et al., 2004; Schweizer et al., 2008).

Since somatosensory stimulation and training of motor skills may substantially alter the extent and the more fine-grained somatotopy of the homunculus, the investigation into training or rehabilitation induced changes would profit from an undemanding assessment, available in a clinical setting. In the current study we therefore addressed the question whether high-density diffuse-optical imaging of the sensory SI hand areal is spatially sensitive enough to somatotopically differentiate and map the representations of thumb (first) and little (fifth) finger to vibrotactile stimulation.

MATERIALS AND METHODS

SUBJECTS

Eight right-handed volunteers (mean age 31.3 ± 4.5 years, three females) without any history of neurological or psychiatric disorders were investigated. The study was approved by the local ethics committee at Charité University Hospital Berlin and written consent was obtained from each subject prior to investigation.

STIMULI AND PROCEDURE

Participants were seated in an EEG chair in a sound-attenuated, dimly lit room. Somatosensory stimulation was elicited by vibrotactile stimuli applied by rotating brushes (10 mm diameter surface) mounted into a glove at the position of the tips of the first and fifth finger. The timing of brushes was controlled by Cogent (Wellcome Department of Imaging Neuroscience, London, UK), a stimulus toolbox that runs in the Matlab environment (The Mathworks, Natick, MA, USA). During the experiment each subject received 24 runs of a 5-s vibrotactile stimulus on either the first or fifth finger of the left hand (**Figure 1D**). The application of the tactile stimuli was temporally jittered (mean SOA 20 s, range 16–24 s) and appeared in a pseudo-randomized sequence to avoid stimulus expectation and to optimize the data for an analysis based on the sluggish vascular response (Birn et al., 2002).

Prior to vibrotactile stimulation subjects performed 10 repetitions of self-paced finger tapping of the left hand without wearing the glove to assess the motor areas. The timing of finger tapping was guided by the noise of the rotating brushes, to exclude confounding auditory and arousal effects. The finger-tapping experiment was identical to the somatosensory experiment with respect to timing and temporal jitter. Activation in the motor area is a robust signal that has been reported in a number of studies (Obrig et al. 1996). In the present study finger tapping served as a control condition. Because the motor homunculus is located on the precentral gyrus we expected the somatosensory activation to be posterior to the motor response. OI data were continuously acquired during vibrotactile stimulation and tapping tasks.

To project functional activation patterns on the individual brain anatomy, an anatomical T1-weighted MPRAGE MRI scan was acquired for each individual subject (TR = 94 ms, TE = 4 ms, flip angle 12°, voxel size 1 × 1 × 1 mm 1.5 T, Magnetom Vision, Siemens, Erlangen, Germany). For a subsequent co-registration of OT-results and anatomical structures the corners of the imaging grid were marked on the scalp. Before MR scanning, vitamin-E capsules were fixed at the marked head positions using double-sided self adhesive tape (**Figure 1C**).

OPTICAL IMAGING DATA ACQUISITION

Optical imaging was performed using a DYNOT 232 optical tomography imager (NIRx Medizintechnik GmbH, Berlin, Germany). To achieve high spatial sampling of about 0.75-cm IOD, a rectangular

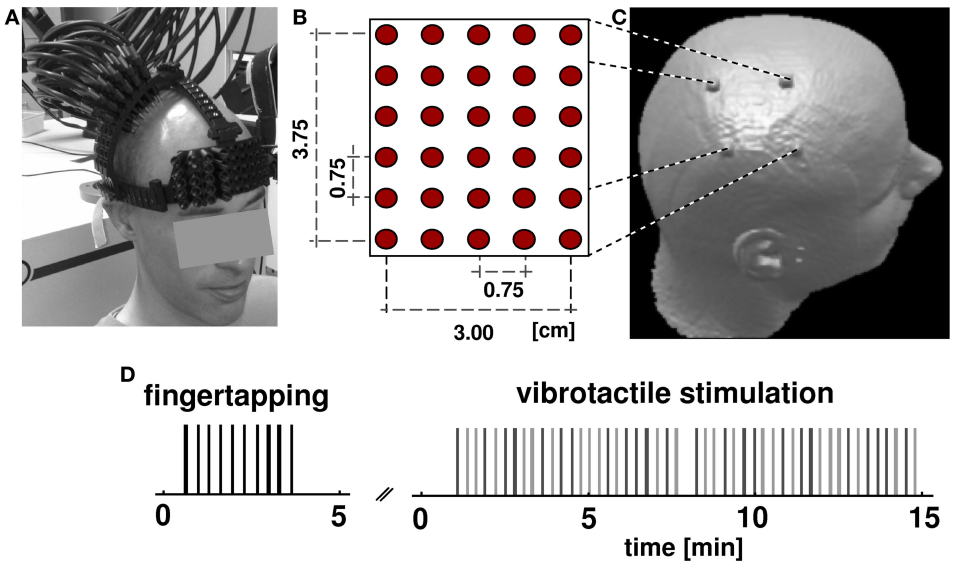

FIGURE 1 | Experimental design. (A) Subjects wore an open scaffolding fiber optic holder, consisting of semi-elastic plastic stripes running along the head circumference just above the ears and along the midline. Arched support members which positioned the fiber optic tips over the right pericentral region were attached to this support structure. Fibers were individually spring loaded to maintain a mild constant pressure onto the skin to provide stable optical contact. **(B)** The optical probes form a rectangular array of 30 fibers with inter-optode distance of 0.75 cm. **(C)** After NIRS acquisition, subjects received an anatomical MR scan with fiducial marks positioned at the corner of the probe array allowing the subsequent alignment of functional optical and structural MRI data. **(D)** Subjects underwent two consecutive sessions, a finger tapping task and vibrotactile stimulation. In both tasks the occurrence of an event (vertical bars: black for tapping, light gray for first finger, dark gray for fifth finger) was jittered over time. The whole optical imaging procedure took less than 20 min.

array consisting of 30 fibers was arranged over the right pericentral area using an open scaffolding structure and individually spring-loaded fibers. This design allowed for an easy access of the fiber tips for parting the hair before placing an optode and also ensured stable optical contact. Five horizontal and six vertical rows of probes covered an area of 3.00 cm × 3.75 cm (**Figures 1A,B**). The imager employs time-multiplexed source illumination and utilizes each optical fiber as both source and detector. The resulting 900 source-detector combinations with variable IODs (0–4.80 cm distance) sample different sub-volumes beneath the probe array and allow investigating functional activation by means of an optical tomography approach (Barbour et al., 2001). For the vibrotactile and finger-tapping task data at two wavelengths (760 and 830 nm) were acquired continuously at a rate of 1.9 Hz.

DATA ANALYSIS

The first task was to locate the optical probe array with respect to cortical anatomy. Anatomical MR-images of each subject were segmented using standard routines implemented in the Statistical Parametric Mapping software (SPM8, Wellcome Trust, University College London, UK). Images were divided into gray and white matter following SPM's Bayesian algorithm on the tissue probability maps for white and gray matter. This yielded the voxels of gray matter underneath the pad. The localization of the fiducials was determined from raw images. Based on the individual three-dimensional gray matter maps the fiducial marks of the probe array were then projected on the calculated gray matter surface. The localization of the central sulcus was judged by four independent experts based on the preprocessed anatomical MR-images. For this purpose the individual's anatomical image was rotated so as to provide a perpendicular view onto the area enclosed by the fiducial marks (similar to the perspective seen in **Figure 1C**). The topographic view of the anatomical cortex reconstruction was then subjected to a 2-D transformation to superimpose the fiducials' location with the corners of the optical reconstruction map. Subjects for whom the central sulcus and/or the presumed activation areas were located outside the area enclose by the fiducial marks were excluded from further analysis.

Next, optical imaging data of both tasks were band pass-filtered between 0.033 and 0.5 Hz (Butterworth, second order). From these we reconstructed volumetric image time series of HbO and HbR concentration changes using the normalized-difference method described in Barbour et al. (2001) and Pei et al. (2001), as implemented in NAVI software package (NIRx Medical Technologies LLC, Glen Head, NY, USA). The algorithm achieves fast image reconstruction by truncated singular value decomposition (tSVD) inversion of a pre-calculated image operator. The operator, or weight matrix, is generated by solving the optical diffusion equation on a finite element method (FEM) mesh which was obtained from a generic anatomical MRI image of the human head and which considered the specific source-detector configuration of our experiment.

The depth-sensitivity of the true 3-D image reconstruction allows for ready distinction of extra-cerebral artifacts from cerebral activity. Stimulus-related activity was observed only in subsurface areas, which were selected as regions of interest (ROI) for further processing and display. No further method of surface–signal correction, such as a nearest-neighbor signal subtraction (Zeff et al., 2007), was employed. All data sets were carefully checked for

motion artifacts; however, because of the rigid mounting of the fibers and the relatively short experimental period, no correction for any such artifacts was deemed necessary.

Images were reconstructed on a sub-volume of this FEM mesh being congruent with the region of the optical fiber array on the subject. For both, the finger-tapping task and the vibrotactile stimulation, a general linear model (GLM) was calculated to estimate the effect of hemodynamic changes within this specific three-dimensional sub-volume. For the tapping task a design matrix consisting of a 0–1 boxcar predictor was convolved with a hemodynamic response function with a peak at 5 s (Boynton et al., 1996). For the vibrotactile data two independent predictors were applied for stimulation periods of first and fifth digit, respectively. Thus, for each voxel of the sub-volume T-values were derived for HbR and HbO data in each condition. To assess the maxima of activation for the two tactile and the motor conditions we created a series of two-dimensional images of the area covered by the probe array. This roughly corresponds to a slice orientation tangential to the head surface as can be constructed by 3D-MR datasets. A further sub-division of the volume into concentric shells parallel to the optical head model surface was not necessary because size and position revealed a rather planar surface of the probe array. For each condition T-value maps based on the changes in HbR were derived from layers of a medium depth (mean 5.4 mm, SD 1.65 mm). The maps showing a strong hemodynamic response were averaged and superimposed on the corresponding anatomical image and finally thresholded at 90% of the absolute maximum (**Figure 2**).

RESULTS

Three of eight subjects were excluded from the analysis because the probe array for these subjects was not localized over the pericentral region and hence did not include the putative hand area of the motor and somatosensory homunculus.

One subject revealed no focal motor activation during finger-tapping; therefore we do not report on the results of this subject.

Figure 2 shows the activation maps for the remaining four subjects. T-value maps based on HbR-changes were superimposed on individual anatomical images. The four subjects show a maximum hemodynamic response to finger tapping located on the precentral gyrus. In contrast, the hemodynamic response to

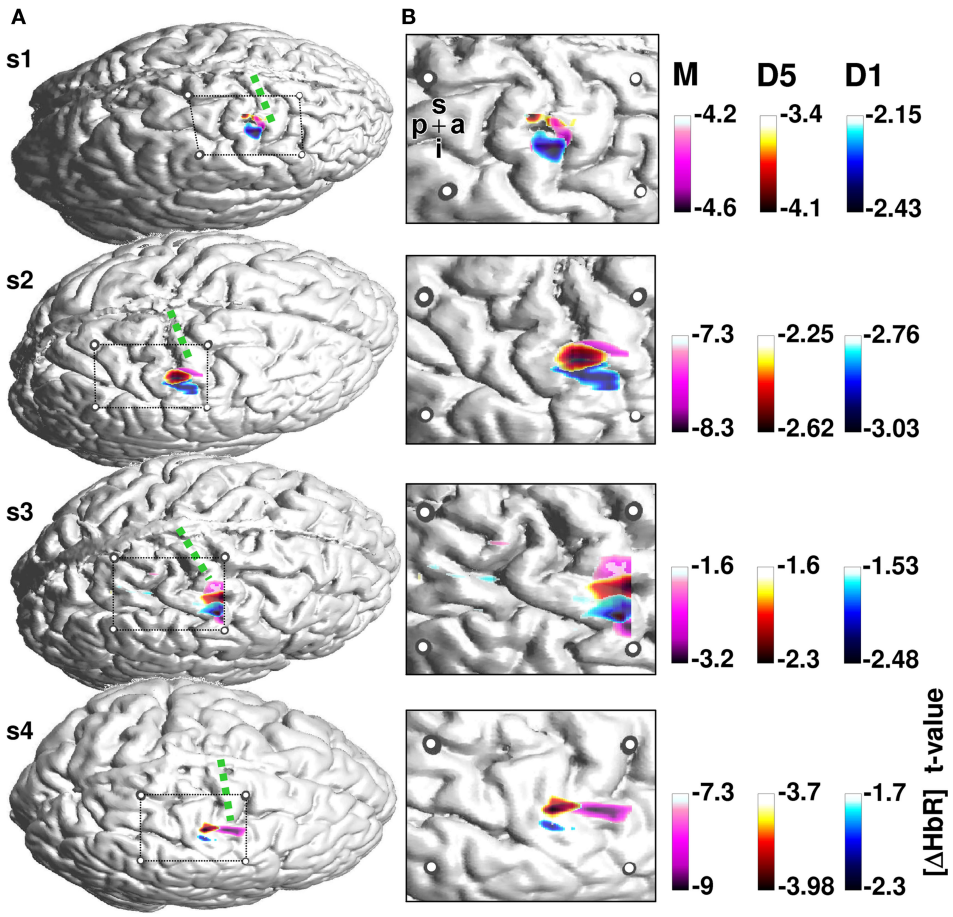

FIGURE 2 | Activation maps for the finger tapping and vibrotactile finger stimulation. (A) Individual cortical anatomy of the four subjects (s1–s4) recovered from anatomical MRI. Circles represent the positions of the fiducial marks projected onto the cortical surface. These allow the location of the cortical area covered by the optical array. The array covers the pre and postcentral gyrus. Precentral gyrus is denoted with a green dotted line. HbR T-maps for finger tapping (pink) and vibrotactile stimulation of first (blue) and fifth (red) finger, respectively, were superimposed on the anatomical image. **(B)** Magnified section of the probe array with underlying anatomical structures and thresholded T-values. Letters p, a, i, s denote the posterior to anterior and inferior to superior directions of the images.

somatosensory stimulation is located on the postcentral gyrus. Besides this anterior-posterior differentiation, the localization of the activation to first versus fifth finger stimulation differed with respect to their maximal amplitude.

Across all four subjects the activation elicited by stimulation of the fifth finger was located more superior along the central sulcus compared to first finger stimulation. The temporal evolution of the hemodynamic response is illustrated in **Figure 3**. Mean changes of HbR and HbO across all runs are shown for the 5 s stimulation period and the ensuing 8 s of rest. Data for first and fifth finger of subject 2 are shown. Clearly both conditions led to an increase in HbO (red) and a decrease in HbR (blue) with the typical vascular response latency peaking 5–7 s after stimulus onset (0 s on the time axis). After thresholding of the results at their absolute maxima, maps revealed different locations of the activation patterns of first and fifth finger stimulation. Vibrotactile stimulation of the first finger led to a more inferior and anterior activation pattern compared to the pattern of the fifth finger in a lateral 2D-view of the brain. This differential localization held for both HbO and HbR. Although HbO and HbR showed slight differences with respect to size and temporal dynamics of the activation patterns, both parameters followed typical dynamics of the vascular response with an increased focal oxygenation resulting from a rise of blood volume and flow velocity. The latter overcompensates the oxygen uptake and thus yields an increased washout of HbR. The anatomical structures subjacent to the fiber array confirmed that the hemodynamic changes to first and fifth finger stimulation originated from the postcentral gyrus.

DISCUSSION

We demonstrated that high-density optical imaging allows for a fine-grained resolution of functional cortical activations in the pericentral motor and somatosensory cortices. The data showed spatially separated activations in response to vibrotactile stimulation posterior to those during motor performance. Also a differentiation between somatosensory representations of the first and fifth finger was unequivocally seen in four subjects. The spatial distribution is in line with the well-known anatomical homuncular organization in the pre and postcentral gyrus which was shown by the projection of the functional imaging results onto the individuals'

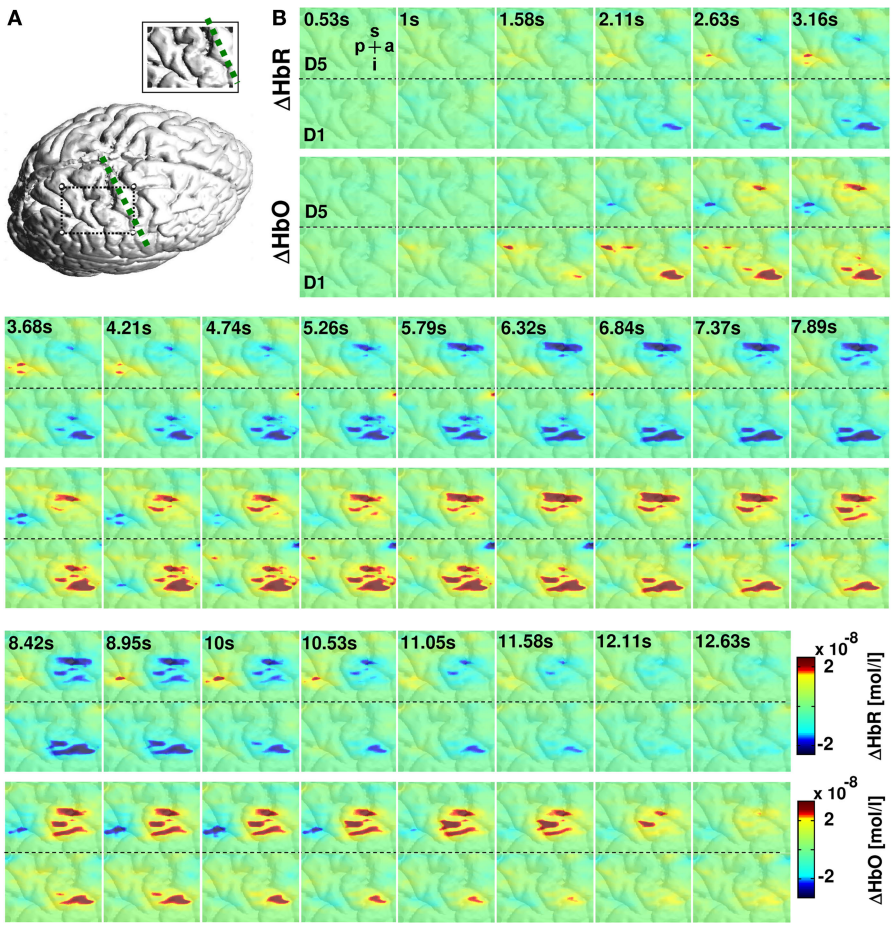

FIGURE 3 | Hemodynamic changes in response to vibrotactile stimulation. **(A)** Cortical surface rendering of subject 2 with an inset showing the area covered by the probe array. **(B)** Colored panels depict the averaged hemodynamic changes from this subject for HbR (upper row) and HbO (lower row) to 5-s vibrotactile stimulation of the fifth and first finger. The vibrotactile stimulation started at 0 s. Vibrotactile stimulation of first and fifth finger yielded to a decrease in HbR (blue) and an increase in HbO (red) with a hemodynamic peak latency of 5–7 s. Letters p, a, i, s denote the posterior to anterior and inferior to superior directions of the images.

structural MRIs. Our results confirm reports of similar approaches using high-density optical imaging (Zeff et al., 2007; White and Culver, 2010) and extend the application of the methodology to the somatosensory system. First we discuss the findings with regard to previous work on non-invasive imaging of the homuncular organization of the somatosensory cortex, followed by the discussion of relevant limitations and, more importantly, the perspectives of this approach.

Electrophysiological methods provided the first successful demonstration that the homuncular organization is accessible to non-invasive techniques in healthy adults. MEG (Baumgartner et al., 1991; Hari et al., 1993; Nakamura et al., 1998) and EEG (Buchner et al., 1995) located differential sources in the pericentral region notably also providing first evidence that this representation can be altered by plastic changes in disease (Elbert et al., 1998; Braun et al., 2003). While these latter findings show the high sensitivity of MEG and EEG to subtle changes in source amplitude and orientation, the same sensitivity constitutes a fundamental limitation of electrophysiological imaging related to the inverse problem of all localization approaches. With the advent of blood oxygen level dependence-(BOLD) fMRI, a number of groups used the inherent advantage of MRI supplying a high-resolution structural image on which the functional activation can be individually mapped (Sakai et al., 1995; Lin et al., 1996; Gelnar et al., 1998; Kurth et al., 1998; Stippich et al., 1999; Francis et al., 2000; Nelson and Chen, 2008; Schweizer et al., 2008; Weibull et al., 2008). Some of these studies were able to produce functional maps highly similar to Penfield's invasively assessed maps. In these images stimulation of the thumb results in the most lateral, anterior and inferior position, followed by the other fingers orderly along the central sulcus in a superior to medial direction (Maldjian et al., 1999; Kurth et al., 2000; van Westen et al., 2004; Schweizer et al., 2008).

Our results confirm that sensitivity of optical imaging is sufficient to detect similarly subtle differences in the lateral distribution of activation foci. Sensitivity to a functional activation paradigm across studies is somewhat arbitrary depending on the exact stimulation protocol, individual anatomy, and a number of issues of the analytical tools and assumptions. A key question is how such an approach can be useful for future research. Here, one apparent concern is the rather high exclusion rate of half of our subjects. Three subjects were excluded due to a wrong localization of the pad with respect to cortical anatomy. This is somewhat at odds with the comparatively small inter-individual variance of the central sulcus with reference to the 10–20 system. Using magnetic resonance imaging, Steinmetz et al. (1989) reported a 1.2 cm rostral to caudal variation of the central sulcus (16 subjects) when relating cortical anatomy to the grid referenced by the external bony landmarks. This point, determined in sagittal slices 4 cm from midline and with respect to the line defined by the vertex point (Cz) and the pre-auricular point, referred to the location of the middle finger representation of the motor and sensory homunculi. Another MR-study reported inter-individual variances of the same order, when cortical anatomy was related to the 10–10 system (Koessler et al., 2009). Across 16 subjects the standard deviations of the C4 electrode position, close to the central sulcus, was below 10 mm (SD for C4: $x = 4.6$ mm, $y = 8.3$ mm, $z = 6.4$ mm). It may be possible that our projection of the optical probes and the cortical surface has added to the variance of the pad's location in the excluded subjects. Additionally, the central sulcus was located by a rather simple expert-rating approach using preprocessed representations of individuals' brain surface. Since the focus in this paper is on the approach rather than an anatomical question, we used this quite conservative inclusion criterion. In clinical applications structural imaging data will be available in most patients, thus information on the individual anatomy and more importantly individual lesions will usually allow for an informed positioning of the probe array. Furthermore powerful novel projection algorithms have been proposed (Okamoto et al., 2004; Custo et al., 2010) for low-density imaging and are currently being developed for high-density tomographic data.

Another subject was excluded since motor performance did not elicit reliable activation. There are two reasons for using a reliable response to finger tapping as an inclusion criterion. Firstly, motor-related activation has been shown to be much more robust not only in optical (Obrig et al., 1996) but also in BOLD-contrast imaging, partially due to the fact that somatosensory feedback is inherent to natural motor performance. Additionally the hemodynamic response to finger tapping was expected to project to the precentral gyrus (M1 and premotor areas). Hence to judge the potential of high-resolution optical imaging we considered it mandatory to differentiate in both an anterior-posterior and a medio-lateral dimension.

What are the limitations of the approach? Clearly parts of the brain located in deep sulcal structures with some distance to the surface cannot be reached by optical approaches. The resolution of sub-divisions of SI, as it has been shown in primates (Merzenich et al., 1978; Kaas et al., 1979; Nelson et al., 1980; Sur et al., 1982; Pons et al., 1985), may be beyond the lateral resolution even of high-density optical approaches. The somatotopic organization is most pronounced in area 3b, and in area 3a located on the posterior wall of the central sulcus. These factors may contribute to the issue of precision of our approach. For high-resolution MRI differentiations of the sub-divisions of SI have been reported (Eickhoff et al., 2005; Schweizer et al., 2008). Refining co-registration with structural MRI and re-localizing the center of the image pad to optimally cover the area of interest may enhance the accuracy of the here presented approach. However, considering some fundamental limitations of diffuse-optical tomography we think that such sub-differentiation will be beyond even more sophisticated methodological approaches. The limitations inherent to non-invasive optical imaging can be divided into three fields. (i) The underlying *physical* principles of photon transport in strongly scattering media restrict the precision of the reconstruction of the sampled tissue. This is due to the fact that strong assumptions concerning the background optical properties are mandatory. Deviations from the assumed optical properties in the individual clearly limit precision. (ii) *Anatomically,* the variability of gyral structure and the thickness of the extra-cerebral tissue reduce the spatial accuracy of the derived activation foci. Since optical imaging does not supply anatomical information, the measured activation pattern can only be projected onto a gyral map when relying on external landmarks and cranio–cerebral correlations with the 10–10/10–20 electrode placement system (Okamoto et al., 2004) or when a structural MRI is performed in the individual subject. (iii) *Physiologically,* systemic changes in hemodynamics must be

considered. This notorious issue in optical imaging may lead to a contamination of the vascular response with respect to amplitude but also timing (Boden et al., 2007). In high-resolution approaches this may be considered a lesser issue, since the high focality of the response is an intrinsic argument for the cortical origin of the detected changes. However, when comparing amplitude and temporal dynamics between groups or in their development over time, this may introduce another source of noise.

Bearing these issues in mind, we are confident that future application of high-density optical imaging is complementary to vascular (fMRI) and electrophysiological imaging (EEG). As it has been demonstrated in a large number of studies, optical imaging has a potential in applications in which fMRI application is problematic, notably in infant research. The present approach may be specifically suited to be applied in clinical and rehabilitative research. In a multimodal scenario structural and potentially functional information can be gathered in an initial MRI-based assessment. During the course of rehabilitative therapy optical imaging could serve as a convenient tool to monitor plasticity in a predefined region of interest. Another promising perspective is the simultaneous application high-density optical imaging with EEG or MEG (Obrig et al., 2002; Mackert et al., 2004). Beyond basic issues of neurovascular coupling (Koch et al., 2009) the respective strengths of a high sensitivity to brief events (EEG) and the integration over slower processes inherent to vascular techniques like optical imaging has as yet not been fully explored. The latter may be of relevance especially when plastic changes during stimulation and training are the focus of research. Our present data and the pioneering work of other groups (Zeff et al., 2007; White and Culver, 2010) can be considered a huge step towards an increase of reliability and applicability of optical imaging in such fields of research.

ACKNOWLEDGMENTS

Financial support of the EU (NEST 012778, EFRE 20002006 2/6, nEUROpt 201076), and BMBF (BNIC, Bernstein Center for Computational Neuroscience, German-Polish cooperation FK: 01GZ0710) are gratefully acknowledged. Support was also provided by NIH grants R42NS050007, R44NS049734 to R. L. Barbour.

REFERENCES

Barbour, R. L., Graber, H. L., Pei, Y., Zhong, S., and Schmitz, C. H. (2001). Optical tomographic imaging of dynamic features of dense-scattering media. *J. Opt. Soc. Am. A. Opt. Image Sci. Vis.* 18, 3018–3036.

Baumgartner, C., Doppelbauer, A., Sutherling, W. W., Zeitlhofer, J., Lindinger, G., Lind, C., and Deecke, L. (1991). Human somatosensory cortical finger representation as studied by combined neuromagnetic and neuroelectric measurements. *Neurosci. Lett.* 134, 103–108.

Birn, R. M., Cox, R. W., and Bandettini, P. A. (2002). Detection versus estimation in event-related fMRI: choosing the optimal stimulus timing. *Neuroimage* 15, 252–264.

Boas, D. A., Chen, K., Grebert, D., and Franceschini, M. A. (2004). Improving the diffuse optical imaging spatial resolution of the cerebral hemodynamic response to brain activation in humans. *Opt. Lett.* 29, 1506–1508.

Boden, S., Obrig, H., Kohncke, C., Benav, H., Koch, S. P., and Steinbrink, J. (2007). The oxygenation response to functional stimulation: is there a physiological meaning to the lag between parameters? *Neuroimage* 36,100–107.

Boynton, G. M., Engel, S. A., Glover, G. H., and Heeger, D. J. (1996). Linear systems analysis of functional magnetic resonance imaging in human V1. *J. Neurosci.* 16, 4207–4221.

Braun, C., Schweizer, R., Heinz, U., Wiech, K., Birbaumer, N., and Topka, H. (2003). Task-specific plasticity of somatosensory cortex in patients with writer's cramp. *Neuroimage* 20, 1329–1338.

Buchner, H., Adams, L., Muller, A., Ludwig, I., Knepper, A., Thron, A., Niemann, K., and Scherg, M. (1995). Somatotopy of human hand somatosensory cortex revealed by dipole source analysis of early somatosensory evoked potentials and 3D-NMR tomography. *Electroencephalogr. Clin. Neurophysiol.* 96, 121–134.

Custo, A., Boas, D. A., Tsuzuki, D., Dan, I., Mesquita, R., Fischl, B., Grimson, W. E., and Wells, W. (2010). Anatomical atlas-guided diffuse optical tomography of brain activation. *Neuroimage* 49, 561–567.

Eickhoff, S., Walters, N. B., Schleicher, A., Kril, J., Egan, G. F., Zilles, K., Watson, J. D., and Amunts, K. (2005). High-resolution MRI reflects myeloarchitecture and cytoarchitecture of human cerebral cortex. *Hum. Brain Mapp.* 24, 206–215.

Elbert, T., Candia, V., Altenmuller, E., Rau, H., Sterr, A., Rockstroh, B., Pantev, C., and Taub, E. (1998). Alteration of digital representations in somatosensory cortex in focal hand dystonia. *Neuroreport* 9, 3571–3575.

Foerster, O. (1931). The cerebral cortex in man. *Lancet* 221, 309–312.

Francis, S. T., Kelly, E. F., Bowtell, R., Dunseath, W. J., Folger, S. E., and McGlone, F. (2000). fMRI of the responses to vibratory stimulation of digit tips. *Neuroimage* 11, 188–202.

Gelnar, P. A., Krauss, B. R., Szeverenyi, N. M., and Apkarian, A. V. (1998). Fingertip representation in the human somatosensory cortex: an fMRI study. *Neuroimage* 7, 261–283.

Grocott, M., Richardson, A., Montgomery, H., and Mythen, M. (2007). Caudwell Xtreme Everest: a field study of human adaptation to hypoxia. *Crit. Care* 11, 151.

Hari, R., Karhu, J., Hamalainen, M., Knuutila, J., Salonen, O., Sams, M., and Vilkman, V. (1993). Functional organization of the human first and second somatosensory cortices: a neuromagnetic study. *Eur. J. Neurosci.* 5, 724–734.

Jackson, H. J. (1863). Convulsive spasms of the right hand and arm preceding epileptic seizures. *Med. Times. Gaz.* 1, 589.

Kaas, J. H., Nelson, R. J., Sur, M., Lin, C. S., and Merzenich, M. M. (1979). Multiple representations of the body within the primary somatosensory cortex of primates. *Science* 204, 521–523.

Koch, S. P., Werner, P., Steinbrink, J., Fries, P., and Obrig, H. (2009). Stimulus-induced and state-dependent sustained gamma activity is tightly coupled to the hemodynamic response in humans. *J. Neurosci.* 29, 13962–13970.

Koessler, L., Maillard, L., Benhadid, A., Vignal, J. P., Felblinger, J., Vespignani, H., and Braun, M. (2009). Automated cortical projection of EEG sensors: anatomical correlation via the international 10-10 system. *Neuroimage* 46, 64–72.

Kurth, R., Villringer, K., Mackert, B. M., Schwiemann, J., Braun, J., Curio, G., Villringer, A., and Wolf, K. J. (1998). fMRI assessment of somatotopy in human Brodmann area 3b by electrical finger stimulation. *Neuroreport* 9, 207–212.

Kurth, R., Villringer, K., Curio, G., Wolf, K. J., Krause, T., Repenthin, J., Schwiemann, J., Deuchert, M., and Villringer, A. (2000). fMRI shows multiple somatotopic digit representations in human primary somatosensory cortex. *Neuroreport* 11, 1487–1491.

Lin, W., Kuppusamy, K., Haacke, E. M., and Burton, H. (1996). Functional MRI in human somatosensory cortex activated by touching textured surfaces. *J. Magn. Reson. Imaging* 6, 565–572.

Mackert, B. M., Wubbeler, G., Leistner, S., Uludag, K., Obrig, H., Villringer, A., Trahms, L., and Curio, G. (2004). Neurovascular coupling analyzed non-invasively in the human brain. *Neuroreport* 15, 63–66.

Maldjian, J. A., Gottschalk, A., Patel, R. S., Detre, J. A., and Alsop, D. C. (1999). The sensory somatotopic map of the human hand demonstrated at 4 Tesla. *Neuroimage* 10, 55–62.

Merzenich, M. M., Kaas, J. H., Sur, M., and Lin, C. S. (1978). Double representation of the body surface within cytoarchitectonic areas 3b and 1 in "SI" in the owl monkey (*Aotus trivirgatus*). *J. Comp. Neurol.* 181, 41–73.

Miyai, I., Tanabe, H. C., Sase, I., Eda, H., Oda, I., Konishi, I., Tsunazawa, Y., Suzuki, T., Yanagida, T., and Kubota, K. (2001). Cortical mapping of gait in humans: a near-infrared spectroscopic topography study. *Neuroimage* 14, 1186–1192.

Nakamura, A., Yamada, T., Goto, A., Kato, T., Ito, K., Abe, Y., Kachi, T., and Kakigi, R. (1998). Somatosensory homunculus as drawn by MEG. *Neuroimage* 7, 377–386.

Nelson, A. J., and Chen, R. (2008). Digit somatotopy within cortical areas of the postcentral gyrus in humans. *Cereb. Cortex* 18, 2341–2351.

Nelson, R. J., Sur, M., Felleman, D. J., and Kaas, J. H. (1980). Representations of the body surface in postcentral parietal

cortex of *Macaca fascicularis*. *J. Comp. Neurol.* 192, 611–643.

Obrig, H., Hirth, C., Junge-Hulsing, J. G., Doge, C., Wolf, T., Dirnagl, U., and Villringer, A. (1996). Cerebral oxygenation changes in response to motor stimulation. *J. Appl. Physiol.* 81, 1174–1183.

Obrig, H., Israel, H., Kohl-Bareis, M., Uludag, K., Wenzel, R., Muller, B., Arnold, G., and Villringer, A. (2002). Habituation of the visually evoked potential and its vascular response: implications for neurovascular coupling in the healthy adult. *Neuroimage* 17, 1–18.

Okamoto, M., Dan, H., Sakamoto, K., Takeo, K., Shimizu, K., Kohno, S., Oda, I., Isobe, S., Suzuki, T., Kohyama, K., and Dan, I. (2004). Three-dimensional probabilistic anatomical cranio-cerebral correlation via the international 10-20 system oriented for transcranial functional brain mapping. *Neuroimage* 21, 99–111.

Olopade, C. O., Mensah, E., Gupta, R., Huo, D., Picchietti, D. L., Gratton, E., and Michalos, A. (2007). Noninvasive determination of brain tissue oxygenation during sleep in obstructive sleep apnea: a near-infrared spectroscopic approach. *Sleep* 30, 1747–1755.

Pei, Y., Graber, H. L., and Barbour, R. L. (2001). Influence of systematic errors in reference states on image quality and on stability of derived information for DC optical imaging. *Appl. Opt.* 40, 5755–5769.

Penfield, W., and Boldrey, E. (1937). Somatic motor and sensory representation in the cerebral cortex of man as studied by electrical stimulation. *Brain Res.* 60, 389–443.

Penfield, W., and Rasmussen, T. (1950). *The Cerebral Cortex of Man. A Clinical Study of Localization of Function*. New York: Macmillan Company.

Pons, T. P., Garraghty, P. E., Cusick, C. G., and Kaas, J. H. (1985). A sequential representation of the occiput, arm, forearm and hand across the rostro-caudal dimension of areas 1, 2 and 5 in macaque monkeys. *Brain Res.* 335, 350–353.

Sakai, K., Watanabe, E., Onodera, Y., Itagaki, H., Yamamoto, E., Koizumi, H., and Miyashita, Y. (1995). Functional mapping of the human somatosensory cortex with echo-planar MRI. *Magn. Reson. Med.* 33, 736–743.

Schweizer, R., Voit, D., and Frahm, J. (2008). Finger representations in human primary somatosensory cortex as revealed by high-resolution functional MRI of tactile stimulation. *Neuroimage* 42, 28–35.

Steinmetz, H., Furst, G., and Meyer, B. U. (1989). Craniocerebral topography within the international 10-20 system. *Electroencephalogr. Clin. Neurophysiol.* 72, 499–506.

Stippich, C., Hofmann, R., Kapfer, D., Hempel, E., Heiland, S., Jansen, O., and Sartor, K. (1999). Somatotopic mapping of the human primary somatosensory cortex by fully automated tactile stimulation using functional magnetic resonance imaging. *Neurosci. Lett.* 277, 25–28.

Sur, M., Nelson, R. J., and Kaas, J. H. (1982). Representations of the body surface in cortical areas 3b and 1 of squirrel monkeys: comparisons with other primates. *J. Comp. Neurol.* 211, 177–192.

van Westen, D., Fransson, P., Olsrud, J., Rosen, B., Lundborg, G., and Larsson, E. M. (2004). Fingersomatotopy in area 3b: an fMRI-study. *BMC Neurosci.* 5, 28.

Weibull, A., Bjorkman, A., Hall, H., Rosen, B., Lundborg, G., and Svensson, J. (2008). Optimizing the mapping of finger areas in primary somatosensory cortex using functional MRI. *Magn. Reson. Imaging* 26, 1342–1351.

White, B. R., and Culver, J. P. (2010). Phase-encoded retinotopy as an evaluation of diffuse optical neuroimaging. *Neuroimage* 49, 568–577.

Wolf, T., Lindauer, U., Obrig, H., Dreier, J., Back, T., Villringer, A., and Dirnagl, U. (1996). Systemic nitric oxide synthase inhibition does not affect brain oxygenation during cortical spreading depression in rats: a noninvasive near-infrared spectroscopy and laser-Doppler flowmetry study. *J. Cereb. Blood Flow Metab.* 16, 1100–1107.

Zeff, B. W., White, B. R., Dehghani, H., Schlaggar, B. L., and Culver, J. P. (2007). Retinotopic mapping of adult human visual cortex with high-density diffuse optical tomography. *Proc. Natl. Acad. Sci. USA* 104, 12169–12174.

Conflict of Interest Statement: The authors declare that the research was conducted in the absence of any commercial or financial relationships that could be construed as a potential conflict of interest.

Received: 25 February 2010; paper pending published: 30 March 2010; accepted: 26 May 2010; published online: 14 June 2010.

Citation: Koch SP, Habermehl C, Mehnert J, Schmitz CH, Holtze S, Villringer A, Steinbrink J and Obrig H (2010) High-resolution optical functional mapping of the human somatosensory cortex. Front. Neuroenerg. ***2****:12. doi: 10.3389/fnene.2010.00012*

frontiers in
NEUROENERGETICS

ORIGINAL RESEARCH ARTICLE
published: 14 July 2010
doi: 10.3389/fnene.2010.00014

Brain specificity of diffuse optical imaging: improvements from superficial signal regression and tomography

*Nicholas M. Gregg[1], Brian R. White[1,2], Benjamin W. Zeff[1], Andrew J. Berger[3] and Joseph P. Culver[1,2,4]**

[1] *Department of Radiology, Washington University in St. Louis, MO, USA*
[2] *Department of Physics, Washington University in St. Louis, MO, USA*
[3] *The Institute of Optics, University of Rochester, Rochester, NY, USA*
[4] *Department of Biomedical Engineering, Washington University in St. Louis, MO, USA*

Edited by:
David Boas, Massachusetts General Hospital, USA; Massachusetts Institute of Technology, USA; Harvard Medical School, USA

Reviewed by:
Jens Steinbrink, Charité - Universitätsmedizin Berlin, Germany
Yueli Chen, University of Connecticut, USA

***Correspondence:**
Joseph P. Culver, Department of Radiology, Optical Radiology Laboratory, Washington University in St. Louis, 4525 Scott Avenue, Box 8225, St. Louis, MO 63110, USA.
e-mail: culverj@wustl.edu

Functional near infrared spectroscopy (fNIRS) is a portable monitor of cerebral hemodynamics with wide clinical potential. However, in fNIRS, the vascular signal from the brain is often obscured by vascular signals present in the scalp and skull. In this paper, we evaluate two methods for improving *in vivo* data from adult human subjects through the use of high-density diffuse optical tomography (DOT). First, we test whether we can extend superficial regression methods (which utilize the multiple source–detector pair separations) from sparse optode arrays to application with DOT imaging arrays. In order to accomplish this goal, we modify the method to remove physiological artifacts from deeper sampling channels using an average of shallow measurements. Second, DOT provides three-dimensional image reconstructions and should explicitly separate different tissue layers. We test whether DOT's depth-sectioning can completely remove superficial physiological artifacts. Herein, we assess improvements in signal quality and reproducibility due to these methods using a well-characterized visual paradigm and our high-density DOT system. Both approaches remove noise from the data, resulting in cleaner imaging and more consistent hemodynamic responses. Additionally, the two methods act synergistically, with greater improvements when the approaches are used together.

Keywords: neuroimaging, biomedical optics, near-infrared spectroscopy, diffuse optical tomography, artifact removal, image quality

INTRODUCTION

Recent successes using functional near infrared spectroscopy (fNIRS) (Hebden, 2003; Yodh and Boas, 2003; Steinbrink et al., 2006) to study neonatal auditory and language development (Gervain et al., 2008; Saito et al., 2009) and pain responses (Bartocci et al., 2006) highlight the promise of extending fNIRS neuroimaging into populations that are difficult to scan with functional magnetic resonance imaging (fMRI). fNIRS uses near infrared sources and detectors to measure changes in absorption due neurovascular dynamics in response to brain activation, which allows a combination of portable instrumentation, wearable imaging caps, and more comprehensive hemodynamic imaging contrasts. These advantages make fNIRS ideally suited for a range of neuroscience applications in comparison with fMRI (Hebden, 2003; Yodh and Boas, 2003; Steinbrink et al., 2006). Nonetheless, limitations in brain specificity have prevented the technique from performing sophisticated cognitive neuroimaging studies that have become common in fMRI. As instrumentation has improved, the primary source of noise in fNIRS is physiological, arising from hemodynamics unrelated to the desired neural paradigm. While such spurious signals also exist in fMRI, their effect is exacerbated in fNIRS, since every measurement consists of light that has traveled from an extra-cranial source, through the scalp and skull, into the brain, and back out through the scalp and skull to reach a detector. Measurements therefore not only contain confounding signals from systemic sources, but also from hemodynamics localized to the superficial tissue layers. Even when combined into sparse (~3 cm) grids for topographic imaging, NIRS continuous-wave measurement systems have poor spatial sampling and are ill-equipped to discriminate these noise sources (Klaessens et al., 2005; Davis et al., 2006).

Though not yet widely used, progress with diffuse optical tomography (DOT) techniques has begun to provide higher functional neuroimaging performance than fNIRS while maintaining simple instrumentation (Benaron et al., 2000; Bluestone et al., 2001; Hebden et al., 2002; Hebden, 2003; Gibson et al., 2006; Joseph et al., 2006; Zeff et al., 2007; Wylie et al., 2009; White and Culver, 2010a,b). High-density DOT systems sample many source–detector pairs (SD-pairs) at multiple separations. The depth sensitivity of the measurements varies with the source–detector distance: closely spaced SD-pairs sample shallowly, while more widely spaced pairs penetrate deeply. This feature supports two methods for increasing the ability to discriminate signals arising from the brain. First, source–detector distances can be chosen such that some measurements are preferentially sensitive to scalp, skull, and systemic hemodynamic fluctuations, while others sample into the brain. Shallow measurements are then assumed to be a measure of the superficial and systemic noise and can be regressed from deeper pairs. The regressed data should produce a more accurate measure of hemodynamic trends unique to the brain (Saager and Berger, 2005, 2008). Second, overlapping measurements allow tomographic image reconstruction techniques (Barbour et al., 1990; Arridge, 1999; Yodh and Boas, 2003), resulting in an image of hemodynamic changes throughout a three-dimensional volume of the head, spatially separating contributions from deep and shallow sources.

Despite the conceptual illustrations of DOT's feasibility for neuroimaging and the knowledge that superficial contamination can lead to controversies of the interpretation of results (Jasdzewski et al., 2003; Boden et al., 2007) the majority of fNIRS studies are still conducted with sparse, single-distance imaging arrays. Initially the hesitation to switch to DOT was due in part to the complicated instrumentation requirements of early DOT systems. Now, as multiple simple neuroimaging DOT scanners are available, it is necessary to clearly demonstrate the possible improvements from these new techniques using *in vivo* imaging data. Thus, we here evaluate the ability of two methods, superficial signal regression (SSR) and tomography itself, to improve signal quality using *in vivo* measurements of the adult human visual cortex. Our goal is to answer three questions. (1) Can SSR techniques developed for sparse fNIRS arrays be adapted to high-density imaging arrays? This extension is non-trivial for two reasons. DOT inter-optode spacing is determined by the dense grid rather than by considerations of tissue sensitivity, and thus we might not be able to construct an ideal regressor. Also, since every deep measurement is not uniquely paired with a single shallow measurement, some other strategy to define a regression signal is required. Here, we evaluate a simple approach using a single spatially averaged regression signal for the entire measurement set. We will thus test whether this regression method is adequate. (2) How much signal-to-noise is gained by moving from sparse, isolated fNIRS measurements to DOT imaging? And, (3) is the depth-sectioning of DOT itself sufficient to separate multiple tissue layers, or does SSR in combination with DOT provide an added advantage?

MATERIALS AND METHODS

PROTOCOL

Data were acquired using a high-density DOT scanner, developed in-house (Zeff et al., 2007). The optode array consisted of 24 source positions (with light emitting diodes, LEDs, at both 750 and 850 nm) and 28 detector positions (coupled to avalanche photodiodes, APDs) designed to image the visual cortex (**Figure 1A**). Healthy adults were scanned after informed consent, as specified by the Washington University School of Medicine Human Research Protection Office. Subjects sat 70 cm away from a 19-inch LCD screen, and the DOT pad was secured over the visual cortex using hook-and-loop strapping. In this study, we used visual stimulation data acquired in adult humans since visual stimuli activate a well-localized region of cortex and have minimal systemic correlates [as opposed to motor stimuli that can be correlated with increases in blood pressure (Boden et al., 2007)]. Subjects were instructed to look at a crosshair, and a visual stimulus in the lower right visual field spanning a polar angle of 70° and a radial angle of 0.5–1.7° was presented, consisting of 10 s of counter-phase flashing at 10 Hz followed by 30 s of 50% gray screen (**Figure 1B**). A session had between four and eight stimulus repetitions. Data was acquired from a population of nine subjects. Two subjects were had a majority of channels with high signal variance and were excluded due to poor cap fit. Of the remaining seven subjects, one was scanned three times and another was scanned twice, for a total of 10 data sets included in this study.

SUPERFICIAL SIGNAL REGRESSION

Due to the high dynamic range of the DOT system, light is detected from several different source–detector distances. In this paper, we will focus on using the first- and second-nearest neighbors, referring to SD-pairs separated by 1.3 and 3.0 cm, respectively (**Figure 2A**). First-nearest neighbors sample predominantly superficially, sensitive

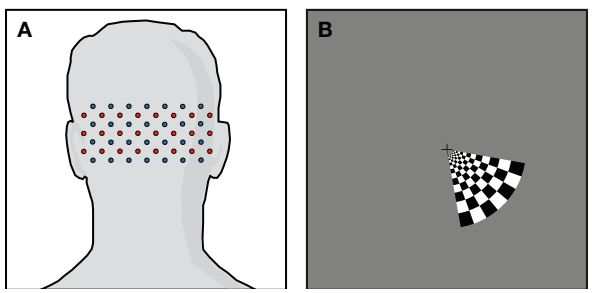

FIGURE 1 | High-density DOT study design. (A) Schematic of the high-density scanning grid placed over the occipital cortex. Sources are in red, detectors in blue. **(B)** The visual stimulus. Black and white regions alternate contrast at 10 Hz. This visual stimulus was presented in a block pattern, consisting of 10 s of visual activation followed by 30 s of 50% gray screen.

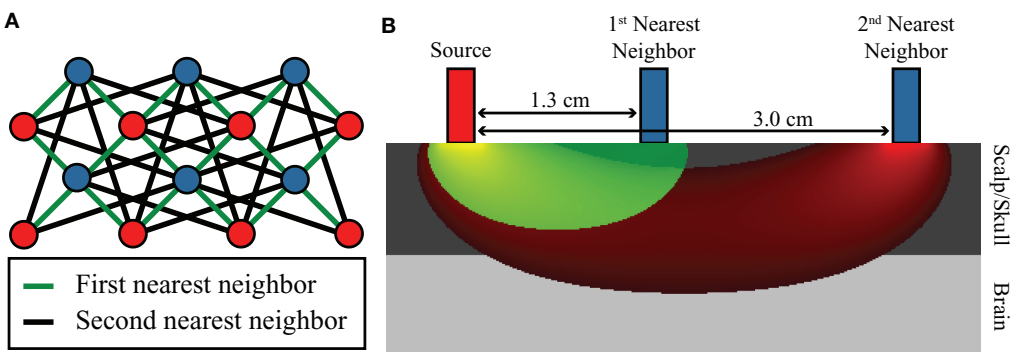

FIGURE 2 | High-density diffuse optical imaging. (A) Schematic of a subsection of a high-density grid. Red dots indicate source positions, and blue dots detector positions. Interconnecting lines define first- and second-nearest neighbor source–detector pairs. **(B)** Illustration of depth sensitivity of SD-pairs with respect to lateral separation using a photon migration simulation in a semi-infinite, homogeneous geometry using 3-mm diameter, exponentially decaying optodes. Sensitivity functions have been truncated at 5% intensity. The most closely spaced SD-pairs (sensitivity in green) sample superficial scalp/skull properties, while more widely spaced SD-pairs (sensitivity in red) are sensitive to both brain and scalp/skull signals.

to scalp and skull properties, while second-nearest neighbors sample into the brain as well as the scalp/skull (**Figure 2B**) (Dehghani et al., 2009). We thus assume that the second-nearest neighbors contain the desired brain signal obscured by noise: $S_{NN2} = S_{brain} + S_{noise}$. Regressing the noise from the second-nearest neighbor data will then, in principle, produce a more accurate measure of brain properties: $S_{NN2} - S_{noise} = S_{brain}$ (Saager and Berger, 2005).

Our hypothesis is that the first-nearest neighbors can be used to construct a measure of this noise, which consists of both global variations and any changes localized to the superficial tissue layers: $S_{NN1} \approx S_{noise} = S_{superficial} + S_{global}$. Specifically, our noise signal is produced by spatially averaging the first-nearest neighbor signals: $y_n = (1/N_{nn})\Sigma_{j=1}^{N_{nn}} y_j$. Here, y_j is the jth first-nearest neighbor pair measurement, N_{nn} is the number of first-nearest neighbors in the array, and y_n is the superficial noise signal. This formulation contains two deviations from sparse fNIRS techniques. First, while one might desire a shorter first-nearest neighbor separation (~0.5 cm) (Saager and Berger, 2008), our separation is constrained by the optode geometry needed for an imaging array. Second, rather than having an individual short-separation regressor for each deep measurement, we have averaged all first-nearest neighbors. These two changes should have the effect of partially mitigating each other, since even if some first-nearest neighbors have small sensitivity to the brain activation, using a large spatial average for the regressor means that local brain activations will not appear in the regressor (see the discussion for more on these effects).

The contribution of this noise signal to all measurements is removed by regression: $y_{i,brain} = y_i - \alpha_i y_n$, where α_i is a temporal correlation factor $\alpha_i = \langle y_i, y_n \rangle / \langle y_n, y_n \rangle$, y_i is the ith unmodified SD-pair time course, and $y_{i,brain}$ is the same SD-pair after SSR. Here the brackets, $<a,b>$ indicate calculation of the inner product between two time courses a and b. Note that this regression against y_n is also performed on each of the individual first-nearest neighbor channels, which will still contain individual variation. When data were processed as SD-pair measures of absorption change (i.e., fNIRS: section "Modified Beer-Lambert law (fNIRS)") this remaining variance in the first-nearest neighbors is not relevant, as we examine only individual second-nearest neighbor channels. However, when performing three-dimensional tomographic reconstructions of volumes of absorbance change (i.e., DOT: section "Diffuse optical tomography reconstructions"), the first-nearest neighbors (with their remaining variance) are used in the reconstruction and contribute to the image.

MODIFIED BEER-LAMBERT LAW (fNIRS)

Measurements of absorbance change were produced from the log-ratio of raw SD-pair data. A band-pass filter (0.02–0.5 Hz) removed pulse and long-term drift. Using the modified Beer-Lambert law (MBL), $\Delta\mu_a = \Delta A / L \cdot dpf$, changes in absorption were determined from absorbance. Here ΔA is the change in absorbance, L is the separation between this measurement's source and detector, and dpf is the differential path-length factor (a term that corrects for light being multiply scattered within the head, and thereby traveling a longer distance than the physical source detector separation). We used values for dpf derived from the work of Duncan et al. (1996) of 5.11 cm^{-1} for 750 nm and 4.67 cm^{-1} for 850 nm.

DIFFUSE OPTICAL TOMOGRAPHY RECONSTRUCTIONS

Diffuse optical tomography reconstructions were generated using a hemispherical head model (Zeff et al., 2007). A finite-element, forward light model (Dehghani et al., 2003) was used to generate a sensitivity matrix for the source/detector array. Using a direct inversion of the sensitivity matrix, SD-pair absorbance measurements were converted into tomographic maps of absorption change (Zeff et al., 2007). A hemispherical shell through the superficial cerebral cortex (1-cm thick centered at a 1-cm depth) was isolated from the full 3D reconstruction for display (shown as a posterior coronal projection, as if looking at the brain from behind with the scalp and skull removed). We can thus spatially remove superficially reconstructed hemodynamics.

HEMOGLOBIN SPECTROSCOPY

For both SD-pair measures and tomographic maps of absorption change, we used the extinction coefficients of oxy- (HbO_2) and deoxyhemoglobin (HbR) to convert from changes in the absorption to concentration changes: ΔHbO_2, ΔHbR, and ΔHbT (total hemoglobin). The extinction coefficients used for HbO_2 are 1.36 and 3.40 $mM^{-1}\,cm^{-1}$ and for HbR are 2.39 and 1.85 $mM^{-1}\,cm^{-1}$ (for 750 and 850 nm, respectively). These coefficients were generated by applying a weighted average over the spectra of our LEDs (Gaussian FWHM ~60 and 45 nm, respectively) to the table of extinction coefficients found in Wray et al. (1988).

EVALUATION OF CONTRAST-TO-NOISE

To quantify the performance of the different neuroimaging methods, we evaluated the contrast-to-noise ratio (CNR) of the retrieved hemodynamic response. Contrast is defined as the peak-height of response (averaged over multiple stimulus presentations). We characterized measurement noise through the standard deviation in the pre-stimulus baseline. We use baseline noise rather than variation in the activation height, since peak height could change from block to block due to factors such as subject attentiveness and direction of gaze that are independent from system or physiological noise. We then judge a method's effectiveness by its improvement in CNR versus fNIRS/MBL processing without SSR. Additionally, both DOT methods create images, which we judge spatially by looking at contrast and noise.

RESULTS

Our goal was to compare the ability to distinguish brain activations using four analysis methods: (1) SD-pair data processed with the MBL without any additional processing, (2) SD-pair data processed using the MBL with SSR, (3) DOT reconstructions, and (4) DOT reconstructions with SSR. First, we examined time traces of the hemodynamic response to the visual stimulus from a single, representative second-nearest neighbor SD-pair generated with and without SSR (methods 1 and 2). If no SSR processing is applied to MBL data, then it is difficult to distinguish individual hemodynamic activations (**Figure 3A**). One reason that this data fails to show canonical responses is that it also contains superficial and systemic variation; using high-density optode arrays we can measure the superficial noise signal (**Figure 3B**). Using SSR to remove this signal from the second-nearest neighbor SD-pair produced a consistent canonical hemodynamic response (**Figure 3C**). While

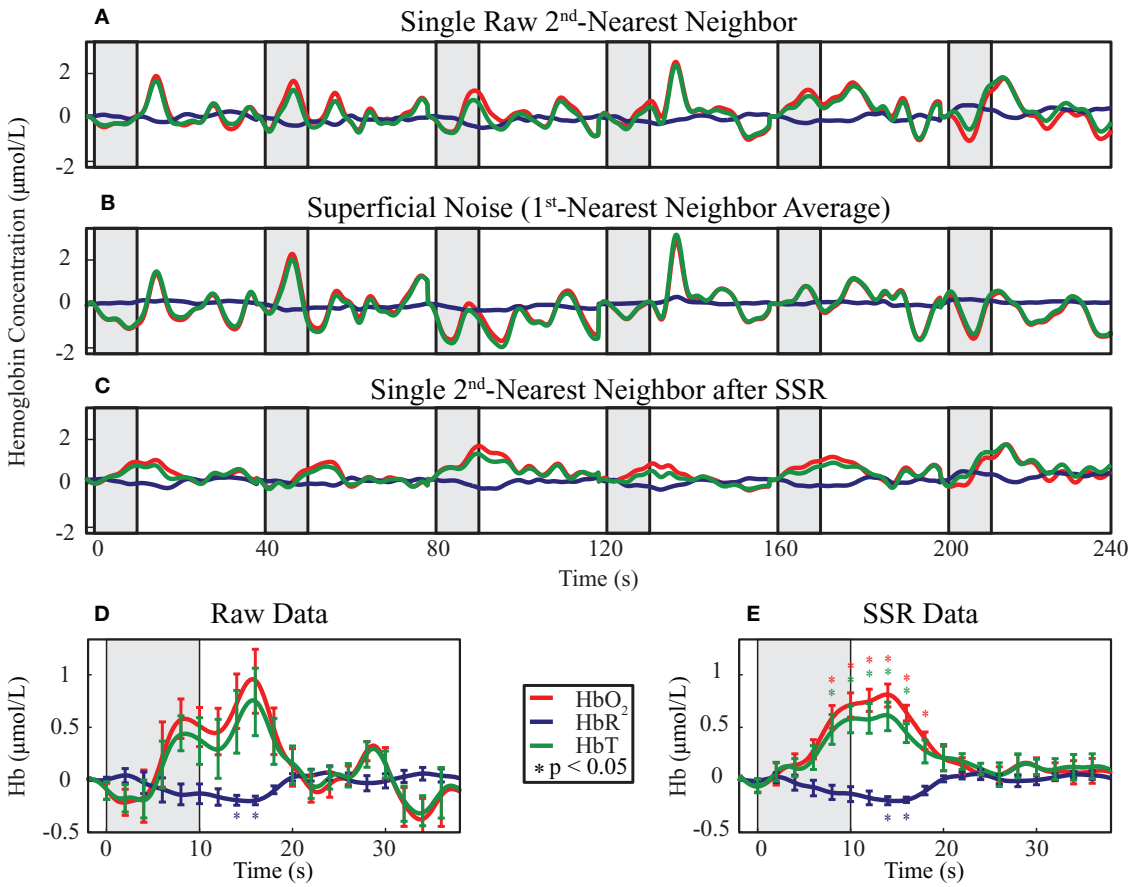

FIGURE 3 | Evaluation of the effect of SSR on SD-pair data during visual stimulation. The gray shaded regions indicate visual stimulus. **(A–C)** Time traces of the hemodynamic response from six consecutive blocks with ΔHbO_2 in red, ΔHbR in blue, and ΔHbT in green. The superficial noise signal **(B)** is regressed from a raw second-nearest neighbor SD-pair **(A)**, producing SSR data **(C)**. Note the consistent clean shape of activation after SSR. **(D,E)** Block-averaged time traces of **(A)** and **(C)**, respectively. Error bars mark standard deviation and asterisks indicate statistically significant deviation from baseline. Note the reduced noise and improved CNR of the activation after SSR.

the expected response shape is visible after block-averaging without SSR (**Figure 3D**), with SSR, activations due to single stimulus presentations are apparent even before block-averaging. Block-averaged SSR data (**Figure 3E**) had reduced noise (error bars denote standard error), improved statistical significance (asterisks mark significant deviation from baseline $p < 0.05$ based on a comparison to the pre-stimulus baseline of *time* = −2 s with a two-tailed *t*-test), and qualitatively improved response shape. In this individual, the responses for both HbO_2 and HbT were non-significant in the data prior to SSR. This improvement in signal quality is quantified through an approximately two-fold improvement in CNR (**Table 1**).

Tomographic images of ΔHbO_2, ΔHbR, and ΔHbT were generated with and without SSR. Reconstructed images of raw ΔHbO_2 data during the peak functional response (13 s after stimulus onset averaged over one second) show inconsistent responses from trial to trial (**Figure 4A**, top row). In contrast, the images of data that have SSR processing show similar activations after each stimulus presentation (**Figure 4A**, bottom row). While both activation maps appear similar after block-averaging (**Figure 4B**), the greater noise in the raw data is reflected in an image of variance over the multiple trials (**Figure 4C**). Noise reduction due to SSR can also be quantified in voxel time traces chosen from the area of peak activation (**Figure 4D**). These traces (**Figures 4E,F**) show the ability of SSR (as with SD-pair data) to reduce noise, improve statistical significance, and qualitatively improve the shape of the hemodynamic response. Comparing CNR of the various methods shows that there are gains through the use of DOT alone, but there is a synergistic effect between SSR and DOT with the signal quality being highest after the utilization of both methods (**Table 1**).

The above exemplary results can be generalized to the group data demonstrating consistent CNR improvement through the use of the SSR method and DOT (**Figure 5**). On average, tomographic image reconstruction and SSR improve CNR in all contrasts. However, some subjects or individual contrasts within a subject fail to show improvement when only one of these methods is used (in no case however, does SSR drastically decrease the data's CNR). In combination, the two depth-discrimination methods improve the CNR of all subjects and all contrasts (with the exception of HbR in one individual). On average, sequential use of SSR and tomography provide a 2.24-, 2.18-, and 3.01-fold improvement in CNR for HbO_2, HbR, and HbT, respectively.

Table 1 | Improvement in the contrast-to-noise ratio (CNR) following the use of SSR and DOT.

Method	CNR			Fold-improvement versus MBL		
	ΔHbO_2	ΔHbR	ΔHbT	ΔHbO_2	ΔHbR	ΔHbT
MBL	3.36	2.70	3.01	N/A	N/A	N/A
MBL with SSR	6.96	5.35	4.79	2.07	1.99	1.59
DOT	4.09	6.34	3.43	1.21	2.35	1.13
DOT with SSR	7.78	7.51	5.26	2.32	2.78	1.75

While both SSR and DOT improve CNR relative to standard fNIRS techniques (the modified Beer-Lambert law), the combination of DOT and SSR results in the lowest noise. This improvement holds for all three contrasts.

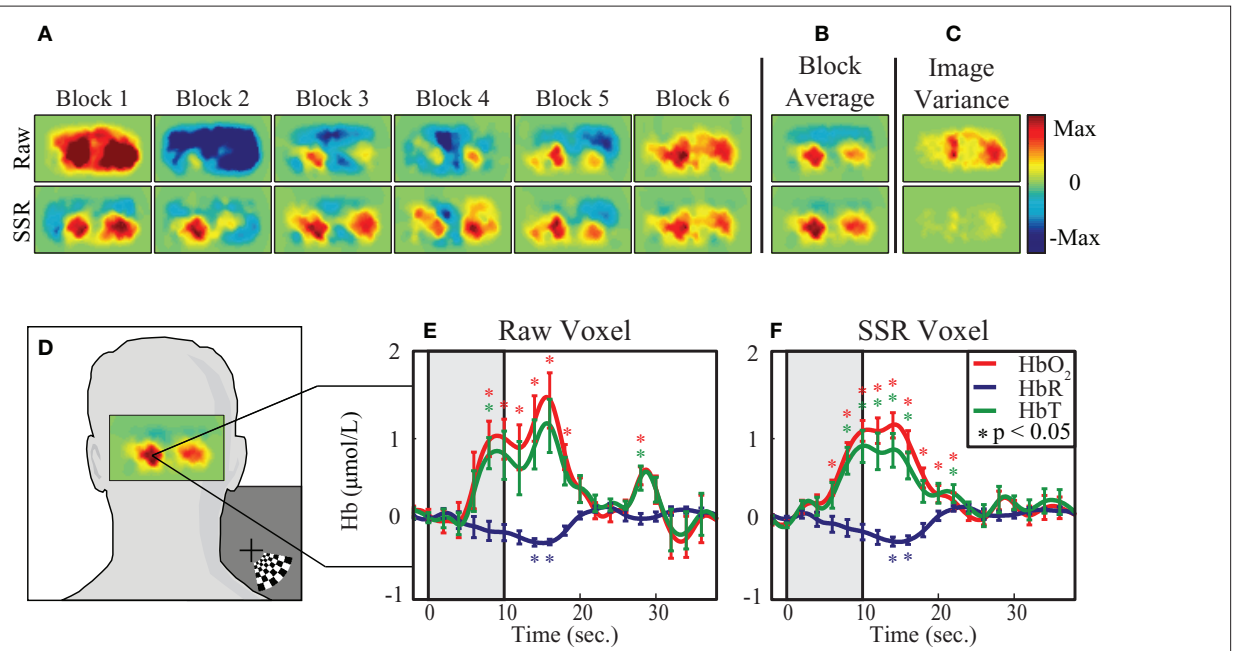

FIGURE 4 | Evaluation of the effect of SSR on imaged data. **(A)** Reconstructed images from a 1-cm thick shell of cortex. Each plot shows 1 s of data at peak activation from six consecutive blocks, without SSR (top row) and with SSR (bottom row) superficial signal regression. **(B)** The block average of the six blocks in **(A)**. **(C)** Image variance is displayed as the standard deviation of each pixel at peak activation across all blocks. Note that while the block-averages appear similar, the image variance plot captures the inconsistency in the raw (non-SSR) data. **(D)** Reconstructed image of cortical response to visual stimulus, overlaid on adult head to show direction of view and the voxel chosen for time trace analysis. **(E,F)** Block-averaged time traces generated from a single voxel of reconstructed data, with and without SSR. Error bars mark standard deviation and asterisks indicate statistically significant deviation from baseline.

DISCUSSION

Limitations in the signal quality of optical signals have hampered the acceptance of fNIRS in clinical practice and cognitive neuroscience research. To date, a number of groups have pursued varying techniques to regress or discriminate physiological noise from optically acquired functional brain signals. One potential method is to use direct peripheral measurements of the hypothesized noise sources (e.g., via a pulse-oximeter or respiration belt), which can then be regressed from the acquired data [as is commonly performed in fMRI (Glover et al., 2000)]. This approach, however, is limited in the number of noise sources it can measure, and additionally it assumes a similarity between blood flow in the periphery and in the head that may not hold in practice. Our lab, as well as others, have used statistical techniques that assume orthogonality or independence between functional brain signals and physiological noise to identify these components (Morren et al., 2004; Zhang et al., 2005; Markham et al., 2009). An additional method for regression is the use of adaptive filtering techniques (Zhang et al., 2007, 2009), which have been used in single-source, multi-detector geometries.

In this paper, we have implemented and evaluated a theoretically and computationally simple regression procedure within the context of a high-density DOT imaging array. This method is amenable to real-time imaging and has been shown to be capable of CNR improvement in each hemoglobin species for ≥ 80% of subjects, both in SD-pair data and in image reconstructions. The use of tomography individually is still helpful, but less impressive. This result might be due to the fact that we are only using first- and second-nearest neighbors in the present analysis. As there is substantial overlap in the sensitivities of these two measurement distances, we might predict that their ability to completely

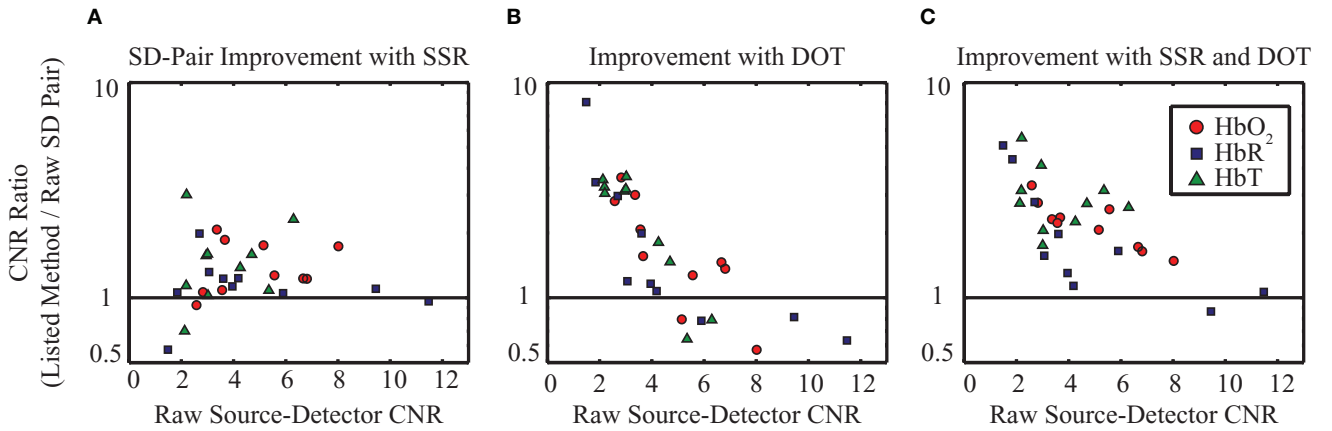

FIGURE 5 | Evaluation of the signal quality of SSR and DOT versus MBL across ten data sets (seven subjects, with some scanned multiple times). All graphs plot the fold-improvement in CNR versus the MBL CNR. ΔHbO_2, ΔHbR, and ΔHbT are denoted in red circles, blue squares, and green triangles, respectively. **(A)** Improvement in CNR due to the use of SSR on SD-pairs. **(B)** Improvement in CNR through the use of tomographic image reconstruction (chosen at the voxel with maximal response). **(C)** Improvement in CNR due to the combined use of SSR and image reconstruction. Note that it is the subjects with the worst initial CNR (farthest to the left) that benefit the most from the evaluated methods.

distinguish two depths to be limited. We expect that future DOT systems with sufficiently higher signal-to-noise to include further source–detector distances would have better depth profiling (Dehghani et al., 2009). The combined effect of SSR and image reconstruction improves the CNR in all 10 datasets for HbO_2 and HbT, and nine of 10 datasets for HbR. SSR and DOT have a synergistic effect to improve the depth-sectioning capabilities of optical imaging.

Additionally, we see that it is the subjects with the worst initial SNR that have the largest improvement after the use of SSR and DOT. This result is possibly because there are two contributions to noise: physiological noise and instrument noise. Since we expect instrument noise to be relatively constant between studies, the variance between subjects results predominantly from the amount of physiological noise present. Subjects with initially poor CNR (and thus high physiological noise) will benefit most from the noise removal techniques described here. Subjects with initially low physiological noise have CNRs limited by instrument noise. We would then expect the present techniques (which are designed to solely remove physiological noise) to have little effect on the CNR of these subjects.

It is important to note that what one refers to as "physiological noise" varies with the context of the experiment. When performing a functional activation study (as here), many normal physiological processes (including pulse, respiration, blood pressure oscillations, and spontaneous neural activity) all qualify as noise as they are undesired variance not related to your experimental paradigm. However, in other circumstances it could be the "noise" that you wish to measure. Resting-state functional connectivity (Biswal et al., 1995; Fox et al., 2005; Fox and Raichle, 2007; White et al., 2009) was originally dismissed as noise in fMRI signals. Additionally, one can extract important information through the examination of optical measurement of pulse and respiratory fluctuations (Wolf et al., 1997; Franceschini et al., 2002, 2006). The SSR method in this paper was designed for examination of task-evoked neural activity; care should be taken in choosing the appropriate noise removal method for each experiment.

While a linear regression should be less powerful than an adaptive filter, our results are more consistent and comprehensive than those previously presented for adaptive filters. Zhang et al. (2009) found that with their filter "71% of the [HbO_2] measurements revealed CNR improvements after adaptive filtering, with a mean improvement of 60%. No CNR improvement was observed for [HbR]." In contrast, our improvement of about 200% in CNR is seen across all hemoglobin species. These results show that effective filtering can be obtained with simple, easily implemented algorithms. However, it also demonstrates that more research needs to be done on the nature of physiological interference in optical signals. We expect that greater knowledge of the sensitivities of different contrasts to physiological processes will yield even higher performing filter algorithms.

While one of the advantages of the proposed method is its ease of use, this simplicity does come at the cost of making assumptions that may not hold in all cases. One limitation is that there are likely several sources that contribute to the measured noise and that the linear combination present in the first-nearest neighbor pairs may not be the same as the linear combination in the second-nearest neighbors. In such a case, simple regression cannot remove all noise, but still has been shown to provide noise-reduction benefits (Saager and Berger, 2008). An extension of the current technique would be a multiple linear regression method combined with direct measurements of other systemic signals (e.g., heart rate, breathing rate, and arterial blood pressure), which would, in principle, provide still better performance. A second limitation is that the averaged first-nearest neighbor signal might include some component sensitive to the brain. In the present adult study this effect is minimal since the brain sensitivity of first-nearest neighbors is low (<5%) and the activations were localized. However, in other applications, such as imaging infants, where the scalp and skull are much thinner and

activations cannot be as easily localized, one would have to take care that the regression did not remove too much of the desired brain response. A third concern is that the superficial noise signal might vary over the surface of head. In this case, one could determine a local measure of the noise using nearby first-nearest neighbors. However, although future work will develop better algorithms, the present paper shows that current data can still be dramatically improved with simply implemented methods.

The average CNR improvement (with the use of both SSR and DOT) of approximately 2.5-fold in hemoglobin absorption data corresponds to a greater than six-fold reduction in the necessary acquisition time required for an equivalent signal quality (assuming that CNR scales as the square root of the total scan time). Decreased acquisition time will have two complementary effects that aid the use of fNIRS in novel environments, such as with young children and hospitalized patients. With increased signal quality, one needs to rely less on the long-term cooperation of the subject and can obtain useful data even if only short scanning windows are available. Conversely, for a fixed session length, decreased time per stimulus allows the use of multiple stimulus paradigms and attempts to decode more complex brain functionality.

We have shown that high-density DOT's overlapping, depth-dependent measurements of the head and brain can be leveraged to perform SSR in addition to three-dimensional image reconstructions. Both of these methods reduce the effect of physiological noise in the acquired neuroimaging data. The extension of SSR to DOT data provides an additional benefit beyond DOT's inherent depth-sectioning capabilities. Improvements in repeatability and signal quality advance DOT towards real-time imaging and greater utility in basic neuroscience and clinical care.

ACKNOWLEDGMENTS

This research was supported in part by NIH grants, R01-EB009233 (Joseph P. Culver), R21-HD057512 (Joseph P. Culver), R21-EB007924 (Joseph P. Culver), T90-DA022871 (Brian R. White), and Cephalogics LLC.

REFERENCES

Arridge, S. R. (1999). Optical tomography in medical imaging. *Inverse Probl.* 15, R41–R93.

Barbour, R. L., Graber, H., Aronson, R., and Lubowsky, J. (1990). Model for 3-D optical imaging of tissue. *IGARSS* 2, 1395–1399.

Bartocci, M., Bergqvist, L. L., Lagercrantz, H., and Anand, K. J. S. (2006). Pain activates cortical areas in the preterm newborn brain. *Pain* 122, 109–117.

Benaron, D. A., Hintz, S. R., Villringer, A., Boas, D., Kleinschmidt, A., Frahm, J., Hirth, C., Obrig, H., van Houten, J. C., Kermit, E. L., Cheong, W. F., and Stevenson, D. K. (2000). Noninvasive functional imaging of human brain using light. *J. Cereb. Blood Flow Metab.* 20, 469–477.

Biswal, B., Yetkin, F. Z., Haughton, V. M., and Hyde, J. S. (1995). Functional connectivity in the motor cortex of resting human brain using echo-planar MRI. *Magn. Reson. Med.* 34, 537–541.

Bluestone, A. Y., Abdoulaev, G., Schmitz, C. H., Barbour, R. L., and Hielscher, A. H. (2001). Three-dimensional optical tomography of hemodynamics in the human head. *Opt. Express* 9, 272–286.

Boden, S., Obrig, H., Kohncke, C., Benav, H., Koch, S. P., and Steinbrink, J. (2007). The oxygenation response to functional stimulation: is there a physiological meaning to the lag between parameters? *Neuroimage* 36, 100–107.

Davis, S. L., Fadel, P. J., Cui, J., Thomas, G. D., and Crandall, C. G. (2006). Skin blood flow influences near-infrared spectroscopy-derived measurements of tissue oxygenation during heat stress. *J. Appl. Physiol.* 100, 221–224.

Dehghani, H., Pogue, B. W., Poplack, S. P., and Paulsen, K. D. (2003). Multiwavelength three-dimensional near-infrared tomography of the breast: initial simulation, phantom, and clinical results. *Appl. Opt.* 42, 135–145.

Dehghani, H., White, B. R., Zeff, B. W., Tizzard, A., and Culver, J. P. (2009). Depth sensitivity and image reconstruction analysis of dense imaging arrays for mapping brain function with diffuse optical tomography. *Appl. Opt.* 48, D137–D143.

Duncan, A., Meek, J. H., Clemence, M., Elwell, C. E., Fallon, P., Tyszczuk, L., Cope, M., and Delpy, D. T. (1996). Measurement of cranial optical path length as a function of age using phase resolved near infrared spectroscopy. *Pediatr. Res.* 39, 889–894.

Fox, M. D., and Raichle, M. E. (2007). Spontaneous fluctuations in brain activity observed with functional magnetic resonance imaging. *Nat. Rev. Neurosci.* 8, 700–711.

Fox, M. D., Snyder, A. Z., Vincent, J. L., Corbetta, M., Van Essen, D. C., and Raichle, M. E. (2005). The human brain is intrinsically organized into dynamic, anticorrelated functional networks. *Proc. Natl. Acad. Sci. U.S.A.* 102, 9673–9678.

Franceschini, M. A., Boas, D. A., Zourabian, A., Diamond, S. G., Nadgir, S., Lin, D. W., Moore, J. B., and Fantini, S. (2002). Near-infrared spiroximetry: noninvasive measurements of venous saturation in piglets and human subjects. *J. Appl. Physiol.* 92, 372–384.

Franceschini, M. A., Joseph, D. K., Huppert, T. J., Diamond, S. G., and Boas, D. A. (2006). Diffuse optical imaging of the whole head. *J. Biomed. Opt.* 11, 054007.

Gervain, J., Macagno, F., Cogoi, S., Pena, M., and Mehler, J. (2008). The neonate brain detects speech structure. *Proc. Natl. Acad. Sci. U.S.A.* 105, 14222–14227.

Gibson, A. P., Austin, T., Everdell, N. L., Schweiger, M., Arridge, S. R., Meek, J. H., Wyatt, J. S., Delpy, D. T., and Hebden, J. C. (2006). Three-dimensional whole-head optical tomography of passive motor evoked responses in the neonate. *Neuroimage* 30, 521–528.

Glover, G. H., Li, T.-Q., and Ress, D. (2000). Image-based method for retrospective correction of physiological motion effects in fMRI: retroicor. *Mag. Reson. Med.* 44, 162–167.

Hebden, J. C. (2003). Advances in optical imaging of the newborn infant brain. *Pathophysiology* 40, 501–510.

Hebden, J. C., Gibson, A., Yusof, R. M., Everdell, N., Hillman, E. M. C., Delpy, D. T., Arridge, S. R., Austin, T., Meek, J. H., and Wyatt, J. S. (2002). Three-dimensional optical tomography of the premature infant brain. *Phys. Med. Biol.* 47, 4155–4166.

Jasdzewski, G., Strangman, G., Wagner, J., Kwong, K. K., Poldrack, R. A., and Boas, D. A. (2003). Differences in the hemodynamic response to event-related motor and visual paradigms as measured by near-infrared spectroscopy. *Neuroimage* 20, 479–488.

Joseph, D. K., Huppert, T. J., Franceschini, M. A., and Boas, D. A. (2006). Diffuse optical tomography system to image brain activation with improved spatial resolution and validation with functional magnetic resonance imaging. *Appl. Opt.* 45, 8142–8151.

Klaessens, J. H. G. M., Hopman, J. C. W., Liem, K. D., van Os, S. H. G., and Thijssen, J. M. (2005). Effects of skin on bias and reproducibility of near-infrared spectroscopy measurement of cerebral oxygenation changes in porcine brain. *J. Biomed. Opt.* 10, 044003.

Markham, J., White, B. R., Zeff, B. W., and Culver, J. P. (2009). Blind identification of evoked human brain activity with independent component analysis of optical data. *Hum. Brain Mapp.* 30, 2382–2392.

Morren, G., Wolf, M., Lemmerling, P., Wolf, U., Choi, J. H., Gratton, E., De Lathauwer, L., and Van Huffel, S. (2004). Detection of fast neuronal signals in the motor cortex from functional near infrared spectroscopy measurements using independent component analysis. *Med. Biol. Eng. Comput.* 42, 92–99.

Saager, R., and Berger, A. (2008). Measurement of layer-like hemodynamic trends in scalp and cortex: implications for physiological baseline suppression in functional near-infrared spectroscopy. *J. Biomed. Opt.* 13, 034017.

Saager, R. B., and Berger, A. J. (2005). Direct characterization and removal of interfering absorption trends in two-layer turbid media. *J. Opt. Soc. Am. A* 22, 1874–1882.

Saito, Y., Fukuhara, R., Aoyama, S., and Toshima, T. (2009). Frontal brain activation in premature infants' response to auditory stimuli in neonatal intensive care unit. *Early Hum. Dev.* 85, 471–474.

Steinbrink, J., Villringer, A., Kempf, F. C. D., Haux, D., Boden, S., and Obrig, H. (2006). Illuminating the BOLD

signal: combined fMRI-fNIRS studies. *Magn. Reson. Imaging* 24, 495–505.

White, B. R., and Culver, J. P. (2010a). Phase-encoded retinotopy as an evaluation of diffuse optical neuroimaging. *Neuroimage* 49, 568–577.

White, B. R., and Culver, J. P. (2010b). A quantitative evaluation of high-density diffuse optical tomography: in vivo resolution and mapping performance. *J. Biomed. Opt*. 15, 026006.

White, B. R., Snyder, A. Z., Cohen, A. L., Petersen, S. E., Raichle, M. E., Schlaggar, B. L., and Culver, J. P. (2009). Resting-state functional connectivity in the human brain revealed with diffuse optical tomography. *Neuroimage* 47, 148–156.

Wolf, M., Duc, G., Keel, M., and Niederer, P. (1997). Continuous noninvasive measurements of cerebral arterial and venous oxygen saturation at the bedside in mechanically ventilated neonates. *Crit. Care Med.* 9, 1579–1582.

Wray, S., Cope, M., Delpy, D. T., Wyatt, J. S., and Reynolds, E. O. R. (1988). Characteristics of the near infrared absorption spectra of cytochrome aa3 and haemoglobin for the non-invasive monitoring of cerebral oxygenation. *Biochim. Biophys. Acta* 933, 184–192.

Wylie, G. R., Graber, H., Voelbel, G. T., Kohl, A. D., DeLuca, J., Pei, Y., Xu, Y., and Barbour, R. L. (2009). Using covariation in the Hb signal to detect visual activation: a near infrared spectroscopy study. *Neuroimage* 47, 473–481.

Yodh, A. G., and Boas, D. A. (2003). "Functional imaging with diffusing light," in *Biomedical Photonics*, ed. T. Vo-Dinh (Boca Raton, FL: CRC Press), 21–1–21–45.

Zeff, B. W., White, B. R., Dehghani, H., Schlaggar, B. L., and Culver, J. P. (2007). Retinotopic mapping of adult human visual cortex with high-density diffuse optical tomography. *Proc. Natl. Acad. Sci. U.S.A.* 104, 12169–12174.

Zhang, Q., Brown, E. N., and Strangman, G. E. (2007). Adaptive filtering to reduce global interference in evoked brain activity detection: a human subject case study. *J. Biomed. Opt*. 12, 064009.

Zhang, Q., Strangman, G. E., and Ganis, G. (2009). Adaptive filtering to reduce global interference in non-invasive NIRS measures of brain activation: how well and when does it work? *Neuroimage* 45, 788–794.

Zhang, Y. H., Brooks, D. H., Franceschini, M. A., and Boas, D. A. (2005). Eigenvector-based spatial filtering for reduction of physiological interference in diffuse optical imaging. *J. Biomed. Opt.* 10, 011014.

Conflict of Interest Statement: Joseph P. Culver and Washington University have financial interests in Cephalogics LLC based on a license of related technology by the University to Cephalogics LLC.

Received: 26 February 2010; paper pending published: 30 March 2010; accepted: 11 June 2010; published online: 14 July 2010. Citation: Gregg NM, White BR, Zeff BW, Berger AJ and Culver JP (2010) Brain specificity of diffuse optical imaging: improvements from superficial signal regression and tomography. Front. Neuroenerg. ***2****:14. doi: 10.3389/fnene.2010.00014*

frontiers in
NEUROENERGETICS

ORIGINAL RESEARCH ARTICLE
published: 30 July 2010
doi: 10.3389/fnene.2010.00019

The biological effect of contralateral forepaw stimulation in rat focal cerebral ischemia: a multispectral optical imaging study

*Janos Luckl[1†], Wesley Baker[2], Zheng-Hui Sun[1], Turgut Durduran[2‡], Arjun G. Yodh[2] and Joel H. Greenberg[1]**

[1] Department of Neurology, University of Pennsylvania, Philadelphia, PA, USA
[2] Department of Physics and Astronomy, University of Pennsylvania, Philadelphia, PA, USA

Edited by:
David Boas, Massachusetts General Hospital, USA; Massachusetts Institute of Technology, USA; Harvard Medical School, USA

Reviewed by:
Ilknur Ay, Massachusetts General Hospital, USA
Bruno Weber, University of Zurich, Switzerland

****Correspondence:***
Joel H. Greenberg, Cerebrovascular Research Center, Department of Neurology, University of Pennsylvania, 415 Stemmler Hall, 3450 Hamilton Walk, Philadelphia, PA 19104-6063, USA.
e-mail: joel@upenn.edu
Present address:
[†]Department of Experimental Neurology, Charite-Universitatsmedizin Berlin, Berlin, Germany.
[‡] ICFO- Institut de Ciències Fotòniques, Mediterranean Technology Park, 08860 Castelldefels (Barcelona), Spain.

Our group has already published the possible neuroprotective effect of contralateral forepaw stimulation in temporary focal ischemia in a study. However, the background is still unclear. In the present study we investigated the possible mechanism by monitoring focal ischemia with multispectral [laser speckle, imaging of intrinsic signals (OIS)] imaging. Sprague–Dawley rats were prepared using 1.2% isoflurane anesthesia. The middle cerebral artery was occluded by photothrombosis (4 mW) and the common carotid artery was ligated permanently. Physiological variables were constantly monitored during the experiment. A 6 × 6 mm area centered 3 mm posterior and 4 mm lateral to Bregma was thinned for laser speckle and OIS imaging. Nine circular regions of interests (0.3 mm in diameter) were evenly spaced on the speckle contrast image for the analysis of peri-infarct flow transients, blood flow, and metabolic changes. Both the sham (n = 7) and forepaw-stimulated animals (n = 7) underwent neurological examinations 24 h after ischemia at which point all animals were sacrificed and the infarct size was determined by triphenyltetrazolium chloride. The physiological variables were in normal range and the experimental protocol did not cause significant differences between groups. Both the neurological scores (sham: 3.6 ± 1.7, stimulated: 4.3 ± 1.4) and the infarct volume (sham: 124 ± 39 mm^3, stimulated: 147 ± 47 mm^3) did not show significant differences between groups. The forepaw stimulation did not increase the intra-ischemic flow neither over the penumbral or the peri-ischemic area. However, the hemoglobin transients related metabolic load ($CMRO_2$) was significantly lower ($p < 0.001$) while the averaged number of hyperemic flow transients were significantly (p = 0.013) higher in the forepaw (sham: 3.5 ± 2.2, stimulated: 7.0 ± 2.3) stimulated animals.

Keywords: optical imaging, focal cerebral ischemia, forepaw stimulation, middle cerebral artery occlusion, photothrombosis, speckle contrast, OIS, flow transients

INTRODUCTION

Although many compounds have been investigated in cerebral ischemia, none have so far proven clinically useful in humans. Therefore, there is an intense interest in developing novel, non-pharmacological therapies. Techniques, such as the production of hypothermia (Yanamoto et al., 1999) and hyperoxemia (Shin et al., 2006), have been investigated intensively, but it remains to be seen how they transfer from laboratory to bedside. The use of electrical/magnetic stimulation represent a new direction in the treatment of various diseases of the central nervous system (CNS). Neuromuscular electrical stimulation (Chae et al., 2008), repetitive transcranial magnetic stimulation (rTMS) (Williams et al., 2009), and epidural cortical stimulation (Brown et al., 2006) all seem to be promising in the rehabilitation (improving motor function and pain) of stroke patients. The successful application of post-stroke stimulation raises the question as to whether patients could benefit from stimulation during acute cerebral ischemia. We previously showed that contralateral forepaw stimulation can reduce tissue injury if administered during temporary cerebral ischemia in the rat (Burnett et al., 2006), and a recent study found that vagal nerve stimulation during ischemia also reduces damage from transient cerebral ischemia (Ay et al., 2009). Since our previous study (Burnett et al., 2005) used only a single laser Doppler (LD) probe to monitor the intra-ischemic events, changes in cerebral blood flow (CBF) due to stimulation remains to be determined despite the promising results.

In the past decade optical imaging [laser speckle imaging (LSI) and imaging of intrinsic signals (OIS)] has became a powerful tool for collecting information on cortical perfusion and metabolism with excellent temporal and spatial resolution (Dunn et al., 2005). In the present study we have used multispectral (LSI and OIS) imaging to determine if contralateral forepaw stimulation in rat has any detectable biological effect on intra-ischemic CBF and/or flow/hemoglobin transients (Strong et al., 2007; Jones et al., 2008; Luckl et al., 2009) during focal brain ischemia.

MATERIALS AND METHODS

PHOTOCHEMICALLY INDUCED DISTAL MIDDLE CEREBRAL ARTERY OCCLUSION

All procedures performed were approved by the Institutional Animal Care and Use Committee of the University of Pennsylvania. Adult male Sprague–Dawley rats (290–320 g) were anesthetized with 4% isoflurane for induction in a mixture of 50% nitrous oxide and 50% oxygen and maintained on 1.2–1.3%

isoflurane (1.0–1.25 MAC) in 70% nitrous oxide and 30% oxygen during surgery and throughout the study. Body temperature was monitored by a rectal probe and maintained at 37.5 ± 0.2°C with a heating blanket regulated by a homeothermic blanket control unit (Harvard Apparatus Limited Holliston, MA, USA). A polyethylene catheter (PE-50) was placed into the tail artery for the measurement of arterial blood pressure and for blood gas sampling. Blood pressure was continuously monitored using a pressure transducer and recorded on a computer based recording system (PowerLab, ADInstruments, Colorado Springs, CO, USA). The right CCA was exposed by a ventral midline incision in the neck and the retraction of the sternocleidomastoid muscle. The exposed artery was surrounded by a snare. The rats were placed into a stereotaxic head holder, and a 6 × 6 mm area centered 3 mm posterior and 4 mm lateral to Bregma was thinned for laser speckle (**Figure 1**). Special attention was paid during surgical preparation to make the skull thickness uniform (Parthasarathy et al., 2008).

A 2-cm vertical incision was made midway between the right eye and the right ear. The temporalis muscle was separated and retracted to expose the zygomatic and squamosal bones. Under an operating microscope (Carl Zeiss, Inc.), a burr hole of 4 mm in diameter was made with a high-speed drill 1 mm rostral to the anterior junction of the zygomatic and squamosal bones, revealing the distal segment of the middle cerebral artery (MCA). The epidural temperature was monitored by probe and maintained at 37.5 ± 0.3°C with a custom-made air ventilator blowing warm air to the dura. The right side of the stereotaxic frame was tilted upward for the imaging and so that the laser could hit the vessel perpendicularly. A laser beam was focused on the artery through a spherical lens of 25 cm focal length. To induce occlusion, a stock solution of Erythosin B dye (MP Biomedicals, Solon, OH, USA), 17 mg/mL in 0.9% saline, was made for intravenous injection (via the tail vein) at a dose of 40 mg/kg. Immediately after injection of the dye, the MCA was irradiated (532 nm) for 5 min with a 4 mW beam from a diode laser (LaserGlow Technologies, model LRS-0532-KFM-00030-03). A thrombus was produced proximally to the Y-shaped juncture of the frontal and parietal branches of the MCA by focusing the laser at that site. An orange fluorescence was immediately observed in the irradiated distal MCA segment under the operating microscope. A white thrombus began to form approximately 4–5 min later within the fluorescent segment and gradually elongated distally. Following the irradiation, the right CCA was occluded permanently by tightening the snare. Since real time speckle imaging was started immediately after the injection of the erythrosin B, we could confirm successful occlusion also by real time flow measurement. Changes in oxygenation and blood flow were monitored through a thinned skull preparation with intrinsic optical imaging (Grinvald et al., 1986; Kohl et al., 2000) and speckle contrast imaging (Briers, 2001; Dunn et al., 2001; Durduran et al., 2004).

IMAGING

We obtained images of changes in CBF by measuring changes in speckle contrast (calculated using 7 × 7 pixel sliding window), C, of the raw speckle intensity images (Briers, 2001). Because the camera exposure time, T, was much greater than the speckle correlation time, τ_c, which is inversely proportional to the CBF (Bonner and Nossal, 1981), we used the simple relation $\tau_c = 2TC^2$ (Ramirez-San-Juan et al., 2008) to relate contrast to CBF. To improve the signal-to-noise ratio, 15 $1/\tau_c$ images were averaged together. Relative CBF images were then derived by normalizing the averaged $1/\tau_c$ images with baseline measurements obtained at the beginning of the data collection with a correction for biological zero ($1/\tau_c$ values when cerebral perfusion was zero) (Ayata et al., 2004; Strong et al., 2006; Zhou et al., 2008). In this study, biological zero images could not be obtained in each animal because the animals were not sacrificed until days after the imaging. Consequently, a group of animals ($n = 6$) was used to determine the biological zero value, which was found to be 9.1 ± 1.2% of baseline.

To monitor oxygenation with intrinsic optical imaging, we acquired spectral intensity images at three wavelengths (540, 580, and 610 nm) and used a modified Beer–Lambert relationship (Arridge et al., 1992) to relate the reflectance attenuation at each wavelength to changes in hemoglobin concentration. In this analysis, we assumed that contributions to the attenuation from chromophores other than oxyhemoglobin (HbO) and deoxyhemoglobin (Hb) and changes in scattering over the wavelength range used are negligible. Furthermore, we generated the differential pathlength factors in the modified Beer–Lambert relation using Monte Carlo simulations that included the geometry of the imaging system (Kohl et al., 2000).

Our imaging instrument is very similar to the one previously described by (Dunn et al., 2003). For speckle imaging, a collimated laser diode (DL7140-201S, 785 nm, 80 mW; Thorlabs, Newton, NJ, USA) driven by a commercial laser diode controller (LDC 500; Thorlabs, Newton, NJ, USA) provided uniform illumination on the skull surface. To acquire spectral images at multiple-wavelengths, a xenon arc lamp (XBO 150 W/1 OFR; OSRAM) was directed through an eight-position filter wheel (FW-1000, Applied Scientific Instrumentation, Inc) and then coupled to a 12-mm fiber bundle illuminating the cortex. The filter wheel was programmed such that external trigger pulses consecutively switched the filter wheel between four positions. Three positions contained 10-nm bandpass filters centered at wavelengths of 540, 580, and 610 nm, with the other position blocked. The laser diode was off while the filter wheel was in the first three positions, but switched on when the filter wheel reached the blocked position, enabling interleaved spectral and speckle imaging with 140 μm spatial resolution every 2 s.

Imaging software (StreamPix; NorPix, Montreal, Quebec, Canada) was used to record images over the right MCA territory acquired by a 12-bit, TEC cooled CCD camera (Uniq; Uniq Vision Inc.) with a field of view of 5 × 5 mm. A 60-mm lens (Schneider-Kreuznach, Apo-Componon 2.8/40, Germany) was used to focus the image, and the aperture was adjusted so that the speckle size matched the pixel dimensions (9.9 × 9.9 μm). Every 2 s, three spectral and 15 speckle images were taken. A program written in the SciWorks software environment (DataWave Technologies, Boulder, CO, USA) that interfaces to an A/D board controlled the timing for the external triggering of the camera and filter wheel, as well as the timing for switching on/off the laser diode.

CALCULATION OF OXYGEN METABOLISM CHANGES

Relative changes in the cerebral metabolic rate of oxygen ($rCMRO_2$) were calculated from the images of CBF, total hemoglobin, and deoxyhemoglobin using the relationship (Mayhew et al., 2000; Jones et al., 2001):

$$rCMRO_2 = \left(1+\frac{\Delta CBF}{CBF_0}\right)\left(1+\gamma_r\frac{\Delta Hb}{Hb_0}\right)\left(1+\gamma_t\frac{\Delta HbT}{HbT_0}\right)^{-1}-1,$$

where the subscript "o" indicates baseline values and the symbol "Δ" indicates changes from baseline values. The parameters γ_r and γ_t are vascular weighting constants proportional to the amount of deoxyhemoglobin and total hemoglobin in venules, respectively, and are assumed to be one in our calculation. Also, while speckle measures relative changes in CBF directly, OIS cannot determine absolute concentrations, so we assumed baseline values of 60 and 40 μM for HbT_0 and Hb_0, respectively (Dunn et al., 2005). The equation for $rCMRO_2$ was derived based on direct measurements of changes in CBF, deoxyhemoglobin and total hemoglobin in the venous compartment. It is assumed, however, that the optical signal from the brain is proportional to that in the venous compartment and further that the relative volume fractions of the arteriole, capillary, and venules compartments does not change. We have shown that this equation is relatively insensitive to changes in these volume fractions (Culver et al., 2003) although in the core of the ischemia the changes may be more appreciably. The flow transients (where $rCMRO_2$ has been calculated) are not in the most ischemic regions and consequently errors based on this assumption are small.

TEMPORAL PROTOCOL AND IMAGE ANALYSIS

Prior to the initiation of imaging, two subdermal electrodes were inserted into the left (contralateral to injury) forepaw between digits 1 and 2 and between 3 and 4. After 5 min of collecting baseline flow and oxygenation data, a 15-min data collection of real time speckle was initiated synchronously with the production of photothrombosis in order to confirm a successful occlusion (**Figure 2**). The occlusion usually occurred in the 4–5th min of the real time speckle sequence. In the remaining 10-min CBF was monitored to exclude the chance of spontaneous reperfusion. After confirming the successful, reperfusion-free occlusion, surface blood flow, and oxygenation were monitored in 15 min long intra-ischemic sequences over a period of 2 h. Laser speckle (15 Hz) and three-wavelength OIS (540, 580, 610 nm) data were obtained every 2 s. Seven animals underwent 2-h forepaw stimulation (2-mA pulses, 5 Hz for 4 s with 3-s rest) starting with the first intra-ischemic (LS + OIS) sequence synchronously and continuing for 120 min, while seven animals did not receive forepaw stimulation. Data from the literature indicate that a 2 mA forepaw electrical stimulus is innocuous (Luo et al., 2009).

The high spatial resolution images were divided into nine equal sectors, and one circular region of interest (ROI, 0.3 mm in diameter; **Figure 1**) was placed in each sector, where care was taken to ensure the ROIs were not over any large blood vessels. Changes in blood flow, hemoglobin, and metabolism in each ROI over time were analyzed.

The average residual cerebral blood flow (rCBF) during the first 120 min of ischemia was calculated as a percentage of the baseline (5 min) prior to the occlusion over each ROI. Both hemoglobin and peri-infarct flow transients (PIFT) were identified by their propagating feature (transients seen in at least two ROIs with appropriate time delay). The occurrence of flow transients over each ROI was calculated as the percentage of the total number of flow transients in each experimental group (Strong et al., 2007; Jones et al., 2008; Luckl et al., 2009). The duration of the flow transients was determined by computing a mean of the laser speckle signal 1 min both prior to and following a peri-infarct flow transient, and then determining the start and the end of the PIFT from the time at which the mean laser speckle signal intercrossed with the ascending or the descending leg of the PIFT (Luckl et al., 2009). The amplitude was obtained as the percent change in CBF. We measured the hypoperfusion and hyperemia components of the amplitudes separately. The duration and the amplitudes of the Hb (Hb, HbO) transients and $CMRO_2$ changes were determined similarly.

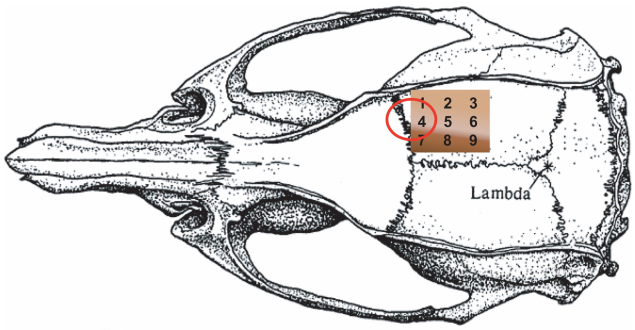

FIGURE 1 | Schematic figure of the thinned skull with the positions of the nine regions of interests (ROI). The shadowing (white line) shows the border zone of the lesion in both groups of animals (no significant difference) after mapping the infarct area with the map of ROIs. The red ellipse indicates the cortical representation of the forepaw as determined by blood oxygen-level dependent imaging (Ghosh et al., 2009) and by OIS in our laboratory.

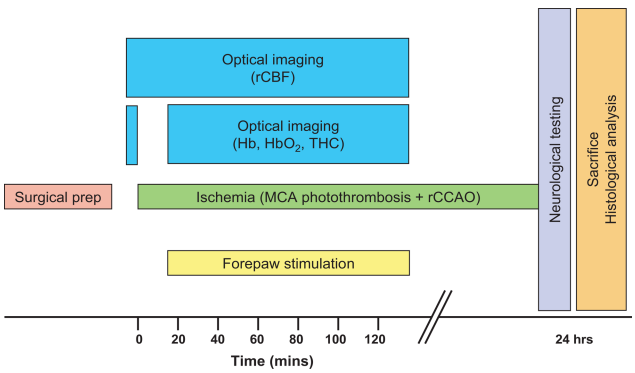

FIGURE 2 | Schematic of study design. Ischemia was produced by direct occlusion of the right middle cerebral artery (MCA) by photothrombosis along with right common carotid artery occlusion (rCCAO), and optical imaging was done during the acute phase of ischemia.

NEUROLOGICAL EVALUATION AND INFARCT VOLUME MEASUREMENT

A neurological evaluation was performed at 24 h post-injury according to the protocol of (De Ryck et al., 1989). Visual placing in forward and sideways directions, tactile placing of the dorsal

and lateral paw surfaces, and proprioceptive placing were tested and scored on a 10-point scale ranging from 10 (no deficit) to 0 (maximum deficit).

Rats were sacrificed 24 h after MCAO. The brain was removed from the skull and was sectioned in the coronal plane at 1.5-mm intervals using a rodent brain matrix. The brain slices were stained with 2% triphenyltetrazolium chloride (TTC), photographed and the infarct volume was determined as described previously (Luckl et al., 2007). We also mapped the infarcted area to the imaging data. The distance between the midline and the border of the infarct zone on the TTC slices was measured and mapped onto the flow and hemoglobin images. According to our sectioning method slices from No. 2 to No. 5 correspond to the thinned area on the skull.

STATISTICAL ANALYSIS

The physiological parameters (baseline and intra-ischemic), the outcomes (infarct size, edema), and the number of flow transients were tested using two-way repeated-measures analysis of variance (ANOVA). When differences were found, a Holm–Sidak test was conducted to probe the origin of differences (control vs stimulated, baseline vs ischemia) and to correct for multiple tests. Neurological scores were examined with a Mann–Whitney rank sum test. A two-way ANOVA with repeated-measures analysis was used to statistically exclude presence of regional heterogeneity in the baseline flow and to compare the mean amplitude of the hemoglobin (oxy, deoxy) transients and the related $CMRO_2$ changes. Region and group (stimulated, non-stimulated) were the independent variables and hemoglobin and $CMRO_2$ transients were dependent variables.

RESULTS

PHYSIOLOGICAL VARIABLES

The physiological variables were in a normal range in each animal (**Table 1**). There were no significant differences in any parameter between the control and stimulated groups. However, occlusion did produce a significant increase in MABP ($p < 0.01$) independent of group (control, stimulated), but in no other physiological parameter did occlusion significantly produces changes.

Table 1 | Physiological variables.

	Control	Stimulated
BASELINE		
Weight (g)	309 ± 19	298 ± 15
MABP (mm Hg)	91 ± 8	97 ± 6
pH	7.46 ± 0.03	7.43 ± 0.04
PO_2 (mm Hg)	126 ± 14	130 ± 24
PCO_2 (mm Hg)	35.9 ± 4.7	39.6 ± 4.9
Core temp (°C)	37.5 ± 0.2	37.5 ± 0.2
Dura temp (°C)	37.5 ± 0.3	37.4 ± 0.3
ISCHEMIA (20 MIN POST-MCAO)		
MABP (mm Hg)	114 ± 15	118 ± 9
pH	7.46 ± 0.04	7.45 ± 0.03
PO_2 (mm Hg)	122 ± 21	122 ± 14
PCO_2 (mm Hg)	35.1 ± 4.9	36.0 ± 5.0
Core temp (°C)	37.6 ± 0.2	37.4 ± 0.2
Dura temp (°C)	37.5 ± 0.2	37.5 ± 0.2
ISCHEMIA (80 MIN POST-MCAO)		
MABP (mm Hg)	113 ± 13	118 ± 8
pH	7.45 ± 0.03	7.44 ± 0.03
PO_2 (mm Hg)	119 ± 18	121 ± 11
PCO_2 (mm Hg)	36.61 ± 3.1	34.2 ± 4.3
Core temp (°C)	37.6 ± 0.2	37.5 ± 0.2
Dura temp (°C)	37.5 ± 0.2	37.5 ± 0.1

Mean ± SD.

HISTOLOGICAL AND NEUROLOGICAL OUTCOME

Both the neurological (sham: 3.6 ± 1.7, stimulated: 4.3 ± 1.4) and the histological (sham: 124 ± 39 mm^3, stimulated: 147 ± 47 mm^3) outcome did not show significant difference between stimulated and control groups. By mapping the infarct zone with the ROI map we found that ROI 7, 8, 9 represents the peri-ischemic area in both groups.

CEREBRAL BLOOD FLOW AND PERI-INFARCT FLOW TRANSIENTS

Two-way ANOVA with repeated measures (animal and ROI) showed that there was a difference in residual blood flow after occlusion between the peri-ischemic area (ROI 7–9) and the ischemic cortex (ROI 1–6) ($p < 0.002$), but no difference between stimulated and non-stimulated animals ($p = 0.658$). The results of laser speckle imaging are presented in **Table 2**. The averaged residual flow after the occlusion was between 47% and 58% of baseline in both groups over the peri-ischemic area. Similarly, there were no differences in residual flow (26–35%) between groups over the ischemic cortex.

The averaged number of flow transients were significantly ($p < 0.05$) higher in the forepaw-stimulated animals (7.0 ± 2.3) compared to the non-stimulated group (3.5 ± 2.3). The flow transients propagate mostly over the peri-ischemic (ROI 7–9) and the penumbral (ROI 4–6) region while the occurrence of flow transients is very low over ROI 1–3 which probably represents the core.

We could distinguish five different morphologies of flow transients as described previously (Luckl et al., 2009). Briefly: (I) monophasic, hyperemic; (II, III) biphasic (hyperemia or hypoperfusion dominant); and (IV, V) monophasic, hypoperfusive (transient or prolonged). The propagation of the flow transients was multi-directional, sometimes giving the impression of being "disordered". In one case, the propagation was bi-directional (splitting) and in another case, a hyperemic, low frequency flow oscillation could be seen over a well-circumscribed part of the ischemic cortex. In early studies with this model we saw the whole cycling propagation pattern described by Graf et al. (2007) in only a few animals probably because we used a representative, but relatively small, "window" size compared to the complete ischemic territory.

HEMOGLOBIN/$CMRO_2$ TRANSIENTS

Tables 3 and 4 summarize the results of OIS imaging. Since the occurrence of transients is very low over the "core" region (ROI 1–3) (**Table 2**) we only examined the data coming from ROI 4–9 in the statistical analysis. Forepaw stimulation significantly ($p < 0.05$) reduces the transient-related $CMRO_2$ changes over ROI 4–9 (penumbra and peri-ischemic area). In concert with this result, we found

Table 2 | Results of laser speckle imaging in the control- (non-stimulated) and forepaw-stimulated groups.

	Control animals			Stimulated animals		
ROI	**rCBF* (%)**	**Occurrence of PIFT** (%)**	**Average duration of PIFT (s)**	**rCBF**	**Occurrence of PIFT (%)**	**Average duration of PIFT (s)**
1	26 ± 7	12	220 ± 40	31 ± 12	8	210 ± 40
2	28 ± 13	8	211 ± 23	29 ± 12	4	201 ± 38
3	27 ± 9	4	222 ± 45	29 ± 15	4	187 ± 20
4	33 ± 16	52	212 ± 43	35 ± 12	49	220 ± 44
5	28 ± 9	32	230 ± 45	30 ± 16	39	242 ± 54
6	33 ± 13	32	242 ± 51	35 ± 12	45	246 ± 50
7	53 ± 18	100	256 ± 59	58 ± 12	100	260 ± 72
8	47 ± 9	100	217 ± 55	48 ± 13	100	250 ± 42
9	54 ± 8	96	227 ± 52	57 ± 18	94	242 ± 56

**Average relative cerebral blood flow (rCBF) over the first 120 min of ischemia as a percent of pre-ischemic flow*
***Frequency of peri-infarct flow transients (PIFT) in region of interest (ROI) as a percent of total number of PIFTs in the group.*

Table 3 | Changes in oxygen concentrations and cerebral oxygen metabolism in animals during forepaw stimulation (mean ± SD).

	Parameters	**ROI_4**	**ROI_5**	**ROI_6**	**ROI_7**	**ROI_8**	**ROI_9**
$CMRO_2$	Change %	30.9 ± 9.1	26.7 ± 8.1	22.4 ± 3.7	34.3 ± 9.4	35.4 ± 3.9	36.7 ± 10.6
HbO	Amplitude (μM)	15 ± 12.4	12.2 ± 9.4	7.6 ± 1.6	20.4 ± 12.9	23.2 ± 10.3	19.4 ± 6.7
	Duration (s)	262 ± 100	248 ± 54	246 ± 48	250 ± 74	260 ± 30	232 ± 54
Hb	Amplitude (μM)	5.9 ± 1.1	6.5 ± 1.5	4.4 ± 1.1	6.9 ± 1.1	6.4 ± 1.1	7.7 ± 2.3
	Duration (s)	252 ± 7.2	230 ± 42	256 ± 46	202 ± 44	176 ± 18	174 ± 30

Table 4 | Change in oxygen concentrations and cerebral oxygen metabolism in control animals (mean ± SD).

	Parameters	**ROI_4**	**ROI_5**	**ROI_6**	**ROI_7**	**ROI_8**	**ROI_9**
$CMRO_2$	Change %	47.6 ± 8.8	35.8 ± 5.0	32.6 ± 5.0	46.4 ± 12.3	48.2 ± 9.6	47 ± 13.7
HbO	Amplitude (μM)	22 ± 19.1	17.1 ± 2.6	27.4 ± 2.7	33 ± 15.7	29.9 ± 13.5	20.3 ± 9.3
	Duration (s)	234 ± 80	276 ± 32	292 ± 54	284 ± 76	282 ± 68	270 ± 56
Hb	Amplitude (μM)	9.9 ± 7.4	7.4 ± 3.5	7.5 ± 3.3	9.9 ± 4.3	7.8 ± 2.7	8.1 ± 2.3
	Duration (s)	254 ± 44	252 ± 66	278 ± 89	200 ± 32	170 ± 40	196 ± 78

also that the mean amplitude (peak to peak) of oxy and deoxy Hb transients were smaller in the stimulated animals, although these differences were not significant (**Figures 3 and 4**). We also did not find significant differences between groups with respect to the average duration of hemoglobin (oxy, deoxy) transients.

DISCUSSION

Our study provides a multispectral, optical imaging analysis of intra-ischemic CBF and metabolism during contralateral forepaw stimulation. The results show that forepaw stimulation can significantly modify the number of PIFT and the transients-related metabolic load in the ischemic hemisphere (contralateral to stimulated forepaw).

Although, our previous study (Burnett et al., 2006) clearly showed that forepaw stimulation has neuroprotective effect in transient focal ischemia, the present study in permanent ischemia did not demonstrate differences in outcome measurements between groups. It should be stressed that this study was designed only to look for any possible biological effect of contralateral forepaw stimulation. We produced a permanent ischemia by photothrombosis, but applied forepaw stimulation only for 2 h. The photothrombosis model of distal MCA occlusion was chosen since it allowed for the dura to remain intact during the surgery and therefore was less invasive than more direct MCA occlusion techniques for the production of permanent focal cerebral ischemia (Chen et al., 1986).

The original hypothesis on the possible beneficial effect of contralateral forepaw stimulation in ischemia was that functional stimulation might increase the intra-ischemic blood flow through collaterals. When we did not see any significant blood flow change in our original study (Burnett et al., 2006) in which a single laser Doppler probes was positioned over the ischemic region, we attributed this to the fact that only a single small region in the MCA was sampled. Similarly, we could not see increase in flow by laser speckle

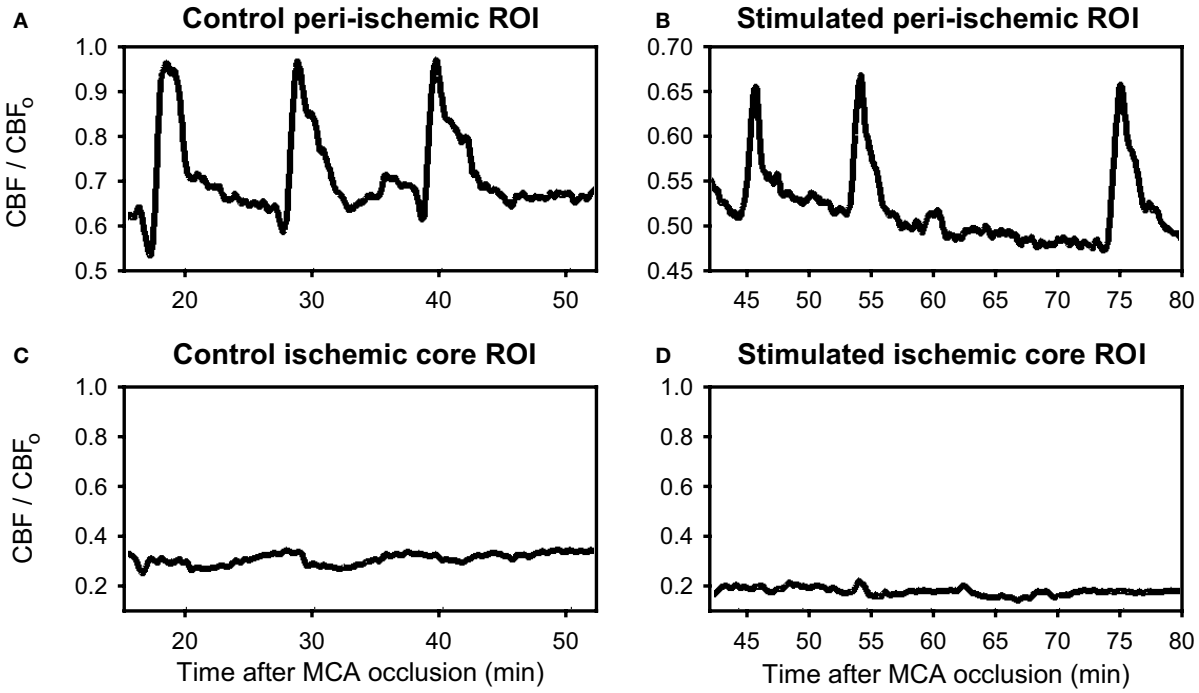

FIGURE 3 | Demonstration of flow transients in relative cerebral blood flow (CBF/CBF$_o$) in peri-ischemia regions. (A, B) and in the ischemic core **(C, D)** from a typical rat not receiving forepaw stimulation during ischemia **(A, C)** and from a rat receiving forepaw stimulation during ischemia **(B, D).** The "o" subscript refers to the parameter prior to MCA occlusion. Note the significant flow transients in the peri-ischemic territory (ROIs 7–9), whereas the occurrence of the transients over the ischemic core (ROIs 1-3) was very low.

in the forepaw-stimulated animals in the present study. There was no significant difference in residual flow between groups even over the peri-ischemic (ROI 7–9, watershed zone between MCA and anterior cerebral artery) region.

The averaged number of flow transients, however, was significantly higher in the forepaw-stimulated animals. In addition, we also found that the mean amplitude of oxy- and deoxy Hb transients was smaller although non-significantly in the stimulated animals, and forepaw stimulation significantly reduced the transient-related $CMRO_2$ changes over ROI 4–9 (penumbra and peri-ischemic area). It is important to note that we detected these changes over the whole (6×6 mm) monitored region which is larger than the cortical representation area of the forepaw (**Figure 1**). This significant "mismatch" indicates at first sight that the underlying mechanism is probably not related to a possible input of stimulation into the ischemic cortex. However, data from the literature suggest that the flow transients show a cyclic propagation pattern around the core. Although our "window" was relatively small for detecting the full circling pattern, our data suggest that a significant proportion of flow transients propagate through the forepaw area. Our results also indicate that at least a part of the forepaw area is peri-ischemic with rCBF over 50% of baseline. Such level of ischemia still allows synaptic activity and some cortical input (Hossmann, 1994; Burnett et al., 2005). We speculate that the forepaw area in the cortex may include a small territory at the ACM–ACA watershed zone where spreading depolarizations and the corresponding flow/hemoglobin transients can be modified through electrical stimulation.

In various animal models of cerebrovascular disease, spreading depolarization (SD) has been found to contribute to ischemic injury through its high metabolic and excitotoxic impact (Nedergaard and Astrup, 1986). SDs increase cerebral metabolic rate by 71% (Piilgaard and Lauritzen, 2009) in non-ischemic rat cortex. The metabolic load due to the transients in our control animals over the peri-ischemic cortex with CBF around 50% of control was 46–48% while the $CMRO_2$ change was 30–35% over the penumbra. Forepaw stimulation decreases this metabolic load significantly by 30–45% over both penumbral and peri-ischemic tissue.

The expansion of the core coincides with the occurrence of repetitive spreading depolarizations (Hossmann, 1996; Shin et al., 2006). In a distal MCAO model of mice each subsequent spreading depolarization expanded the core by an additional 19% (Shin et al., 2006). Our experience with filament occlusion in rat shows that the number of flow transients clearly correlate with the histological outcome but not in a definite stepwise fashion (Luckl et al., 2009). Similarly, NADH fluorescence studies in focal ischemia showed that recurrent depolarization increases the severity of neuronal injury but only a proportion of spreading depolarizations enlarge the core (Higuchi et al., 2002; Sasaki et al., 2009). In the present study we found that the number of flow transients were significantly higher in the stimulated group. Taking the outcome measurements into consideration, it is likely that a certain percent of transients with the decreased metabolic load is non-injurious. Whether forepaw stimulation increases the "real" number of transients or increases only the speed of these transients around the core remains unanswered in this study.

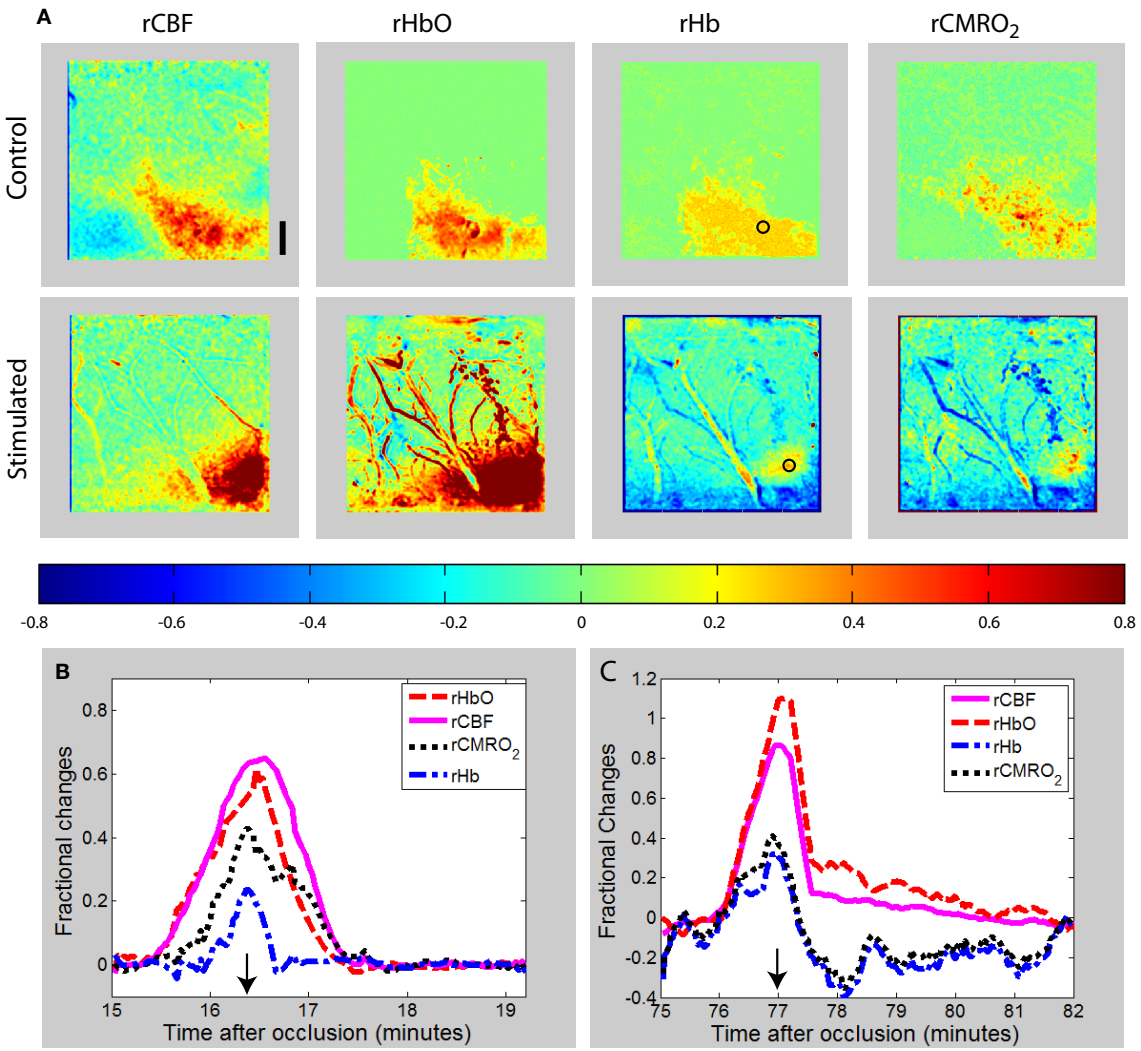

FIGURE 4 | (A) Maps of changes in relative blood flow (rCBF), relative oxyhemoglobin (rHbO), relative deoxyhemoglobin (rHb), and relative oxygen consumption ($rCMRO_2$) during a transient in the peri-ischemia cortex of a exemplar control (non-stimulated) and forepaw-stimulated animal. In both animals, the transient is moving toward the right of the image (caudally). The color bar indicates fractional decreases or increases of each parameter with respect to its level just prior to the start of the transient. The time course of the parameters for the region of interest shown by the circular ROI in the rHb images is shown for the control **(B)** and stimulated **(C)** animal, with the images shown in **(A)** obtained at the time indicated by the arrows. Scale bar is 1 mm.

The site of the MCA occlusion may influence the outcome of the experiment. With this model (distal photothrombotic occlusion of the MCA) we found that the propagation of the flow/Hgb transients was confined mostly to ROI 7–9. In a filament occlusion study (proximal occlusion of the MCA) with a "window" in a similar position, we found that the propagation pattern of the PIFTs is more conservative (fronto-caudal) with the transients traveling through the entire observational area and the occurrence of the flow transients being close to 100% over each ROI (Luckl et al., 2009). The explanation might be that the distal occlusion of the MCA induces an infarct only in the parietal lobe while the proximal MCAO affects a larger volume (parietal and temporal lobe) making the diameter and the extent of the presumed cycling larger. Taking into consideration that the location and the extent of the forepaw area may vary in animals, the chance that a flow transient propagates through the forepaw area and that it can be modulated by forepaw stimulation is presumably higher in proximal MCAO than in the distal MCAO model. Differences in hemodynamics in different stroke models may also determine the effect of stimulation. For example distal occlusion of the MCA leaves the proximal branches patent while these are closed during proximal MCA occlusion (filament occlusion). The inability to see any appreciable increases in the present study using imaging, which monitors a large region does suggest that forepaw stimulation during photothrombotic occlusion of the distal MCA in the rat does not increase blood flow in the ischemic or peri-ischemic territory. This is not to say that blood flow would not be altered in other focal ischemia models.

Strictly speaking, the theory of laser speckle imaging assumes that the speckle intensities over time are Gaussian with mean zero (Lemieux and Durian, 1999). This assumption breaks down in the

presence of static scatterers, such as the thinned skull of the rat, because the speckle pattern due to static scattering is constant over time. Several methods have been proposed to account for the presence of static scattering when doing speckle imaging (Li et al., 2006; Zakharov et al., 2006; Parthasarathy et al., 2008; Zakharov et al., 2009). We employed Zakharov et al.'s algorithm, which determines the static contribution in the speckle pattern by cross-correlating sequential speckle images (Zakharov et al., 2009). Based on our findings, neglecting the effect of the skull and other static scattering elements introduces a systematic underestimation in flow changes of less than 5%. However, this would not affect the conclusions when comparing the transients between stimulation and control groups.

The equation used to calculate changes in $CMRO_2$ is based on many assumptions (Culver et al., 2003; Jones et al., 2008) which may not be valid in ischemia, and particularly in the ischemic core. For this reason, we have limited our calculations of $rCMRO_2$ to the peri-ischemic and penumbral portions of the cortex. The derivation of this equation assumes that the volume fraction of the vascular compartments (arteriole, capillary, venule) from which the optical signal originates does not change. In a previous publication we argue that ischemia can lead to a 9–21% underestimation in the calculated $rCMRO_2$ (Culver et al., 2003). However, since the changes in the microvascular hemodynamics appear to be similar in the stimulated and non-stimulated animals, these errors will be comparable and our conclusions will not be significantly affected.

With multispectral optical imaging we have taken the first step in deciphering the possible influence of forepaw stimulation on ischemic tissue. Based on the results we speculate that forepaw stimulation exerts its effect probably through the cortical representation of the forepaw by modulating the nature of the propagating flow/metabolic transients. The next step would be to investigate the impact of a different stimulation paradigm (increasing frequency or amplitude, etc.). Since we did not record DC potentials it would be also important to check the effect of stimulation directly on spreading depolarizations especially over the forepaw area.

ACKNOWLEDGMENT

This study was supported by National Institutes of Health grant NS057400.

REFERENCES

Arridge, S. R., Cope, M., and Delpy, D. T. (1992). The theoretical basis for the determination of optical pathlengths in tissue: temporal and frequency analysis. *Phys. Med. Biol.* 37, 1531–1560.

Ay, I., Lu, J., Ay, H., and Gregory, S. A. (2009). Vagus nerve stimulation reduces infarct size in rat focal cerebral ischemia. *Neurosci. Lett.* 459, 147–151.

Ayata, C., Dunn, A. K., Gursoy-OZdemir, Y., Huang, Z., Boas, D. A., and Moskowitz, M. A. (2004). Laser speckle flowmetry for the study of cerebrovascular physiology in normal and ischemic mouse cortex. *J. Cereb. Blood Flow Metab.* 24, 744–755.

Bonner, R., and Nossal, R. (1981). Model for laser Doppler measurements of blood flow in tissue. *Appl. Optics* 20, 2097–2107.

Briers, J. D. (2001). Laser Doppler, speckle and related techniques for blood perfusion mapping and imaging. *Physiol. Meas.* 22, R35–R66.

Brown, J. A., Lutsep, H. L., Weinand, M., and Cramer, S. C. (2006). Motor cortex stimulation for the enhancement of recovery from stroke: a prospective, multicenter safety study. *Neurosurgery* 58, 464–473.

Burnett, M. G., Detre, J. A., and Greenberg, J. H. (2005). Activation-flow coupling during graded cerebral ischemia. *Brain Res.* 1047, 112–118.

Burnett, M. G., Shimazu, T., Szabados, T., Muramatsu, H., Detre, J. A., and Greenberg, J. H. (2006). Electrical forepaw stimulation during reversible forebrain ischemia decreases infarct volume. *Stroke* 37, 1327–1331.

Chae, J., Sheffler, L., and Knutson, J. (2008). Neuromuscular electrical stimulation for motor restoration in hemiplegia. *Top. Stroke Rehabil.* 15, 412–426.

Chen, S. T., Hsu, C. Y., Hogan, E. L., Maricq, H., and Balentine, J. D. (1986). A model of focal ischemic stroke in the rat: reproducible extensive cortical infarction. *Stroke* 17, 738–743.

Culver, J. P., Durduran, T., Furuya, D., Cheung, C., Greenberg, J. H., and Yodh, A. G. (2003). Diffuse optical tomography of cerebral blood flow, oxygenation, and metabolism in rat during focal ischemia. *J. Cereb. Blood Flow Metab.* 23, 911–924.

De Ryck, M., Van, R. J., Borgers, M., Wauquier, A., and Janssen, P. A. (1989). Photochemical stroke model: flunarizine prevents sensorimotor deficits after neocortical infarcts in rats. *Stroke* 20, 1383–1390.

Dunn, A. K., Bolay, H., Moskowitz, M. A., and Boas, D. A. (2001). Dynamic imaging of cerebral blood flow using laser speckle. *J. Cereb. Blood Flow Metab.* 21, 195–201.

Dunn, A. K., Devor, A., Bolay, H., Andermann, M. L., Moskowitz, M. A., Dale, A. M., and Boas, D. A. (2003). Simultaneous imaging of total cerebral hemoglobin concentration, oxygenation, and blood flow during functional activation. *Opt. Lett.* 28, 28–30.

Dunn, A. K., Devor, A., Dale, A. M., and Boas, D. A. (2005). Spatial extent of oxygen metabolism and hemodynamic changes during functional activation of the rat somatosensory cortex. *Neuroimage* 27, 279–290.

Durduran, T., Burnett, M. G., Yu, G., Zhou, C., Furuya, D., Yodh, A. G., Detre, J. A., and Greenberg, J. H. (2004). Spatiotemporal quantification of cerebral blood flow during functional activation in rat somatosensory cortex using laser-speckle flowmetry. *J. Cereb. Blood Flow Metab.* 24, 518–525.

Ghosh, A., Sydekum, E., Haiss, F., Peduzzi, S., Zorner, B., Schneider, R., Baltes, C., Rudin, M., Weber, B., and Schwab, M. E. (2009). Functional and anatomical reorganization of the sensory-motor cortex after incomplete spinal cord injury in adult rats. *J. Neurosci.* 29, 12210–12219.

Graf, R., Nakamura, H., Vollmar, S., Dohmen, C., Sakawitz, B., Bosche, B., Dunn, A., and Strong, A. J. (2007). Cycling propagation of spontaneous spreading depolarizations around ischemic foci: evidence from experimental and clinical assessments. Program No. 765. 9 2007 Neuroscience Meeting Planner. San Diego, CA: Society for Neuroscience. Online.

Grinvald, A., Segal, M., Kuhnt, U., Hildesheim, R., Manker, A., Anglister, L., and Freeman, J. A. (1986). Real-time optical mapping of neuronal activity in vertebrate CNS in vitro and in vivo. *Soc. Gen. Physiol Ser.* 40, 165–197.

Higuchi, T., Takeda, Y., Hashimoto, M., Nagano, O., and Hirakawa, M. (2002). Dynamic changes in cortical NADH fluorescence and direct current potential in rat focal ischemia: relationship between propagation of recurrent depolarization and growth of the ischemic core. *J. Cereb. Blood Flow Metab.* 22, 71–79.

Hossmann, K. A. (1994). Viability thresholds and the penumbra of focal ischemia. *Ann. Neurol.* 36, 557–565.

Hossmann, K. A. (1996). Periinfarct depolarizations. *Cerebrovasc. Brain Metab. Rev.* 8, 195–208.

Jones, M., Berwick, J., Johnston, D., and Mayhew, J. (2001). Concurrent optical imaging spectroscopy and laser-Doppler flowmetry: the relationship between blood flow, oxygenation, and volume in rodent barrel cortex. *Neuroimage* 13, 1002–1015.

Jones, P. B., Shin, H. K., Boas, D. A., Hyman, B. T., Moskowitz, M. A., Ayata, C., and Dunn, A. K. (2008). Simultaneous multispectral reflectance imaging and laser speckle flowmetry of cerebral blood flow and oxygen metabolism in focal cerebral ischemia. *J. Biomed. Optics* 13, 044007.

Kohl, M., Lindauer, U., Royl, G., Kuhl, M., Gold, L., Villringer, A., and Dirnagl, U. (2000). Physical model for the spectroscopic analysis of cortical intrinsic optical signals. *Phys. Med. Biol.* 45, 3749–3764.

Lemieux, P., and Durian, D. (1999). Investigating non-Gaussian scattering processes by using nth-order intensity correlation functions. *J. Opt. Soc. Am.* 16, 1651–1664.

Li, P., Ni, S., Zhang, L., Zeng, S., and Luo, Q. (2006). Imaging cerebral blood flow through the intact rat skull with temporal laser speckle imaging. *Opt. Lett.* 31, 1824–1826.

Luckl, J., Keating, J., and Greenberg, J. H. (2007). Alpha-chloralose is a suitable anesthetic for chronic focal cerebral ischemia studies in the rat: a comparative study. *Brain Res.* 1191, 157–167.

Luckl, J., Zhou, C., Durduran, T., Yodh, A. G., and Greenberg, J. H. (2009). Characterization of periinfarct flow transients with laser speckle and

Doppler after middle cerebral artery occlusion in the rat. *J. Neurosci. Res.* 87, 1219–1229.

Luo, Z., Yu, M., Smith, S. D., Kritzer, M., Du, C., Ma, Y., Volkow, N. D., Glass, P. S., and Benveniste, H. (2009). The effect of intravenous lidocaine on brain activation during non-noxious and acute noxious stimulation of the forepaw: a functional magnetic resonance imaging study in the rat. *Anesth. Analg.* 108, 334–344.

Mayhew, J., Johnston, D., Berwick, J., Jones, M., Coffey, P., and Zheng, Y. (2000). Spectroscopic analysis of neural activity in brain: increased oxygen consumption following activation of barrel cortex. *Neuroimage* 12, 664–675.

Nedergaard, M., and Astrup, J. (1986). Infarct rim: effect of hyperglycemia on direct current potential and [14C]2-deoxyglucose phosphorylation. *J. Cereb. Blood Flow Metab.* 6, 607–615.

Parthasarathy, A. B., Tom, W. J., Gopal, A., Zhang, X., and Dunn, A. K. (2008). Robust flow measurement with multi-exposure speckle imaging. *Opt. Express* 16, 1975–1989.

Piilgaard, H., and Lauritzen, M. (2009). Persistent increase in oxygen consumption and impaired neurovascular coupling after spreading depression in rat neocortex. *J. Cereb. Blood Flow Metab.* 29, 1517–1527.

Ramirez-San-Juan, J. C., Ramos-Garcia, R., Guizar-Iturbide, I., Martinez-Niconoff, G., and Choi, B. (2008). Impact of velocity distribution assumption on simplified laser speckle imaging equation. *Opt. Express* 16, 3197–3203.

Sasaki, T., Takeda, Y., Taninishi, H., Arai, M., Shiraishi, K., and Morita, K. (2009). Dynamic changes in cortical NADH fluorescence in rat focal ischemia: evaluation of the effects of hypothermia on propagation of peri-infarct depolarization by temporal and spatial analysis. *Neurosci. Lett.* 449, 61–65.

Shin, H. K., Dunn, A. K., Jones, P. B., Boas, D. A., Moskowitz, M. A., and Ayata, C. (2006). Vasoconstrictive neurovascular coupling during focal ischemic depolarizations. *J. Cereb. Blood Flow Metab.* 26, 1018–1030.

Strong, A. J., Anderson, P. J., Watts, H. R., Virley, D. J., Lloyd, A., Irving, E. A., Nagafuji, T., Ninomiya, M., Nakamura, H., Dunn, A. K., and Graf, R. (2007). Peri-infarct depolarizations lead to loss of perfusion in ischaemic gyrencephalic cerebral cortex. *Brain* 130, 995–1008.

Strong, A. J., Bezzina, E. L., Anderson, P. J., Boutelle, M. G., Hopwood, S. E., and Dunn, A. K. (2006). Evaluation of laser speckle flowmetry for imaging cortical perfusion in experimental stroke studies: quantitation of perfusion and detection of peri-infarct depolarisations. *J. Cereb. Blood Flow Metab.* 26, 645–653.

Williams, J. A., Imamura, M., and Fregni, F. (2009). Updates on the use of non-invasive brain stimulation in physical and rehabilitation medicine. *J. Rehabil. Med.* 41, 305–311.

Yanamoto, H., Nagata, I., Nakahara, I., Tohnai, N., Zhang, Z., and Kikuchi, H. (1999). Combination of intraischemic and postischemic hypothermia provides potent and persistent neuroprotection against temporary focal ischemia in rats. *Stroke* 30, 2720–2726.

Zakharov, P., Volker, A., Buck, A., Weber, B., and Scheffold, F. (2006). Quantitative modeling of laser speckle imaging. *Opt. Lett.* 31, 3465–3467.

Zakharov, P., Volker, A. C., Wyss, M. T., Haiss, F., Calcinaghi, N., Zunzunegui, C., Buck, A., Scheffold, F., and Weber, B. (2009). Dynamic laser speckle imaging of cerebral blood flow. *Opt. Express* 17, 13904–13917.

Zhou, C., Shimazu, T., Durduran, T., Luckl, J., Kimberg, D. Y., Yu, G., Chen, X. H., Detre, J. A., Yodh, A. G., and Greenberg, J. H. (2008). Acute functional recovery of cerebral blood flow after forebrain ischemia in rat. *J. Cereb. Blood Flow Metab.* 28, 1275–1284.

Conflict of Interest Statement: The authors declare that the research was conducted in the absence of any commercial or financial relationships that could be construed as a potential conflict of interest.

Received: 23 February 2010; paper pending published: 30 March 2010; accepted: 05 July 2010; published online: 30 July 2010.

Citation: Luckl J, Baker W, Sun Z-H, Durduran T, Yodh AG and Greenberg JH (2010) The biological effect of contralateral forepaw stimulation in rat focal cerebral ischemia: a multispectral optical imaging study. Front. Neuroenerg. ***2****:19. doi: 10.3389/fnene.2010.00019*

frontiers in
NEUROENERGETICS

ORIGINAL RESEARCH ARTICLE
published: 06 August 2010
doi: 10.3389/fnene.2010.00022

Detection of neural action potentials using optical coherence tomography: intensity and phase measurements with and without dyes

Taner Akkin[1]*, David Landowne[2] and Aarthi Sivaprakasam[1]

[1] *Department of Biomedical Engineering, University of Minnesota, Minneapolis, MN, USA*
[2] *Department of Physiology and Biophysics, University of Miami, Miami, FL, USA*

Edited by:
David Boas, Massachusetts General Hospital, USA; Massachusetts Institute of Technology, USA; Harvard Medical School, USA

Reviewed by:
Vivek Srinivasan, Massachusetts General Hospital, USA
Ricky Wang, Oregon Health and Science University, USA

***Correspondence:**
Taner Akkin, Department of Biomedical Engineering, University of Minnesota, 7-105 Hasselmo Hall, 312 Church Street SE, Minneapolis, MN 55455, USA.
e-mail: akkin@umn.edu

We review the use of optical coherence tomography (OCT) for detection of neural activity, and present a new approach for depth-localization of neural action potentials (APs) using voltage-sensitive dyes as contrast agents in OCT. A stained squid giant axon is imaged by spectral-domain OCT. Changes in the intensity and phase of back-scattered light coming from regions around the membrane are measured during AP propagation. The depth-resolved change in back-scattered intensity coincides with the arrival of AP at the measurement area, and is synchronous with the changes in transmitted light intensity and reflection-mode cross-polarized light intensity measured independently. The system also provides depth-resolved phase changes as an additional indication of activity. With further investigation our results could open a new era in functional imaging technology to localize neural activity at different depths *in situ*.

Keywords: OCT, spectral domain, neural activity, voltage-sensitive, fast signals

INTRODUCTION

Indications of neural activity are usually classified in "slow" and "fast" categories. The slow signals occur in a few seconds to minutes, and, as e.g., hemodynamic response probed by functional magnetic resonance imaging, they represent indirect measurements of neural activity. On the other hand, the fast signals occur in the millisecond timescale and are directly correlated to changes in membrane potential. Electrical measurements of membrane potential using external or internal electrodes are studied widely for neural activity, but the use of electrodes in many applications is not feasible, and its invasive nature can easily induce irreversible damage to nerve fibers. Besides, spatial resolution of the external electrical measurements is typically low. As the development of new methods that directly assess neural activity becomes a pressing need, a variety of optical techniques and contrasts are being investigated for imaging neural structure and function with high spatial and temporal resolutions.

The use of optical instrumentation to study neural activity dates to late 1940s. During action potential (AP) propagation in neural tissue light scattering, absorption, birefringence, fluorescence, and volume changes have been reported (Cohen, 1973). Imaging with voltage-sensitive dyes has become an important part of neuroscience for observing membrane potential in single and multiple neurons (Homma et al., 2009). However, the techniques have not produced information to locate the APs at different depths. Development of new techniques and improvement of current approaches are essential to obtain a useful test for neural function. For instance, imaging the activity with optical slices rather than in physical slices (e.g., brain slices) would be a major advancement in functional assessment of neural tissue.

Optical coherence tomography (OCT) is a non-invasive technique that uses reflected/back-scattered light to construct depth-resolved images of tissue. Recent OCT based techniques have potential to study AP related minute changes at different depths. The techniques have the additional advantage of being less invasive than many other measurements, because they work in reflection geometry, which means the source and detector are on the same side of the nerve. Here, we review the related work in this area, and present new data for depth-localization of neural activity in squid giant axons (SGA) stained with a voltage-sensitive near-infrared dye. Real-time cross-sectional images of a spectral-domain OCT (SD-OCT) system were used to select center portion of the SGA for functional interrogation. By monitoring the same depth profile over time, we acquired M-mode SD-OCT images while electrical current stimulus pulses were applied to the axon to initiate propagated APs. Analysis of the intensity and phase of the interferometric signal showed local changes on a millisecond time scale. The results are also compared with the changes in transmitted light intensity, reflection-mode cross-polarized light intensity and electrical APs, which are recorded simultaneously with the SD-OCT signal. Since the dye approach is known to be extremely fast and linear, our technique may be developed as a depth-resolved optical voltmeter measuring local changes in membrane potential.

MATERIALS AND METHODS

OPTICAL COHERENCE TOMOGRAPHY

Optical coherence tomography is a depth-resolved, high-resolution, non-invasive technique that employs low-coherence interferometry to image biological tissue up to a depth of a few millimeters. It is similar to ultrasound imaging except that reflected/back-scattered

near-infrared light is used rather than acoustic waves. **Figure 1** illustrates a basic fiber-based OCT system in time and spectral domains. The systems can be implemented in bulk optical setups or with single mode fibers. Light from a broadband source such as a superluminescent diode or mode-lock Ti:Sapphire laser is typically split into the reference and sample arms. Interference of light returning from these arms to the fiber coupler (or beamsplitter) produces the axial information. Time-domain OCT (Huang et al., 1991) utilizes both axial (A-line) and lateral (B-line) scanners to construct cross-sectional images from amplitude of the photo-detector signal. At a given time, the photo-detector signal represents a single depth location when the optical path length of the reference arm matches that of the location within the sample. Thus, this method may have limited use for detecting neural activity.

The axial resolution Δz (~2–20 μm) of the OCT systems is determined by the center wavelength λ_0 and spectral bandwidth $\Delta\lambda$ of the light source. For a Gaussian spectrum, Δz is given by $\Delta z = \left(2\ln(2)/\pi\right)\left(\lambda_0^2/\Delta\lambda\right)$. High axial resolution requires a short temporal coherence provided by broad bandwidth light sources. The lateral resolution Δx, on the other hand, is determined by sample path optics that focuses the beam on the sample, and given by $\Delta x = 4\lambda f/\pi d$, where d is the spot size on the lens with the focal length f. High lateral resolution requires a lens with high numerical aperture (NA), and correspondingly a small beam spot at the focus.

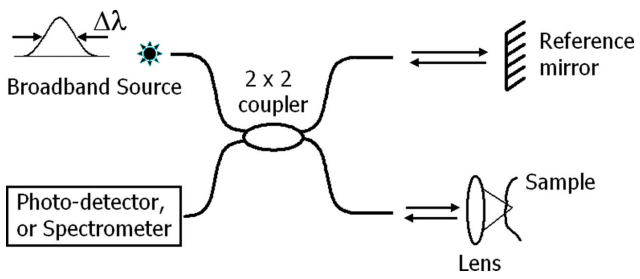

FIGURE 1 | Generic system for optical coherence tomography (OCT). In time-domain OCT, a photo-detector detects interferometric fringes while the reference mirror is scanned in axial direction. In spectral-domain OCT, the reference mirror is stationary, and a spectrometer records the modulations on the optical spectrum due to interference, which is then used in calculation of the axial information for all depth points, simultaneously.

Unlike in time-domain OCT, the reference mirror of the Michelson interferometer is not scanned in SD-OCT (also known as Fourier-domain OCT). Instead, SD-OCT uses a spectrometer to record interference of back-scattered light from all depth points simultaneously (Fercher et al., 1995). Then, a Fourier transform algorithm relates the spectral modulations in k-space to information along the axial direction. This allows imaging a depth profile (A-line) in ~10–50 μs (integration time of the spectrometer); thus, provides adequate temporal resolution for the fast signals of neural activity for a full depth profile. To show the operation of SD-OCT, a reflector was placed in the sample arm. Interference between the reference and sample light resulted in modulations on the optical spectrum (**Figure 2A**). After spectral shaping, which is not required, the Fourier transform algorithm produced the spatial information along an A-line. **Figure 2B** shows the magnitude of the signal in linear scale. The peak at 220 μm is the envelope of the coherence function and corresponds to the reflection from the sample surface. The width of the coherence function determines the axial resolution. By scanning the beam over a sample, SD-OCT produces real-time images, which helps selecting a particular region of neural tissue for functional study.

There are various types of OCT that use intensity, phase or polarization properties of light for imaging microstructure, blood flow, or birefringence properties of tissues. The readers are referred to review articles (e.g., Fercher et al., 2003) or books (e.g., Drexler and Fujimoto, 2008) for detailed description of the concepts and principles.

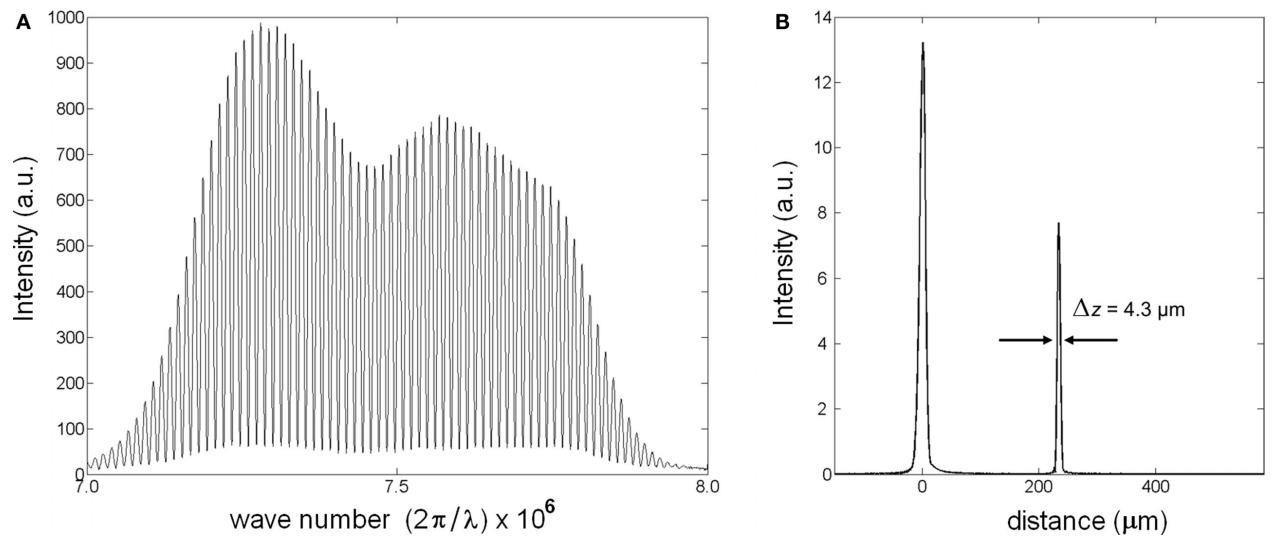

FIGURE 2 | Description of SD-OCT measurement. (A) Strong modulation on optical spectrum (λ = 835 nm; Δλ = 75 nm) is due to a reflective surface in the sample arm. **(B)** The peak at 0 is a Fourier transform of the source spectrum, the peak at 220 μm is the reflector causing modulations on the spectrum.

PHASE-SENSITIVE OPTICAL COHERENCE TOMOGRAPHY

Coherence functions consist of interferometric fringes. Let us consider a time-domain system. For low coherent light sources with Gaussian spectral density, the interference term I can be described by a Gaussian envelope and sinusoidal fringes as

$$I(\tau) \propto e^{-(\tau/4a)^2} \cos(2\pi f \tau + \varphi + \phi_N), \quad (1)$$

where τ is the temporal delay between light in sample and reference paths, $a = (\ln 2)^{1/2}/\Delta\omega$ and $\Delta\omega$ is angular optical frequency width of the source, f is the frequency of fringes that is determined by the scanner or a modulator in the reference arm, φ is the phase carrying physically relevant information about a sample, and ϕ_N is the phase noise in the interferometer due to environmental perturbations. For a reliable phase measurement, phase noise should be cancelled by a common-mode phase noise rejection scheme. This can be achieved by a common path interferometric setup or a differential phase operation provided by dual channel interferometers. In the latter approach noise ϕ_N is cancelled by computing phase difference between two channels/points, $\Delta\varphi = \varphi_1 - \varphi_2$. $\Delta\varphi$ is proportional to the optical path length difference (Δp) between the observation points, $\Delta p = (\lambda_0/4\pi)\Delta\varphi$. As a result, the Δp measurement yields sub-wavelength sensitivity, which is useful to monitor minute changes in refractive index or geometrical size of samples. This approach has been utilized for detecting AP related minute changes from a single point in crustacean nerve (Akkin et al., 2004; Fang-Yen et al., 2004).

The phase information is readily available in SD-OCT, as well (Choma et al., 2005; Joo et al., 2005). By using the phase of the complex valued depth profile, which is obtained by a discrete Fourier transform algorithm, changes in optical path length can be quantified for a full depth profile simultaneously. SD-OCT can reject the phase noise by common path implementations that doesn't utilize a separate reference arm or by measuring phase difference between two depth locations. The latter was used to report Δp response due to AP propagation in crustacean nerve (Akkin et al., 2007) and SGA (Akkin et al., 2009). Using a fiber-based SD-OCT, we recorded interference between the front and back surfaces of a fixed glass slide for 1 s with a temporal resolution of 34.1 μs. The standard deviation of the phase measurement (~0.75 mrad) suggested about 50 pm noise for Δp measurements. Signal-to-noise ratio degradation in biological tissue and motion artifacts may worsen the sensitivity; nevertheless, SD-OCT has the time resolution and sensitivity to study the transient changes related to AP propagation at all points along a depth profile. Furthermore, development of single-shot two-dimensional techniques at high imaging speeds (Witte et al., 2009) is promising for functional investigation of neural tissue in cross-sectional optical slices.

PREVIOUS WORK ON DETECTING NEURAL ACTIVITY USING OCT TECHNIQUES

INTENSITY MEASUREMENTS

Time-domain OCT can be applied to detect slow changes in reflectivity/back-scattering during neural activity. OCT was used to detect visually evoked cortical functions of a cat brain *in vivo* (Maheswari et al., 2002, 2003; Rajagopalan and Tanifuji, 2007). Neural activity related local reflectivity changes occurring in a small volume revealed that the optical response was about 1 s or more after the onset of visual stimulus, and lasted for duration of a few seconds (Maheswari et al., 2003). In another study, time-domain OCT reflectance measurements from rat somatosensory cortex during forepaw electrical stimulation showed a functional signal with a time course corresponding to the hemodynamic signal (Aguirre et al., 2006; Chen et al., 2009). Time-domain OCT was also used to report a scattering increase from nerve fibers from abdominal ganglion of sea slug, which was repetitively stimulated over several minutes (Lazebnik et al., 2003). Using the same model, scattering intensity from single neurons was recorded by SD-OCT (Graf et al., 2009).

The most developed medical application of OCT is imaging the anatomy of retinal layers in real-time at micron scale resolution. Since visible light activates retina and induces changes related to the physiology and circuitry of the retina, OCT with its near-infrared beam has potentials for detecting layer-specific retinal activity. Isolated frog retina was used to demonstrate OCT measurement of light-activated near-infrared scattering changes in photoreceptor and ganglion layers (Yao et al., 2005). Then, light-activated reflectivity changes in isolated rabbit retina were observed in the inner/outer segments of the photoreceptor layer and the plexiform layers using time-domain OCT (Bizheva et al., 2006). By using SD-OCT, reflectivity measurements demonstrated non-invasive functional imaging of rat retina *in vivo* (Srinivasan et al., 2006).

PHASE MEASUREMENTS

Conventional time-domain OCT is insensitive to fast (millisecond) and small (nanometer) changes due to AP propagation. On the other hand, differential phase implementations of the technique can probe a single nerve location in depth and a reference surface nearby at the same time with microsecond temporal resolution and sub-nanometer optical path length resolution. Using a phase-sensitive optical low-coherence reflectometer, depth-resolved surface and subsurface changes from nerve bundles dissected from crayfish claw was recorded during AP propagation (Akkin et al., 2004). The measured Δp response was about 1 nm in amplitude, 1 ms in duration and occurred at about the AP arrival time to the optical measurement site. Initial direction of the Δp response was either an increase or a decrease. This may be supported by contact-mode measurements reporting a contraction followed by a slow swelling for a crayfish giant axon (Hill et al., 1977), and swelling followed by contraction for squid giant axon (Iwasa and Tasaki, 1980) due to AP propagation. Using a different differential phase interferometer probing a lobster nerve surface, swelling of about 5 nm in about 10 ms duration was reported (Fang-Yen et al., 2004). SD-OCT was also demonstrated to be able to measure these changes from lobster and crayfish nerve preparations, which showed 0.5–2.5 nm Δp responses within the nerves (Akkin et al., 2007).

More recent SD-OCT phase measurements showed details of the transient changes on SGA during activity (Akkin et al., 2009). Experiments were performed at room and cold temperatures, and in hypertonic solutions to analyze transformation and amplification of the optical (Δp) response. To demonstrate how well the Δp response matches with the electrical AP, and to describe the measurements better, here we present **Figures 3 and 4**. After real-time SD-OCT imaging of axonal cross-sections in a nerve chamber,

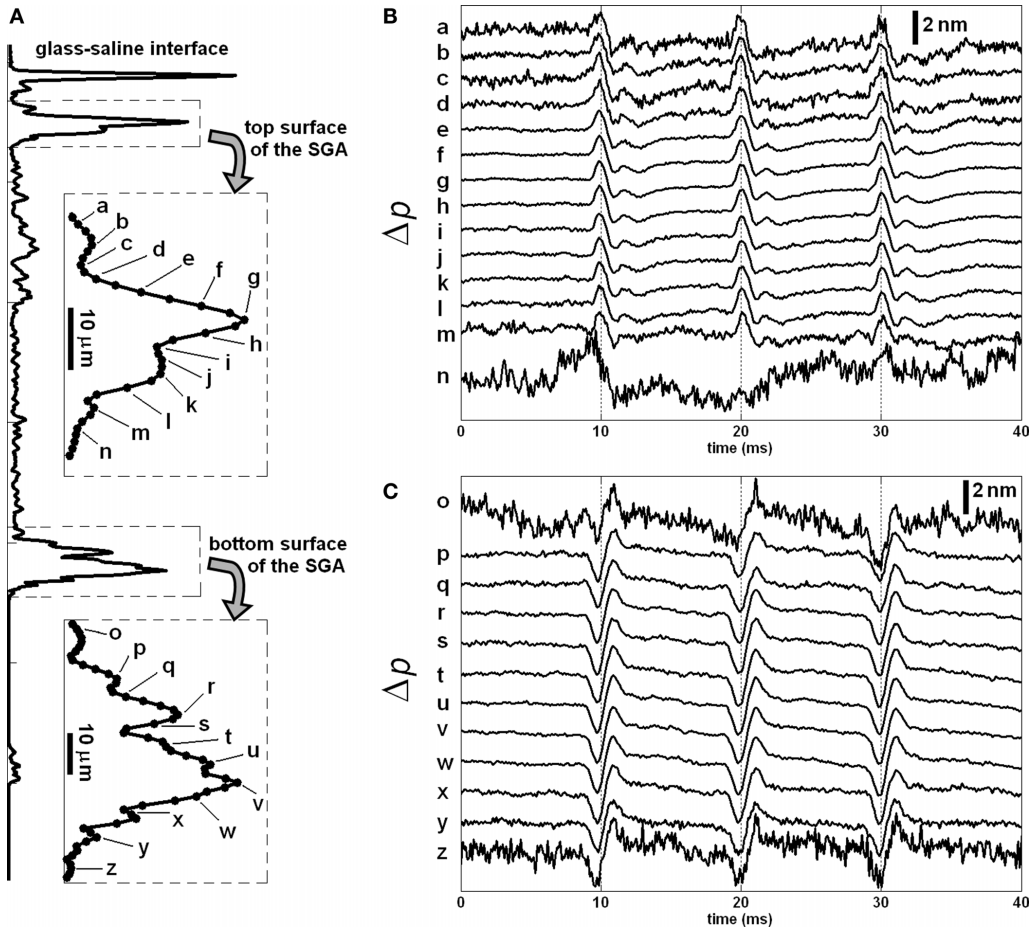

FIGURE 3 | Depth profile of a squid giant axon probed by the SD-OCT (A); the insets show the labels of points, whose responses are given in **(B,C),** and in **Figures 4 and 5.** Δ*p* traces in **(B,C)** are recorded from top and bottom surfaces of the axon with respect to the reference glass, respectively. Each trace in (**B,C)** is an average of 250 responses, and has 5 kHz bandwidth. Diameter of the axon was 410 μm. Saline solution was cold seawater (temperature: 2°C). The timing of the electrical stimulation and electrical AP recording is given in **Figure 4B**.

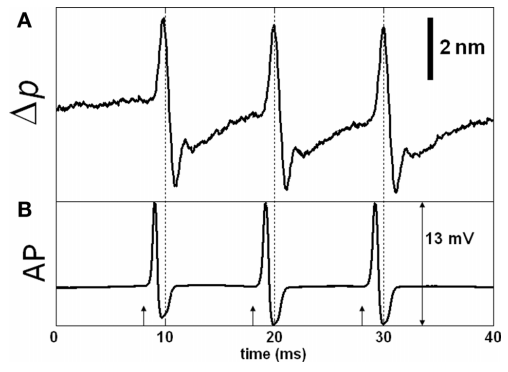

FIGURE 4 | SD-OCT measurement of action potential (AP) related path length change (Δ*p*). Δ*p* trace in **(A)** is measured between the top and bottom surfaces of the axon (points g and v) and is equivalent to subtraction of the corresponding Δ*p* traces in **Figure 3**. The optical response is relatively large compared to most of our results. **(B)** Shows the externally and differentially recorded AP; arrows indicate stimuli (500 μA, 50 μs). Each trace is an average of 250 responses, and has 5 kHz bandwidth.

axonal surfaces as well as a reference glass above the axon were monitored during AP propagations initiated by electrical current pulses. **Figure 3** illustrates the depth profile probed in this experiment, and the Δ*p* responses of many points chosen from the top and bottom surfaces of the axon. The glass surface was used for differential phase measurement to cancel the noise on the signals acquired from a level in the top (**Figure 3B**) or bottom (**Figure 3C**) surfaces of the axon, and not needed for the Δ*p* response (**Figure 4A**) between the top and bottom surfaces of the axon. In **Figure 3**, an upward change in Δ*p* indicates a decrease, and a downward change indicates an increase in optical path length between a surface and the reference glass. In **Figure 4A**, an upward change in Δ*p* indicates an increase in optical path length between the top and bottom surfaces of the axon, and a downward change represents a decrease. These figures also show repeatability of the response as a train of three pulses were applied as shown together with the corresponding AP recording in **Figure 4B**. The arrival of each AP to the optical recording area is approximately at the zero-crossings of the electrical signal (9.5, 19.5, and 29.5 ms). Each trace in **Figures 3 and 4** is an average of 250 records and has 5 kHz

bandwidth. The shape and timing of the AP related responses were similar for those points located on the same surface. Clearly, the signal-to-noise ratio was better for the points having higher amplitudes, which are plotted and labeled in the insets of **Figure 3A**. Dots in the insets are about 1.1 μm apart.

Results showed that the Δ*p* response measured between the top and bottom surfaces of the axon ranged from sub-nanometers to 21 nm on a millisecond time scale (Akkin et al., 2009). The responses were mostly biphasic. The initial direction of the first event was constant for a given location, but alternated for different locations in about equal frequency of occurrence. Hence, these transient events appeared to have local characteristics. Mean values of Δ*p* response was 1.1 nm at room temperature (20–21°C) and 1.65 nm in cold (~2°C). For most of the Δ*p* responses, which were below 1.2 nm, the mean values at room temperature and in the cold were 0.57 and 0.68 nm, respectively. This suggests that cooling for most of squid giant axon data increased the Δ*p* response by about 19%. Increasing the NaCl levels in saline solution (seawater) decreased the diameter of the axon as expected and produced significantly larger Δ*p* responses during AP propagation. These SD-OCT phase measurements and possible mechanisms are discussed in Akkin et al. (2009). However, the mechanistic origins of the changes producing the optical signals are not yet conclusive. The lack of knowledge hampers improvements in the assessment of activity for both simple and complex neural tissues.

In addition to the phase measurements (Δ*p* response), we analyzed the same SD-OCT data set used in **Figures 3 and 4** to obtain an AP indicator based on changes in back-scattered/reflected light intensity. **Figure 5** shows the variations in the SD-OCT intensity signal (Δ*I*) for many points on the top surface of the squid giant axon. The intensity traces in **Figure 5** are also averages of 250 records and have 5 kHz bandwidth. It is clear that the Δ*I* traces are noisier compared to the Δ*p* traces of **Figure 3**. All Δ*I* responses were less than 1% of the intensity level given in **Figure 4A**. Moreover, the shapes and directions of the Δ*I* traces varied significantly between the points. No Δ*I* response was observed for the bottom surface and the other points on the top surface of the axon. We did not observe a Δ*I* response frequently, which is consistent with the very small (10^{-6} to 10^{-5}) changes in light scattering observed without depth resolution by Cohen et al. (1972).

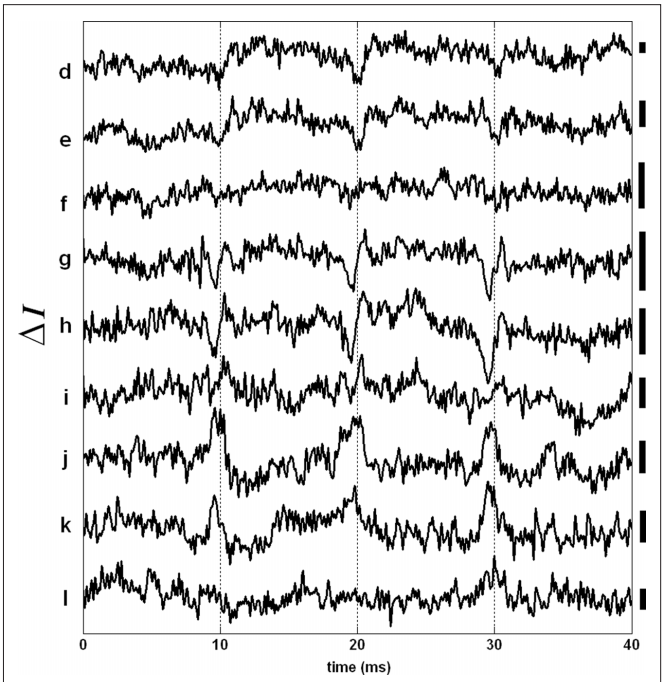

FIGURE 5 | AP related changes in the SD-OCT intensity signal (Δ*I* response). Each trace has a label that corresponds to a particular level in the depth profile shown in **Figure 3A**. Bars on the right represent 0.25% change of the corresponding intensity level. Other locations did not produce a detectable Δ*I* response. Each trace is an average of 250 responses, and has 5 kHz bandwidth.

DYE CONTRAST IN OCT

Most intrinsic optical signals of neural activity are small and require signal averaging. On the other hand, imaging with voltage-sensitive dyes has increasingly become an important part of neuroscience for studying neural activity in various models. Many dyes are commercially available, and there is a demand for near-IR dyes as the longer wavelengths can penetrate more in the scattering tissue. Near-IR dyes will also be good for retinal studies, since they don't excite the photoreceptor cells. The fluorescence dyes, because of use in reflection geometry, are more desirable for many applications. Function in neurons in a superficial plane can be imaged by conventional techniques, but axial (depth) sectioning is not inherently provided. In other words, function of cells lying behind other cells in the light path could not be distinguished. We believe that OCT is a potential candidate to fill this gap. Although OCT does not require exogenous chemicals, we used a voltage-sensitive dye as an OCT contrast agent for depth-resolved detection of neural activity. The preliminary data presented here is encouraging and shows feasibility of the approach.

Figure 6A illustrates the sample arm configuration of our fiber-based SD-OCT system, which was not polarization sensitive, but we used polarization optics to observe reflection-mode cross-polarized light intensity with detector D_R. Another detector (D_T) was used to observe AP related changes in transmitted light intensity due to absorption or scattering changes. Collimated light (λo: 835 nm, Δλ: 75 nm) with a diameter of 2.4 mm enters to a Wollaston prism at its divergence angle; therefore, linearly polarized light is directed and focused on a squid giant axon that is oriented 45° with respect to the incoming polarization state.

Light from two broadband superluminescent diodes were combined to improve the axial resolution. The envelope of **Figure 2A** suggests the spectral characteristics of the combined source and **Figure 2B** shows the corresponding axial resolution. The reference arm of the SD-OCT consisted of an attenuator and a stationary reflector. In the detection arm, a custom built spectrometer contains a 75-mm achromatic collimator, 1200 lines/mm transmission grating and 100 mm achromatic lens, which focuses the optical spectrum on a line scan CCD camera.

The experiment was performed at Marine Biological Laboratory (Woods Hole, MA, USA). A dissected giant axon of squid (*Loligo pealeii*) was stained with a near-infrared dye (IR-144, Eastman Kodak Co., 1 mg/ml in sea water). Structures and characteristics of IR-144 and several other IR dyes can be found in Webb et al.

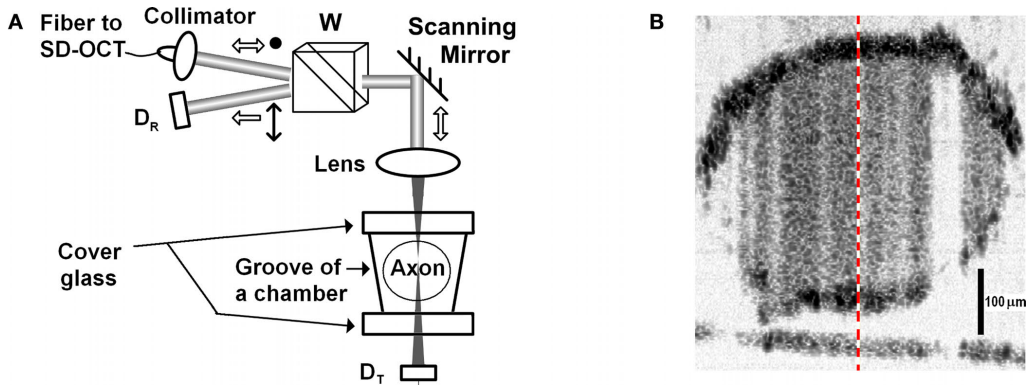

FIGURE 6 | (A) SD-OCT sample arm configuration, D: detector, W: Wollaston prism**. (B)** Image of a 420-µm diameter stained squid giant axon. The-dashed line indicates the A-line probed in the experiment.

(1975). The axon was placed in a nerve chamber (description in Akkin et al., 2009) and kept in a cold environment (~2°C) during the experiment. By scanning the beam over the sample, the SD-OCT system displayed cross-sectional images of the axon in real-time. **Figure 6B** shows the logarithmic representation of the reflectivity image with 43 dB dynamic range. The axial and lateral resolutions were 4.3 µm in tissue (5.9 µm in air) and 21 µm, respectively. The optical power on the axon did not exceed 1 mW. After selecting the center of the axon, the beam was stationary at the center (M-mode imaging) to observe the AP related changes.

Simultaneous with the SD-OCT measurement, the two detectors (D_R, D_T) measured changes in transmitted light intensity and reflection-mode cross-polarized light intensity. **Figure 7** shows the photo-detector signals that are not depth-resolved, and the differentially and externally recorded electrical AP. The arrows represent the current pulses (500 µA, 50 µs) applied to the squid giant axon. Each record consisted of three stimuli to show the repeatability of the responses. Each trace is an average of 250 records to reveal the details. With the arrival of each AP to the optical recording area (approximately zero-crossings at 10, 20, and 30 ms), the transmitted light intensity (**Figure 7A**) was temporarily reduced by about 0.15% followed by an increase making the response biphasic. The back-scattered cross-polarized signal (**Figure 7B**) resulted in a detectable signal as well. Since this signal was not detectable for the unstained axon studied above, it may indicate an enhancement of the dye for the reflected signal. An earlier study (Ross et al., 1977) reported transmission-mode cross-polarized intensity change from the edge of an axon stained with *merocyanine-rhodamine*, but did not show a detectable signal at the center of the axon. Therefore, the cross-polarized signal measured at the center of the axon in reflection geometry may be enhanced further by utilizing the edges. Moreover, **Figure 7B** suggests the use of polarization-sensitive OCT systems for functional neural imaging.

We used SD-OCT to look for dye dependent changes in back-scattered light intensity near the surfaces of the stained squid giant axon because the largest voltage changes occur across the axon membrane. We simultaneously measured intensity and phase

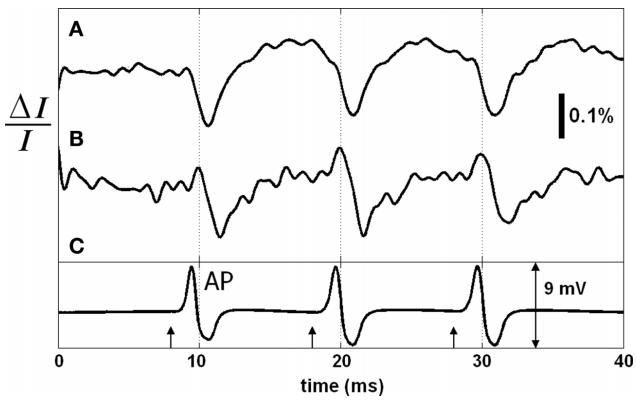

FIGURE 7 |Transmitted light intensity change (A), and reflected cross-polarized light intensity change (B) during AP propagation in the stained squid giant axon. Electrical action potential recording is in **(C)**; arrows indicate stimuli (500 µA, 50 µs). Each trace is an average of 250 responses. Saline solution was cold seawater (temperature: 2°C).

changes of the SD-OCT signals from the same axon. **Figure 8A** shows the depth profile probed in this experiment with labels indicating points, whose responses were presented in this and next figures. To utilize the phase signals, common-mode phase noise was removed by subtracting the phase of a glass–saline interface above the squid giant axon from the phase of the measurement points. Then the phase difference ($\Delta\varphi$) was converted to single-pass optical path length change (Δp) for convenience, $\Delta p(z) = (\lambda_0/4\pi)\Delta\varphi(z)$, and plotted as a function of time. The Δp traces in **Figure 8B** shows similar responses for the four points chosen from the top surface of the axon. Other points on the same surface produced similar Δp responses, as well. Such traces may also be obtained without the use of dye (Akkin et al., 2009). The top surface of the axon produced less than 1% intensity change for a few points as shown in **Figure 8C**; whereas multiple points for the bottom surface produced different results.

Figure 9 shows the intensity and phase signals of SD-OCT for eight points located at the inner side of the bottom surface of the axon. Even though separations of the points are less than the axial

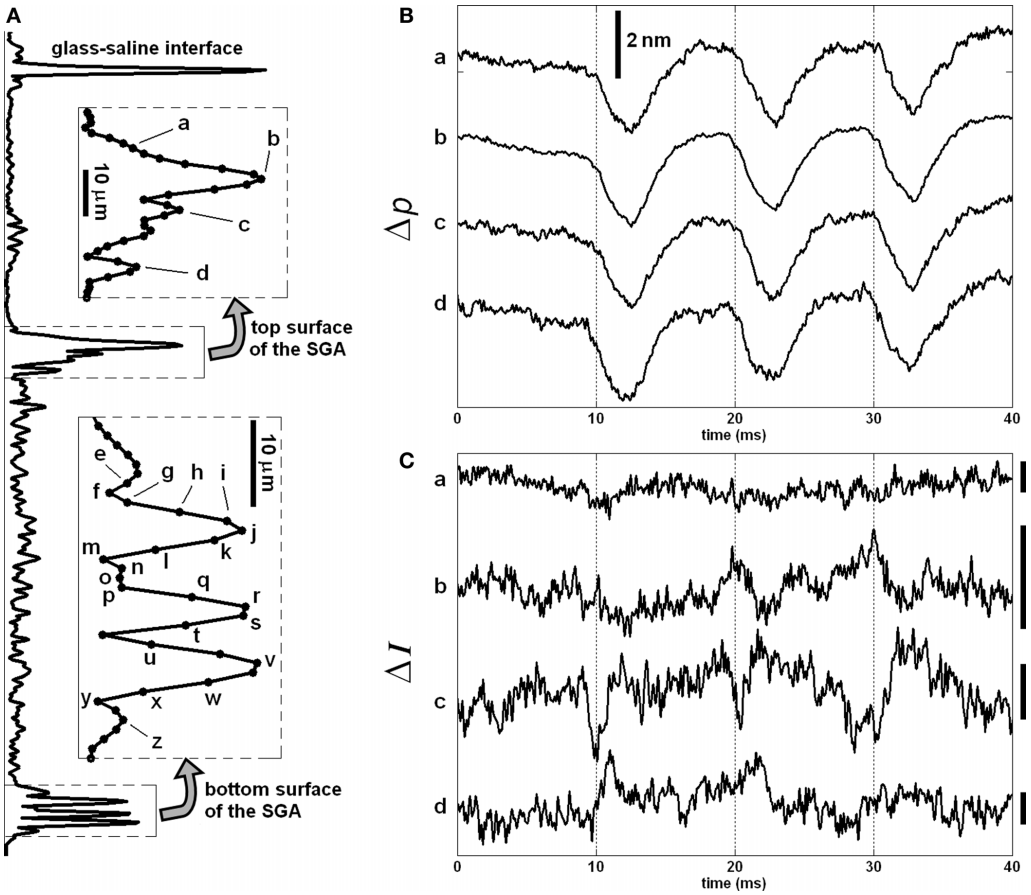

FIGURE 8 | Depth profile of the stained squid giant axon probed by the SD-OCT (A), and Δp (B) and ΔI (C) responses of the top surface of the axon. The insets show the labels of points, whose responses are given in **(B,C)**, and the next figures. Bars in **(C)** represent 0.5% change of the corresponding intensity level. Each trace is an average of 250 responses, and has 5 kHz bandwidth. The AP is given in **Figure 7C**.

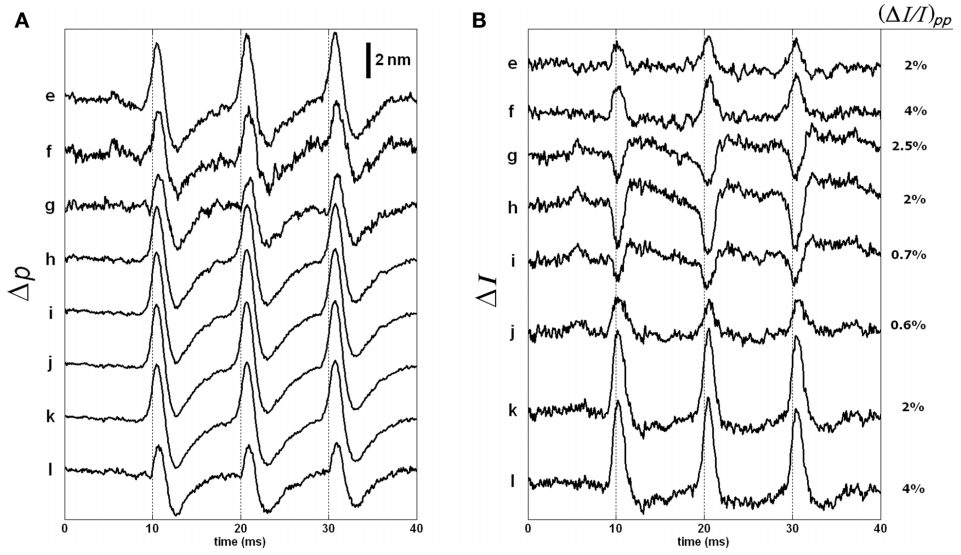

FIGURE 9 | Δp (A) and ΔI (B) responses of the eight points located at the inner side of the bottom surface of the stained axon. Each trace is an average of 250 responses, and has 5 kHz bandwidth. The AP is given in **Figure 7C**.

resolution, we provide these to describe the nature of the responses. Both Δp and ΔI responses are highly correlated with the arrival of APs to the measurement area (simultaneously recorded APs are shown in **Figure 7C**). The Δp traces for the eight points are similar to each other (**Figure 9A**). The intensity traces are shown in **Figure 9B**. The amplitude and sign of the ΔI responses varied for different points. Moreover, the biphasic feature observed for the Δp response was not apparent for most of the ΔI responses. By normalizing the ΔI responses by the intensity at the corresponding levels, we obtained the peak-to-peak normalized intensity changes as shown in the right side of the figure. These values represent a large increase in the signal-to-noise ratio over the results obtained with unstained axons.

The responses of points m, n, o, and p are shown in **Figure 10** as they represent different characteristics. The Δp responses of points m and p are very much different than the Δp responses of all other points. The point m with the smallest intensity level produced the largest normalized intensity change that was about 13%. For this point, the shape and timing of the Δp and ΔI responses were comparable, which is perhaps related to the low intensity level. Point p, on the other hand, produced a triphasic Δp response, but not a detectable ΔI response. Points n and o produced large Δp responses (about 13 nm and 11 nm, respectively) in the same direction, but the signs of their ΔI responses were in opposite directions. The sign of the intensity change was different at different locations within the coherence length. This requires further investigation.

Figure 11 shows the responses of the remaining points. The Δp traces were similar to those in **Figure 9A**. The ΔI responses and their normalized peak-to-peak changes are given in **Figure 11B**. As shown, the ΔI responses for points on the outer side of the bottom surface were difficult to detect.

Figures 9–11 reveal an unexpected complexity of signals associated with APs at different depths within the cellular sheath that surrounds the squid giant axon. Assuming the Δp responses were caused by displacements, the observed intensity changes are too large to be explained by about 6 nm shift of a 4.3-μm coherence function, which should produce about 0.4% change at the full-width-half

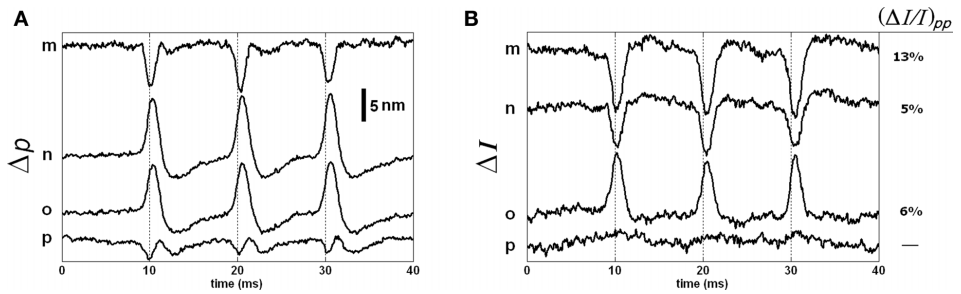

FIGURE 10 | Δp (A) and ΔI (B) responses of the four points located within the bottom surface of the stained axon. Each trace is an average of 250 responses, and has 5 kHz bandwidth. The AP is given in **Figure 7C**.

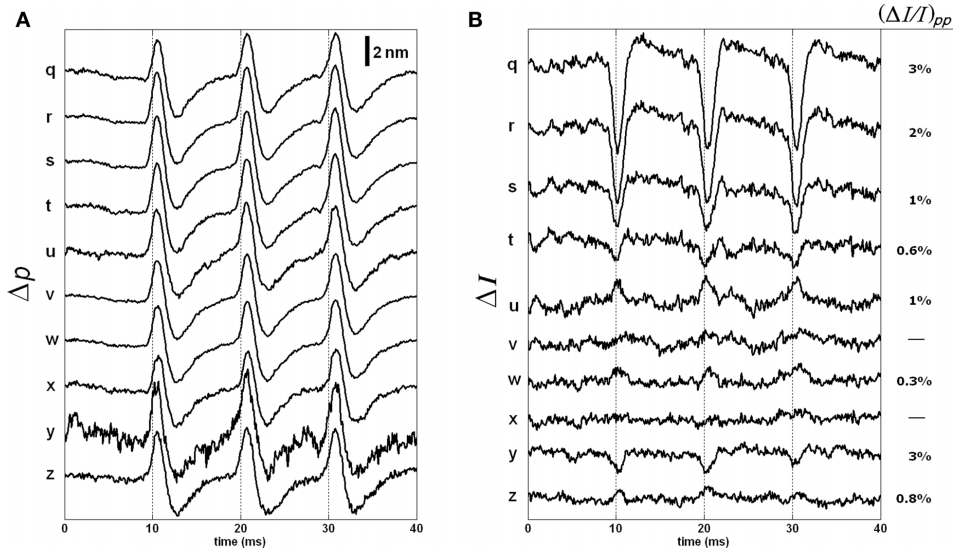

FIGURE 11 | Δp (A) and ΔI (B) responses of the 10 points located at the outer side of the bottom surface of the stained axon. Each trace is an average of 250 responses, and has 5 kHz bandwidth. The AP is given in **Figure 7C**.

maxima and less at the higher levels. Another important point is that the timing and the shape of these dye intensity and phase signals are different. The phase signals peaked little after (0.3–0.5 ms) the intensity signals and lasted longer for most points. This suggests that the dye intensity signal may be directly related to the local potential changes, and the phase signal may result from AP-induced structural changes. While more work is needed to understand the mechanisms of the AP related phase and intensity signals of OCT, its depth-resolved signals clearly provides more information than the conventional transmission-mode recording, and it works in reflection geometry.

CONCLUSION

We utilized SD-OCT intensity measurement on a squid giant axon stained with a voltage-sensitive dye to localize the activity in depth. Although OCT does not require exogenous chemicals, preliminary data demonstrated that the stained axon produce significant change in local back-scattered light intensity around the membrane during AP propagation. The phase signals of SD-OCT are available as well, and changes in transmitted light intensity and reflected cross-polarized light intensity were also reported for the same axon. The results suggest a need for the development of new dyes for specific wavelength regions that OCT systems operate; so that voltage induced changes in absorption or scattering properties can be captured in reflection geometry and with depth-sectioning capability. More work will be needed to understand the mechanism underlying these optical signals associated with the passage of APs. The development of the SD-OCT technique to identify functional and dysfunctional areas within the nerve has tremendous advantages in functional neural imaging. The technique would enable us to compare the local structural and potential changes with high spatial and temporal resolutions, and be used as an alternative or supportive tool to electrophysiology. The approach has potential to produce critical data, which could increase the understanding of functioning nerve and aid future diagnostic applications.

ACKNOWLEDGMENTS

This work was supported in part by a research grant from the NIH (EB006588, co-funded by National Institute of Biomedical Imaging and Bioengineering (NIBIB) and National Eye Institute (NEI)), and by the Hartline and MacNichol Jr. Fellowship at the Marine Biological Laboratory, Woods Hole, MA, USA. Authors thank Dr. L. B. Cohen for his encouragement and support that include providing the dye.

REFERENCES

Aguirre, A. D., Chen, Y., Fujimoto, J. G., Ruvinskaya, L., Devor, A., and Boas, D. A. (2006). Depth-resolved imaging of functional activation in the rat cerebral cortex using optical coherence tomography. *Opt. Lett.* 31, 3459–3461.

Akkin, T., Davé, D. P., Milner, T. E., and Rylander, H. G. III. (2004). Detection of neural activity using phase-sensitive optical low-coherence reflectometry. *Opt. Express* 12, 2377–2386.

Akkin, T., Joo, C., and de Boer, J. F. (2007). Depth resolved measurement of transient structural changes during action potential propagation. *Biophys. J.* 93, 1347–1353.

Akkin, T., Landowne, D., and Sivaprakasam, A. (2009). Optical coherence tomography phase measurement of transient changes in squid giant axons during activity. *J. Membr. Biol.* 231, 35–46.

Bizheva, K., Pflug, R., Hermann, B., Povazay, B., Sattmann, H., Qiu, P., Anger, E., Reitsamer, H., Popov, S., Taylor, J. R., Unterhuber, A., Ahnelt, P., and Drexler, W. (2006). Optophysiology: depth-resolved probing of retinal physiology with functional ultrahigh-resolution optical coherence tomography. *Proc. Natl. Acad. Sci. U.S.A.* 103, 5066–5071.

Chen, Y., Aguirre, A. D., Ruvinskaya, L., Devor, A., Boas, D. A., and Fujimoto J. G. (2009). Optical coherence tomography (OCT) reveals depth-resolved dynamics during functional brain activation. *J. Neurosci. Methods* 178, 162–173.

Choma, M. A., Ellerbee, A. K., Yang, C., Creazzo, T. L., and Izatt, J. A. (2005). Spectral-domain phase microscopy. *Opt. Lett.* 30, 1162–1164.

Cohen, L. B. (1973). Changes in neuron structure during action potential propagation and synaptic transmission. *Physiol. Rev.* 53, 373–418.

Cohen, L. B., Keynes, R. D., and Landowne, D. (1972). Changes in light scattering that accompany the action potential in squid giant axons: potential-dependent components. *J. Physiol.* 224, 701–725.

Drexler, W., and Fujimoto, J. G. (eds). (2008). *Optical Coherence Tomography: Technology and Applications*. New York, NY: Springer.

Fang-Yen, C., Chu, M. C., Seung, H. S., Dasari, R. R., and Feld, M. S. (2004). Noncontact measurement of nerve displacement during action potential with a dual-beam low-coherence interferometer. *Opt. Lett.* 29, 2028–2030.

Fercher, A. F., Drexler, W., Hitzenberger, C. K., and Lasser, T. (2003). Optical coherence tomography – principles and applications. *Rep. Prog. Phys.* 66, 239–303.

Fercher, A. F., Hitzenberger, C. K., Kamp, G., and Elzaiat, S. Y. (1995). Measurement of intraocular distances by backscattering spectral interferometry. *Opt. Commun.* 117, 43–48.

Graf, B. W., Ralston, T. S., Ko, H.-J., and Boppart, S. A. (2009). Detecting intrinsic scattering changes correlated to neuron action potentials using optical coherence imaging. *Opt. Express* 17, 13447–13457.

Hill, B. C., Schubert, E. D., Nokes, M. A., and Michelson, R. P. (1977). Laser interferometer measurement of changes in crayfish axon diameter concurrent with action potential. *Science* 196, 426–428.

Homma, R., Baker, B. J., Jin, L., Garaschuk, O., Konnerth, A., Cohen, L. B., Bleau, C. X., Canepari, M., Djurisic, M., and Zecevic, D. (2009). Wide-field and two-photon imaging of brain activity with voltage- and calcium-sensitive dyes. *Methods Mol. Biol.* 489, 43–79.

Huang, D., Swanson, E. A., Lin, C. P., Schuman, J. S., Stinson, W. G., Chang, W., Hee, M. R., Flotte, T., Gregory, K., Puliafito, C. A., and Fujimoto, J. G. (1991). Optical coherence tomography. *Science* 254, 1178–1181.

Iwasa, K., and Tasaki, I. (1980). Mechanical changes in squid giant axons associated with production of action potentials. *Biochem. Biophys. Res. Commun.* 95, 1328–1331.

Joo, C., Akkin, T., Cense, B., Park, B. H., and de Boer, J. F. (2005). Spectral-domain optical coherence phase microscopy for quantitative phase-contrast imaging. *Opt. Lett.* 30, 2131–2133.

Lazebnik, M., Marks, D. L., Potgieter, K., Gillette, R., and Boppart, S. A. (2003). Functional optical coherence tomography for detecting neural activity through scattering changes. *Opt. Lett.* 28, 1218–1220.

Maheswari, R. U., Takaoka, H., Homma, R., Kadono, H., and Tanifuji, M. (2002). Implementation of optical coherence tomography (OCT) in visualization of functional structures of cat visual cortex. *Opt. Commun.* 202, 47–54.

Maheswari, R. U., Takaoka, H., Kadono, H., Homma, R., and Tanifuji, M. (2003). Novel functional imaging technique from brain surface with optical coherence tomography enabling visualization of depth resolved functional structure in vivo. *J. Neurosci. Methods* 124, 83–92.

Rajagopalan U. M., and Tanifuji, M. (2007). Functional optical coherence tomography reveals localized layer-specific activations in cat primary visual cortex in vivo. *Opt. Lett.* 32, 2614–2616.

Ross, W. N., Salzberg, B. M., Cohen, L. B., Grinvald, A., Davila, H. V., Waggoner, A. S., and Wang, C. H. (1977). Changes in absorption, fluorescence, dichroism, and birefringence in stained giant axons: optical measurement of membrane potential. *J. Membr. Biol.* 33, 141–183.

Srinivasan, V. J., Wojtkowski, M., Fujimoto, J. G., and Duker, J. S. (2006). In vivo measurement of retinal physiology with high-speed ultrahigh-resolution optical coherence tomography. *Opt. Lett.* 31, 2308–2310.

Webb, J. P., Webster, F. G., and Plourde, B. E. (1975). Sixteen new IR laser dyes. *IEEE J. Quantum Electron.* 11, 114–119.

Witte S., Baclayon, M., Peterman, E. J., Toonen, R. F., Mansvelder, H. D., and Groot, M. L. (2009). Single-shot two-dimensional full-range optical coherence tomography achieved by dispersion control. *Opt. Express* 17, 11335–11349.

Yao, X-C., Yamauchi, A., Perry, B., and George, J. S. (2005). Rapid optical coherence tomography and recording functional scattering changes from activated frog retina. *Appl. Opt.* 44, 2019–2023.

Conflict of Interest Statement: The authors declare that the research was conducted in the absence of any commercial or financial relationships that could be construed as a potential conflict of interest.

Received: 19 February 2010; paper pending published: 31 March 2010; accepted: 14 July 2010; published online: 06 August 2010.

Citation: Akkin T, Landowne D and Sivaprakasam A (2010) Detection of neural action potentials using optical coherence tomography: intensity and phase measurements with and without dyes. Front. Neuroenerg. ***2****:22. doi: 10.3389/fnene.2010.00022*

frontiers in
NEUROENERGETICS

ORIGINAL RESEARCH ARTICLE
published: 11 August 2010
doi: 10.3389/fnene.2010.00015

Does neural input or processing play a greater role in the magnitude of neuroimaging signals?

Sam Harris, Myles Jones, Ying Zheng and Jason Berwick*

Department of Psychology, University of Sheffield, Sheffield, UK

Edited by:
David Boas, Massachusetts General Hospital, USA; Massachusetts Institute of Technology, USA; Harvard Medical School, USA

Reviewed by:
Hellmuth Obrig, Charité – Universitätsmedizin Berlin, Germany; Max Planck Institute of Human Cognitive and Brain Sciences, Germany
Maria Angela Franceschini, Harvard Medical School, USA

***Correspondence:**
Jason Berwick, Department of Psychology, University of Sheffield, Western Bank, Sheffield, South YorkShire S10 2TN, UK.
e-mail: j.berwick@sheffield.ac.uk

An important constraint on how hemodynamic neuroimaging signals such as fMRI can be interpreted in terms of the underlying evoked activity is an understanding of neurovascular coupling mechanisms that actually generate hemodynamic responses. The predominant view at present is that the hemodynamic response is most correlated with synaptic input and subsequent neural processing rather than spiking output. It is still not clear whether input or processing is more important in the generation of hemodynamics responses. In order to investigate this we measured the hemodynamic and neural responses to electrical whisker pad stimuli in rat whisker barrel somatosensory cortex both before and after the local cortical injections of the $GABA_A$ agonist muscimol. Muscimol would not be expected to affect the thalamocortical input into the cortex but would inhibit subsequent intra-cortical processing. Pre-muscimol infusion whisker stimuli elicited the expected neural and accompanying hemodynamic responses to that reported previously. Following infusion of muscimol, although the temporal profile of neural responses to each pulse of the stimulus train was similar, the average response was reduced in magnitude by ~79% compared to that elicited pre-infusion. The whisker-evoked hemodynamic responses were reduced by a commensurate magnitude suggesting that, although the neurovascular coupling relationships were similar for synaptic input as well as for cortical processing, the magnitude of the overall response is dominated by processing rather than from that produced from the thalamocortical input alone.

Keywords: neurovascular coupling, synaptic activity, muscimol, barrel cortex, whisker

INTRODUCTION

To produce maps of cortical activation modern neuroimaging techniques such as fMRI rely on changes in hemodynamic variables occurring in close proximity to localized increases of neural activity. This relationship, termed neurovascular coupling, is still not completely understood. Following experiments both in anesthetized (Lauritzen, 2001; Jones et al., 2004; Logothetis, 2007; Rauch et al., 2008) and awake animals (Goense et al., 2008), the predominant view is that the hemodynamic response is more closely associated with synaptic activity rather than with spiking output (Lauritzen, 2001; Jones et al., 2004; Logothetis, 2007; Rauch et al., 2008). However, an unresolved issue is whether the hemodynamic response is more representative of the synaptic activity associated with the direct input into an area of cortex or subsequent intra-cortical processing (Mangia et al., 2009). Recent studies in the anesthetized rat have suggested that in both cortical (Radhakrishnan et al., 2007; Franceschini et al., 2008) and sub-cortical (Angenstein et al., 2009) structures, intra-regional processing could be more important than the initial evoked input to a brain region in generating accompanying hemodynamic responses. This has important consequences for the interpretation of data from neuroimaging techniques such as the Blood Oxygen Level dependent (BOLD) fMRI signal as it would allow accurate interpretation of cerebral hemodynamics in terms of stimulus processing. Although these studies (Radhakrishnan et al., 2007; Franceschini et al., 2008; Angenstein et al., 2009) strongly suggested intra-regional processing was more associated with hemodynamic signals than with input, they did not dissociate the two and examine the accompanying hemodynamics. Therefore to test this idea directly it would be advantageous to manipulate a neural system to clearly disassociate the input from the cortical processing. To further this aim, we measured the hemodynamic and neural responses to 16s electrical whisker pad stimuli in rat barrel cortex using 2-dimensional optical imaging spectroscopy (2D-OIS) and multi-channel electrophysiology both before and after inactivation of cortical processing by local cortical injection of the γ-aminobutyric acid type A ($GABA_A$) receptor agonist muscimol. As based on previous work (Higley and Contreras, 2007) cortical muscimol infusion would not be expected to affect the thalamocortical input into the cortex but inhibit subsequent intra-cortical processing. This pharmacological manipulation allowed assessment of the separate contributions of cortical input and subsequent processing to the accompanying evoked hemodynamic response. Intra cerebral infusions of this agonist have recently been successfully used to assess the contribution of inhibitory cortical activity to "paired-pulse" whisker inhibition (Higley and Contreras, 2007) and to study the effect of GABAergic tone on neurovascular coupling in the cerebellum (Caesar et al., 2003, 2008). Our data suggest, that although the quantitative neurovascular coupling relationships for cortical input and intra-cortical processing are similar, intra-cortical processing accounts for a the majority of the neurovascular response evoked by sensory stimuli.

MATERIALS AND METHODS

ANIMAL PREPARATION AND SURGERY

All procedures were performed in accordance with the 1986 Animal (scientific procedures) Act, under approval from the UK Home Office. Female Hooded Lister rats of 230–330 g were kept in a 12-h dark/light cycle at a temperature of 22°C, with food and water supplied *ad libitum*. Animals were anesthetized with urethane at 1.25 g/kg i.p., additional doses of 0.1 ml urethane were administered if required. Atropine was administered at 0.4 mg/kg s.c. to lessen mucous secretions during surgery. Temperature was maintained at 37°C using a homoeothermic blanket (Harvard Apparatus) through rectal temperature monitoring during surgery and experimental procedures. The animals were tracheotomized, allowing artificial ventilation and recording of end-tidal CO_2. Blood gas measurements and end-tidal CO_2 measurements were taken to allow correct adjustment of ventilator parameters to keep the animal within physiological limits. Femoral arteries and veins were cannulated to allow the measurement of mean arterial blood pressure (MABP) and drug infusion. Phenylephrine was infused at 0.13–0.26 mg/h to maintain MABP between 100–110 mmHg (Golanov et al., 1994; Nakai and Maeda, 1999). Animals were placed in a stereotaxic frame (Kopf instruments). The skull overlying the somatosensory cortex was thinned to translucency with a dental drill, with the skull surface cooled with saline. A circular plastic 'well' (20-mm diameter) was attached over the thinned area of the skull using dental cement. The well was filled with saline, to reduce specularities from the skull surface.

2-DIMENSIONAL SPECTROSCOPY (2D-OIS) IMAGING

A Dalsa 1M30P camera operating in 4 × 4 binning mode recorded images of the cortical surface and each image pixel represented 75 × 75 um The camera has a quantum efficiency of 28% at 500 nm. The cortical surface was illuminated with four wavelengths of light using a Lambda DG-4 high-speed filter changer (Sutter Instrument Company, Novato, CA, USA) and light source that was synchronized to camera image capture. The four wavelengths were specifically chosen as two pairs (495 nm ± 31 FWHM and 559 nm ± 16 FWHM; 575 nm ± 14 FWHM and 587 nm ± 9 FWHM). The wavelengths in each pair were chosen such that they had a similar total absorption coefficient and thus sample the same tissue volume but have specific absorption coefficients for oxyhemoglobin (HbO_2) and deoxyhemoglobin (Hbr) that are as different as is possible to maximize signal to noise ratio. The frame rate of the camera was 32 Hz, which was synchronized to the filter switching, thereby giving an 8 Hz effective frame rate for each wavelength and therefore the subsequent estimates of hemodynamics. To create spatio-temporal "maps" of cortical hemodynamics the data were subject to Spectral analysis using a path length scaling algorithm (PLSA) described in detail previously (Berwick et al., 2005, 2008). Briefly the algorithm uses modified Beer-Lambert Law with a path length correction factor. We estimated the concentration of hemoglobin in tissue at a concentration 104 μM based on previous measurements (Kennerley et al., 2005) and the saturation was calculated on a pixel by pixel basis (Berwick et al., 2008). The spectral analysis produced 2D images over time, of oxyhemoglobin (HbO_2), deoxyhemoglobin (Hbr), and total hemoglobin (Hbt).

EXPERIMENTAL PROCEDURES

Subcutaneous stainless steel stimulation electrodes insulated to within 2 mm of the tip were inserted in a posterior direction between rows A/B and C/D of the left whisker pad of the rat ensuring the whole whisker pad was stimulated when electrical stimuli were applied. Stimuli produced no change in MABP, pCO_2 or heart rate suggesting that electrical whisker pad stimuli did not produce any systemic changes that could affect cortical hemodynamics of interest.

Localization of whisker region for electrode placement

An initial 2D-OIS experiment was performed to localize whisker barrel cortex for accurate placement of a multi-channel electrode. Brief whisker pad stimuli (2 s) were presented to localize whisker barrel cortex. Electrical whisker pad stimuli (1.2 mA, 2 s, 5 Hz) were presented for 30 trials with a 26 s inter-stimulus interval. Data from individual trials were averaged and subjected to the spectral analysis. Images of hemodynamic changes were co-registered with images of the cortical surfaces to guide electrode placement. A very small whole in the thinned skull directly above the selected location was made with a dental drill and the bone removed. The dura was then pierced with a 27 gauge needle. A 16-channel electrode coupled with a fluidic probe loaded with Muscimol (75-μm spacing, Neuronexus technologies Inc, concentration of Muscimol 0.125 μg per μl), was inserted normal to the cortical surface, to a depth of 1200 μm. The probe was coupled to a pre-amp and data acquisition device (Medusa Bioamp, TDT, Florida); using a custom written script in MATLAB (Mathworks).

Experimental paradigm

Following accurate electrode placement, concurrent electrophysiological measures of neural activity were recorded while accompanying cortical hemodynamics were measured simultaneously with 2D-OIS. Once the electrode was inserted a control experiment was performed which consisted of 30 trials with an inter-stimulus interval of 70 s. Stimulation occurred after 19 s in each trial (1.2 mA 16 s at 5 Hz). Data was trial averaged and then subjected to the same spectroscopy analysis as described above. Simultaneously neural activity was collected across all 16 channels of the multi-electrode at a sampling frequency of 6.1 KHz for a period of 26.7 s starting 5.2 s before stimulation onset within each trial. After this experiment 1 μl of muscimol was infused over a period of 1 min using a 10-μl Hamilton syringe and syringe pump (World Precision Instruments Inc). After the muscimol had been allowed to take effect the long stimulation 2D-OIS and simultaneous neural activity paradigm was repeated.

Electrophysiological data analysis

The 16-channel neural data was analyzed by performing current source density (CSD) analysis. Recordings were averaged over trials, with stimulus onset "jittered" within a 20-ms window to reduce effects of 50 Hz mains noise. The resultant evoked field potential recordings were sampled at 6 kHz with 16-bit resolution. The CSD analysis has been described in detail previously (Martindale et al., 2003). The field potentials were used to obtain spatio-temporal estimates of the current sources and sinks within the cortical layers (Nicholson and Freeman, 1975; Mitzdorf, 1985). The current sink

with the greatest amplitude was located ~500 μm below the surface of the brain. This corresponds to layer IV, which receives direct somatosensory input from the ventral posterior thalamus. The main current sink in layer IV, which is believed to be a result of excitatory post synaptic activity (EPSP) in the barrel, was taken as our neural activity measure and will be referred to as the CSD Sink.

Post-mortem cytochrome oxidase histology to confirm location of somatosensory cortex

Following most experiments post-mortem brain tissue was prepared for subsequent histological analysis. The histological methods have been explained previously (Zheng et al., 2001) and as such is only described briefly here. Rats were transcardially perfused with saline, followed by 4% paraformaldehyde and finally photographic emulsion (Jessops Ltd) to enable visualization of surface cortical vessels in histogical sections. Brains were removed and the right cortex was separated from the rest of the cerebrum and compressed to a thickness of 2 mm. A cryostat was used to section the cortex into slices tangential to its surface. An initial surface slice of 200 μm was sectioned to ensure visualization of the surface blood vessels, and then subsequent 50-μm sections were taken. The slices were placed into an incubation medium in a dark room at 37°C to allowing stain for cytochrome oxidase to visualize barrel representations; this is a modified version of the procedure described by Wong-Riley and Welt (1980). The photographic emulsion in the vessels in histological sections was developed after staining. Photomicrographs of the resultant histological sections of cortex were taken and the images were linearly warped to each other by locating corresponding features by eye.

RESULTS

SPATIAL ANALYSIS OF THE HEMODYNAMIC RESPONSE BEFORE AND AFTER MUSCIMOL INJECTION

Hemodynamic responses were recorded from the right somatosensory whisker barrel cortex of urethane anesthetized rats following presentation of 16 s electrical stimulation of the left whisker pad. The electrode (with fluidic port attached) placement was accurately placed into the cortex as demonstrated by an *in vivo* CCD camera "gray-level" image of the cortical surface (**Figure 1A**). An image of combined photomicrographs of post-mortem histology of the cortical surface and the underling cortical barrels is shown for comparison (**Figure 1B**). It can be seen the electrode and fluidic port have been inserted into the cortex in the region of whisker barrel B1. For this representative animal two regions of interest (ROI) were chosen from which to examine the resultant time series of cortical hemodynamics following pixel averaging. One ROI was selected near to the electrode tip and a second from anterior whisker barrels distal to electrode placement. To assess the spatial extent of the hemodynamic response prior and post muscimol infusion, an average response image was created by averaging all images collected during the entire stimulus presentation period (16 s) for Hbt, HbO_2 and Hbr (**Figures 1C,E**). For the whisker-evoked hemodynamics collected prior to muscimol infusion (control, **Figure 1C**) a large increase over the whole whisker barrel cortical region can be observed for both Hbt and HbO_2; whereas Hbr showed a large decrease over the whole whisker region particularly in the "draining" cortical veins. Examination of the time series of the response for the two ROI selected (**Figure 1D**) demonstrates that the response in the anterior barrels (dotted lines) distal to the electrode is only slightly larger than from the region immediately surrounding the electrode tip (solid lines). Following infusion of muscimol the spatial extent and magnitude of the hemodynamic response elicited by whisker stimuli was altered compared to that observed prior to muscimol infusion. By observation of spatial images calculated by averaging images collected during stimulus presentation (**Figure 1E**), Hbt, HbO_2 and Hbr around the electrode tip were attenuated compared to those elicited prior to muscimol infusion and with respect to the ROI distal to the electrode. This can also be observed in the time series responses from the two ROI (**Figure 1F**) which demonstrate that the hemodynamic response around the electrode tip has been substantially reduced following muscimol infusion whereas the response from the distal region of interest being relatively unaffected.

TIME SERIES OF ANIMAL AVERAGED CORTICAL HEMODYNAMIC RESPONSES (N = 8)

A region of interest was selected around the electrode tip in each animal Hemodynamic data was pixel averaged to create a time series for each animal and then data was subsequently averaged across animals (**Figure 2**). The "control" hemodynamic response elicited by 16 s whisker stimuli prior to muscimol infusion was similar to that described previously (Berwick et al., 2005). It consisted of an immediate large increase in Hbt and HbO_2 that peaked after ~5 s, follow by a decrease to an elevated plateau that lasted for the remainder of stimulus presentation before returning to baseline. The Hbr response was characterized by a small increase within the first second of stimulation, usually referred to as the "deoxy dip" followed by a large decrease below baseline reaching a minima at ~5 s slowly returning to baseline after stimulus cessation. Despite displaying a similar time course to that elicited by whisker stimuli prior to muscimol infusion, following muscimol infusion all aspects of the hemodynamic were substantially attenuated in magnitude (**Figure 2**).

Neural activity assessed by current source density analysis (CSD)

By using a combined multi-channel electrode and infusion fluidic port we were able to monitor the neural response locally at the site of muscimol infusion. CSD analysis converts laminar field potentials evoked by whisker stimuli into current sinks and sources as a function of cortical depth (Nicholson and Freeman, 1975; Mitzdorf, 1985). The neural response to whisker stimuli for a representative animal in the pre-muscimol infusion "control" condition (**Figure 3A**) showed the characteristic evoked superficial source with an accompanying underlying sink centered at Layer IV. The 'heat map' representation of the CSD analysis was derived by averaging of all 80 impulses (16 s stimulation at 5 Hz) of the electrical whisker pad stimulus train presented. This current sink in layer IV represents active excitatory post synaptic potentials in response to each electrical whisker pad impulse. We selected this current sink as our measure of neural activity and averaged across animals. (**Figure 3B**). It can be seen the largest neural response was elicited by the first impulse of the stimulus train with responses to subsequent impulses of the train being at

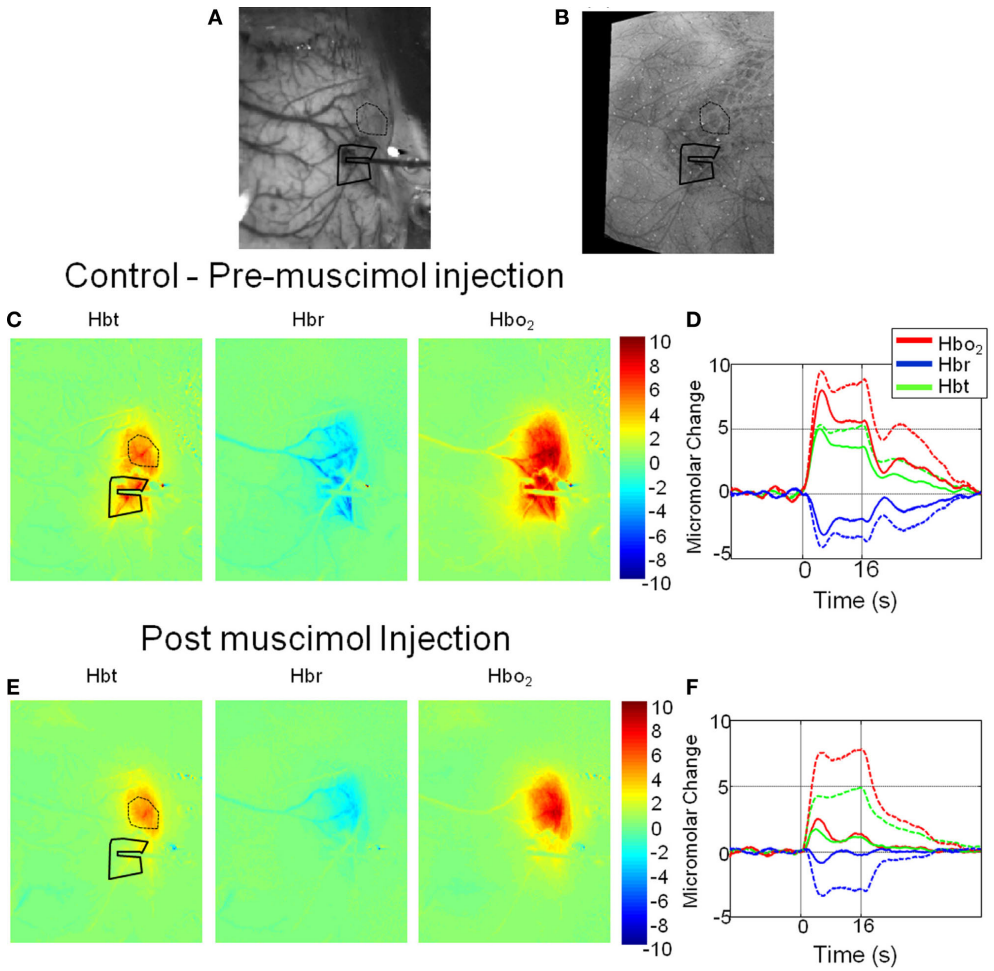

FIGURE 1 | Hemodynamic responses in a representative animal before and after local cortical infusion of muscimol. (A) *In vivo* gray level CCD camera image of the somatosensory cortical surface. The electrode with drug infusion probe attached is visible on the right hand side of the image. **(B)** An image of combined photomicrographs of post-mortem histological sections of the cortical surface and the underling cortical barrels from Layer IV. **(C)** Total blood volume (Hbt), Deoxyhemoglobin (Hbr) and Oxyhemoglobin (HbO_2) responses to 16-s electrical stimulation of the whisker pad. Each image represents an average change in micromolar concentration from baseline over the 16-s stimulation period. **(D)** Time series of hemodynamics response prior to muscimol infusion from a region of interest around the electrode tip (solid lines) and an additional ROI distal to the electrode in the more anterior whisker barrels (dotted lines). **(E)** Hemodynamic response images post muscimol injection. **(F)** Time series of hemodynamics response post muscimol infusion from a region of interest around the electrode tip (solid lines) and an additional ROI distal to the electrode in the more anterior whisker barrels (dotted lines).

a lower but similar magnitude. Following infusion of muscimol the spatial profile of the results of CSD analysis are similar to that observed prior to muscimol infusion but are greatly reduced in magnitude (**Figure 3C**). The sink in layer IV appeared to be less broad in time than the control response. Examination of the animal averaged time series of the layer IV sink (**Figure 3D**) showed that the response to the first impulse of the stimulus train was reduced compared to that elicited prior to muscimol infusion. There was also a large reduction in magnitude of responses to subsequent impulses of the stimulus train compared to the control condition. When these "CSD-sink time series" were averaged across each impulse of the stimulus train (**Figure 3E**) it can be seen that the size of the sinks elicited were smaller and displayed more of a temporally transient nature compared those elicited prior to muscimol infusion.

Statistical analysis

The sum (Σ) of the time series of Hbt and the layer IV CSD-sink were calculated for each animal (**Table 1**). As total hemoglobin concentration (Hbt) is the sum of oxyhemoglobin and deoxyhemoglobin concentration and during the hemodynamic response function the increases in Hbo and decreases in Hbr are correlated (Jones et al., 2001, 2002) it was decided to select the magnitude of Hbt changes as the dependent variable for statistical analysis of hemodynamics. A one-way repeated measures (pre or post muscimol injection) MANOVAs with two dependent variables (Hbt and CSD magnitude) suggested that the injection of muscimol caused a significant change in response size (size: Wilks' Lambda = 0.15, hypothesis df = 2, error df = 6, $F = 16.93, P = 0.003$). Subsequent univariate's ANOVA suggested that both Hbt and CSD responses were significantly reduced

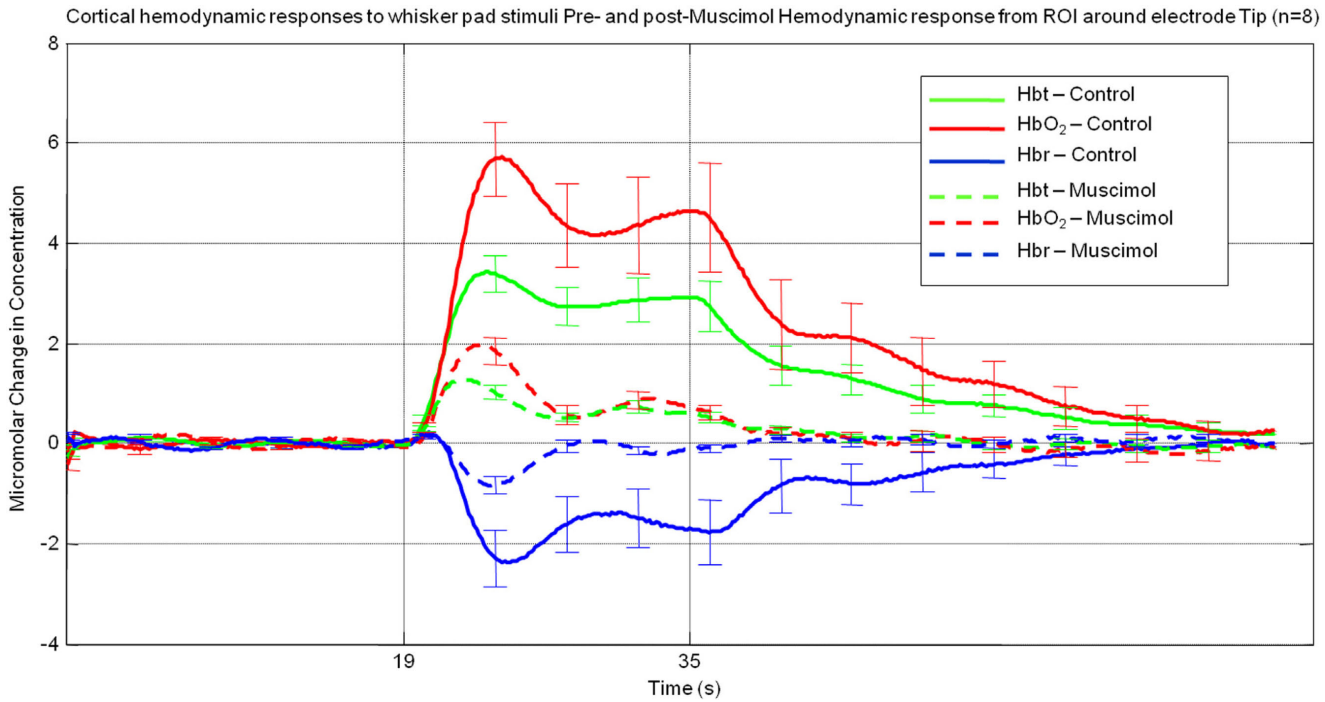

FIGURE 2 | Average hemodynamic responses across animals ($n = 8$) from a region of interest proximal to electrode tip pre (solid lines) and post (dashed lines) muscimol infusion. (Error bars = SEM).

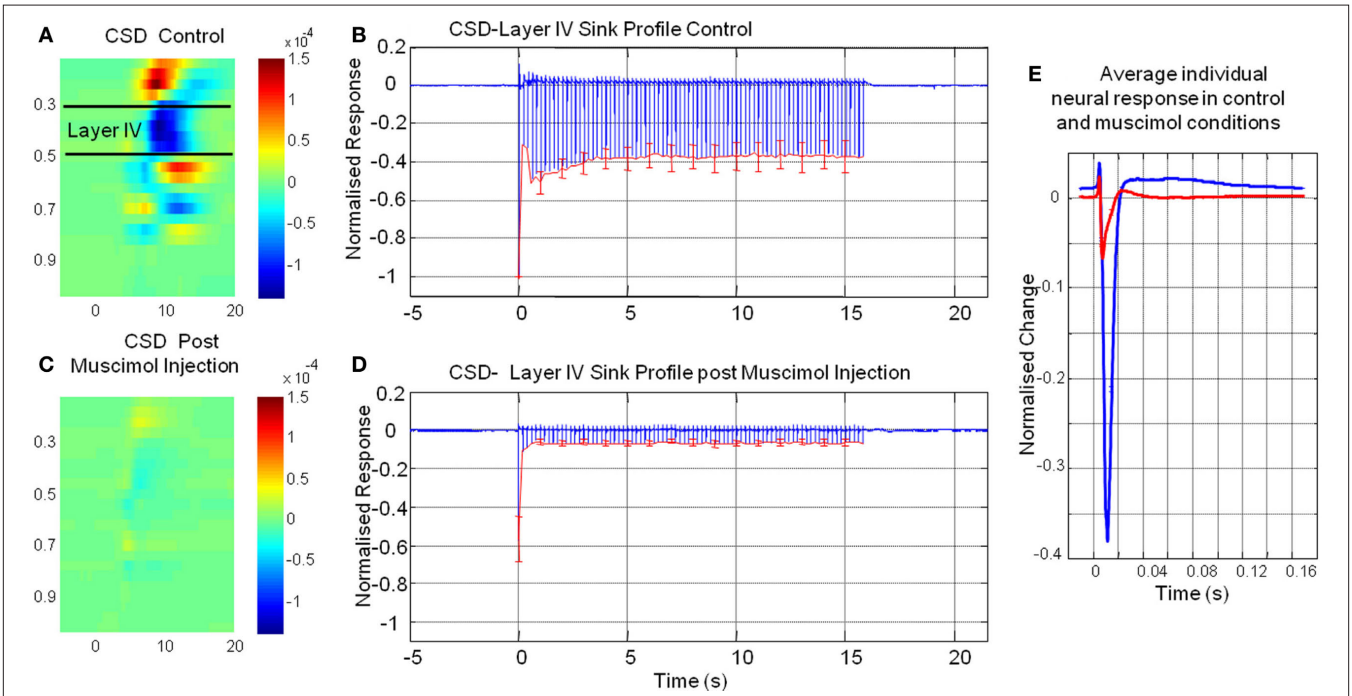

FIGURE 3 | The results of current source density (CSD) of multi laminar local field potential responses elicited by electrical whisker pad stimuli pre and post muscimol infusion. (A) Representative animal impulse averaged CSD response prior to muscimol infusion. **(B)** Time series of layer IV CSD-sink averaged across animals before muscimol infusion. **(C)** Averaged CSD response post muscimol infusion for the same animal as in **(A)**. **(D)** Time series of layer IV CSD-sink averaged across animals post muscimol infusion **(E)** Time series of impulse averaged layer IV CSD-sink response pre (blue) and post (red) muscimol injection (error bars = SEM).

Table 1 | Magnitude of hemodynamic and neuronal responses before and after muscimol infusion.

Animal	Hbt control	Hbt muscimol	CSD-sink control	CSD-sink muscimol
1	416.1	117.0	0.09	0.01
2	262.6	106.3	0.09	0.04
3	217.5	95.7	0.20	0.04
4	347.6	77.4	0.17	0.03
5	417.9	42.4	0.24	0.03
6	325.8	116.6	0.11	0.07
7	375.2	73.1	0.57	0.10
8	136.8	57.3	0.08	0.02
Mean	312.4	87.5	0.19	0.04
(% Reduction)		(72%)		(79%)
SEM	35.2	9.8	0.06	0.01

even if Bonferroni corrected. (Hbt: $F = 39.487$, $P = < 0.0001$; CSD: $F = 8.694$, $P = 0.021$). The reductions in neural and hemodynamics responses were similar (79 and 72% respectively). Therefore even though the magnitude of response has reduced, the quantitative relationships of neurovascular coupling were similar before and after muscimol infusion suggesting the neurovascular coupling mechanisms are conserved for input and processing.

DISCUSSION

The aim of the current study was to assess the neurovascular relationships for input and cortical processing and whether they had equal contributions to the overall neurovascular response elicited by sensory stimuli. We first performed a 16 s whisker stimulation in control conditions and then repeated the same stimulation following local cortical infusion of the $GABA_A$ receptor agonist muscimol. Muscimol was infused to prevent the whisker stimulus driven thalamocortical information being processed by further by the cortex (Higley and Contreras, 2007).

The time series of current sink in layer IV following muscimol infusion (**Figure 3** far right panel) was far more transient than that elicited by whisker stimuli prior to infusion. It has been shown that, in addition to the synaptic activity due to thalamic input, whisker stimuli also evoke longer latency synaptic activity in layer IV due to cortical interactions. Thus, it appears that it is this longer latency synaptic activity associated with intra-cortical processing that is (Ebner and Armstrong-James, 1990) absent from the time series of CSD-sink following muscimol infusion. Furthermore, Higley and Contreras (2007) showed a similar change in time series of CSD from layer IV evoked by whisker stimuli following intra-cortical musicmol infusion. They made recordings from thalamus and suggested that the thalamocortical input was unchanged by intra-cortical muscimol infusion. This is also suggestive the sink at layer IV provides a measure of intra-cortical processing and thalamic input, the former being disrupted by muscimol infusion.

The data suggests that although the neurovascular relationships were similar between input and processing a vast majority of the magnitude of the response was due to processing. Most studies investigating neurovascular coupling with fMRI or other techniques have concluded that the hemodynamic response is due to synaptic input and cortical processing but have not tried to disassociate the two. Two recent findings have, like this study suggested that the hemodynamic response is due to the processing of information rather than the input. Franceschini et al. (2008) measured the somatosensory evoked potentials (SEPs) evoked by forepaw stimuli and accompanying cortical hemodynamics with diffuse optical imaging tomography. They found that the N1 and P2 aspects of the field potential predicted the evoked hemodynamics better than did the P1. As P1 is more associated with synaptic input than the N1 and P2 measures of the field potential they suggested that the hemodynamic response was more associated with cortical processing than synaptic input. Angenstein et al. (2009) directly electrically stimulated the perforant pathway of the hippocampus in anesthetized rats and measured spiking output and the accompanying BOLD fMRI signal. They found that perforant pathway stimuli that evoked the same spiking output in hippocampus had variable accompanying BOLD responses and thus the variability in the BOLD response must have been due to differences in intra-regional processing. They therefore concluded that the evoked BOLD response depended more on the local processing of neural activity than the output or input activity. The current study confirms and extends these recent findings by measuring more local changes of neurovascular coupling (Layer IV current sink and local changes in hemoglobin), and by actively disassociating between the synaptic activity associated with input and intra-cortical processing with the use of muscimol infusion.

The results of the present investigation differ from those obtained in studies performed in rat cerebellum (Caesar et al., 2003, 2008) following local muscimol infusion. In these studies muscimol application had little effect on field potential magnitude whereas the blood flow responses were reduced at superficial cerebellar cortical depths. These authors suggested that GABAergic tone, at least in the cerebellum, plays a role in the relay of excitatory input into blood flow responses. Comparison of these results and those of the current study highlight the potential differences in neurovascular responses between different brain areas.

LIMITATIONS OF CURRENT STUDY

The main limitation of the current study is the assumption that the input from the thalamus is not affected by cortical application of muscimol. This is an important issue because there are far greater corticothalamic descending projections than the thalamocortical projections ascending into the cortex. Recently Higley and Contreras (2007) investigated whether effective cortical neural inhibition following presentation of stimuli to two whiskers was generated in the cortex or a property of sub-cortical interactions. Their experiment was similar that conducted here in that, CSD analysis of neural responses to whisker stimulus were observed before and after cortical application of muscimol (CSD responses also very similar cf Figure 2A, Higley and

Contreras, 2007). However, unlike the present investigation they also made concurrent electrophysiological measurements of thalamic neural activity and showed that the cortical application of muscimol had no effect on the whisker-evoked responses in the thalamus. This provides good evidence that in our study that the thalamic input to the cortex would be unaffected by muscimol application to the cortex.

CONCLUSION

The results of this study show that although the quantitative neurovascular coupling relationship is similar for both cortical input and intra-cortical processing a great majority of the measured neurovascular response is driven by intra-cortical processing. These results may have important implications for the interpretation and understanding of cortical fMRI signals.

REFERENCES

Angenstein, F., Kammerer, E., and Scheich, H. (2009). The BOLD response in the rat hippocampus depends rather on local processing of signals than on the input or output activity. A combined functional MRI and electrophysiological study. *J. Neurosci.* 29, 2428–2439.

Berwick, J., Johnston, D., Jones, M., Martindale, J., Martin, C., Kennerley, A. J., Redgrave, P., and Mayhew, J. E. (2008). Fine detail of neurovascular coupling revealed by spatiotemporal analysis of the hemodynamic response to single whisker stimulation in rat barrel cortex. *J. Neurophysiol.* 99, 787–798.

Berwick, J., Johnston, D., Jones, M., Martindale, J., Redgrave, P., McLoughlin, N., Schiessl, I., and Mayhew, J. E. (2005). Neurovascular coupling investigated with two-dimensional optical imaging spectroscopy in rat whisker barrel cortex. *Eur. J. Neurosci.* 22, 1655–1666.

Caesar, K., Offenhauser, N., and Lauritzen, M. (2008). Gamma-aminobutyric acid modulates local brain oxygen consumption and blood flow in rat cerebellar cortex. *J. Cereb. Blood Flow Metab.* 28, 906–915.

Caesar, K., Thomsen, K., and Lauritzen, M. (2003). Dissociation of spikes, synaptic activity, and activity-dependent increments in rat cerebellar blood flow by tonic synaptic inhibition. *Proc. Natl. Acad. Sci. U.S.A.* 100, 16000–16005.

Ebner, F. F., and Armstrong-James, M. A. (1990). Intracortical processes regulating the integration of sensory information. *Prog. Brain Res.* 86, 129–141.

Franceschini, M. A., Nissila, I., Wu, W., Diamond, S. G., Bonmassar, G., and Boas, D. A. (2008). Coupling between somatosensory evoked potentials and hemodynamic response in the rat. *Neuroimage* 41, 189–203.

Goense, J. B., Ku, S. P., Merkle, H., Tolias, A. S., and Logothetis, N. K. (2008). fMRI of the temporal lobe of the awake monkey at 7 T. *Neuroimage* 39, 1081–1093.

Golanov, E. V., Yamamoto, S., and Reis, D. J. (1994). Spontaneous waves of cerebral blood flow associated with a pattern of electrocortical activity. *Am. J. Physiol.* 266, R204–R214.

Higley, M. J., and Contreras, D. (2007). Cellular mechanisms of suppressive interactions between somatosensory responses *in vivo*. *J. Neurophysiol.* 97, 647–658.

Jones, M., Berwick, J., Johnston, D., and Mayhew, J. (2001). Concurrent optical imaging spectroscopy and laser-Doppler flowmetry: the relationship between blood flow, oxygenation, and volume in rodent barrel cortex. *Neuroimage* 13, 1002–1015.

Jones, M., Berwick, J., and Mayhew, J. (2002). Changes in blood flow, oxygenation, and volume following extended stimulation of rodent barrel cortex. *Neuroimage* 15, 474–487.

Jones, M., Hewson-Stoate, N., Martindale, J., Redgrave, P., and Mayhew, J. (2004). Nonlinear coupling of neural activity and CBF in rodent barrel cortex. *Neuroimage* 22, 956–965.

Kennerley, A. J., Berwick, J., Martindale, J., Johnston, D., Papadakis, N. and Mayhew, J. E., (2005). Concurrent fMRI and optical measures for the investigation of the hemodynamic response function. *Magn. Reson. Med.* 54, 354–365.

Lauritzen, M. (2001). Relationship of spikes, synaptic activity, and local changes of cerebral blood flow. *J. Cereb. Blood Flow Metab.* 21, 1367–1383.

Logothetis, N. K. (2007). The ins and outs of fMRI signals. *Nat. Neurosci.* 10, 1230–1232.

Mangia, S., Giove, F., Tkac, I., Logothetis, N. K., Henry, P. G., Olman, C. A., Maraviglia, B., Di Salle, F., and Ugurbil, K. (2009). Metabolic and hemodynamic events after changes in neuronal activity: current hypotheses, theoretical predictions and *in vivo* NMR experimental findings. *J. Cereb. Blood Flow Metab.* 29, 441–463.

Martindale, J., Mayhew, J., Berwick, J., Jones, M., Martin, C., Johnston, D., Redgrave, P., and Zheng, Y. (2003). The hemodynamic impulse response to a single neural event. *J. Cereb. Blood Flow Metab.* 23, 546–555.

Mitzdorf, U. (1985). Current source-density method and application in cat cerebral cortex: investigation of evoked potentials and EEG phenomena. *Physiol. Rev.* 65, 37–100.

Nakai, M., and Maeda, M. (1999). Scopolamine-sensitive and resistant components of increase in cerebral cortical blood flow elicited by periaqueductal gray matter of rats. *Neurosci. Lett.* 270, 173–176.

Nicholson, C., and Freeman, J. A. (1975). Theory of current source-density analysis and determination of conductivity tensor for anuran cerebellum. *J. Neurophysiol.* 38, 356–368.

Radhakrishnan, I., Nissila, I., Wu, W., Diamond, S. G., Bonmassar, G., Boas, D. A., and Franceschini, M. A. (2007). Studying the neurovascular coupling with evoked potentials and hemodynamic signals. *Soc. Neurosci.* 316.4.

Rauch, A., Rainer, G., and Logothetis, N. K. (2008). The effect of a serotonin-induced dissociation between spiking and perisynaptic activity on BOLD functional MRI. *Proc. Natl. Acad. Sci. U.S.A.* 105, 6759–6764.

Wong-Riley, M. T., and Welt, C. (1980). Histochemical changes in cytochrome oxidase of cortical barrels after vibrissal removal in neonatal and adult mice. *Proc. Natl. Acad. Sci. U.S.A.* 77, 2333–2337.

Zheng, Y., Johnston, D., Berwick, J., and Mayhew, J. (2001). Signal source separation in the analysis of neural activity in brain. *Neuroimage* 13, 447–458.

Conflict of Interest Statement: The authors declare that the research was conducted in the absence of any commercial or financial relationships that could be construed as a potential conflict of interest.

Received: 22 January 2010; paper pending published: 30 March 2010; accepted: 25 June 2010; published online: 11 August 2010.

Citation: Harris S, Jones M, Zheng Y and Berwick J (2010) Does neural input or processing play a greater role in the magnitude of neuroimaging signals? Front. Neuroenerg. ***2****:15. doi: 10.3389/fnene.2010.00015*

frontiers in
NEUROENERGETICS

ORIGINAL RESEARCH ARTICLE
published: 27 August 2010
doi: 10.3389/fnene.2010.00023

Linear superposition of sensory-evoked and ongoing cortical hemodynamics

Mohamad Saka, Jason Berwick and Myles Jones*

The Centre for Signal Processing in NeuroImaging and Systems Neuroscience, Department of Psychology, University of Sheffield, Sheffield, South Yorkshire, UK

Edited by:
David Boas,
Massachusetts General Hospital, USA; Massachusetts Institute of Technology, USA; Harvard Medical School, USA

Reviewed by:
Ivo Vanzetta,
Institut de Neurosciences Cognitives de la Méditerranée, France
Amir Shmuel, McGill University, Canada

****Correspondence:***
Myles Jones, The Centre for Signal Processing in NeuroImaging and Systems Neuroscience, Department of Psychology, Western Bank, University of Sheffield, Sheffield, South Yorkshire S10 2TN, UK.
e-mail: m.jones@sheffield.ac.uk

Modern non-invasive brain imaging techniques utilize changes in cerebral blood flow, volume and oxygenation that accompany brain activation. However, stimulus-evoked hemodynamic responses display considerable inter-trial variability even when identical stimuli are presented and the sources of this variability are poorly understood. One of the sources of this response variation could be ongoing spontaneous hemodynamic fluctuations. To investigate this issue, 2-dimensional optical imaging spectroscopy was used to measure cortical hemodynamics in response to sensory stimuli in anesthetized rodents. Pre-stimulus cortical hemodynamics displayed spontaneous periodic fluctuations and as such, data from individual stimulus presentation trials were assigned to one of four groups depending on the phase angle of pre-stimulus hemodynamic fluctuations and averaged. This analysis revealed that sensory evoked cortical hemodynamics displayed distinctive response characteristics and magnitudes depending on the phase angle of ongoing fluctuations at stimulus onset. To investigate the origin of this phenomenon, "null-trials" were collected without stimulus presentation. Subtraction of phase averaged "null trials" from their phase averaged stimulus-evoked counterparts resulted in four similar time series that resembled the mean stimulus-evoked response. These analyses suggest that linear superposition of evoked and ongoing cortical hemodynamic changes may be a property of the structure of inter-trial variability.

Keywords: optical-imaging, brain-imaging, barrel cortex, spontaneous fluctuations

INTRODUCTION

The changes in blood flow, volume and oxygenation that accompany brain activation are collectively referred to as the hemodynamic response. Cerebral hemodynamics are of interest to cognitive neuroscience as they form the basis of non-invasive human brain imaging techniques such as Blood Oxygenation Level Dependent (BOLD) fMRI (Kwong et al., 1992; Ogawa et al., 1992). However, stimulus-evoked hemodynamic responses are known to display considerable inter-trial variability (Aguirre et al., 1998); and the sources of this variation are poorly understood. The ubiquitous low frequency fluctuations in "resting state" hemodynamics (Biswal et al., 1995; Mayhew et al., 1996; Lowe et al., 1998; Obrig et al., 2000; Spitzer et al., 2001; Greicius et al., 2003; Majeed et al., 2009) could be one possible source of the variation in subsequent stimulus-evoked responses. Understanding whether ongoing and evoked hemodynamics sum linearly is an important prerequisite for developing methods to reduce inter-trial variability. In the case of multiple successive stimulus presentations (Malonek et al., 1997) both linear (Martindale et al., 2003) and non-linear (Cannestra et al., 1998) summation has been reported. In the case of ongoing and evoked hemodynamics, a recent study suggests that ongoing hemodynamic activity may contribute to the variation in stimulus-evoked hemodynamic responses (Fox et al., 2006b), in a similar fashion to that in which resting cortical activity contributes to the variance in evoked neural responses (Arieli et al., 1996). Fox and colleagues measured task related BOLD signal changes in motor cortex and found inter-trial variability. Subsequent subtraction of coherent spontaneous BOLD fluctuations from the cortex contralateral to that activated by the task, reduced inter-trial variability and therefore suggested a superposition of evoked and ongoing hemodynamics. Another approach for examining the role of spontaneous pre-stimulus fluctuations in the trial-to-trial variability of stimulus-evoked neurophysiological data, is to group trials based on some property of their pre-stimulus time series, average trials in each group and examine whether the mean groups responses differ (Sauseng et al., 2007). To investigate whether this approach could confirm and extend the findings of Fox et al. (2006b) we first recorded whisker pad stimulus-evoked cortical hemodynamics in the rodent barrel cortex of anesthetized rodents with 2-dimensional optical imaging spectroscopy (2D-OIS, Devor et al., 2003; Berwick et al., 2005, 2008). This allowed measurement of the individual components of the hemodynamic response (oxyhemoglobin, deoxyhemoglobin and total hemoglobin) at a higher temporal resolution than that afforded by fMRI. Data was examined on a trial by trial basis and grouped based on pre-stimulus hemodynamics. As hemodynamic fluctuations are oscillatory in nature (Mayhew et al., 1996), an identical magnitude of hemodynamics occurs at two distinct phases (e.g., 0° and 180°). Therefore if trials were grouped based on the magnitude of hemodynamic activity at stimulus onset, information regarding whether the fluctuation was "rising" or "falling" at this time point would be lost. Therefore the metric of pre-stimulus hemodynamic activity chosen to "classify" individual trials, was not the magnitude of pre-stimulus hemodynamic activities but their phase angle at stimulus

onset. Individual trials were then averaged according to the phase of their pre-stimulus hemodynamic fluctuations. This revealed that cortical hemodynamics display distinct responses to sensory stimuli depending on the phase of pre-stimulus fluctuations. To investigate the origin of this phenomenon, null trials of identical duration were collected where no stimuli were presented. Phase averaged "null trial data" was then used to investigate whether ongoing and evoked hemodynamics linearly superpose by examining times series produced by subtracting phase averaged "null trial data" from phase averaged stimulus-evoked trials.

MATERIALS AND METHODS

ANIMAL PREPARATION (N = 6)

Female Hooded Lister rats weighing between 250 g and 400 g were kept in a 12-h dark/light cycle environment at a temperature of 22°C with food and water *ad libitum*. Prior to surgery, animals were anesthetized with urethane (1.25 g/kg i.p.). Rectal temperature was maintained at 37°C throughout surgical and experimental procedures using a homeothermic blanket (Harvard). Animals were tracheotomized to allow artificial ventilation and measurement of end-tidal CO_2. Ventilation parameters were adjusted to maintain blood gas measurements and end-tidal CO_2 within physiological limits. The femoral vein and artery were cannulated to allow drug infusion and measurement of mean arterial blood pressure respectively. Phenylephrine (0.13–0.26 mg/hr) was infused to maintain blood pressure between physiological limits (MABP, 100–110 mmHg). Animals were placed in a stereotaxic frame (Kopf Instruments) and the skull overlying the somatosensory cortex was thinned to translucency with a dental drill under constant cooling with saline. A plastic "well" was attached to the thinned skull and filled with saline (37°C) to reduce specularities from the skull surface. All procedures were carried out in accord with Home Office regulations.

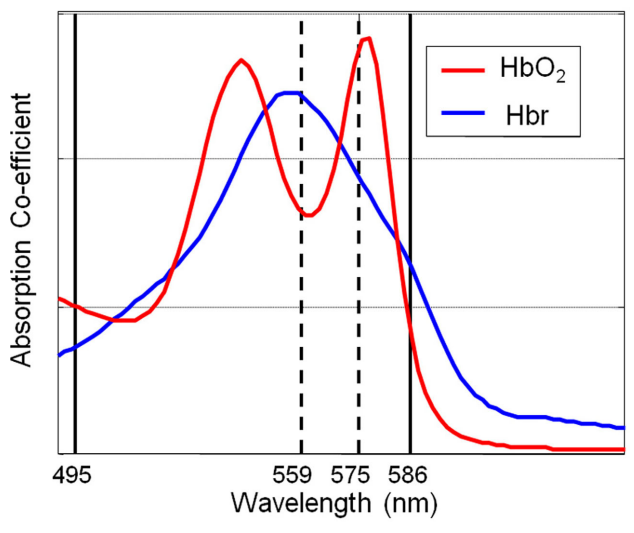

FIGURE 1 | A schematic diagram of the absorption spectra of oxyhemoglobin (HbO_2) and deoxyhemoglobin (Hbr) displaying the choices of wavelengths of filters for the incident illumination used for optical imaging spectroscopy.

2D OPTICAL IMAGING SPECTROSCOPY ESTIMATES OF HEMOGLOBIN CHANGES

Images of the cortical surface were collected with a high-speed CCD camera. The cortex was sequentially illuminated with four wavelengths (two pairs) of light (495 ± 31 and 587 ± 9 nm FWHM; 559 ± 16 nm and 575 ± 14 FWHM) with a Lambda DG-4 high-speed filter changer (Sutter Instrument, Novato, CA, USA) and stabilized 300W xenon arc light source (**Figure 1**). The wavelengths in each pair are chosen such that they sample a similar same tissue volume. However, for each of the two wavelengths in each pair, one is associated with a greater absorption co-efficient for oxyhemoglobin than deoxyhemoglobin and the other is associated with a greater absorption co-efficient for deoxyhemoglobin than oxyhemoglobin. The camera data collection (30 Hz) was synchronized to filter changing such that each subsequent image was collected with a different wavelength of cortical illumination. This "multi-wavelength" optical imaging data was subject to spectral analysis using a modified beer Lambert law that corrects for the wavelength dependency of photon path length (Mayhew et al., 1999) and has been used previously to analyze this form of spectroscopic data (Berwick et al., 2005, 2008). This allowed estimation of changes in total hemoglobin concentration (Hbt), oxyhemoglobin concentration (HbO_2) and deoxyhemoglobin concentration (Hbr). As data from each of the four wavelengths of illumination were required for spectral estimates of hemoglobin changes the effective sampling frequency was that of the camera frame rate divided by 4 (30/4 = 7.5). The baseline value of cortical Hbt was set at 104 μM which was estimated by a previous MRI study in rodent (Kennerley et al., 2005).

STIMULUS PRESENTATION, PARADIGMS AND DATA ANALYSIS

All stimulus presentation was controlled through a 1401plus (CED Ltd, UK) running custom-written code with stimulus onset time locked to the CCD camera. Electrical stimulation of the whole whisker pad was delivered via stainless steel electrodes inserted in an anterior direction each side of the whisker pad (Mayhew et al., 2000; Jones et al., 2001, 2002, 2004, 2005; Sheth et al., 2003). All electrical stimuli were presented for 3 s at 1 Hz with a 0.3 ms individual pulse width at an intensity of 1.2 mA (Jones et al., 2004, 2005, 2008). No change in MABP, heart rate or PCO_2 were observed at this stimulus intensity suggesting that the measured hemodynamic responses were not contaminated by systemic physiological changes. Trials were 24-s long with a 1-s inter-trial interval. Stimulation occurred on the 8th second of each trial. Experimental runs consisted of 30 trials. In each experimental run, either stimuli were presented or else data with identical parameters were collected without presenting stimuli. 6–9 experimental runs (180–270 trials) where stimuli were presented (termed "stimulus-evoked") and 6–8 experimental runs (180–240 trials) where stimuli were not presented (termed "nulls") were collected for each animal ($n = 6$).

For each animal, trial averaged images of total Hbt changes following stimulus presentation were analyzed using a signal source separation algorithm (Molgedey and Schuster, 1994) as previously described (Zheng et al., 2001). This procedure has been shown on numerous occasions to localize spatially discrete activations of barrel cortex which show excellent concordance with cytochrome oxidase histology in tangential (Jones et al., 2001, 2002) and coronal

sections (Jones et al., 2004). "Barrel maps" were registered with images of cortical surface for selection of a region of interest (ROI). A parenchymal ROI was selected in the center of the active barrel region avoiding overlying surface vasculature. This ROI was used to provide time series of hemodynamics for each "stimulus-evoked" or "null" trial for each animal.

TRIAL AVERAGING ACCORDING TO PHASE OF SPONTANEOUS PRE-STIMULUS HEMODYNAMIC FLUCTUATIONS

A Hilbert transform (Matlab ™ function "Hilbert") was used to calculate the phase of the ongoing pre-stimulus fluctuations in Hbt. Briefly, this technique assumes the time series to be the real part of a complex signal and determines the imaginary part. The phase is calculated as the inverse tangent of the ratio of the imaginary and real signals (Pikovsky et al., 2001). This allows calculation of the instantaneous phase of an ongoing time series even if the time series is not precisely sinusoidal (Haslinger et al., 2006) and has been extensively used to characterize EEG data (Le Van Quyen et al., 2001; Le Van Quyen and Bragin, 2007). For clarity phase angle is expressed in degrees (rather than radians) and between 0 and 360. Trials were then assigned to one of four groups (0–90°; 90–180°; 180–270°; 270–360°) based on the phase of the ongoing fluctuations in Hbt immediately before stimulus onset. In the case of trials in which stimuli were not presented, phase was calculated for an identical period (8 s) of the time series and trials were again averaged based on the phase found at the 8-s time point (corresponding to the time of stimulus onset in the stimulus presentation trials. Again trials were then assigned to one of four groups (0°–90°; 90°–180°; 180°–270°; 270°–360° and averaged).

RESULTS

THE TRIAL AND ANIMAL AVERAGED WHISKER EVOKED CORTICAL HEMODYNAMIC RESPONSE

Trial and animal averaging revealed the characteristic cortical hemodynamic response elicited by stimulation of the whisker pad as measured by optical imaging spectroscopy (**Figure 2**). Following stimulus onset there was an increase in total Hbt and an increase in oxyhemoglobin (HbO_2) concentration. Changes in deoxyhemoglobin (Hbr) concentration were biphasic displaying a small early increase shortly after stimulus onset, then decreasing below pre-stimulus baseline.

INDIVIDUAL TRIAL DATA DISPLAYS INTER-TRIAL VARIABILITY AND SPONTANEOUS PRE-STIMULUS FLUCTUATIONS

However, examination of individual trials suggested that stimulus-evoked hemodynamic responses displayed considerable inter-trial variability (**Figure 3**). Twenty trials of the stimulus-evoked changes in hemodynamics from a single subject are shown for example (**Figure 3**). Individual trial data show variability in response magnitude and contain low frequency spontaneous fluctuations in the pre-stimulus "baseline" period. Indeed examination of trials in which stimuli were not presented reveals low frequency fluctuations

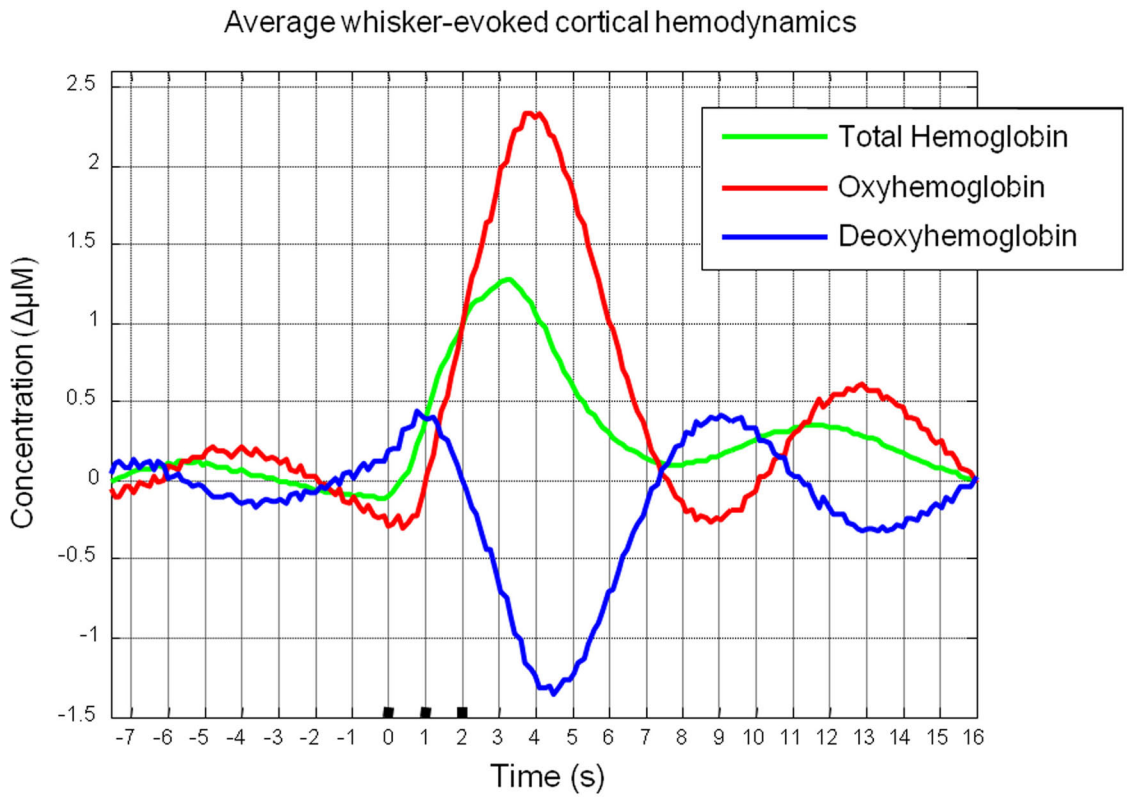

FIGURE 2 | Mean cortical hemodynamics in response to sensory stimuli as measured by optical imaging spectroscopy. Changes in Total Hemoglobin (Hbt), oxyhemoglobin (HbO_2) and deoxyhemoglobin (Hbr) following presentation of electrical whisker pad stimuli (3 s, 1 Hz, 1.2 mA).

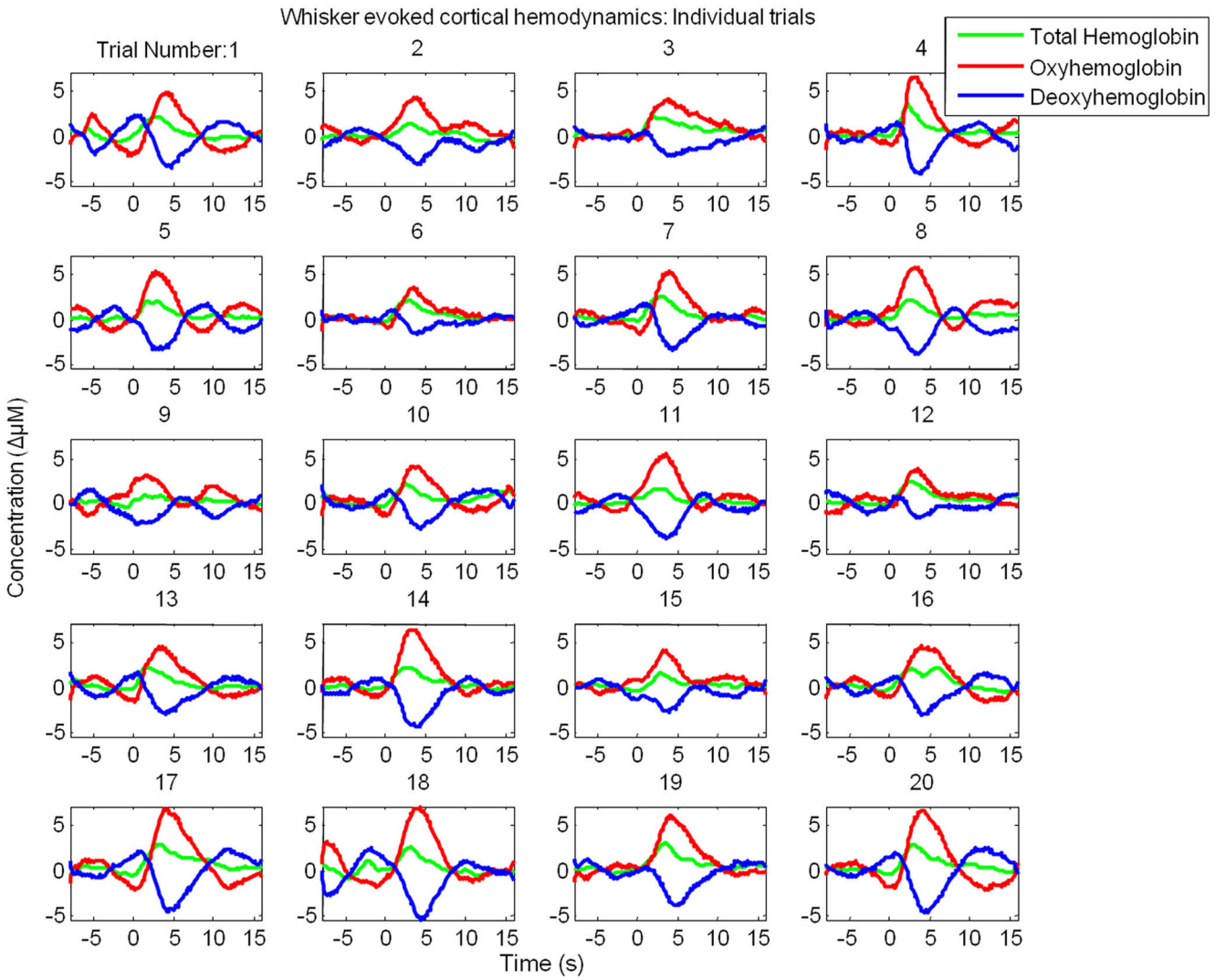

FIGURE 3 | Cortical hemodynamic responses display considerable inter-trial variability. Twenty individual "un-averaged" trials of the changes in Total Hemoglobin (Hbt), oxyhemoglobin (HbO_2) and deoxyhemoglobin (Hbr) following presentation of electrical whisker pad stimuli (3 s, 1 Hz, 1.2 mA) as measured by optical imaging spectroscopy.

in Hbt, HbO_2 and Hbr (**Figure 4A**). The frequency of these low frequency fluctuations was ~0.1 Hz (**Figure 4B**) as previously reported (Mayhew et al., 1996; Spitzer et al., 2001; Majeed et al., 2009). Hbt fluctuations led those of HbO_2, while HbO_2 and Hbr were approximately in anti-phase (**Figure 4A**). It can be observed that hemodynamics contain low frequency fluctuations with higher frequency "noise" superimposed on the time series (**Figures 4A,B**). These higher frequency fluctuations are orders of magnitude lower than the predominant fluctuations at ~ 0.1 Hz (**Figure 4C**). The data were smoothed using a Savitzky–Golay filter with a 3rd order polynominal to remove higher frequency components from the data. It can be seen that this does not alter the phase, frequency or magnitude of the data (**Figure 4C**). It simply removes the higher frequency "noise" which is well outside the frequency range of the low frequency fluctuations (**Figure 4**) and therefore do not require more sophisticated removal techniques. The source of this higher frequency component is most likely to be due to breathing as animals are artificially respirated at a rate of between 1–2 Hz and in individual animals (e.g., **Figure 4E**) a peak at similar frequency (~1.2 Hz in this case) can be seen in the Fourier transform of both the end-tidal CO_2 trace and the cortical hemodynamics.

AVERAGING TRIALS ACCORDING TO THE PHASE OF SPONTANEOUS PRE-STIMULUS HEMODYNAMIC FLUCTUATIONS AT STIMULUS ONSET

Data was examined on a trial by trial basis and grouped based on pre-stimulus hemodynamics. The question arises as to which metric of pre-stimulus hemodynamics to use to classify trials. As hemodynamic fluctuations are oscillatory in nature (Mayhew et al., 1996; Majeed et al., 2009) at any particular time point their time series could be classified by phase or magnitude. As an identical magnitude of hemodynamics could occur at two distinct phases (e.g., 0° and 180°), if trials were grouped based on the

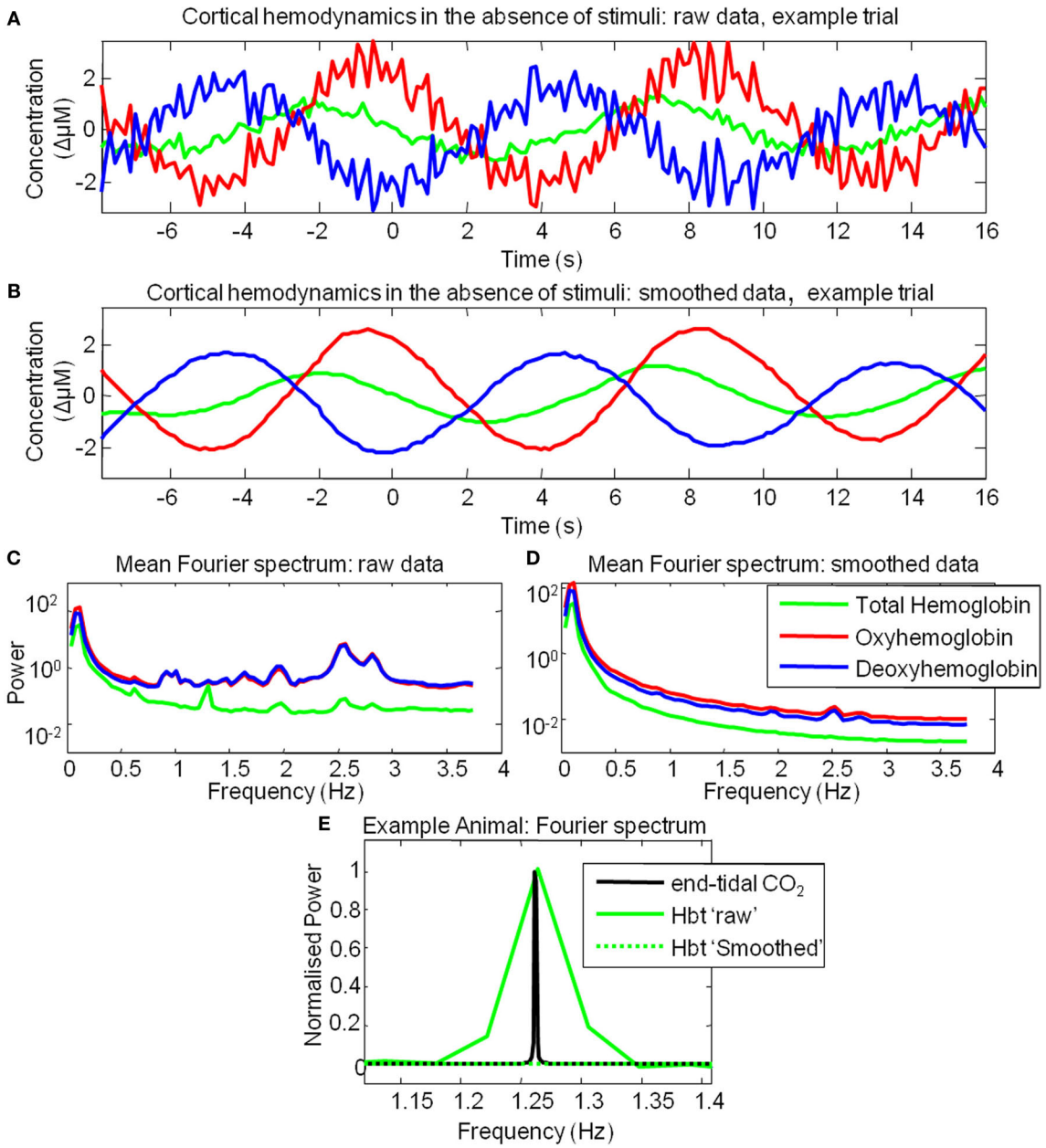

FIGURE 4 | Cortical hemodynamics display low frequency fluctuations in the absence of stimulus presentation. (A) The time series of the changes in Total Hemoglobin (Hbt), oxyhemoglobin (HbO_2) and deoxyhemoglobin (Hbr) from of a single example trial where stimulus was not presented. **(B)** The same data as **(A)** smoothed with a Savitzky–Golay filter. **(C)** Mean power spectra of all trials in which stimuli were not presented. **(D)** Mean power spectra of all trials in which stimuli were not presented following smoothing procedure. **(E)** Fourier spectrum of total Hbt and end-tidal PCO_2 measurements from an example animal.

magnitude of hemodynamic activity at stimulus onset, information regarding whether the fluctuation was "rising" or "falling" at this time point would be lost. Therefore the metric of pre-stimulus hemodynamic activity chosen to "classify" individual trials, was their phase angle at stimulus onset. The Hilbert transform was used to calculate the phase of each data point of the pre-stimulus period of Hbt (**Figure 5**). The Hilbert transform is advantageous in that it can track the instantaneous phase of a time series even if the time series is not perfectly sinusoidal or periodic, from as little data as 3 data points. However, this means that this method could be relatively sensitive to noise. Notwithstanding, reasonable estimates of phase of the raw data can be obtained (**Figure 5A**) albeit with "noise" commensurate with that in the original time series and "difficulty" at some time points. As such, before the Hilbert transform was used to estimate phase the data was first smoothed using a Savitzky–Golay filter with a 3rd order polynominal to remove higher frequency components (**Figures 4,5**). Following filtering, it can clearly be seen that the Hilbert transform is accurately tracking the ongoing phase of the predominant 0.1 Hz component (**Figure 5D**).

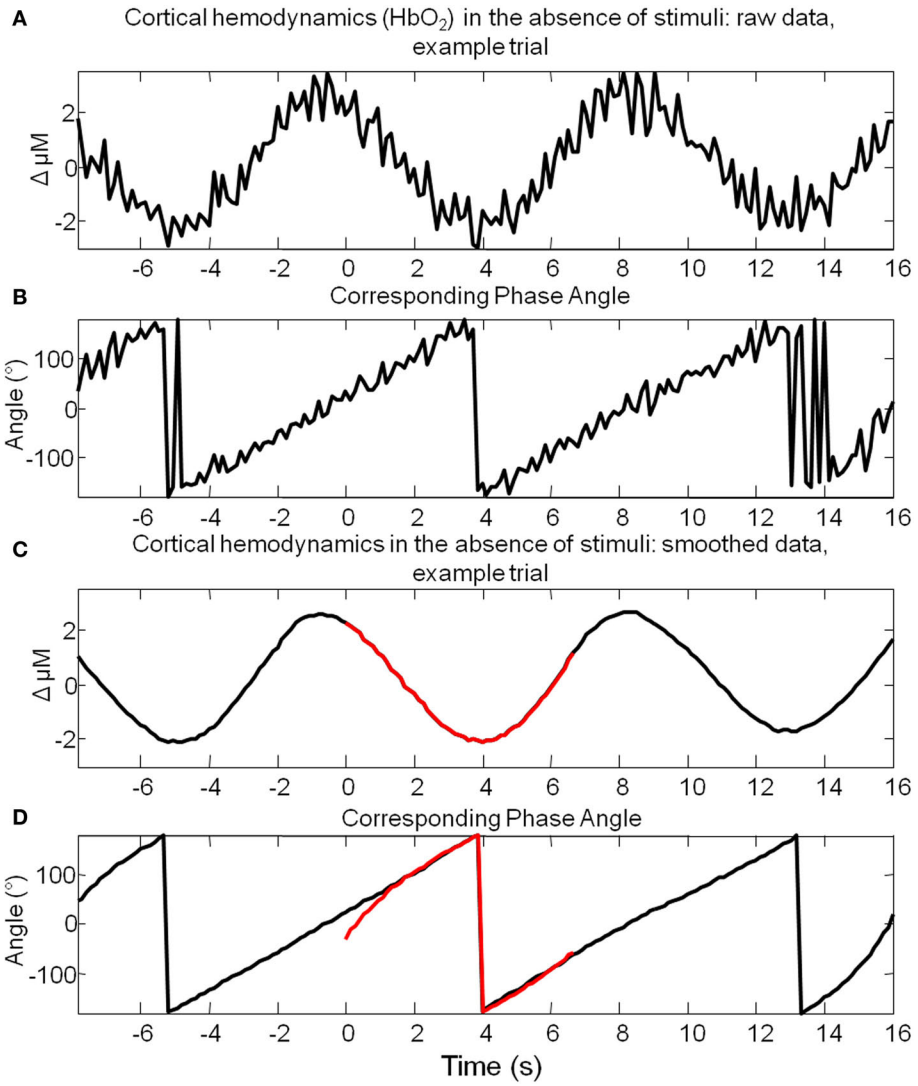

FIGURE 5 | Hilbert transform allows estimation of the instantaneous phase of spontaneous cortical hemodynamic fluctuations. (A) The time series of the changes in oxyhemoglobin (HbO_2) from a single example trial where stimuli were not presented. **(B)** The phase angle for each time point of the data presented in **(A)** calculated using the Hilbert transform. **(C)** The same data as that presented in **(A)**, smoothed with a Savitzky–Golay filter. **(D)** The phase angle for each time point of the data presented in **(C)** calculated using the Hilbert transform. A small section of **(C)** is highlighted in red and the phase calculated from these time points alone is highlighted in red in **(D)**. This suggests that a commensurate estimate of phase can be obtained after tracking only several seconds of data to that obtained by tracking the phase of the data for 8 s preceding these time points.

A total of 1404 trials were taken from six animals and were ranked according to their phase at the time point of stimulus onset. Phase was calculated for the 8-s pre-stimulus period for each trial. To demonstrate this was a sufficient time period to reliably estimate the phase at the time point of stimulus onset, an 8-s subsection of a longer time series is shown (highlighted in red **Figure 5C**). After several seconds (~2 s) the estimate of phase for this segment (**Figure 5D**) is similar than that obtained by tracking the phase of the time series preceding this segment. This suggests that 8 s is a sufficient time period to estimate the phase of these fluctuations. Trials regardless of subject origin were then assigned to one of four groups according to the phase angle of the spontaneous hemodynamic fluctuations (0°–90°; 90°–180°; 180°–270°; 270°–360°) in Hbt at the single time point before stimulus onset. Examination of the pre-stimulus time series in each of the phase groups suggests that the analysis procedure is effective (**Figure 6B**) in that each mean phase averaged time series differs from one another and appears to display an expected appropriate time course. To illustrate this further an artificial sine wave is shown for comparison (**Figure 6A**). Furthermore this averaging procedure does not alter the frequency of the low frequency components as the Fourier spectrum of the pre-stimulus phase averaged time series is similar to that observed for data collected in the absence of stimuli (**Figure 6C** compared to **Figure 4C**).

Subsequent "phase-averaged" total hemoglobin responses evoked by sensory stimuli were of differing magnitudes (**Figure 6D**). The magnitude of the stimulus-evoked increases in Hbt was smallest in the 0°–90° group, followed by in the 270°–360° group and 90°–180°

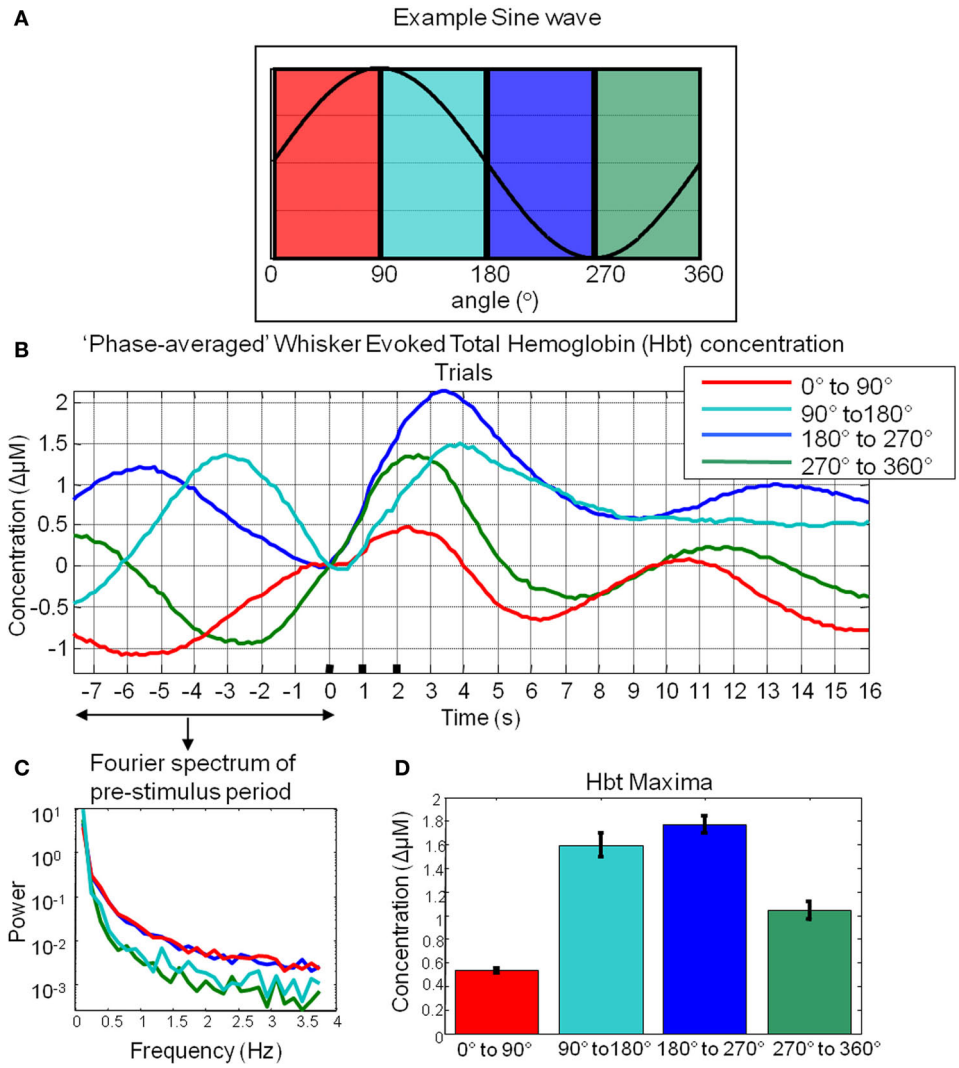

FIGURE 6 | Cortical total hemoglobin responses to sensory stimuli. (A) An artificial sine wave with respect to angle in degrees is shown for reference. **(B)** Hbt responses to sensory stimuli were grouped based on the phase of their pre-stimulus fluctuations at stimulus onset and averaged. **(C)** Power spectra of pre-stimulus fluctuations following phase averaging procedure. **(D)** Mean maxima of Hbt changes evoked by sensory stimuli depending on the phase of pre-stimulus fluctuations at stimulus onset.

group and was largest in the 180°–270° group (**Figure 6**). Trials were treated as subjects for statistical analyses. An independent groups ANOVA suggested that Hbt maxima differed significantly in these phase groups ($F = 86.614$, df error = 1284, $p = 0.000$). Bonferroni corrected *post hoc* tests suggested the Hbt maxima in each phase group differed significantly ($p = 0.000$) from one another apart from between the 90°–180°group and the 180°–270° group ($p = 0.520$).

"NULL" TRIALS IN WHICH STIMULI WERE NOT PRESENTED

To investigate the possible origin of this phenomenon, data from trials in which no stimuli were presented were also averaged based on the phase of their Hbt fluctuations at a time point that corresponded to stimulus onset (8 s in each trial) in the stimulus presentation trials. This resulted in phase averaged time series that were identical to phase averaged stimulus-evoked responses during the "pre-stimulus" period (compare **Figure 7A and Figure 7B**). However, the time series differed after stimulus presentation with the phase averaged null trials providing an indication of the average "behavior" of the hemodynamics for each phase group had a stimulus not occurred. In the case of the phase averaged "null" trials there appears to be a slight dampening of the fluctuations after a certain period (approximately 10 s). This is because the fluctuations are not perfectly sinusoidal and periodic and as such, averaging trials together that are grouped for phase at a certain time point does not result in an infinite time series of unvarying amplitude. To investigate whether the differences in stimulus-evoked responses in each phase group were due to superposition of ongoing and evoked hemodynamics, phase averaged "nulls" were subtracted from phase averaged stimulus-evoked responses. This subtraction resulted in four similar time series that closely resembled the time series of the mean of all trials without phase averaging (**Figure 7C**). Slight

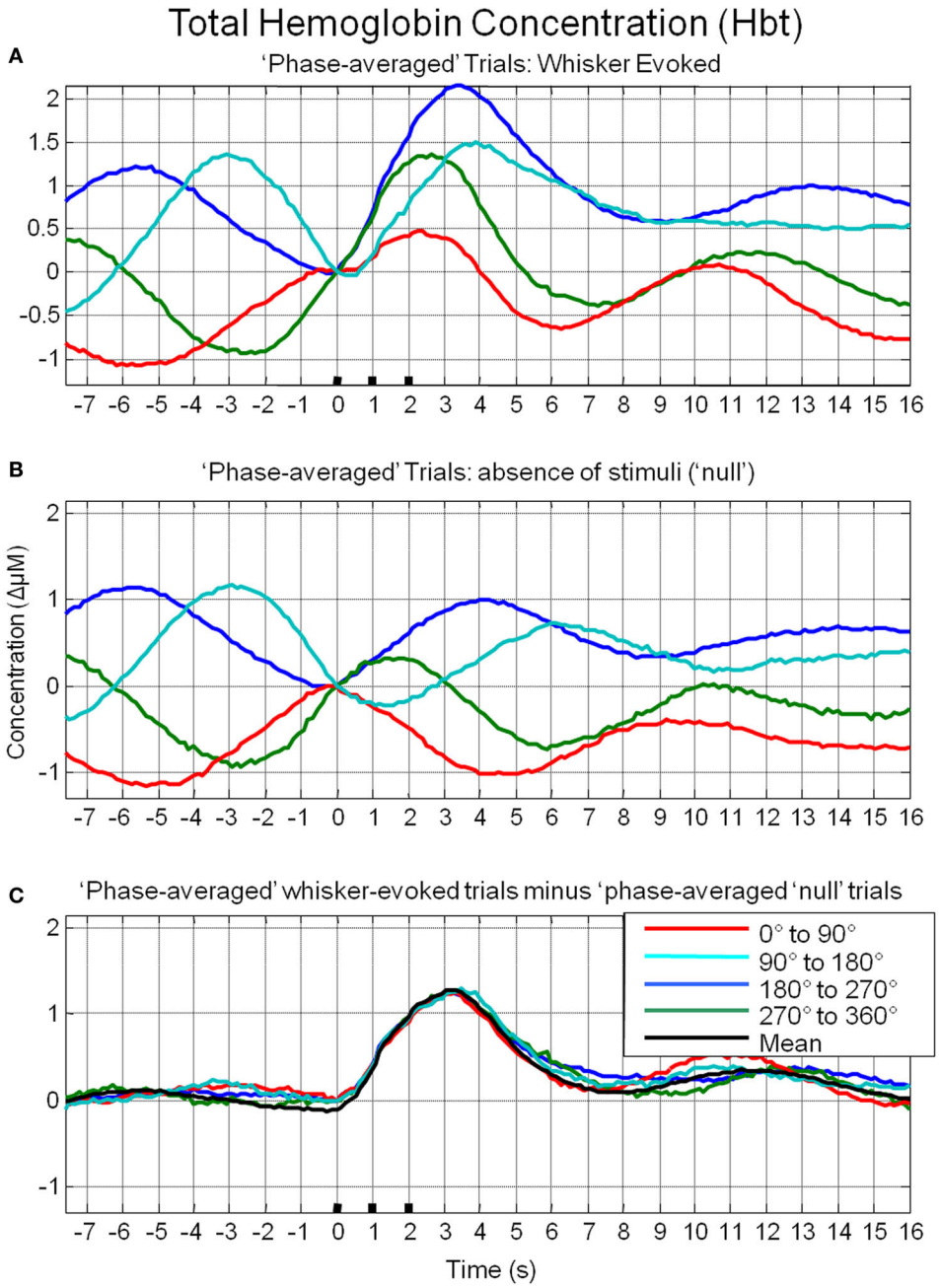

FIGURE 7 | Linear superposition of sensory-evoked and ongoing cortical total hemoglobin concentration changes (Hbt). (A) Hbt responses to sensory stimuli were grouped based on the phase of their pre-stimulus fluctuations at stimulus onset and averaged. **(B)** Hbt trial data without presentation of sensory stimuli ("nulls") are grouped based on the phase of their pre-stimulus fluctuations at the same time point within each trial and averaged. **(C)** Subtraction of the phase averaged stimulus-evoked responses from their phase averaged null counterpart results in four similar time series.

differences between the "phase averaged responses" and the mean response may have been due to non-identical trial numbers in each of the phase groups. Similar phenomenon could be observed in the other components of the hemodynamic response as measured by optical imaging spectroscopy, oxyhemoglobin (HbO_2, **Figure 8A**) and deoxyhemoglobin (Hbr, **Figure 9A**). When changes in oxyhemoglobin concentration were averaged on the basis of their phase at stimulus onset they also displayed differences in magnitudes (**Figure 8**). Likewise, subtraction of phase averaged HbO_2 null trials from phase averaged stimulus-evoked trials also resulted in four similar time series. A commensurate phenomenon was observed for changes in Hbr (**Figure 9**).

An additional analysis was performed to investigate whether these phenomena were due to simply averaging subsets of trials rather than the suggested averaging of trials based on their phase at stimulus onset (**Figure 10**). Trials were randomly allocated to four

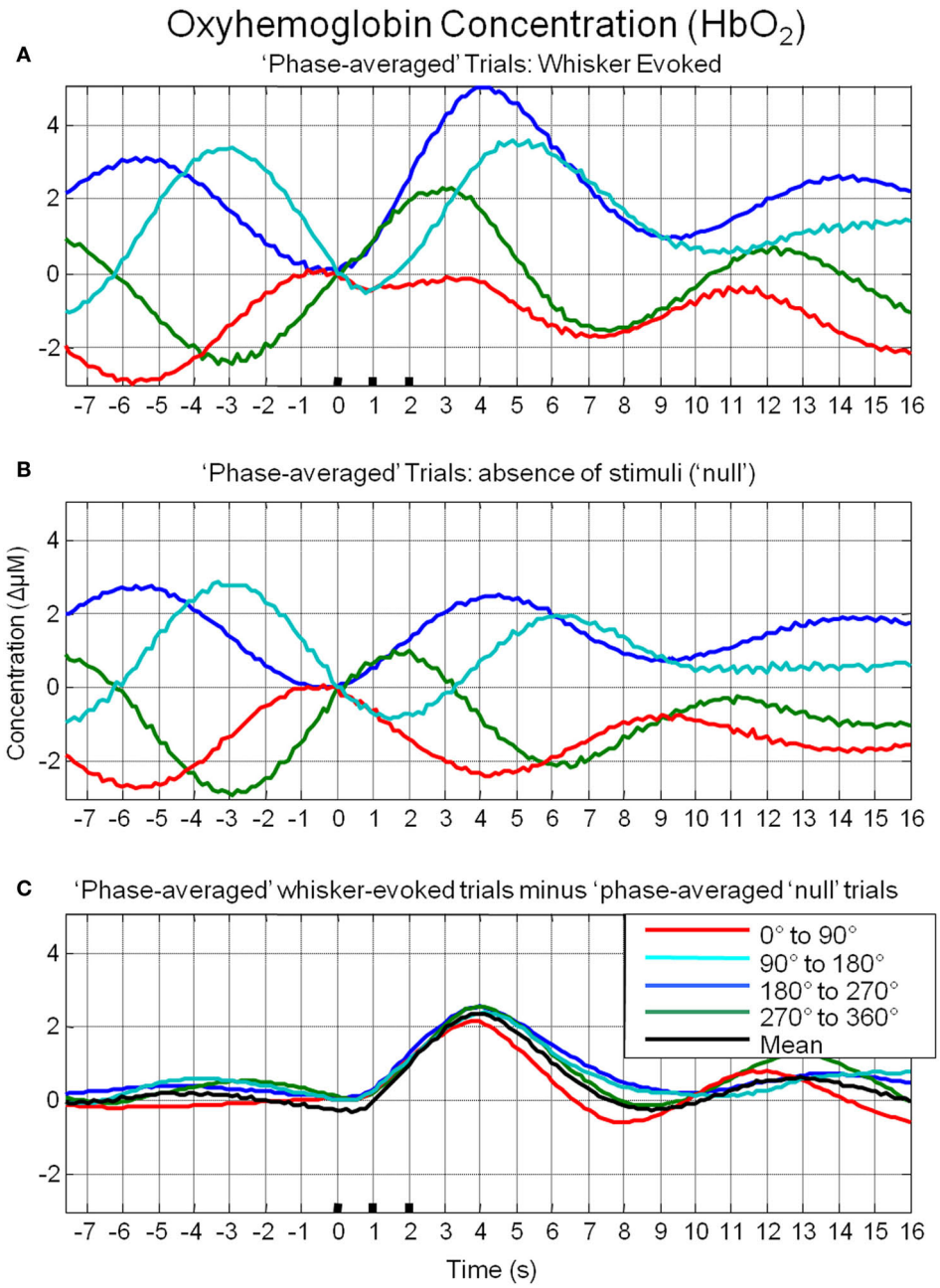

FIGURE 8 | Linear superposition of sensory-evoked and ongoing cortical oxyhemoglobin concentration changes (HbO_2). (A) HbO_2 responses to sensory stimuli were grouped based on the phase of their pre-stimulus fluctuations at stimulus onset and averaged. **(B)** HbO_2 trial data without presentation of sensory stimuli ("nulls") are grouped based on the phase of their pre-stimulus fluctuations at the same time point within each trial and averaged. **(C)** Subtraction of the phase averaged stimulus-evoked responses from their phase averaged null counterpart results in four similar time series.

groups and averaged. It can be clearly seen that in case of stimulus-evoked responses, group averaging resulted in four similar time series that closely resembled the mean of all trials. In the case of trials where stimuli were not presented, this resulted in time series in which little remnants of spontaneous fluctuations remained. Unsurprisingly, subtraction of the phase averaged stimulus-evoked responses from their phase averaged null counterparts produced little alteration of the "group-averaged" time series.

DISCUSSION

The data and analyses presented here extend and confirm the finding of Fox et al. (2006b) by further demonstrating interaction between stimulus-evoked and ongoing cortical hemodynamics. The data and analyses presented here suggest that depending on the phase of ongoing cortical hemodynamic fluctuations at stimulus onset, stimulus-evoked hemodynamics display different magnitudes and temporal dynamics. To investigate the origin of the interaction

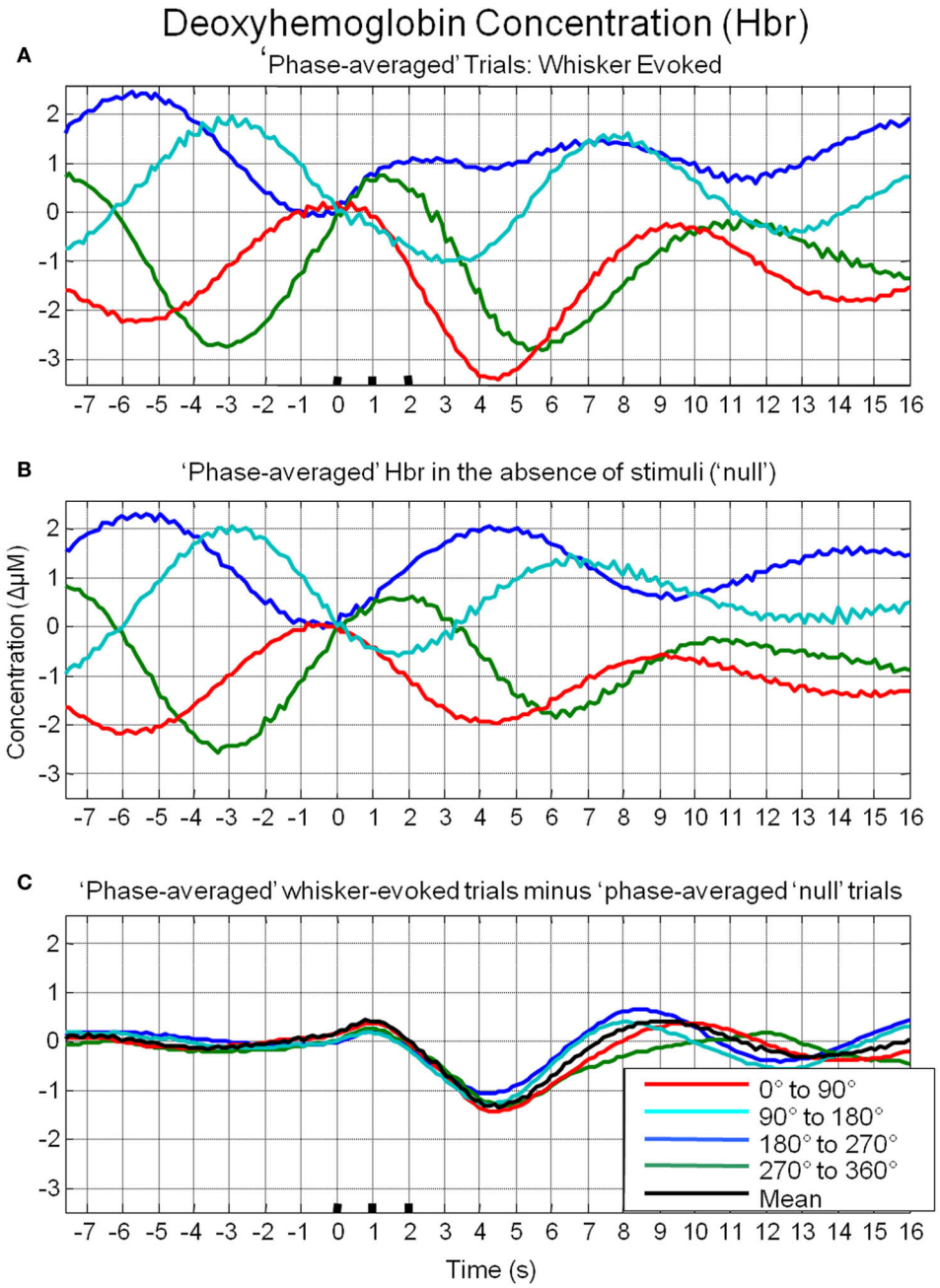

FIGURE 9 | Linear superposition of sensory-evoked and ongoing cortical deoxyhemoglobin concentration changes (Hbr). (A) Hbr responses to sensory stimuli were grouped based on the phase of their pre-stimulus fluctuations at stimulus onset and averaged. **(B)** Hbr trial data without presentation of sensory stimuli ("nulls") are grouped based on the phase of their pre-stimulus fluctuations at the same time point within each trial and averaged. **(C)** Subtraction of the phase averaged stimulus-evoked responses from their phase averaged null counterpart results in four similar time series.

between spontaneous and motor-evoked fMRI signals, Fox and colleagues utilized the coherent fluctuations from the contralateral motor cortex that was not activated by task demands (Fox et al., 2006b). Subtraction of these spontaneous fluctuations on a trial-to-trial basis removed a significant component of the variability of the stimulus-evoked responses (Fox et al., 2006b). As in the somatosensory system of the anesthetized rodent, sensory stimuli have been shown to elicit changes in metabolic and hemodynamic parameters in cortex both ipsilateral and contralateral to the sensory stimulus (Devor et al., 2008) adopting a similar approach to Fox and colleagues in this animal model would have resulted in the subtraction of sensory responses rather than just coherent spontaneous fluctuations. Thus rather than compare coherent fluctuations from contralateral barrel cortex during stimulus presentation, we collected data in the absence of stimuli from the same barrel cortex ROI selected for stimulus-evoked trials. The use of optical

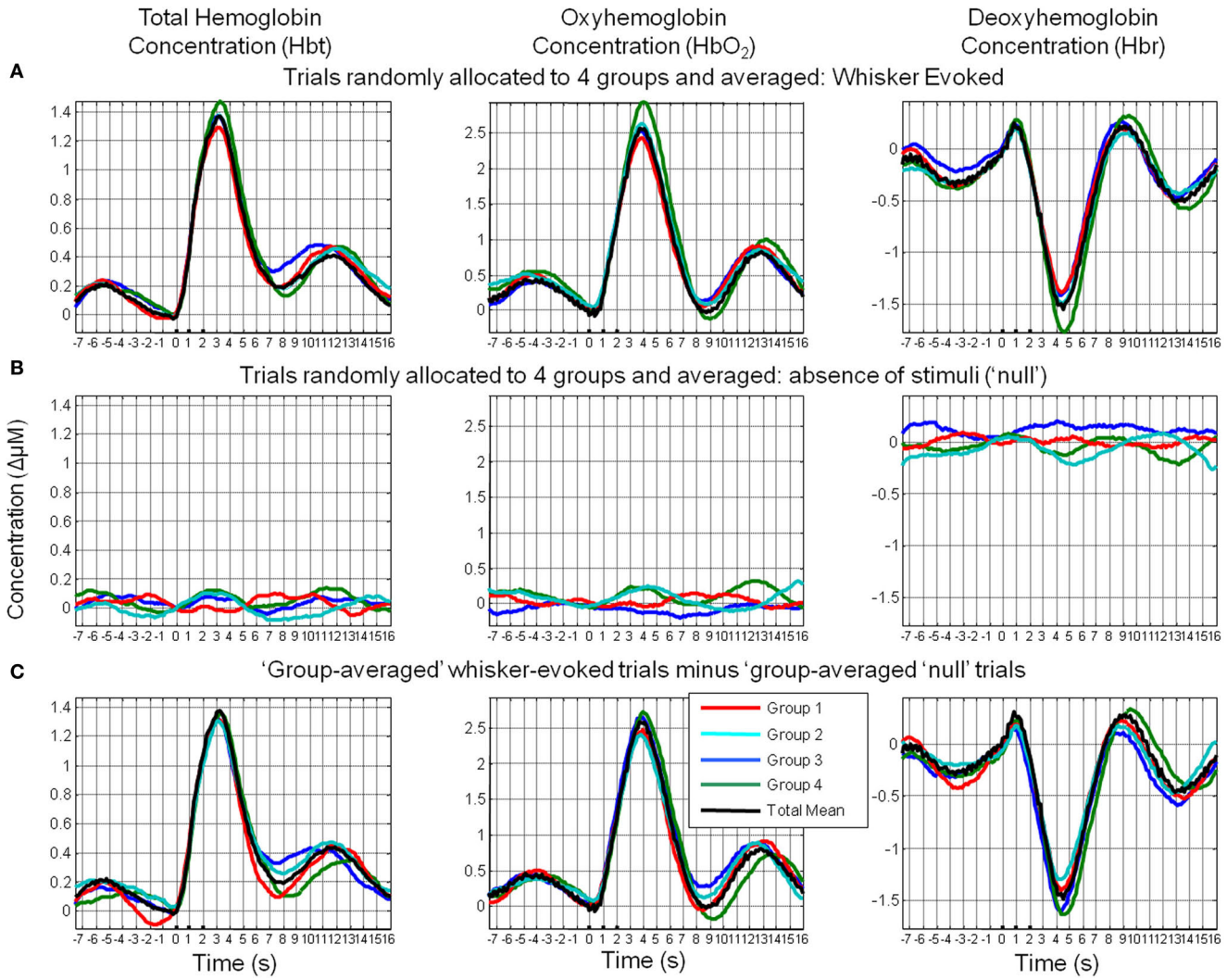

FIGURE 10 | Random assignment of sensory-evoked and ongoing cortical total hemodynamics to four groups. (A) Hemodynamic responses to sensory stimuli were randomly assigned to one of four groups and averaged. **(B)** Hemodynamic trial data without presentation of sensory stimuli ("nulls") were randomly assigned to one of four groups and averaged. **(C)** Subtraction of the group-averaged stimulus-evoked responses from their "group-averaged" null counterparts.

techniques also enabled measurement of the different aspects of the hemodynamic response that underlie the fMRI response. In addition, for each aspect of the hemodynamic response: HbO_2, Hbr and Hbt, these "null" trials were also sorted on the basis of their phase at the time point corresponding to stimulus presentation in the stimulus-evoked trials. Phase averaged null trials were subtracted from their phase averaged counterparts and the similarity of the resultant time series strongly suggests a linear superposition of ongoing and evoked cortical hemodynamics.

Spontaneous fluctuations in hemodynamic based brain imaging signals have also become of interest to cognitive neuroscience as they display temporal coherence in functionally related neuroanatomical structures and as such, fMRI data collected in the absence of stimuli or tasks (often termed "resting state") is now routinely used to assess functional connectivity (Biswal et al., 1995; Lowe et al., 1998; Hampson et al., 2002; Greicius et al., 2003; van de Ven et al., 2004; Fox et al., 2005, 2006a). However, the 0.1 Hz fluctuation investigated here typically forms the upper limit of the frequency spectrum of fluctuations used in such studies for connectivity analysis, as the data is pre-filtered below this frequency before subsequent correlation analyses are conducted. Vincent et al. (2007) inferred functional connectivity from spontaneous fMRI signals in both human subjects and non-human primates. They filtered their data into different frequency ranges depending on species, which may suggest that spontaneous fMRI fluctuations may have different predominant frequencies between species. However, Obrig et al. (2000) reviewed studies making transcranial Doppler sonography (Zhang et al., 1998a,b), near infrared spectroscopy (Elwell et al., 1996, 1999) and fMRI (Mitra et al., 1997) measures of spontaneous fluctuations in cerebral hemodynamics in humans and Laser Doppler flowmetry (Golanov and Reis, 1996) or optical (Mayhew et al., 1996) measures of cerebral hemodynamics in animals. They found that the majority of studies reported fluctuations at ~ 0.1 Hz regardless of species. Notwithstanding the variety of frequencies that may be present in cerebral hemodynamics, we

chose to investigate the 0.1 Hz component due to its ubiquitous presence in previous research (Obrig et al., 2000). The question arises as to the origin of the fluctuations at the 0.1 Hz frequency. There is increasing evidence that spontaneous fluctuations in hemodynamic fMRI signals in general are related to spontaneous neural activity. Logothetis et al. (2001) was able to generate a BOLD fMRI impulse response function by deconvolving "spontaneous" fMRI data with simultaneous measures of LFP from primate. A correlation between spontaneous LFP, MUA, action potential rate and fMRI fluctuations at an appropriate temporal lag over large regions in the visual cortex was found in this animal model in a subsequent study (Shmuel and Leopold, 2008) when the anesthetized and paralyzed animals viewed either a gray image (seven animals) or were in complete darkness (two animals). However, the 0.1 Hz oscillation in particular, has also been hypothesized to be vaso- or myogenic in origin (Morita et al., 1995) due to similar 0.1 Hz oscillations in hemodynamics being found in peripheral tissues in addition to brain, such as the testes (Damber et al., 1983; Mayhew et al., 1998). However, a recent study making MRI measures of spontaneous BOLD fluctuations in rat found that connectivity maps could be created from both the more typically used slower frequency components and the 0.1 Hz oscillation (Majeed et al., 2009). This could suggest the 0.1 Hz is in some way related to spontaneous activity or functionally connected regions happened to have correlated vasogenic 0.1 Hz oscillations. Friston et al. (2000) convolved a hemodynamic impulse response function with simulated stochastic neural activity and found the resulting time series strongly resembled the characteristic 0.1 Hz spontaneous fluctuations recorded in optical studies (Mayhew et al., 1996; Spitzer et al., 2001) suggesting that the time course of 0.1 Hz hemodynamic fluctuations could be produced by spontaneous neural activity despite the fact that spontaneous neural activity may occur at a different temporal scale. Golanov et al. (1994) demonstrated temporal concordance of spontaneous EEG burst preceding CBF oscillations, some of which were in frequencies around the 0.1 Hz range. Future work using combined electrophysiology and optical measures of hemodynamics may provide further information whether the 0.1 Hz hemodynamics oscillations are related to spontaneous activity. Regardless of the origin of the 0.1 Hz component the present investigation demonstrates how it may contribute to the variability in stimulus-evoked responses. A finding which may prove to be useful in interpreting individual trials of hemodynamic based neuroimaging data.

CONCLUSION

The present investigation demonstrates that stimulus-evoked cortical hemodynamics may demonstrate inter-trial variability based on attributes of pre-stimulus ongoing fluctuations.

ACKNOWLEDGMENTS

This work was supported by MRC New Investigator Award G0501127. The authors would like to thank Mr Michael Bruyns-Haylett for commenting on a draft of the manuscript and Professors John Mayhew and Peter Redgrave for their continued support. We would also like to thank Drs David Johnston, Ying Zheng, Ian Devonshire and Chris Martin for helpful comments. Particularly thanks to Dr Robert Haslinger (MGH) for advice on the use of the Hilbert transform and Dr Michael Fox for suggesting the comparison of "null" and stimulus-evoked trials. We also thank the technical staff of the Psychology Department: Marion Simkins, Natalie Walton and Malcom Benn.

REFERENCES

Aguirre, G. K., Zarahn, E., and D'Esposito, M. (1998). The variability of human, BOLD hemodynamic responses. *Neuroimage* 8, 360–369.

Arieli, A., Sterkin, A., Grinvald, A., and Aertsen, A. (1996). Dynamics of ongoing activity: explanation of the large variability in evoked cortical responses. *Science* 273, 1868–1871.

Berwick, J., Johnston, D., Jones, M., Martindale, J., Martin, C., Kennerley, A. J., Redgrave, P., and Mayhew, J. E. (2008). Fine detail of neurovascular coupling revealed by spatiotemporal analysis of the hemodynamic response to single whisker stimulation in rat barrel cortex. *J. Neurophysiol.* 99, 787–798.

Berwick, J., Johnston, D., Jones, M., Martindale, J., Redgrave, P., McLoughlin, N., Schiessl, I., and Mayhew, J. E. (2005). Neurovascular coupling investigated with two-dimensional optical imaging spectroscopy in rat whisker barrel cortex. *Eur. J. Neurosci.* 22, 1655–1666.

Biswal, B., Yetkin, F. Z., Haughton, V. M., and Hyde, J. S. (1995). Functional connectivity in the motor cortex of resting human brain using echo-planar MRI. *Magn. Reson. Med.* 34, 537–541.

Cannestra, A. F., Pouratian, N., Shomer, M. H., and Toga, A. W. (1998). Refractory periods observed by intrinsic signal and fluorescent dye imaging. *J. Neurophysiol.* 80, 1522–1532.

Damber, J. E., Lindahl, O., Selstam, G., and Tenland, T. (1983). Rhythmical oscillations in rat testicular microcirculation as recorded by laser Doppler flowmetry. *Acta Physiol. Scand.* 118, 117–123.

Devor, A., Dunn, A. K., Andermann, M. L., Ulbert, I., Boas, D. A., and Dale, A. M. (2003). Coupling of total hemoglobin concentration, oxygenation, and neural activity in rat somatosensory cortex. *Neuron* 39, 353–359.

Devor, A., Hillman, E. M., Tian, P., Waeber, C., Teng, I. C., Ruvinskaya, L., Shalinsky, M. H., Zhu, H., Haslinger, R. H., Narayanan, S. N., Ulbert, I., Dunn, A. K., Lo, E. H., Rosen, B. R., Dale, A. M., Kleinfeld, D., and Boas, D. A. (2008). Stimulus-induced changes in blood flow and 2-deoxyglucose uptake dissociate in ipsilateral somatosensory cortex. *J. Neurosci.* 28, 14347–14357.

Elwell, C. E., Owen-Reece, H., Wyatt, J. S., Cope, M., Reynolds, E. O., and Delpy, D. T. (1996). Influence of respiration and changes in expiratory pressure on cerebral haemoglobin concentration measured by near infrared spectroscopy. *J. Cereb. Blood Flow Metab.* 16, 353–357.

Elwell, C. E., Springett, R., Hillman, E., and Delpy, D. T. (1999). Oscillations in cerebral haemodynamics. Implications for functional activation studies. *Adv. Exp. Med. Biol.* 471, 57–65.

Fox, M. D., Corbetta, M., Snyder, A. Z., Vincent, J. L., and Raichle, M. E. (2006a). Spontaneous neuronal activity distinguishes human dorsal and ventral attention systems. *Proc. Natl. Acad. Sci. U.S.A.* 103, 10046–10051.

Fox, M. D., Snyder, A. Z., Zacks, J. M., and Raichle, M. E. (2006b). Coherent spontaneous activity accounts for trial-to-trial variability in human evoked brain responses. *Nat. Neurosci.* 9, 23–25.

Fox, M. D., Snyder, A. Z., Vincent, J. L., Corbetta, M., Van Essen, D. C., and Raichle, M. E. (2005). The human brain is intrinsically organized into dynamic, anticorrelated functional networks. *Proc. Natl. Acad. Sci. U.S.A.* 102, 9673–9678.

Friston, K. J., Mechelli, A., Turner, R., and Price, C. J. (2000). Nonlinear responses in fMRI: the Balloon model, Volterra kernels, and other hemodynamics. *Neuroimage* 12, 466–477.

Golanov, E. V., and Reis, D. J. (1996). Cerebral cortical neurons with activity linked to central neurogenic spontaneous and evoked elevations in cerebral blood flow. *Neurosci. Lett.* 209, 101–104.

Golanov, E. V., Yamamoto, S., and Reis, D. J. (1994). Spontaneous waves of cerebral blood flow associated with a pattern of electrocortical activity. *Am. J. Physiol.* 266, R204–R214.

Greicius, M. D., Krasnow, B., Reiss, A. L., and Menon, V. (2003). Functional connectivity in the resting brain: a network analysis of the default mode hypothesis. *Proc. Natl. Acad. Sci. U.S.A.* 100, 253–258.

Hampson, M., Peterson, B. S., Skudlarski, P., Gatenby, J. C., and Gore, J. C. (2002). Detection of functional connectivity using temporal correlations in MR images. *Hum. Brain Mapp.* 15, 247–262.

Haslinger, R., Ulbert, I., Moore, C. I., Brown, E. N., and Devor, A. (2006). Analysis of LFP phase predicts sensory response of barrel cortex. *J. Neurophysiol.* 96, 1658–1663.

Jones, M., Berwick, J., Hewson-Stoate, N., Gias, C., and Mayhew, J. (2005). The effect of hypercapnia on the neural and hemodynamic responses to somatosensory stimulation. *Neuroimage* 27, 609–623.

Jones, M., Berwick, J., Johnston, D., and Mayhew, J. (2001). Concurrent optical imaging spectroscopy and laser-Doppler flowmetry: the relationship between blood flow, oxygenation, and volume in rodent barrel cortex. *Neuroimage* 13, 1002–1015.

Jones, M., Berwick, J., and Mayhew, J. (2002). Changes in blood flow, oxygenation, and volume following extended stimulation of rodent barrel cortex. *Neuroimage* 15, 474–487.

Jones, M., Devonshire, I. M., Berwick, J., Martin, C., Redgrave, P., and Mayhew, J. (2008). Altered neurovascular coupling during information-processing states. *Eur. J. Neurosci.* 27, 2758–2772.

Jones, M., Hewson-Stoate, N., Martindale, J., Redgrave, P., and Mayhew, J. (2004). Nonlinear coupling of neural activity and CBF in rodent barrel cortex. *Neuroimage* 22, 956–965.

Kennerley, A. J., Berwick, J., Martindale, J., Johnston, D., Papadakis, N., and Mayhew, J. E. (2005). Concurrent fMRI and optical measures for the investigation of the hemodynamic response function. *Magn. Reson. Med.* 54, 354–365.

Kwong, K. K., Belliveau, J. W., Chesler, D. A., Goldberg, I. E., Weisskoff, R. M., Poncelet, B. P., Kennedy, D. N., Hoppel, B. E., Cohen, M. S., Turner, R., Cheng, H-M., Brady, T. J., and Rosen, B. R. (1992). Dynamic magnetic resonance imaging of human brain activity during primary sensory stimulation. *Proc. Natl. Acad. Sci. U.S.A.* 89, 5675–5679.

Le Van Quyen, M., and Bragin, A. (2007). Analysis of dynamic brain oscillations: methodological advances. *Trends Neurosci.* 30, 365–373.

Le Van Quyen, M., Foucher, J., Lachaux, J., Rodriguez, E., Lutz, A., Martinerie, J., and Varela, F. J. (2001). Comparison of Hilbert transform and wavelet methods for the analysis of neuronal synchrony. *J. Neurosci. Methods* 111, 83–98.

Logothetis, N. K., Pauls, J., Augath, M., Trinath, T., and Oeltermann, A. (2001). Neurophysiological investigation of the basis of the fMRI signal. *Nature* 412, 150–157.

Lowe, M. J., Mock, B. J., and Sorenson, J. A. (1998). Functional connectivity in single and multislice echoplanar imaging using resting-state fluctuations. *Neuroimage* 7, 119–132.

Majeed, W., Magnuson, M., and Keilholz, S. D. (2009). Spatiotemporal dynamics of low frequency fluctuations in BOLD fMRI of the rat. *J. Magn. Reson. Imaging* 30, 384–393.

Malonek, D., Dirnagl, U., Lindauer, U., Yamada, K., Kanno, I., and Grinvald, A. (1997). Vascular imprints of neuronal activity: relationships between the dynamics of cortical blood flow, oxygenation, and volume changes following sensory stimulation. *Proc. Natl. Acad. Sci. U.S.A.* 94, 14826–14831.

Martindale, J., Mayhew, J., Berwick, J., Jones, M., Martin, C., Johnston, D., Redgrave, P., and Zheng, Y. (2003). The hemodynamic impulse response to a single neural event. *J. Cereb. Blood Flow Metab.* 23, 546–555.

Mayhew, J., Hu, D., Zheng, Y., Askew, S., Hou, Y., Berwick, J., Coffey, P. J., and Brown, N. (1998). An evaluation of linear model analysis techniques for processing images of microcirculation activity. *Neuroimage* 7, 49–71.

Mayhew, J., Johnston, D., Berwick, J., Jones, M., Coffey, P., and Zheng, Y. (2000). Spectroscopic analysis of neural activity in brain: increased oxygen consumption following activation of barrel cortex. *Neuroimage* 12, 664–675.

Mayhew, J., Zheng, Y., Hou, Y., Vuksanovic, B., Berwick, J., Askew, S., and Coffey, P. (1999). Spectroscopic analysis of changes in remitted illumination: the response to increased neural activity in brain. *Neuroimage* 10, 304–326.

Mayhew, J. E., Askew, S., Zheng, Y., Porrill, J., Westby, G. W., Redgrave, P., Rector, D. M., and Harper, R. M. (1996). Cerebral vasomotion: a 0.1-Hz oscillation in reflected light imaging of neural activity. *Neuroimage* 4, 183–193.

Mitra, P. P., Ogawa, S., Hu, X., and Ugurbil, K. (1997). The nature of spatiotemporal changes in cerebral hemodynamics as manifested in functional magnetic resonance imaging. *Magn. Reson. Med.* 37, 511–518.

Molgedey, L., and Schuster, H. G. (1994). Separation of a mixture of independent signals using time delayed correlations. *Phys. Rev. Lett.* 72, 3634–3637.

Morita, Y., Hardebo, J. E., and Bouskela, E. (1995). Influence of cerebrovascular sympathetic, parasympathetic, and sensory nerves on autoregulation and spontaneous vasomotion. *Acta Physiol. Scand.* 154, 121–130.

Obrig, H., Neufang, M., Wenzel, R., Kohl, M., Steinbrink, J., Einhaupl, K., and Villringer, A. (2000). Spontaneous low frequency oscillations of cerebral hemodynamics and metabolism in human adults. *Neuroimage* 12, 623–639.

Ogawa, S., Tank, D. W., Menon, R., Ellermann, J. M., Kim, S. G., Merkle, H., and Ugurbil, K. (1992). Intrinsic signal changes accompanying sensory stimulation: functional brain mapping with magnetic resonance imaging. *Proc. Natl. Acad. Sci. U.S.A.* 89, 5951–5955.

Pikovsky, A., Rosenblum, M., and Kurths, J. (2001). *Synchronization - A Universal Concept in Nonlinear Sciences*. Cambridge, UK: Cambridge.

Sauseng, P., Klimesch, W., Gruber, W. R., Hanslmayr, S., Freunberger, R., and Doppelmayr, M. (2007). Are event-related potential components generated by phase resetting of brain oscillations? A critical discussion. *Neuroscience* 146, 1435–1444.

Sheth, S., Nemoto, M., Guiou, M., Walker, M., Pouratian, N., and Toga, A. W. (2003). Evaluation of coupling between optical intrinsic signals and neuronal activity in rat somatosensory cortex. *Neuroimage* 19, 884–894.

Shmuel, A., and Leopold, D. A. (2008). Neuronal correlates of spontaneous fluctuations in fMRI signals in monkey visual cortex: Implications for functional connectivity at rest. *Hum. Brain Mapp.* 29, 751–761.

Spitzer, M. W., Calford, M. B., Clarey, J. C., Pettigrew, J. D., and Roe, A. W. (2001). Spontaneous and stimulus-evoked intrinsic optical signals in primary auditory cortex of the cat. *J. Neurophysiol.* 85, 1283–1298.

van de Ven, V. G., Formisano, E., Prvulovic, D., Roeder, C. H., and Linden, D. E. (2004). Functional connectivity as revealed by spatial independent component analysis of fMRI measurements during rest. *Hum. Brain Mapp.* 22, 165–178.

Vincent, J. L., Patel, G. H., Fox, M. D., Snyder, A. Z., Baker, J. T., Van Essen, D. C., Zempel, J. M., Snyder, L. H., Corbetta, M., and Raichle, M. E. (2007). Intrinsic functional architecture in the anaesthetized monkey brain. *Nature* 447, 83–86.

Zhang, R., Zuckerman, J. H., Giller, C. A., and Levine, B. D. (1998a). Transfer function analysis of dynamic cerebral autoregulation in humans. *Am. J. Physiol.* 274, H233–H241.

Zhang, R., Zuckerman, J. H., and Levine, B. D. (1998b). Deterioration of cerebral autoregulation during orthostatic stress: insights from the frequency domain. *J. Appl. Physiol.* 85, 1113–1122.

Zheng, Y., Johnston, D., Berwick, J., and Mayhew, J. (2001). Signal source separation in the analysis of neural activity in brain. *Neuroimage* 13, 447–458.

Conflict of Interest Statement: The authors declare that the research was conducted in the absence of any commercial or financial relationships that could be construed as a potential conflict of interest.

Received: 25 January 2010; paper pending published: 03 May 2010; accepted: 14 July 2010; published online: 27 August 2010.
Citation: Saka M, Berwick J and Jones M (2010) Linear superposition of sensory-evoked and ongoing cortical hemodynamics. Front. Neuroenerg. 2:23. doi: 10.3389/fnene.2010.00023

frontiers in
NEUROENERGETICS

ORIGINAL RESEARCH ARTICLE
published: 15 September 2010
doi: 10.3389/fnene.2010.00128

Imaging retinal blood flow with laser speckle flowmetry

Anja I. Srienc, Zeb L. Kurth-Nelson and Eric A. Newman*

Department of Neuroscience, University of Minnesota, Minneapolis, MN, USA

Edited by:
Anna Devor, University of California San Diego, USA

Reviewed by:
Gabriel A. Silva, University of California San Diego, USA
Chris Shaffer, Cornell University, USA

****Correspondence:***
Eric A. Newman, Department of Neuroscience, University of Minnesota, 321 Church St. SE, Minneapolis, MN 55455, USA.
e-mail: ean@umn.edu

Laser speckle flowmetry (LSF) was initially developed to measure blood flow in the retina. More recently, its primary application has been to image baseline blood flow and activity-dependent changes in blood flow in the brain. We now describe experiments in the rat retina in which LSF was used in conjunction with confocal microscopy to monitor light-evoked changes in blood flow in retinal vessels. This dual imaging technique permitted us to stimulate retinal photoreceptors and measure vessel diameter with confocal microscopy while simultaneously monitoring blood flow with LSF. We found that a flickering light dilated retinal arterioles and evoked increases in retinal blood velocity with similar time courses. In addition, focal light stimulation evoked local increases in blood velocity. The spatial distribution of these increases depended on the location of the stimulus relative to retinal arterioles and venules. The results suggest that capillaries are largely unresponsive to local neuronal activity and that hemodynamic responses are mediated primarily by arterioles. The use of LSF to image retinal blood flow holds promise in elucidating the mechanisms mediating functional hyperemia in the retina and in characterizing changes in blood flow that occur during retinal pathology.

Keywords: retina, choroid, blood flow, arterioles, capillaries, functional hyperemia, laser speckle flowmetry

INTRODUCTION

Laser speckle flowmetry (LSF) has been successfully employed to measure blood flow in the CNS for three decades. It has the distinct advantage over other methods of monitoring blood flow, such as laser Doppler flowmetry, as it can produce two-dimensional images of blood flow with high spatial and temporal resolution.

The principals underlying LSF have been described in detail elsewhere (Fercher and Briers, 1981; Dunn et al., 2001; Yuan et al., 2005). Briefly, when an optically rough surface is illuminated with coherent light, a speckle pattern is produced as the incident light is reflected off of surfaces lying at different depths. Some areas of the surface appear bright due to constructive interference while other areas appear dark due to destructive interference. If the surface is stationary, the speckle pattern of bright and dark spots will remain stationary as well. However, if the surface moves (e.g., blood cells moving through vessels), the speckle pattern will blur with time. Thus, a stationary region on the surface will have a high speckle contrast while a moving region will have a low speckle contrast when imaged over the appropriate time window (Yuan et al., 2005). In practice, local speckle contrast is calculated by imaging a surface with a digital camera and computing the standard deviation of brightness divided by the mean brightness over a small array of pixels. The resulting speckle contrast value is used to evaluate relative velocity. With modern computational techniques, speckle contrast can be calculated and speckle images analyzed almost instantaneously.

Although LSF has been used in many studies to monitor blood flow in the cortex (Bolay et al., 2002; Ayata et al., 2004; Durduran et al., 2004), the very first use of LSF was to monitor blood flow in the retina. The first studies (Fercher and Briers, 1981; Briers and Fercher, 1982) were conducted in the early 1980s, before it was practical to calculate speckle contrast with digital techniques. Instead, the retina was imaged on film and speckle contrast images were obtained with high-pass spatial filtering optical techniques. The resulting images displayed patterns of blood flow in the human retina, with arterioles and venules highlighted because the velocity of blood flow was greatest in these vessels.

More recently, LSF has been used to monitor blood flow in the retina using digital cameras and computational techniques to calculate speckle contrast images. Retinal vessels have been imaged in rabbit (Tamaki et al., 1994) and rat (Cheng et al., 2008) retinas and changes in blood flow have been monitored in response to varying intraocular pressure and varying levels of inspired oxygen. LSF has also been employed to investigate the effects of glaucoma therapies on retinal circulation in rabbits (Tamaki et al., 1997b), monkeys (Ishii and Araie, 2000), and people (Koseki et al., 2008) and to monitor the choroidal circulation in patients with polypoidal choroidal vasculopathy (Watanabe et al., 2008).

We now describe results obtained using LSF to image blood flow in the *in vivo* rat retina. The goals of this project were twofold. First, we wanted to develop a technique to combine LSF with laser scanning confocal microscopy of the retina. This would allow us to monitor spatial and temporal patterns of retinal blood flow with LSF while simultaneously monitoring the diameter of retinal vessels with confocal line scans. An added benefit of this technique is that a second channel of the confocal microscope can generate spatially and temporally defined visual stimuli to activate retinal photoreceptors.

The second goal of this project was to determine whether blood flow is regulated at the local level in the retina. In the brain, localized increases in neuronal activity lead to spatially restricted increases in blood flow (Iadecola and Nedergaard, 2007). This hemodynamic response, termed functional hyperemia, supplies active neurons with needed oxygen and nutrients. Previous work using laser Doppler flowmetry and other techniques (Riva et al., 2005) has shown that global stimulation of the retina results in global increases in retinal blood flow. In addition, an fMRI study has demonstrated that when

one-half of the retina is stimulated with light, blood flow increases in that half, but not the other half of the retina (Duong et al., 2002). However, fMRI does not currently have the resolution to accurately determine the spatial extent of the functional hyperemia response in the retina. Laser speckle flowmetry, in contrast, is ideally suited to mapping the spatial extent of blood flow increases evoked by focal stimulation (Dunn et al., 2001; Ayata et al., 2004).

We describe in this report methods for successfully combining LSF and laser scanning confocal microscopy to monitor blood flow in the retina of the anesthetized rat. With this combined imaging system, we use confocal microscopy to stimulate photoreceptors in restricted retinal regions while simultaneously monitoring arteriole diameter with confocal line scans. At the same time, we use LSF to visualize spatial patterns of blood flow changes. We find that, as in the brain, focal stimulation of retinal photoreceptors does indeed produce localized increases in blood flow in the retinal circulation. Spatial patterns of functional hyperemia responses suggest that blood flow is regulated primarily by first and second order arterioles in the retina, but not by capillaries or venules.

MATERIALS AND METHODS

IN VIVO RETINA PREPARATION

Experiments were performed on male Long-Evans rats (250–350 g). Animals were treated in accordance with the guidelines of the Institutional Animal Care and Use Committee of the University of Minnesota. The initial surgery was performed under isoflurane anesthesia (2%). The femoral vein and artery on the left side were cannulated for drug administration and monitoring of blood pressure. The animal was placed in a modified stereotaxic holder with a three-point head restraint. The cornea and conjunctiva of the right eye were numbed with proparacaine hydrochloride (0.5% solution) and the pupil dilated with atropine sulfate (1% solution). The stereotaxic holder was fixed to a movable stage below an upright microscope that served to image the retina for both LSF and confocal microscopy. An IV bolus of atropine (0.1 mg/kg) was delivered prior to any eye manipulations to counter the oculocardiac reflex, which can reduce blood pressure.

Following surgery, anesthesia was maintained for the duration of the experiment by continuous infusion of α-chloralose (55 mg/kg/h). A soluble form of α-chloralose (α-chloralose-HBC-complex, Sigma) was used. Animals were paralyzed with gallamine triethiodide (initial bolus of 15 mg/kg and continuous infusion at 15 mg/kg/h) to prevent eye movements. Depth of anesthesia was assessed by monitoring heart rate and blood pressure and anesthesia infusion adjusted accordingly. Core body temperature was monitored and maintained at 37°C (TC-1000 Temperature Controller, CWE). Blood oxygen saturation level and heart rate (MouseOx, Starr Life Sciences Corp), arterial blood pressure (Pressure Monitor BP-1, World Precision Instruments), and end-tidal CO_2 (microCapStar, CWE) were monitored continuously. Blood gases and pH were sampled periodically (Instrumentation Laboratory Gem Premier 3000). The animal was artificially ventilated (40–50 breaths/min; CWE SAR-830-P) and blood oxygen saturation level, end-tidal CO_2 and mean arterial pressure maintained within physiological limits (92–97%, 35–45 mm Hg, and 90–115 mm Hg respectively) by adjusting the ventilator breath rate and pressure and the O_2 level of the inspired air.

RETINAL IMAGING

The retina was viewed through the cornea and lens with an Olympus BX61W1 upright microscope and 4× and 10× dry objectives. The refractive properties of the cornea were neutralized by placing goniscopic prism solution and a contact lens (5.4 mm fundus laser lens, Ocular Instruments) over the cornea (**Figure 1A**). A CoolSnap ES digital CCD camera (Photometrics) was attached to the phototube of the microscope for LSF. The retina was imaged simultaneously with an Olympus FluoView 1000 laser scanning confocal microscope. Light from the retina was separated by a dichroic mirror (T600lpxr, Chroma Technology) in the microscope, with 808 nm light passing through to the LSF digital camera and 400–600 nm wavelengths reflected into the confocal scanner (**Figure 1B**). An 808 nm bandpass filter was placed in front of the LSF camera to block residual visible wavelengths.

LASER SPECKLE FLOWMETRY

Retinal blood flow was monitored by LSF. The retina was illuminated with 808 nm infrared light from a laser diode (200 mW, L808P200, ThorLabs) and imaged with the digital camera. The retina was illuminated by focusing light from the laser diode onto one end of an optical fiber (240 μm diameter) and placing the other end of the fiber against the globe. The end of the optical fiber was positioned on the eye at a 35° angle from the horizontal, approximately 1.5 mm below the limbus. The precise position of the end of the optical fiber was adjusted to maximize signals from the retinal vasculature and minimize signals from the choroidal circulation. The infrared beam emerging from the optical fiber was sufficiently dim as to not cause damage to the eye and was kept on continuously.

Images of the retina were acquired with a 40 ms exposure time. In preliminary experiments, we found that shorter exposure times reduced the speckle signals in smaller vessels, while longer exposure times decreased the signals in larger vessels (Yuan et al., 2005). Two-dimensional LSF images were calculated using a custom MatLab routine. Raw images were spatially binned into 5 × 5 pixel arrays and speckle contrast values computed using the following relation (Dunn et al., 2001),

$$\text{Speckle contrast value} = \frac{\text{standard deviation of pixels in array}}{\text{mean intensity of pixels in array}} \quad (1)$$

LSF ratio images, showing changes in blood flow produced by light stimulation, were computed by first averaging all speckle images acquired before a stimulus and the images acquired during a stimulus and dividing the latter averaged image by the former. Ratio images were low pass filtered to reduce noise. In ratio images, regions with values less than 1 (decreased speckle contrast) indicate areas of stimulus-induced increase in blood flow.

The relative velocity of blood flow can be derived from speckle contrast values using a computationally intensive relation (Fercher and Briers, 1981). However, over the limited range of speckle contrast values that we observed experimentally (0.2–0.4), relative velocity values can be approximated using the following relation (Cheng and Duong, 2007),

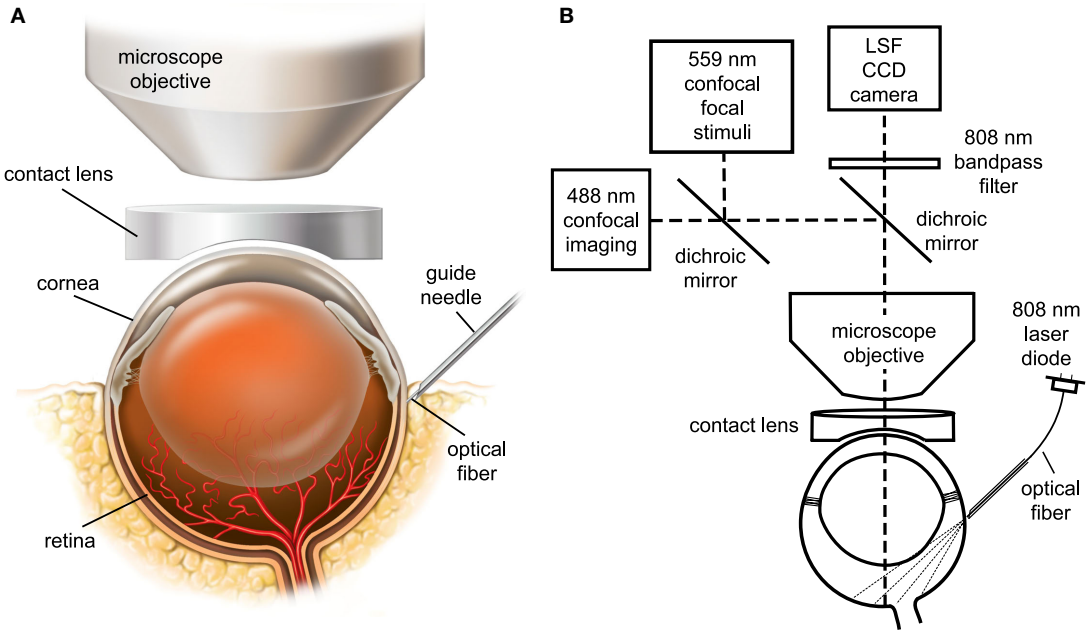

FIGURE 1 | The *in vivo* rat preparation for monitoring retinal blood flow with simultaneous laser speckle flowmetry (LSF) and confocal microscopy. **(A)** The retina is imaged through an upright microscope and a contact lens placed over the cornea. A hypodermic needle serves as a guide tube for an optical fiber for LSF illumination. **(B)** The retina is illuminated for LSF by 808 nm light passing though an optical fiber that is inserted into the hypodermic needle guide tube. The retina is imaged simultaneously for LSF and confocal microscopy. A dichroic mirror directs the appropriate wavelengths of light from the retina to the LSF camera and the confocal microscope. An 808 nm bandpass filter prevents confocal excitation or emission light from entering the LSF camera. The confocal microscope has a primary scanner (488 nm) for imaging retinal vessels and a secondary scanner for generating 559 nm stimulating light.

$$\text{Velocity} \propto \frac{1}{(\text{speckle contrast})^2} \quad (2)$$

We used this relation to compute blood velocity images from speckle contrast images. As above, images showing changes in blood velocity were obtained by computing blood velocity ratio images. Blood velocity images obtained during light stimulation were divided by those obtained during a pre-stimulus period.

CONFOCAL MICROSCOPY

The diameter of retinal arterioles was monitored with laser scanning microscopy. Blood vessels were labeled by IV injection of dextran–fluorescein (2,000,000 MW, 1 ml, 3% solution) and imaged with 488 nm illumination. The luminal diameter of the vessels was assessed with confocal line scans drawn perpendicular to the vessel. In the resulting distance vs. time line scan images (see **Figure 4B**) vessel dilation is seen as a widening of the bright lumen of the vessel. Luminal diameter vs time graphs were calculated using a custom MatLab routine.

LIGHT STIMULATION

Retinal photoreceptors were stimulated by light generated by the secondary (SIM) scanner of the FluoView 1000 laser scanning confocal microscope. Using the SIM scanner, the wavelength, intensity and scanning of a laser beam can be controlled independently of light from the primary scanner, which was used to acquire line scan images of retinal vessels.

We stimulated retinal photoreceptors with a 12 Hz flickering 559 nm light of 15 s duration. The luminous flux of the stimulus was 0.02 lumens. A flicker frequency of 12 Hz was chosen because it produces a maximal functional hyperemia response in many species (Riva et al., 2005). A flicker rate of 12 Hz with a duty cycle of 50% was generated by scanning a 135 by 20 μm region of the retina with the secondary confocal scanner. With a pixel dwell time of 100 μs, this elongated horizontal rectangle was scanned downwards in 42 ms. At the end of the scan, the 559 nm light was blanked and the beam returned to the top of the rectangle. The return scan took an additional 42 ms. When the scan is repeated continuously, a flickering 12 Hz light is produced. Although the dimensions of the scanned rectangle were chosen to generate the appropriate stimulus frequency, the rectangular region is sufficiently small compared to the overall size of the retina to be useful for mapping localized hemodynamic responses.

Retinal photoreceptors were also stimulated with a 12 Hz diffuse white light having a luminous flux of 1.9 lumens falling on the eye. Light from a fiber optic illuminator was gated with an electromechanical shutter and focused onto the eye through a fiber bundle. This light effectively stimulated the entire retinal surface.

RESULTS

SIMULTANEOUS CONFOCAL AND LSF IMAGING OF THE RETINA

We imaged the retina through the cornea and lens using an upright microscope though which confocal and laser speckle images were obtained simultaneously. The refractive properties of the cornea

were neutralized with a contact lens placed between the eye and the microscope objective lens (**Figure 1A**). For LSF, the retina was illuminated with 808 nm infrared light (**Figure 1B**). This wavelength is well outside the absorption range of photoreceptor photopigments (Jacobs et al., 2001). Thus, retinal photoreceptors and neurons were not stimulated by the LSF illumination light.

Arterioles and venules, which radiate from the optic disc, can be visualized simultaneously by confocal microscopy and LSF. This is illustrated in **Figure 2**, where a confocal image of retinal vessels is shown in **Figure 2A**, a raw laser speckle image acquired simultaneously in **Figure 2B**, a computed laser speckle contrast image in **Figure 2C** and a computed blood velocity image in **Figure 2D**. In the confocal image (**Figure 2A**), primary arterioles and venules, filled with fluorescent dye, radiate from the optic disc at the bottom left. Arterioles can be distinguished from venules by their smaller diameter. Secondary and tertiary arterioles, branching from the primary vessels, are clearly seen in this image, as are retinal capillaries. In the raw speckle image (**Figure 2B**), the larger vessels are seen as regions of reduced speckle contrast. They appear smoother than surrounding retinal areas, which are more speckled. When a speckle contrast image (**Figure 2C**) is computed from the raw image, the larger vessels appear darker. This is because blood is flowing more rapidly through the larger vessels, resulting in blurring of the speckles and lowering of the speckle contrast. Computed speckle contrast (Eq. 1) is invariant with incident illumination. Thus, the intensity of the speckle contrast image (excluding the major vessels) is relatively uniform, even though the intensity of the raw speckle image (**Figure 2B**) varies greatly. When a blood velocity image (**Figure 2D**) is computed from the speckle contrast image, vessels with high blood velocity appear brighter. Blood velocity is roughly proportional to pixel intensity in this image and is greatest in the primary arterioles and venules.

ILLUMINATION OF THE RETINA

The LSF in the retina has previously been achieved using a custom fundus camera that allows on-axis illumination of coherent light that passes through the cornea and lens (Tamaki et al., 1994). However, when using an upright microscope to obtain simultaneous LSF and confocal images, on-axis illumination is difficult to implement in practice. Reflection of the coherent light off of the microscope lenses and the contact lens produces strong interference patterns which obscure portions of the LSF images.

Instead of using on-axis illumination, we have employed an off-axis method of illumination. Light from an 808 nm laser diode is directed through an optical fiber and onto the sclera at the appropriate position and angle to illuminate the retinal area being imaged (**Figure 1B**). Sufficient light passes through the sclera and the retinal pigment epithelium to illuminate the retina. This trans-scleral

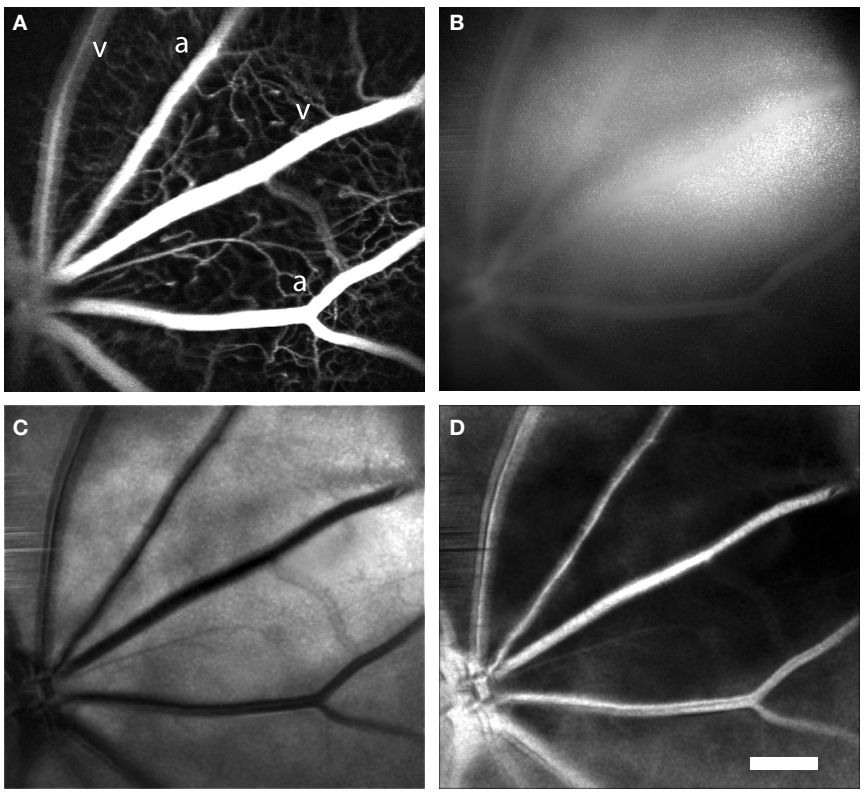

FIGURE 2 | Laser speckle flowmetry of retinal blood vessels. (A) Confocal image of retinal blood vessels labeled with dextran-fluorescein. Primary arterioles and venules are seen radiating from the optic disc (at the lower left). **(B)** Raw speckle image acquired simultaneously from the same retina as **(A)**. Note that there is less speckling in the regions corresponding to the major vessels. **(C)** Speckle contrast image calculated from **(B)**. Dark lines indicate regions of reduced speckle contrast, generated by blood flowing rapidly through the primary retinal vessels. **(D)** Blood velocity image calculated from **(C)**. The brighter areas indicate greater blood velocity. In this and subsequent figures, primary arterioles and venules are labeled "a" and "v," respectively. Scale bar for all panels, 250 μm.

illumination pathway is aided by the use of infrared light, which passes through tissue more easily than does visible light. Depending on the precise position of the optical fiber illuminating the globe, either the retinal vasculature or the choroidal circulation is imaged. When the optical fiber is positioned 1–2 mm posterior to the limbus, the retinal circulation is visualized (**Figure 3A**). The pattern of arterioles and venules corresponds to the fluorescence confocal image of the fluorescein-filled vessels (**Figure 3B**). In some preparations, indistinct splotches, as well as the retinal vessels, are seen in speckle contrast and blood velocity images (**Figure 3A**, arrowheads). These splotches are out of focus choroidal vessels. As the focus is shifted to the plane of the choroid and the end of the illuminating fiber is moved towards the posterior pole of the globe, the choroidal circulation becomes more distinct (**Figure 3C**). The splotches seen in images of the retinal vessels correspond to the larger choroidal vessels (**Figure 3C**, arrowheads). Although LSF images of choroidal vessels are of reduced quality, one must bear in mind that the vessels are imaged through 350 μm of tissue and a heavily pigmented layer, the retinal pigment epithelium. The size and branching patterns of the choroidal vessels imaged with LSF resemble those seen in corrosion casts of the choroidal vasculature (**Figure 3D**).

LIGHT-EVOKED CHANGES IN ARTERIOLE DIAMETER

We monitored light-evoked changes in retinal circulation using both confocal microscopy and LSF. Retinal arterioles dilate in response to light stimulation (Riva et al., 2005). This dilation can be quantified with confocal line scans. A line oriented perpendicular to an arteriole (**Figure 4A**, yellow line) is repeatedly scanned for the duration of a trial. The resulting line scan image (**Figure 4B**) displays the vessel diameter as a function of time. When retinal photoreceptors are stimulated (**Figure 4B**, white bar), the vessel dilates. A plot of vessel diameter vs. time (**Figure 4D**, trace 2) shows that light evokes a rapid increase in vessel diameter with a latency of approximately 1 s. Typically, a flickering light evoked a biphasic response consisting of a transient dilation lasting around 5 s followed by a sustained increase in vessel diameter. In a series of trials,

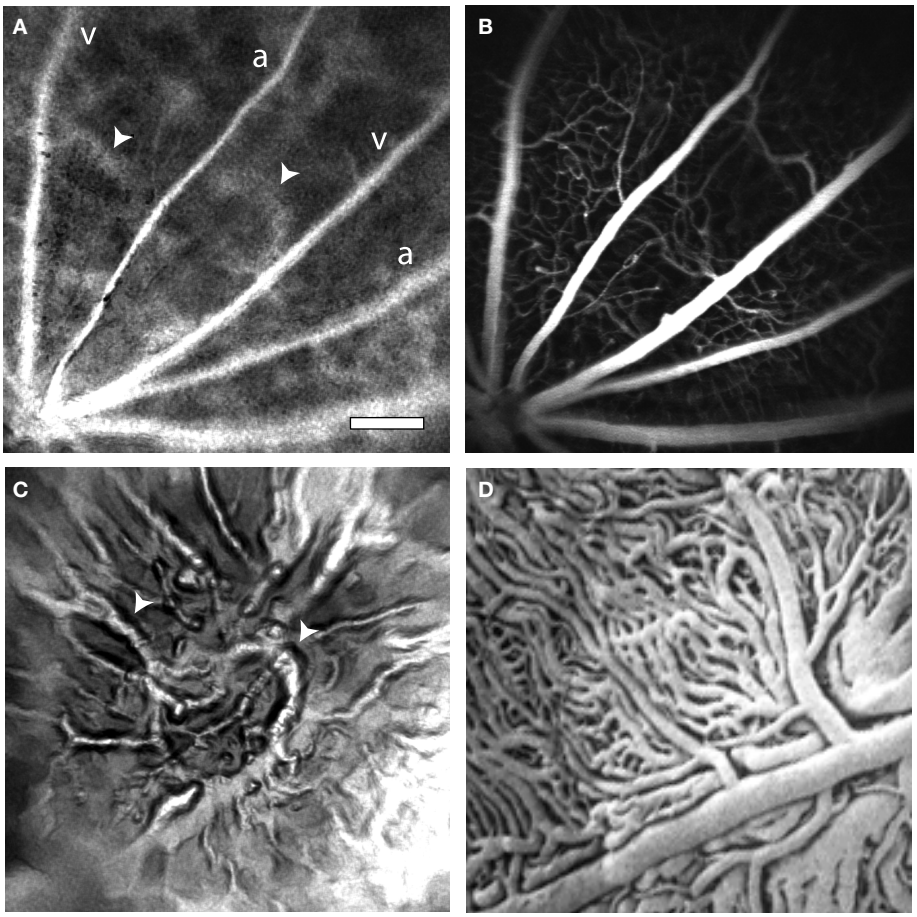

FIGURE 3 | Laser speckle flowmetry of the retinal and choroidal vasculature. (A) A blood velocity image of retinal vessels. In addition to the primary arterioles and venules, indistinct splotches (arrowheads), which are generated by choroidal vessels, are seen. **(B)** Confocal image of the retinal vasculature from the same retinal region as **(A)**. **(C)** A blood velocity image of choroidal vessels in the same preparation as **(A)** and **(B)**. The image was obtained by adjusting the focal plane of the microscope and moving the illuminating optical fiber toward the posterior pole of the globe. The splotches visible in **(A)** correspond to major choroidal vessels (arrowheads) visible in **(C)**. **(D)** A corrosion cast of the choroidal vasculature of the rat, reproduced at the same magnification as the other panels. Note that the size and branching patterns of the vessels are similar to those in **(C)**. From Bhutto and Amemiya (2001), used with permission. Scale bar for all panels, 250 μm.

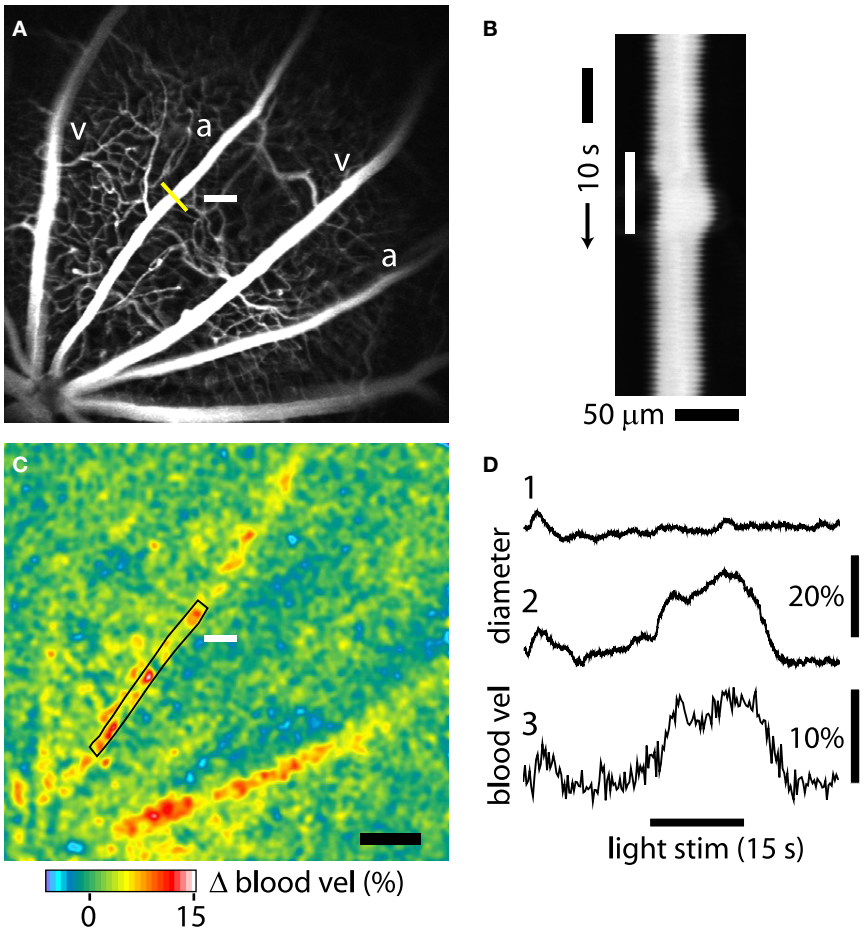

FIGURE 4 | Light-evoked changes in retinal blood flow measured with confocal microscopy and LSF. (A) Confocal image of retinal vessels. The diameter of the upper arteriole was measured with confocal line scans (yellow line). The nearby white bar indicates the location of the flickering light stimulus in panels **(A)** and **(C)**. Scale bar for panels **(A)** and **(C)**, 250 µm. **(B)** Line scan image obtained from the arteriole in **(A)**. Distance [across the yellow line in **(A)**] is plotted as a function of time. A flickering light [white bar in **(B)**] evokes vessel dilation, indicated by the widening of the vessel cross section. The uneven edges of the vessel are caused by a respiratory movement artifact. **(C)** Blood velocity ratio image, showing the light-evoked change in velocity, calculated at 2–5 s after onset of the stimulus. The flickering light evoked large blood velocity increases in the two primary arterioles and smaller increases in the venules. **(D)** Time course of the light-evoked responses. (Trace 1) Change in arteriole diameter [measured at the yellow line in **(A)**] evoked by the onset of the 488 nm line scan excitation light, at the beginning of the trace. The flickering light stimulus was not turned on. The small response decayed within 10 s. (Trace 2) The same conditions as trace 1, except that the flickering light stimulus (black bar at bottom) was turned on. (Trace 3) change in blood velocity within the same arteriole, measured in the rectangular region indicated in **(C)**. Changes in light-evoked arteriole diameter and blood velocity were similar.

vessel dilation averaged 8.87 ± 0.71% (S.E.M.; $n = 60$, six animals) of baseline diameter. Latency to the onset of dilation (time to 50% peak amplitude) was 1.51 ± 0.06 s ($n = 52$, six animals).

Changes in blood velocity were monitored simultaneously with vessel diameter using LSF. Hemodynamic responses were analyzed by calculating blood velocity images from raw speckle images using Eqs 1 and 2. Changes in blood velocity were visualized by calculating blood velocity ratio images. Averaged velocity images obtained during the transient phase of the light response (2–5 s following stimulus onset) were divided by the averaged images obtained prior to stimulation. Six to 15 ratio images from sequential trials were averaged together to improve signal to noise. In these averaged pseudocolor ratio images, increased blood velocity is indicated by yellows, reds and white. The velocity ratio image for the trial illustrated in **Figure 4C**, shows a prominent light-evoked increase in blood velocity in the primary arteriole adjacent to the stimulus as well as in a neighboring primary arteriole. Smaller velocity increases are seen in the primary venules. The time course of velocity within one of the arterioles (measured within the boxed area in **Figure 4C**) is illustrated in **Figure 4D**, trace 3. It has a similar time course to the dilation measured in the same vessel (**Figure 4D**, trace 2).

Line scan measurements of arteriole diameter were made using 488 nm light, which stimulates retinal photoreceptors as well as exciting the dye used to image vessels. Although the intensity of the 488 nm light was far dimmer (typically 400-fold) than the 559 nm light used to stimulate retinal photoreceptors, onset of the line scan light did, in many trials, evoke a vascular response. However, as shown in **Figure 4D**, both the increase in vessel diameter (trace 2) and the increase in blood velocity (trace 3) evoked by the onset of the line scan light were substantially smaller

than the responses evoked by the 559 nm flickering stimulus. In addition, the response to the onset of the line scan light decayed rapidly (**Figure 4D**, trace 1), well before the flickering stimulus was turned on. It should be noted that the 488 nm light was not turned on when only blood velocity, and not vessel diameter, was monitored (**Figure 5**).

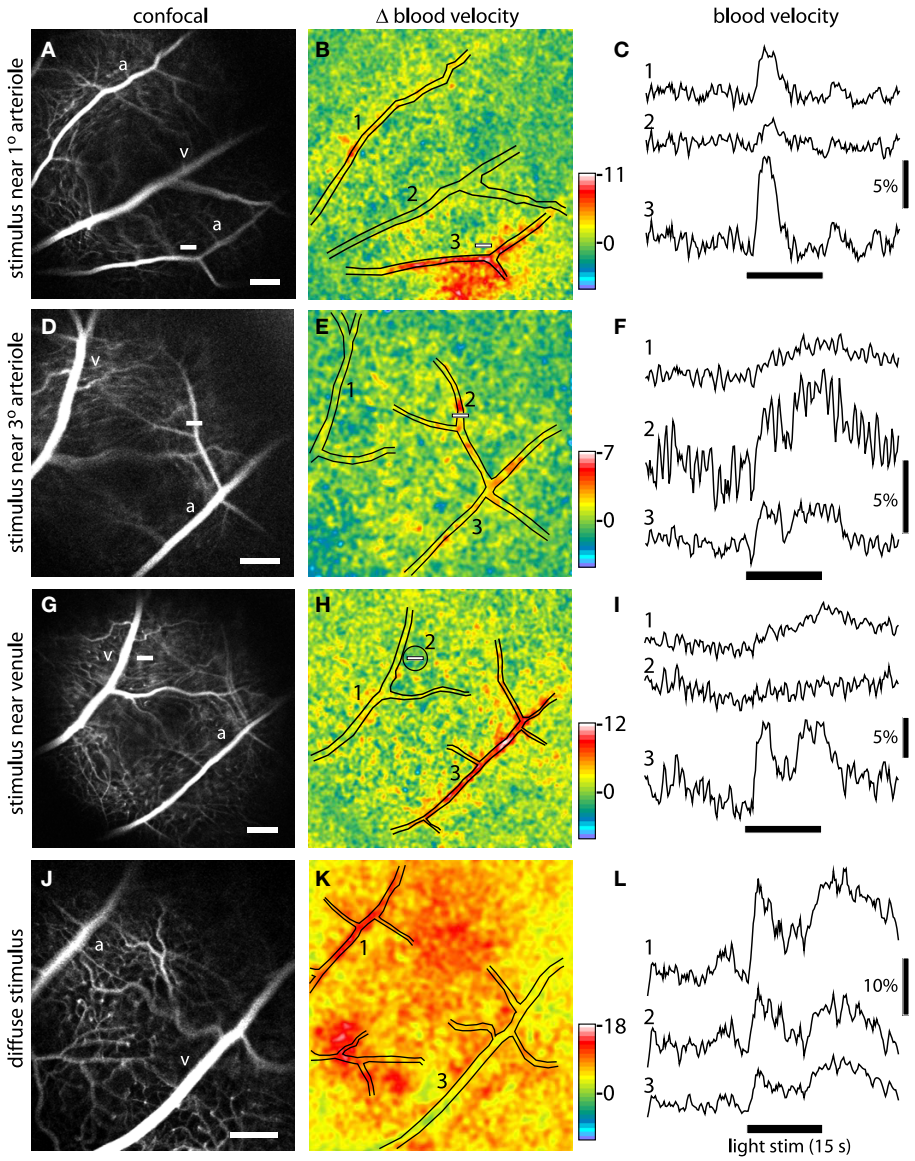

FIGURE 5 | Blood velocity increases evoked by focal and diffuse light stimulation. Each row in the figure represents a different stimulus condition. Top three rows, the retina was stimulated with a focal, 15 s flickering light. Bottom row, the retina was stimulated with a diffuse 15 s flickering light. The left panels of each row show confocal images of the retina. Scale bars (at the bottom right of each panel), 250 μm. The middle panels show blood velocity ratio images for the same retinal regions. The pseudocolor images show the change in blood velocity at 2–5 s after stimulus onset and the pseudocolor scale bars indicates Δ velocity in percent. The locations of the large vessels are indicated by black lines. The small white bars in the left and middle panels indicate the locations of the focal stimulus. The right panels show the time course of blood velocity changes evoked by the light stimulus (black bars below the traces) for selected retinal regions. The region where each measurement was made is indicated by the numbers in the middle panels. Except when otherwise noted, blood velocity was measured within arterioles or venules. **(A–C)** The retina was stimulated near a branch point of first and second order arterioles. Blood velocity was measured in a non-stimulated arteriole (1), a venule (2), and the stimulated arteriole (3). Increased blood velocity was greatest within and in the regions immediately surrounding the stimulated arteriole. **(D–F)** The stimulus was near a third order arteriole. Blood velocity was measured in a venule (1), the stimulated third order arteriole (2), and the upstream first order arteriole (3). Increased blood velocity was greatest within the stimulated third order arteriole. **(G–I)** The stimulus was in a capillary bed, near a first order venule. Blood velocity was measured in the stimulated venule (1), a 200 μm diameter region surrounding the stimulus (2), and a distant arteriole (3). Increased blood velocity was small in the stimulated region and nearby venule but much larger in the arteriole. **(J–L)** The retina was stimulated uniformly by a diffuse light. Blood velocity was measured in an arteriole (1), across the entire imaged region of the retina (2), and a venule (3). Increased blood velocity was greatest in the primary arterioles and in regions supplied by arteriole branches.

LIGHT-EVOKED CHANGES IN BLOOD FLOW

Increases in blood flow evoked by retinal stimulation have been characterized using a number of techniques (Riva et al., 2005). However, the spatial extent of these increases has not previously been determined. It is not known, for instance, whether a spatially restricted light stimulus will evoke a localized increase in blood flow or whether the increase will spread far beyond the illuminated region.

We have now characterized retinal blood flow responses to focal stimulation using a combination of LSF and confocal microscopy. We stimulated retinal photoreceptors with a 559 nm, 12 Hz flickering light generated by the confocal microscope. This stimulus illuminated a 135 × 20 μm region on the retinal surface (see Materials and Methods). Changes in blood velocity evoked by this stimulus were monitored with LSF using 808 nm illumination.

We found that the spatial pattern of blood velocity increase evoked by this focal stimulus varied depending on the location of the stimulus relative to retinal arterioles and venules. When the stimulus was near a primary arteriole, increased blood velocity was greatest in that arteriole and in the region immediately surrounding the vessel (**Figure 5B**). In many cases, other nearby primary arterioles also showed large velocity increases (**Figures 4C and 5B**). The time course and amplitude of the velocity increase was calculated for regions corresponding to the stimulated primary arteriole and nearby arterioles and venules. Light-evoked velocity increases in the arterioles and venules typically had similar time courses (**Figure 5C**), but the velocity increases in the arterioles were larger than were the increases in the venules (**Figure 6**). The peak velocity increase in the stimulated primary arteriole averaged 7.60 ± 0.83% (n = 10, seven animals) and had a latency of 1.49 ± 0.12 s (n = 9, six animals). The amplitude of the velocity increase in the adjacent primary venule was smaller, averaging 2.44 ± 0.48%, with a latency of 1.95 ± 0.22 s (n = 6, four animals).

When the focal stimulus was near a second or third order arteriole, increased blood velocity was seen within the stimulated vessel and in upstream arterioles serving the vessel (**Figure 5E**). The time course of the velocity increase was similar in the stimulated vessel and in upstream vessels. However, the observed temporal similarity of these responses may be due to the fact that our sampling rate (4 Hz) was not fast enough to detect small changes in response latency. It should also be borne in mind that when an increase in blood velocity is observed within a vessel, that increase could be due to active dilation of that vessel or to dilation of upstream arterioles, causing an increase in the pressure head to the vessel.

Blood velocity increases were somewhat smaller when the focal stimulus was distant from first, second, and third order arterioles (**Figures 5G and 6**). In these cases, the largest velocity increases were seen in primary arterioles, even though they were some distance from the stimulus (**Figures 5H,I**, trace 3). Responses were smaller in venules and in regions near the stimulus (**Figures 5H,I**, traces 1 and 2). Peak blood velocity increases in the primary arteriole nearest to the stimulus averaged 6.47 ± 0.85% (n = 10, seven animals) and had a latency of 1.42 ± 0.10 s (n = 10, seven animals). Responses in the nearest primary venule averaged 2.07 ± 0.54% (n = 10, seven animals) and had a latency of 1.58 ± 0.21 s (n = 8, six animals). Responses averaged 2.08 ± 0.59% (n = 10, seven animals) and had a latency of 1.22 ± 0.21 s (n = 5, five animals) in a region 200 μm in diameter centered on the stimulus. We also measured the amplitude of blood velocity increase in an annular region 200–400 μm from the stimulus to determine whether the local response was restricted to the area of stimulation. The velocity increase in this annular region was 2.25 ± 0.60% (n = 10, seven animals), not significantly different from the response in the 200 μm diameter region centered on the stimulus.

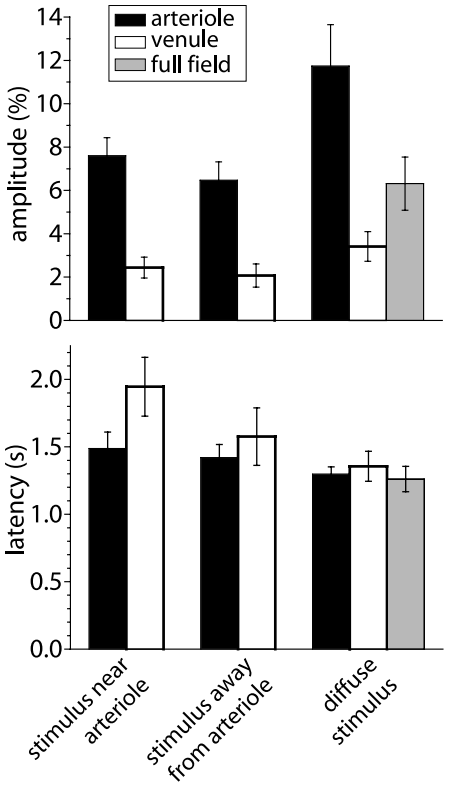

FIGURE 6 | Amplitude and latency of blood velocity increases measured with LSF. Shown are mean response amplitude (peak change in blood velocity) and latency (time to 50% peak amplitude) for responses evoked under three different stimulus conditions: a focal stimulus near a primary arteriole, a focal stimulus far from 1°, 2°, or 3° arterioles, and a diffuse stimulus. Blood velocity was measured within primary arterioles (back bars), within primary venules (open bars), and, for diffuse stimulation, over the entire visible retina (gray bars). Error bars, SEM.

Activation of a local region of the cerebral cortex sometimes evokes decreased blood flow in regions distant from the central region of increased blood flow (Harel et al., 2002; Devor et al., 2005). In our retinal experiments, we never observed a consistent decrease in blood velocity in response to focal light stimulation, regardless of the location of the stimulus. However, such a decrease could have occurred outside the field of view of our imaging system.

A diffuse flickering white light also evoked increased retinal blood velocity. As expected, blood velocity increases were more uniformly distributed across the retina (**Figure 5K**) than were increases evoked by focal stimulation. Velocity increases were larger in some retinal regions than others. These regions were generally associated with second and third order arterioles (**Figure 5K**). Velocity increases were greatest in primary arterioles (11.74 ± 1.91%;

latency; 1.30 ± 0.05 s, $n = 8$, five animals; **Figure 6**) as well as in regions near primary and secondary arterioles. Increases were substantially smaller in primary venules (3.41 ± 0.68%, $n = 8$, five animals; latency; 1.36 ± 0.11 s, $n = 6$, four animals). Blood velocity increases averaged over the entire viewable retina equaled 6.31 ± 1.23% ($n = 8$, five animals; latency; 1.26 ± 0.09 s, $n = 7$, five animals) (**Figure 5L**, trace 2).

DISCUSSION

We have described methods for combining LSF and laser scanning confocal microscopy to monitor blood flow in the retina. Using this combined imaging system, blood velocity changes were measured with LSF and arteriole diameter monitored with confocal line scans while retinal photoreceptors were stimulated by modulating the laser light from the secondary scanner of the confocal microscope. In contrast to other methods of measuring blood flow, LSF has the distinct advantage of permitting blood velocity to be monitored with high spatial and temporal resolution.

We illuminated the retina for LSF with 808 nm light delivered through an optical fiber pressed against the sclera. This method has several advantages. First, photoreceptors are largely insensitive to this infrared wavelength. Thus, retinal blood flow can be monitored without stimulating retinal neurons. Second, either the retinal vasculature or the choroidal circulation can be imaged with LSF, depending on the position of the illuminating optical fiber. Although LSF has previously been used to monitor choroidal blood flow in patients with polypoidal choroidal vasculopathy (Watanabe et al., 2008) and flow in the sub-foveal region of healthy subjects (Tamaki et al., 1997a), our work is, to our knowledge, the first to image blood flow in an extended network of choroidal vessels in the healthy eye. This technique may prove useful in future studies of the regulation of choroid blood flow under normal and pathological conditions.

Many previous studies have characterized retinal blood flow changes evoked by light stimulation (Riva et al., 2005). However, this is the first study to evaluate the spatial distribution of blood flow increases evoked by focal stimulation. We found that focal retinal stimulation evoked local increases in blood flow. This demonstrates that the retina has the ability to control blood flow at a local level. As in the brain, local control of blood flow in the retina allows needed oxygen and nutrients to be supplied to active neurons efficiently, without increasing the supply to inactive retinal regions.

Activity-dependent increases in blood flow in the brain were first described well over a century ago (Mosso, 1880; Roy and Sherrington, 1890). Yet, the identity of the vessels which mediate this functional hyperemia response remains in question. Earlier studies suggested that a large fraction of hemodynamic resistance in the brain lay within large cerebral arteries (Faraci and Heistad, 1990) or smaller, precapillary arterioles (Zweifach, 1974) and it was thought that dilation of these vessels was responsible for increased blood flow (Iadecola, 2004; Lipowsky, 2005). More recently, it has been suggested that capillaries may contribute to the regulation of blood flow in the brain. A theoretical study suggested that up to 70% of the total hemodynamic resistance in the brain vasculature lies in the capillary bed (Boas et al., 2008). In addition, pericytes, which control capillary diameter, have been shown to contract or relax in response to neurotransmitters and neuronal activity (Kawamura et al., 2003; Wu et al., 2003; Peppiatt et al., 2006).

The LSF results presented here bear on this issue and suggest that in the retina, activity-dependent blood flow changes are controlled largely by arterioles and that capillaries contribute little to the response. If capillary dilation contributed to functional hyperemia, focal stimulation of a region devoid of arterioles would result in increased blood flow to that region. However, we found the opposite to be true. When the retina was stimulated near a primary venule or in a region distant from arterioles, little increase in blood velocity was seen in the stimulated region. Rather, blood velocity increases were largest in the arterioles serving the stimulated region. In addition, blood velocity increases in the stimulated region of the retina were no larger than in an annulus surrounding this region. These results suggest that capillaries do not actively dilate in response to local neuronal activity and that more distant arterioles mediate the functional hyperemia response. The results must be interpreted with caution, however, as our LSF technique may not be sensitive enough to detect small changes in blood velocity in the capillary bed.

Previous studies have demonstrated that local arteriole dilations can be propagated upstream, leading to the dilation of larger arterioles and arteries feeding the stimulated vessels (Iadecola et al., 1997; Erinjeri and Woolsey, 2002). Our LSF results are consistent with this view. When a focal retinal stimulus was near a second or third order arteriole, increased retinal blood velocity was observed, not only near the stimulated arteriole, but also near the primary, upstream arteriole (**Figure 5E**).

We found that light-evoked velocity increases in primary venules were smaller than those observed in primary arterioles. This result appears at first to be paradoxical, as all blood flowing into the retina through primary arterioles must exit the retina through the venules. We attribute this discrepancy to the fact that primary venules in the retina are significantly larger in diameter than primary arterioles. Thus, for the same increase in total blood flux, velocity would increase to a smaller extent in venules than in arterioles. The differences in observed velocity increases are also attributable to the different time courses of the responses in arterioles and venules. Blood velocity amplitudes were measured during the initial, transient phase of the response (2–5 s after stimulus onset) while, in some cases, responses in venules were larger during the sustained portion of the response (**Figure 5I**, trace 1).

We believe that the combined use of LSF and confocal microscopy holds great promise for studying the regulation of blood flow, both in the normal retina and in the retina under pathological conditions. A few examples illustrate the potential of this preparation.

- Preliminary experiments from our laboratory demonstrate that retinal glial cells can be labeled with Ca^{2+} indicator dyes and filled with caged-Ca^{2+} compounds introduced into the vitreous humor through a hypodermic needle inserted through the sclera. Photolysis of caged-Ca^{2+} by short wavelength pulses delivered by a confocal microscope generate Ca^{2+} increases in the labeled glial cells. The role of glial cells in regulating retinal blood flow can be evaluated using this technique (Metea and Newman, 2006; Takano et al., 2006).

- Preliminary studies show that ischemia can be produced in a restricted region of the retina by photothrombosis generated by confocal illumination and bleaching of a photo-labile dye, such as rose bengal (Ding et al., 2009). The effect of the thrombolytic lesion on blood flow in the penumbra can then be studied with LSF.
- Preliminary experiments demonstrate that blood vessels and blood flow in the mouse retina can be imaged with the same LSF/confocal microscopy techniques we describe here for the rat.

The potential of this preparation for characterizing mechanisms mediating functional hyperemia in health and disease will be expanded tremendously with the use of transgenic mouse lines.

ACKNOWLEDGMENTS

We thank Anusha Mishra and Tess Kornfield for comments on the manuscript and Michael Burian for technical assistance. Supported by Fondation Leducq, NIH EY004077, and NIH TRINOD Training Grant.

REFERENCES

Ayata, C., Dunn, A. K., Gursoy-Ozdemir, Y., Huang, Z., Boas, D. A., and Moskowitz, M. A. (2004). Laser speckle flowmetry for the study of cerebrovascular physiology in normal and ischemic mouse cortex. *J. Cereb. Blood Flow Metab.* 24, 744–755.

Bhutto, I. A., and Amemiya, T. (2001). Microvascular architecture of the rat choroid: corrosion cast study. *Anat. Rec.* 264, 63–71.

Boas, D. A., Jones, S. R., Devor, A., Huppert, T. J., and Dale, A. M. (2008). A vascular anatomical network model of the spatio-temporal response to brain activation. *Neuroimage* 40, 1116–1129.

Bolay, H., Reuter, U., Dunn, A. K., Huang, Z., Boas, D. A., and Moskowitz, M. A. (2002). Intrinsic brain activity triggers trigeminal meningeal afferents in a migraine model. *Nat. Med.* 8, 136–142.

Briers, J. D., and Fercher, A. F. (1982). Retinal blood-flow visualization by means of laser speckle photography. *Invest. Ophthalmol. Vis. Sci.* 22, 255–259.

Cheng, H., and Duong, T. Q. (2007). Simplified laser-speckle-imaging analysis method and its application to retinal blood flow imaging. *Opt. Lett.* 32, 2188–2190.

Cheng, H., Yan, Y., and Duong, T. Q. (2008). Temporal statistical analysis of laser speckle images and its application to retinal blood-flow imaging. *Opt. Express* 16, 10214–10219.

Devor, A., Ulbert, I., Dunn, A. K., Narayanan, S. N., Jones, S. R., Andermann, M. L., Boas, D. A., and Dale, A. M. (2005). Coupling of the cortical hemodynamic response to cortical and thalamic neuronal activity. *Proc. Natl. Acad. Sci. U.S.A.* 102, 3822–3827.

Ding, S., Wang, T., Cui, W., and Haydon, P. G. (2009). Photothrombosis ischemia stimulates a sustained astrocytic Ca2+ signaling in vivo. *Glia* 57, 767–776.

Dunn, A. K., Bolay, H., Moskowitz, M. A., and Boas, D. A. (2001). Dynamic imaging of cerebral blood flow using laser speckle. *J. Cereb. Blood Flow Metab.* 21, 195–201.

Duong, T. Q., Ngan, S. C., Ugurbil, K., and Kim, S. G. (2002). Functional magnetic resonance imaging of the retina. *Invest. Ophthalmol. Vis. Sci.* 43, 1176–1181.

Durduran, T., Burnett, M. G., Yu, G., Zhou, C., Furuya, D., Yodh, A. G., Detre, J. A., and Greenberg, J. H. (2004). Spatiotemporal quantification of cerebral blood flow during functional activation in rat somatosensory cortex using laser-speckle flowmetry. *J. Cereb. Blood Flow Metab.* 24, 518–525.

Erinjeri, J. P., and Woolsey, T. A. (2002). Spatial integration of vascular changes with neural activity in mouse cortex. *J. Cereb. Blood Flow Metab.* 22, 353–360.

Faraci, F. M., and Heistad, D. D. (1990). Regulation of large cerebral arteries and cerebral microvascular pressure. *Circ. Res.* 66, 8–17.

Fercher, A. F., and Briers, J. D. (1981). Flow visualization by means of single-exposure speckle photography. *Opt. Commun.* 37, 326–330.

Harel, N., Lee, S. P., Nagaoka, T., Kim, D. S., and Kim, S. G. (2002). Origin of negative blood oxygenation level-dependent fMRI signals. *J. Cereb. Blood Flow Metab.* 22, 908–917.

Iadecola, C. (2004). Neurovascular regulation in the normal brain and in Alzheimer's disease. *Nat. Rev. Neurosci.* 5, 347–360.

Iadecola, C., and Nedergaard, M. (2007). Glial regulation of the cerebral microvasculature. *Nat. Neurosci.* 10, 1369–1376.

Iadecola, C., Yang, G., Ebner, T. J., and Chen, G. (1997). Local and propagated vascular responses evoked by focal synaptic activity in cerebellar cortex. *J. Neurophysiol.* 78, 651–659.

Ishii, K., and Araie, M. (2000). Effect of topical Latanoprost-timolol combined therapy on retinal blood flow and circulation of optic nerve head tissue in cynomolgus monkeys. *Jpn. J. Ophthalmol.* 44, 227–234.

Jacobs, G. H., Fenwick, J. A., and Williams, G. A. (2001). Cone-based vision of rats for ultraviolet and visible lights. *J. Exp. Biol.* 204, 2439–2446.

Kawamura, H., Sugiyama, T., Wu, D. M., Kobayashi, M., Yamanishi, S., Katsumura, K., and Puro, D. G. (2003). ATP: a vasoactive signal in the pericyte-containing microvasculature of the rat retina. *J. Physiol. (Lond.)* 551.3, 787–799.

Koseki, N., Araie, M., Tomidokoro, A., Nagahara, M., Hasegawa, T., Tamaki, Y., and Yamamoto, S. (2008). A placebo-controlled 3-year study of a calcium blocker on visual field and ocular circulation in glaucoma with low-normal pressure. *Ophthalmology* 115, 2049–2057.

Lipowsky, H. H. (2005). Microvascular rheology and hemodynamics. *Microcirculation* 12, 5–15.

Metea, M. R., and Newman, E. A. (2006). Glial cells dilate and constrict blood vessels: a mechanism of neurovascular coupling. *J. Neurosci.* 26, 2862–2870.

Mosso, A. (1880). Sulla circolazione del sangue nel cervello dell'uomo. *Mem. Real Acc. Lincei* 5, 237–358.

Peppiatt, C. M., Howarth, C., Mobbs, P., and Attwell, D. (2006). Bidirectional control of CNS capillary diameter by pericytes. *Nature* 443, 700–704.

Riva, C. E., Logean, E., and Falsini, B. (2005). Visually evoked hemodynamical response and assessment of neurovascular coupling in the optic nerve and retina. *Prog. Retin. Eye Res.* 24, 183–215.

Roy, C. S., and Sherrington, C. S. (1890). On the regulation of the blood-supply of the brain. *J. Physiol. (Lond.)* 11, 85–108.

Takano, T., Tian, G. F., Peng, W., Lou, N., Libionka, W., Han, X., and Nedergaard, M. (2006). Astrocyte-mediated control of cerebral blood flow. *Nat. Neurosci.* 9, 260–267.

Tamaki, Y., Araie, M., Kawamoto, E., Eguchi, S., and Fujii, H. (1994). Noncontact, two-dimensional measurement of retinal microcirculation using laser speckle phenomenon. *Invest. Ophthalmol. Vis. Sci.* 35, 3825–3834.

Tamaki, Y., Araie, M., Tomita, K., Nagahara, M., Tomidokoro, A., and Fujii, H. (1997a). Real-time measurement of human optic nerve head and choroid circulation, using the laser speckle phenomenon. *Jpn. J. Ophthalmol.* 41, 49–54.

Tamaki, Y., Araie, M., Tomita, K., and Tomidokoro, A. (1997b). Effect of topical timolol on tissue circulation in optic nerve head. *Jpn. J. Ophthalmol.* 41, 297–304.

Watanabe, G., Fujii, H., and Kishi, S. (2008). Imaging of choroidal hemodynamics in eyes with polypoidal choroidal vasculopathy using laser speckle phenomenon. *Jpn. J. Ophthalmol.* 52, 175–181.

Wu, D. M., Kawamura, H., Sakagami, K., Kobayashi, M., and Puro, D. G. (2003). Cholinergic regulation of pericyte-containing retinal microvessels. *Am. J. Physiol. Heart Circ. Physiol.* 284, H2083–H2090.

Yuan, S., Devor, A., Boas, D. A., and Dunn, A. K. (2005). Determination of optimal exposure time for imaging of blood flow changes with laser speckle contrast imaging. *Appl. Opt.* 44, 1823–1830.

Zweifach, B. W. (1974). Quantitative studies of microcirculatory structure and function. I. Analysis of pressure distribution in the terminal vascular bed in cat mesentery. *Circ. Res.* 34, 843–857.

Conflict of Interest Statement: The authors declare that the research was conducted in the absence of any commercial or financial relationships that could be construed as a potential conflict of interest.

Received: 03 March 2010; paper pending published: 01 April 2010; accepted: 06 August 2010; published online: 15 September 2010.

*Citation: Srienc AI, Kurth-Nelson ZL and Newman EA (2010) Imaging retinal blood flow with laser speckle flowmetry. Front. Neuroenerg. **2**:128. doi: 10.3389/fnene.2010.00128*